

A PIPELINE FOR CONSTRUCTING OPTIMIZED
N-BODY MODELS OF INTERACTING GALAXIES

by

Allen S. Harvey Jr.

A Dissertation

Submitted to the

Graduate Faculty

of

George Mason University

In Partial fulfillment of

The Requirements for the Degree

of

Doctor of Philosophy

Computational Sciences and Informatics

Committee:

_____ Dr. John Wallin, Dissertation Director

_____ Dr. Kirk Borne, Committee Chair

_____ Dr. Daniel Carr, Committee Member

_____ Dr. Rainald Löhner, Committee Member

_____ Dr. Chi Yang, Committee Member

_____ Dr. Maria Dworzecka, Director, School of
Physics, Astronomy, and Computational
Sciences

_____ Dr. Donna Fox, Associate Dean for Academic
and Student Affairs, College of Science

_____ Dr. Peggy Agouris, Dean, College of
Science

Date: _____ Spring Semester 2015
George Mason University
Fairfax, VA

A Pipeline for Constructing Optimized N-Body Models of Interacting Galaxies

A dissertation submitted in partial fulfillment of the requirements for the degree of
Doctor of Philosophy at George Mason University

By

Allen S. Harvey Jr.

Master of Science

George Mason University, 2007

Bachelor of Science

State University of New York, College at Brockport, 2003

Director: Dr. John Wallin, Professor

Middle Tennessee State University

Department of Physics and Astronomy

Department of Computer Science

Spring Semester 2015

George Mason University

Fairfax, VA

Copyright © 2015 by Allen S. Harvey Jr.
All Rights Reserved

Dedication

I owe my love of science to watching plenty of Star Trek when I was younger. One of the things that has always stuck with me was the purpose of life in its vision of the future: to better one's self and one's fellow man. My pursuit of education has enriched my life, and I hope that the work I have accomplished in this dissertation contributes to our understanding of the universe. It is with that hope that I dedicate this dissertation to my twin children, Alexander and Arianna, so that the future is a better place due in small part to my contribution to the world.

Acknowledgments

My advisor, John Wallin, has taught me so much during my time at George Mason University. It was an honor and a privilege to have him serve as my advisor for this effort. When he left George Mason University to grow another Computational Sciences department at another school, Middle Tennessee State University, he did not abandon me. Thanks to the video conferencing technologies of Microsoft's Skype and Google's Hangouts, we were able to keep in contact on a routine basis to work on problems and keep my focus where it needed to be. His commitment to me was unwavering, and for that I am extremely grateful. Similarly, I would like to extend my thanks to fellow George Mason University alumni, Anthony Holincheck, who's own dissertation is the backbone to mine. Without his research and accomplishments, none of mine would have been possible. I am fortunate to have had the opportunity to collaborate with both of you on this project.

My wife has been patient with me since I began my first semester at George Mason University nearly 11 years ago. During the time I earned my Masters of Science and continued into the doctoral program, she too completed her Masters of Education. I know the time has felt like forever to her, but I promise we are almost there. Her support at home, particularly providing more than her fair share of parenting of our infant twins born during this final stretch, has been enormous to me.

I would also like to thank my employer, Engility Corporation, for its financial assistance which allowed me to pursue my education at George Mason University, to include the research for this dissertation. While working at Engility, I have had the privilege to support the United States Department of Defense's Defense Threat Reduction Agency in computational matters pertaining to nuclear technology research and development. My government client Mark Sward permitted me to use computer hours of the Department of Defense's High Performance Computing Modernization Program's supercomputer systems. A special thanks goes to all those in support of those tremendous assets. These systems were invaluable to me in prototyping and developing the techniques and processes used throughout this dissertation while other computing resources were coming online at the Middle Tennessee State University.

Table of Contents

	Page
List of Tables	x
List of Figures	xiv
Abstract	xxvi
1 Introduction	1
1.1 A Brief History of the Study of Interacting Galaxies	3
1.2 Dynamics of Galaxies and Mergers	6
1.3 Computational Methods	9
1.4 An Existing Pipeline	12
1.5 A Pipeline Extension for Constructing Models of Interacting Galaxies	14
1.5.1 A Pipeline Alternative - Identikit	17
2 Modeling Galaxies	20
2.1 SPAM - A Restricted Three-Body Model	21
2.2 MASS99 - An N-Body Model	25
2.2.1 Enhancements to MASS99	26
2.3 GADGET-2 - An N-Body Model	28
2.4 AMR Models	29
2.5 N-Body Generators	30
2.5.1 MASS99	32
2.5.2 NEMO	33
2.5.3 Starscream	33
3 Restricted Three-Body to N-Body	35
3.1 Initial Conditions	35
3.1.1 Dynamical Friction	36
3.1.2 Tuning Dynamical Friction	39
3.2 A Progenitor Galaxy	43
3.3 Default N-Body Values	45
3.4 Early-time Galaxy Instability	46

4	Assembling the Pipeline	55
4.1	Determining the Quality of an N-Body Model	55
4.2	Finding Optimal N-Body Models	61
4.3	Simulation Size	63
4.4	MASS99 to GADGET-2 Comparisons	64
4.4.1	GADGET-2 Snapshot Toolbox	66
4.5	Pipeline Execution	67
4.5.1	N-Body Optimizer - optimizeDF.py	67
4.5.2	Creating N-Body Models - runController.pl	69
4.5.3	Finding Best Matches between Simulations - bestMatch.pl	70
4.5.4	Evaluating Morphology - morphologyChecker.py	70
4.6	Set of Interacting Galaxies	70
4.7	Computational Resources	72
4.7.1	Garnet	74
4.7.2	Diamond	75
4.7.3	Babbage	75
5	Simulation Results	77
5.1	Results for each Pair of Galaxies	77
5.1.1	SDSS 587722984435351614 (Arp 240)	78
5.1.2	SDSS 587724234257137777 (Arp 290)	87
5.1.3	SDSS 587726033843585146 (Arp 142)	93
5.1.4	SDSS 587727177926508595 (Arp 318)	99
5.1.5	SDSS 587727178988388373 (Arp 256)	105
5.1.6	SDSS 587727222471131318 (UGC 11751)	111
5.1.7	SDSS 587728676861051075 (Arp 104)	117
5.1.8	SDSS 587729227151704160	123
5.1.9	SDSS 587731913110650988 (Arp 285)	129
5.1.10	SDSS 587732136993882121 (Arp 214)	135
5.1.11	SDSS 587732772130652231 (NGC 4320)	141
5.1.12	SDSS 587733080814583863 (NGC 4669)	147
5.1.13	SDSS 587734862680752822 (Arp 255)	153
5.1.14	SDSS 587735043609329845 (Arp 82)	159
5.1.15	SDSS 587735665840881790 (Arp 239)	165

5.1.16	SDSS 587736523764334706 (Arp 274)	171
5.1.17	SDSS 587736941981466667 (Arp 199)	177
5.1.18	SDSS 587738569246376675 (Arp 57)	183
5.1.19	SDSS 587738569249390718	189
5.1.20	SDSS 587739153356095531 (Arp 247)	195
5.1.21	SDSS 587739407868690486 (Arp 241)	201
5.1.22	SDSS 587739505541578866 (Arp 313)	207
5.1.23	SDSS 587739646743412797 (Arp 107)	213
5.1.24	SDSS 587739647284805725 (Arp 294)	219
5.1.25	SDSS 587739707420967061 (Arp 172)	225
5.1.26	SDSS 587739720308818095 (Arp 218)	231
5.1.27	SDSS 587739721376202860 (Arp 302)	237
5.1.28	SDSS 587739721900163101 (Arp 242)	243
5.1.29	SDSS 587739810496708646 (Arp 72)	249
5.1.30	SDSS 587739845393580192 (Arp 101)	255
5.1.31	SDSS 587741391565422775 (Arp 58)	261
5.1.32	SDSS 587741532784361481 (Arp 105)	267
5.1.33	SDSS 587741534400217110 (Arp 97)	273
5.1.34	SDSS 587741602030026825 (Arp 305)	279
5.1.35	SDSS 587741722819493915 (Arp 106)	285
5.1.36	SDSS 587741817851674654 (NGC 2802/2803)	291
5.1.37	SDSS 587741829658181698 (Arp 301)	297
5.1.38	SDSS 587742010583941189 (Arp 89)	303
5.1.39	SDSS 587742014353702970 (Arp 87)	309
5.1.40	SDSS 587742571610243080 (Arp 191)	315
5.1.41	SDSS 587745402001817662 (Arp 237)	321
5.1.42	SDSS 587746029596311590 (Arp 181)	327
5.1.43	SDSS 587747120521216156 (Arp 146)	333
5.1.44	SDSS 588007005230530750 (Arp 143)	339
5.1.45	SDSS 588011124116422756 (Arp 238)	345
5.1.46	SDSS 588013383816904792	351
5.1.47	SDSS 588017604696408086 (Arp 297)	357

5.1.48	SDSS 588017604696408195 (NGC 5753/5755)	363
5.1.49	SDSS 588017702948962343 (Arp 173)	369
5.1.50	SDSS 588017978901528612 (Arp 84)	375
5.1.51	SDSS 588018055130710322 (UGC 10650)	381
5.1.52	SDSS 758874299603222717 (Arp 112)	387
5.1.53	SDSS 758877153600208945 (Arp 70)	393
5.1.54	SDSS 1237678620102623480	399
5.2	Pipeline Evaluation	405
6	Analysis and Discussion	408
6.1	Dynamical Friction	408
6.2	Orbital Elements and System Parameters	410
6.2.1	Indicators of N-Body Model Quality	411
6.2.2	Indicators of N-Body Modeling Difficulty	417
6.2.3	Other Elements and Parameters	421
6.3	Velocity Profiles	427
6.4	Including Gas Dynamics	428
6.5	Other Future Work	434
6.5.1	Optimizing Additional Model Parameters	434
6.5.2	Metrics for Optimization	435
6.5.3	Comparisons using Observational Data	436
6.5.4	Alternative Progenitor Galaxies	437
7	Conclusion	438
7.1	The Pipeline for Constructing Optimized N-Body Models	439
7.2	Enhancements to the Pipeline	440
7.2.1	Targeted Efforts for Future Work for the Entire Pipeline	441
A	A General Purpose Volume Renderer for Meshless Data	443
A.1	Abstract from Submitted Draft to Astronomy & Computing	443
A.2	Introduction	443
A.3	Motivation	444
A.3.1	Why VisIt?	446
A.4	Algorithm and Approach	448
A.5	Challenges	452
A.6	Summary	458

Bibliography	461
------------------------	-----

List of Tables

Table	Page
5.1 Summary for SDSS 587722984435351614	78
5.2 Orbital Elements & Dynamical Friction for SDSS 587722984435351614 . . .	83
5.3 Summary for SDSS 587724234257137777	87
5.4 Orbital Elements & Dynamical Friction for SDSS 587724234257137777 . . .	90
5.5 Summary for SDSS 587726033843585146	93
5.6 Orbital Elements & Dynamical Friction for SDSS 587726033843585146 . . .	96
5.7 Summary for SDSS 587727177926508595	99
5.8 Orbital Elements & Dynamical Friction for SDSS 587727177926508595 . . .	102
5.9 Summary for SDSS 587727178988388373	105
5.10 Orbital Elements & Dynamical Friction for SDSS 587727178988388373 . . .	108
5.11 Summary for SDSS 587727222471131318	111
5.12 Orbital Elements & Dynamical Friction for SDSS 587727222471131318 . . .	114
5.13 Summary for SDSS 587728676861051075	117
5.14 Orbital Elements & Dynamical Friction for SDSS 587728676861051075 . . .	120
5.15 Summary for SDSS 587729227151704160	123
5.16 Orbital Elements & Dynamical Friction for SDSS 587729227151704160 . . .	126
5.17 Summary for SDSS 587731913110650988	129
5.18 Orbital Elements & Dynamical Friction for SDSS 587731913110650988 . . .	132
5.19 Summary for SDSS 587732136993882121	135
5.20 Orbital Elements & Dynamical Friction for SDSS 587732136993882121 . . .	138
5.21 Summary for SDSS 587732772130652231	141
5.22 Orbital Elements & Dynamical Friction for SDSS 587732772130652231 . . .	144
5.23 Summary for SDSS 587733080814583863	147
5.24 Orbital Elements & Dynamical Friction for SDSS 587733080814583863 . . .	150
5.25 Summary for SDSS 587734862680752822	153

5.26	Orbital Elements & Dynamical Friction for SDSS 587734862680752822 . . .	156
5.27	Summary for SDSS 587735043609329845	159
5.28	Orbital Elements & Dynamical Friction for SDSS 587735043609329845 . . .	162
5.29	Summary for SDSS 587735665840881790	165
5.30	Orbital Elements & Dynamical Friction for SDSS 587735665840881790 . . .	168
5.31	Summary for SDSS 587736523764334706	171
5.32	Orbital Elements & Dynamical Friction for SDSS 587736523764334706 . . .	174
5.33	Summary for SDSS 587736941981466667	177
5.34	Orbital Elements & Dynamical Friction for SDSS 587736941981466667 . . .	180
5.35	Summary for SDSS 587738569246376675	183
5.36	Orbital Elements & Dynamical Friction for SDSS 587738569246376675 . . .	186
5.37	Summary for SDSS 587738569249390718	189
5.38	Orbital Elements & Dynamical Friction for SDSS 587738569249390718 . . .	192
5.39	Summary for SDSS 587739153356095531	195
5.40	Orbital Elements & Dynamical Friction for SDSS 587739153356095531 . . .	198
5.41	Summary for SDSS 587739407868690486	201
5.42	Orbital Elements & Dynamical Friction for SDSS 587739407868690486 . . .	204
5.43	Summary for SDSS 587739505541578866	207
5.44	Orbital Elements & Dynamical Friction for SDSS 587739505541578866 . . .	210
5.45	Summary for SDSS 587739646743412797	213
5.46	Orbital Elements & Dynamical Friction for SDSS 587739646743412797 . . .	216
5.47	Summary for SDSS 587739647284805725	219
5.48	Orbital Elements & Dynamical Friction for SDSS 587739647284805725 . . .	222
5.49	Summary for SDSS 587739707420967061	225
5.50	Orbital Elements & Dynamical Friction for SDSS 587739707420967061 . . .	228
5.51	Summary for SDSS 587739720308818095	231
5.52	Orbital Elements & Dynamical Friction for SDSS 587739720308818095 . . .	234
5.53	Summary for SDSS 587739721376202860	237
5.54	Orbital Elements & Dynamical Friction for SDSS 587739721376202860 . . .	240
5.55	Summary for SDSS 587739721900163101	243
5.56	Orbital Elements & Dynamical Friction for SDSS 587739721900163101 . . .	246
5.57	Summary for SDSS 587739810496708646	249

5.58	Orbital Elements & Dynamical Friction for SDSS 587739810496708646 . . .	252
5.59	Summary for SDSS 587739845393580192	255
5.60	Orbital Elements & Dynamical Friction for SDSS 587739845393580192 . . .	258
5.61	Summary for SDSS 587741391565422775	261
5.62	Orbital Elements & Dynamical Friction for SDSS 587741391565422775 . . .	264
5.63	Summary for SDSS 587741532784361481	267
5.64	Orbital Elements & Dynamical Friction for SDSS 587741532784361481 . . .	270
5.65	Summary for SDSS 587741534400217110	273
5.66	Orbital Elements & Dynamical Friction for SDSS 587741534400217110 . . .	276
5.67	Summary for SDSS 587741602030026825	279
5.68	Orbital Elements & Dynamical Friction for SDSS 587741602030026825 . . .	282
5.69	Summary for SDSS 587741722819493915	285
5.70	Orbital Elements & Dynamical Friction for SDSS 587741722819493915 . . .	288
5.71	Summary for SDSS 587741817851674654	291
5.72	Orbital Elements & Dynamical Friction for SDSS 587741817851674654 . . .	294
5.73	Summary for SDSS 587741829658181698	297
5.74	Orbital Elements & Dynamical Friction for SDSS 587741829658181698 . . .	300
5.75	Summary for SDSS 587742010583941189	303
5.76	Orbital Elements & Dynamical Friction for SDSS 587742010583941189 . . .	306
5.77	Summary for SDSS 587742014353702970	309
5.78	Orbital Elements & Dynamical Friction for SDSS 587742014353702970 . . .	312
5.79	Summary for SDSS 587742571610243080	315
5.80	Orbital Elements & Dynamical Friction for SDSS 587742571610243080 . . .	318
5.81	Summary for SDSS 587745402001817662	321
5.82	Orbital Elements & Dynamical Friction for SDSS 587745402001817662 . . .	324
5.83	Summary for SDSS 587746029596311590	327
5.84	Orbital Elements & Dynamical Friction for SDSS 587746029596311590 . . .	330
5.85	Summary for SDSS 587747120521216156	333
5.86	Orbital Elements & Dynamical Friction for SDSS 587747120521216156 . . .	336
5.87	Summary for SDSS 588007005230530750	339
5.88	Orbital Elements & Dynamical Friction for SDSS 588007005230530750 . . .	342
5.89	Summary for SDSS 588011124116422756	345

5.90	Orbital Elements & Dynamical Friction for SDSS 588011124116422756 . . .	348
5.91	Summary for SDSS 588013383816904792	351
5.92	Orbital Elements & Dynamical Friction for SDSS 588013383816904792 . . .	354
5.93	Summary for SDSS 588017604696408086	357
5.94	Orbital Elements & Dynamical Friction for SDSS 588017604696408086 . . .	360
5.95	Summary for SDSS 588017604696408195	363
5.96	Orbital Elements & Dynamical Friction for SDSS 588017604696408195 . . .	366
5.97	Summary for SDSS 588017702948962343	369
5.98	Orbital Elements & Dynamical Friction for SDSS 588017702948962343 . . .	372
5.99	Summary for SDSS 588017978901528612	375
5.100	Orbital Elements & Dynamical Friction for SDSS 588017978901528612 . . .	378
5.101	Summary for SDSS 588018055130710322	381
5.102	Orbital Elements & Dynamical Friction for SDSS 588018055130710322 . . .	384
5.103	Summary for SDSS 758874299603222717	387
5.104	Orbital Elements & Dynamical Friction for SDSS 758874299603222717 . . .	390
5.105	Summary for SDSS 758877153600208945	393
5.106	Orbital Elements & Dynamical Friction for SDSS 758877153600208945 . . .	396
5.107	Summary for SDSS 1237678620102623480	399
5.108	Orbital Elements & Dynamical Friction for SDSS 1237678620102623480 . .	402

List of Figures

Figure	Page
1.1 Galaxy Classification	4
1.2 Feedback Mechanisms	7
1.3 A Pipeline for Constructing Multi-Method Models of Interacting Galaxies .	13
1.4 A Pipeline for Constructing Optimized N-Body Models of Interacting Galaxies	15
2.1 Parallel Profiling of MASS99	27
3.1 Dynamical friction between one large body and N smaller bodies	37
3.2 Dynamical Friction Between Two N-Bodies	38
3.3 Trajectories from Varying Dynamical Friction	41
3.4 Final Configurations of Massless Particles from Restricted Three-Body Simulation	42
3.5 Evolution of a Unit Progenitor Galaxy	44
3.6 Ring in the Disc	47
3.7 Energy vs Time of Unit Galaxy	48
3.8 Initial Distribution of Disc Particles by NEMO	51
3.9 Energy vs Time of a MASS99 and NEMO Galaxy Model	52
3.10 Scatter Plots of Radial Velocity vs Radius	53
4.1 Grids over SPAM Models	57
4.2 Grids over N-Body Models	58
4.3 N-Body Trajectories with Varying Simulation Size	64
4.4 Comparison between MASS99 and GADGET-2	65
4.5 N-Body Model Optimization Process	68
4.6 54 Galaxies for the Pipeline	71
5.1 Images for SDSS 587722984435351614	80
5.2 Simulation XZ Projections for SDSS 587722984435351614	81
5.3 Simulation YZ Projections for SDSS 587722984435351614	81

5.4	Line of Sight Velocity Plots for SDSS 587722984435351614	82
5.5	Trajectory Plots for SDSS 587722984435351614	85
5.6	Metrics for Best N-Body Simulation of SDSS 587722984435351614	86
5.7	Images for SDSS 587724234257137777	88
5.8	Simulation XZ Projections for SDSS 587724234257137777	89
5.9	Simulation YZ Projections for SDSS 587724234257137777	89
5.10	Line of Sight Velocity Plots for SDSS 587724234257137777	90
5.11	Trajectory Plots for SDSS 587724234257137777	91
5.12	Metrics for Best N-Body Simulation of SDSS 587724234257137777	92
5.13	Images for SDSS 587726033843585146	94
5.14	Simulation XZ Projections for SDSS 587726033843585146	95
5.15	Simulation YZ Projections for SDSS 587726033843585146	95
5.16	Line of Sight Velocity Plots for SDSS 587726033843585146	96
5.17	Trajectory Plots for SDSS 587726033843585146	97
5.18	Metrics for Best N-Body Simulation of SDSS 587726033843585146	98
5.19	Images for SDSS 587727177926508595	100
5.20	Simulation XZ Projections for SDSS 587727177926508595	101
5.21	Simulation YZ Projections for SDSS 587727177926508595	101
5.22	Line of Sight Velocity Plots for SDSS 587727177926508595	102
5.23	Trajectory Plots for SDSS 587727177926508595	103
5.24	Metrics for Best N-Body Simulation of SDSS 587727177926508595	104
5.25	Images for SDSS 587727178988388373	106
5.26	Simulation XZ Projections for SDSS 587727178988388373	107
5.27	Simulation YZ Projections for SDSS 587727178988388373	107
5.28	Line of Sight Velocity Plots for SDSS 587727178988388373	108
5.29	Trajectory Plots for SDSS 587727178988388373	109
5.30	Metrics for Best N-Body Simulation of SDSS 587727178988388373	110
5.31	Images for SDSS 587727222471131318	112
5.32	Simulation XZ Projections for SDSS 587727222471131318	113
5.33	Simulation YZ Projections for SDSS 587727222471131318	113
5.34	Line of Sight Velocity Plots for SDSS 587727222471131318	114
5.35	Trajectory Plots for SDSS 587727222471131318	115

5.36	Metrics for Best N-Body Simulation of SDSS 587727222471131318	116
5.37	Images for SDSS 587728676861051075	118
5.38	Simulation XZ Projections for SDSS 587728676861051075	119
5.39	Simulation YZ Projections for SDSS 587728676861051075	119
5.40	Line of Sight Velocity Plots for SDSS 587728676861051075	120
5.41	Trajectory Plots for SDSS 587728676861051075	121
5.42	Metrics for Best N-Body Simulation of SDSS 587728676861051075	122
5.43	Images for SDSS 587729227151704160	124
5.44	Simulation XZ Projections for SDSS 587729227151704160	125
5.45	Simulation YZ Projections for SDSS 587729227151704160	125
5.46	Line of Sight Velocity Plots for SDSS 587729227151704160	126
5.47	Trajectory Plots for SDSS 587729227151704160	127
5.48	Metrics for Best N-Body Simulation of SDSS 587729227151704160	128
5.49	Images for SDSS 587731913110650988	130
5.50	Simulation XZ Projections for SDSS 587731913110650988	131
5.51	Simulation YZ Projections for SDSS 587731913110650988	131
5.52	Line of Sight Velocity Plots for SDSS 587731913110650988	132
5.53	Trajectory Plots for SDSS 587731913110650988	133
5.54	Metrics for Best N-Body Simulation of SDSS 587731913110650988	134
5.55	Images for SDSS 587732136993882121	136
5.56	Simulation XZ Projections for SDSS 587732136993882121	137
5.57	Simulation YZ Projections for SDSS 587732136993882121	137
5.58	Line of Sight Velocity Plots for SDSS 587732136993882121	138
5.59	Trajectory Plots for SDSS 587732136993882121	139
5.60	Metrics for Best N-Body Simulation of SDSS 587732136993882121	140
5.61	Images for SDSS 587732772130652231	142
5.62	Simulation XZ Projections for SDSS 587732772130652231	143
5.63	Simulation YZ Projections for SDSS 587732772130652231	143
5.64	Line of Sight Velocity Plots for SDSS 587732772130652231	144
5.65	Trajectory Plots for SDSS 587732772130652231	145
5.66	Metrics for Best N-Body Simulation of SDSS 587732772130652231	146
5.67	Images for SDSS 587733080814583863	148

5.68	Simulation XZ Projections for SDSS 587733080814583863	149
5.69	Simulation YZ Projections for SDSS 587733080814583863	149
5.70	Line of Sight Velocity Plots for SDSS 587733080814583863	150
5.71	Trajectory Plots for SDSS 587733080814583863	151
5.72	Metrics for Best N-Body Simulation of SDSS 587733080814583863	152
5.73	Images for SDSS 587734862680752822	154
5.74	Simulation XZ Projections for SDSS 587734862680752822	155
5.75	Simulation YZ Projections for SDSS 587734862680752822	155
5.76	Line of Sight Velocity Plots for SDSS 587734862680752822	156
5.77	Trajectory Plots for SDSS 587734862680752822	157
5.78	Metrics for Best N-Body Simulation of SDSS 587734862680752822	158
5.79	Images for SDSS 587735043609329845	160
5.80	Simulation XZ Projections for SDSS 587735043609329845	161
5.81	Simulation YZ Projections for SDSS 587735043609329845	161
5.82	Line of Sight Velocity Plots for SDSS 587735043609329845	162
5.83	Trajectory Plots for SDSS 587735043609329845	163
5.84	Metrics for Best N-Body Simulation of SDSS 587735043609329845	164
5.85	Images for SDSS 587735665840881790	166
5.86	Simulation XZ Projections for SDSS 587735665840881790	167
5.87	Simulation YZ Projections for SDSS 587735665840881790	167
5.88	Line of Sight Velocity Plots for SDSS 587735665840881790	168
5.89	Trajectory Plots for SDSS 587735665840881790	169
5.90	Metrics for Best N-Body Simulation of SDSS 587735665840881790	170
5.91	Images for SDSS 587736523764334706	172
5.92	Simulation XZ Projections for SDSS 587736523764334706	173
5.93	Simulation YZ Projections for SDSS 587736523764334706	173
5.94	Line of Sight Velocity Plots for SDSS 587736523764334706	174
5.95	Trajectory Plots for SDSS 587736523764334706	175
5.96	Metrics for Best N-Body Simulation of SDSS 587736523764334706	176
5.97	Images for SDSS 587736941981466667	178
5.98	Simulation XZ Projections for SDSS 587736941981466667	179
5.99	Simulation YZ Projections for SDSS 587736941981466667	179

5.100	Line of Sight Velocity Plots for SDSS 587736941981466667	180
5.101	Trajectory Plots for SDSS 587736941981466667	181
5.102	Metrics for Best N-Body Simulation of SDSS 587736941981466667	182
5.103	Images for SDSS 587738569246376675	184
5.104	Simulation XZ Projections for SDSS 587738569246376675	185
5.105	Simulation YZ Projections for SDSS 587738569246376675	185
5.106	Line of Sight Velocity Plots for SDSS 587738569246376675	186
5.107	Trajectory Plots for SDSS 587738569246376675	187
5.108	Metrics for Best N-Body Simulation of SDSS 587738569246376675	188
5.109	Images for SDSS 587738569249390718	190
5.110	Simulation XZ Projections for SDSS 587738569249390718	191
5.111	Simulation YZ Projections for SDSS 587738569249390718	191
5.112	Line of Sight Velocity Plots for SDSS 587738569249390718	192
5.113	Trajectory Plots for SDSS 587738569249390718	193
5.114	Metrics for Best N-Body Simulation of SDSS 587738569249390718	194
5.115	Images for SDSS 587739153356095531	196
5.116	Simulation XZ Projections for SDSS 587739153356095531	197
5.117	Simulation YZ Projections for SDSS 587739153356095531	197
5.118	Line of Sight Velocity Plots for SDSS 587739153356095531	198
5.119	Trajectory Plots for SDSS 587739153356095531	199
5.120	Metrics for Best N-Body Simulation of SDSS 587739153356095531	200
5.121	Images for SDSS 587739407868690486	202
5.122	Simulation XZ Projections for SDSS 587739407868690486	203
5.123	Simulation YZ Projections for SDSS 587739407868690486	203
5.124	Line of Sight Velocity Plots for SDSS 587739407868690486	204
5.125	Trajectory Plots for SDSS 587739407868690486	205
5.126	Metrics for Best N-Body Simulation of SDSS 587739407868690486	206
5.127	Images for SDSS 587739505541578866	208
5.128	Simulation XZ Projections for SDSS 587739505541578866	209
5.129	Simulation YZ Projections for SDSS 587739505541578866	209
5.130	Line of Sight Velocity Plots for SDSS 587739505541578866	210
5.131	Trajectory Plots for SDSS 587739505541578866	211

5.132	Metrics for Best N-Body Simulation of SDSS 587739505541578866	212
5.133	Images for SDSS 587739646743412797	214
5.134	Simulation XZ Projections for SDSS 587739646743412797	215
5.135	Simulation YZ Projections for SDSS 587739646743412797	215
5.136	Line of Sight Velocity Plots for SDSS 587739646743412797	216
5.137	Trajectory Plots for SDSS 587739646743412797	217
5.138	Metrics for Best N-Body Simulation of SDSS 587739646743412797	218
5.139	Images for SDSS 587739647284805725	220
5.140	Simulation XZ Projections for SDSS 587739647284805725	221
5.141	Simulation YZ Projections for SDSS 587739647284805725	221
5.142	Line of Sight Velocity Plots for SDSS 587739647284805725	222
5.143	Trajectory Plots for SDSS 587739647284805725	223
5.144	Metrics for Best N-Body Simulation of SDSS 587739647284805725	224
5.145	Images for SDSS 587739707420967061	226
5.146	Simulation XZ Projections for SDSS 587739707420967061	227
5.147	Simulation YZ Projections for SDSS 587739707420967061	227
5.148	Line of Sight Velocity Plots for SDSS 587739707420967061	228
5.149	Trajectory Plots for SDSS 587739707420967061	229
5.150	Metrics for Best N-Body Simulation of SDSS 587739707420967061	230
5.151	Images for SDSS 587739720308818095	232
5.152	Simulation XZ Projections for SDSS 587739720308818095	233
5.153	Simulation YZ Projections for SDSS 587739720308818095	233
5.154	Line of Sight Velocity Plots for SDSS 587739720308818095	234
5.155	Trajectory Plots for SDSS 587739720308818095	235
5.156	Metrics for Best N-Body Simulation of SDSS 587739720308818095	236
5.157	Images for SDSS 587739721376202860	238
5.158	Simulation XZ Projections for SDSS 587739721376202860	239
5.159	Simulation YZ Projections for SDSS 587739721376202860	239
5.160	Line of Sight Velocity Plots for SDSS 587739721376202860	240
5.161	Trajectory Plots for SDSS 587739721376202860	241
5.162	Metrics for Best N-Body Simulation of SDSS 587739721376202860	242
5.163	Images for SDSS 587739721900163101	244

5.164	Simulation XZ Projections for SDSS 587739721900163101	245
5.165	Simulation YZ Projections for SDSS 587739721900163101	245
5.166	Line of Sight Velocity Plots for SDSS 587739721900163101	246
5.167	Trajectory Plots for SDSS 587739721900163101	247
5.168	Metrics for Best N-Body Simulation of SDSS 587739721900163101	248
5.169	Images for SDSS 587739810496708646	250
5.170	Simulation XZ Projections for SDSS 587739810496708646	251
5.171	Simulation YZ Projections for SDSS 587739810496708646	251
5.172	Line of Sight Velocity Plots for SDSS 587739810496708646	252
5.173	Trajectory Plots for SDSS 587739810496708646	253
5.174	Metrics for Best N-Body Simulation of SDSS 587739810496708646	254
5.175	Images for SDSS 587739845393580192	256
5.176	Simulation XZ Projections for SDSS 587739845393580192	257
5.177	Simulation YZ Projections for SDSS 587739845393580192	257
5.178	Line of Sight Velocity Plots for SDSS 587739845393580192	258
5.179	Trajectory Plots for SDSS 587739845393580192	259
5.180	Metrics for Best N-Body Simulation of SDSS 587739845393580192	260
5.181	Images for SDSS 587741391565422775	262
5.182	Simulation XZ Projections for SDSS 587741391565422775	263
5.183	Simulation YZ Projections for SDSS 587741391565422775	263
5.184	Line of Sight Velocity Plots for SDSS 587741391565422775	264
5.185	Trajectory Plots for SDSS 587741391565422775	265
5.186	Metrics for Best N-Body Simulation of SDSS 587741391565422775	266
5.187	Images for SDSS 587741532784361481	268
5.188	Simulation XZ Projections for SDSS 587741532784361481	269
5.189	Simulation YZ Projections for SDSS 587741532784361481	269
5.190	Line of Sight Velocity Plots for SDSS 587741532784361481	270
5.191	Trajectory Plots for SDSS 587741532784361481	271
5.192	Metrics for Best N-Body Simulation of SDSS 587741532784361481	272
5.193	Images for SDSS 587741534400217110	274
5.194	Simulation XZ Projections for SDSS 587741534400217110	275
5.195	Simulation YZ Projections for SDSS 587741534400217110	275

5.196	Line of Sight Velocity Plots for SDSS 587741534400217110	276
5.197	Trajectory Plots for SDSS 587741534400217110	277
5.198	Metrics for Best N-Body Simulation of SDSS 587741534400217110	278
5.199	Images for SDSS 587741602030026825	280
5.200	Simulation XZ Projections for SDSS 587741602030026825	281
5.201	Simulation YZ Projections for SDSS 587741602030026825	281
5.202	Line of Sight Velocity Plots for SDSS 587741602030026825	282
5.203	Trajectory Plots for SDSS 587741602030026825	283
5.204	Metrics for Best N-Body Simulation of SDSS 587741602030026825	284
5.205	Images for SDSS 587741722819493915	286
5.206	Simulation XZ Projections for SDSS 587741722819493915	287
5.207	Simulation YZ Projections for SDSS 587741722819493915	287
5.208	Line of Sight Velocity Plots for SDSS 587741722819493915	288
5.209	Trajectory Plots for SDSS 587741722819493915	289
5.210	Metrics for Best N-Body Simulation of SDSS 587741722819493915	290
5.211	Images for SDSS 587741817851674654	292
5.212	Simulation XZ Projections for SDSS 587741817851674654	293
5.213	Simulation YZ Projections for SDSS 587741817851674654	293
5.214	Line of Sight Velocity Plots for SDSS 587741817851674654	294
5.215	Trajectory Plots for SDSS 587741817851674654	295
5.216	Metrics for Best N-Body Simulation of SDSS 587741817851674654	296
5.217	Images for SDSS 587741829658181698	298
5.218	Simulation XZ Projections for SDSS 587741829658181698	299
5.219	Simulation YZ Projections for SDSS 587741829658181698	299
5.220	Line of Sight Velocity Plots for SDSS 587741829658181698	300
5.221	Trajectory Plots for SDSS 587741829658181698	301
5.222	Metrics for Best N-Body Simulation of SDSS 587741829658181698	302
5.223	Images for SDSS 587742010583941189	304
5.224	Simulation XZ Projections for SDSS 587742010583941189	305
5.225	Simulation YZ Projections for SDSS 587742010583941189	305
5.226	Line of Sight Velocity Plots for SDSS 587742010583941189	306
5.227	Trajectory Plots for SDSS 587742010583941189	307

5.228	Metrics for Best N-Body Simulation of SDSS 587742010583941189	308
5.229	Images for SDSS 587742014353702970	310
5.230	Simulation XZ Projections for SDSS 587742014353702970	311
5.231	Simulation YZ Projections for SDSS 587742014353702970	311
5.232	Line of Sight Velocity Plots for SDSS 587742014353702970	312
5.233	Trajectory Plots for SDSS 587742014353702970	313
5.234	Metrics for Best N-Body Simulation of SDSS 587742014353702970	314
5.235	Images for SDSS 587742571610243080	316
5.236	Simulation XZ Projections for SDSS 587742571610243080	317
5.237	Simulation YZ Projections for SDSS 587742571610243080	317
5.238	Line of Sight Velocity Plots for SDSS 587742571610243080	318
5.239	Trajectory Plots for SDSS 587742571610243080	319
5.240	Metrics for Best N-Body Simulation of SDSS 587742571610243080	320
5.241	Images for SDSS 587745402001817662	322
5.242	Simulation XZ Projections for SDSS 587745402001817662	323
5.243	Simulation YZ Projections for SDSS 587745402001817662	323
5.244	Line of Sight Velocity Plots for SDSS 587745402001817662	324
5.245	Trajectory Plots for SDSS 587745402001817662	325
5.246	Metrics for Best N-Body Simulation of SDSS 587745402001817662	326
5.247	Images for SDSS 587746029596311590	328
5.248	Simulation XZ Projections for SDSS 587746029596311590	329
5.249	Simulation YZ Projections for SDSS 587746029596311590	329
5.250	Line of Sight Velocity Plots for SDSS 587746029596311590	330
5.251	Trajectory Plots for SDSS 587746029596311590	331
5.252	Metrics for Best N-Body Simulation of SDSS 587746029596311590	332
5.253	Images for SDSS 587747120521216156	334
5.254	Simulation XZ Projections for SDSS 587747120521216156	335
5.255	Simulation YZ Projections for SDSS 587747120521216156	335
5.256	Line of Sight Velocity Plots for SDSS 587747120521216156	336
5.257	Trajectory Plots for SDSS 587747120521216156	337
5.258	Metrics for Best N-Body Simulation of SDSS 587747120521216156	338
5.259	Images for SDSS 588007005230530750	340

5.260	Simulation XZ Projections for SDSS 588007005230530750	341
5.261	Simulation YZ Projections for SDSS 588007005230530750	341
5.262	Line of Sight Velocity Plots for SDSS 588007005230530750	342
5.263	Trajectory Plots for SDSS 588007005230530750	343
5.264	Metrics for Best N-Body Simulation of SDSS 588007005230530750	344
5.265	Images for SDSS 588011124116422756	346
5.266	Simulation XZ Projections for SDSS 588011124116422756	347
5.267	Simulation YZ Projections for SDSS 588011124116422756	347
5.268	Line of Sight Velocity Plots for SDSS 588011124116422756	348
5.269	Trajectory Plots for SDSS 588011124116422756	349
5.270	Metrics for Best N-Body Simulation of SDSS 588011124116422756	350
5.271	Images for SDSS 588013383816904792	352
5.272	Simulation XZ Projections for SDSS 588013383816904792	353
5.273	Simulation YZ Projections for SDSS 588013383816904792	353
5.274	Line of Sight Velocity Plots for SDSS 588013383816904792	354
5.275	Trajectory Plots for SDSS 588013383816904792	355
5.276	Metrics for Best N-Body Simulation of SDSS 588013383816904792	356
5.277	Images for SDSS 588017604696408086	358
5.278	Simulation XZ Projections for SDSS 588017604696408086	359
5.279	Simulation YZ Projections for SDSS 588017604696408086	359
5.280	Line of Sight Velocity Plots for SDSS 588017604696408086	360
5.281	Trajectory Plots for SDSS 588017604696408086	361
5.282	Metrics for Best N-Body Simulation of SDSS 588017604696408086	362
5.283	Images for SDSS 588017604696408195	364
5.284	Simulation XZ Projections for SDSS 588017604696408195	365
5.285	Simulation YZ Projections for SDSS 588017604696408195	365
5.286	Line of Sight Velocity Plots for SDSS 588017604696408195	366
5.287	Trajectory Plots for SDSS 588017604696408195	367
5.288	Metrics for Best N-Body Simulation of SDSS 588017604696408195	368
5.289	Images for SDSS 588017702948962343	370
5.290	Simulation XZ Projections for SDSS 588017702948962343	371
5.291	Simulation YZ Projections for SDSS 588017702948962343	371

5.292	Line of Sight Velocity Plots for SDSS 588017702948962343	372
5.293	Trajectory Plots for SDSS 588017702948962343	373
5.294	Metrics for Best N-Body Simulation of SDSS 588017702948962343	374
5.295	Images for SDSS 588017978901528612	376
5.296	Simulation XZ Projections for SDSS 588017978901528612	377
5.297	Simulation YZ Projections for SDSS 588017978901528612	377
5.298	Line of Sight Velocity Plots for SDSS 588017978901528612	378
5.299	Trajectory Plots for SDSS 588017978901528612	379
5.300	Metrics for Best N-Body Simulation of SDSS 588017978901528612	380
5.301	Images for SDSS 588018055130710322	382
5.302	Simulation XZ Projections for SDSS 588018055130710322	383
5.303	Simulation YZ Projections for SDSS 588018055130710322	383
5.304	Line of Sight Velocity Plots for SDSS 588018055130710322	384
5.305	Trajectory Plots for SDSS 588018055130710322	385
5.306	Metrics for Best N-Body Simulation of SDSS 588018055130710322	386
5.307	Images for SDSS 758874299603222717	388
5.308	Simulation XZ Projections for SDSS 758874299603222717	389
5.309	Simulation YZ Projections for SDSS 758874299603222717	389
5.310	Line of Sight Velocity Plots for SDSS 758874299603222717	390
5.311	Trajectory Plots for SDSS 758874299603222717	391
5.312	Metrics for Best N-Body Simulation of SDSS 758874299603222717	392
5.313	Images for SDSS 758877153600208945	394
5.314	Simulation XZ Projections for SDSS 758877153600208945	395
5.315	Simulation YZ Projections for SDSS 758877153600208945	395
5.316	Line of Sight Velocity Plots for SDSS 758877153600208945	396
5.317	Trajectory Plots for SDSS 758877153600208945	397
5.318	Metrics for Best N-Body Simulation of SDSS 758877153600208945	398
5.319	Images for SDSS 1237678620102623480	400
5.320	Simulation XZ Projections for SDSS 1237678620102623480	401
5.321	Simulation YZ Projections for SDSS 1237678620102623480	401
5.322	Line of Sight Velocity Plots for SDSS 1237678620102623480	402
5.323	Trajectory Plots for SDSS 1237678620102623480	403

5.324	Metrics for Best N-Body Simulation of SDSS 1237678620102623480	404
5.325	Qualitative Assessment of the N-Body Pipeline	406
6.1	Pie Chart of Pipeline Performance	409
6.2	Distributions of Dynamical Friction	411
6.3	Scatterplot of Inclinations	413
6.4	Scatterplot of the Longitude of the Ascending Node	414
6.5	Scatterplot of Inclinations	415
6.6	Scatterplot of Specific Orbital Energy	416
6.7	Boxplots of the Change in Specific Orbital Energy	417
6.8	Scatterplot of Distances of Closes Approach	418
6.9	Boxplots of Distances of Closes Approach	419
6.10	Model Quality as a Function of Reduced Mass	420
6.11	Scatterplot of Eccentricity	422
6.12	Scatterplot of Argument of Perapsis	423
6.13	Change in Argument of Perapsis	424
6.14	Scatterplot of Semi-Major Axes	425
6.15	Stacked Bar Chart of Orbits as Determined by the N-Body Model	426
6.16	Rotated Line of Sght Velocity of Arp 241	428
6.17	Morphology Change Due to Gas Dynamics	430
6.18	Trajectory Plots for Arp 82 with Gas	432
6.19	Metric Changes Due to Gas Dynamics	433
6.20	Systems with Different Galaxy Types	437
A.1	Simple N-Body Visualization	445
A.2	Visualization of a Cell-Centered Dataset	449
A.3	Visualization of a Node-Centered Dataset	450
A.4	Meshless Visualization With Varying Glyph Sizes	451
A.5	Splatting Particles with Gradients	452
A.6	Volume Rendered Visualization of a Meshless Dataset	453
A.7	Volume Rendered Images of Interacting Galxies	457
A.8	Visualization Controls in VisIt	458
A.9	Meshless Volume Rendering Using the Alpha Channel	459

Abstract

A PIPELINE FOR CONSTRUCTING OPTIMIZED N-BODY MODELS OF INTERACTING GALAXIES

Allen S. Harvey Jr., PhD

George Mason University, 2015

Dissertation Director: Dr. John Wallin

Galaxies form the building blocks of our understanding of a hierarchical evolution of the universe. Galaxies interact with other galaxies by impacting each other's gravitational fields, exchanging mass, spurring star formation, and even by merging. As sky surveys continue to capture images of interacting galaxies as they were in a snapshot of time so long ago, simulations of their evolution are needed to understand how they have arrived at their observed state. Restricted three-body simulations have advanced to produce realistic gravitational potentials to rapidly model interacting galaxies. Much research has been conducted to advance the creation and convergence of these models to obtain good matches to observed galaxies. Unfortunately, these models lack the physics for rich and realistic tidal features, gas dynamics, stellar black holes, and star formation, among others, that necessitate the use of higher fidelity models, such as N-Body gravity methods. The parameters describing the interacting galaxies from a restricted three-body simulation can be backwards integrated to estimate reasonable initial parameters for the galaxies well before their observed state. However, the backwards and forward integration in time of these simulations must be tuned by carefully choosing a tuning scalar to capture the dynamical

friction of the interacting galaxies.

This dissertation presents a prototype pipeline to link computationally efficient restricted three-body simulations of galaxy interactions to full, high resolution N-Body simulations. The software iterates between both classes of simulations to converge on the best match to an observed galaxy merger state. The system begins with a state vector from a merger at its peri-center as determined by the restricted three-body simulation code, SPAM, with an uncertain value for a dynamical friction scalar. The pipeline uses this vector to backwards integrate another SPAM model that systematically varies a scalar for dynamical friction and determines initial conditions to use for evolution of in an N-Body simulation. These initial conditions are used to create, scale, and reposition unit galaxy models for use in an N-Body simulation of the users choice, and creates the necessary input deck for it. For each simulation, a scoring metric is calculated to determine the quality of fit that the N-Body simulation has in regards to the original SPAM simulation. The scores from each simulation are used in a second order Newton-Raphson optimization step to iterate on values of dynamical friction. This dissertation demonstrates the use of the pipeline to model 54 pairs of interacting galaxies. These models in most cases greatly improve upon the accuracy of faster running models in identifying a set of parameters to define each interacting galaxy with relatively small computational investment. The resulting parameters can be used by higher resolution simulations with more complete sets of physics, such as gas dynamics and star formation, to more readily compare to observational data.

Chapter 1: Introduction

We can glean insights into our universe's past, present, and future through meticulous observations of the night's sky. By collecting photons at different frequencies and times, we can gauge the sizes, compositions, orientations, and velocities of heavenly bodies. The predominant theories on the evolution of universe however cannot be defined by these observational features alone. We must place them in a framework based upon physics and mathematics. The prevailing theory of an expanding, cold dark matter universe, or Λ CDM, predicts that nearly 80% of all matter in the universe is dark, i.e. not directly observable. Galaxy models support these theories, as only the inclusion of dark matter allows these galaxy models to stabilize and match their observable features (Blumenthal et al., 1984). Significant richness in the universe comes from the configuration of dark matter in halos, resulting from the interactions between multiple galaxies. The visible components of galaxies may not appear to merge, but their dark matter may combine hierarchically for form larger, more complex features.

To accurately model what the actual configuration of the universe is as observed today in a region of space, galaxies and their evolutions must be modeled accurately as well, as they are carriers of dark matter. For this reason, galaxies are the building blocks of all hierarchical cosmological models. Unfortunately, it's not always possible to model the observable features of a galaxy and understand its history and formation. Many galaxies observed today are believed to be the result of close encounters or even complete mergers with other galaxies over billions of years. The idea of galaxy evolution was first suggested by Edwin Hubble in the mid-1920s, although his particular theory of galaxy evolution didn't involve galaxy interactions (Hubble, 1927). During interactions of these spiral galaxies, their stars, dust, and gases may be stripped away or spread over large regions

in which tidal distortions can be created, star formation can be enhanced, shockwaves can ripple through them, and complete mergers can occur given the right initial conditions. Over time, most of the dust and gases become consumed as fuel in star and other stellar body formations. Many of these resulting galaxies are relatively inert and elliptical in configuration.

Astronomers have developed models of individual galaxies, and even pairs of galaxies interacting with one another that have relatively good agreement with theories or some observations. It is not uncommon for the development of a model of a particular galaxy or system with good kinematics and morphology to take several months by an experienced modeler (Hammer et al., 2009). To overcome this challenge, others have developed means of automating the search of parameter space to fit models to real galaxy systems (Barnes and Hibbard, 2009). In other cases, a model is constructed and the sets of observational data are investigated to see if it matches any observed system. Modern sky surveys, such as the Sloan Digital Sky Survey have measured the properties of over 900,000 galaxies to search through. Future surveys, such as those conducted by the Large Synoptic Survey Telescope, will identify and characterize well over 50 billion galaxies, with over 10 million of those belonging to systems of interacting galaxies (LSST Science Collaboration et al., 2009). Modeling one and two at a time in great detail will not allow scientists to develop cosmological scale models of regions of the universe using real galaxies, necessitating a great deal of effective and efficient automation. For the time being, cosmological scale models populate their volume statistically with a range of galaxies and allow them and their dark matter to interact and evolve.

Because observational data of galaxies are only obtained at a snapshot in their existence, models of galaxies are needed to understand how they originated and how they might further evolve. This dissertation extends the work of the Merger Wars project, which through citizen science and machine learning techniques, it has found a way to rapidly determine many of the initial parameters used to describe and define a galaxy

(Holincheck, 2013). More specifically, the work presented in this dissertation is a continuation of the rapid modeling and simulation pipelining approach of another dissertation topic, *A Pipeline for Constructing a Catalog of Multi-method Models of Interacting Galaxies* (Holincheck, 2013). Where as the Merger Wars project relied on a restricted three-body model of the galaxies called SPAM, this dissertation evolves 54 galaxy pairs using higher fidelity N-Body models that take into account more than just a simple approximation of the gravitational potential. Through high performance computing, these pairs can be studied in great detail, the accuracy of the lower resolution models better defined, and other phenomena such as star formation rates and nuclear activity can be compared to other observational data. This pipeline extension will enable other researchers to quickly and easily investigate their models over a wide range of galaxy pairs, offering new avenues of validation presently not feasible to explore today.

1.1 A Brief History of the Study of Interacting Galaxies

The study of interacting galaxies can be traced to the early part of the 20th century. Edwin Hubble attempted to classify galaxies into two major categories: ellipticals and spirals (Hubble, 1927). In his classification scheme, spirals were further broken into two major types, barred or non-barred. Some of the galaxies he studied could not be easily classified into such general categories and were binned as irregular galaxies, lacking the clear features expected from an elliptical or spiral galaxy. Over the next several decades refinements were made to Hubble's classification scheme, and quantitative metrics were added to it, such as color and luminosity (de Vaucouleurs, 1962). De Vaucouleurs also expanded on the form of galaxies, leading to a classification scheme based on four major galaxy classes: ellipticals, lenticulars, spirals, and irregulars. This revised scheme further broke down lenticulars and spirals into families (ordinary or barred) and those into varieties (ringed or s-shaped). These two classes are further broken down into stages, which are

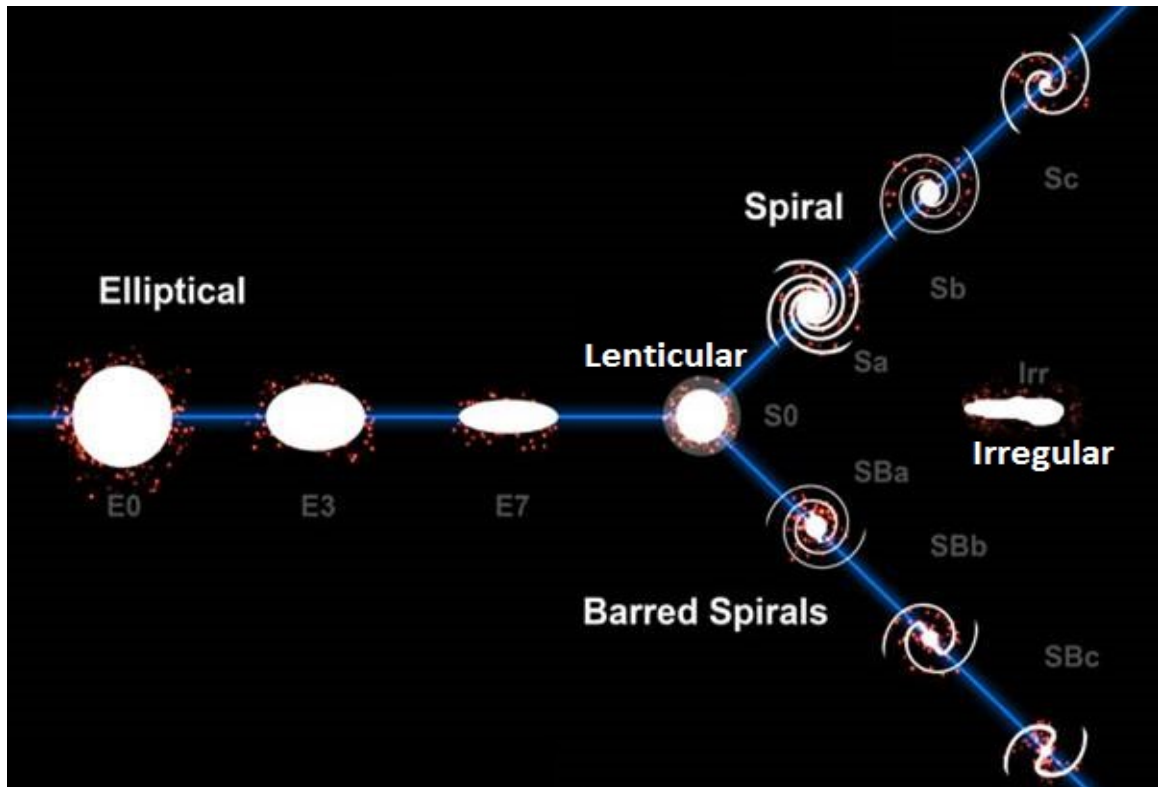


Figure 1.1: Hubble's galaxy classification scheme as revised by De Vaucouleurs to include elliptical, lenticular, spiral, and irregular galaxies. Image obtained and modified with permission from *Nova Celestia* (Sulehria, 2005)

unique to their class.

Even with improvements to classification schemes, astronomers could not neatly classify the increasing number of galaxies being cataloged. Systems were being observed with a diverse set of morphological features, such as long tidal tails, galactic bridges, and distorted discs. In 1966, Halton Arp published an atlas of more than 300 galaxies that could not be classified by existing means and attempted his own scheme (Arp, 1966). At the time, the prevalent theories discredited the likelihood that galaxies could merge and that gravity alone could explain many of the rich features observed. In 2007, the Galaxy Zoo project began to use citizen scientists to classify over 1 million galaxies from the Sloan Digital Sky Survey and received over 100 million classifications (Lintott et al. (2011) and Willett et al. (2013)). This unprecedented attempt at classifying galaxies showed there are likely more

revisions that will need to be made to the classic classification schemes.

During the 1960s and 1970s, numerical experiments using two masses to define a gravitational field and a set of massless particles to trace the fields showed that it is possible for gravity alone to explain the observation of features seen in many of the irregular shaped galaxies. This class of simulations can be grouped together as restricted three-body simulations. Simulations also showed the impact the kinematics of the galaxies could have on the shape of tidal features, causing them to be tight during fast interactions and broad during slower ones. These models could not explain all features observed, but helped to change the prevailing theories at the time. In the 1980s, an alternative methodology called the Multiple Three-Body Algorithm (MTBA or M3BA) was developed by Borne as a hybrid technique between restricted three-body and full N-Body, sharing the computational efficiency of a restricted three-body method with the more accurate gravitational physics of an N-Body method, particularly when it applied to elliptical galaxies, as discussed in Borne (1984) and Borne (1988a). Later investigations showed that the coupling these tidal features caused by gravitational fields could also impact the distribution of gases within the galaxies and thus impact star formation rates throughout the galaxies (Toomre, 1972).

In the 1980s, the Lambda Cold Dark Matter (Λ CDM) theory of the universe popularized the idea that the universe, once hot after The Big Bang, had cooled (Blumenthal et al., 1984). As the universe expanded, dark matter dynamically cooled and condensed into localized structures. These structures led to the formation of higher density regions of gas that were trapped in these gravitational wells. Over time, these local structures grew into larger structures that became the seeds of early galaxies. Eventually the cooling of gas in these regions triggered star formation which led to galaxies. In time, these systems can be attracted to other systems and hierarchically merge. This leads to a great interest in galaxies and interacting galaxies for the modern theory of the universe's evolution.

Although there is a preference by many researchers to exploit high performance computing to simulate ever larger galaxies with greater resolution as resources allow, the

study of interacting galaxies has continued using more sophisticated approximations of the physics within a galaxy. Restricted three-body simulations have refined their description of the gravitational fields and incorporated changes to the kinematics of the system to better match higher resolution models of the same systems (Holincheck and Wallin, 2015). These advancements contribute to the current study of interacting galaxies today by allowing a large number of systems to be investigated very quickly. Such advancements are needed as modern day sky surveys are discovering more and more galaxies and systems are identified that cannot be classified or understood without the use of simulation.

1.2 Dynamics of Galaxies and Mergers

When looking at the optical emissions of galaxies through a telescope, we can see that they are predominantly made up of stars. By looking at other wavelengths from atomic transitions, we know that typical spiral galaxies have 10-20% of their directly observable mass in the form of gas and dust. About 95% of this gas consists of HI (neutral hydrogen), HII (single ionized hydrogen), H₂ (molecular hydrogen) and helium, while 5% consists of oxygen, nitrogen, and carbon-monoxide. Other low Z elements can be found as dust throughout the galaxy. Together, the gas and dust are known as the inter-stellar medium or ISM, and roughly 50% of it can be found along the galactic disks of spiral galaxies. A very detailed description of the ISM can be found in the literature by Ferrire (2001).

Although galaxies have lifespans of billions of years and appear relatively stationary to an observer over days, months, or even years, there are active and complex processes going on all the time. Throughout a galaxy's life, stars are born, radiate energy, and eventually die. Gas may dissipate, condense, radiate energy to cool, or absorb energy to heat up. And not to be forgotten, gravity is always acting between these bodies.

The above interactions or feedback may appear simple at first, but much more is happening. While stars are undergoing nuclear fusion, photons are radiated expelling energy.

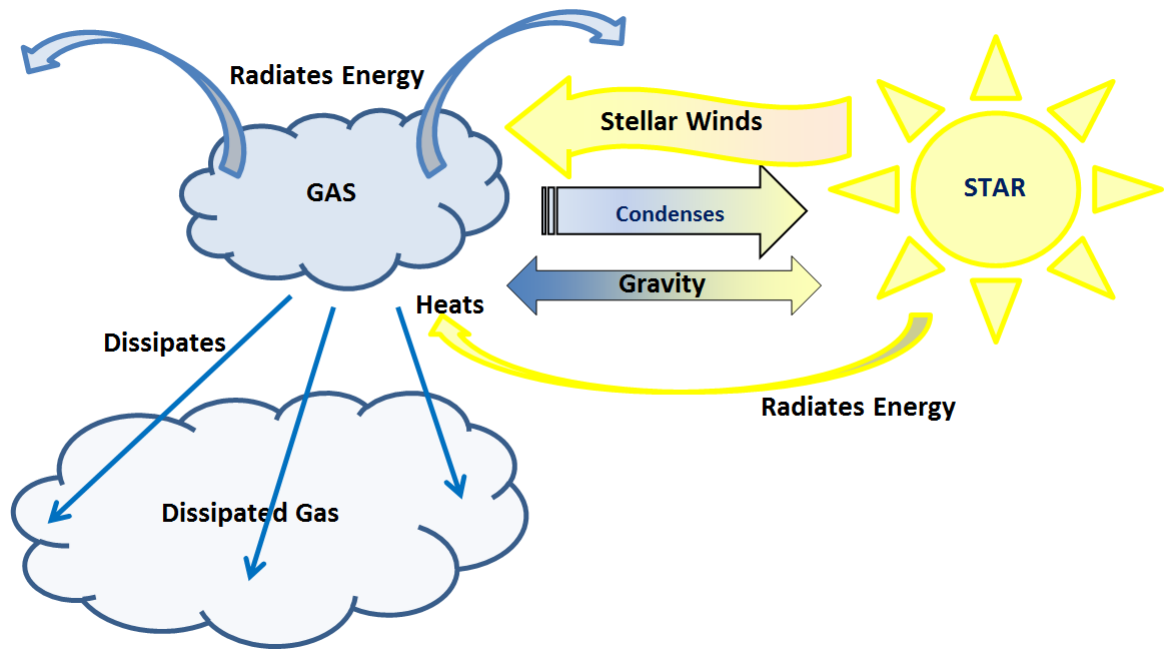


Figure 1.2: Several feedback mechanisms exist between stars and their surrounding gas. Gases may heat, cool, dissipate, or condense while stars may heat, cool, and release winds

When these photons are absorbed by the interstellar gas, molecular hydrogen may dissociate and molecules and atoms may become ionized. As stars (typically type O & B stars) release ionized material, gas, and energy into the surrounding regions through ejections or winds amounting to a tremendous amount of energy and momentum that may heat, dissipate, or disperse the ISM. This will decrease the gas density and may lower temperatures. These effects can be greatly magnified if a star were to go nova or supernova. The shockwaves created in this way that ripple through the ISM may both disperse it or sweep up enough material to make it extremely dense along the shock front. This may also heat the gas and then lead to it emitting x-rays. The increased density may lead to further star formation while the increased dispersion can potentially lower the density of the ISM enough that star formation will never occur unless another body acts upon it.

As gas cools, it tends to do so first adiabatically before radiatively. Over time, pockets

of gas may become dense enough to form stars due to collisions or loss of angular momentum. This collapse, however, may be opposed by the electromagnetic fields created through ionized cosmic radiation that may be passing through the ISM. This radiation acts as a stabilizer to prevent the gas from collapsing onto itself due to self-gravity.

Although figure 1.2 depicts a single body of gas interacting with a single star, in actuality a body or pocket of gas may interact with several stars. Likewise, several pockets of gas may interact with a single star. Even more, multiple pockets of gas and dust may interact with each other, exchanging angular momentum and energy through collisions and radiation. Stars however tend not to interact with each other directly and are considered to be collision-less. This is one reason why the ISM often can be thought of as a continuum while stars cannot.

When taken as a whole, these interactions over a large region containing many stars and ISM give rise to the dynamics we can observe in snapshots in time that are taking place in galaxies. As galaxies pass near each other, interactions take place between stars and ISM of the opposing galaxies. Outer portions of the galaxies may begin to morph as tidal forces begin to appear. As first speculated by Zwicky in the 1950s and later confirmed, this can be seen as thin tails of stars with the ISM beginning to form on the outer regions of the galaxies, and even bridges may form between them, linking them together. These tails may become thin and dense and become a source of high star formation rate in these galaxies, particularly at the tips of the tails (Struck, 2006). If the galaxies pass through each other, the morphology may be more drastic, and the bodies may not separate but in fact merge. Over time, morphological features may subside as gravity works to restore angular momentum. As galaxies pass near each other, the increased gravity may result in gas concentrating along the disk due to tidal forces, leading to increased star formation rates (Noguchi, 1998). In any case, neither galaxy will ever be the same again.

1.3 Computational Methods

In the field of computational astrophysics, there are four major techniques used to model gravity and the interstellar medium. These are N-Body methods, smooth-particle hydrodynamics, particle-mesh (also known as particles-in-cell or PIC), and continuum methods using adaptive mesh refinement or AMR. Each method has its strengths and weaknesses, and today many codes that model galaxies and their interactions use a combination of methods. Specific examples of such codes will be discussed later.

Early computational capabilities available to astronomers were crude and limited. In the 1960s and 1970s, Eulerian based methods that attempted to treat stars and the interstellar medium as a continuum were impractical to use as they required significant data storage and processing to advance in time. Understanding that gravity from discrete stars accounted for most of the movement and evolution of galaxies, Lagrangian methods were used. The most common were N-Body methods in which stars were approximated as collision-less macro-bodies and modeled using the Boltzmann Equation. These methods were relatively efficient compared to Lagrangian methods and could easily scale in size. Toomre & Toomre were able to show that test particles in dynamically shifting gravitational fields (e.g. restricted three-body codes) were all that's needed to replicate galaxy features such as arms and tides (Toomre, 1972). Although a significant approximation of a real system that would have billions or trillions of discrete entities, the ability of such a restricted approach to mimic observable features was remarkable.

N-Body codes, however, did have a significant draw back. The gravitational potential each object experiences is based on the relative mass and locations of all other entities in the model domain. This naturally led to algorithms with numerical complexity on the order of $O(N^2)$. In the 1980s, Appel (1985) and Barnes and Hut (1986) revolutionized N-Body methods for astrophysics by incorporating two major ideas. The first was to organize the data spatially. This was accomplished through tree data-structures. One type of tree useful

is the k-d tree in which objects are iteratively subdivided equally along the dimension of greatest extent. In other words, there are two children for every parent in the tree, and new generations are born until the leaves in the tree have no more than one member. This tree is balanced and can be searched with complexity $O(N \log N)$, a tremendous algorithmic improvement. An alternative tree approach is to use oct-trees (3D) or quad-tree (2D). These trees, used by Barnes & Hut, would subdivide each parent into 8 (or 4 in 2D) equal volumes that did not guarantee to create a balanced tree. Like the k-d tree, the children nodes are subdivided until no more than 1 particle exists in each. The benefit this offers is that all the particles within a branch are spatially local to each other. The second advancement came from the idea that nodes of the tree containing more than one particle with some ratio of size and distance away from a particle elsewhere in the tree can be approximated as a point source. This reduces the number of explicit interactions that need to be computed, greatly reducing runtimes. Higher order multi-pole expressions for those nodes of many particles can be used to improve the accuracy of the computation.

One Eulerian technique for modeling the gravity of an N-Body system is the Particle-Mesh Method. This technique keeps gravity localized to particles that can move, but the gravitational potential is computed over a mesh by solving Poisson's equation. A major advancement was made by Villumsen (1989) when Green's functions using Fast Fourier Transformations (FFT) were introduced as a new, faster way to solve Poisson's equation for gravitational potential. This offered increased computational efficiency at the expense of limiting high resolution to small regions. The technique also naturally supports periodic boundary conditions.

The aforementioned techniques principally dealt with stars and dark matter, but not gas dynamics. Gas and the interstellar medium are treated as a continuum in the two remaining methods, smooth-particle dynamics (Lagrangian) and strictly mesh-based Eulerian methods (popularized with the advent of adaptive mesh refinement). Smooth-particle hydrodynamics (SPH) has been overwhelmingly the method of choice for astronomers in

the N-Body community. The implementation approach of SPH can be similar to N-Body, and it offers a natural way to maintain high resolutions in areas of high densities and velocities while being memory efficient. This has been very important when the complementary N-Body methods would push the limit of the number of particles they could run. Mesh based methods, using finite-difference/volume/element approaches naturally ensured that dust and the interstellar media could occupy the entire simulation domain and have been relatively straight forward to implement as well. Solving Euler's equations for fluxes in mass, velocity, and energy have unfortunately relied on very inefficient uniform grids that swamp the memory available to the machines on which they were run while trying to achieve an acceptable resolution. Over the past 10-20 years, the introduction of mesh based techniques such as adaptive mesh refinement have overcome the reliance on strictly uniform meshes, making some of these approaches more memory and computational efficient than SPH methods (Trac, 2003). Today gas dynamics for galaxies are split into these two major camps. It is further argued that these Eulerian approaches are much more accurate than SPH, particularly at higher dimensions where SPH has difficulty tracking shocks (Vazza, 2001), a phenomena linked to high rates of star formation. Kang (2004) also observed that SPH models tend to have high uncertainties in properties such as temperature and entropy in low density regions due to statistical artifacts of that methodology.

Accurate, high resolution galaxy modeling codes cannot rely on solely modeling stars or gases in hopes of accurately modeling specific galaxies and interactions of galaxies. To this day most codes either are strictly particle based, relying on N-Body methods and SPH, or they use mesh-based codes that utilize adaptive mesh refinement for gas dynamics and a particle-mesh approach for stars. Subtle variations between codes do exist, but these are the two major approaches used today by and large. No code is known to exist that combines the efficiency of an N-Body model for gravity with the accuracy and efficiency of an AMR method for gas dynamics.

1.4 An Existing Pipeline

The subject of the dissertation by Holincheck established a pipeline methodology that begins with observational data of a pair of interacting galaxies and ends with a model or models of the system along with orbital parameters to describe its orbit¹. A diagram of the process can be seen in figure 1.3. This pipeline uses redshift and luminosity data to establish physical scales and masses respectively of the galaxies. Through the use of citizen scientists in the Merger Wars project and the restricted three-body simulation software SPAM, the parameter space defining the orientations of the galaxies and orbital elements of the system are determined. This is made possible by the reversibility of the restricted three-body method. Candidate values for the system are backwards integrated by the restricted three-body method and then forward integrated with massless test or tracer particles. Once the simulation returns to the starting time ($t=0$), the massless particles should mimic the morphology of the system. Citizen scientists or automated fitness functions evaluate the quality of the resulting simulation of matching the target system. As resources permit, more candidate conditions are run, hopefully resulting in a handful of high quality models for the system. If more than one candidate system has a high fitness, additional comparisons are made until the best overall model is determined. In general, there should only be a couple models with a high fitness if there are pronounced tidal and other morphological features of the system, as there are only a few ways, if that, to orient the galaxies in a system to generate those features, increasing the uniqueness of these models. In some cases there may be two potential models to match the system, usually with the orientation of the galaxies in respect to the viewer causing a difference. Borne (1988a) discusses how using the velocity data from the observed system and noting the parity of the tidal features can typically be used to determine exactly which model is permissible.

Relying on a restricted three-body model of a system cannot capture all phenomena an

¹The orbit is the relative path or trajectory the secondary galaxy experiences if the primary galaxy is held and fixed at the origin in Cartesian space.

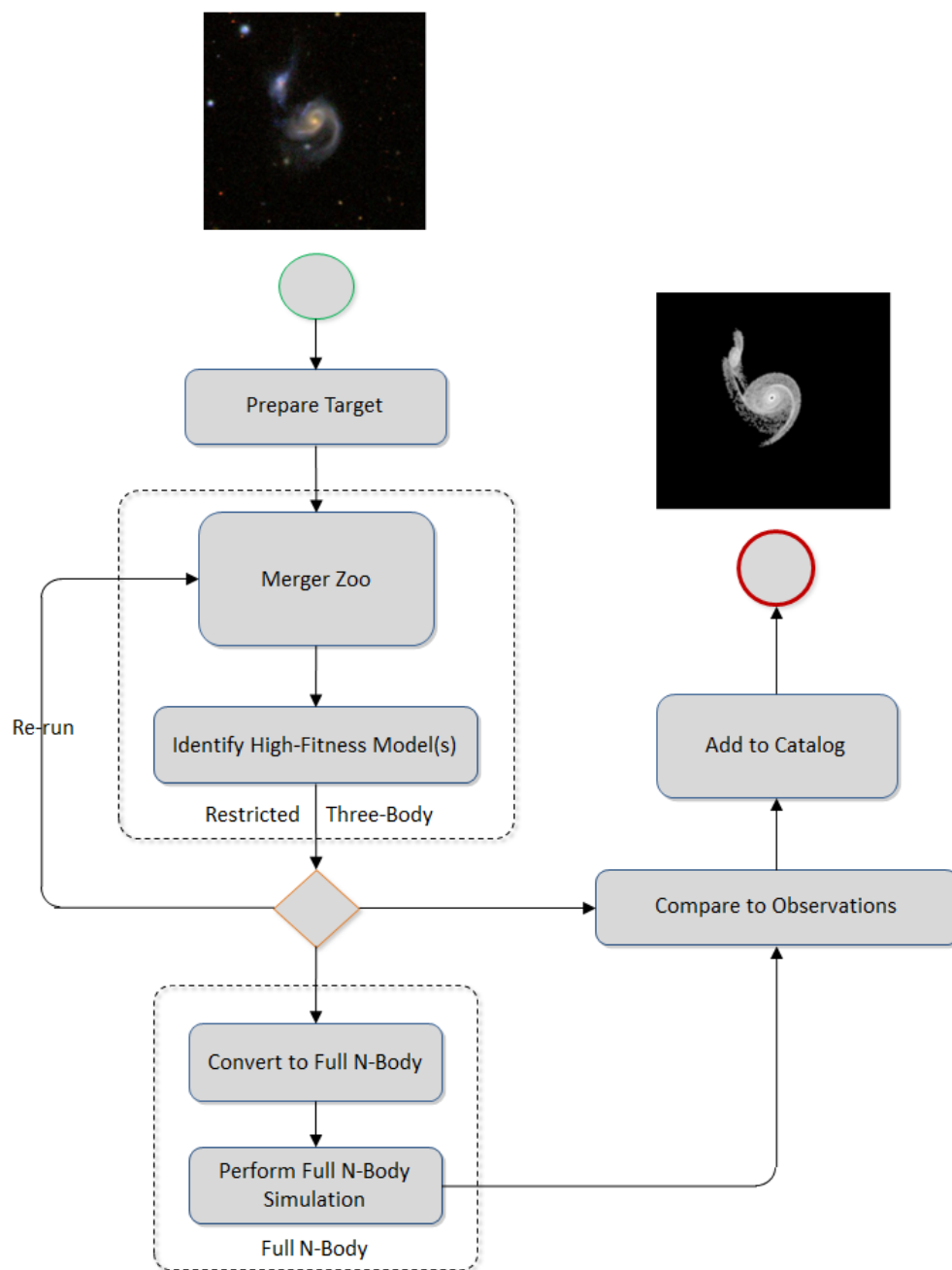


Figure 1.3: A Pipeline for constructing multi-method models of interacting galaxies

astronomer would like to know about the system, such as luminosity, star formation rate, heating, cooling, and gas distribution to name a few. Understanding and determining these features require higher fidelity simulations that incorporate additional physics. The pipeline suggests full N-Body methods (discussed later) as one approach to achieve such higher fidelity simulations. These simulations can be initialized again by backwards integrating any of the best restricted three-body simulations and using the size, orientation, positions, and velocities of the galaxies as new initial conditions. Once the high fidelity simulations are integrated, they too can be judged for quality by matching the observational data before being recorded as a good representation of the target system. These higher fidelity simulations were not included in the Holincheck dissertation.

1.5 A Pipeline Extension for Constructing Models of Interacting Galaxies

The preceding pipeline suggested and recommended to convert the best restricted three-body simulations to N-Body simulations and make additional comparisons to observational data before accepting any into a catalog. The process implies this should be straight forward, however several questions arise, such as should we expect the N-Body simulation to agree with the restricted three-body simulation? After all, the N-Body simulation allows all particles to interact with one another as opposed to a couple interacting with a field. How does one determine if an N-Body simulation is a good match to observational data? Can information about the N-Body simulation be used to refine the restricted three-body model of a system? This dissertation answers those questions as the original pipeline for creating multi-method models is extended to support optimal N-Body models.

Being an extension to figure 1.3, the new process in figure 1.4 looks remarkably similar at first. All of the changes come in the N-Body section of the pipeline. Like before, this section will receive as input a restricted three-body model with a high fitness. This is provided

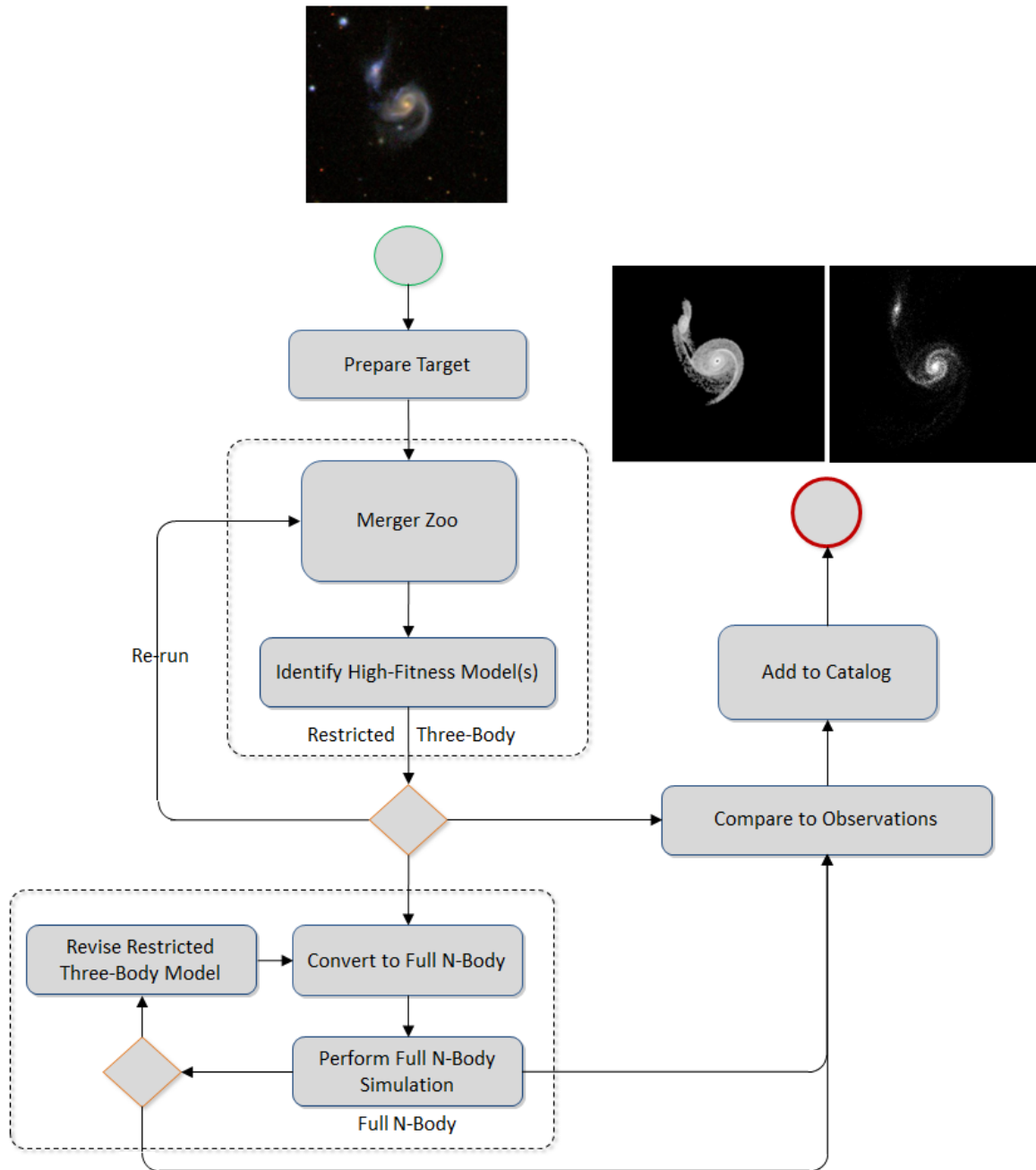


Figure 1.4: A Pipeline for constructing optimized N-Body models of interacting galaxies

by means of a state vector describing the system of interacting galaxies at the same time its target observational data represents. This state vector includes the orientation of the discs in both galaxies, their masses, their disc radii, and the relative position and velocity of the secondary galaxy. This state vector is found by evaluating many different restricted three-body models which are all computationally inexpensive. Before an N-Body simulation can be constructed, the state vector must be used to backwards integrate a restricted three-body model to determine initial conditions for the higher fidelity simulation. Generally, backwards integrating until the system reaches the apocenter of its orbit will be sufficient to start an N-Body simulation before each galaxy begins to show signs of an interaction. The state vector describing the restricted three-body model at this point in time when the apocenter is reached can be used to construct two progenitor galaxy models in the N-Body simulation.

The N-Body simulation is forward integrated in time until a good match to a target system can be found. Ideally, this would occur at the same time the original state vector represented. However, given the additional physics in an N-Body simulation, this is not always the case. Similar to restricted three-body phase of the pipeline, the N-Body phase also needs to evaluate the quality of the simulation. Whereas the earlier phase is either scored qualitatively by citizen scientists or quantitatively through automated fitness functions against observational data, the N-Body simulations can be scored against the same data or the restricted three body simulations themselves. It is usually preferable to only compare a simulation to actual data to determine how well the model represents reality, but by comparing to another model already deemed to be a very good representation of the data, we can compare against variables for which there is no observational data, such as its position along the Z axis or in V_x or V_y space. In this dissertation, we focus on comparisons against the restricted three-body model to exercise the pipeline process.

If the N-Body fitness is not good enough, its initial conditions can be modified to result in a new N-Body simulation to be compared against the restricted three-body simulation

or observational data. One way to do this is by adjusting a scalar for dynamical friction used in the restricted three-body model. These models are reversible, meaning that if a value in the model is changed and then the system is backwards integrated in time and then forward integrate from there, the system will pass through the same point at which it started. However, when it is backwards integrated, its trajectory will change, resulting in multiple changes to the initial conditions of the next N-Body simulation. By applying an optimization step, intelligent modifications can be made to this scalar to limit the number of computationally expensive N-Body simulations needed to achieve a better match to a target data set. Once an acceptable model or models have been found, a comparison can be made one last time against observational data before being added to a catalog. This dissertation will focus on the feasibility of and implementation of the pipeline extension necessary to ensure quality N-Body models can be determined for a catalog by simulating 54 real systems of interacting galaxies.

1.5.1 A Pipeline Alternative - Identikit

The challenge of exploring the parameter space to rapidly generate models of interacting galaxies is not new. Computationally inexpensive methods such as restricted three-body and MTBA have been used to simulate many potential models of a system until the dynamics and features of a simulation are in good agreement with observations. Borne, Hoessel, and Balcells in the 1980s successfully generated a large number of simulations using the MTBA methodology to model several binary galaxy systems (Balcells et al., 1989; Borne, 1988b; Borne et al., 1988; Borne and Hoessel, 1988). However, generating candidate models and matching those to observations was done manually.

In 2009, the Identikit software package was released to add automation to explore parameter space for models in a similar manner to the pipeline presented in this dissertation, but with some stark differences (Barnes and Hibbard, 2009). At its core, Identikit is a hybrid N-Body and test particle tracing simulation model that models a pair of interacting

galaxies by defining the mass ratio of the pair, their disk orientations, orbital parameters (specifically eccentricity and pericenter). Both galaxies are constructed with the same mass model (based on a Navarro halo profile, Hernquist bulge profile, and van der Kruit & Searle disk profile) using equal massive particle masses, and test particles distributed on exactly circular orbits to capture the behavior of the disks. Hybrid simulations are run using the Zeno astronomical package to span the allowable parameter space of the variables used to define the galaxies. A user then selects different times during the orbit, length & velocity scaling factors, centers of mass & velocity for the system, and viewing orientations to search for a best match to observational data.

In the second major release of the Identikit package in 2011, graphical user interface tools were created to allow the user to select regions of interest in the matching process (primarily tidal tails) (Barnes, 2011). The software can now automatically search through time and orientations to calculate a score as a measure of how well the resulting simulation matches the target data set in X , Y , and V_z space. This allows the user to focus on the score values to pick out prospective good matches for further investigation.

The short coming of the Identikit approach is that phase space is not always well explored. Individual users can only look through a few hundred cases themselves. They are guided by experience in how to find a good match to the system rather than by a thorough exploration of the phase space associated with the problem.

In our pipeline approach, similar parameters are used to define the pair of interacting galaxies, and likewise, both approaches are broken into two major but differing phases. Our first phase searches for parameters of the interacting galaxies through the use of Citizen Scientists or fitness functions (Holincheck, 2013). These parameters are honed in upon through the use of a restricted three-body simulation, SPAM. Whereas Identikit picks an orbit and forward integrates the galaxies on it, SPAM simulations are setup at the time of the observed interaction, backwards integrated to the apocenter of their orbit, and forward integrated back to the observed time to see how the test tracer particles visualize the disk,

galactic bridges, and tidal features. In effect, the viewing parameters Identikit adjusts post simulation are part of our original simulation.

To improve the fidelity of the parameters to determine better initial conditions for our galaxies, a limited set of N-Body simulations are used in conjunction with a restricted three-body simulation by varying its dynamical friction. This process also uses an automated scoring methodology in determining a quality of fit to the observed data in X,Y, and Z space (the score can take into account V_x , V_y , & V_z but does not presently), but also adds an optimization step to efficiently search the range of dynamical friction. In essence, our approach uses fast running simulations to explore the parameter space and identify good matches to observational data, and it relies on a much smaller set of more costly N-Body simulations to fine tune the parameter choices. This is in contrast to the Identikit approach which uses costly N-Body simulations to explore much of the parameter space and then applies fast running observational related methods on each N-Body simulation to find the the best matches. It is expected that the approach relying on fewer executions of the more complex algorithm (i.e., the N-Body method) should in theory should identify good matches to data faster than the other.

In this dissertation, our approach is applied to 54 real interacting pairs to reliably search for reasonable initial parameters describing each galaxy that would result in an interaction similar to what was observed. The Identikit methodology has been applied to a smaller set of interacting galaxies - 36 fictitious interactions in which the real initial conditions are known exactly to assess the methodology and four real systems: NGC 52578, The Mice, the Antennae, and NGC 2623 (Privon et al. (2013), Mortazavi and Lotz (2014)). Unfortunately, the sets of galaxies modeled by each approach do not overlap. While the Identikit interactions have focused on galaxy pairs with mass ratio $\mu = 1.0$ (the system is capable of different mass ratios) and equal size galaxies, the simulations in this dissertation span reduced mass ratios of 0.1 to 30, with each disk having its own diameter.

Chapter 2: Modeling Galaxies

The Sloan Digital Sky Survey (SDSS) contains a massive amount of observational data to be mined and processed using existing galaxy models and analytical methods to test theories and thus improve our understanding of the mechanisms that take part in galaxies and their mergers. By studying such large datasets, we can improve our confidence in existing and new theories, while at the same time gain a better understanding of the evolution of the universe by better understanding its building blocks. The Galaxy Zoo projects have led efforts in citizen science and machine learning to qualitatively classify galaxies and scope current and initial properties of the galaxies undergoing a merger event (Darg, 2010). Such properties include galaxy type, orientation, velocity, configuration, and mass. However, understanding the dynamics of the each system is the only way to fully understand the physical processes that lead to star formation, galaxies merging, and the growth of central black holes. The particular characteristics of the orbital interactions are directly tied to the evolution of these systems. Since the dynamics of a merger is directly tied to the formation of tidal features, using n-body codes to model tidal features ultimately gives us an understanding of the dynamical conditions that drive the evolution of the merger.

Traditionally, a scientist would have to apply recipes of galaxy configurations to a code to achieve a stable galaxy and then relax, perturb, excite, or equilibrate the system to learn how different mergers evolve. Creating models that reproduce the tidal features of merging systems has traditionally been an extremely time consuming process. In order to model more than a handful of these systems, a method is needed to systematically search through the parameter space to find the initial conditions and current dynamical state of the system. Holincheck (2013) created a crowd sourced pipeline for doing this search and determined the dynamical states for over 62 interacting systems. Although

Holincheck’s models provide a good starting place for understanding mergers, they use a relatively simple approximation for the physics of the interaction. Self-consistent gravity and ultimately hydrodynamics must be included to fully model these mergers. When included, the resulting models of systems of interacting galaxies can be used to test theories on the physical behaviors that likely occurred to reach the current merger state. Once automated, studies can be performed on thousands of galaxies to discover trends and prove or disprove theories. Until existing theories can be applied to such a large set of mergers, uncertainty will remain in physical processes and galaxy configurations and compositions (e.g., active galaxies, globular clusters, central black holes, and dark matter halos).

There are several software packages developed over the past 20 years that have great significance to the computational astrophysical community. These items span galaxy model input generators, simple restricted three-body models, N-Body method models, and more recently Adaptive Mesh Refinement Models. This chapter will highlight some of the significant computer codes that contain models for galaxies that will be referenced and discussed throughout this dissertation, particularly those that contributed to the development of our pipeline. Access to the source code for each software package was available for inspection, modification, and compiling.

2.1 SPAM - A Restricted Three-Body Model

SPAM¹ is a restricted three-body, gravitational model written in Fortran90 originally developed by Wallin et al. (1990) and enhanced by Holincheck during the original pipeline creation (Holincheck and Wallin, 2015). In SPAM, two galaxies are each approximated as a single macro-body with its own mass. The third body comes into play as set of massless tracer particles used to map out the gravitational fields of the two galaxies - one set of particles will belong solely to one galaxy and the other set to the other galaxy; the set of massless particles is referred to as the third body in the restricted three-body method.

¹Stellar Particle Animation Model

Because the test or tracer particles are massless, they do not directly contribute to the motion of the two galaxies, but they will trace out the features of the galaxy, such as the discs and tidal tails, by experiencing an acceleration due to gravity experienced by the gravitational potential created by the two macro-particles. In SPAM, these test particles are distributed radially along the plane of the disc component of each galaxy, proportional to $1/r$, $\exp(-r/r_0)$, or $\exp(-r^2/a + r \times b + c)$, and uniformly in the azimuthal direction². All particles are integrated over time using the same integration scheme in time and space³. By limiting the gravity component to the two macro-particles, SPAM and other restricted three-body models are able to compute the trajectories of the galaxies over several crossing distances in just a few seconds on a single CPU. Toomre (1972), Wallin et al. (1990), Borne (1984), and Petsch and Theis (2008) have shown that this methodology performs well when used to match observed morphologies of real pairs of galaxies.

So far, the preceding description of SPAM could describe other restricted three-body models. However, there are two significant differences between it and most other restricted three-body models. The first is that SPAM allows the user to select between one of three gravitational potentials. The first potential uses a softening length treatment as seen in equation 2.1, which corresponds to an acceleration experienced by each particle defined by equation 2.2.

$$\phi(r) = \frac{GM}{\epsilon} \left[\frac{\pi}{2} - \tan^{-1} \left(\frac{r}{\epsilon} \right) \right] \quad (2.1)$$

$$\vec{a} = -\frac{GM}{(r^2 + \epsilon^2)} \hat{r} \quad (2.2)$$

This equation for acceleration is common to many N-Body methods. Although it has been used in many models of interacting systems, it cannot capture the potential associated with a dark matter halo accurately. A second option in the code uses a Modified

²For our use of SPAM throughout this dissertation, the $1/r$ profile was used exclusively

³SPAM uses a leapfrog integration scheme with a Runge-Kutta 4 method

Newtonian Dynamics (MOND) potential described by Scarpa (2006), in which the acceleration described in equation 2.2 is modified as a_{mond} in equation 2.3 within which a_0 is the constant $1.2 \times 10^{-8} \text{ cm s}^{-2}$.

$$a_{mond} = a \left(\frac{1}{2} + \frac{1}{2} \sqrt{1 + \left(\frac{2a_0}{a} \right)^2} \right)^{\frac{1}{2}} \quad (2.3)$$

The MOND model was developed to explain the flat rotation curves in galaxies without using dark matter. It is not widely accepted in the astrophysical community and is not used in this study. This is noted only for completeness.

The third potential is constructed from a three component system that can be used to describe the distribution of mass within a spiral galaxy. In this approach, the acceleration becomes a function of the radial distance between particles and the center of each galaxy, and is defined simply as:

$$\vec{a} = \frac{GM_{total}(r)}{r^2} \hat{r} \quad (2.4)$$

where the function of massing being the sum of the mass of the bulge, disc, and halo of the galaxy at distance r .

$$M_{total}(r) = M_{disc}(r) + M_{halo}(r) + M_{bulge}(r) \quad (2.5)$$

The equations for the mass distribution were derived by Hernquist (1993) and can be found in many self-consistent N-Body models. He defines the halo mass distribution as:

$$M(r)_{halo} = \frac{4\pi\alpha_{halo}}{r^2} \frac{1}{2\sqrt{\pi^3}} \int_0^r \frac{\exp(-x^2)}{x^2 + q_{halo}^2} x^2 dx \quad (2.6)$$

in which

$$q_{halo} = \frac{\gamma_{halo}}{r_c} \quad (2.7)$$

and

$$\alpha_{halo} = \frac{1}{1 - q_{halo} \sqrt{\pi} \exp[q_{halo}^2] (1 - \text{erf}(q_{halo}))} \quad (2.8)$$

where r_c is the cutoff radius of the halo & γ is the core radius of the halo. The bulge is defined in equation 2.9 as:

$$M(r)_{bulge} = 4\pi \exp\left(\frac{-r^2}{h_{bulge}^2}\right) \int_0^r \exp\left[\frac{-x^2}{h_{bulge}^2}\right] x^2 dx \quad (2.9)$$

where h_{bulge} is the size or radius of the bulge. Finally, the disc is defined in equation 2.10 as:

$$M(r)_{disc} = \frac{1}{2h_{disc}^2} \int_0^r \exp\left[\frac{-x}{h_{disc}}\right] x^2 dx \quad (2.10)$$

where h_{disc} is the size or radius of the disc.

This Hernquist potential is used exclusively in this study. It closely matches the potential we use in the MASS99 and GADGET-2 codes described in the next section.

Typically when one uses any model of a galaxy system, each galaxy is defined by a progenitor model, and it is during the forward integration in time that the interesting physics take place, which hopefully leads to the desired morphology. SPAM is unique in that it allows the user to forward or backwards integrate the model in time. If backwards integration is requested, only the two particles representing the galaxies are used. This simple interaction allows the integration to be reversible. Once the system has been backwards integrated to a specified time, then the massless particles are added around each galaxy. Once completed, the simulation forward integrates back to time equal to 0 (when it started)

and continues integrating to the user specified time. In the pipeline defined in figures 1.3 and 1.4, the SPAM model parameters are defined at time equal to 0, which corresponds to the epoch in which the target system has been observed. It is by backwards integrating and then forward integrating, we can see the massless particles capturing the morphology of the system. In this way, SPAM's model parameters connect the current dynamical state of the system with its pre-encounter conditions.

Restricted three-body methods have run-time advantages over all other galaxy modeling methods since the bulk of the physics is captured by two particles, making computation trivial. Even by including thousands of massless particles which do not contribute to the gravitational potential of the system, the runtime only changes linearly, that is the addition of N massless particles the code's execution time will scale $\approx O(N)$. In this dissertation, all simulations using SPAM utilized 50,000 particles, with the particles being distributed to each galaxy by the mass ratio of the system. On a modest laptop computer, most simulations took on the order of one minute to complete allowing the system to evolve over one crossing distance. This number of particles were sufficient to observe the desired morphological structures.

2.2 MASS99 - An N-Body Model

MASS99⁴ is a hierarchical, N-Body tree code developed at George Mason University over the past 15 years (Antunes and Wallin (2001), Antunes and Wallin (2007)). It includes gas dynamics by means of smooth particle hydrodynamics (SPH), includes star formation models, and is parallelized to work any cluster supporting openMPI and the Intel or GNU Fortran90 or newer compilers. The implementation of the N-Body component of MASS99 is largely the same as other N-Body codes based on the original Barnes-Hut algorithm. Macro-particles used to define dark matter and stars are on one tree, while SPH particles

⁴Multi-physics Astrophysical Simulation Software

representing gas belong to a different tree. MASS99 allows the user to turn on or off the far distance mass approximation of collections of particles far from the particle whose force is being calculated and supports the inclusion of quadrupole moments to improve accuracy of force calculations. MASS99 offers multiple time marching and integration schemes to choose from to control runtimes versus accuracy.

Although fundamentally similar to other N-Body methods, MASS99 implements parallelization differently than many others. MASS99 achieves most of its parallelization by breaking its overall tree data structure into a series of smaller, trees that can be walked locally and whose particles can be walked on the remote trees. This helps to keep each computational node active. The Message Passing Interface (MPI) is used to share data in this way.

2.2.1 Enhancements to MASS99

During the beginning of this dissertation, MASS99 was ported to a few large, distributed memory clusters at various Department of Defense Supercomputing Resource Centers (DSRCs). This was done to support the potential need of simulating many systems of interacting galaxies with a very large number of particles (hundreds of thousands to a billion). This provided access to the Intel profiling tools to assess how efficiently the code was using the clusters nodes. This led to the discovery that a significant amount of time was spent by nodes either waiting to receive data or for other nodes to complete their work. The scheduling and balancing of the order in which gravity particles are shared between nodes was optimized by scheduling smaller transfers first, which keeps nodes busier processing data with less time waiting on other nodes to complete larger tasks; the throughput of processing particles was improved.

Additional work was made on the model during this project to convert it to a hybrid OpenMP/MPI model. The code continues to parallelize the N-Body problem into a set

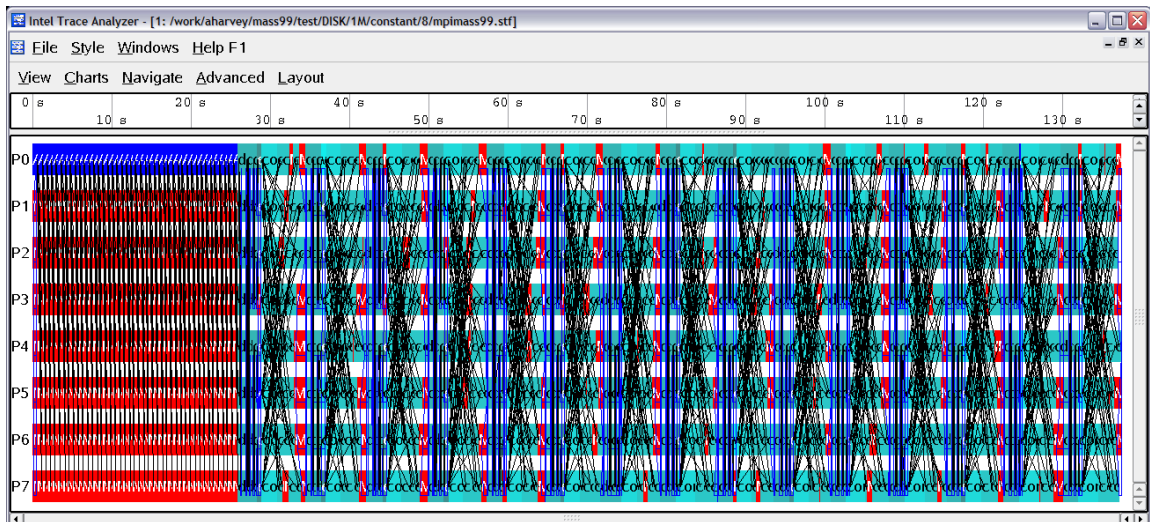


Figure 2.1: Tools such as Intels ITAC have been used to help identify excessive wait times and later optimize the parallelization efficiency of MASS99. After optimization, most nodes are waiting for data or to move to the next phase at the same time. This can be seen by the bands of cyan and red blocks.

of trees, one for each MPI process. However, by limiting the number of MPI processes on each computational node (and therefore the number of trees on each node), OpenMP threads can be used to take advantage of the threading capability of the node (e.g., multi-core or hyper-threading) by processing sections of the node's own tree in parallel. This has the benefit that there will be fewer network communications needed to share data between nodes. This saves time in packaging, scheduling, and transferring data. Benchmarks have shown an approximately 30% speedup and computational efficiency with this enhancement when using multiprocessing nodes with 8-16 computational cores.

Advancements have also been made in terms of input and output (IO) for the MASS99. Under this effort, MASS99 has been enhanced to output its data for analysis and visualization in the SILO file format with the option to create these files using HDF5. SILO, developed by Lawrence Livermore National Laboratory for the storage of scientific data, is supported by a variety of visualization tools, such as VisIt and Paraview. By using HDF5, more ways are available for other models and tools to query and interact with the

files. Support for the SILO format also allows for efficient parallel IO. This is accomplished by allowing each node to write a portion of the dataset to different files, and a master file containing information associating files with datasets. Due to the nature in which the master tree of particles is constructed within MASS99, no appreciable performance gains are achieved by parallel input of the initial condition files within MASS99, as a single node ultimately controls the tree generation. However, visualization software packages such as *VisIt* can read these multiple files in parallel because visualization does not require the reconstruction of the original master tree.

These enhancements to MASS99 allow it to take advantage of the increasingly higher core density of nodes within computer clusters and third party analysis tools. Although the objective of the pipeline described within this dissertation is to allow for the creation of N-Body models of interacting galaxy systems, the optimal creation is likely to require several N-Body simulations for each system. Since N-Body methods are significantly more computationally expensive than restricted three-body methods, anything that can speed up their use is of great importance. This model is one that is used with the pipeline in this study.

2.3 GADGET-2 - An N-Body Model

GADGET-2⁵ is a freely available software package supporting galaxy simulations all the way up to cosmological scale simulations (Springel, 2005). It was developed by Volker Springel at the Max-Planck Institute for Astrophysics and was first released to the public in March 2000 (Version 1). Although it supports the modeling of individual galaxies, its primary focus was to better understand the structure of the universe at cosmological scales, at which the formation of and interaction of galaxies play an important role.

Like MASS99, it is a hierarchal tree code using oct-trees to model collisionless macro-particles to represent the stars within galaxies. It also includes the use of SPH to model

⁵Galaxies with Dark matter and Gas intEract, Version 2

gas dynamics, as well as the additional physics needed to model larger scale, cosmological evolution, to include the cosmological expansion of space. GADGET-2 supports a full suite of star formation/gas dynamics interactions beyond basic gas dynamics. However, physics pertaining to star formation is not contained in the publicly available version of the code (a version of GADGET-2 with star formation physics is available on a case by case basis from its developers). This capability will be made available in GADGET-3 when it is made publically available. GADGET-2 is also parallelized with MPI and can be run on a wide variety of systems. It does not, however, support a hybrid MPI/openMP mode as MASS99 does now.

Although its current version was released roughly ten years ago, it is still the most widely used publicly available N-Body simulation today. It is used throughout many universities and institutes around the world because the source code is available, allowing easy access to enhance or replace any physics in it. This does have the side effect that, due to a lack of oversight on the code, nearly every major user’s version of GADGET-2 is different. Because GADGET-2 is so prevalent in the astronomical community, many visualization packages have the ability to natively read GADGET-2’s *snapshot* file format, such as the free and open source scientific visualization system *VisIt* from Lawrence Livermore National Laboratory (Childs, 2011). Given the prevalence of GADGET-2 in the astronomical community, we do use GADGET-2 as one of the N-Body software packages supported in our pipeline.

2.4 AMR Models

Whereas the previously discussed codes were Lagrangian based models, there exist many freely available, open-source, adaptive mesh refinement models. Such codes include Enzo developed by a collaboration with UC San Diego, Stanford, Princeton, Columbia, MSU, CU Boulder, CITA, McMaster, SMU, and UC Berkeley (O’Shea et al., 2004), FLASH from the University of Chicago (Fryxell et al., 2000), and AstroBEAR from the University of

Rochester (Cunningham et al., 2009). Each of these codes support hydrodynamics and magneto-hydrodynamics over regular, Cartesian grids and are parallelized with MPI. AstroBEAR has primarily been used to investigate shocks and flows of the interstellar medium, Enzo for cosmological scale simulations to understand the structure of the universe, and FLASH which can be used anywhere between the nuclear flash of a star being born to the hierarchical structure of the universe. Each of these codes contain a wealth of physical models, including radiation transport, self-gravity, metallicity-dependent heating and cooling, star formation, and more. Although there are large user communities for some of these tools, they are not designed specifically for galaxy modeling (although Enzo does support N-Body modeling by a particle-in-cell approach). In addition, these packages have a significantly greater learning curve than the more accessible N-Body tree-code based packages. Although it should conceptually be possible to link our pipeline to any of these models, it is not demonstrated in this dissertation.

2.5 N-Body Generators

A common theme across nearly all software tools that support the modeling of a galaxy, let alone modeling of interacting galaxies, is that they tend not to provide a way of supplying the initial setup of a galaxy, i.e., they do generate an initial galaxy model. Typically the modeler must turn to another model that uses a galaxy recipe to determine the initial distribution of macro-particle positions and velocities to define the stars, gas, and dark matter in each galaxy desired. Fortunately, there are some freely available tools that can generate these initial distributions of particles that can then be used by tools such as GADGET-2.

The most common recipe for constructing a model of galaxies was developed by Hernquist (1993). As we described in section 2.1, this model was also the basis for the potential used in the SPAM code. This is a three component model representing the halo, bulge,

and disc. Particles are randomly sampled such that they follow the mass functions as defined in equations 2.6 to 2.10. Velocities for the particles are often defined such that their dispersions in spherical coordinates can be defined by a distribution function.

$$F(v, r) = 4\pi \left(\frac{1}{2\pi\sigma^2} \right)^{3/2} v^2 \exp(-v^2/2\sigma_r^2) \quad (2.11)$$

Equation 2.11 defines the distribution function of the speed, v , of each particle as a function of its distance from r , the center of mass. Here σ is the standard deviation of the distribution function and v_r is the radial component of the velocity. Due to the asymmetries of the bulge and disc, their distribution functions are much more complex, and the reader should refer to the original paper by Hernquist (1993) for more detail. This method appears to be the most widely used recipe for creating initial conditions of spiral galaxies that will be stable under self gravity.

Another common family of models was developed by Michie and Bodenheimer (1963) but popularized by King (1966). These models assume a constant temperature through a sphere of stellar media (this could be dark matter, stars, or gas). They use a cutoff in the energy to prevent the mass at the center of system from becoming infinite otherwise. The King family can be described by the distribution function:

$$f_K(\mathcal{E}) = \begin{cases} \rho_1 (2\pi\sigma^2)^{-3/2} (e^{\mathcal{E}/\sigma^2} - 1) & \mathcal{E} > 0; \\ 0 & \mathcal{E} \leq 0. \end{cases} \quad (2.12)$$

where the temperature, T , of the system relates to the standard deviation of the system's energy, \mathcal{E} , and its mass by:

$$\sigma^2 = k_B T / m \quad (2.13)$$

The constant ρ_1 in equation 2.12 relates the potential energy of the system, Ψ , with the

temperature and density of the system, as seen in equation 2.14.

$$\rho = \rho_1 e^{\Psi/\sigma^2} \quad (2.14)$$

For specific details on relating equations 2.12 - 2.14 to particle positions and velocities, the reader can refer to King (1966) or Binney (1994). By carefully defining the scale and temperature of a King model, good fits to lower isothermal spheres and elliptical galaxies can be found.

2.5.1 MASS99

The MASS99 software package has built-in support for an N-Body generator using Hernquist's formulation for spiral galaxies and multiple King models for elliptical galaxies and lower isothermal spheres. It creates a spiral galaxy using user specified masses and sizes for the halo, bulge, and disc, as well as the total number of particles to use along with the fractional amount that should be assigned to each component. For the King family of models, a ratio of the energy of the system is specified.

MASS99 also includes a program *CREATE99* that will construct a galaxy of user specified number of particles, mass, and size. Another included program is *SCALE99* that will allow the user to rotate the galaxy around each axis, scale it by size, mass, and velocity, and displace it in space. MASS99 can write the resulting particle locations and velocities to its own internal format, ascii, and a GADGET-2 snapshot format (this was an additional enhancement made during this study).

2.5.2 NEMO

NEMO⁶ is a stellar dynamics toolbox created by Barnes, Hut, and Teuben, and is maintained at the University of Maryland (Barnes et al., 2010). The toolbox includes many tools and models that may be useful for modeling a large variety of stellar dynamics, to include N-Body propagators with and without SPH, visualization tools, and analysis tools. Included in this collection are a handful of galaxy generating models, including magalie (Boily et al., 2001) which implements a modified formulation of the Hernquist model by not directly calculating velocity dispersions but instead matching the velocity to the mass distribution. Magalie uses similar inputs as MASS99 for defining a simple Hernquist model, such as number of particles and scale lengths, but the major difference is that the mass of the disk is fixed at 1.0 mass unit. Because magalie is entirely unitless without prompting the user for scale parameters, one has to take care how the system is defined when trying to use or compare it with other models. The NEMO package includes many tools that can allow the galaxy model to be read and written to a variety of file formats.

2.5.3 Starscream

Yet another generator freely available is *Starscream*⁷ developed by (Billings, 2008). Like many of the other generators, it also has origins that can be traced back to the original recipe developed by Hernquist. Starscreams exact implementation however was developed by Springel and White (1999), which uses aspects of the Hernquist model, although it does lack a bulge. Although fundamentally based on Hernquists original approach described earlier, Starscream uses relationships between the halo mass distributions with aspects of an NFW dark matter halo profile described by Springel et al. (2005). The disc is

⁶NEMO is not an acronym, or at least is not one today. The original code developed by Barnes was referred to as NEMO and that name, all capitalized, has remained ever since. The current developers enjoy teasing users with acronyms the name could stand for but does not and pointing out other acronyms that do spell out the same name.

⁷Starscream is lovingly named after everyone's favorite backstabber from the 1980's children's television cartoon *The Transformers*.

modeled after Springel and White (1999), in which the mass distribution follows equation 2.15.

$$\rho_d(R, z) = \frac{M_d}{4\pi z_0 R_d^2} e^{-R/R_d} \text{sech}^2\left(\frac{z}{z_0}\right) \quad (2.15)$$

The velocity is determined from an analytic function based on a purely exponential disc. There is, however, no separate component for a bulge. Unlike most other generator codes, solving for the potential is done by means of a particle mesh method as opposed to integrating shells in 1D. Another major distinction is that Starscream can be better described as a library of routines that allows a user to construct their own static model of a galaxy. That means the user must create their own C code setting variables defining the overall scales of the galaxy, constants for numerical integration, and how the galaxy should be positioned and rotated. In one code the user can define and build many galaxies and combine them so they immediately can be read by another N-Body code. Starscream natively supports writing to the GADGET-2 snapshot file format.

Chapter 3: Restricted Three-Body to N-Body

In the top half of pipeline by Holincheck and the pipeline defined by this dissertation, at least one restricted three-body model of an interacting galaxy system with a high fitness should be available for construction of an N-Body model and simulation. With our restricted three-body simulator, SPAM, we have a state vector describing the system at the observed time of the system's interaction. We can backwards integrate the system once again to obtain a state vector at some point earlier in time to use as a state vector to begin constructing the equivalent N-Body model. Although the SPAM model only gives us some approximate bulk properties of interaction, including the mass of each galaxy, the disc radii, disc orientation, and relative velocity and position between the two galaxies, it does provide an accurate physical model of the processes in the interaction. Developing a physically self-consistent N-Body model required the tuning of these initial orbital parameters. In addition to tuning these parameters, we must have an approach to determine the number of particles to use, how the mass should be distributed between the dark matter halo, disc, bulge, and gas, what the velocities of individual particles should be, etc. This chapter will explore the challenges and approaches taken to connect the computationally efficient restricted three-body models from the SPAM code to the self-consistent N-Body models from the MASS99 and GADGET-2 codes.

3.1 Initial Conditions

As stated earlier, we must backwards integrate our SPAM models to determine a new state vector to define the parameters needed by an N-Body generator, such as CREATE99. In a restricted three-body model, significant computational savings are had by only having

to directly account for the interactions between two particles, namely the center of each galaxy, whereas an N-Body model potentially has a direct interaction between all N particles. Because of both close encounters between individual particles and the bulk response of the ensemble to larger perturbations, it is this simplification in a three-body model that will cause the most significant differences between it and a self-consistent N-Body model. One of the most significant factors that drive these differences is the physical phenomena of dynamical friction. Although dynamical friction is approximated in the SPAM code, the tuning of the dynamical friction parameters is critical to match the orbits and morphology of the restricted three-body approach to those from a self-consistent N-Body code.

3.1.1 Dynamical Friction

Imagine two bodies of different masses with a relative velocity such that the distance between them is closing, and the gravity each body exerts on each other has no impact on that initial velocity. Also assume that the gravitational attraction is insufficient to cause a collision of the bodies, as seen in figure 3.1. As the distance closes between these two bodies, the smaller body will be deflected towards the larger body, as it will experience a larger gravitational force and change in momentum than the larger body. This deflection will lead the smaller object to move closer towards the larger body's displacement vector. Now imagine instead of one smaller body, there are many bodies with less mass than the larger body. In fact, the total mass of the smaller bodies may still be less than the larger body. In this case, many of these small bodies will be deflected towards the larger body's trajectory vector, creating a wake of small bodies. Collectively these small bodies will create a sizeable gravitational attraction with the larger body along its trajectory, and it also explains the tendency for larger bodies passing through regions of smaller bodies to lose momentum, potentially collapse, and allow systems to relax.

Another way of looking at dynamical friction is for a case where at least one body is approximated as a larger macro-body. As the macro-body approaches a field of smaller

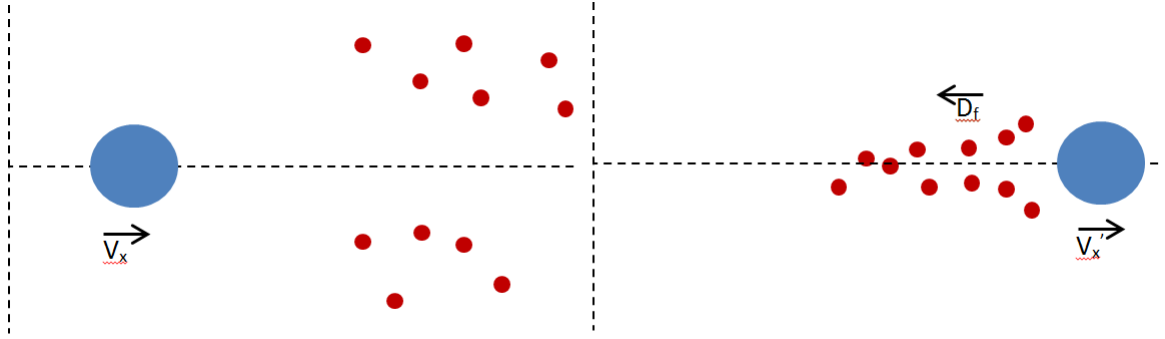


Figure 3.1: A large body (blue sphere) moves a velocity V_x towards a collection of much smaller bodies (red spheres) [left]. When the large body passes through the region of smaller bodies, the mutual gravitational attraction will resemble a wake behind larger body, resulting in an appreciable gravitational or drag force opposite its original trajectory [right].

bodies with gravity as the principal force, all bodies will be attracted towards each other. The smaller particles will tend to accelerate faster due larger relative changes in momentum and its conservation within the entire system. As the macro-body passes through a field of particles, those particles once accelerating will be slowing down as they still experience a force of attraction with the larger body; the particles will be leaving a gravitational potential well. This also holds true for the macro-body, as it should be slowing down as it moves beyond the center of mass of the system. If the system is reduced to just a few macro-bodies such that they are allowed to occupy some of the same space (such as treating a collection of stars of a galaxy as a single body), then there will just be a single, large force of attraction between those overlapping bodies when they are near each other. To account for the forces that should be applied on the outside of the macro-bodies of particles that should be behind it, a drag force is introduced through dynamical friction. This effective drag was defined by Chandrasekhar (1943) and coined dynamical friction. His mathematical formulation of dynamical friction is commonly referred to as *Chandrasekhar's Dynamical Friction Formula*, as seen in equation 3.1.

$$\frac{d\vec{v}_M}{dt} = -16\pi^2 G^2 M m_a \ln \Lambda \left[\int_0^{v_M} dv_a v_a^2 f(v_a) \right] \frac{\vec{v}_M}{v_M^3} \quad (3.1)$$

In this classical equation for dynamical friction, a body of interest with mass M interacts with another body m_a which has a velocity distribution function f . The $\ln \Lambda$ factor is known as the Coulomb logarithm or the coefficient of dynamical friction. It is this logarithm that is typically tuned experimentally until its effect on the deceleration of a system in a restricted three-body model allows it to better match a full N-Body model. Analytic expressions have been defined by Chandrasekhar (1943), Kim (2003), and others to capture dynamical friction, and a coefficient of dynamical friction is often defined as a function of the system's relaxation time.

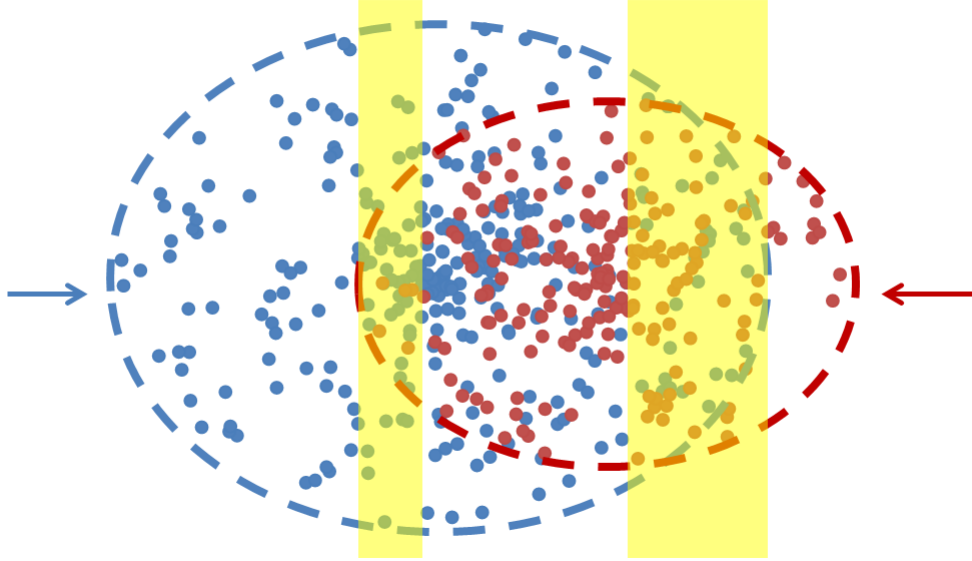


Figure 3.2: Red particles in the leftmost shaded region and blue particles in the rightmost shaded region should introduce a drag on the relative motion of the other body of particles.

In the SPAM code, the distribution of the dark matter and its velocity dispersion is approximated using the Hernquist model. By assuming that the velocity of the dark matter

distribution function described in *Chandrasekhar's Dynamical Friction Formula* is Maxwellian, then equation 3.1 becomes (Binney, 1994):

$$\frac{d\vec{v}_M}{dt} = -\frac{4\pi G^2 M \rho \ln \Lambda}{v_M^3} \left[\text{erf}(X) - \frac{2X}{\sqrt{\pi}} e^{-X^2} \right] \vec{v}_M \quad (3.2)$$

For convenience, X relates the velocity to the velocity dispersion, σ , by:

$$X = \frac{\vec{v}_M}{\sigma} \quad (3.3)$$

Because the motion of the restricted three-body model in each galaxy is predominantly along the plane of the disc, the velocity dispersion is just the radial velocity dispersion, allowing us to define it as:

$$v_r^2 = \frac{G}{\rho(r)} \int_0^r \frac{\rho(r)m(r)}{r^2} dr \quad (3.4)$$

Taken altogether, we can see that the allowable range of values for the coefficient of dynamical friction must be ≥ 0 , otherwise particles would be accelerated and not decelerated. In dimensionless units used by SPAM, typical values for the coefficient of dynamical friction is on the order of 10^{-3} .

3.1.2 Tuning Dynamical Friction

Dynamical friction is typically set to a reasonable value based on experience simulating particular systems or it must be tuned. In the first half of the pipeline process to determine high fitness models using SPAM, its coefficient was set to 0.001. Recall it is the distribution of the tracer particles to capture morphology and relative location of the galaxies that are used to determine the fitness of the restricted three-body models. We know that dynamical friction must be tuned if a restricted three-body model hopes to share the same orbital

trajectory as an N-Body model that does not have a need for a dynamical friction adjustment. So although the N-Body portion of our pipeline may receive a state vector of a high fitness restricted three-body model, we may need to fine tune the coefficient of dynamical friction.

Thanks to the reversibility of restricted three-body methods, even when dynamical friction is tuned, the model returns the galaxies to the same locations they were in when the fitness was assessed. As can be seen in figure 3.3, changing the coefficient just a small amount can have a significant impact on the trajectories. Our objective is to tune the coefficient such that the initial conditions found from the backwards integration will yield a trajectory that arrives at the same point in space as the restricted three-body as when it was assessed.

There is one unavoidable and unfortunate side effect of tuning dynamical friction in our models. Since the orbital trajectory changes depend on dynamical friction, tuning the coefficient of dynamical friction actually changes the model of our encounter. Fortunately, these changes generally do not result in large changes of the systems' tidal features. For most systems, we can tune the dynamical friction and the resulting orbits of the encounter without greatly changing the resulting morphology of the system.

When the coefficient of dynamical friction is not overly large, the configuration of the particles at time equal to 0.0 (i.e., the time the original restricted three-body model best matched the target observation and the time from which the model is backwards integrated) should be qualitatively very similar. An example of this can be seen in figure 3.4. However, when trying to judge how well our N-Body models compare to the restricted three-body models, only the configuration using the dynamical friction from earlier in the pipeline should be used, as that was the configuration already deemed to be a good fit to the observed system. This means that the restricted three-body portion of our pipeline will potentially submit a different model to a model catalog than the restricted three-body model that helps to define a good N-Body model.

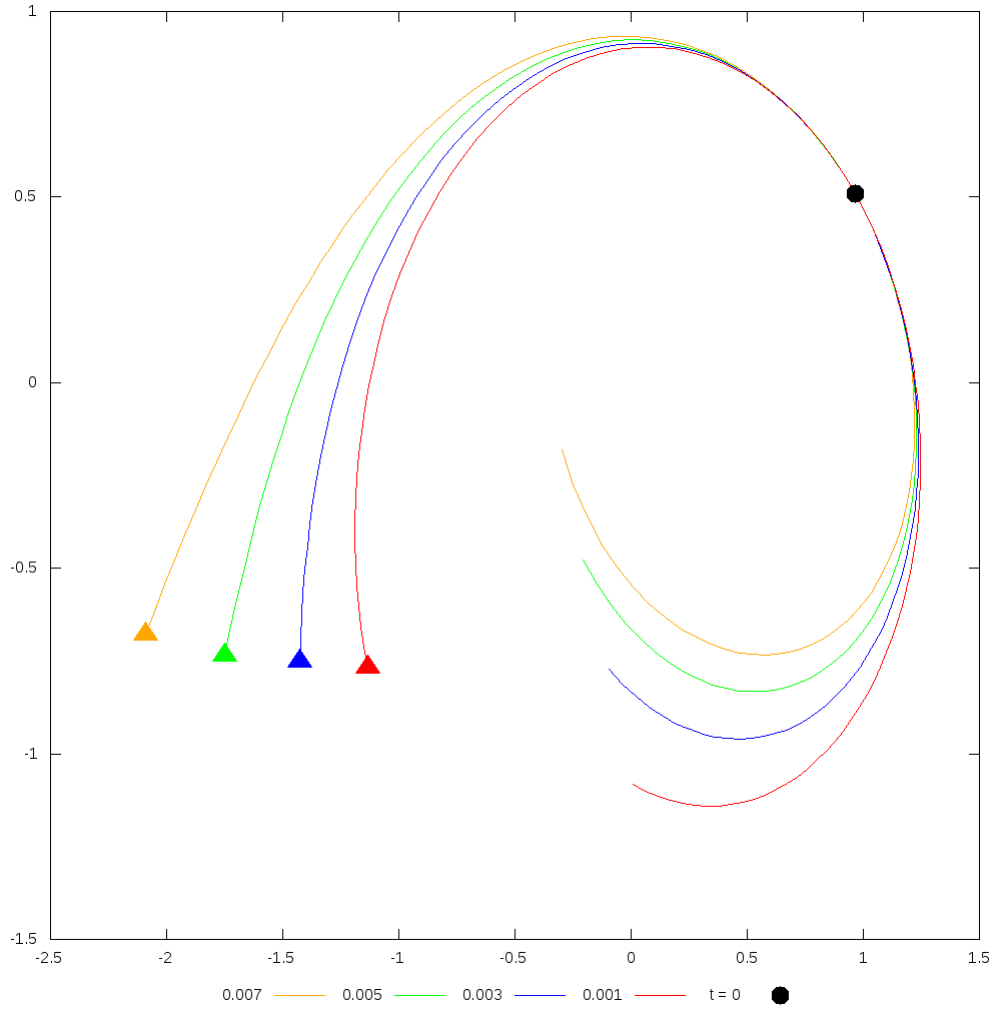


Figure 3.3: A small change in the coefficient dynamical friction can have significant changes in the trajectories of a restricted three-body simulation. Each orbit was backwards and forwarded integrated in time from the same starting location, denoted by a black circle. Filled triangles denote the end of backwards integration or the earliest point in time along the trajectory in the XY plane.

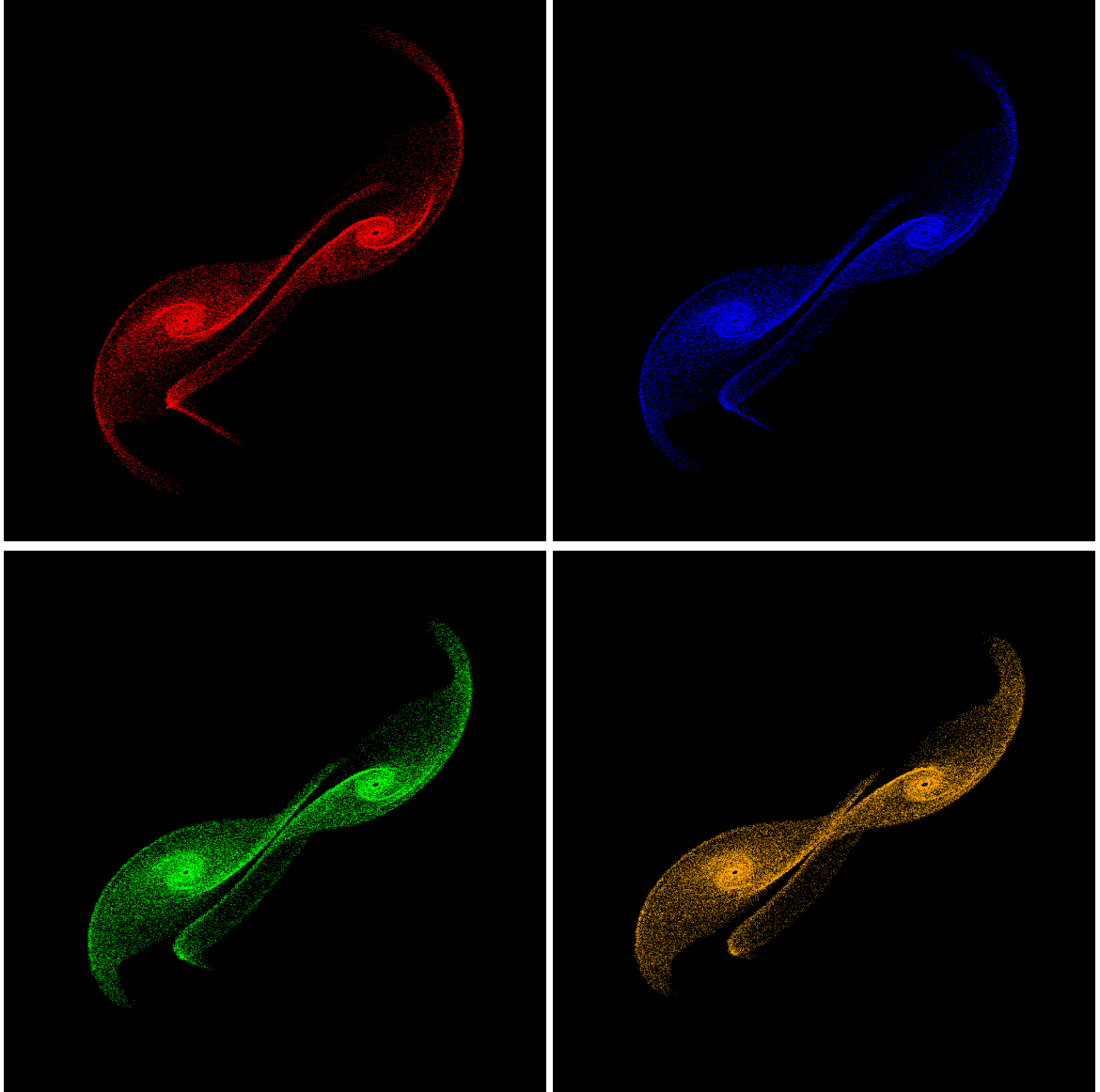


Figure 3.4: The configurations of the same model from SPAM when adjusting the coefficient of dynamical friction, observed at time at 0.0. Small changes in dynamical friction may cause large changes in the orbits as seen in figure 3.3, but changes to the final configuration of particles should be much less noticeable.

3.2 A Progenitor Galaxy

For our pipeline to be robust, we would like to have one or just a few a base models of a single galaxy that can serve as a progenitor for the galaxies in the systems we ultimately wish to model. We begin by using the default disc based model in MASS99 as described earlier. Toomre (1977) hypothesized that many mergers that ultimately formed or appear to be resulting in elliptical galaxies started as two disc based galaxies. The Merger Hypothesis as it has become to be known has been supported by several detailed studies of mergers of binary systems, such as those by Borne and Richstone (1991) and Aarseth and Fall (1980). This makes choosing a disc based model a reasonable choice for our standard progenitor galaxy. The MASS99 model defines a galaxy with masses of 5.8 units for the halo, 1.33 for the disc, and 0.33 for the bulge. It also defines the disc with a radius of 10 units and truncates the halo to this distance as well. If we stay with this model, it obviously will not allow us to match any real system or even a restricted three body simulation. The MASS99 code also includes a scaling and displacement tool, *SCALE99*. This tool allows us to scale the default galaxy model to any system size we want. To make matching the initial conditions found by SPAM or any other restricted three-body simulation easier, we scale this galaxy to a unit galaxy, that is we normalize the entire mass of the system to 1.0 and the radius to 1.0. In the process, velocity and other variables are scaled as appropriate.

Alternatively, we could edit the parameters of the galaxy generator directly to give us the same unit galaxy or another galaxy with the size and mass we want. However, this would require more development and tweaking of the input decks and in some cases source code of the generators. By aiming for a unit progenitor galaxy model, our pipeline can be streamlined by allowing anyone to easily specify their own progenitor model to scale. This can save computational time on the backend of running a pipeline process as scaling a unit galaxy to the size one wants is much faster than creating an unscaled galaxy up front. Additionally, most N-Body generators rotate and displace a galaxy separate from

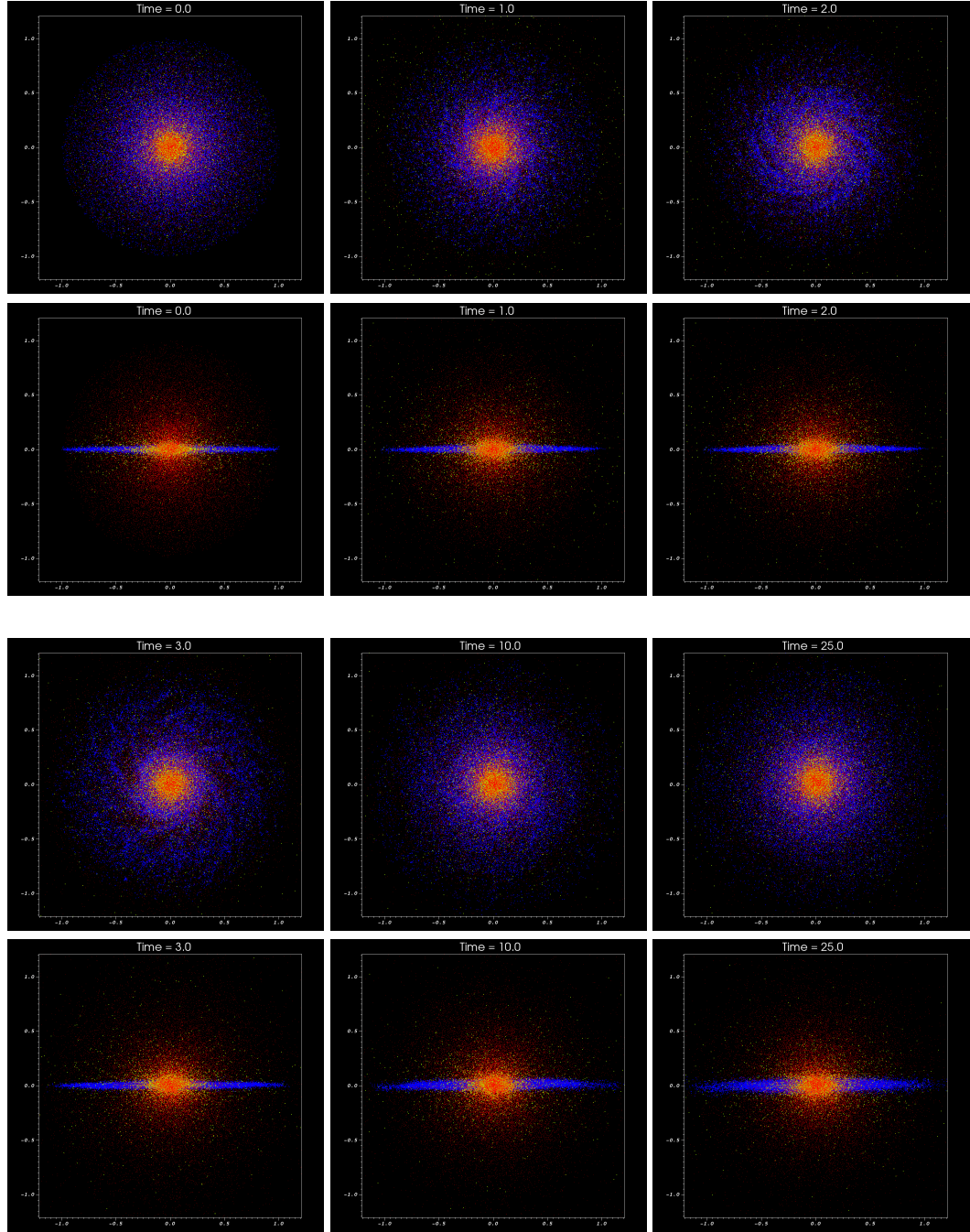


Figure 3.5: The unit progenitor galaxy as created using CREATE99 evolved on its own over time. This model contains a halo (red), bulge (yellow) and disc (blue). The disc is shown from the top down and edge on at several points during the simulation using 10^5 particles.

creating the initial distribution of particles, so scaling the galaxy during those steps too does not add any appreciable work.

An added benefit of using a scaled galaxy approach is it allows us to build a catalog of unit galaxy models that can be pulled off the shelf and used in our pipeline. For example we have constructed unit galaxies of varying sizes, halo mass distributions (where the cutoff radius is not always equal to the disc radius), and formatted for different N-Body propagators (e.g. MASS99 and GADGET-2). These unit progenitor galaxies do not have to be the galaxy with its initial distribution of particles either. They could be evolved by themselves with an N-Body integrator to allow the galaxy to come into equilibrium. If that is done, subsequent scaling of such a system will still work by scaling the actual positions of the particles in the equilibrated system by the desired radius. For example, if the target system has radius of 5.0 but the equilibrated system has its largest radius at 1.5, then the scaled galaxy's furthestest particles from center of mass will be at 7.5.

3.3 Default N-Body Values

Automating running of our N-Body pipeline requires finding settings for the N-Body codes that seem to work well for a wide variety of problems without the need for user intervention. To maintain a high degree of compatibility with the restricted three-body portion of our pipeline, we adapt the same dimensionless scaling parameters as SPAM. Therefore we use:

mass 1.989×10^{33} g (or 1 solar mass)

distance 3.086×10^{21} cm (or 1 kilo parsec)

velocity 207.4 cm/s

For both N-Body tools, we default to a simple variable time step method. The initial time step, dt , is set to:

$$dt = \min(r_i) / \sqrt{N} \quad (3.5)$$

where r_i is the disc radius of the i -th galaxy in the system and N is the number of particles we want to run. We also allow dt to grow by 10 and shrink by 10. The total simulation time is set to twice the time SPAM backwards integrates to find initial conditions. For example, if SPAM backwards integrates to $t = -6.5$ (in SPAM's time reference), then our N-Body simulation will start at time equal to 0.0 and go until time equals 13.0.

Softening lengths also need to be specified for N-Body model. Convenient values for each particle type used in GADGET-2 are:

gas $.05 * \min(r_i)$

halo $.016 * \min(r_i)$

disc $.00144 * \min(r_i)$

bulge $.00324 * \min(r_i)$

where again a parameter is scaled by the minimum radius used. For MASS99, we set the softening length of gas to 0.15 and everything else to 0.05. All other settings for MASS99 and GADGET-2 use their respective defaults. It should be noted that changing these values does not greatly affect the final morphology of the system.

3.4 Early-time Galaxy Instability

If the galaxy model is stable and in a state of equilibrium, then its kinetic, potential, and total energy should remain constant during its evolution. The configuration of the galaxy will change as it evolves, i.e., structures such as spiral arms may form. During testing

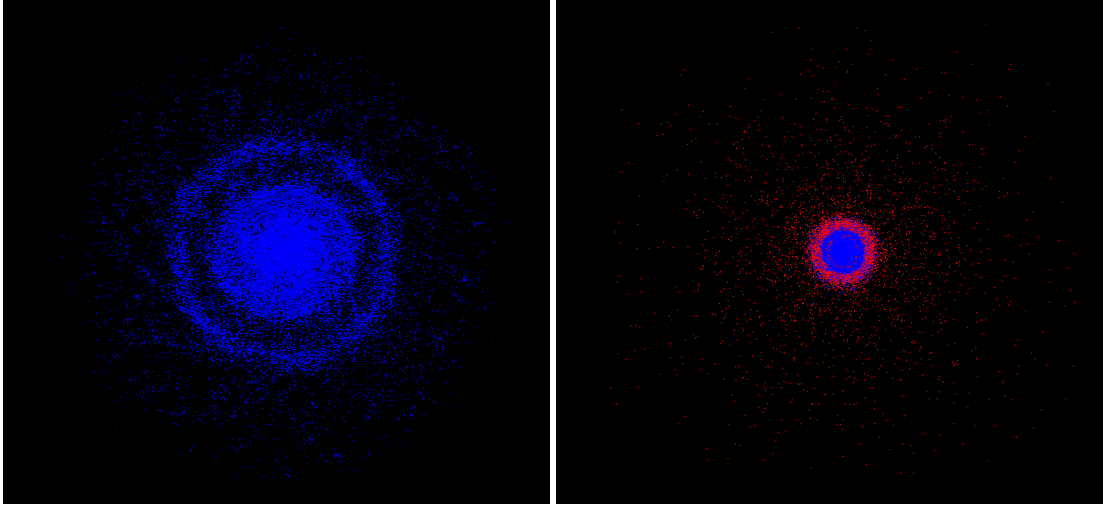


Figure 3.6: As a progenitor galaxy evolves in time, rings form in the disc as it partially collapses and expands before stabilizing. The disc (blue) is alone on the left, while the disc and halo (red) are on the right.

however, the evolution of some galaxies showed oscillations, including the base progenitor galaxy described earlier. Although some stabilization of the system is expected, the degree of oscillations warranted extra attention. These oscillations can be seen in their disks as rings forming in the early time of their evolutions. Upon further investigation, the energy of these galaxies was not constant during the oscillations period, but was once the galaxies equilibrated. For rapid modeling on N-Body models in a pipeline, the galaxies should be in equilibrium at the time they begin to pass near each other. If they are not in equilibrium, each galaxy should be evolved individually (i.e., not under the influence of a nearby galaxy) until equilibrium is reached, and then allowed to interact with each other. If not using progenitor models from a catalog of pre-evolved galaxies, this individualized equilibrium would add significant computational cost to an eventual pipeline. This ramification led to a search for the cause of initial galaxy instability.

The initial search for the cause of instability began with the galaxy generation model in MASS99. By systematically turning off the bulge and disk components, the energy instability was still seen in the halo component. This is not surprising since nearly 80% of the

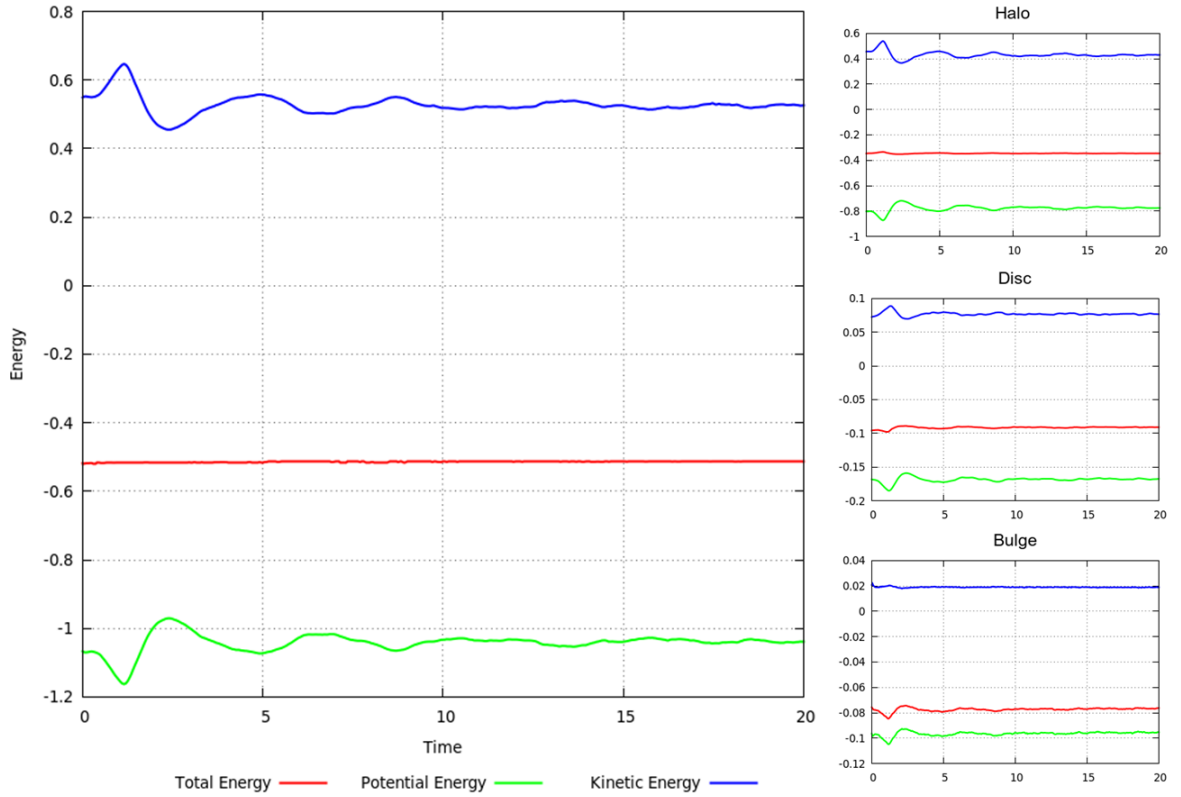


Figure 3.7: The total energy versus time of the unit galaxy created from MASS99. All three components experience an oscillation in kinetic and potential energy while total energy remains conserved.

system's energy is contained in the halo. Several attempts were made to understand where the instability was coming from, including not using a unit galaxy but instead parameters from the examples in the original Hernquist paper (Hernquist, 1993), changing scaling parameters in the Hernquist model formulation, and scaling the velocities of the halo particles. These attempts were not fruitful - some changes enhanced the problem, while others caused the oscillations to flip (expand-collapse-expand as opposed to collapse-expand-collapse). In order to cross validate the implementation of the MASS99 Hernquist model, efforts shifted to other galaxy model generators such as Starscream and NEMO.

Starscream allows us to generate galaxy models based upon the Hernquist model prescription for use with GADGET-2. Using the Starscream libraries to define a galaxy is easy

and straightforward, and the default values in the library yield a galaxy that at first glance is similar to the galaxies generated by MASS99. However, evolving this isolated galaxy with GADGET-2 proved that this was not the case. The default model and slight variants of it yielded galaxies that would rapidly expand and never collapse or come back together. Having not seen the MASS99 galaxies behave in such a way, an attempt was made to match the default conditions used by MASS99 with Starscream in case there was an unknown problem with sample models the software created. The parameters mostly matched between the two codes to create a few different galaxies models, with the exception that Starscream explicitly required a virial velocity for the galaxy, whereas MASS99 computes this value based on the user parameters; a value for the virial velocity was chosen for Starscream that was approximately what MASS99 computed. However, the concentration of the galaxy (the ratio of the disc radius to tidal radius) required to approximately match the physical scales of the galaxies was three magnitudes larger in Starscream. For comparison, most King and Hernquist models use a concentration between 1 and 10. This led to a deeper investigation into the Starscream code as to the source of these discrepancies.

Examination of the Starscream source code offered some explanations on the difficulties of generating models that would work as expected with GADGET-2 and helped identify sources of errors. In the source code, the computation of the disk scale length was split over two lines, but the first line was not terminated properly, so the compiler used, GNU, did not know that the expression was supposed to carry onto the second line. Another error was found in the equations for computing the angular momentum of the disk. The distribution functions for particle positions along the galaxy's radius had discontinuities near its center, although correcting these made no appreciable impact on the galaxy evolution. There did appear to be inconsistencies when determining velocity dispersions in the halo and disc by both using model input parameters to calculate some aspects of the dispersion, and then later recomputing those same input values based on the actual configuration of the galaxy. This should yield similar values, but many tests showed estimates

to be off by a couple orders of magnitude.

While debugging the code, the code’s author was contacted who confirmed that development had effectively ceased, the model was not verified or validated, and no further development would be made. The author does however provide animations of galaxies interacting and not behaving as we have seen, showing that the code once could produce stable galaxies with the right initial conditions or scaling. Attempts were made to use previous releases of the software package, but they did not solve our problems. With the inability to make Starscream work for our unit galaxies, we cannot recommend the current release of the software to be used to generate progenitor galaxies for our pipeline.

Instead of debugging Starscream further, attention shifted to another galaxy model generator, NEMO. The particle configurations generated by NEMO are not written in formats that can be read by MASS99 or GADGET-2. Several years ago NEMO was distributed with codes that aided in file conversion, including to another format that could be read by GADGET-2. Unfortunately, these capabilities have long gone neglected and could not compile with any version of the GNU Compiler Collection (GCC) and documentation is extremely sparse. It is unknown if there is a problem with the source code or the compilers.

Fortunately, the AMUSE¹ project from the Leiden Observatory offers a very powerful astrophysical file translation capability which includes reading and writing to and from NEMO and GADGET-2 file formats (Pelupessy et al., 2013). AMUSE uses Python to rapidly assemble a variety of astrophysics simulations. After some trial and error and bug reporting to the AMUSE developers, AMUSE was able to read the binary NEMO files and write the particle information to a GADGET-2 version 1 snapshot file to serve as initial conditions. AMUSE currently does not support a file format that MASS99 can read, although in the future a GADGET-2 snapshot reader for MASS99 would be easy to implement and would complement its current snapshot writer.

¹The Astrophysical Multi-purpose Software Environment

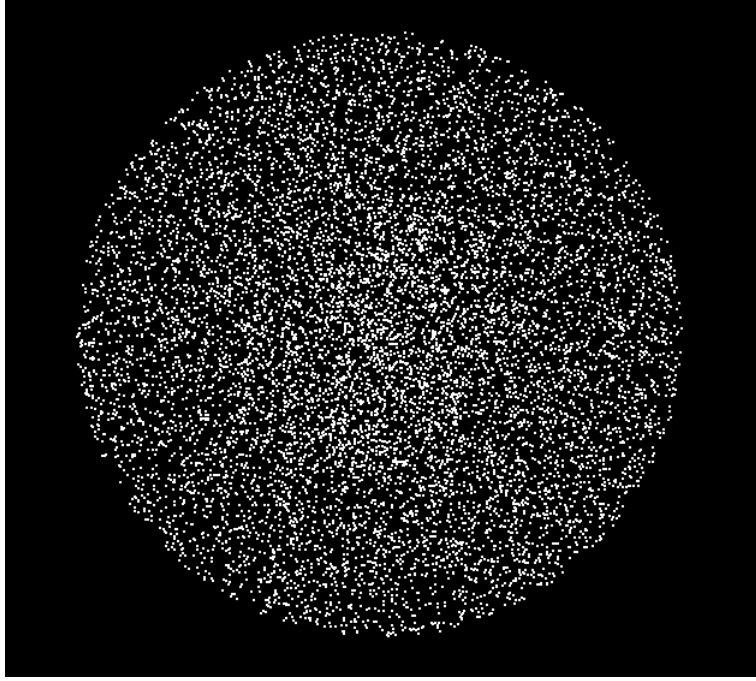


Figure 3.8: NEMO distributes particles uniformly across the disc in a Hernquist model.

To compare the NEMO/magalie Hernquist model implementation to MASS99's implementation, the masses used in the default MASS99 model were scaled to match those defined in NEMO/magalie. Both models were forward integrated in time using the same input decks² for GADGET-2, with the only difference being the binary files providing the initial conditions for the macro-particles of each galaxy. The simulations were evolved to 10 time units, with particle positions and velocities outputted every 0.01 time units, as well as system energy.

Despite using the same parameters to define the galaxy generated by MASS99 and NEMO, the total energy is different for each system, with the MASS99 simulation having approximately 50

Figure 3.10 shows another way of looking at the evolution of the galaxy models by means of a scatter plot. Unlike the other visualizations which show the positions of each

²The input for a GADGET-2 simulation is broken into a parameter file and a particle distribution file. Both simulations used the same parameter files, but different particle distribution files

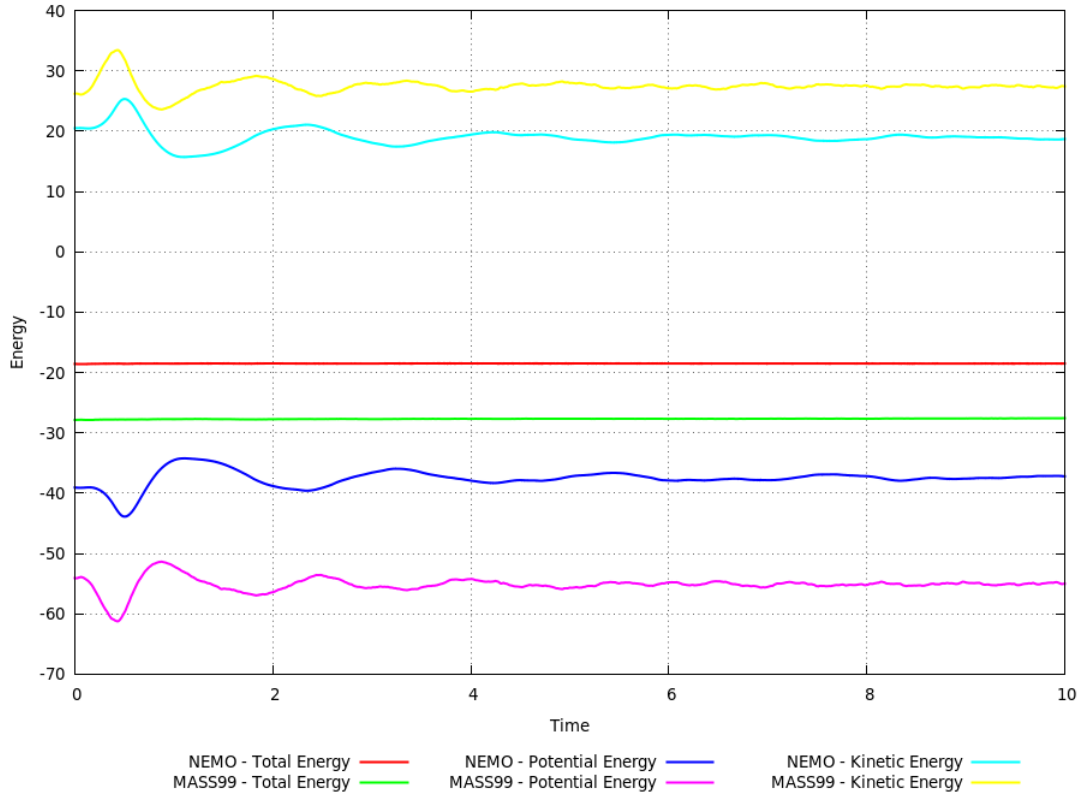


Figure 3.9: The total energy versus time of a Hernquist model implemented in MASS99 and NEMO. Both models use the same size disc and mass of the halo, disc, and bulge.

particle in a cartesian plane, these plots show the position of particles along the radius from their center of masses and the jitter along the Y axis corresponds to the radial velocity. This gives us an indication if particles are coming into or out of the core of the galaxy. Both models exhibit similar behavior, with oscillations appearing in early times in the disc, which corresponds to a bifurcation in the distribution of particles in the halo - many halo particles are fired out of the core, creating a ripple in the halo's density. We believe it is this ripple in the halo at early times that leads to the early instability. Fortunately, when the halo appears to undergo a violent relaxation, the system is able to stabilize.

Further investigations into other galaxy models in MASS99, such as a King Model and several lower isothermal spheres showed similar behavior in which the kinetic and potential energy of the system fluctuates in the early stages of a simulation. Additional changes

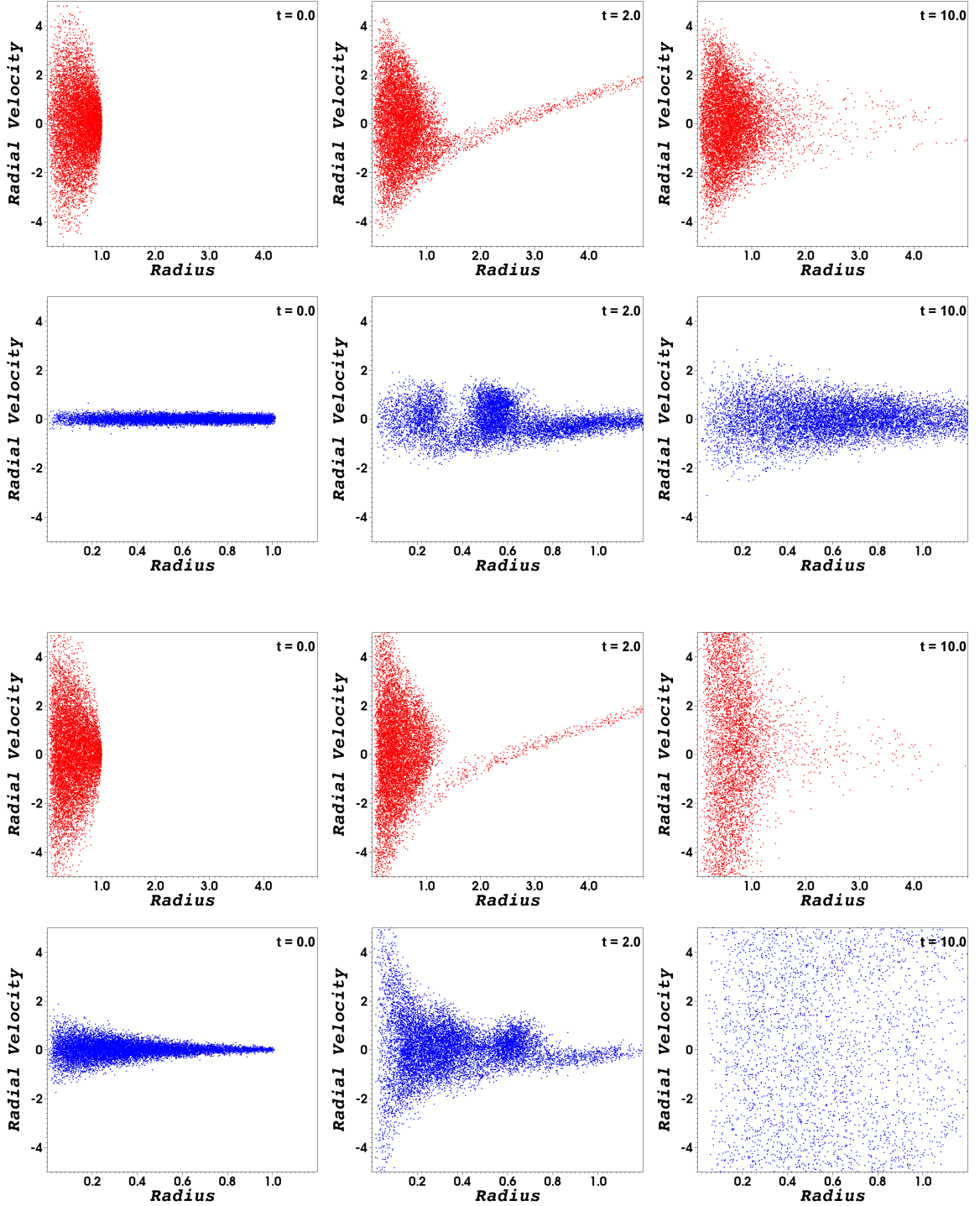


Figure 3.10: Scatter plots of the radial component of velocity versus radius of the NEMO (top two rows) and MASS99 (bottom two rows) galaxy models. Both codes exhibit a strong bifurcation of their halos (blue) early in the simulation as halo particles are ejected from the core, and waves or rings in the discs (red) can be seen at about the same time. The velocity dispersion in NEMO is much less than MASS99 at late time.

to the numerical controls on the N-Body models (such as softening lengths, timestep sizes, error tolerances, particle count, etc.) did not make any appreciable change. The only change that ever seemed to help was distributing the mass of the system over larger radii - the oscillations remained, but their time scales and amplitudes changed. We are surprised that we have not been able to find similar detailed observations in literature, only references to phenomena describing how systems can equilibrate early on, such as through violent relaxation. The original paper by Hernquist describing the formulation of the galaxy makes no reference to the time necessary to equilibrate the system. In fact, our models do appear to agree very well with the images of the galaxy model in that paper. It is possible that a period of time for relaxation of the model is required but was not explicitly captured if the moments in simulation time looked at did not exhibit the oscillations. Our recommendation is to proceed with caution when choosing a progenitor galaxy and its resulting time scales. It is possible that oscillations may occur, making matching the morphology between models and data difficult. If this becomes an problem, the progenitor can always be an already evolved and equilibrated galaxy model. We will show later that oscillations tend be unobserved when tidal forces between two galaxies with reduced masses of 1.0 or less interact.

Chapter 4: Assembling the Pipeline

Up until this point we have discussed much of the process required to develop an N-Body model of a system of interacting galaxies from a state vector of a restricted three-body simulation deemed to be a good match to observational data. If one wants to create the initial N-Body model and declare success, then there is not a need to do much more. However for reasons discussed earlier, such as choosing the right initial conditions, there will be a need to optimize the selection of N-Body model parameters to obtain a better match to the larger observational system or to the morphology displayed in the restricted three-body model. This chapter discusses how we automate the process of building an N-Body model, assess its morphology, and how we automate making model adjustments.

4.1 Determining the Quality of an N-Body Model

A good N-Body model of an actual system of interacting galaxies when projected into the plane of the sky should exhibit a strong similarity in the morphology of the system as well as in the positions of centers of each galaxy. Implicitly, morphology includes overall galaxy size and orientation. Although observational data is what is mostly used to validate a model, the observational data from sky surveys such as SDSS limits our ability to validate or improve upon a model in two dimensions, i.e. along an XY projection. We can determine the redshifts and associated line-of-sight velocities of the galaxies and features within the galaxies using spectroscopic imaging of systems. Although such data is relatively rare for most galaxy interactions, spectrographic imaging surveys such as MaNGA¹

¹The Mapping Nearby Galaxies at Apache Point Observatory (MaNGA) is a sky survey project that will capture spectroscopic measurements across the face of over 10,000 galaxies. Included will be velocity related data of the systems.

are beginning to become available (Bundy, 2015).

In our pipeline, we choose to use the restricted three-body model's output data as a surrogate for observational data. Although purists may find this unsettling, it offers us the ability to match the morphology of a system using well defined positions and velocities in \mathbb{R}^3 space. Another advantage of using a surrogate model for observational data is that our models can offer as much resolution as we have computational resources and time, whereas observational data is limited to the resolution of the sensor used to collect the data. By utilizing higher resolution modeled data than observational data, we are more likely to find a unique solution. Of course, all of this is predicated on the assumption that our restricted-three body model is itself a high quality match to the target system, which must be the case if a restricted three-body model has made it to the N-Body portion of the pipeline. Although nothing precludes the use of observational data as part of the N-Body matching process, our pipeline only explicitly makes use of surrogate data.

We do not want to suggest that there is only one or necessarily a best metric to compute that will judge the quality of fit of our N-Body models to restricted three-body models. Our pipeline makes use of nine different, although related, metrics that utilize spatial positional data only. For each galaxy in the restricted three-body model, we fit a regular grid over its XY, XZ, and YZ projections using the point in time that best matched the observational data (i.e. $t = 0.0$ in SPAM's simulation's point of reference). Figure 4.1 shows the two grids in the XY plane created for a system. In that figure, the grid of the secondary galaxy is significantly smaller than that for the primary galaxy. In the case of a standard two interacting galaxy system, this defines six grids total. The grids have the same logical dimensions, that is they are all of size $N \times N$, where $N = n+1$. The grids only slightly extend past the particle extents, with the grid widths, d , of each spatial dimension, i , being defined by equation 4.1. Of special note, the grids are not centered around the center of masses of each galaxy.

$$d_i = (\max_i - \min_i) * (1 + \frac{1}{n}) \quad (4.1)$$

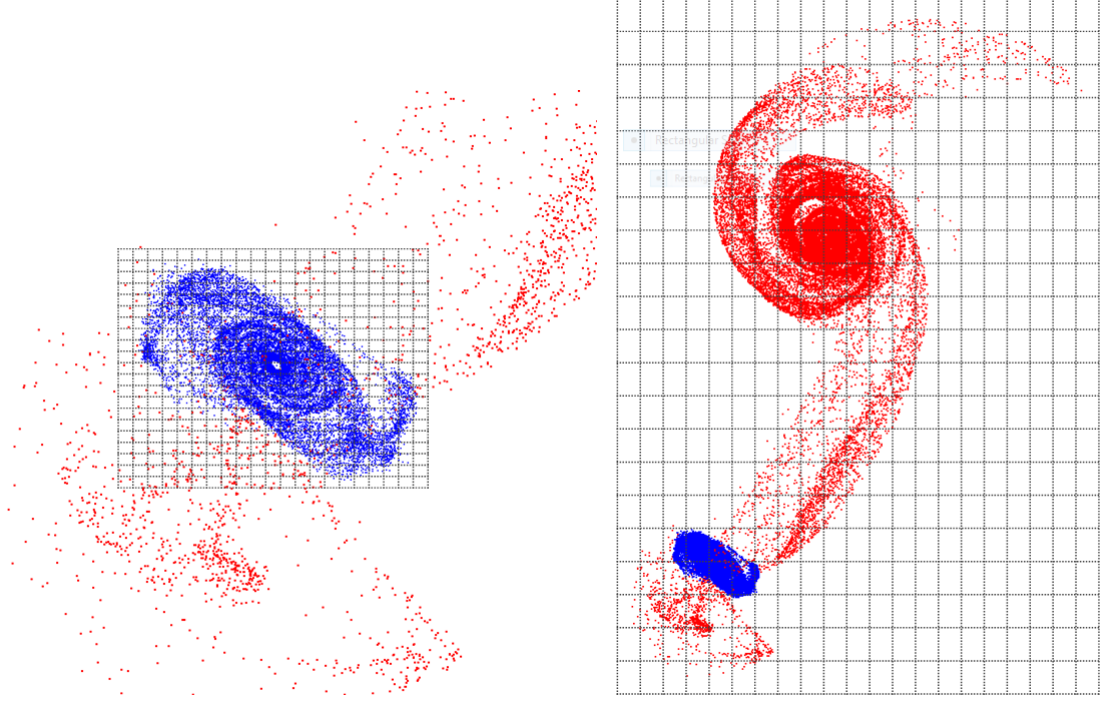


Figure 4.1: A regular grid is placed over each galaxy (red and blue) in the XY, XZ, and YZ projections. Particles belonging to a galaxy are only represented in the particular grid associated with that galaxy. The dimensionality of each grid is the same, even if its spatial size differs.

For each grid that covers a galaxy and projection plane, we count the number of particles only from the galaxy the grid belongs to from the restricted three-body model in each cell or bin. The counts are then normalized, giving us the fraction of particles of the galaxy within each bin. By using a relatively small value for N , we keep these grids small and fast to compute. However, by utilizing projections from these three orthogonal planes, we are able to capture morphology by sampling data within a three-dimensional cube. This is substantially faster than creating a three-dimensional, regular grid over each galaxy (or the system) and avoids issues of oversampling in areas where there are few particles.

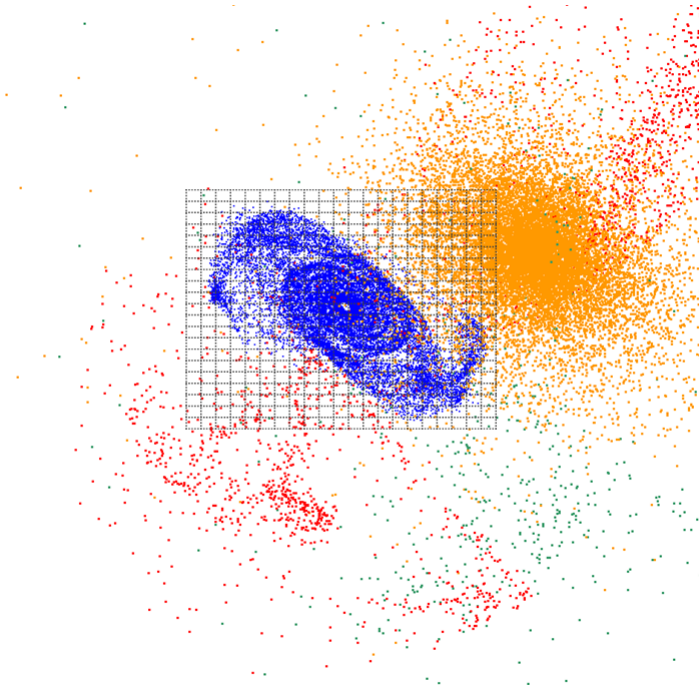
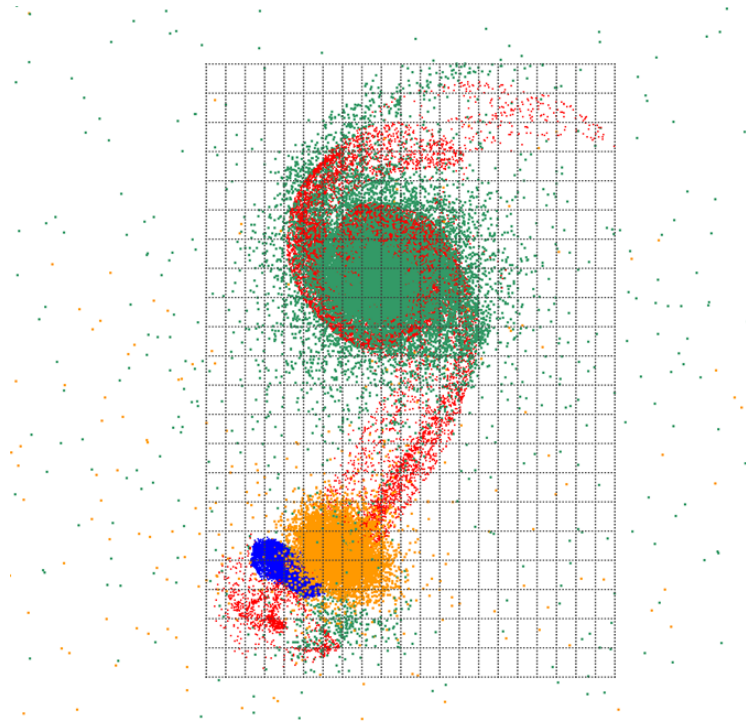


Figure 4.2: The regular grids over the primary galaxy of the restricted three-body simulation (red) will typically encompass most of the primary galaxy of the N-Body simulation (green). However, this may not be the case with the secondary galaxies of the restricted three body and N-Body simulations (blue and orange).

After counting particles from the restricted three-body simulation, the positions of the galaxies from a candidate N-Body simulation are displaced such that the center of masses of the primary galaxies are in the same location. In SPAM, the center of mass of the primary galaxy is always at the origin, so displacing the N-Body simulation only requires the calculation of the center of mass of its primary galaxy. Without changing the original grids, we bin the visible² particles of each galaxy in the N-Body simulations and normalize the counts by the total number of visible particles belonging to each galaxy. As seen in figure 4.2, generally the grid for the primary galaxy will encompass most of the visible N-Body particles from its primary galaxy. However, unless the trajectories of the secondary galaxy are a very good match, a significant number of the secondary galaxy's particles may be outside its grid.

Although the bins of a grid are all equal in size, we do not treat them with the same importance. This is largely because the exact ends of the tails of tidal features have the most uncertainty in any model. We want to have as best possible agreement with the tails to help guide us towards the best or optimal N-Body model, but we do not want to try as hard as getting the locations of the galaxies correct. As such, we introduce a weighting of each cell of a grid in the form:

$$w_{i,j} = \frac{1}{\sqrt{(i - (N - 1)/2)^2 + (j - (N - 1)/2)^2 + 1}} \quad (4.2)$$

where the cells are indexed by i and j . We can also provide a weight for all particles that fell outside the grids by defining a special weight:

$$w_o = \frac{1}{\sqrt{(-1 - (N - 1)/2)^2 + (-1 - (N - 1)/2)^2 + 1}} \quad (4.3)$$

Now we can compute metrics based on a weighted l_2 -norm for each of the six grids by

²we consider all particles except for those belonging to the dark matter halo to be visible

way of:

$$M_{p,g} = \sqrt{w_o \left(1 - \frac{\sum_{i,j} G_{i,j}}{G_{total}}\right)^2 + \sum_{i,j} w_{i,j} (S_{i,j} - G_{i,j})^2} \quad (4.4)$$

where a metric $M_{p,g}$ is defined for each plane p and galaxy g using the counts in bins S from our restricted three-body model, bins G from our N-Body model, and G_{total} is the total number of particles in a galaxy. Three more metrics can be defined by taking vector norms of these six grid based metrics, as:

$$M_1 = \sqrt{M_{xy,1}^2 + M_{xz,1}^2 + M_{yz,1}^2} \quad (4.5)$$

$$M_2 = \sqrt{M_{xy,2}^2 + M_{xz,2}^2 + M_{yz,2}^2} \quad (4.6)$$

$$M_{system} = \sqrt{M_1^2 + M_2^2} \quad (4.7)$$

In each of the metrics, the lowest value is best (this corresponds to less deviation between the target and simulation). In our pipeline, we will focus primarily on metric M_2 which captures the morphology and location of the secondary galaxy. In general, metric M_1 and the other metrics corresponding to the primary galaxy are not that suggestive on the quality of our N-Body model to fit to surrogate data. That is primarily because the center of mass of the primary galaxy is adjusted such that it is at the origin in both simulations. The metrics will compute a strong fit so long as a significant amount of the galaxy's mass is near that point. There are occasions, however, where fitting a model to the primary galaxy is most important, in which case the user can select one of its metrics to use. For the secondary galaxy, its metrics tend to provide a very good indication of both its morphology and position. Although the last metric can provide a good match to the overall system, in

most experiments we have seen the same best N-Body model found using metrics M_2 and M_{system} . Due to the increased sensitivity of M_2 , any determinations of best N-Body models mentioned in this dissertation will be based on this metric unless otherwise specified.

4.2 Finding Optimal N-Body Models

Our pipeline to find optimal matches of an N-Body simulation to observational data or surrogate data requires a way to automatically explore the space of model parameters. Equipped with several different metrics to compute the goodness of fit, we can evaluate how any one of those values change as model parameters change. If the restricted three-body models provided to the N-Body portion of the pipeline does not come with a target dataset to match against, we re-run SPAM and save its configuration of massless particles at $t = 0$ to become our surrogate dataset.

To find an optimal N-Body model, we begin by defining the function $f(\ln\Lambda)$ in which the best metric value is returned for the value of dynamical friction used to generate an N-Body simulation. We search for the best use of dynamical friction by using Newton's method (equation 4.8) to find the minimum of the function.

$$\ln\Lambda_{n+1} = \ln\Lambda_n - \epsilon \frac{f'(\ln\Lambda_n)}{f''(\ln\Lambda_n)} \quad (4.8)$$

For each iteration of Newton's method, we make four perturbations to the current n -th value of dynamical friction, where the perturbations correspond to $\pm h$ & $\pm 2h$, where $h = 0.001$, and $\epsilon = 0.0001$. This provides five different sets of initial conditions to use to build different N-Body models to evaluate. After each N-Body simulation is completed, our metrics are evaluated at every output dump. This allows us to see how well the N-Body simulation matches the target dataset over time. Although all metrics are computed, we must choose one. By default, we use the metric corresponding to the overall quality

of fit of three spatial projections of the secondary galaxy. For each simulation, we record the smallest value of the metric and the time at which it occurred. This means that the resolution of our best metric value and its corresponding time is limited to the frequency at which simulation snapshots are saved to disc. By default, we have set our N-Body simulations to save the particle distributions 101 times during the simulation (they are saved at equal intervals).

Having computed a metric at five different values of dynamical friction, we can update equation 4.8 with second order, central finite-difference approximations to the derivatives. This allows us to explore the space around a another value of dynamical friction until we have converged upon a solution or too many iterations have been used (defined by the user). During experimentation, we found that the method would continue to refine dynamical friction to 10 or more decimal places. To speed up determination of an optimal choice of dynamical friction, we limited the smallest change (i.e. the step size) in dynamical friction to $1e-5$. This speeds up our optimization process by often having to evaluate stencils using values of dynamical friction of which a model was already created. We take advantage of this fact by writing a file containing the values of all metrics computed within the folder each N-Body model is run from. If the optimization method finds this file, It knows it does not need to rerun that particular N-Body model. We also do not allow dynamical friction to become negative. If the points in the finite difference stencils go negative, we reduce the width from h to $h/2$ to avoid this from happening. By limited the step size and reusing past simulations, we can fairly efficiently use a small number of Newton Method iterations (typically 10 or less).

Once our Newton Method has converged to a solution or reached the maximum number of iterations, we scan the function $f(\ln\Lambda)$ evaluations for the minimum value. We do this just in case the last value evaluated by the method was not in fact the smallest value. Alternatively, we could have sampled uniformly across the function $f(\ln\Lambda)$ and used Newton's Method and interpolation on that. We choose not to do so for three reasons. First,

sampling the parameter space is likely to be more exhaustive and therefore computationally intensive than more intelligently searching for the best value from the beginning. Second, although we are making an assumption that our function is smoothly varying, it may not actually be. Although the resulting plot of our metric versus dynamical friction may appear smooth, it is possible that the time corresponding to the metric for different dynamical friction values can vary. This is particularly true for metrics belonging to the secondary galaxy if it is located on opposite sides of its target during a simulation. This does not always happen, but sometimes does. Lastly, although this implementation of Newton’s Method focused solely on dynamical friction, the methodology can be extended to change any number of parameters. Newton’s Method for higher dimensionality of functions is much more efficient than sampling over each dimension parametrically.

4.3 Simulation Size

Generally with N-Body models, the more particles that are run, the greater the resolution of the resulting simulation. Although true, there is a point at which we see little return on computational investment in the ability of our N-Body models to provide an improvement in matching the positions or trajectories of galaxies and their morphology. While many users of N-Body models will often try to push the number of particles run into the tens of millions to billions, we see in figure 4.3 that as little as 30,000 particles split between both galaxies is sufficient to match trajectories. In our simulations, we default to 50,000 particles total for each system. This is the same number of particles used by Holincheck as part of the earlier pipeline in the SPAM simulations. Additional particles will help with visualization of discs to make potentially easier qualitative comparisons between our N-Body models and observational data, but given the coarseness of the bins in our morphology matching algorithm and weighting, this number of particles should make the same fitness determination using 50,000 particles as 50,000,000 particles.

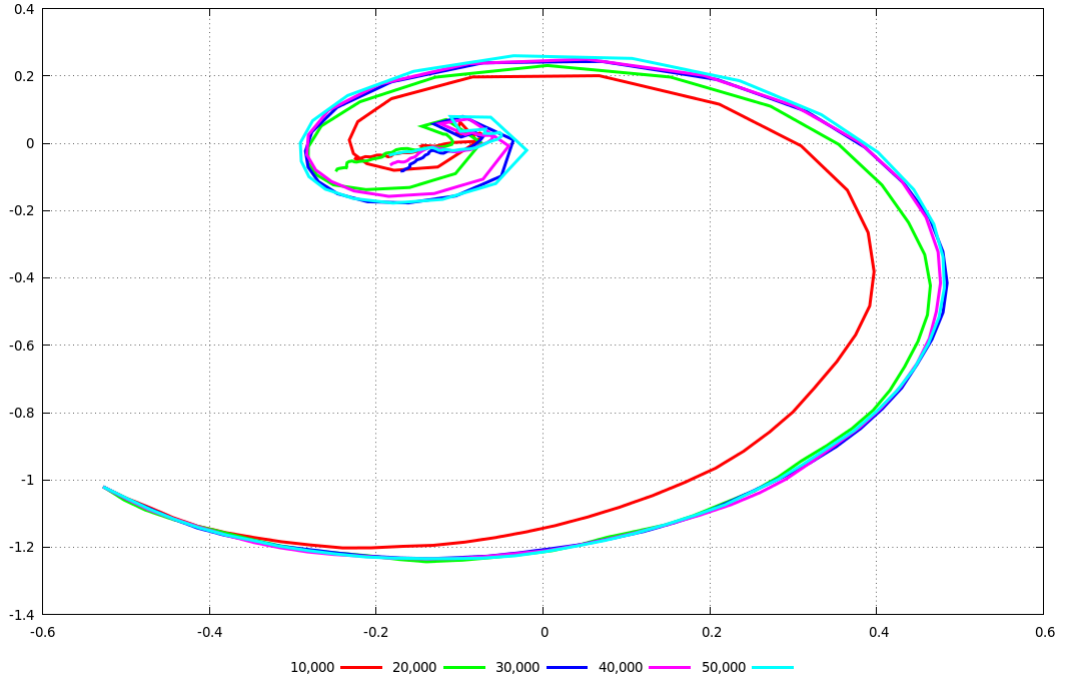


Figure 4.3: The relative trajectories of a pair of interacting galaxies begin to converge on each other for simulation sizes of 30,000 particles.

4.4 MASS99 to GADGET-2 Comparisons

During development of our pipeline for creating N-Body models from restricted three-body models, there were some difficulties regarding energy conservation (discussed earlier) and scalability. To investigate the source of these problems, we turned to another N-Body code, GADGET-2, to see if it exhibited any of the same problems. As it turned out, any issues we had mapping a restricted three-body model to MASS99 or unexpected behavior in the evolution of a galaxy manifested in GADGET-2 too; both MASS99 and GADGET-2 behave very similarly, predicting the same features, good and bad, at the same time in a simulation. As can be seen in figure 4.4, MASS99 and GADGET-2 can reproduce the same morphology and trajectories (as seen in the match of locations in space) of a system of interacting galaxies. The simulations are not exactly the same as they both

use slightly different approximations to the gravitational potential from far away particles, time integration schemes, and softening lengths. However, from our experience, GADGET-2 offered better strong and weak scalability than MASS99, despite our enhancements to support hybrid OpenMP/MPI parallelization in MASS99.

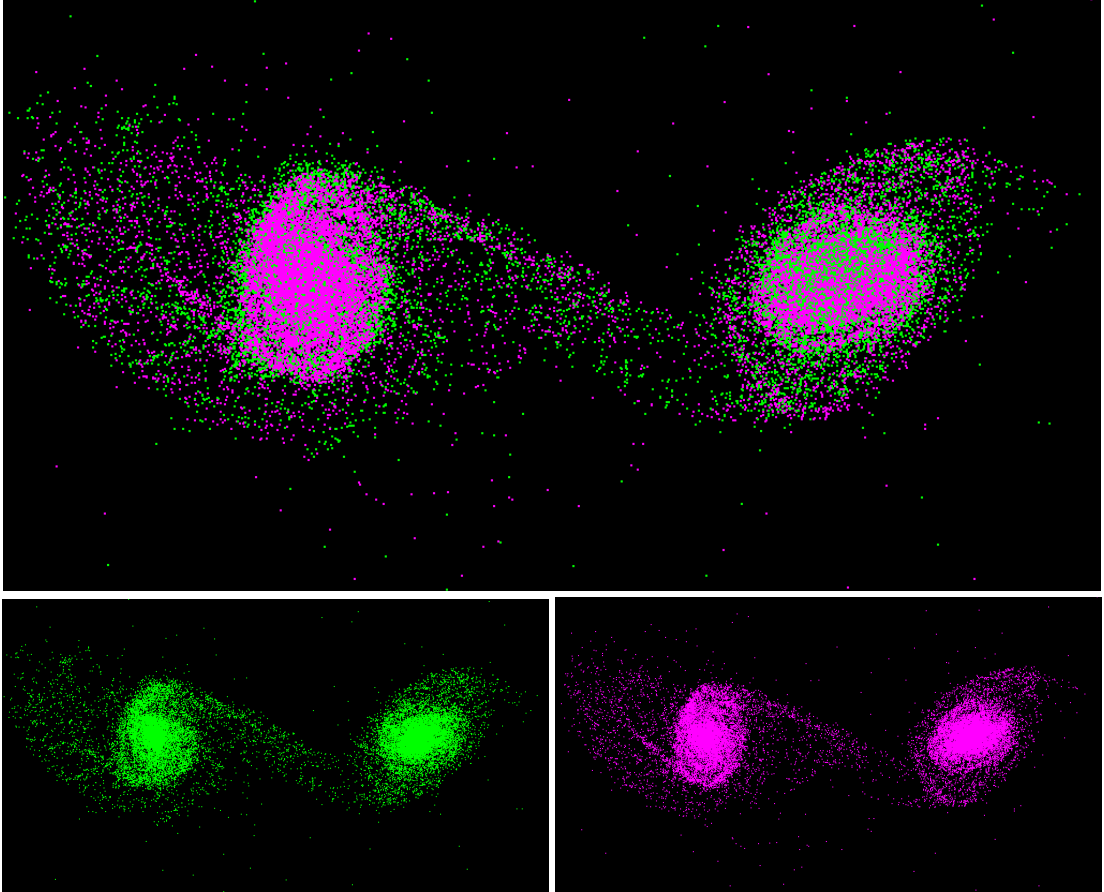


Figure 4.4: Arp 240 as modeled to the same point in time using GADGET-2 (green) and MASS99 (magenta). Both codes evolve the galaxies more or less the same, with small differences in their morphologies, although both exhibit tidal features and a galactic bridge.

Given the substantially larger user community of GADGET-2, we decided to build native support for GADGET-2 in our pipeline. MASS99 support is also provided because it can be used to construct progenitor galaxies and adding or modifying physics in it is

much more streamlined than it is in GADGET-2. All simulation results presented in this dissertation are based on using GADGET-2 as the N-Body propagator unless otherwise noted.

Whereas MASS99 provided support tools to create, scale, displace, and merge galaxies, GADGET-2 did not. This required the development of complimentary tools for GADGET-2 models to be used by our pipeline.

4.4.1 GADGET-2 Snapshot Toolbox

Python was chosen to implement an easy to use core library of functions that could be used to read, write, and manipulate GADGET-2 Snapshot Version 2.0 files. The use of a scripting language allows us to easily and rapidly construct programs like those already available for MASS99 (to include *gadget2_scaler.py*, *gadget2_displacer.py*, & *gadget2_merger.py*) and develop custom analysis tools. By not having to be compiled, this code is easy for others to make modifications to support additional needs and requirements, and it increases portability. The object oriented nature of Python allows us to treat the Snapshot formatted file as an object that we can load into memory and easily manipulate just as we would a compiled code. This core library, *snapshot.py* has the following methods available:

load(filename) - loads a GADGET-2 snapshot version 2.0 file

center - calculates and returns the center of mass and velocity of the system

centerN(N) - calculates and returns the center of mass and velocity of the Nth galaxy in the system

mass - returns the mass of the system

massN(N) - returns the mass of the Nth galaxy in the system

toCenter - displaces the system to its center of mass

store - store the current state of the model to a new GADGET-2 snapshot version 2.0 file

dump(filename) - store the positions, velocities, mass, and particle identification number to a space delimited ascii file

rotate(θ, ϕ, ψ) - rotate the system by three Euler angles

scaleMass(M) - scale the mass of the system by M

scaleRadius(R) - scale the distance of the system by R

displace(X, Y, Z) - displace the system in cartesian space by X, Y, and Z amounts

displaceVelocity(U, V, W) - displace the system's velocities by U, V, and W amounts

merge(G) - merge the current model with another GADGET-2 model, G

4.5 Pipeline Execution

Our restricted three-body to N-Body pipeline prototype has been automated with a series of Perl and Python scripts and has been tested in Linux environments on personal computers and high performance clusters. In general, we use Python scripts for portions of the pipeline that may need to use our GADGET-2 toolbox written in Python, and we use Perl for all other portions. Had development of our pipeline begun with the consideration for using GADGET-2, we may have not used Perl at all and gone entirely with Python. There are four main scripts that enable our process: *optimizeDF.py*, *runController.pl*, *bestMatch.pl*, and *morphologyChecker.py*.

4.5.1 N-Body Optimizer - *optimizeDF.py*

This script handles and runs the entire optimization process. It begins by receiving a state vector from a restricted three-body model (in our prototype, this is SPAM). If a target data

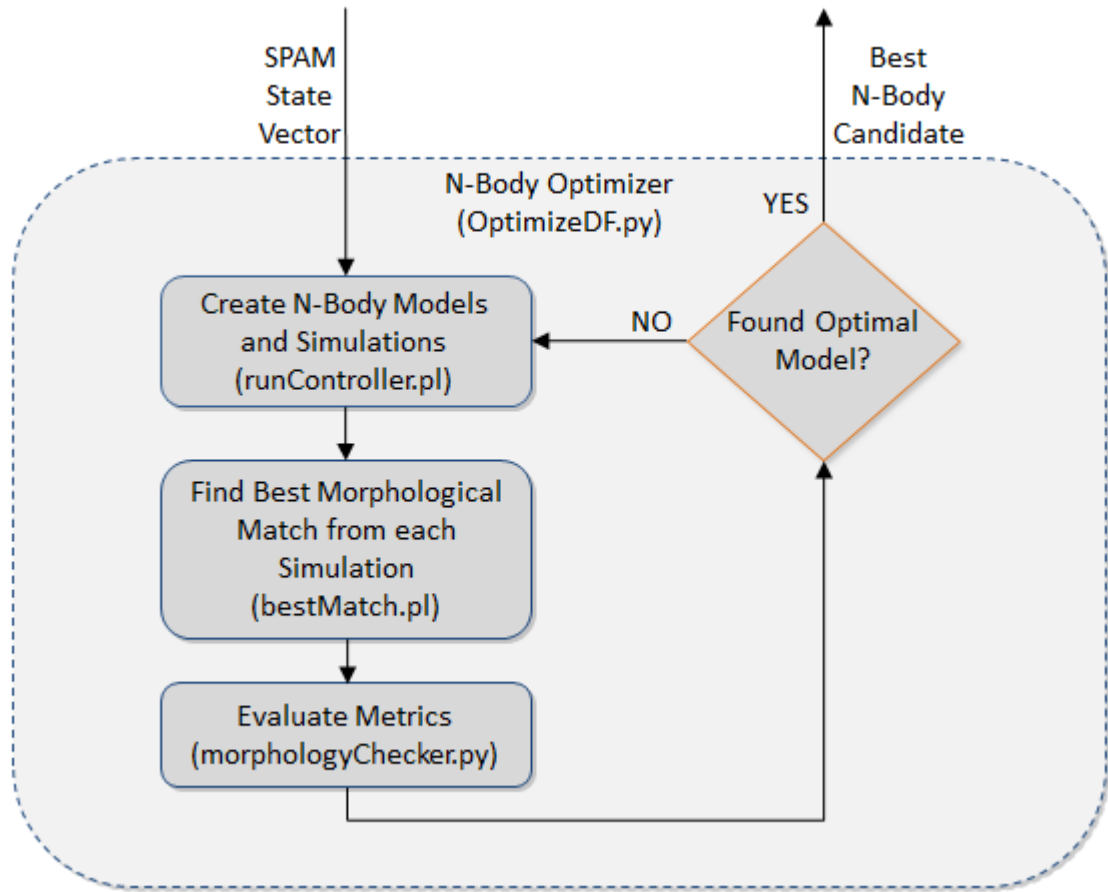


Figure 4.5: A series of Perl and Python scripts are used to automate our pipeline that starts with a restricted three-body state vector and determines the best N-Body model that matches it.

file to use for matching is not provided, SPAM backwards and forwards integrates this state vector’s model to have a dataset with massless particles that capture the morphology of the system. The script also determines variations of dynamical friction to use, creating four additional state vectors. Each of the five state vectors are sent to another script, *runController.pl* where N-Body models will be created, simulated, and best metrics reported. With the metrics received, the code determines if it has converged on a good match to the surrogate data defined by the original restricted three-body model. If it has not, new simulations are created and this inner loop continues. If it has, then it returns (by writing to a

file), which value of dynamical friction led to the best match.

This optimization routine allows the user to specify whether or not GADGET-2 or MASS99 should be used for the optimization process. It also allows the user to specify the size convergence criteria, step size when changing dynamical friction, and whether or not a precomputed progenitor galaxy model should be used. By default, we use a step size of $1e-3$, convergence criteria of $1e-5$, and allow MASS99 to create progenitor galaxies on the fly. The user must also identify which metric should be used to determine when an N-Body model is a good enough fit to a target dataset.

4.5.2 Creating N-Body Models - *runController.pl*

This script is responsible for creating simulations in SPAM, MASS99, and GADGET-2. It reads another script, *settings.pl*, which contains default values for an arbitrary interacting galaxy model simulation (this script simply loads default values for many parameters). Included are all the parameters that define a restricted three-body state vector: whether the simulations should be used in parallel or not (and optionally what mode should be used, such as OpenMP, MPI, or Hybrid), number of threads to use, the number of particles for the system, and the starting and ending times of the simulation. Most of these settings can be overridden by command line arguments, particularly by providing a state vector in the form of a comma separated list to the argument *runstring*. The tool to use for the simulation, SPAM, GADGET-2, or MASS99 must be specified as a command line argument.

If instructed to create an N-Body model for simulation, should it require starting earlier in time as specified by the user, a modified version of SPAM is run that returns the state vector corresponding to that time after backwards integration is complete. If it requires starting earlier in time but that time is not defined, then it will do so in the same manner SPAM was backwards integrated in the Merger Wars activity. *RunController.pl* will create a progenitor galaxy using MASS99 unless one is specified in a command line

argument. After such a model becomes available, it calls either the MASS99 or newly developed GADGET-2 support codes to scale, rotate, and displace it. A second galaxy model is made available in a similar way, and then combined with the first galaxy. The code then uses another script containing functions to create the input file for the corresponding N-Body model. Lastly, the N-Body simulation is started using any parallelization options specified by the user.

4.5.3 Finding Best Matches between Simulations - *bestMatch.pl*

After each simulation is completed, *bestMatch.pl* is used to help determine the metrics discussed earlier that evaluate how well a simulation matches another dataset. It's main use is to automate calls to another script, *morphologyChecker.py*, by providing it with each simulation output dump file. When complete, this script writes a data file containing every metric evaluated for each dump file. Each copy of this file created from each simulation is made available to the overall optimization routine for it to pick which which metric the user wants to focus on.

4.5.4 Evaluating Morphology - *morphologyChecker.py*

The final script in the N-Body portion of our pipeline receives a target simulation output file from SPAM, the number of particles in the primary and secondary galaxy (necessary to properly parse the SPAM output file), and an output file from an N-Body simulation to evaluate. Metrics are computed in accordance to the methodology discussed earlier in this chapter. Once computed, they are returned to the script that invoked this one.

4.6 Set of Interacting Galaxies

The proposed pipeline in this dissertation has been tested with 54 systems of interacting galaxies observed as part of the Sloan Digital Sky Survey. These systems were among

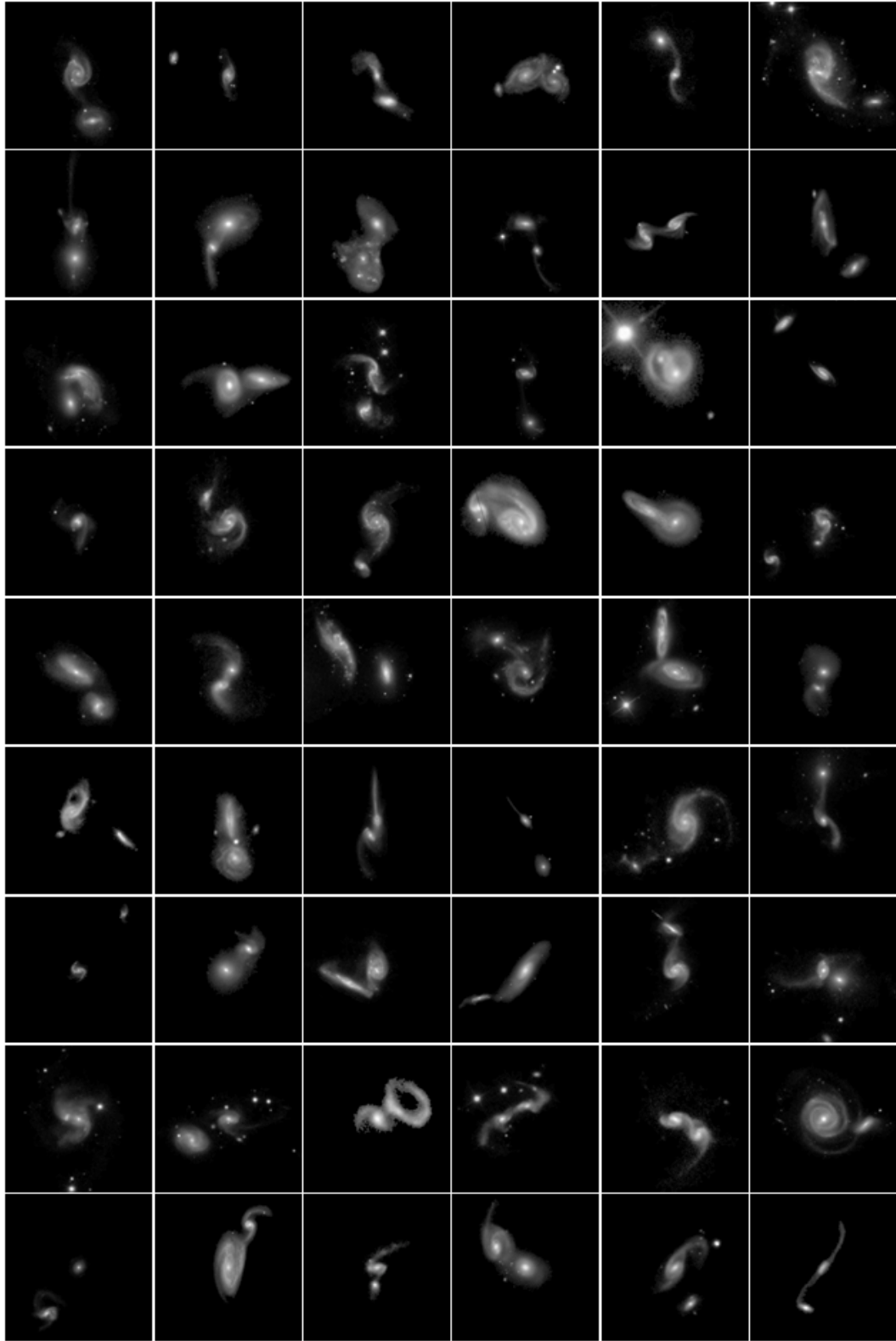


Figure 4.6: 54 galaxies from the SDSS with restricted three-body models created with SPAM by Holincheck for use in our pipeline.

62 systems studied by Holincheck in development of his pipeline to find high quality restricted three-body models. The eight systems we have not included here came from the Hubble Space Telescope's catalog "Galaxies Gone Wild!" (Evans, 2008). When developing the restricted three-body models for all of these systems, these eight systems did not have as detailed spectroscopic data compared to those from the SDSS. The 54 systems and their associated N-Body models still represent a significantly larger set of real systems to be studied than has appeared in any other publication to date.

The SPAM code and citizen scientists were instrumental in determining model parameters for interacting galaxies. Merger Wars was a citizen science project under the Galaxy Zoo (an NSF funded project) in which people would successively pick between two candidate final configurations of galaxy models simulated with SPAM to determine which one best matched the target configuration. After hundreds of thousands of runs were computed (an average of 50,000+ models were run for each system), a state vector for each system was saved and cataloged in accordance with the pipeline seen in figures 1.3 & 1.4. This was a substantial component to restricted three-body modeling portion of the pipelines by Holincheck and the one presented in this dissertation. These state vectors containing the mass and sizes of the galaxies, as well as their disc orientations, relative displacement and speed between one another, and dynamical friction value used, were made available for the study that this dissertation describes before Holincheck's work was published.

4.7 Computational Resources

The computational requirements for running many N-Body models do not come cheaply. With hundreds to hundreds of thousands of potential interacting galaxy systems to study in the future, a single typical PC is inadequate if one wants results in a timely manner, although it is fine for studying a just a few systems. In this dissertation, our study of 54 systems from Holincheck's dissertation has required the use of multiple computing

clusters that have allowed us to learn what strategies work well in our pipeline. During its development, tens of thousands of N-Body simulations were conducted.

The two biggest factors for consideration when studying many systems with N-Body simulations are CPU runtime and data storage. For example, consider an N-Body tree code with 100,000 particles spread between halos, discs, and bulges. These simulations can take between 30 minutes and several hours on an Intel i7 Ivory Bridge quad core processor using OpenMP to achieve some degree of parallelization in a code such as MASS99 or GADGET-2. The time largely depends on the strength of the interaction between the galaxies in the simulation. For comparison, a restricted three-body model using just gravity with 100,000 tracer particles can take just a few seconds. To explore 50+ two-body systems and search for optimal initial conditions of the systems to achieve the greatest agreement with observable or surrogate data would require hundreds of hours on the same computer. Should greater resolution in morphology be required thereby increasing the number of particles into the millions or billions, the runtime demands will soar. Run times will also increase as additional physics are used, such as gas dynamics and star formation. As all these simulations are taking place, data files are written periodically. Because the pipeline inspects the data files after a simulation has completed, all data files must be saved until that time. Even after inspection, data files may still be needed for visualization or to investigate behavior that changed as system parameters changed. Again, take for example a single GADGET-2 simulation of one million particles that produces output files on the order of 50 megabytes. Determining the point at which a system best aligns to our data requires on the order of 100 output dumps, or at least 5 gigabytes per simulation. If multiple simulations are needed to find an optimal model, potentially hundreds of gigabytes of storage would be needed. With more physics and particles, this increases even more. It is not unreasonable to expect hundreds of systems to easily consume many terabytes of storage. Of course data storage can be recovered by removing simulations corresponding to poor models.

Higher fidelity simulations than the ones used in this dissertation will likely require several times more particles than we have used and running them on a single computational node will be infeasible, both from a data storage and a processing perspective. Therefore, high performance computing must be considered when using an N-Body pipeline, particularly in the form of clusters. Another challenge with producing many simulations with their data storage requirements is having access to the data afterwards for analysis and visualization. Even with today's high speed broad band internet access, it is not reasonable to transfer hundreds of gigabytes on a daily basis to desktops and workstations, be it due to network latency, quality of service, or data throttling. To mitigate this problem, the Department of Energy's client/server visualization program *VisIt*, has been our preferred data analysis and visualization solution. This allows data to be processed on the remote systems and only the visualizations and processed data need to be transferred over a network.

During the development of this pipeline, several clusters were utilized for simulation and analysis. We detail the characteristics of the systems below.

4.7.1 Garnet

Garnet is a Cray XE6, 1260 node, distributed memory cluster at the United States Army Engineering, Research, and Development Center in Vicksburg, Mississippi, made operational in early 2012. It consists of AMD Opteron 64-bit 16-Core CPUs running at 2.5 GHz. Each node has two such processors and 64 gigabytes of memory, giving it an actual maximum processing capability of 403 teraflops. Access to the machine was generously provided by the Department of Defense High Performance Computing Modernization Program and The Defense Threat Reduction Agency (DTRA). Use of the equipment was contingent on maintaining affiliation with DTRA through my employment with TASC, Inc. (now owned by Engility Corporation). Due to the extensive user community of the cluster, simulations could only be few in number and utilize 128 nodes or fewer to maintain an acceptable

return of submitted jobs. This system allowed us to experiment with ways to determine good initial conditions applicable for a variety of interacting galaxy systems.

4.7.2 Diamond

Diamond is a 1920 node, distributed memory cluster at the United States Army Engineering, Research, and Development Center in Vicksburg, Mississippi, made operational in 2012. It consists of Intel Xeon Nehalem-EP -4-Core CPUs running at 2.8 Ghz. Each node has two such processors and 48 gigabytes of memory, giving it an actual maximum processing capability of 172 teraflops. Access to the machine was generously provided by the Department of Defense High Performance Computing Modernization Program and The Defense Threat Reduction Agency (DTRA). Use of the equipment was contingent on maintaining affiliation with DTRA through my employment with TASC, Inc. (now owned by Engility Corporation). Due to the extensive user community of the cluster, simulations could only be few in number and utilize 128 nodes or fewer to maintain an acceptable return of submitted jobs. Like Garnet, Diamond played a crucial role during the early development of our pipeline by allowing several different approaches to matching morphology and positions of galaxies in the systems modeled.

4.7.3 Babbage

Babbage is a 40 node, distributed memory cluster using dual AMD Opteron 6134 Processors per node, with a theoretical processing ability of 11.7 teraflops at Middle Tennessee State University. Each node is capable of 16 simulation threads. While the system was under construction and coming on-line, the MASS99 code was used to understand the initial impact of dynamical friction on choosing optimal starting configurations for the 54 galaxy pairs. This activity played an important role in defining the policies and capabilities of the system. Once Babbage became fully operational, fine tuning of our pipeline and final results were all computed on this system. Although Babbage is a much smaller system than

Diamond and Garnet, its smaller set of users meant that we could have access to larger number of nodes more quickly than we could have on the larger systems with many times more users.

Chapter 5: Simulation Results

In this Chapter we present the simulation results for each of the 54 systems modeled. We then discuss the overall effectiveness of the pipeline approach and differences seen between the restricted three-body simulations and N-Body simulations.

5.1 Results for each Pair of Galaxies

In the next 54 subsections of this Chapter, each of the SDSS targets from the Merger Wars project is presented. We begin each section with a quick discussion of the key findings of the N-Body simulations with optimized dynamical friction and a series of tables describing the system. Next we show projections of the restricted three-body simulation and both the initial N-Body simulation and the final N-Body simulation with optimized dynamical friction informing its initial conditions. A target image to match provided by Merger Wars is also presented. We then show a plot of the line of sight velocity from the SPAM simulation and both N-Body simulations, followed by a table of the orbital parameters at the time of the best match to observational data and the SPAM simulation respectively. Each section ends with plots of the trajectories of the simulations and plots of the various metrics used to determine the best N-Body simulation.

Although this chapter is very dense with figures and plots traditionally saved for an appendix, most of the systems modeled exhibit unique qualities and issues that must be recognized to support the broader discussion of the effectiveness of our pipelined approach of modeling systems of interacting galaxies with N-Body simulations. The overall quality of N-Body simulations and number of good matches to our targets will show that it is possible to model many systems with our approach.

5.1.1 SDSS 587722984435351614 (Arp 240)

Each subsection in this chapter is labeled with the primary name of the target system as identified by the Sloan Digital Sky Survey and its more common astronomical name if available. Each subsection begins with a brief discussion of the major findings of the simulation results. In this subsection, Arp 240 shows a very good qualitative fit to both the SPAM simulation and observed image. The galaxies appear better connected in the N-Body simulations than in the SPAM simulation; in the restricted three-body simulation, the connecting tails are easily distinguishable. However, given the criteria in which SPAM applies dynamical friction, the two galaxies do not interact closely enough to cause its treatment to take effect, therefore this system as modeled with SPAM does not vary when adjusting the dynamical friction scalar. Furthermore, the system appears to be in a hyperbolic orbit.

The three part table that follows contains information about the system. The first part contains the system's name, any aliases from other catalogs, the right ascension, declination, and redshift. The second part contains the relative position and velocity of the secondary galaxy in the system as determined by the Merger Wars effort, the subject of another dissertation (Holincheck, 2013). The third and final part of the table lists the mass of each galaxy (this includes the halo, bulge, and disk), radius of the disk, the disc orientation (defined by angles ϕ and θ), and softening length ϵ as determined by the Merger Wars effort too.

Table 5.1: Identification Information and Merger Zoo summary for SDSS 587722984435351614.

Name	Aliases	RA (hms)	Dec (dms)	Redshift
SDSS 587722984435351614	Arp 240, NGC 5257/5258	13:39:52.8	+0:50:23.4	0.022676

R_x	R_y	R_z	V_x	V_y	V_z
-9.93853	-4.5805	15.43348	-1.54025	-2.97899	4.69234

	Primary Galaxy	Secondary Galaxy
mass	34.41671	29.49607
radius	2.97913	4.2501
ϕ	301.0°	35.5°
θ	310.80745°	321.98757°
ϵ	0.3	0.3

The rest of the subsection shows a series of figures taken from the simulations. The first figures are presented in a quad format showing the target system as retrieved by the SDSS in the upper left, the best matching SPAM simulation (which always occurs at the half way mark in its simulation) in the upper right, the initial N-Body simulation in the lower left, and lastly the N-Body simulation using the optimal value for dynamical friction as determined by our pipeline approach in the lower right. Each of the SPAM simulations used 50,000 particles for their systems to capture the appearance of the disc while the N-Body simulations used the same number of particles, but they were split across the halo, bulge, and disc. As such, the N-Body simulations may have similar tidal features as the SPAM simulations, but they will appear much less dense due to fewer particles available for the visualization. The N-Body simulations are only visualizing the particles belonging to the disc and bulge. Furthermore, the N-Body simulations are viewed at the point in time that the optimization methodology finds the simulation to be in best agreement with the SPAM simulation.

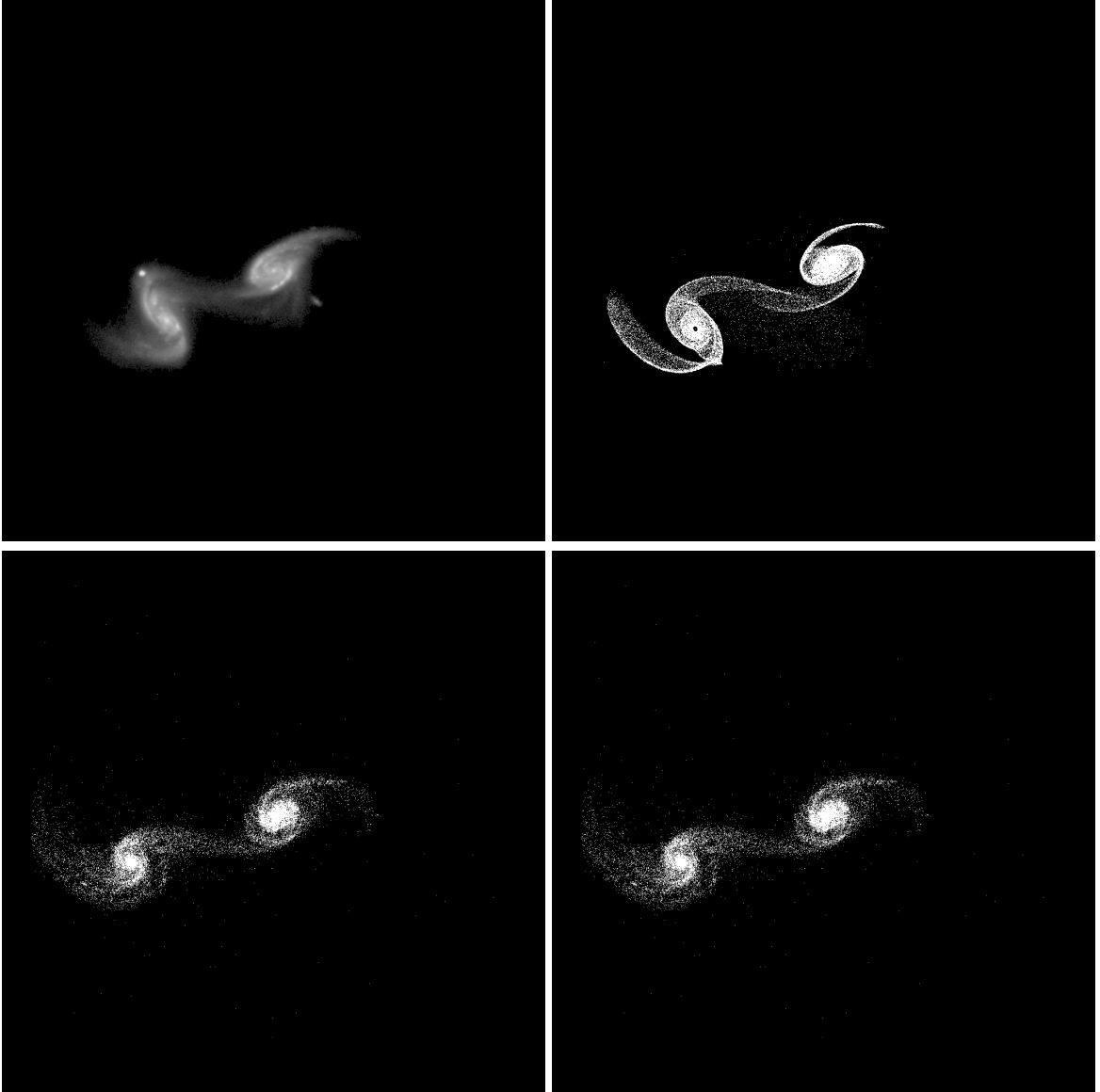


Figure 5.1: Target image (top-left), best SPAM match from Merger Wars (top-right), initial N-Body match (bottom-left), and best N-Body match (bottom-right) for SDSS 587722984435351614

Although we only have one view of the target system, the SPAM simulations allow us to rotate the system to view it from other angles. The next two figures show the system rotated and projected on the XZ and YZ planes. Although a system may appear or may not appear to have strong agreement between the SPAM simulation and the N-Body simulations, the opposite may be true when viewed from another perspective.



Figure 5.2: XZ projections of best SPAM match from Merger Wars (left), initial N-Body match (middle), and best N-Body match (right) for SDSS 587722984435351614



Figure 5.3: YZ projections of best SPAM match from Merger Wars (left), initial N-Body match (middle), and best N-Body match (right) for SDSS 587722984435351614

Velocity along the line of sight or V_z in our simulations is integrated along the Z direction to be used to match to future velocity datasets. One of the projects during the current

phase of the SDSS project, the “Mapping Nearby Galaxies at APO” or MaNGA, is collecting spectroscopic data of thousands of galaxies that can provide us with velocity data. Unfortunately at this time data is not available for any of our systems. However, we are able to make comparisons of the velocity between the N-Body and SPAM simulations. We do expect minor disagreement at the centers of the galaxies if the bulge is not represented by the SPAM simulations, but the discs and tidal features should be in good agreement for a good overall match. These figures were integrated using a 400x400 grid for each system.

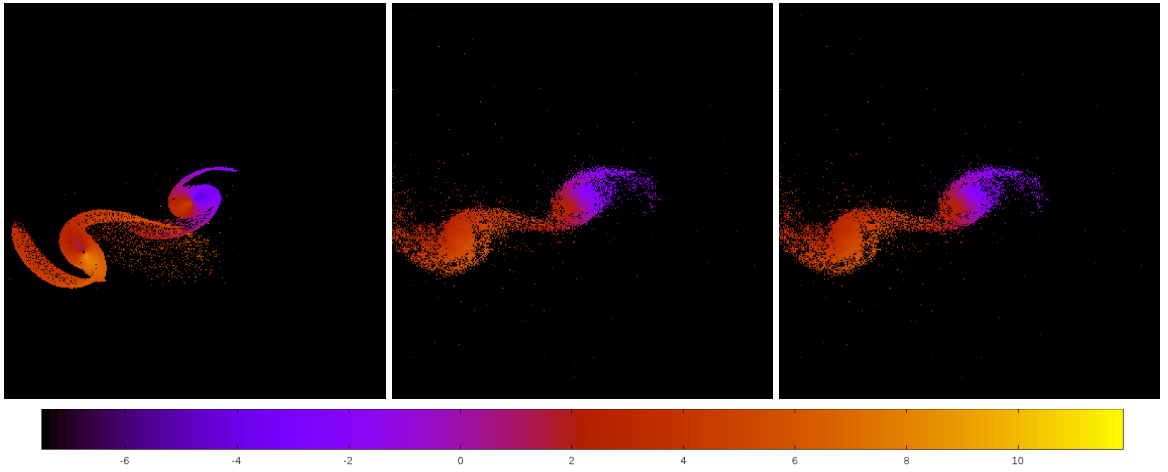


Figure 5.4: Line of sight velocity plots of best SPAM match from Merger Wars (left), initial N-Body match (middle), and best N-Body match (right) for SDSS 587722984435351614

The next table summarizes the orbital parameters of the system as it is at the time of best match to the observational data for SPAM and the N-Body simulations, and it includes data about the best match. Included are:

- a - the semi-major axis (negative for hyperbolic orbits)
- e - the eccentricity
- r_c - the radius of closest approach (the pericenter distance for elliptical orbits, center for circular orbits, and periapse distance for hyperbolic orbits)

- i - the inclination
- Ω - right-ascension of the ascending node
- ω - argument of periapse
- ν - true anomaly
- t_n - the time step in the simulation when the best match occurs (the corresponding SPAM and N-Body simulations will always span the same amount of time)
- $\ln\Lambda$ - the value of dynamical friction used in the simulation (this value does not matter at the time of SPAM's best match and is reported as N/A)

Table 5.2: Orbital Elements & Dynamical Friction for SDSS 587722984435351614

	SPAM Simulation	Initial N-Body Simulation	Best N-Body Simulation
a	-1.006	-1.301	-1.301
e	14.324	12.121	12.121
r_c	13.400	14.474	14.474
i	56.051°	55.593°	55.593°
Ω	133.041°	133.260°	133.260°
ω	7.539°	2.255°	2.255°
ν	71.999°	70.557°	70.557°
t_n	50	57	57
$\ln\Lambda$	N/A	1.00E-03	1.00E-03

These orbital parameters do not define the entirety of the system's orbit, only as it appears momentarily at the time the best match is found. In some simulations, the dynamical friction may be the same for the initial simulation and the optimized simulation, and in some cases it may be zero (or rounded to zero).

The next figures show the trajectories of the secondary galaxy relative to the primary galaxy for each simulation in the XY, XZ, and YZ planes. The starting location of each

trajectory is marked with a triangle colored by the simulation it corresponds to. Because SPAM and GADGET simulations start at the same locations, the triangles will be drawn on top of one another. At the time of best match, a square glyph is drawn on the orbit. In general, the SPAM simulations start at the best match, backwards integrate to find different starting locations for the N-Body simulations, and then forward integrate to 2 times the backwards integration time. Because of this, the squares for the SPAM simulations should overlap each other. When orbits are very close to one another, it may not be easy to tell them apart, but rest assured they are all drawn in the figures.

The last plots show how the metrics vary over time (by time output file) for the N-Body simulation corresponding to the best determination of dynamical friction to use. There are nine possible metrics to view - four correspond to the primary galaxy, four to the secondary galaxy, and one for both. These plots provide a means to see if one metric should be used over another and to judge the uncertainty that the best match should really be defined at the time found by the pipeline. When reading the plots, the best matches occur during the minimum values of a metric. Some systems show very sharp valleys, while others show broad valleys or appear noisy over time. In general, the primary galaxy metrics will be noisy if there are not strong tidal features to match.

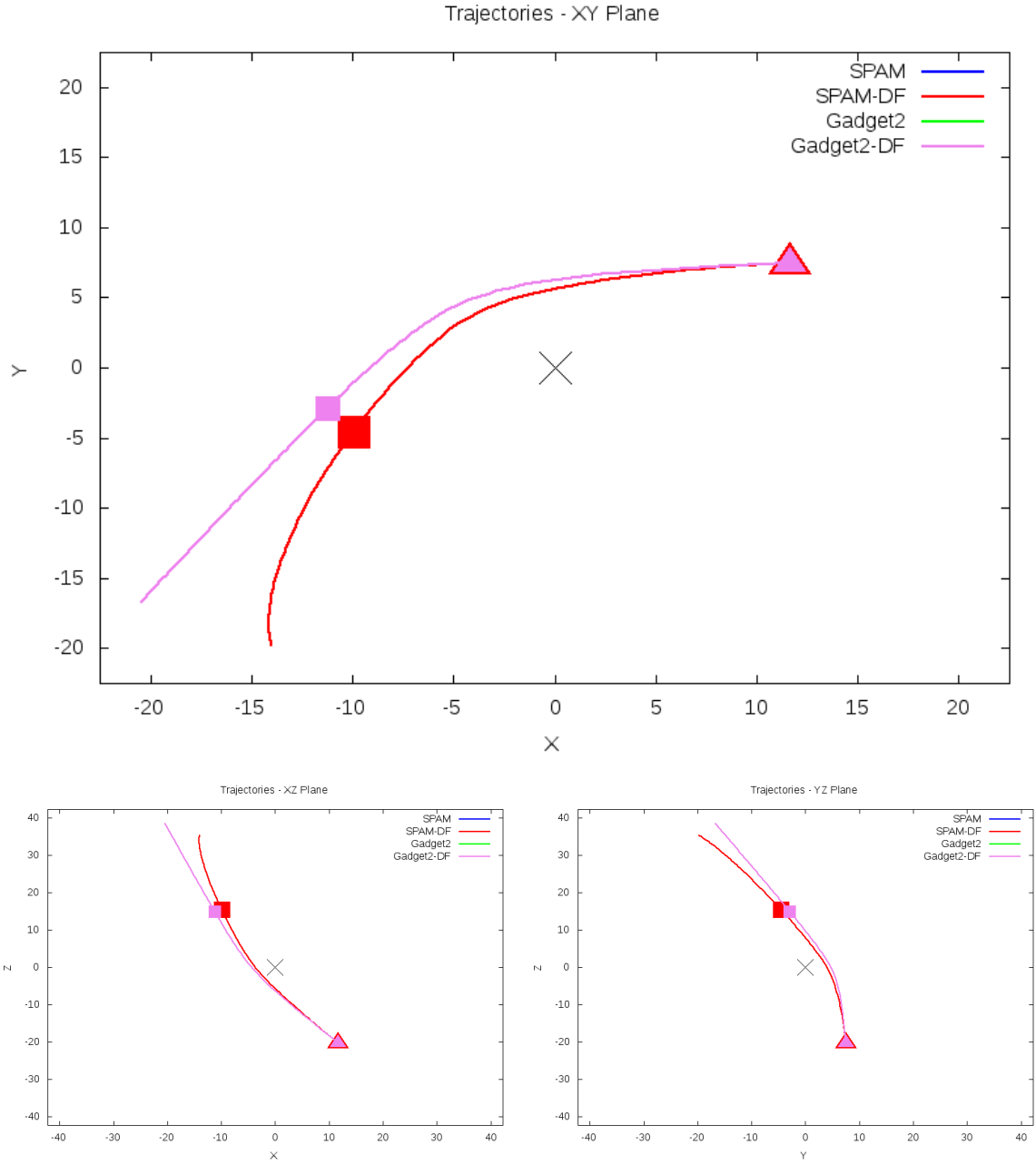


Figure 5.5: Trajectory plots of best SPAM match from Merger Wars, initial N-Body match, and best N-Body match for SDSS 587722984435351614

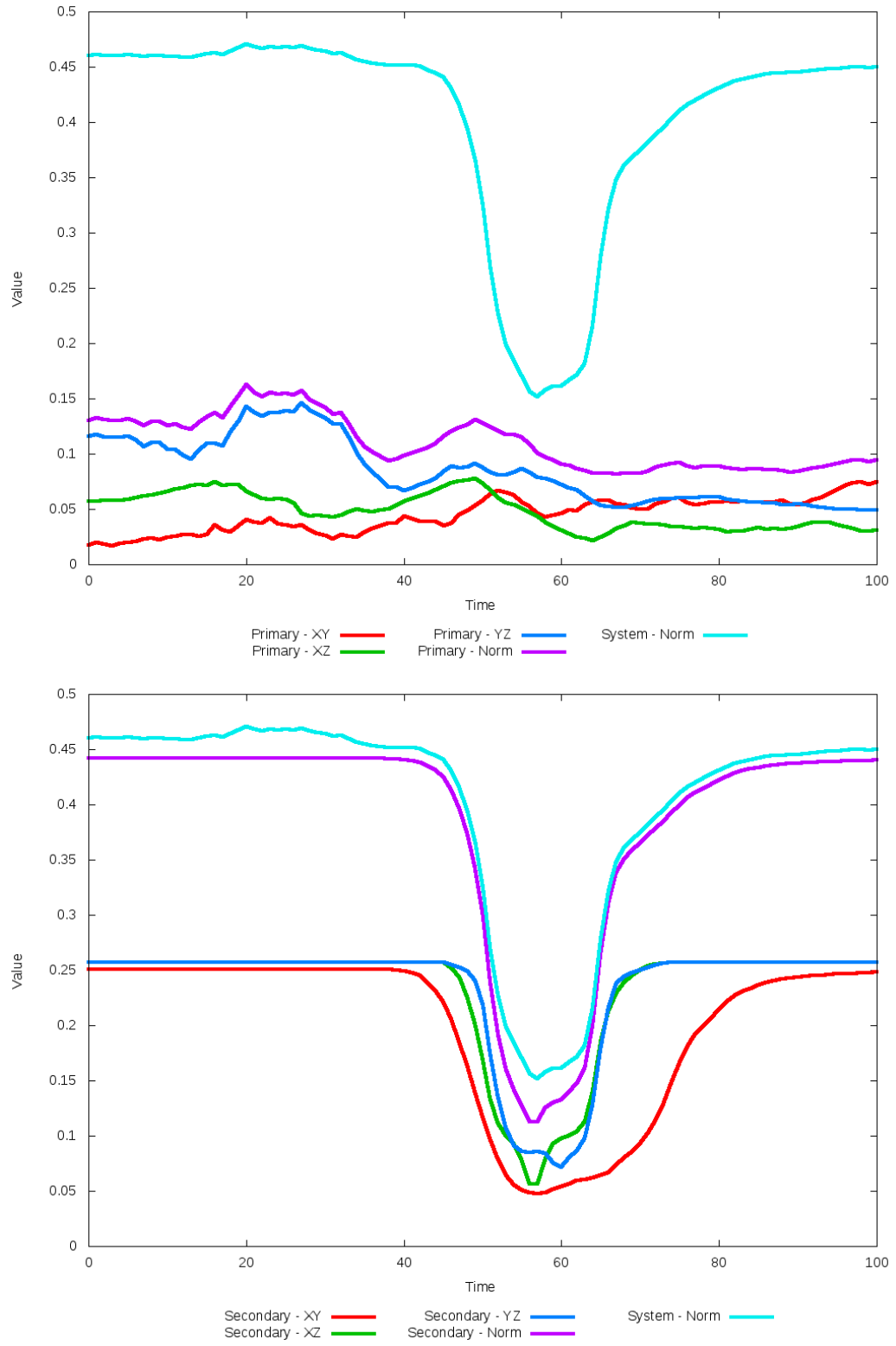


Figure 5.6: All metrics versus simulation time of the best N-Body simulation for SDSS 587722984435351614

5.1.2 SDSS 587724234257137777 (Arp 290)

Arp 290 shows a remarkable improvement in its quality of fit to the SPAM simulation from Merger Wars when dynamical friction is optimized. However, the optimization routine found the best agreement between the N-Body simulation and SPAM simulation with a dynamical friction value of essentially zero. This is not unexpected as the galaxies are at an early stage of their interaction. The location of the secondary galaxy is consistent with the location of the observational data and SPAM simulation, their trajectories are nearly identical, and line of sight velocities are consistent between each simulation. Furthermore, the change in dynamical friction changes the orbit from being hyperbolic to elliptical.

Table 5.3: Identification Information and Merger Zoo summary for SDSS 587724234257137777.

Name	Aliases	RA (hms)	Dec (dms)	Redshift
SDSS 587724234257137777	Arp 290, IC 195/196	2:03:49.7	+14:44:19.1	0.012162

R_x	R_y	R_z	V_x	V_y	V_z
1.08119	-1.66798	-2.06826	-0.18438	-0.39693	-0.02919

	Primary Galaxy	Secondary Galaxy
mass	0.51654	0.36192
radius	0.94043	0.43877
ϕ	12.97415°	135.11902°
θ	97.54035°	305.01225°
ϵ	0.3	0.3

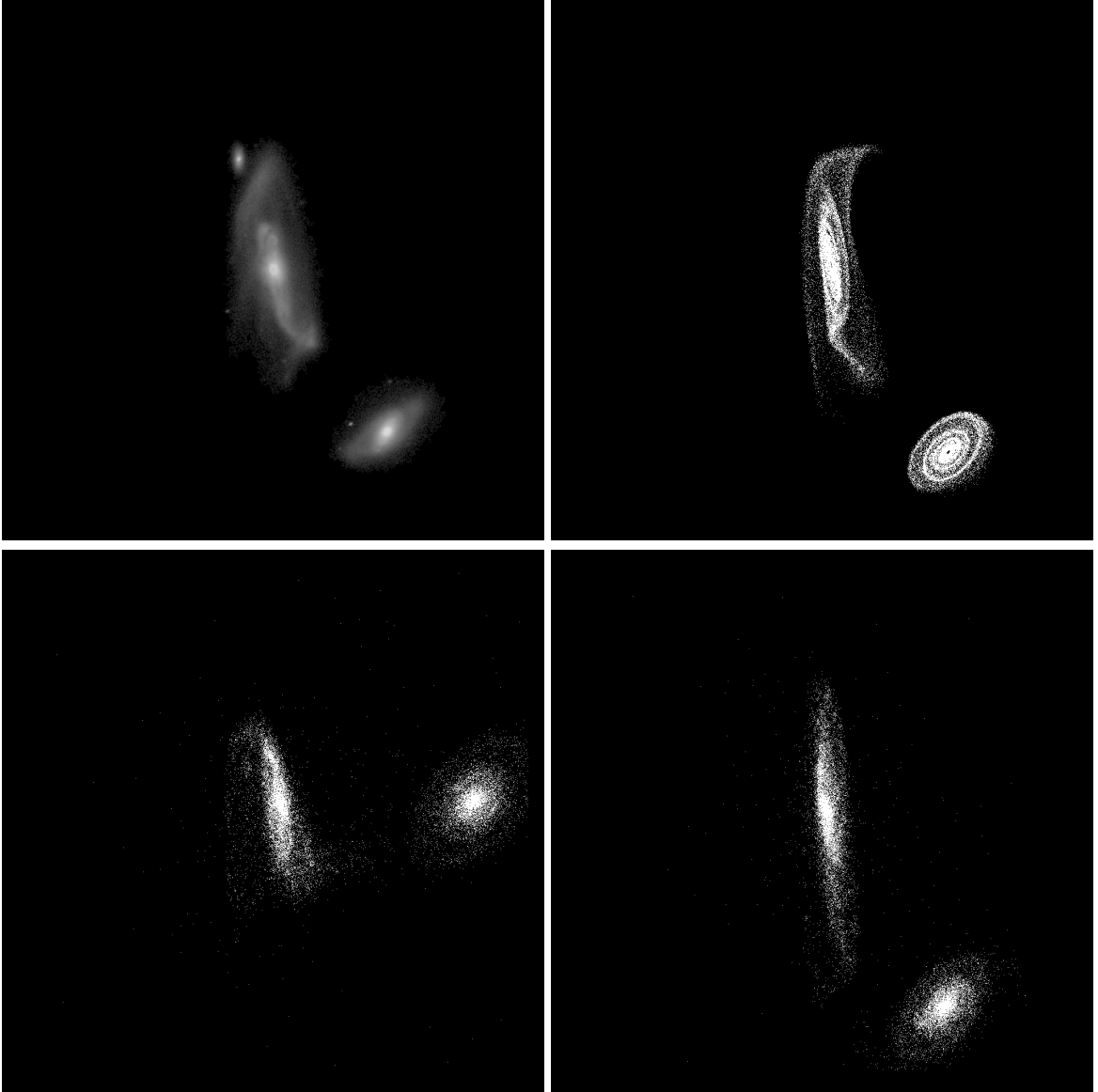


Figure 5.7: Target image (top-left), best SPAM match from Merger Wars (top-right), initial N-Body match (bottom-left), and best N-Body match (bottom-right) for SDSS 587724234257137777

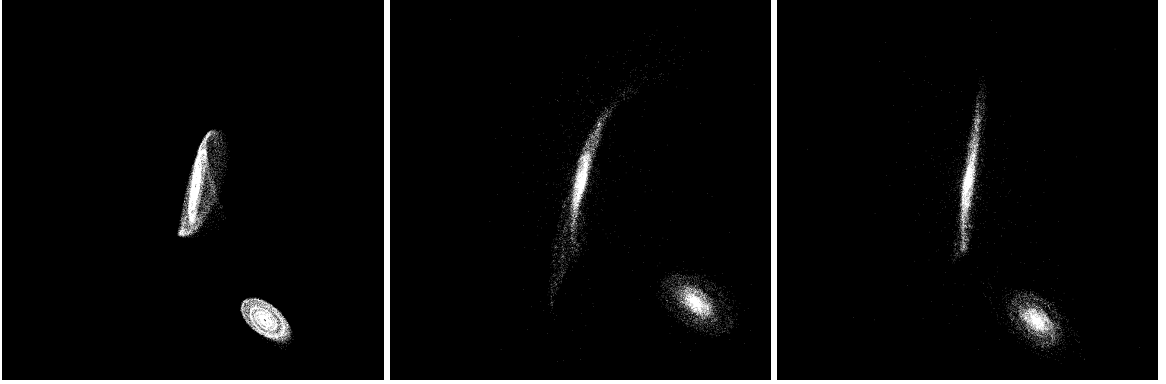


Figure 5.8: XZ projections of best SPAM match from Merger Wars (left), initial N-Body match (middle), and best N-Body match (right) for SDSS 587724234257137777

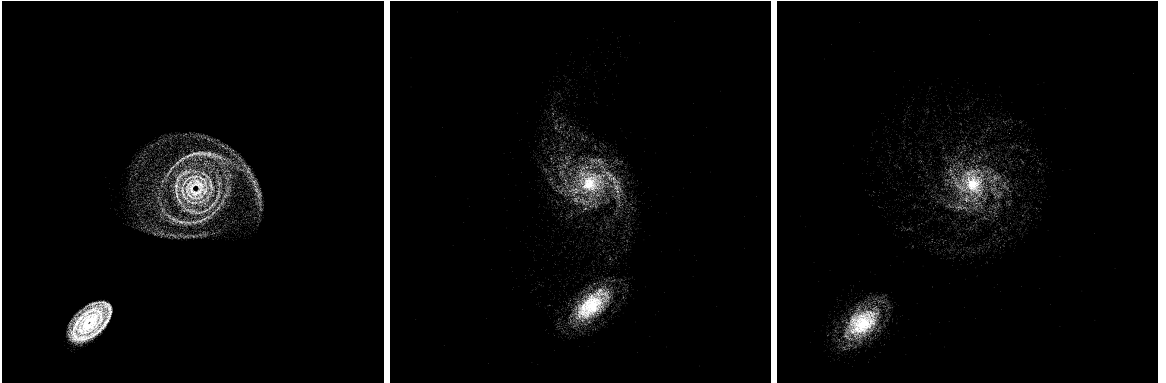


Figure 5.9: YZ projections of best SPAM match from Merger Wars (left), initial N-Body match (middle), and best N-Body match (right) for SDSS 587724234257137777

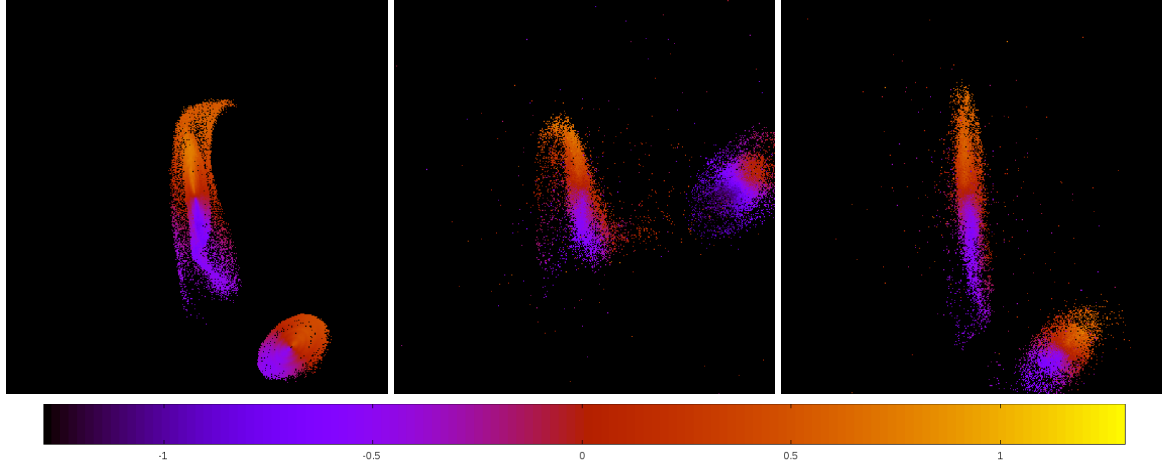


Figure 5.10: Line of sight velocity plots of best SPAM match from Merger Wars (left), initial N-Body match (middle), and best N-Body match (right) for SDSS 587724234257137777

Table 5.4: Orbital Elements & Dynamical Friction for SDSS 587724234257137777

	SPAM Simulation	Initial N-Body Simulation	Best N-Body Simulation
a	-9.667	-1.068	53.440
e	1.508	4.137	0.909
r_c	4.908	3.351	4.841
i	130.072°	129.469°	129.838°
Ω	241.868°	241.165°	241.238°
ω	249.005°	192.228°	240.896°
ν	40.571°	54.278°	48.765°
t_n	50	35	55
$\ln\Lambda$	N/A	1.00E-03	0.00E+00

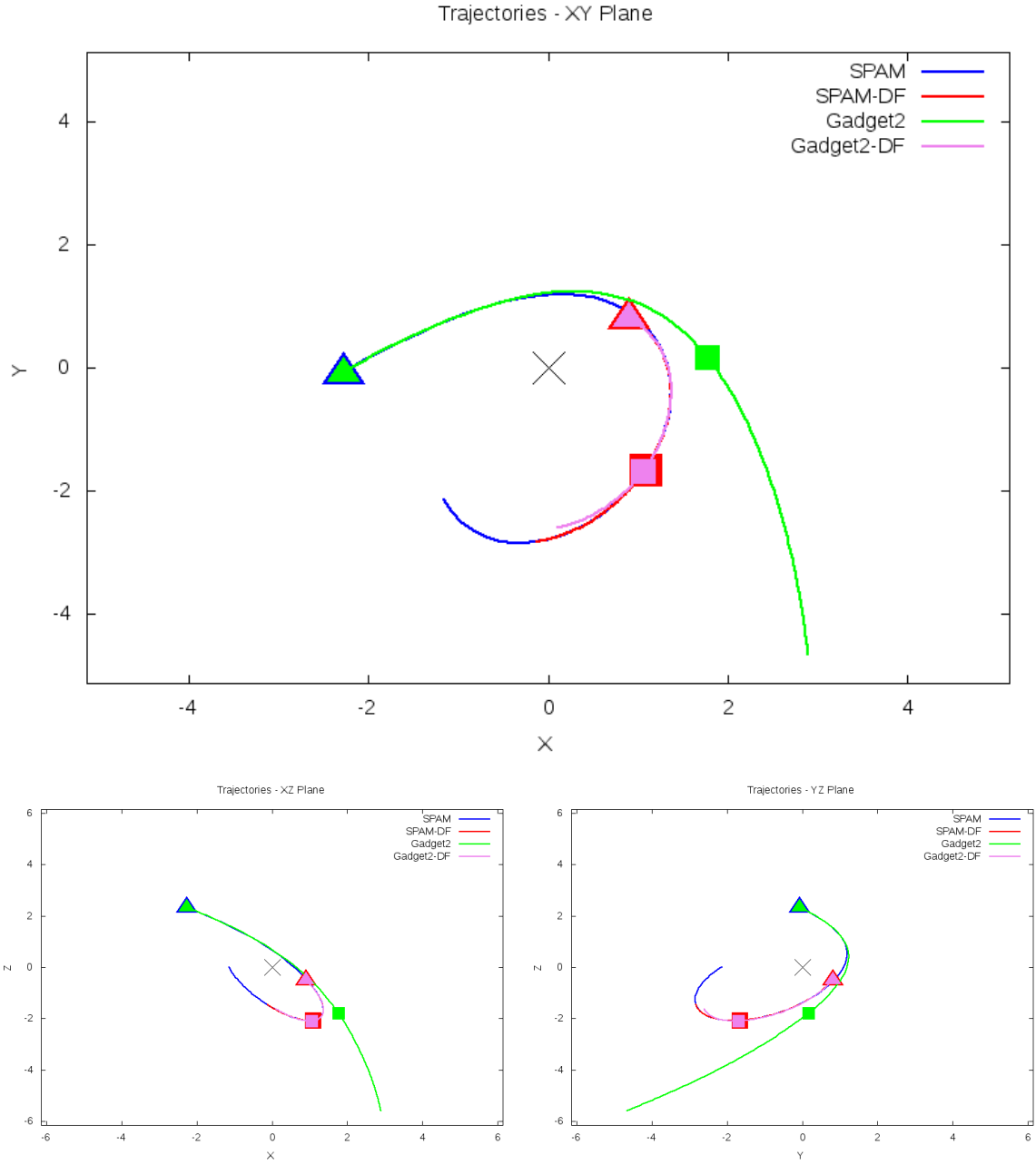


Figure 5.11: Trajectory plots of best SPAM match from Merger Wars, initial N-Body match, and best N-Body match for SDSS 587724234257137777

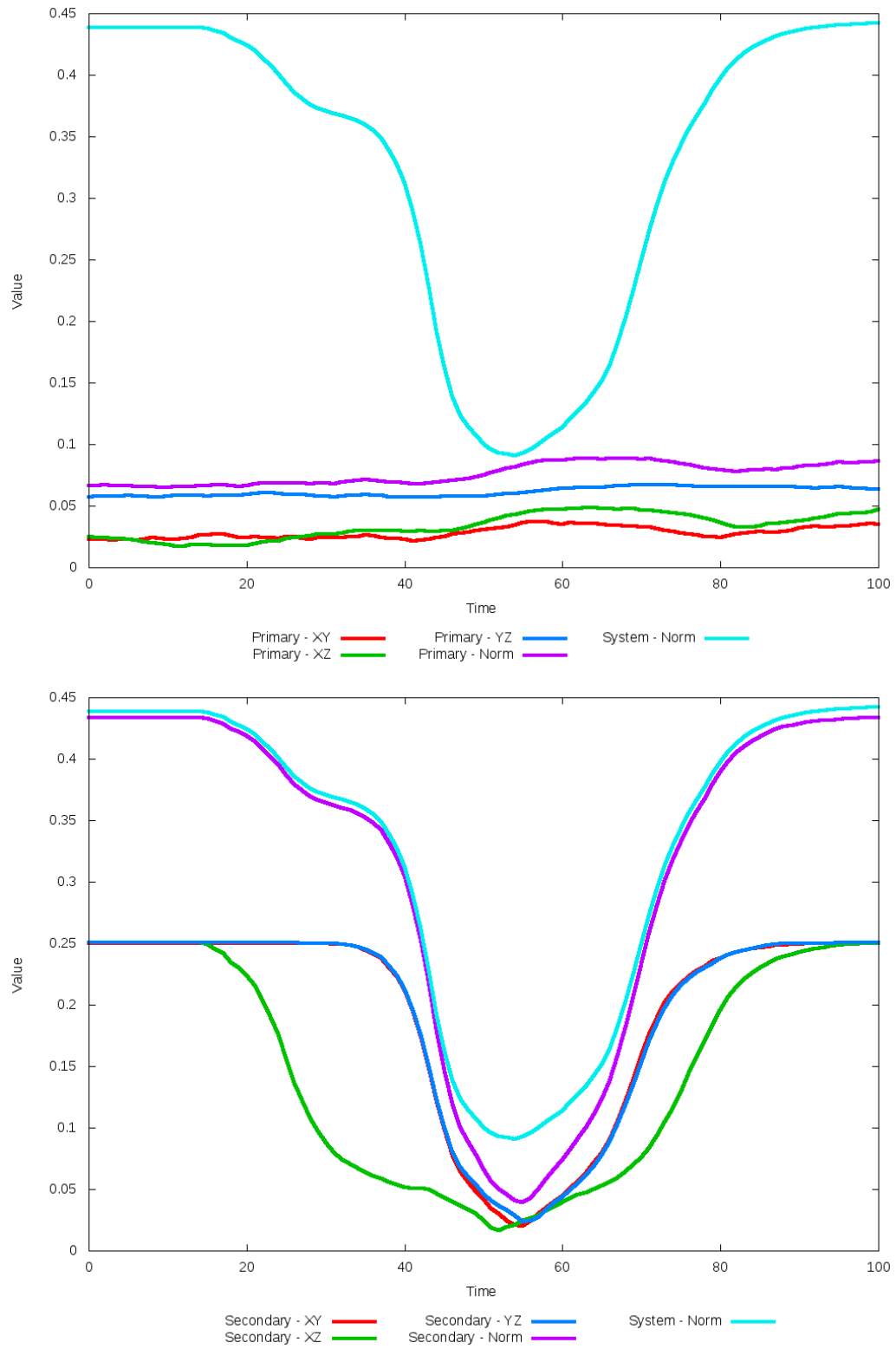


Figure 5.12: All metrics versus simulation time of the best N-Body simulation for SDSS 587724234257137777

5.1.3 SDSS 587726033843585146 (Arp 142)

Arp 142’s N-Body simulations exhibit only a moderate quality of fit to observational data and SPAM simulation. The tidal features in the N-Body simulations are broader and appear more diffuse than the restricted three-body simulation, and as a consequence they lack the rich features too. The features are so broad that the remaining nucleus of the primary galaxy is far from the galaxy’s center of mass. Although the trajectories of the elliptical orbits are in good agreement from their starting locations through the time of best match, V_z is overall more negative in the N-Body simulations than in SPAM. The state vector provided to our pipeline from Merger Wars should be reviewed for other candidates.

Table 5.5: Identification Information and Merger Zoo summary for SDSS 587726033843585146.

Name	Aliases	RA (hms)	Dec (dms)	Redshift
SDSS 587726033843585146	Arp 142, NGC 2936/2937	9:37:44.0	+2:45:36.5	0.023313

R_x	R_y	R_z	V_x	V_y	V_z
-0.49344	-1.43805	0.05985	0.07349	-1.02296	0.89921

	Primary Galaxy	Secondary Galaxy
mass	1.09707	1.54176
radius	1.27761	0.33429
ϕ	48.78911°	43.8006°
θ	50.06943°	135.05795°
ϵ	0.3	0.3

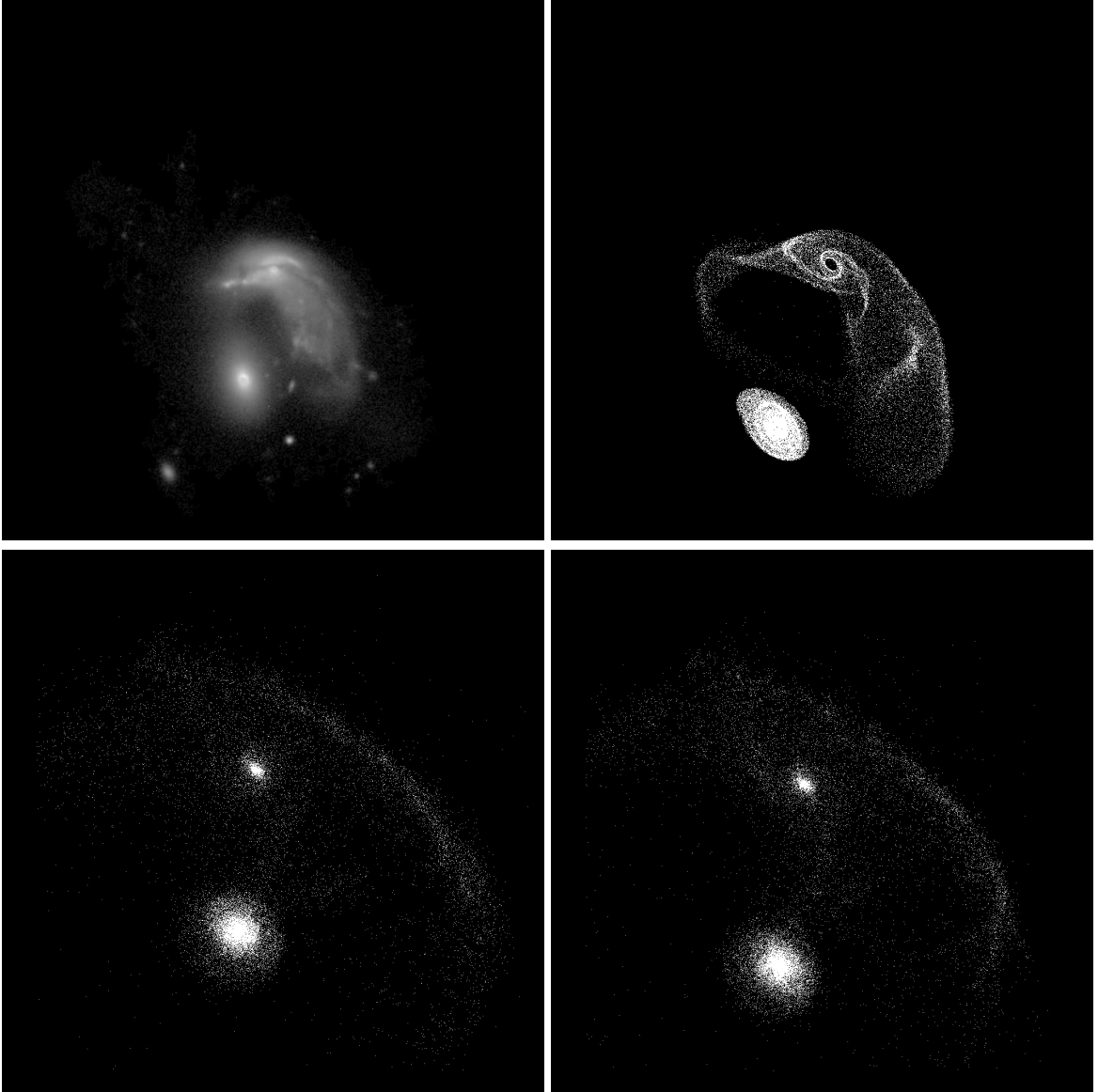


Figure 5.13: Target image (top-left), best SPAM match from Merger Wars (top-right), initial N-Body match (bottom-left), and best N-Body match (bottom-right) for SDSS 587726033843585146

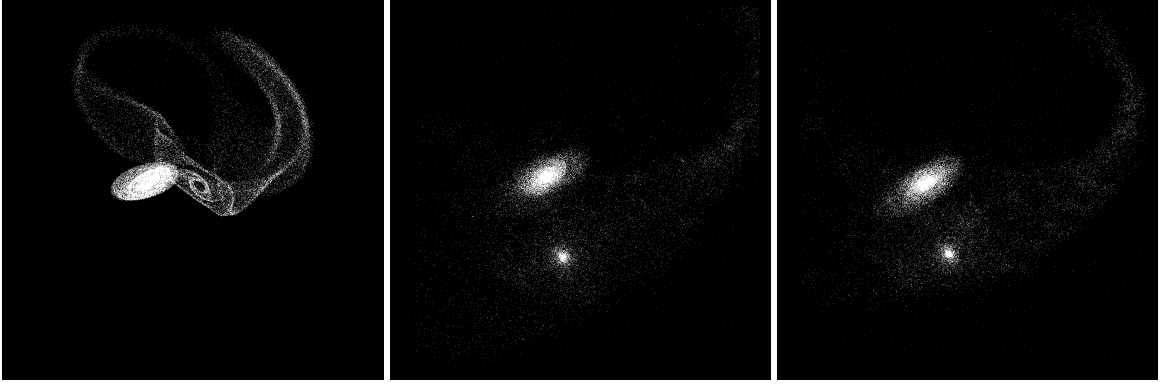


Figure 5.14: XZ projections of best SPAM match from Merger Wars (left), initial N-Body match (middle), and best N-Body match (right) for SDSS 587726033843585146

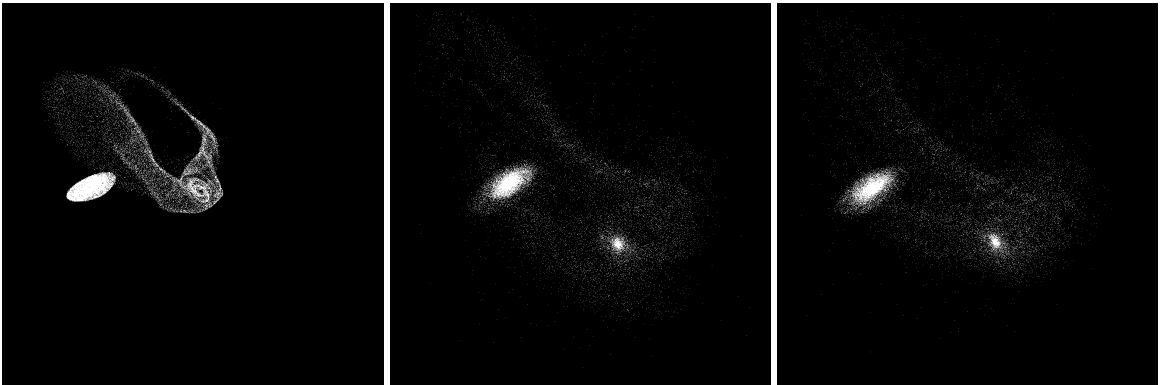


Figure 5.15: YZ projections of best SPAM match from Merger Wars (left), initial N-Body match (middle), and best N-Body match (right) for SDSS 587726033843585146

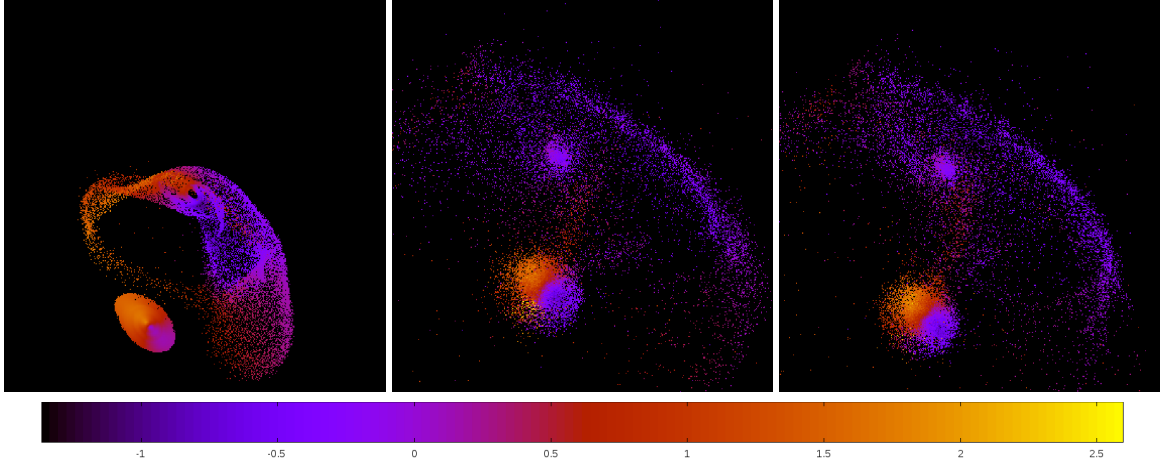


Figure 5.16: Line of sight velocity plots of best SPAM match from Merger Wars (left), initial N-Body match (middle), and best N-Body match (right) for SDSS 587726033843585146

Table 5.6: Orbital Elements & Dynamical Friction for SDSS 587726033843585146

	SPAM Simulation	Initial N-Body Simulation	Best N-Body Simulation
a	-1.208	1.367	3.111
e	2.535	0.652	0.609
r_c	1.855	0.476	1.215
i	65.029°	60.397°	63.961°
Ω	250.011°	246.461°	249.802°
ω	299.587°	199.572°	241.804°
ν	62.174°	164.528°	118.236°
t_n	50	60	61
$\ln\Lambda$	N/A	1.00E-03	1.50E-03

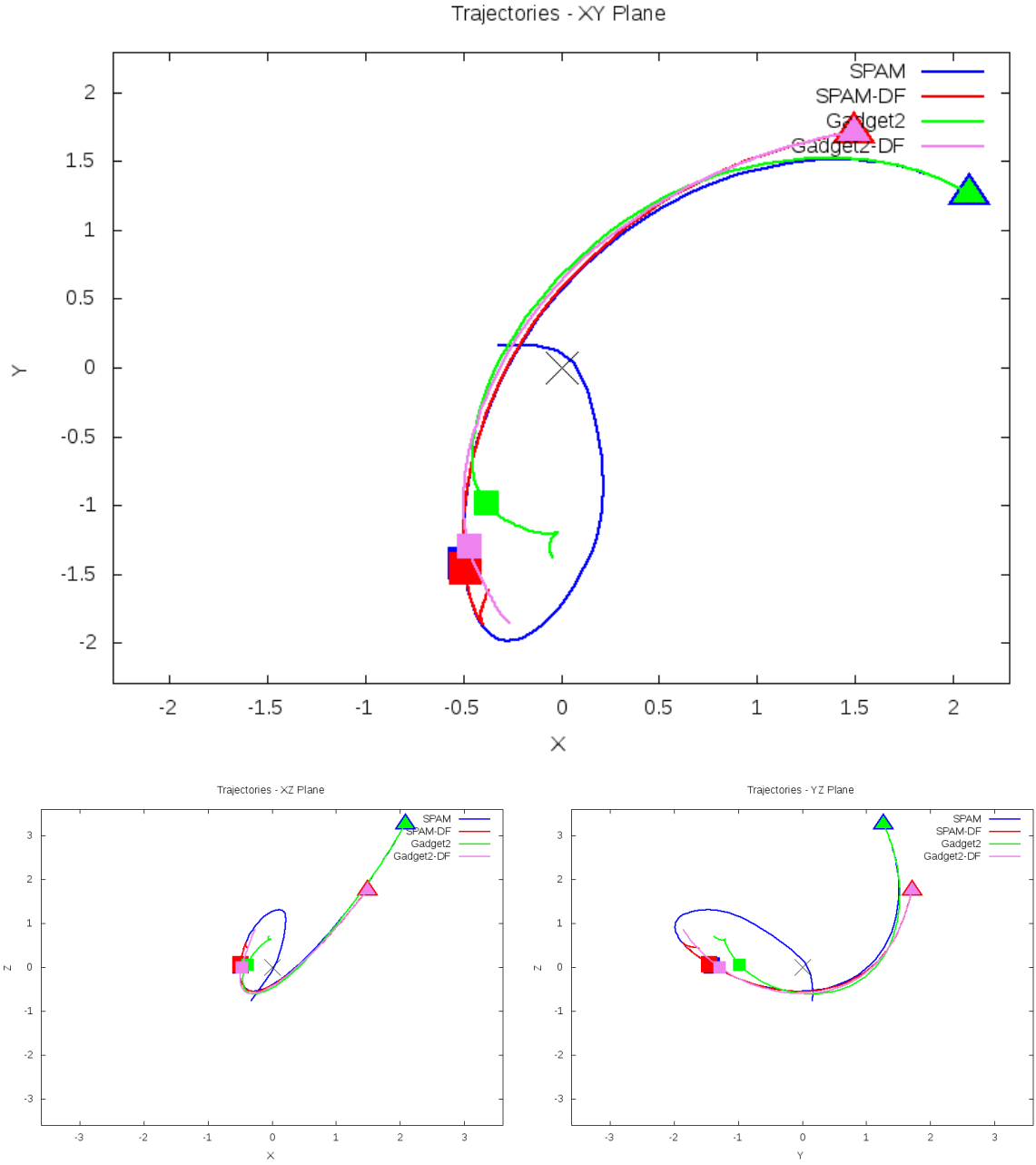


Figure 5.17: Trajectory plots of best SPAM match from Merger Wars, initial N-Body match, and best N-Body match for SDSS 587726033843585146

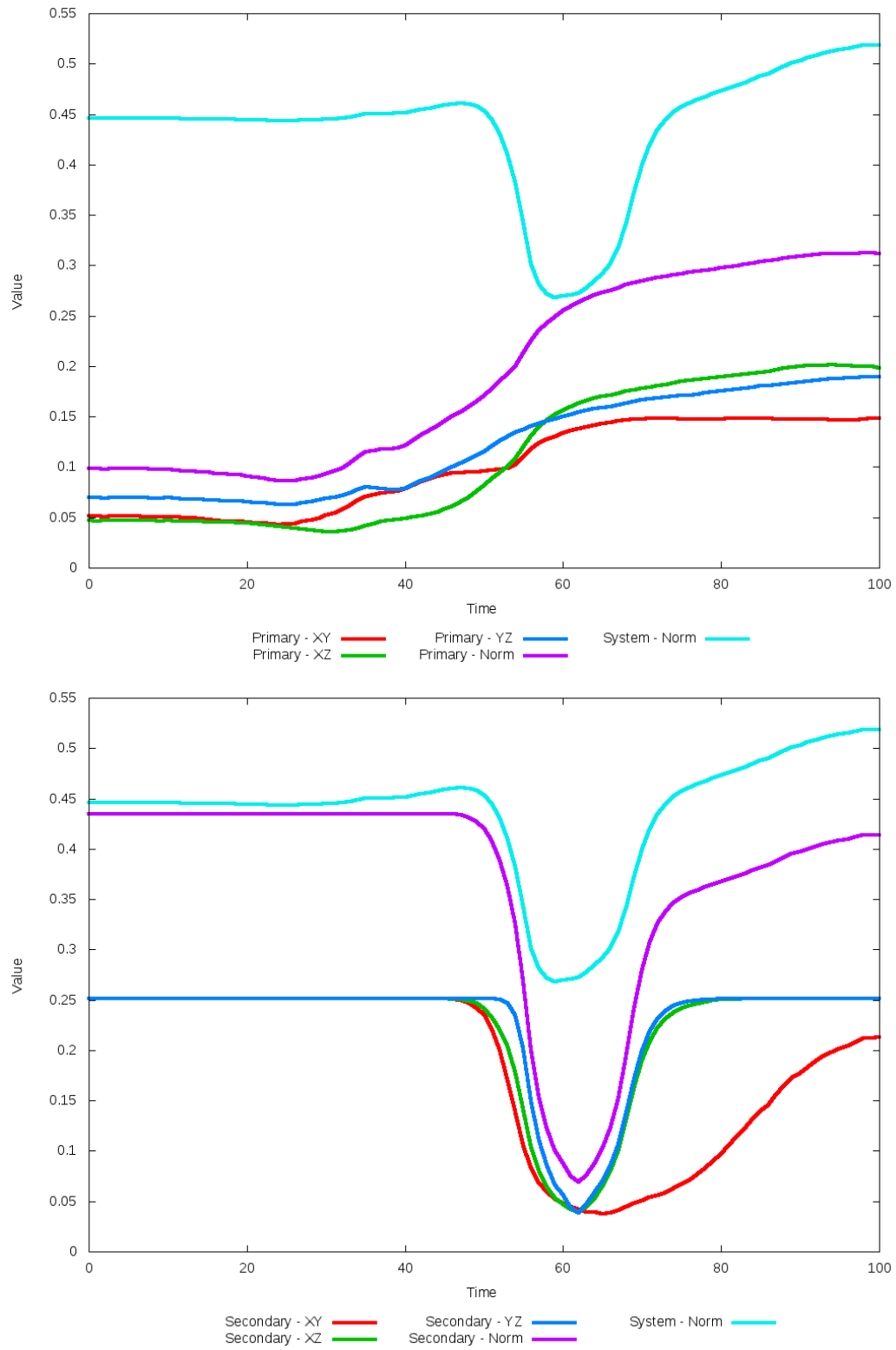


Figure 5.18: All metrics versus simulation time of the best N-Body simulation for SDSS 587726033843585146

5.1.4 SDSS 587727177926508595 (Arp 318)

Arp 318 shows modest agreement between the N-body and SPAM simulations. In the XY projection view of the N-Body simulations, the location of the secondary galaxy with the initial dynamical friction looks to be a better match in the Y-direction than the simulation with optimized dynamical friction, whereas the opposite is true for their locations in the X-direction. Looking at the projections in the XZ and YZ planes shows the optimized dynamical friction cases to be a better match to the SPAM simulation. The change in dynamical friction shows an interesting effect on the hyperbolic orbits of these simulations - the pipeline methodology found a lower value of dynamical friction than the starting value, resulting in the N-Body trajectory straddling the SPAM trajectories. It is possible that allowing the pipeline to explore a finer sampling of dynamical friction values could result in a better overall match.

Table 5.7: Identification Information and Merger Zoo summary for SDSS 587727177926508595.

Name	Aliases	RA (hms)	Dec (dms)	Redshift
SDSS 587727177926508595	Arp 318, NGC 833/835	2:09:24.5	-10:08:09.6	0.013586

R_x	R_y	R_z	V_x	V_y	V_z
0.93974	0.17991	2.66529	0.0	-0.42418	1.16041

	Primary Galaxy	Secondary Galaxy
mass	0.36689	1.02587
radius	0.65803	0.61394
ϕ	6.2096°	95.0°
θ	200.0°	289.23076°
ϵ	0.3	0.3

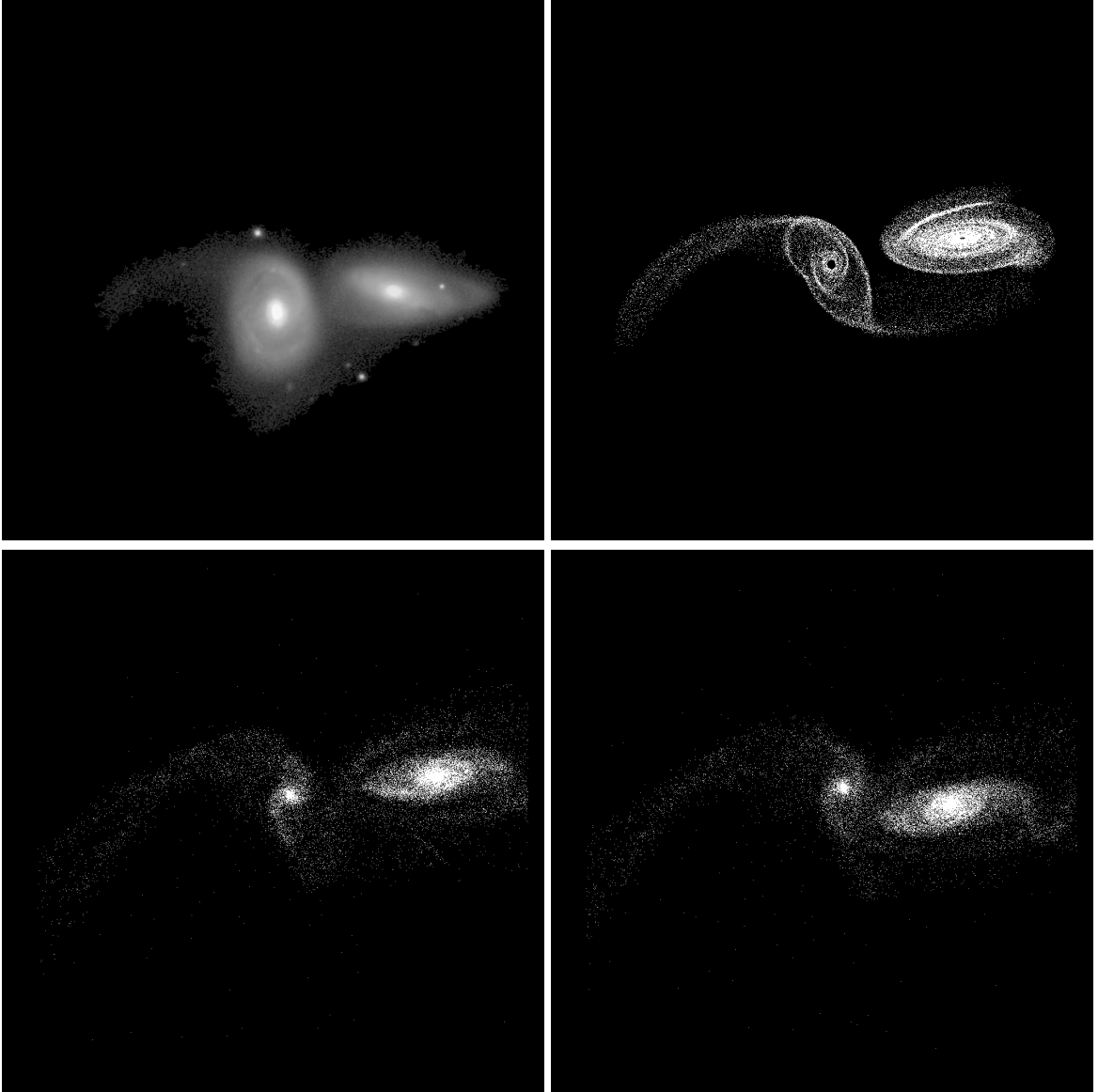


Figure 5.19: Target image (top-left), best SPAM match from Merger Wars (top-right), initial N-Body match (bottom-left), and best N-Body match (bottom-right) for SDSS 587727177926508595

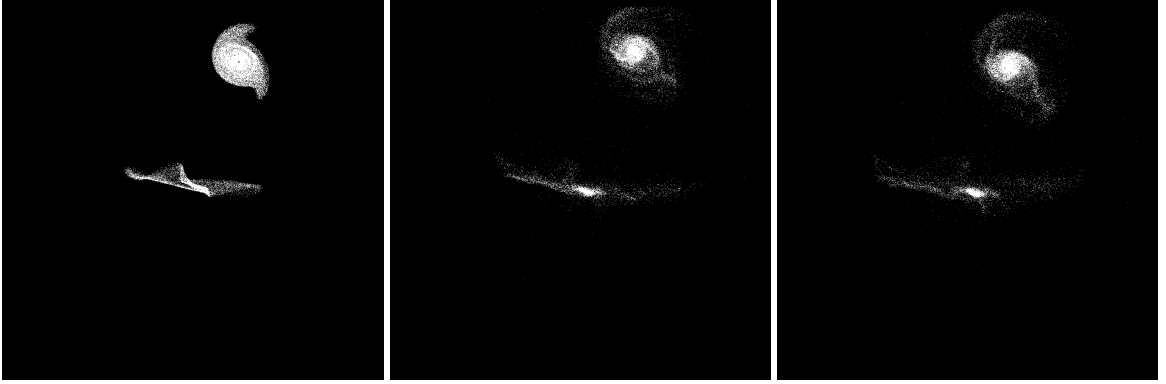


Figure 5.20: XZ projections of best SPAM match from Merger Wars (left), initial N-Body match (middle), and best N-Body match (right) for SDSS 587727177926508595

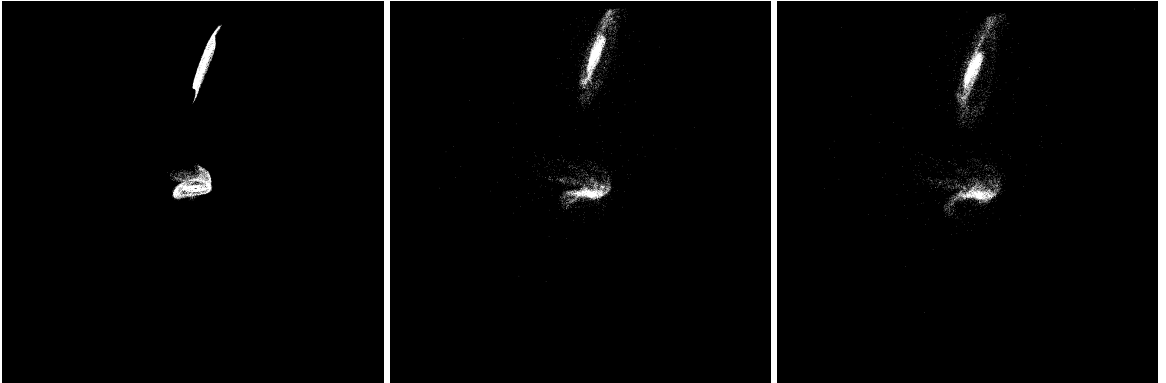


Figure 5.21: YZ projections of best SPAM match from Merger Wars (left), initial N-Body match (middle), and best N-Body match (right) for SDSS 587727177926508595

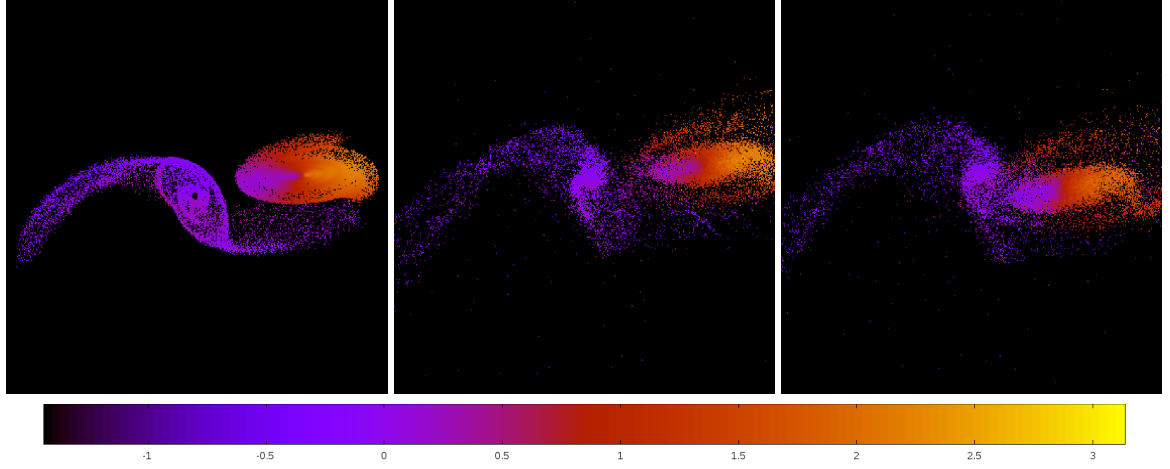


Figure 5.22: Line of sight velocity plots of best SPAM match from Merger Wars (left), initial N-Body match (middle), and best N-Body match (right) for SDSS 587727177926508595

Table 5.8: Orbital Elements & Dynamical Friction for SDSS 587727177926508595

	SPAM Simulation	Initial N-Body Simulation	Best N-Body Simulation
a	-0.405	-0.353	-0.613
e	7.646	8.211	5.121
r_c	2.689	2.543	2.525
i	102.996°	103.287°	103.538°
Ω	50.848°	50.066°	49.878°
ω	8.966°	1.861°	7.646°
ν	66.036°	70.241°	68.605°
t_n	50	51	52
$\ln\Lambda$	N/A	1.00E-03	1.00E-04

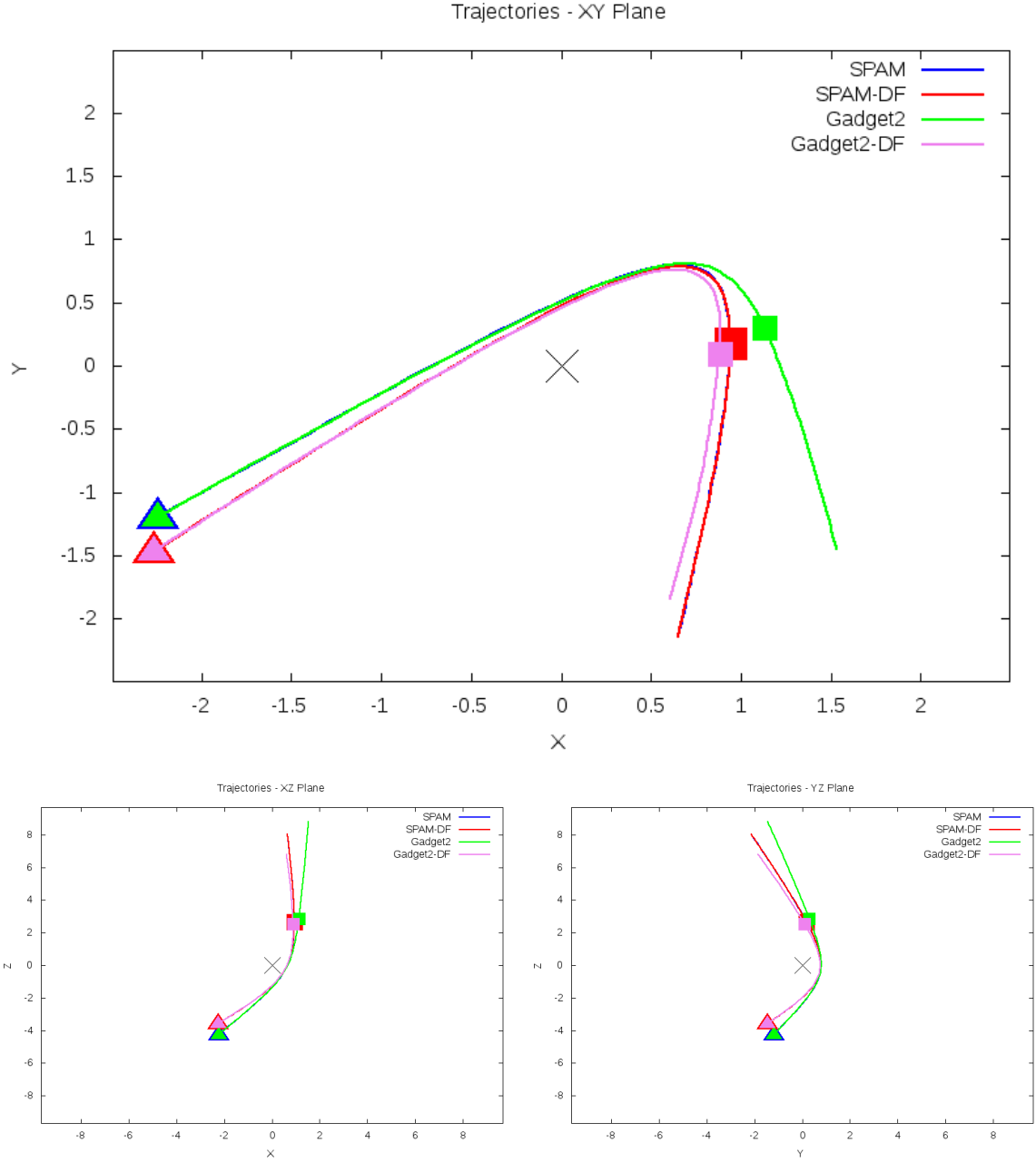


Figure 5.23: Trajectory plots of best SPAM match from Merger Wars, initial N-Body match, and best N-Body match for SDSS 587727177926508595

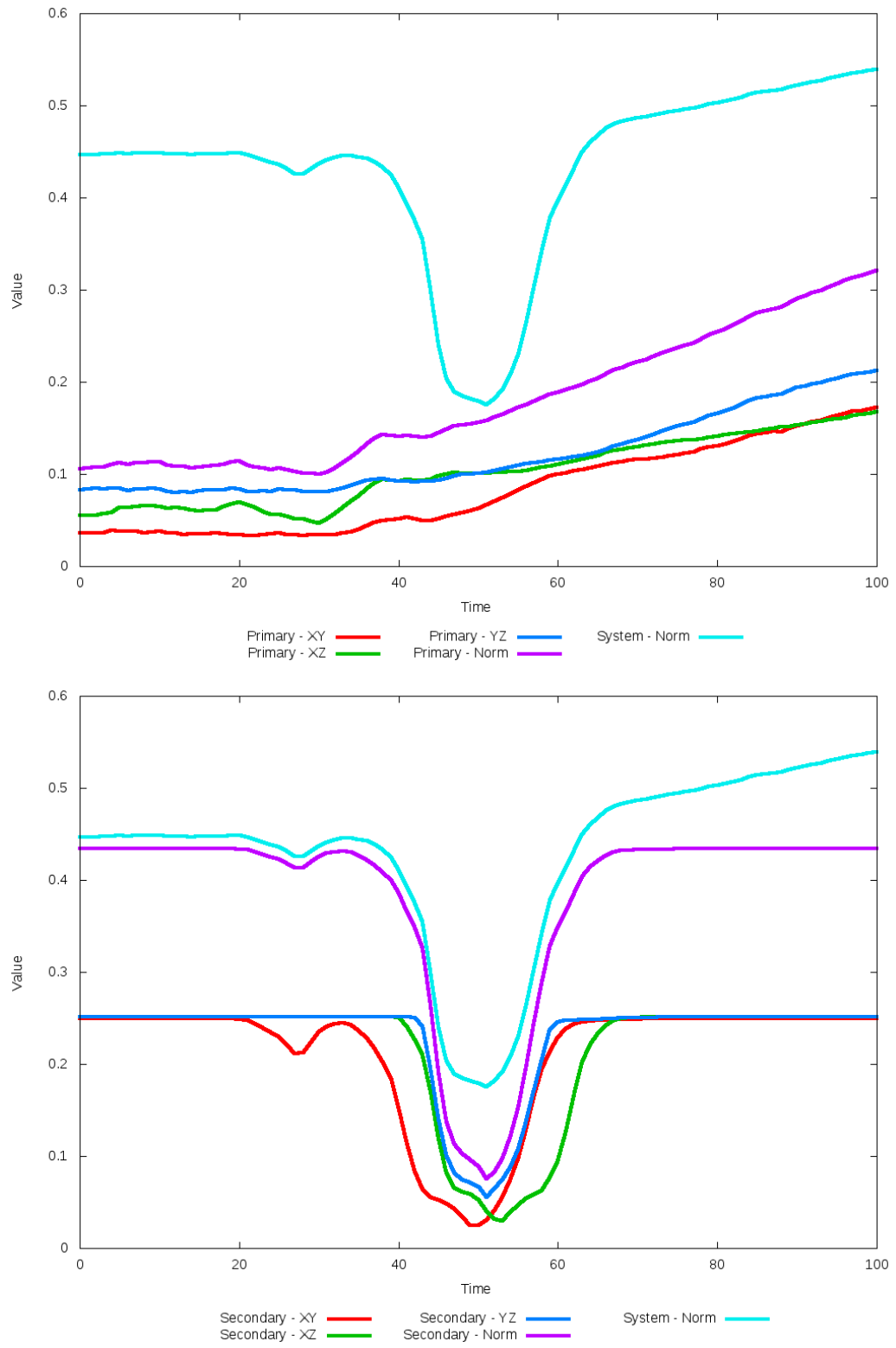


Figure 5.24: All metrics versus simulation time of the best N-Body simulation for SDSS 587727177926508595

5.1.5 SDSS 587727178988388373 (Arp 256)

Arp 256 exhibits good agreement between the N-Body simulations with both the SPAM simulation and observational data, although the N-Body simulations both show broader and longer tidal features than the observational data suggests. Again, the pipeline predicted a dynamical friction scalar at or near zero, with little apparent difference between it and the initial simulation in the XY projection, aside from a change of position in one of the secondary galaxy's tidal tails. However, looking at the XZ and YZ projections shows a more noticeable improvement in the location of the secondary galaxy when compared to the restricted three-body simulation. This agreement would not be found had the metric used in the optimization only looked at the XY plane.

Table 5.9: Identification Information and Merger Zoo summary for SDSS 587727178988388373.

Name	Aliases	RA (hms)	Dec (dms)	Redshift
SDSS 587727178988388373	Arp 256	0:18:50.0	-10:21:41.8	0.027329

R_x	R_y	R_z	V_x	V_y	V_z
-0.40793	-1.92518	1.95772	-1.14918	-1.02439	0.77963

	Primary Galaxy	Secondary Galaxy
mass	1.3042	1.25831
radius	0.94075	0.54373
ϕ	97.78523°	60.52239°
θ	144.60117°	216.50117°
ϵ	0.3	0.3

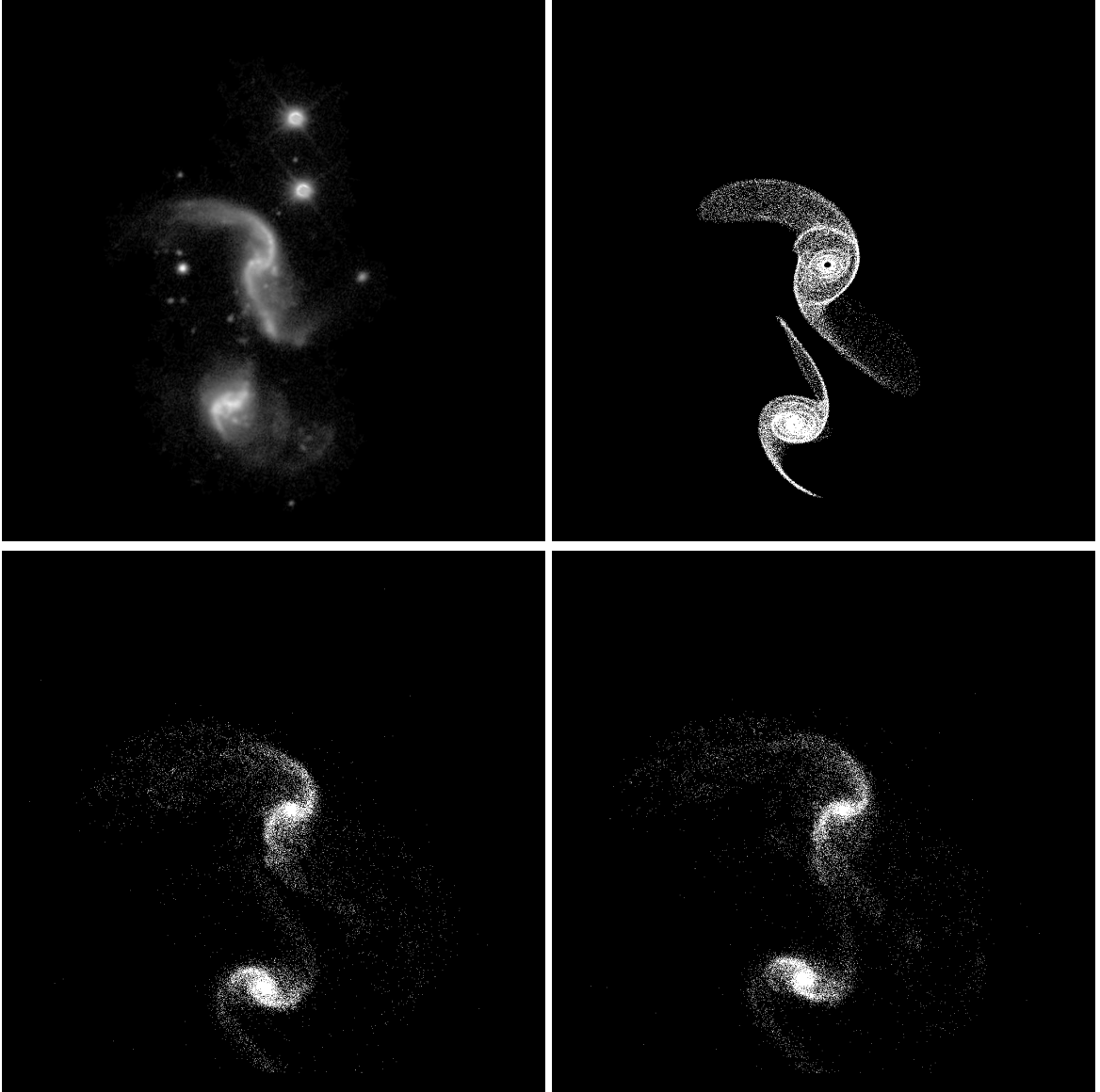


Figure 5.25: Target image (top-left), best SPAM match from Merger Wars (top-right), initial N-Body match (bottom-left), and best N-Body match (bottom-right) for SDSS 587727178988388373

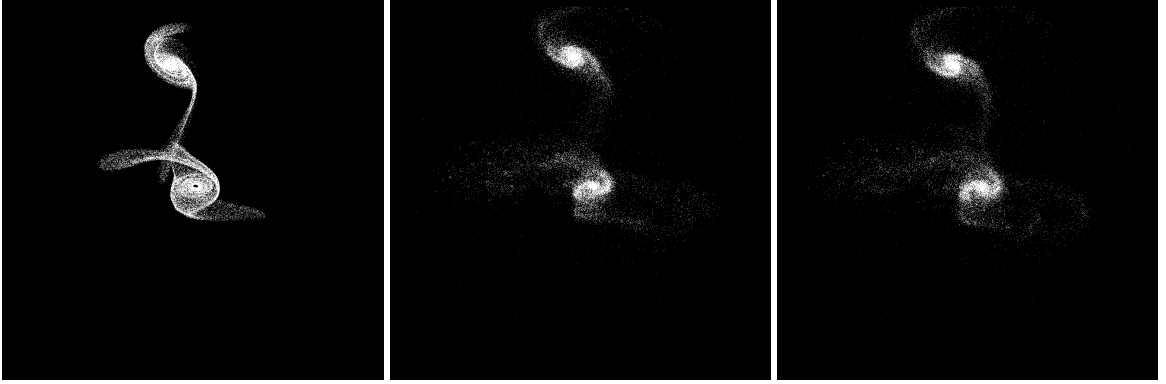


Figure 5.26: XZ projections of best SPAM match from Merger Wars (left), initial N-Body match (middle), and best N-Body match (right) for SDSS 587727178988388373

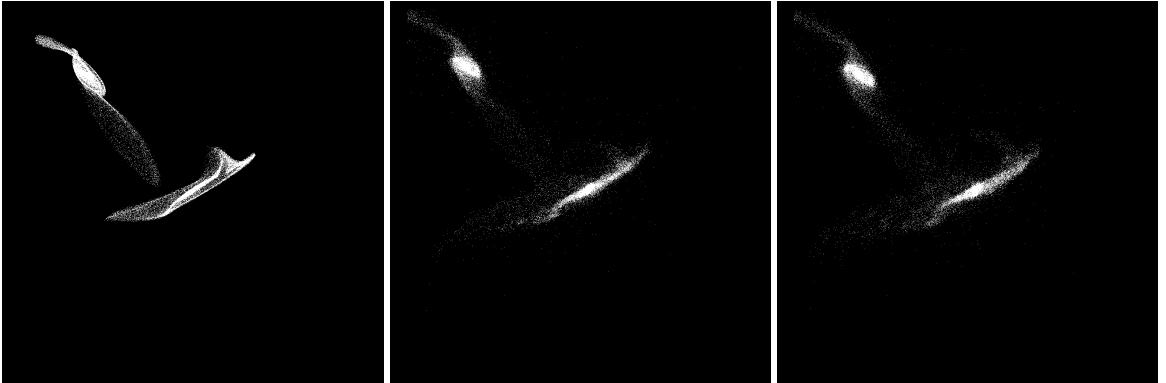


Figure 5.27: YZ projections of best SPAM match from Merger Wars (left), initial N-Body match (middle), and best N-Body match (right) for SDSS 587727178988388373

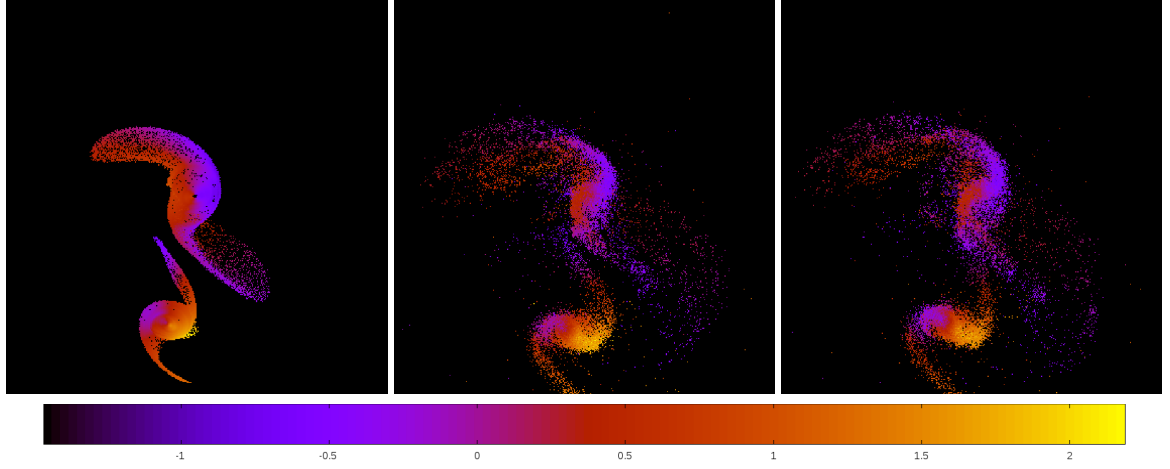


Figure 5.28: Line of sight velocity plots of best SPAM match from Merger Wars (left), initial N-Body match (middle), and best N-Body match (right) for SDSS 587727178988388373

Table 5.10: Orbital Elements & Dynamical Friction for SDSS 587727178988388373

	SPAM Simulation	Initial N-Body Simulation	Best N-Body Simulation
a	-0.509	-0.549	-0.814
e	6.724	6.127	4.471
r_c	2.914	2.817	2.826
i	131.949°	132.833°	132.914°
Ω	14.638°	15.209°	15.110°
ω	45.519°	36.331°	39.485°
ν	62.990°	66.544°	66.080°
t_n	50	51	52
$\ln\Lambda$	N/A	1.00E-03	0.00E+00

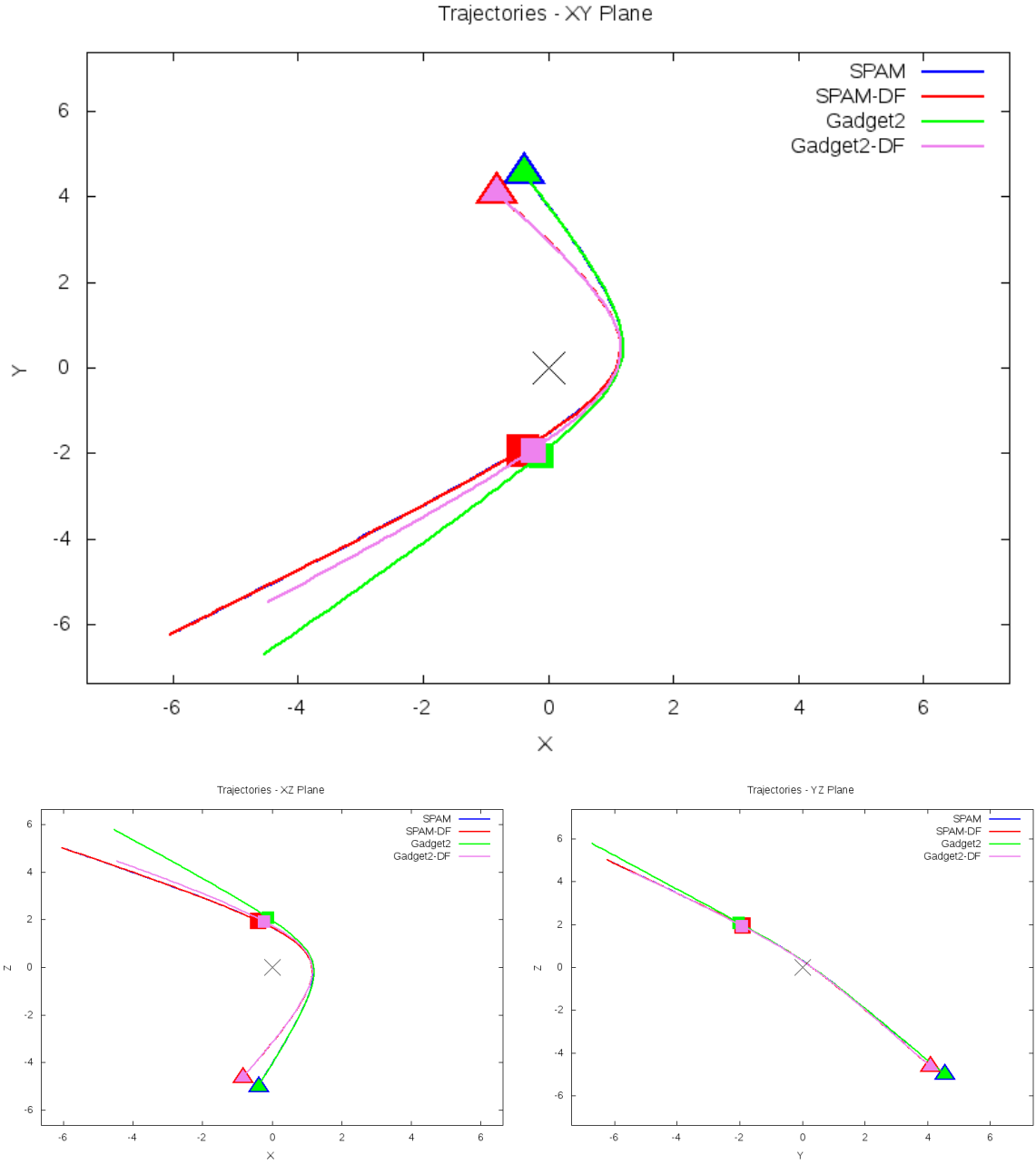


Figure 5.29: Trajectory plots of best SPAM match from Merger Wars, initial N-Body match, and best N-Body match for SDSS 587727178988388373

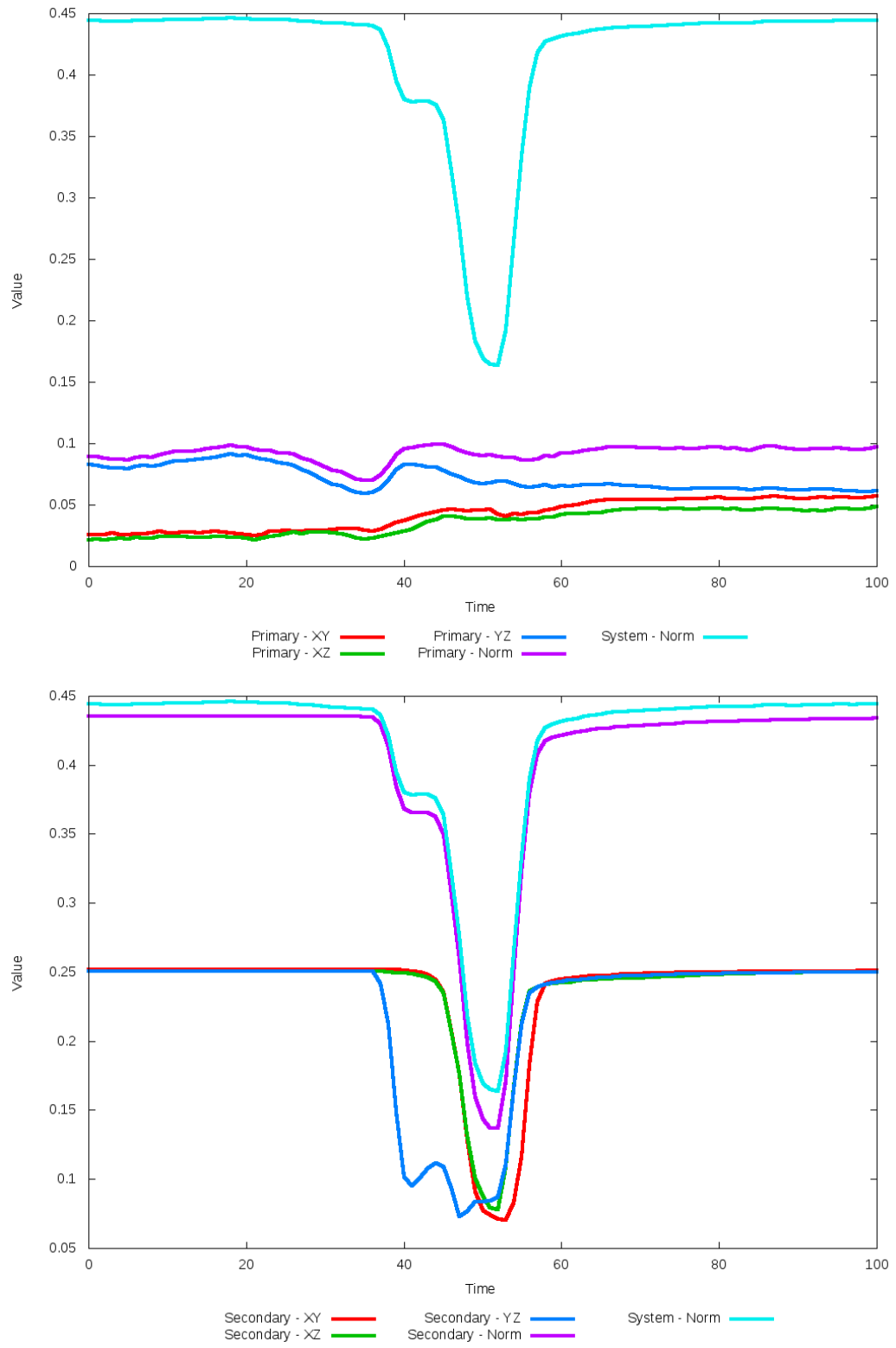


Figure 5.30: All metrics versus simulation time of the best N-Body simulation for SDSS 587727178988388373

5.1.6 SDSS 587727222471131318 (UGC 11751)

UGC 11751's N-Body simulations show very good agreement with observational data and the SPAM simulations. The pipeline's optimal dynamical friction is at or near a value of 0.0 shows its biggest impact through its respective trajectory which shows noticeable improvement, although the trajectory remains hyperbolic. There is also some improvement in the quality of fit when looking at the the line of sight velocity. The optimized N-Body simulation has slightly lower velocities along the disk compared to the initial case (top of the primary galaxy and the right side of the secondary galaxy).

Table 5.11: Identification Information and Merger Zoo summary for SDSS 587727222471131318.

Name	Aliases	RA (hms)	Dec (dms)	Redshift
SDSS 587727222471131318	UGC 11751	21:28:59.3	+11:22:55.0	0.029087

R_x	R_y	R_z	V_x	V_y	V_z
0.66665	-2.12701	1.61528	-0.18579	-0.23147	0.20647

	Primary Galaxy	Secondary Galaxy
mass	0.19195	0.1555
radius	0.81482	0.75573
ϕ	15.0°	87.5°
θ	203.47826°	22.36024°
ϵ	0.3	0.3

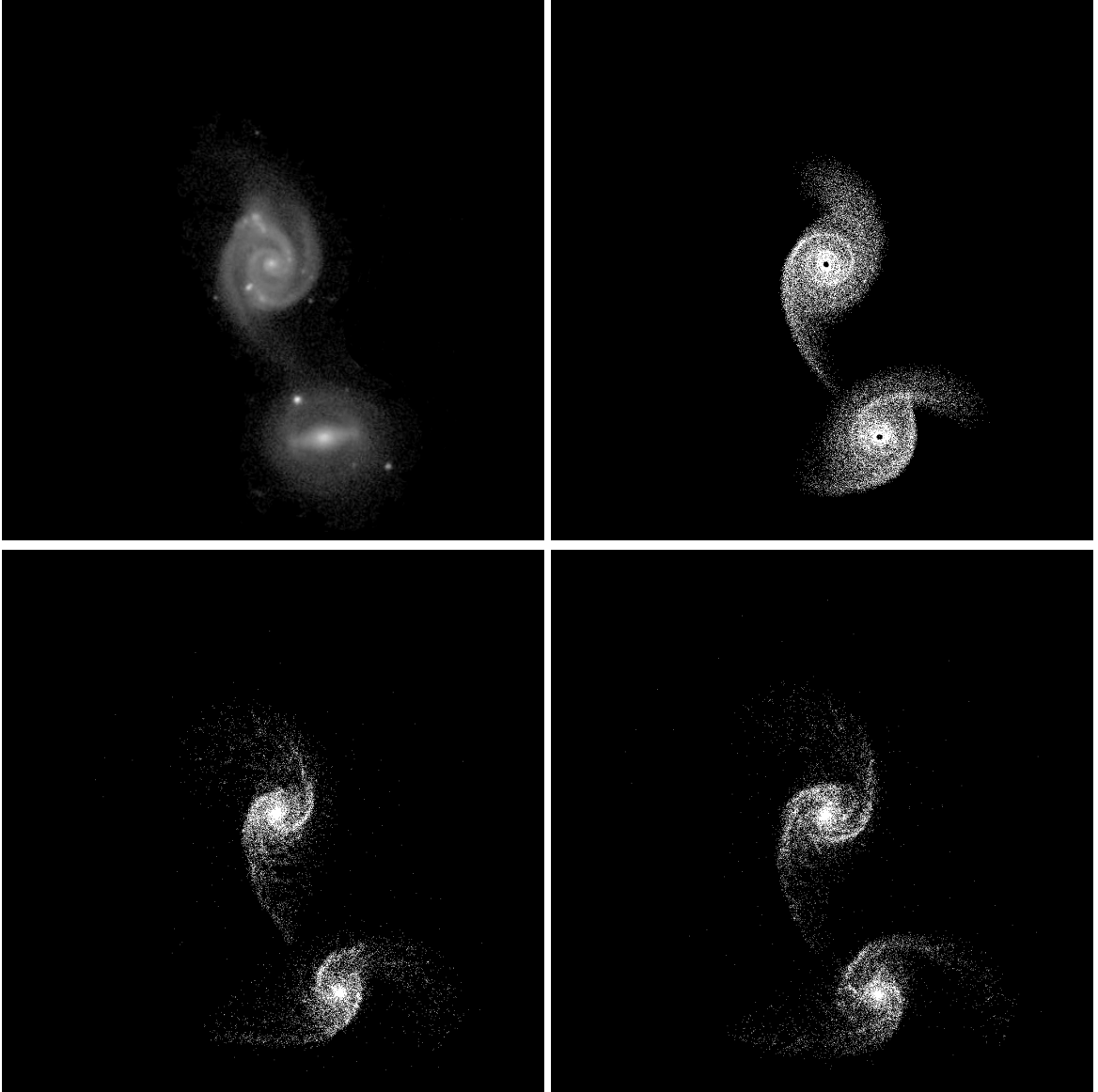


Figure 5.31: Target image (top-left), best SPAM match from Merger Wars (top-right), initial N-Body match (bottom-left), and best N-Body match (bottom-right) for SDSS 587727222471131318

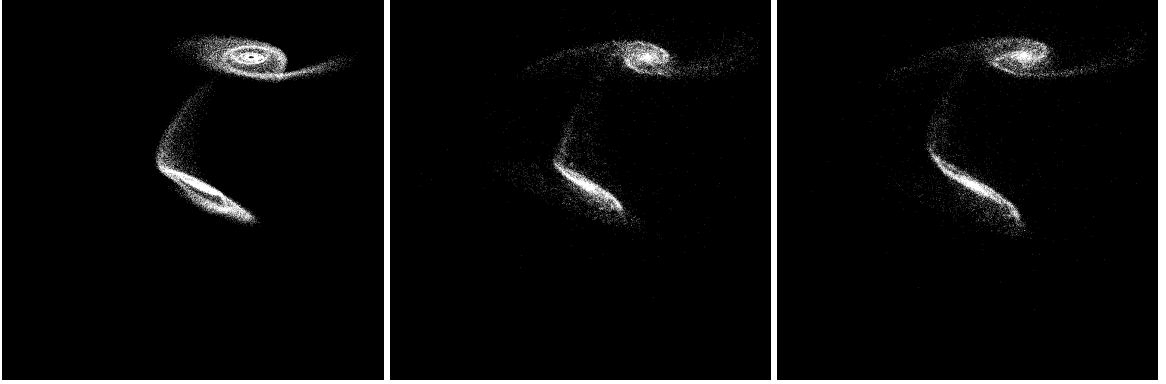


Figure 5.32: XZ projections of best SPAM match from Merger Wars (left), initial N-Body match (middle), and best N-Body match (right) for SDSS 587727222471131318

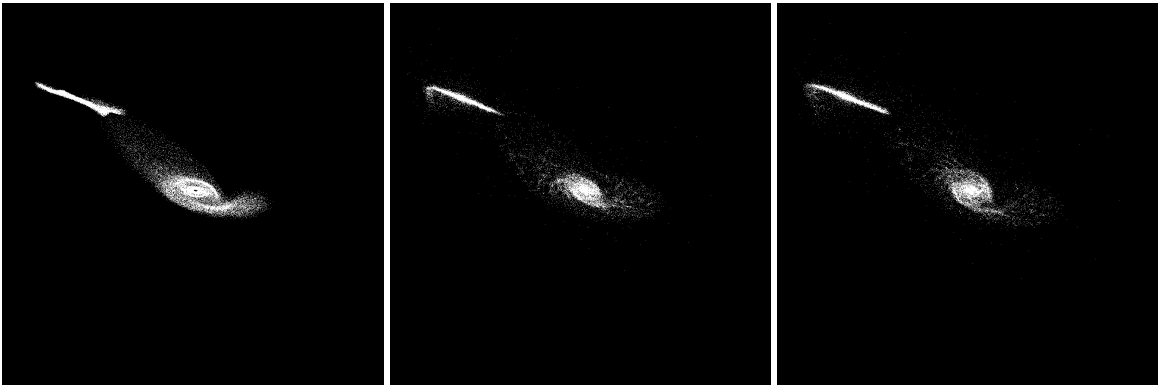


Figure 5.33: YZ projections of best SPAM match from Merger Wars (left), initial N-Body match (middle), and best N-Body match (right) for SDSS 587727222471131318

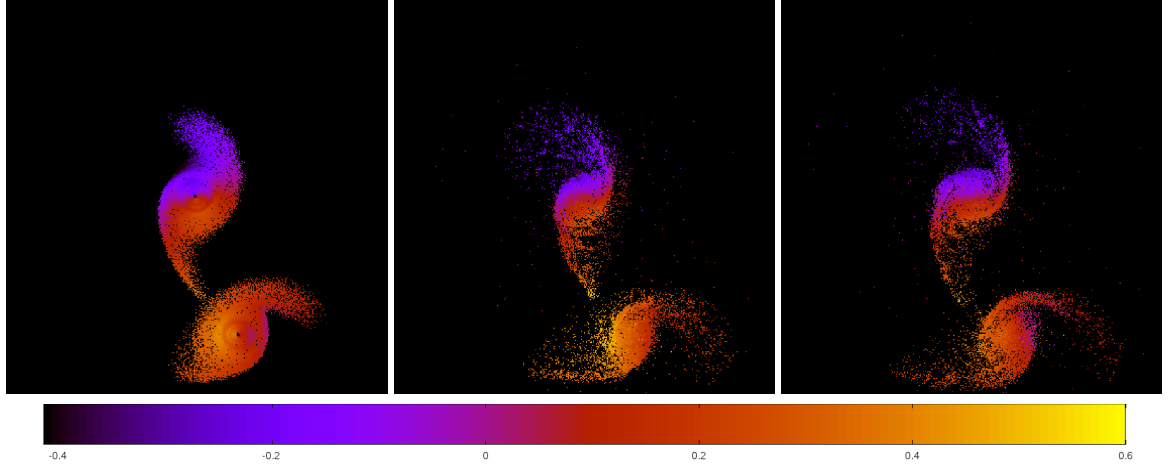


Figure 5.34: Line of sight velocity plots of best SPAM match from Merger Wars (left), initial N-Body match (middle), and best N-Body match (right) for SDSS 587727222471131318

Table 5.12: Orbital Elements & Dynamical Friction for SDSS 587727222471131318

	SPAM Simulation	Initial N-Body Simulation	Best N-Body Simulation
a	-2.502	-1.061	-4.118
e	2.373	3.974	1.843
r_c	3.436	3.155	3.473
i	141.150°	141.845°	141.915°
Ω	351.519°	352.294°	352.166°
ω	7.053°	4.757°	5.767°
ν	62.139°	63.240°	65.045°
t_n	50	44	54
$\ln\Lambda$	N/A	1.00E-03	0.00E+00

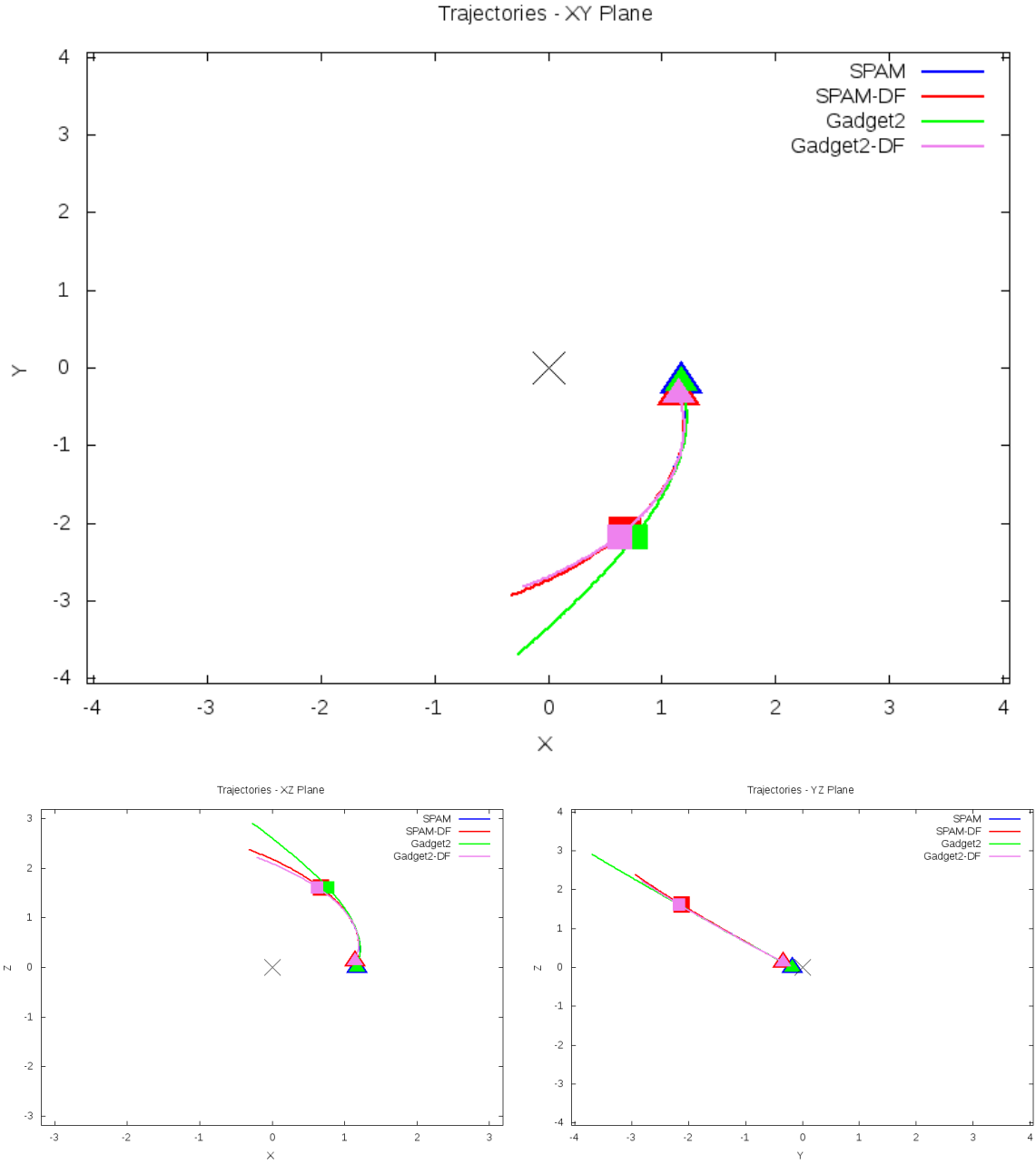


Figure 5.35: Trajectory plots of best SPAM match from Merger Wars, initial N-Body match, and best N-Body match for SDSS 587727222471131318

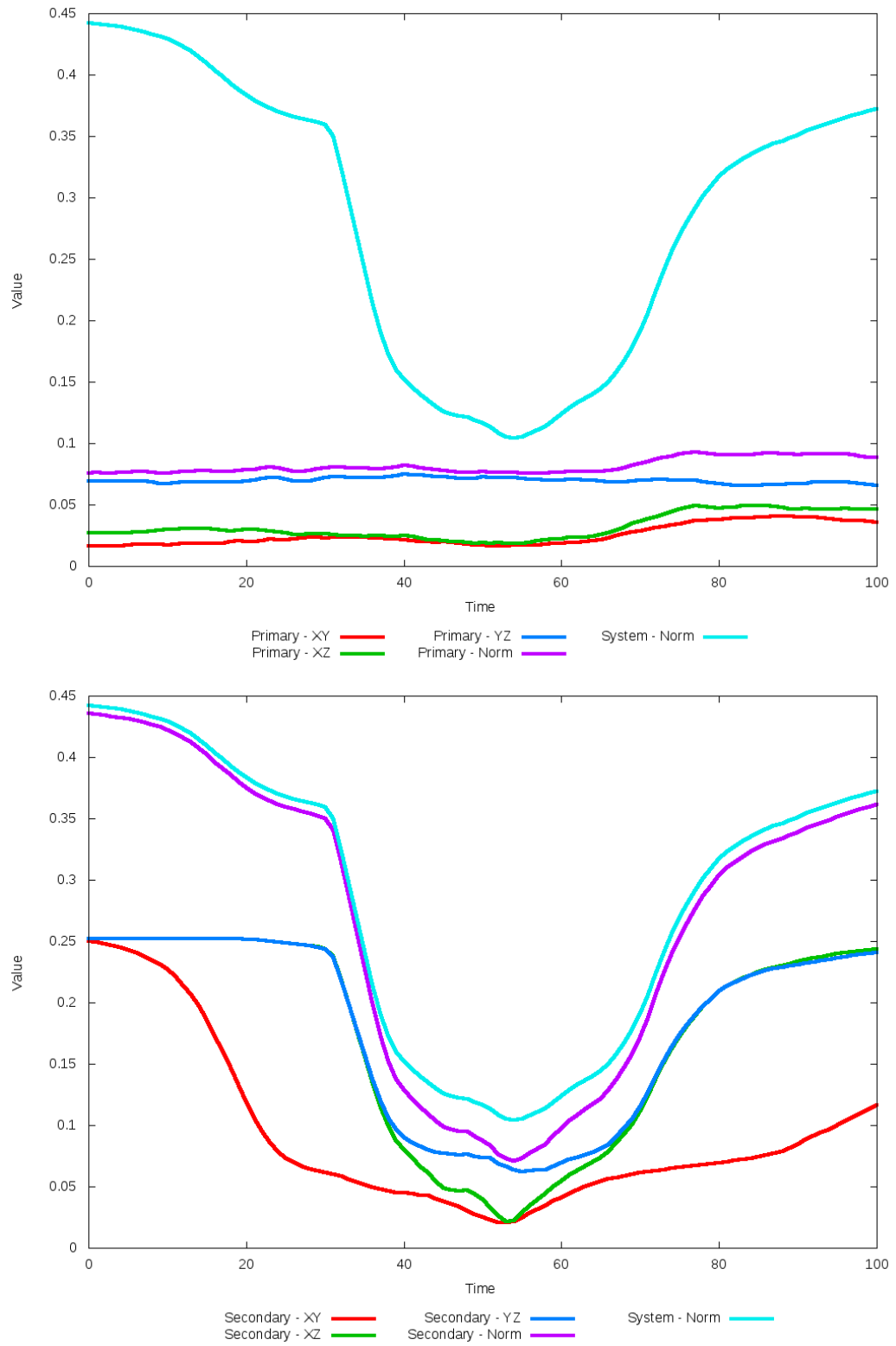


Figure 5.36: All metrics versus simulation time of the best N-Body simulation for SDSS 587727222471131318

5.1.7 SDSS 587728676861051075 (Arp 104)

Arp 104 exhibits a very poor match between the N-Body simulations with the SPAM simulation and observational data. Although the pipeline shows an improvement with change in dynamical friction, the galaxies have essentially merged, which is much different than desired. The restricted three-body simulation predicts a closed orbit with multiple periods while the N-Body simulation shows the merger in less than one. The initial conditions of the galaxies as modeled through Merger Wars need to be revised if there should be hope for an improved match.

Table 5.13: Identification Information and Merger Zoo summary for SDSS 587728676861051075.

Name	Aliases	RA (hms)	Dec (dms)	Redshift
SDSS 587728676861051075	Arp 104, NGC 5216/5218	13:32:10.2	+62:46:02.4	0.009783

R_x	R_y	R_z	V_x	V_y	V_z
0.05958	-0.64055	-0.62252	0.19343	-0.15746	-0.31657

	Primary Galaxy	Secondary Galaxy
mass	0.87551	0.47456
radius	0.09603	0.05894
ϕ	78.08622°	87.64218°
θ	36.69664°	347.76946°
ϵ	0.3	0.3

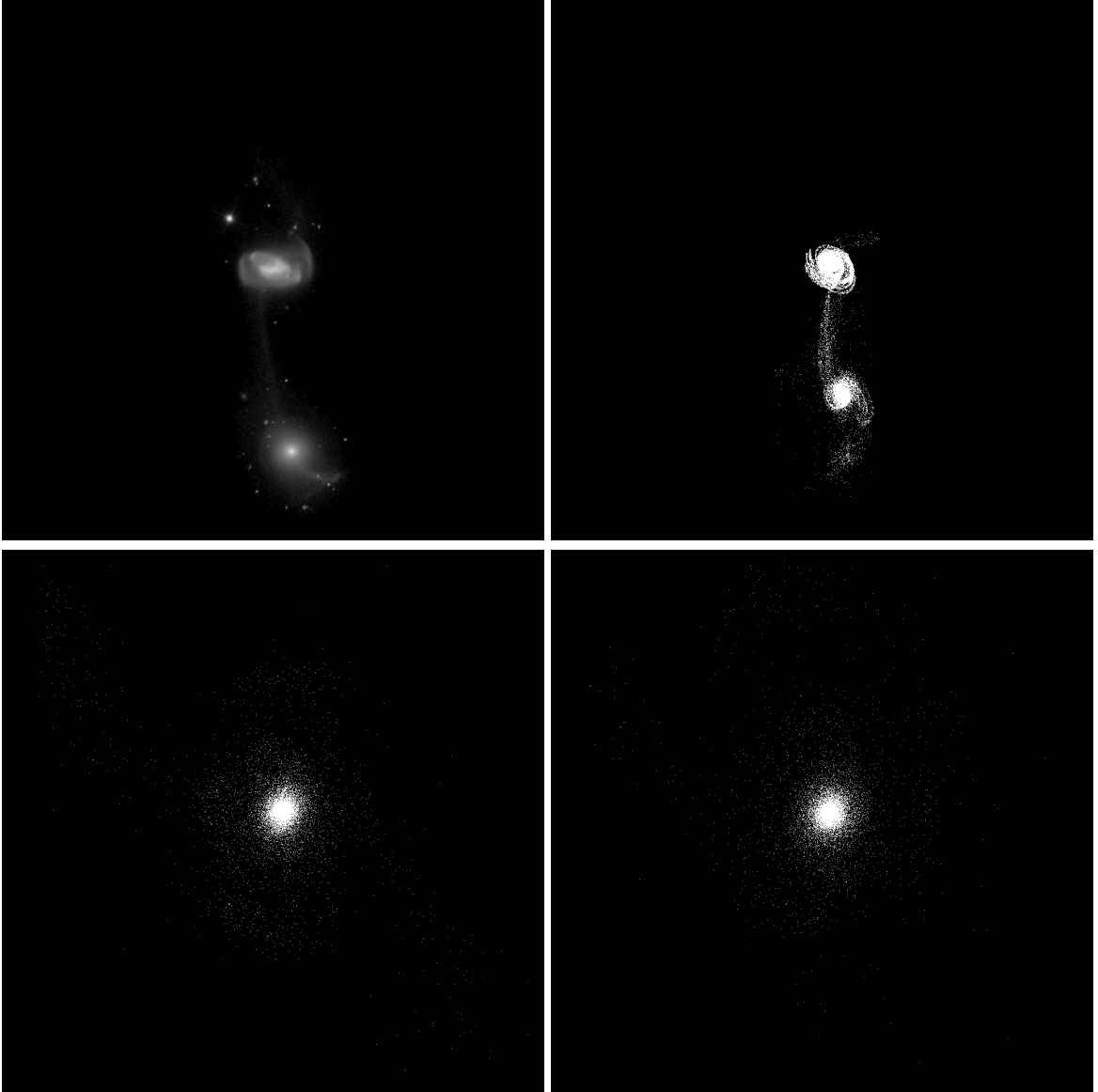


Figure 5.37: Target image (top-left), best SPAM match from Merger Wars (top-right), initial N-Body match (bottom-left), and best N-Body match (bottom-right) for SDSS 587728676861051075

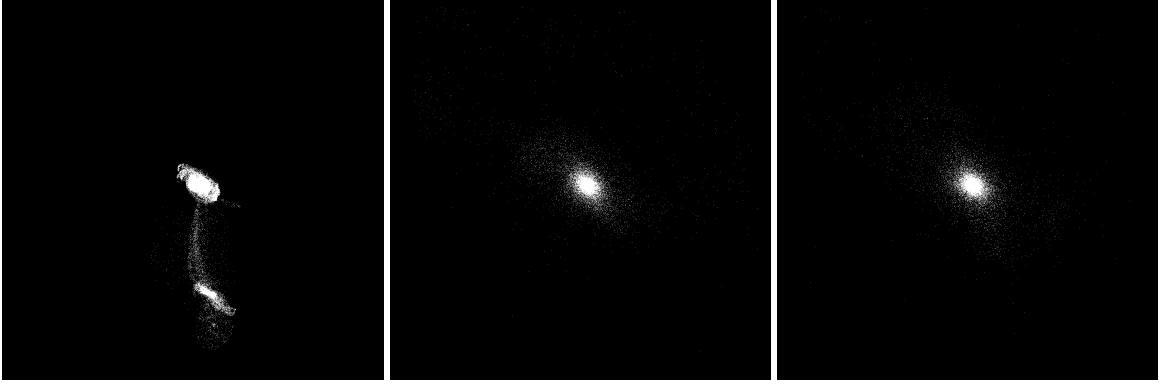


Figure 5.38: XZ projections of best SPAM match from Merger Wars (left), initial N-Body match (middle), and best N-Body match (right) for SDSS 587728676861051075

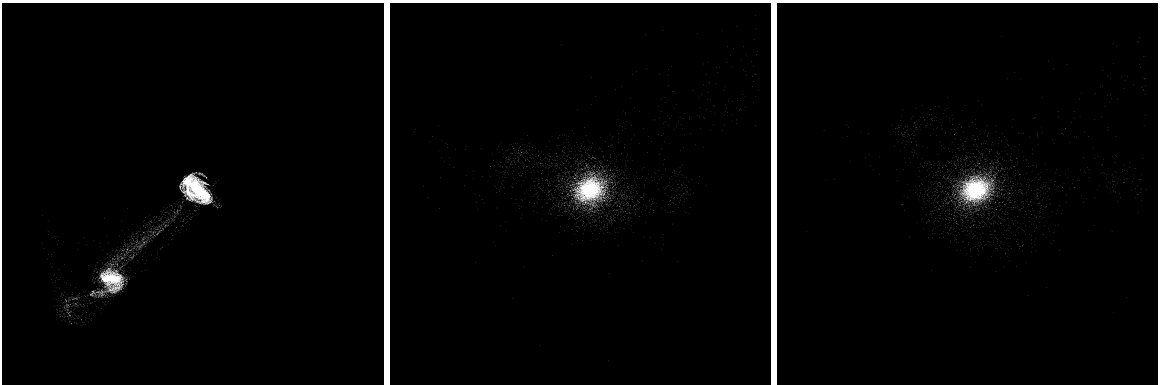


Figure 5.39: YZ projections of best SPAM match from Merger Wars (left), initial N-Body match (middle), and best N-Body match (right) for SDSS 587728676861051075

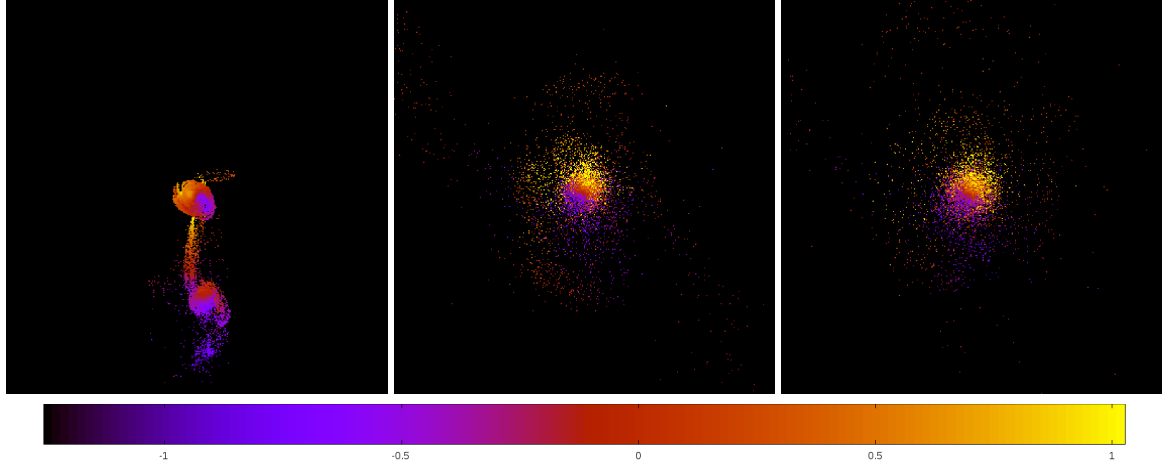


Figure 5.40: Line of sight velocity plots of best SPAM match from Merger Wars (left), initial N-Body match (middle), and best N-Body match (right) for SDSS 587728676861051075

Table 5.14: Orbital Elements & Dynamical Friction for SDSS 587728676861051075

	SPAM Simulation	Initial N-Body Simulation	Best N-Body Simulation
a	1.209	0.174	0.151
e	0.903	1.000	1.000
r_c	0.117	0.000	0.000
i	51.871°	136.095°	112.662°
Ω	45.890°	125.800°	252.787°
ω	76.284°	222.923°	328.477°
ν	165.530°	179.982°	179.951°
t_n	50	26	42
$\ln\Lambda$	N/A	1.00E-03	5.00E-04

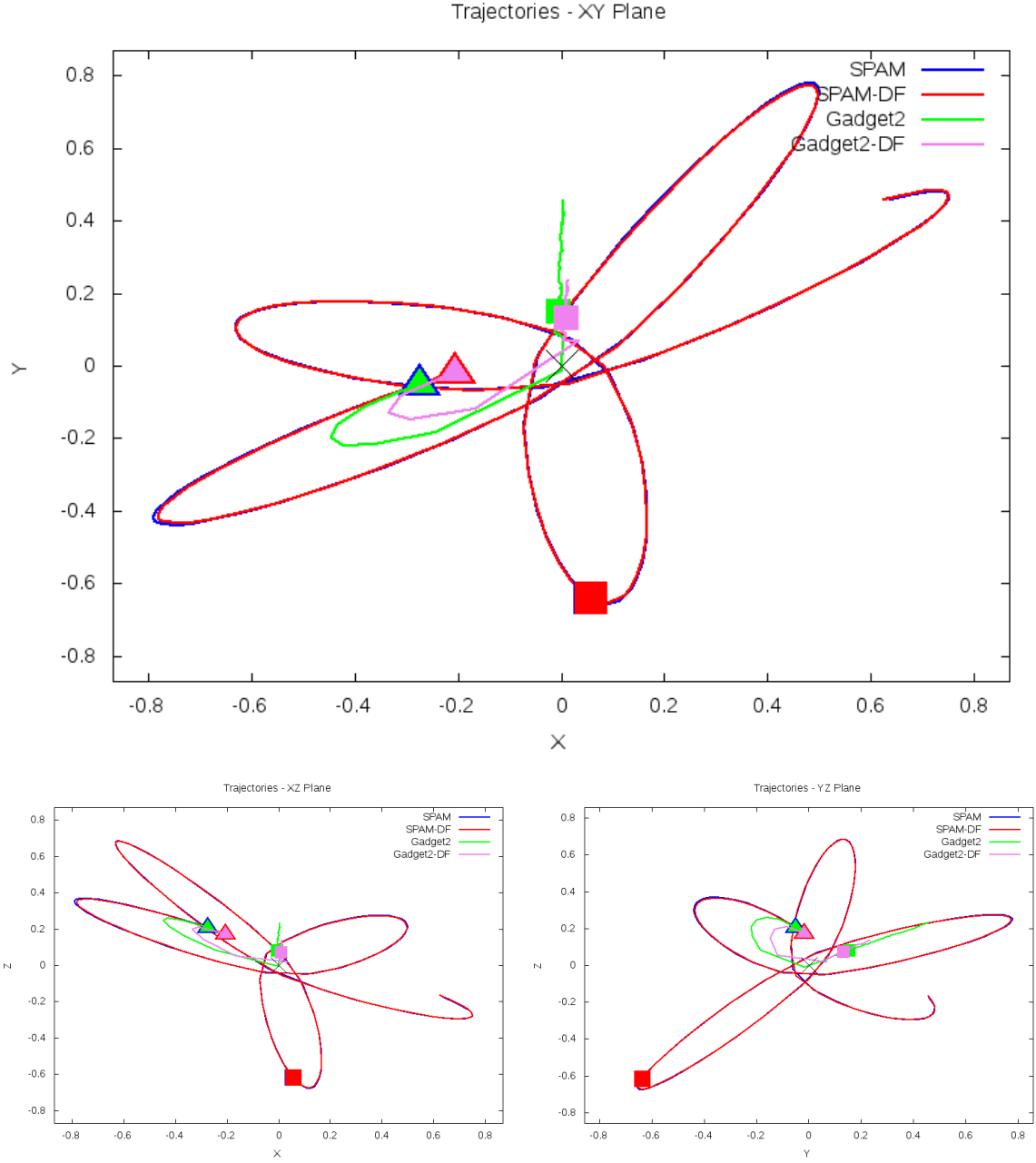


Figure 5.41: Trajectory plots of best SPAM match from Merger Wars, initial N-Body match, and best N-Body match for SDSS 587728676861051075

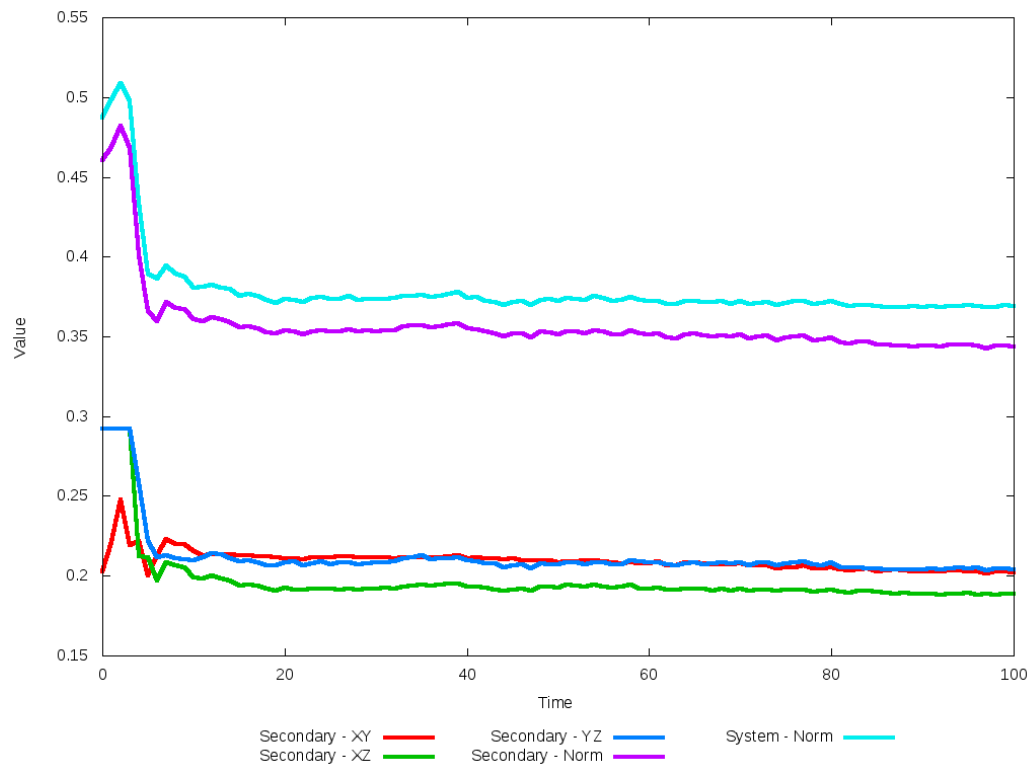
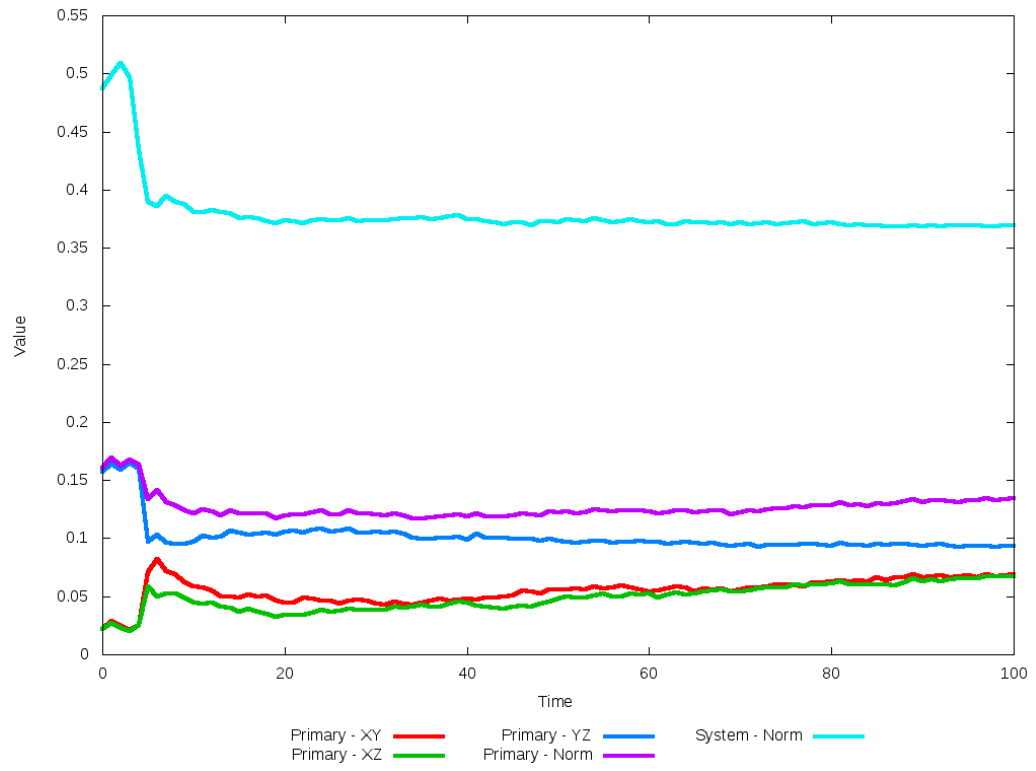


Figure 5.42: All metrics versus simulation time of the best N-Body simulation for SDSS 587728676861051075

5.1.8 SDSS 587729227151704160

The N-Body simulations of this system show modest agreement with the SPAM simulations and observational data. The centers of each galaxy appear to be well positioned to match the restricted three body simulation, but the tidal features of each galaxy are much broader and more diffused in the N-Body simulations. This diffusion does not allow for the appearance of prominent rings as seen in the observational data. The optimized dynamical friction does not present any apparent improvement in matching trajectories or features over the initial case. The inclusion of additional physics in the N-Body simulations, such as gas, may change this behavior.

Table 5.15: Identification Information and Merger Zoo summary for SDSS 587729227151704160.

Name	Aliases	RA (hms)	Dec (dms)	Redshift
SDSS 587729227151704160	2MASS 15530935+5408557	15:53:08.6	+54:08:50.4	0.046756

R_x	R_y	R_z	V_x	V_y	V_z
-0.12623	0.35028	3.35743	-0.12979	0.55971	4.02072

	Primary Galaxy	Secondary Galaxy
mass	0.78258	0.98072
radius	0.30541	0.41196
ϕ	152.77952°	195.62801°
θ	147.22542°	138.42519°
ϵ	0.3	0.3

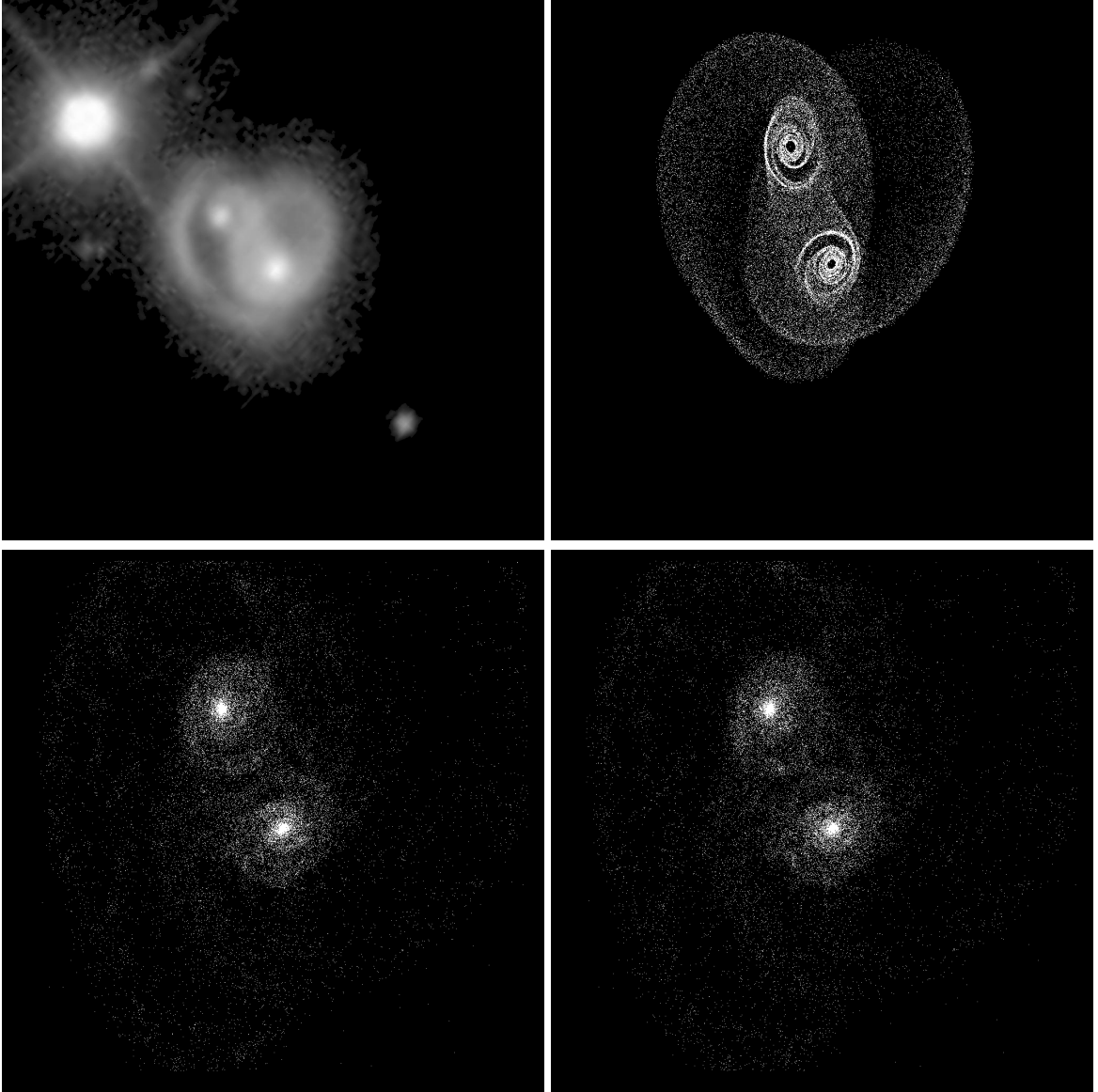


Figure 5.43: Target image (top-left), best SPAM match from Merger Wars (top-right), initial N-Body match (bottom-left), and best N-Body match (bottom-right) for SDSS 587729227151704160

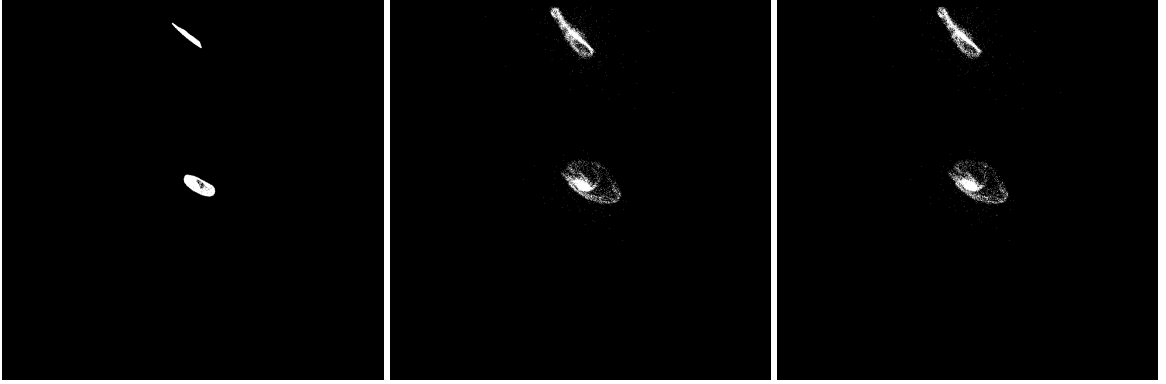


Figure 5.44: XZ projections of best SPAM match from Merger Wars (left), initial N-Body match (middle), and best N-Body match (right) for SDSS 587729227151704160

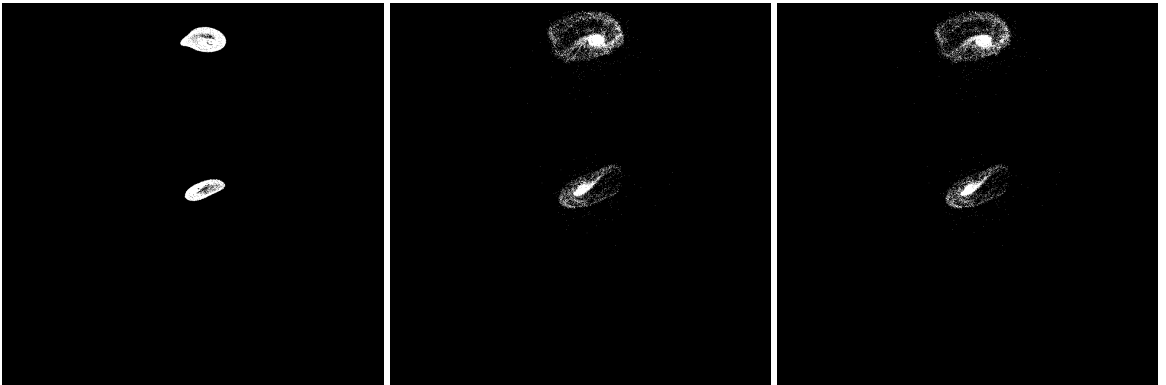


Figure 5.45: YZ projections of best SPAM match from Merger Wars (left), initial N-Body match (middle), and best N-Body match (right) for SDSS 587729227151704160

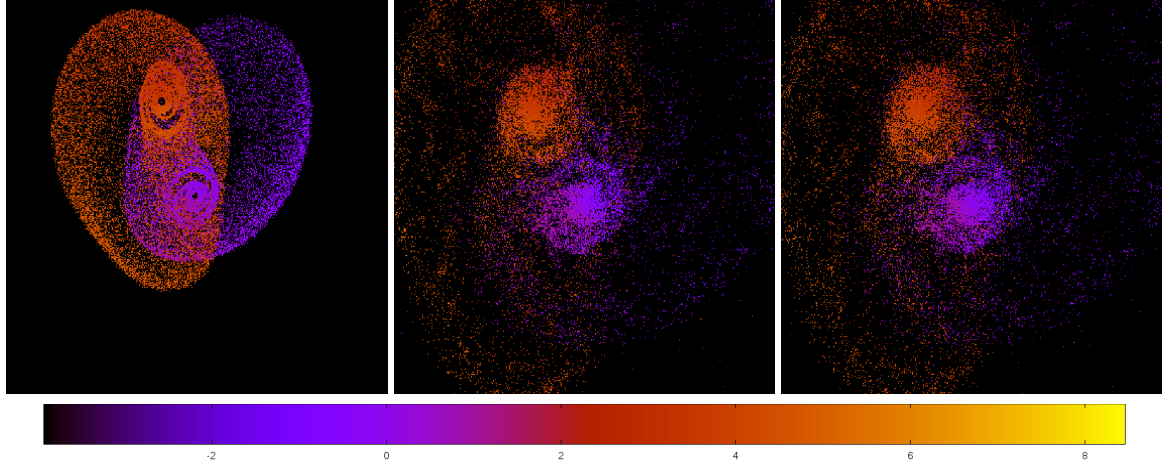


Figure 5.46: Line of sight velocity plots of best SPAM match from Merger Wars (left), initial N-Body match (middle), and best N-Body match (right) for SDSS 587729227151704160

Table 5.16: Orbital Elements & Dynamical Friction for SDSS 587729227151704160

	SPAM Simulation	Initial N-Body Simulation	Best N-Body Simulation
a	-0.054	-0.060	-0.061
e	4.526	4.116	4.100
r_c	0.189	0.187	0.188
i	93.028°	93.368°	93.371°
Ω	261.332°	267.260°	267.132°
ω	354.797°	352.385°	352.333°
ν	100.764°	102.062°	102.104°
t_n	50	52	52
$\ln\Lambda$	N/A	1.00E-03	4.00E-04

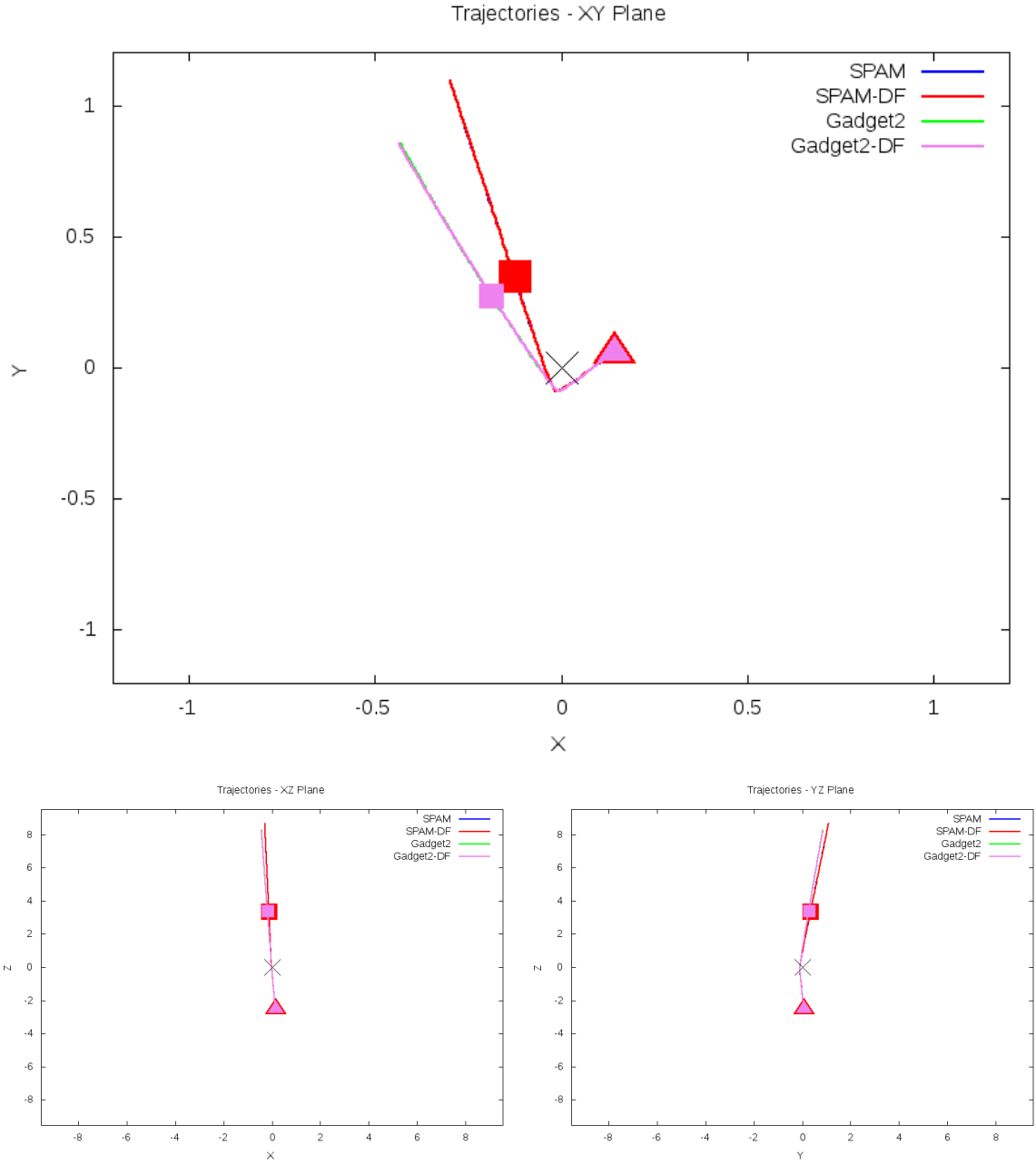


Figure 5.47: Trajectory plots of best SPAM match from Merger Wars, initial N-Body match, and best N-Body match for SDSS 587729227151704160

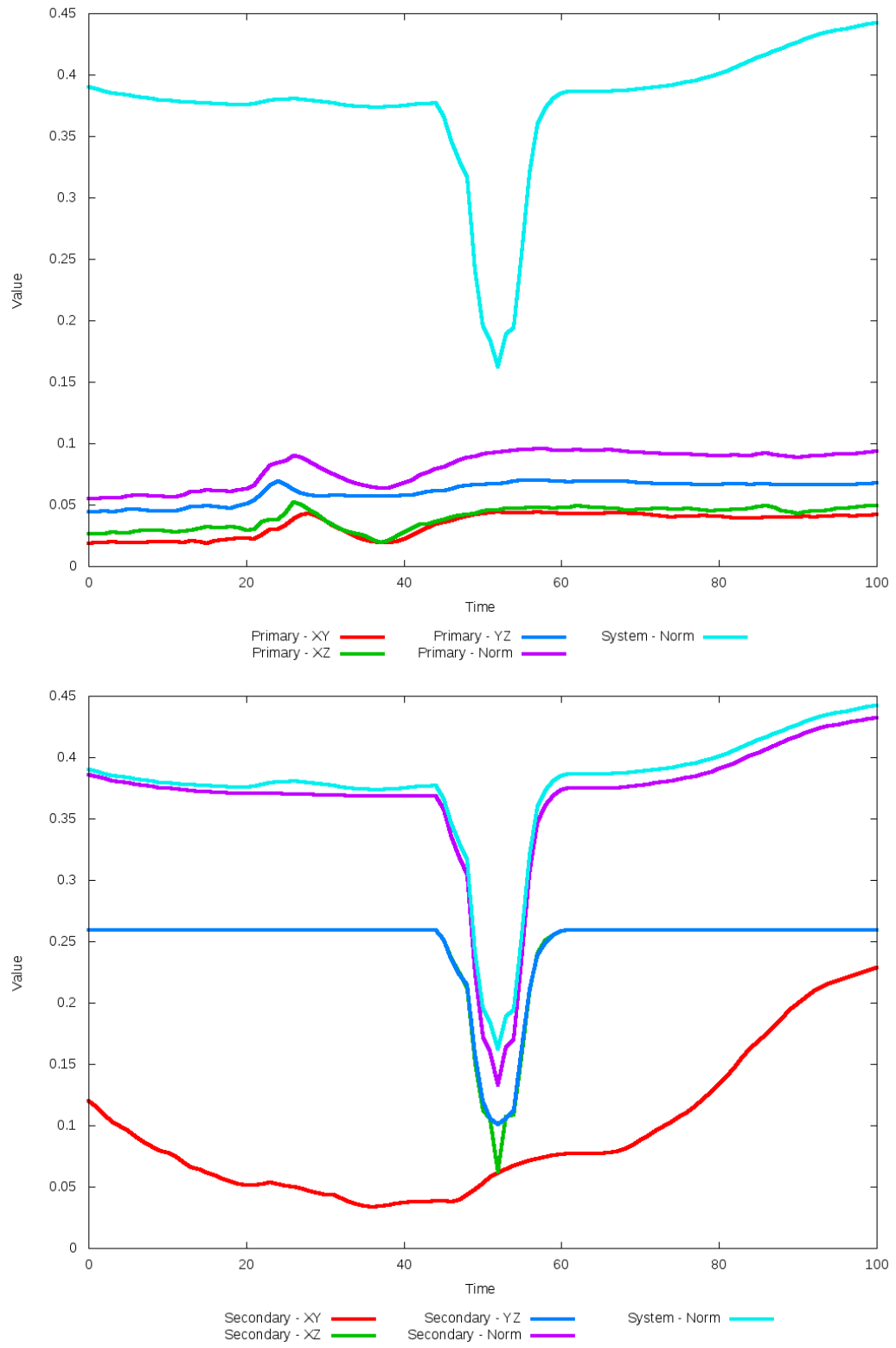


Figure 5.48: All metrics versus simulation time of the best N-Body simulation for SDSS 587729227151704160

5.1.9 SDSS 587731913110650988 (Arp 285)

Arp 285 exhibits very good agreement between the N-Body simulations with both the SPAM simulation and observational data. Again, the pipeline predicted a dynamical friction scalar at or near zero, with little apparent difference between it and the initial simulation in the XY projection. However, looking at the XZ and YZ projections shows a noticeable improvement in the location of the secondary galaxy when compared to the restricted three-body simulation. This agreement would not be found had the metric used in the optimization only looked at the XY plane.

Table 5.17: Identification Information and Merger Zoo summary for SDSS 587731913110650988.

Name	Aliases	RA (hms)	Dec (dms)	Redshift
SDSS 587731913110650988	Arp 285, NGC 2854/2856	9:24:02.9	+49:12:14.1	0.009243

R_x	R_y	R_z	V_x	V_y	V_z
-1.1109	1.42179	1.69164	-0.49869	0.50953	0.08717

	Primary Galaxy	Secondary Galaxy
mass	0.016	0.3198
radius	0.33392	0.38043
ϕ	51.18749°	-35.0°
θ	295.15527°	249.31677°
ϵ	0.3	0.3

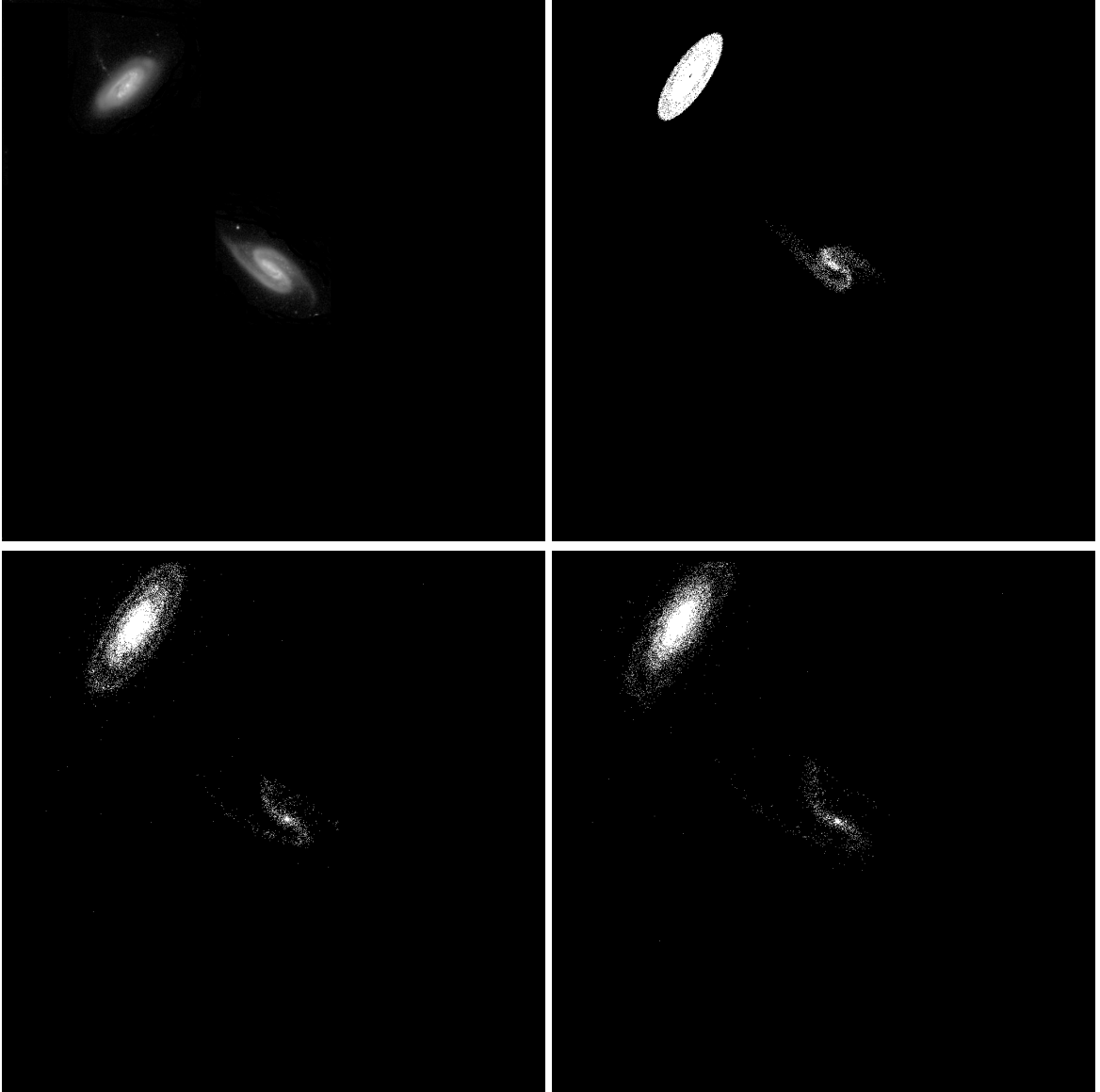


Figure 5.49: Target image (top-left), best SPAM match from Merger Wars (top-right), initial N-Body match (bottom-left), and best N-Body match (bottom-right) for SDSS 587731913110650988

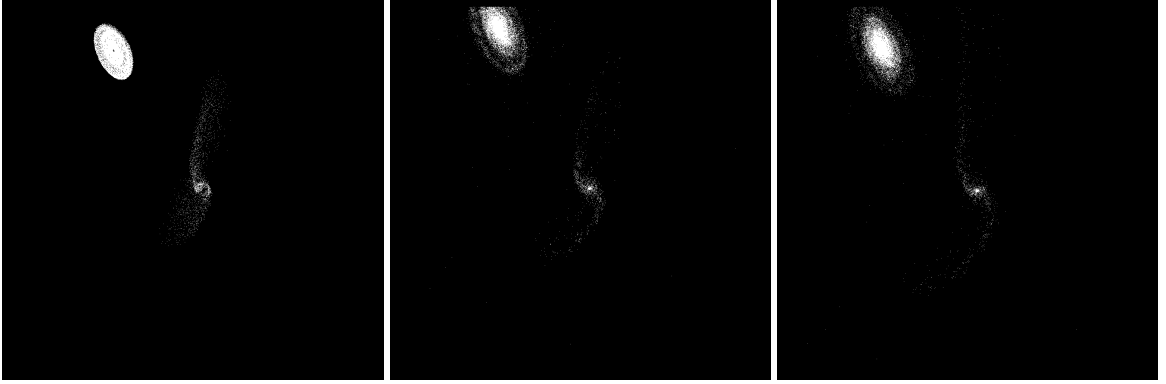


Figure 5.50: XZ projections of best SPAM match from Merger Wars (left), initial N-Body match (middle), and best N-Body match (right) for SDSS 587731913110650988

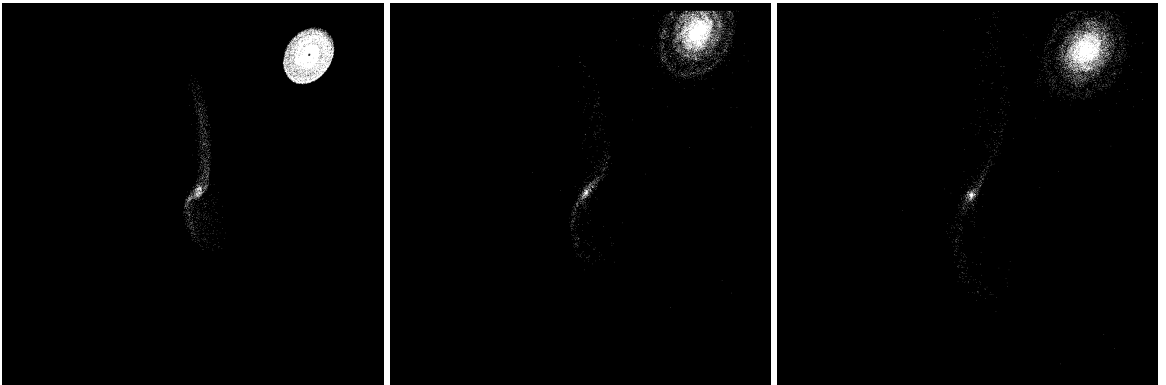


Figure 5.51: YZ projections of best SPAM match from Merger Wars (left), initial N-Body match (middle), and best N-Body match (right) for SDSS 587731913110650988

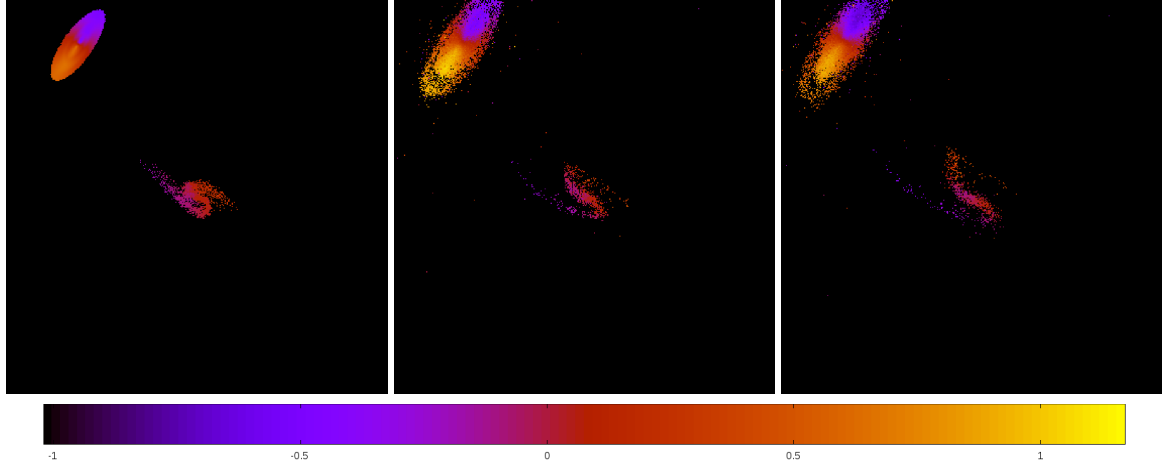


Figure 5.52: Line of sight velocity plots of best SPAM match from Merger Wars (left), initial N-Body match (middle), and best N-Body match (right) for SDSS 587731913110650988

Table 5.18: Orbital Elements & Dynamical Friction for SDSS 587731913110650988

	SPAM Simulation	Initial N-Body Simulation	Best N-Body Simulation
a	-0.061	-0.036	-0.060
e	49.358	80.990	49.483
r_c	2.926	2.842	2.908
i	82.244°	82.933°	83.096°
Ω	315.338°	316.006°	315.781°
ω	82.033°	74.136°	81.106°
ν	54.315°	58.481°	56.001°
t_n	50	47	51
$\ln\Lambda$	N/A	1.00E-03	0.00E+00

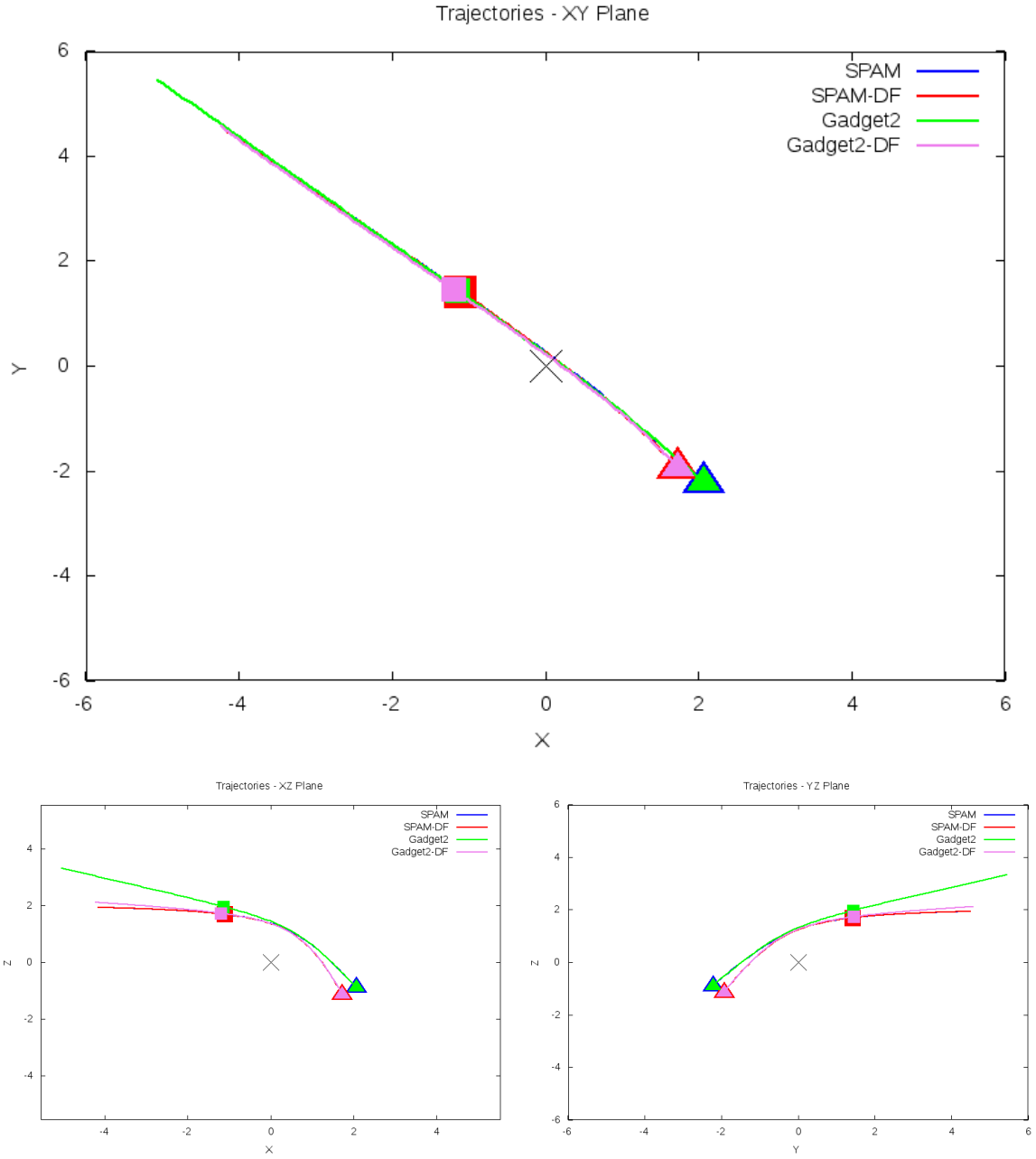


Figure 5.53: Trajectory plots of best SPAM match from Merger Wars, initial N-Body match, and best N-Body match for SDSS 587731913110650988

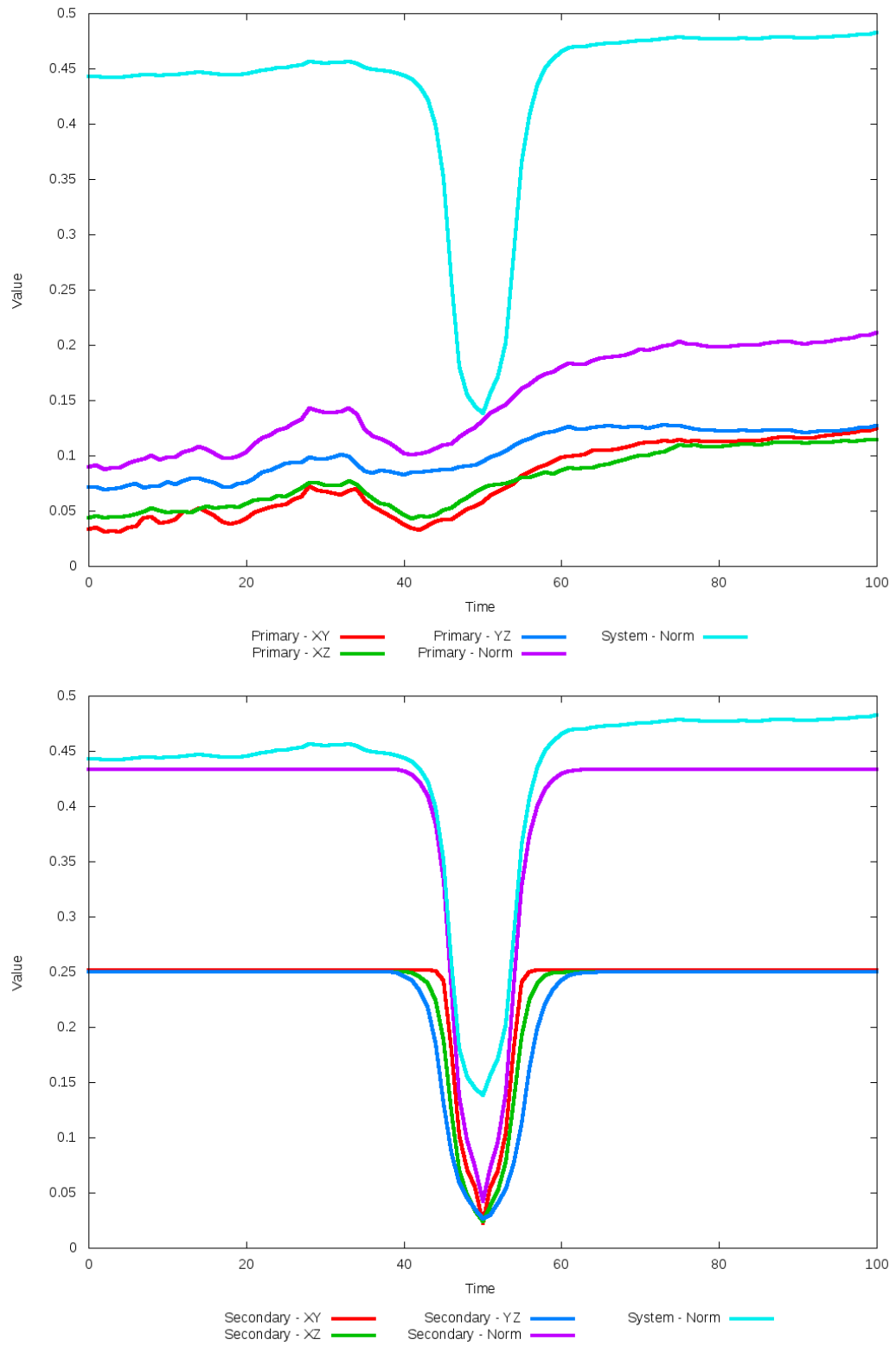


Figure 5.54: All metrics versus simulation time of the best N-Body simulation for SDSS 587731913110650988

5.1.10 SDSS 587732136993882121 (Arp 214)

Arp 214 shows better positional agreement of the secondary galaxy with the optimized dynamical friction found. This is more apparent in the YZ projection and line of sight velocity figures. Although the orientation of the tails in the primary galaxy appear to be a better match in the initial choice of dynamical friction, the shorter tails of the optimized simulation is better in the optimized case. If the optimization were done again using an increased number of output files (i.e. if the time between output files were smaller), then a best match may be found a little longer into the simulation, allowing the primary galaxy to rotate a more.

Table 5.19: Identification Information and Merger Zoo summary for SDSS 587732136993882121.

Name	Aliases	RA (hms)	Dec (dms)	Redshift
SDSS 587732136993882121	Arp 214, NGC 3718/3729	11:32:35.4	+53:04:00.0	0.003312

R_x	R_y	R_z	V_x	V_y	V_z
-2.87284	0.90246	0.0622	-0.33826	0.18874	-0.12684

	Primary Galaxy	Secondary Galaxy
mass	0.11758	0.10218
radius	0.53431	0.4208
ϕ	135.70152°	354.86088°
θ	140.82002°	138.13649°
ϵ	0.3	0.3

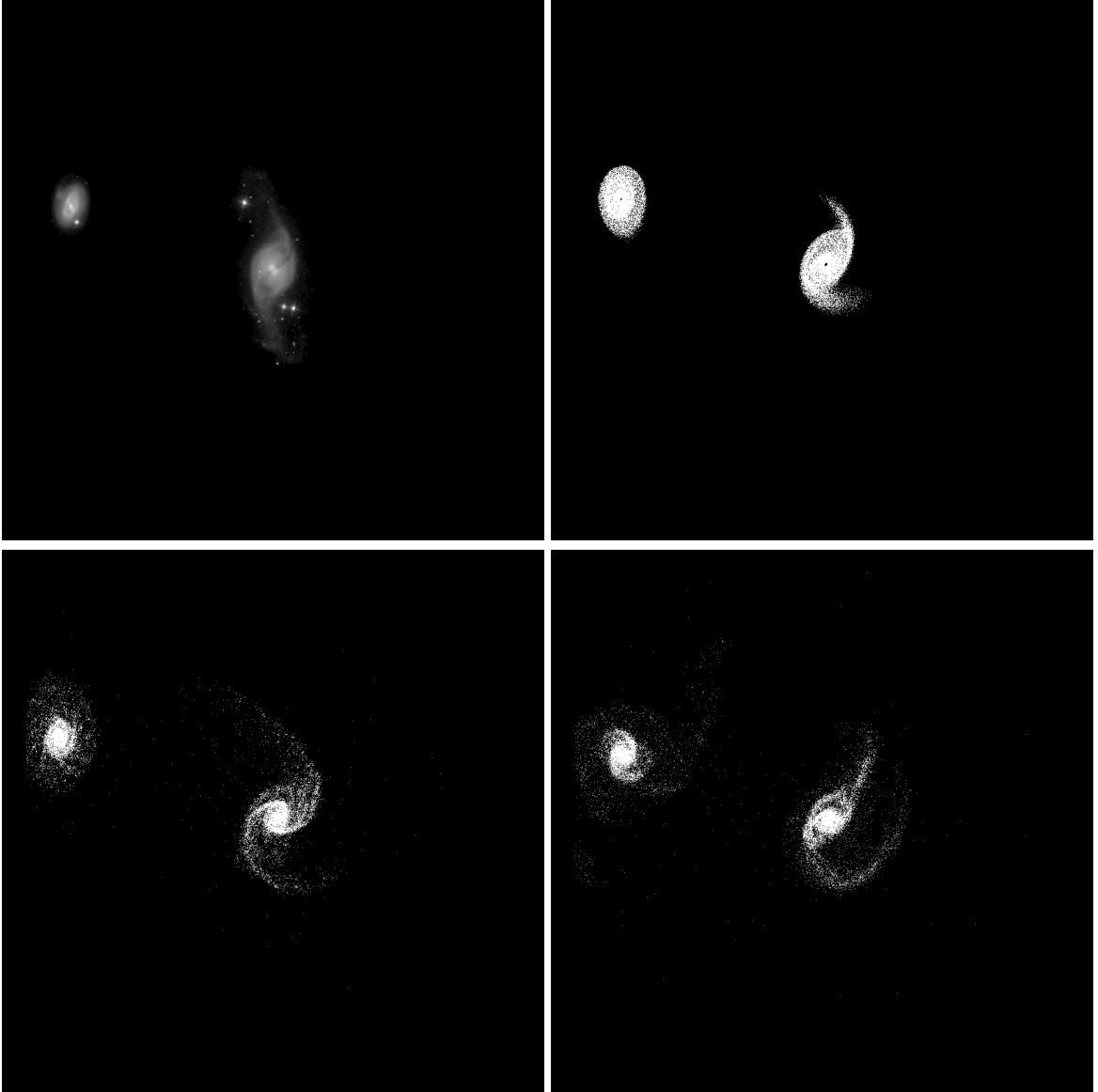


Figure 5.55: Target image (top-left), best SPAM match from Merger Wars (top-right), initial N-Body match (bottom-left), and best N-Body match (bottom-right) for SDSS 587732136993882121

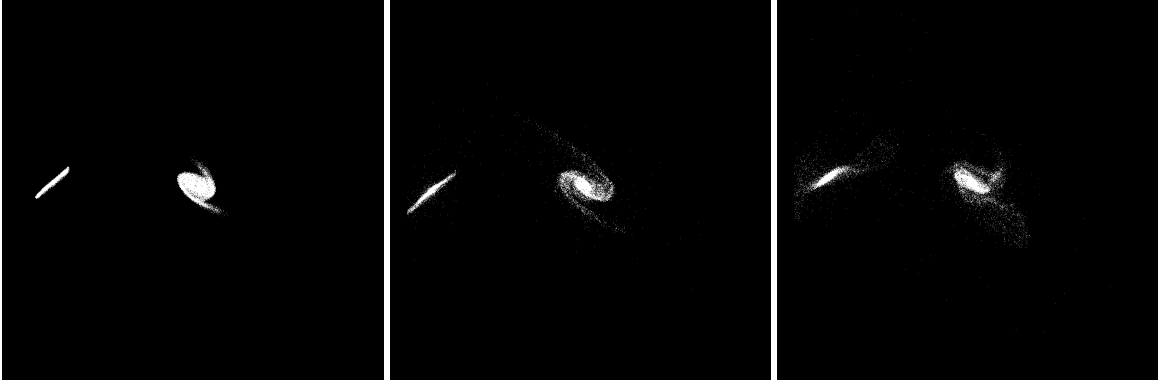


Figure 5.56: XZ projections of best SPAM match from Merger Wars (left), initial N-Body match (middle), and best N-Body match (right) for SDSS 587732136993882121

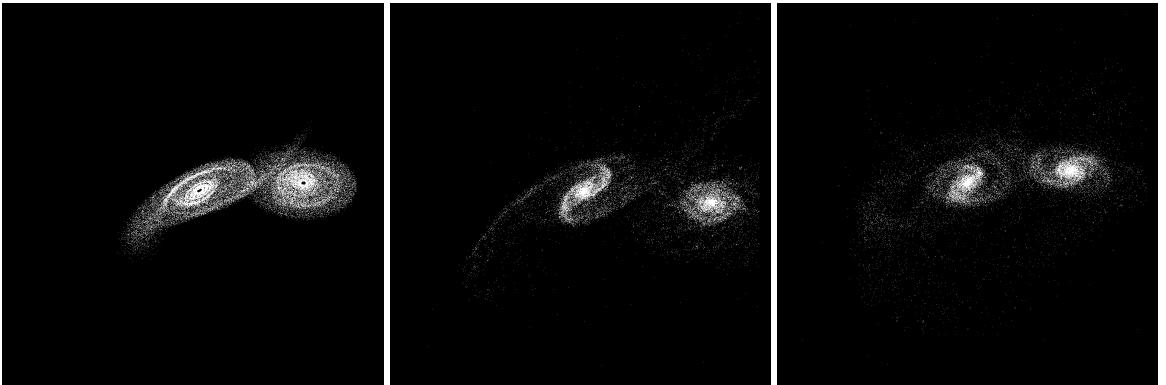


Figure 5.57: YZ projections of best SPAM match from Merger Wars (left), initial N-Body match (middle), and best N-Body match (right) for SDSS 587732136993882121

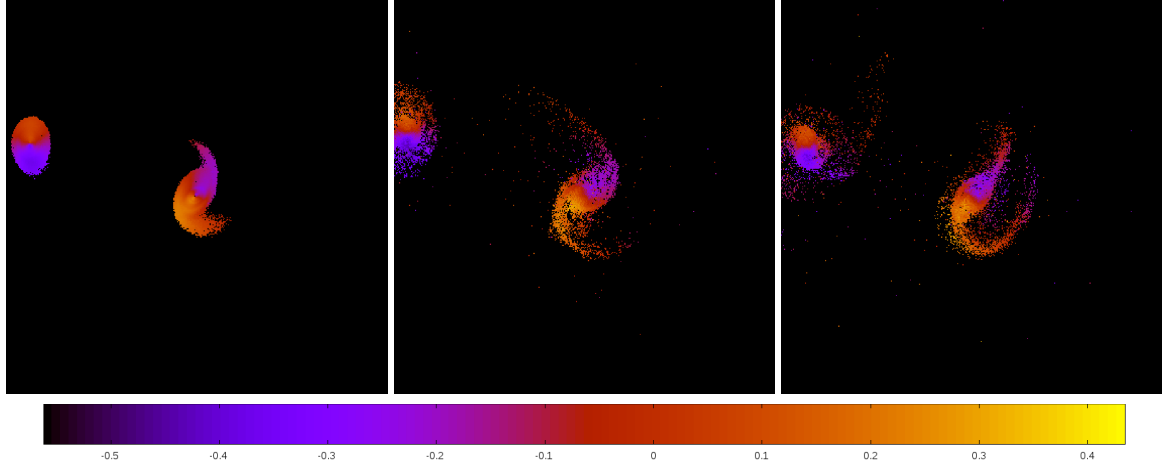


Figure 5.58: Line of sight velocity plots of best SPAM match from Merger Wars (left), initial N-Body match (middle), and best N-Body match (right) for SDSS 587732136993882121

Table 5.20: Orbital Elements & Dynamical Friction for SDSS 587732136993882121

	SPAM Simulation	Initial N-Body Simulation	Best N-Body Simulation
a	-0.840	-0.741	-0.525
e	3.256	3.620	4.466
r_c	1.896	1.942	1.822
i	120.296°	121.708°	121.002°
Ω	341.869°	341.780°	341.701°
ω	94.621°	98.447°	94.189°
ν	83.949°	83.771°	80.948°
t_n	50	55	47
$\ln\Lambda$	N/A	1.00E-03	1.60E-03

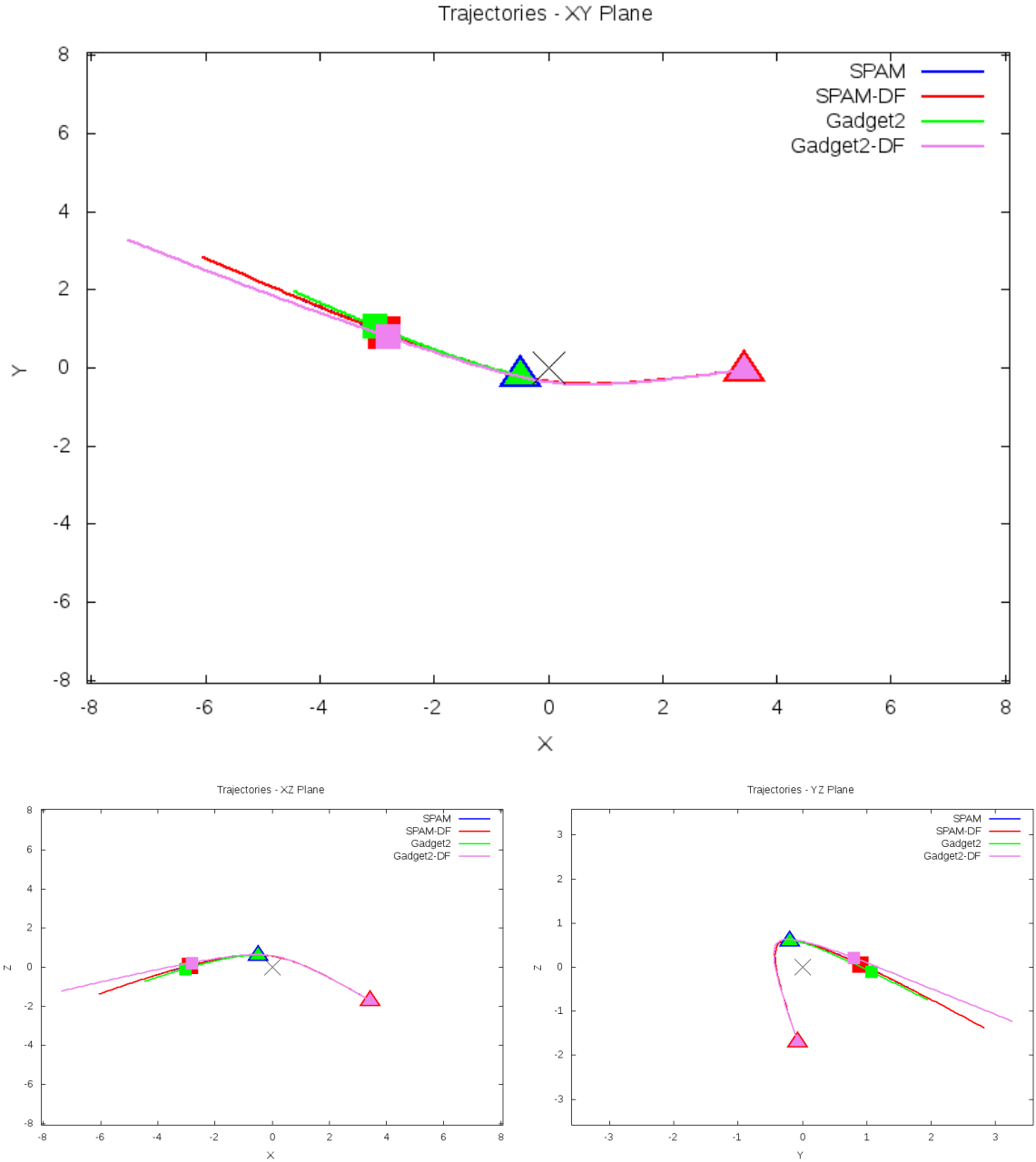


Figure 5.59: Trajectory plots of best SPAM match from Merger Wars, initial N-Body match, and best N-Body match for SDSS 587732136993882121

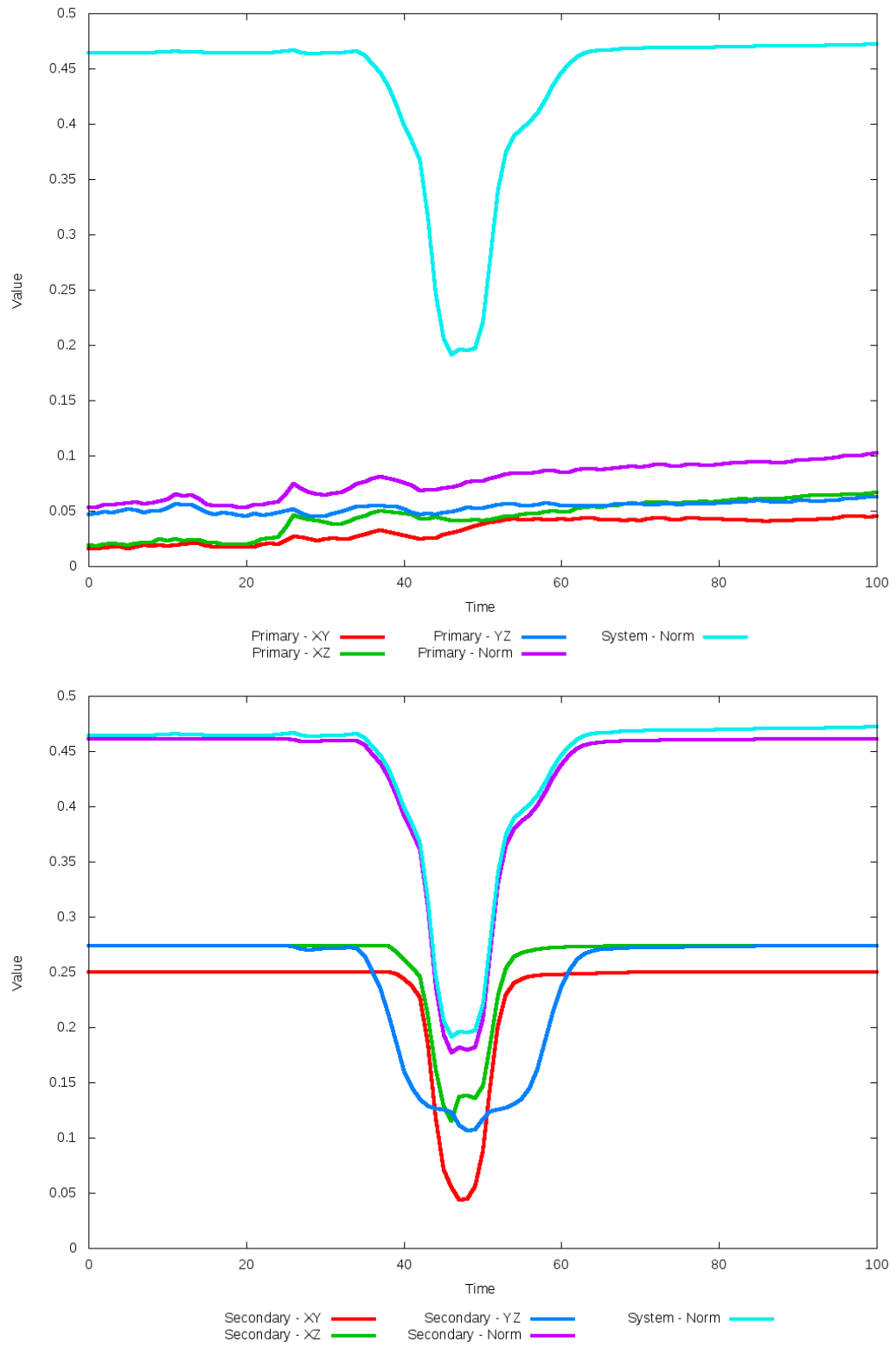


Figure 5.60: All metrics versus simulation time of the best N-Body simulation for SDSS 587732136993882121

5.1.11 SDSS 587732772130652231 (NGC 4320)

NGC 4320 could not be matched to either the SPAM simulation or observational data. The optimization process found the best dynamical friction to be the same as the starting value. The SPAM simulation which already is a questionable match to the target system exhibits multiple orbits. In all N-Body simulations for a range of dynamical friction values, the galaxies very quickly merge. As the systems merge, the metrics used in the optimization process are unable to clearly determine a point in time that best matches SPAM. This system likely needs to be reviewed by the Merger Wars system (or other means) to obtain a different candidate state vector to use in future N-Body simulations.

Table 5.21: Identification Information and Merger Zoo summary for SDSS 587732772130652231.

Name	Aliases	RA (hms)	Dec (dms)	Redshift
SDSS 587732772130652231	NGC 4320, UGC 7452	12:22:57.6	+10:32:52.7	0.026675

R_x	R_y	R_z	V_x	V_y	V_z
-0.10526	0.14243	-0.20682	-2.00321	-0.17917	0.6021

	Primary Galaxy	Secondary Galaxy
mass	0.79131	1.11639
radius	0.47156	0.1715
ϕ	117.875°	147.04046°
θ	326.45962°	65.75701°
ϵ	0.1	0.1

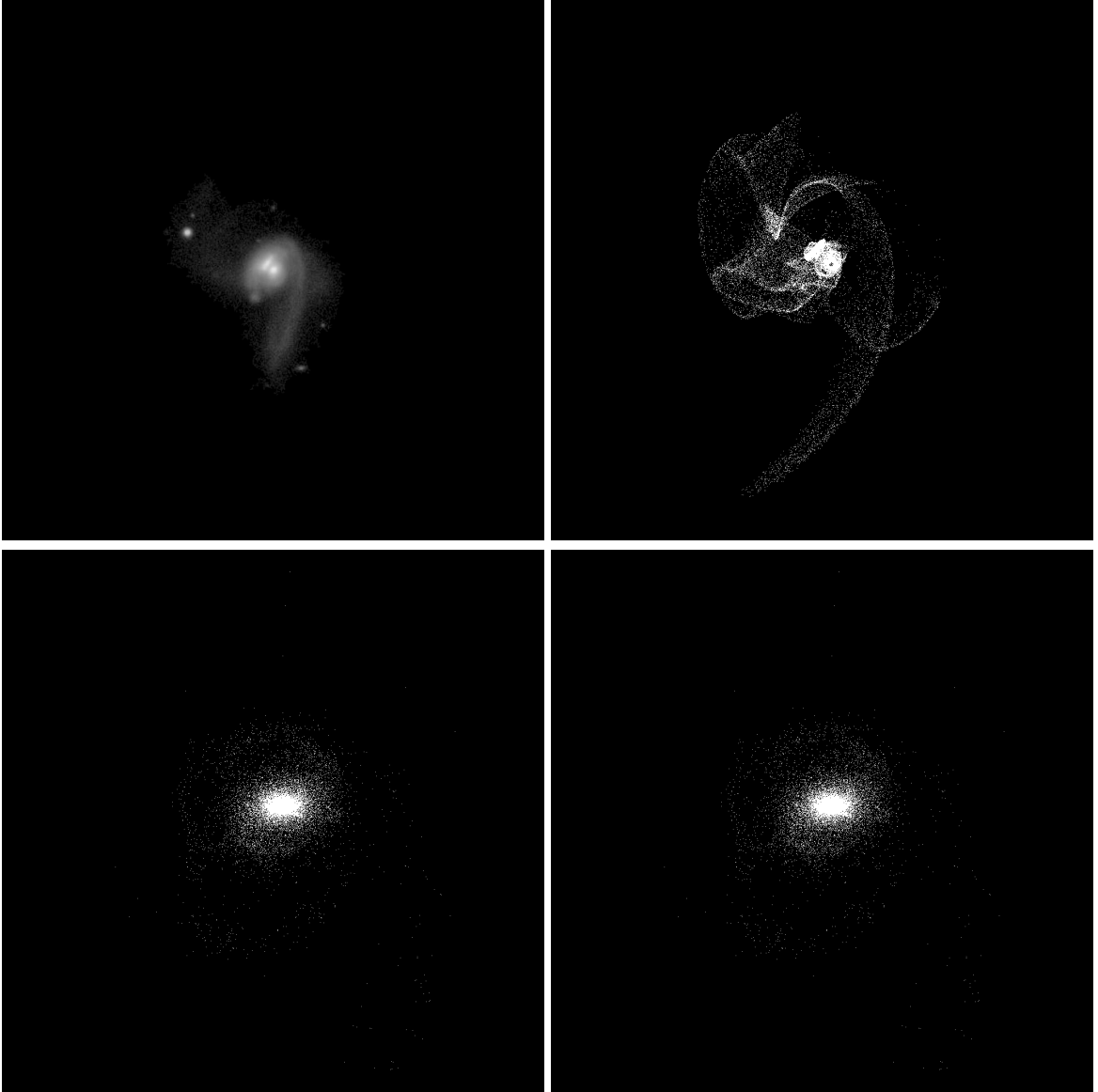


Figure 5.61: Target image (top-left), best SPAM match from Merger Wars (top-right), initial N-Body match (bottom-left), and best N-Body match (bottom-right) for SDSS 587732772130652231

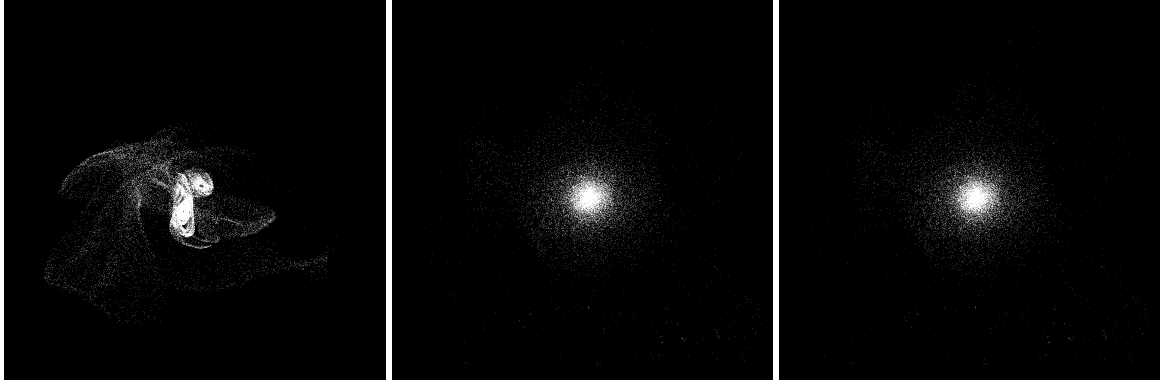


Figure 5.62: XZ projections of best SPAM match from Merger Wars (left), initial N-Body match (middle), and best N-Body match (right) for SDSS 587732772130652231

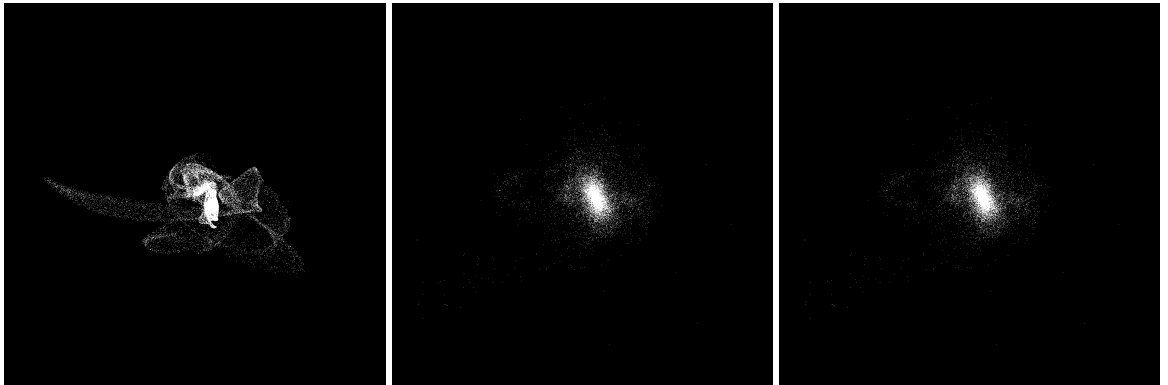


Figure 5.63: YZ projections of best SPAM match from Merger Wars (left), initial N-Body match (middle), and best N-Body match (right) for SDSS 587732772130652231

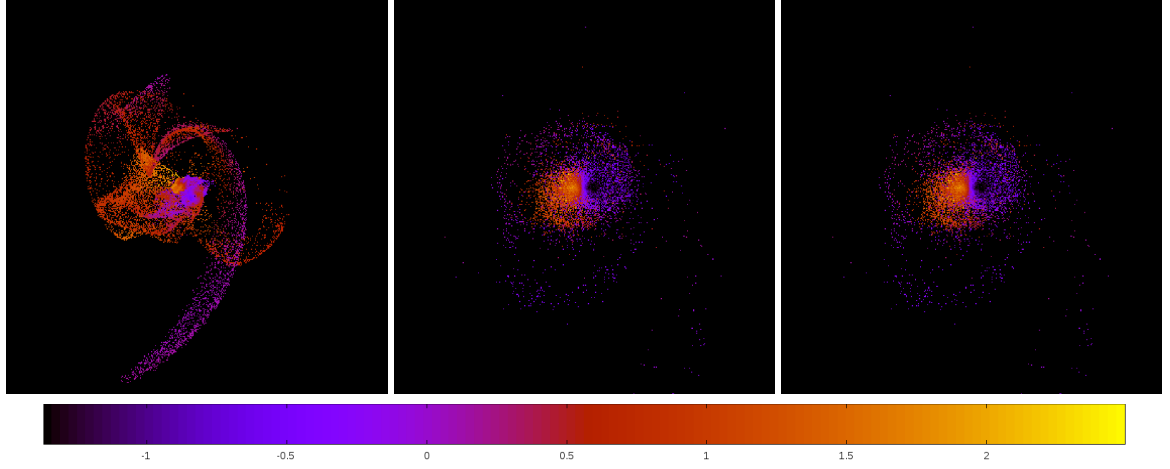


Figure 5.64: Line of sight velocity plots of best SPAM match from Merger Wars (left), initial N-Body match (middle), and best N-Body match (right) for SDSS 587732772130652231

Table 5.22: Orbital Elements & Dynamical Friction for SDSS 587732772130652231

	SPAM Simulation	Initial N-Body Simulation	Best N-Body Simulation
a	-0.934	0.165	0.165
e	1.579	0.999	0.999
r_c	0.541	0.000	0.000
i	57.646°	60.595°	60.595°
Ω	174.179°	221.658°	221.658°
ω	286.992°	54.523°	54.523°
ν	17.441°	180.026°	180.026°
t_n	50	100	100
$\ln\Lambda$	N/A	1.00E-03	1.00E-03

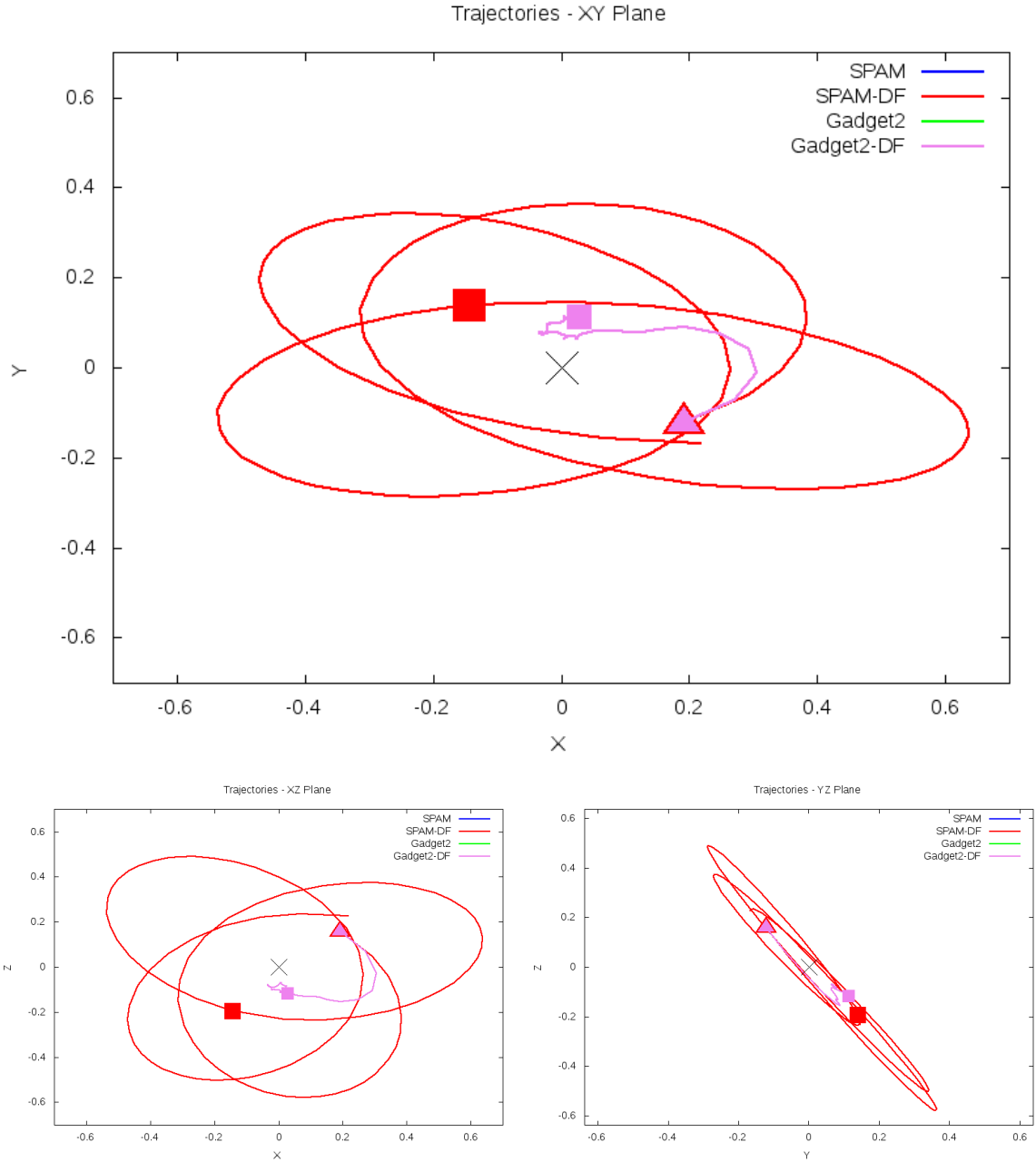


Figure 5.65: Trajectory plots of best SPAM match from Merger Wars, initial N-Body match, and best N-Body match for SDSS 587732772130652231

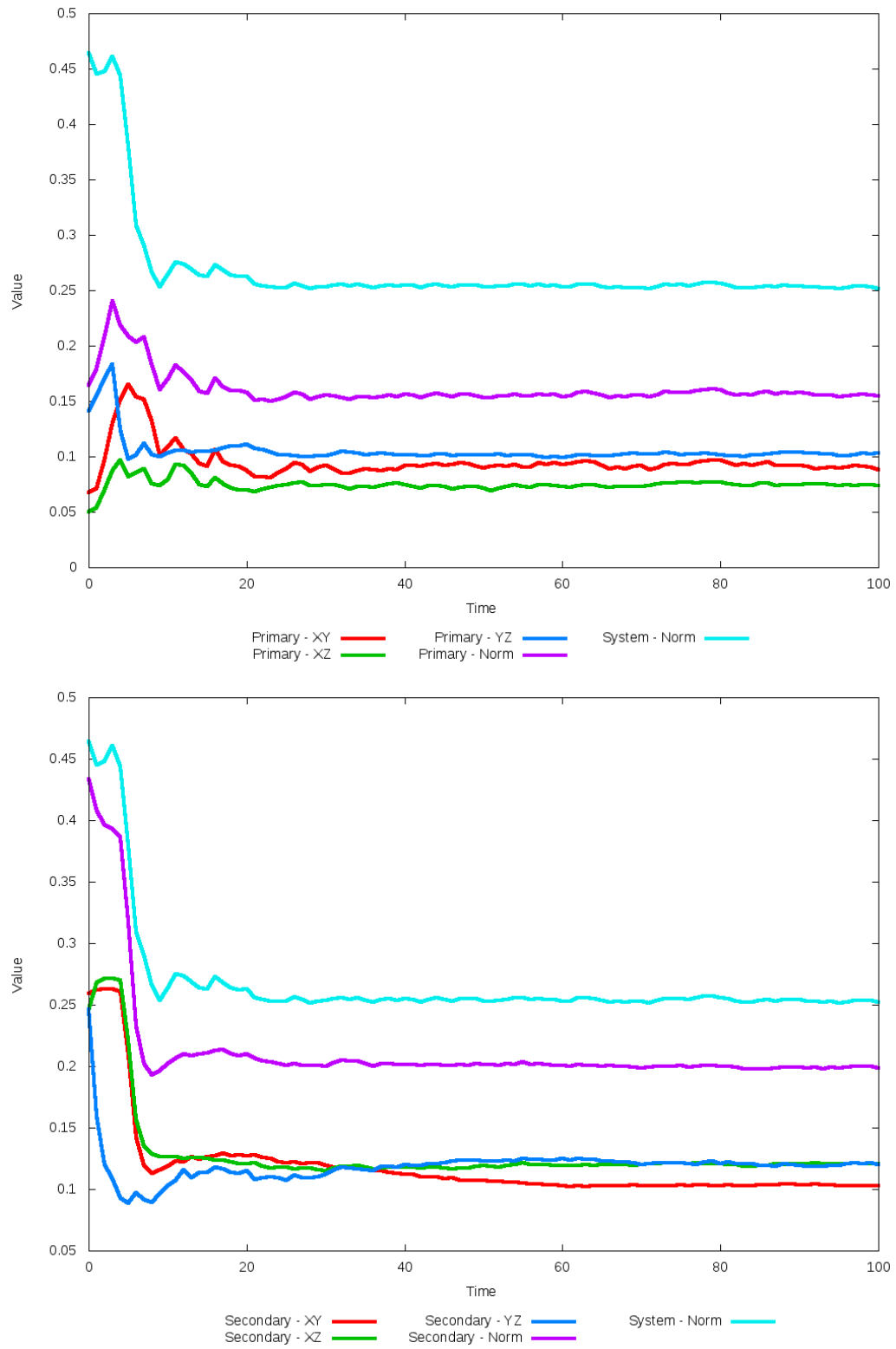


Figure 5.66: All metrics versus simulation time of the best N-Body simulation for SDSS 587732772130652231

5.1.12 SDSS 587733080814583863 (NGC 4669)

NGC 4669 shows a remarkable improvement in its quality of fit to the SPAM simulation from Merger Wars when dynamical friction is optimized. The location of the secondary galaxy is consistent with the location of the observational data and SPAM simulation, their trajectories are nearly identical, and line of sight velocities are consistent between the optimized and SPAM simulations. Although the tidal features of the primary galaxy are not as nearly pronounced in the optimized simulation compared to the observational data, the shape is approximately correct, although they appear more diffused.

Table 5.23: Identification Information and Merger Zoo summary for SDSS 587733080814583863.

Name	Aliases	RA (hms)	Dec (dms)	Redshift
SDSS 587733080814583863	NGC 4669, UGC 7905	12:43:49.4	+54:54:16.4	0.016261

R_x	R_y	R_z	V_x	V_y	V_z
0.08788	-0.63517	1.09776	-0.66456	-0.47795	0.39667

	Primary Galaxy	Secondary Galaxy
mass	0.20617	1.16277
radius	0.27916	0.33541
ϕ	14.93183°	68.71883°
θ	103.69424°	239.11166°
ϵ	0.3	0.3

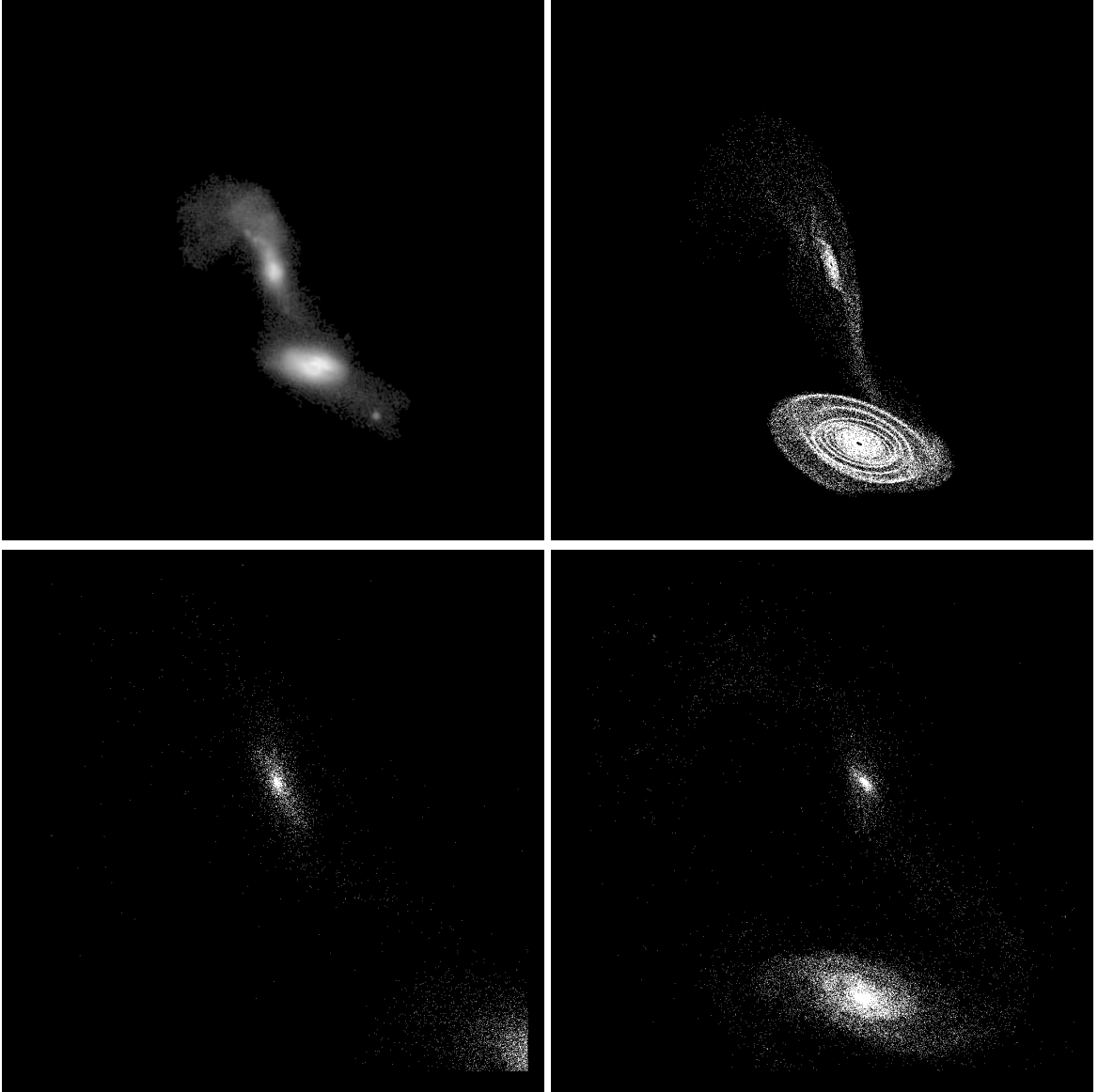


Figure 5.67: Target image (top-left), best SPAM match from Merger Wars (top-right), initial N-Body match (bottom-left), and best N-Body match (bottom-right) for SDSS 587733080814583863

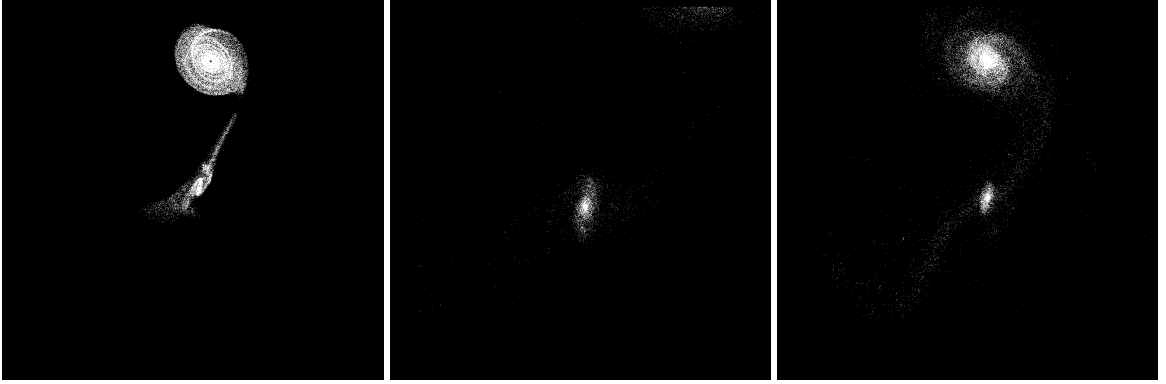


Figure 5.68: XZ projections of best SPAM match from Merger Wars (left), initial N-Body match (middle), and best N-Body match (right) for SDSS 587733080814583863

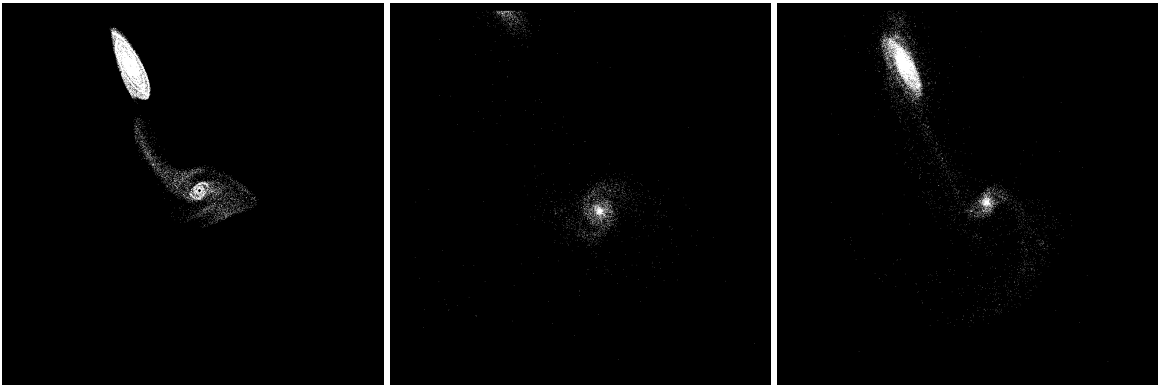


Figure 5.69: YZ projections of best SPAM match from Merger Wars (left), initial N-Body match (middle), and best N-Body match (right) for SDSS 587733080814583863

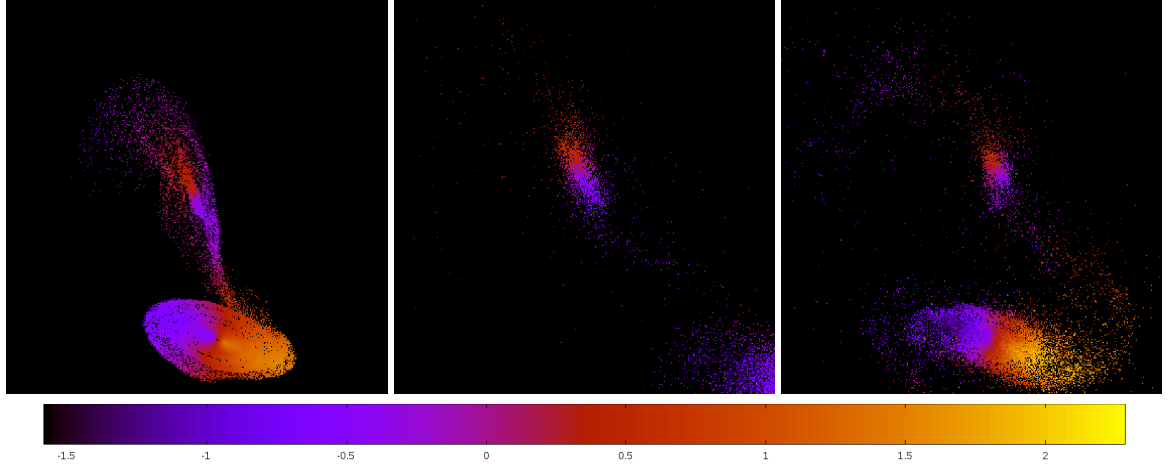


Figure 5.70: Line of sight velocity plots of best SPAM match from Merger Wars (left), initial N-Body match (middle), and best N-Body match (right) for SDSS 587733080814583863

Table 5.24: Orbital Elements & Dynamical Friction for SDSS 587733080814583863

	SPAM Simulation	Initial N-Body Simulation	Best N-Body Simulation
a	-0.616	-1.035	-1.465
e	4.153	4.063	2.200
r_c	1.942	3.169	1.758
i	119.764°	122.800°	120.424°
Ω	19.636°	20.342°	20.855°
ω	50.862°	23.627°	39.182°
ν	44.369°	49.802°	55.909°
t_n	50	64	52
$\ln\Lambda$	N/A	1.00E-03	2.00E-03

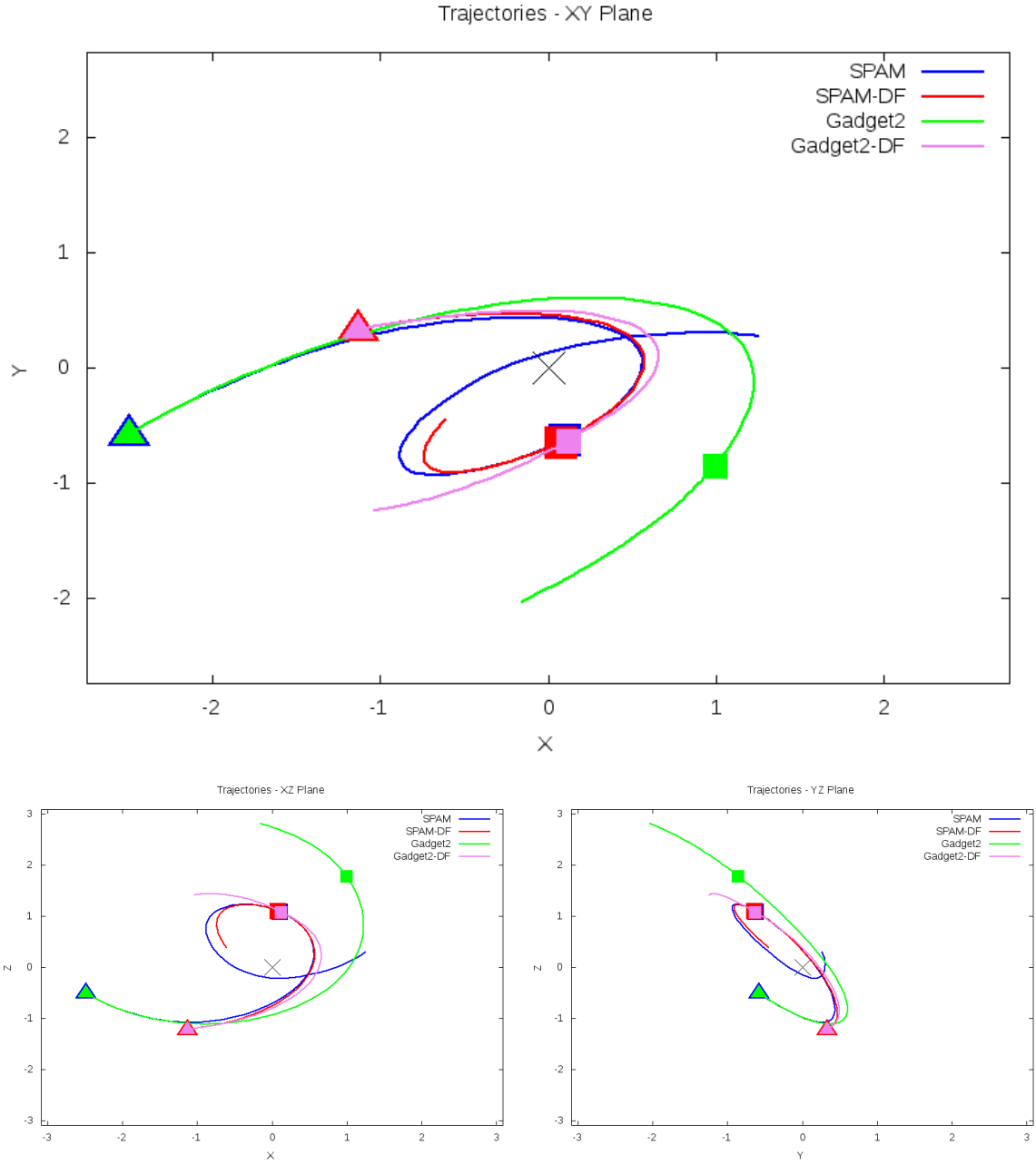


Figure 5.71: Trajectory plots of best SPAM match from Merger Wars, initial N-Body match, and best N-Body match for SDSS 587733080814583863

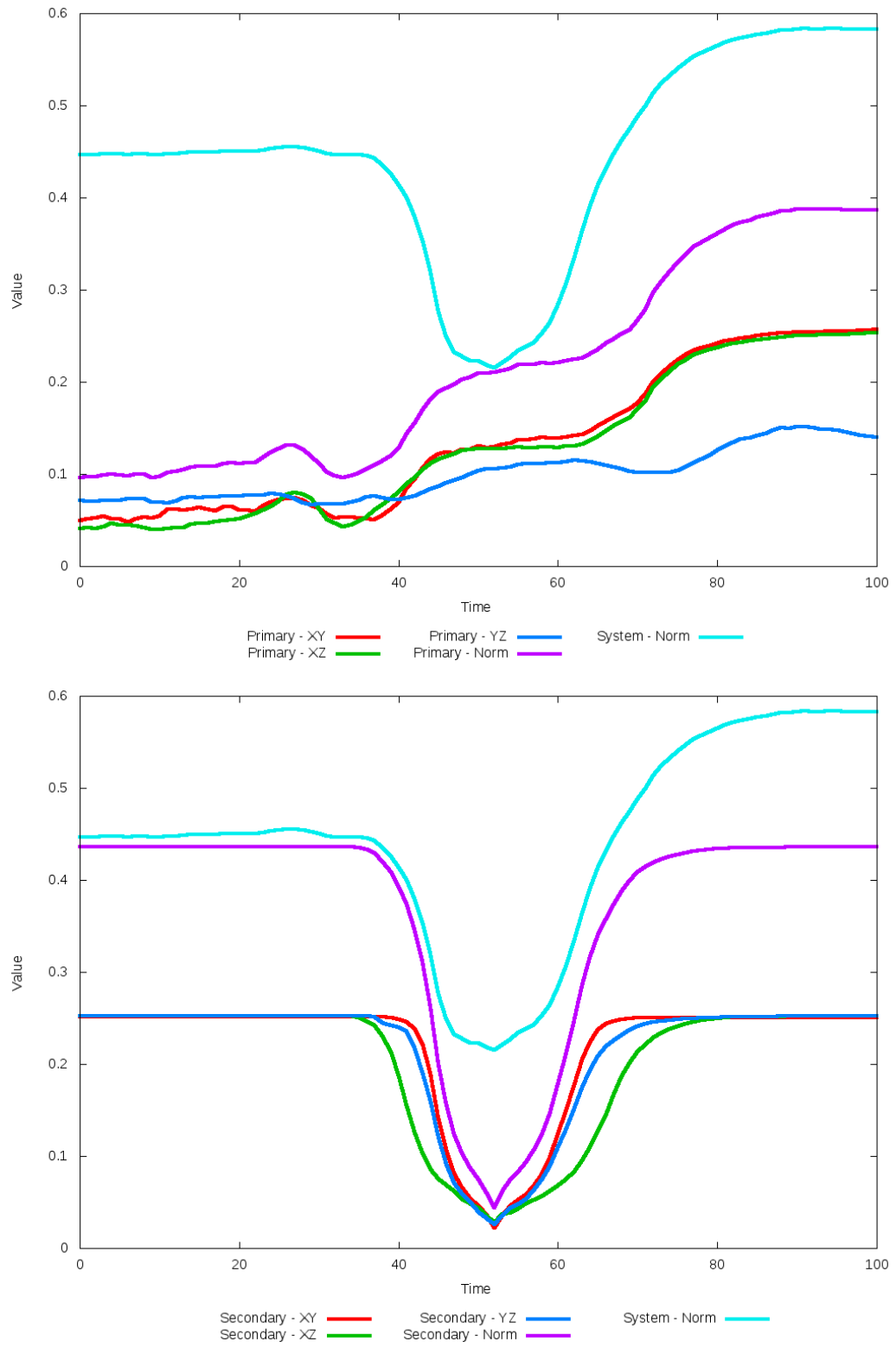


Figure 5.72: All metrics versus simulation time of the best N-Body simulation for SDSS 587733080814583863

5.1.13 SDSS 587734862680752822 (Arp 255)

Arp 255's N-Body simulations show very good agreement to the SPAM simulation and observational data. In particular, the prominent spiral arms in the primary galaxy are all in very good agreement. The optimization was able to find a very slightly better match, although it is difficult to qualitatively see by looking at the figures. Although the SPAM and N-Body simulations visually look very similar, their trajectories are different, particularly along the Y dimension; the N-body runs predict the system to have an elliptical orbit during the interaction while SPAM predicts a hyperbolic orbit.

Table 5.25: Identification Information and Merger Zoo summary for SDSS 587734862680752822.

Name	Aliases	RA (hms)	Dec (dms)	Redshift
SDSS 587734862680752822	Arp 255, UGC 5304	9:53:08.8	+7:51:58.2	0.040858

R_x	R_y	R_z	V_x	V_y	V_z
-1.23326	1.43243	1.17391	-0.24002	-0.52906	0.74803

	Primary Galaxy	Secondary Galaxy
mass	2.30689	0.43804
radius	1.01348	0.78231
ϕ	140.375°	-4.875°
θ	317.51552°	221.36645°
ϵ	0.3	0.3

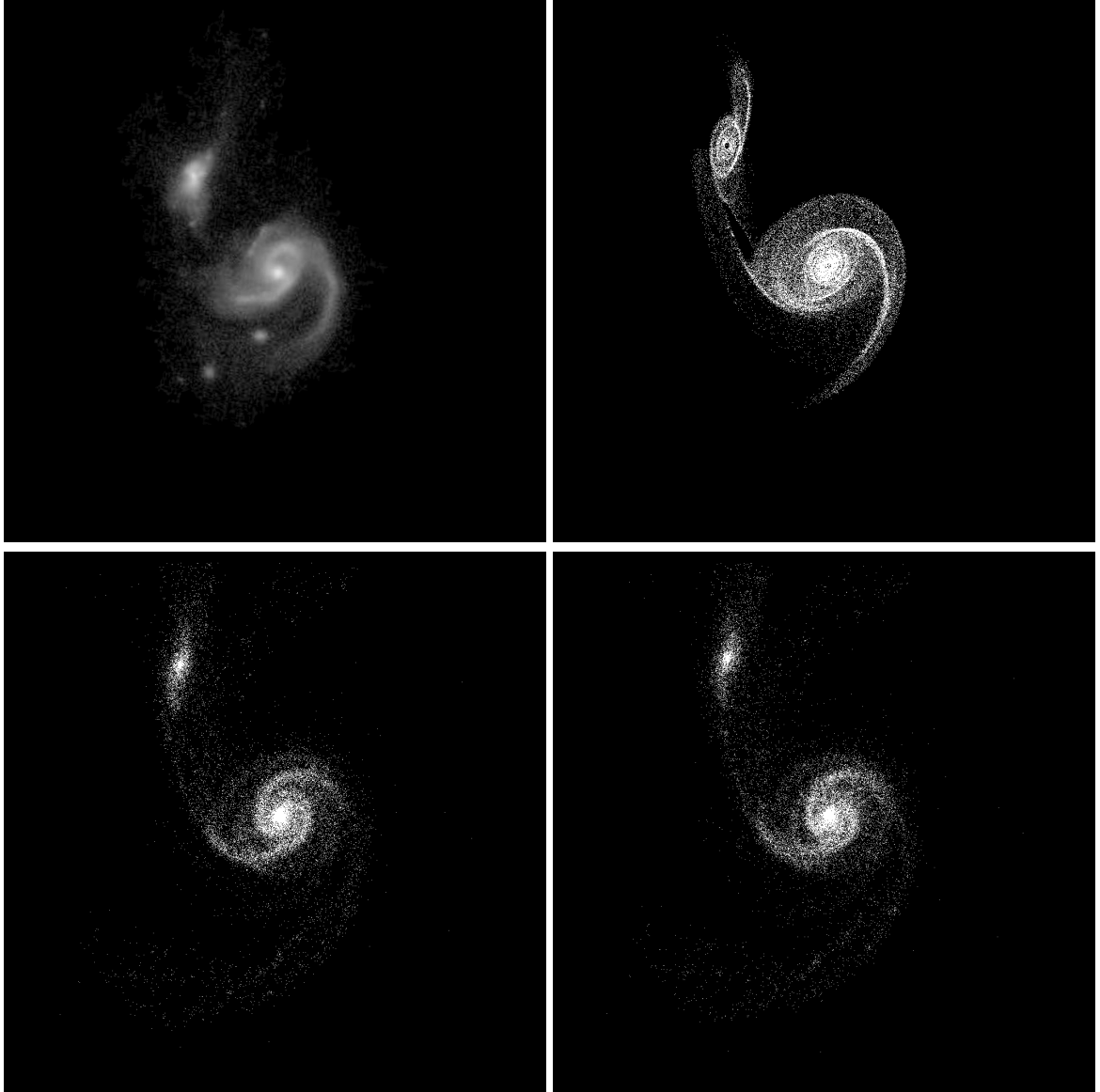


Figure 5.73: Target image (top-left), best SPAM match from Merger Wars (top-right), initial N-Body match (bottom-left), and best N-Body match (bottom-right) for SDSS 587734862680752822

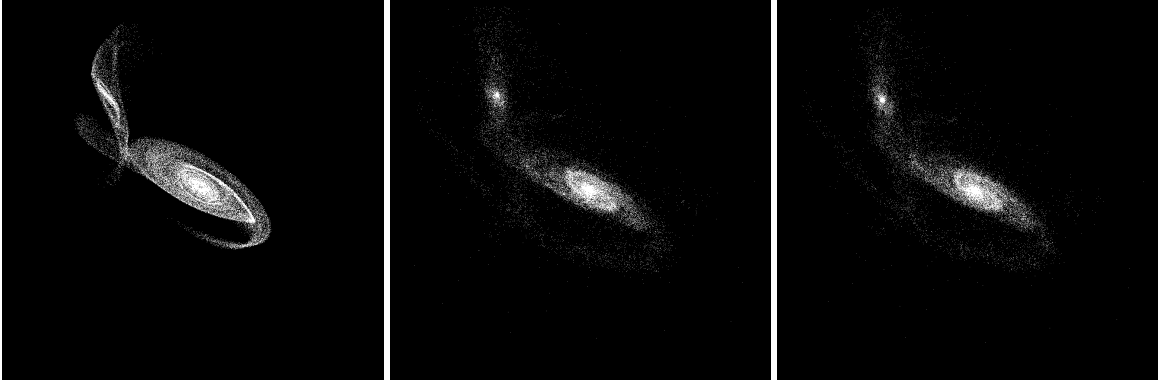


Figure 5.74: XZ projections of best SPAM match from Merger Wars (left), initial N-Body match (middle), and best N-Body match (right) for SDSS 587734862680752822

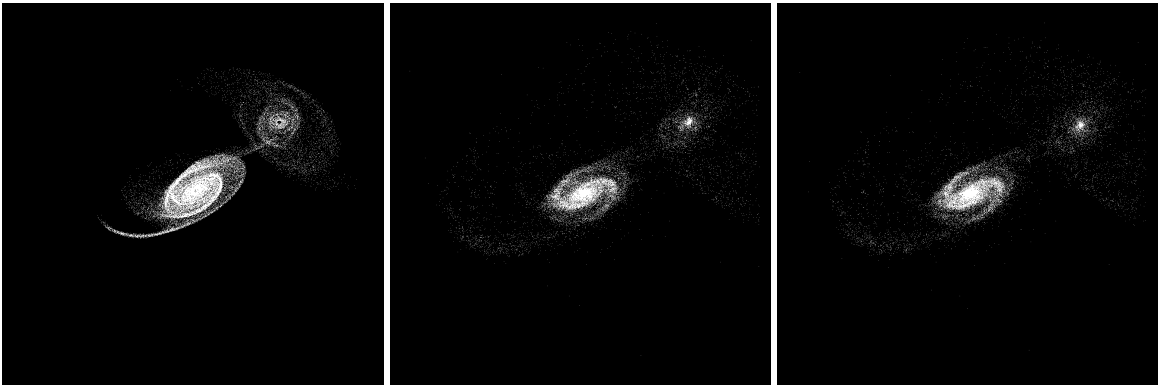


Figure 5.75: YZ projections of best SPAM match from Merger Wars (left), initial N-Body match (middle), and best N-Body match (right) for SDSS 587734862680752822

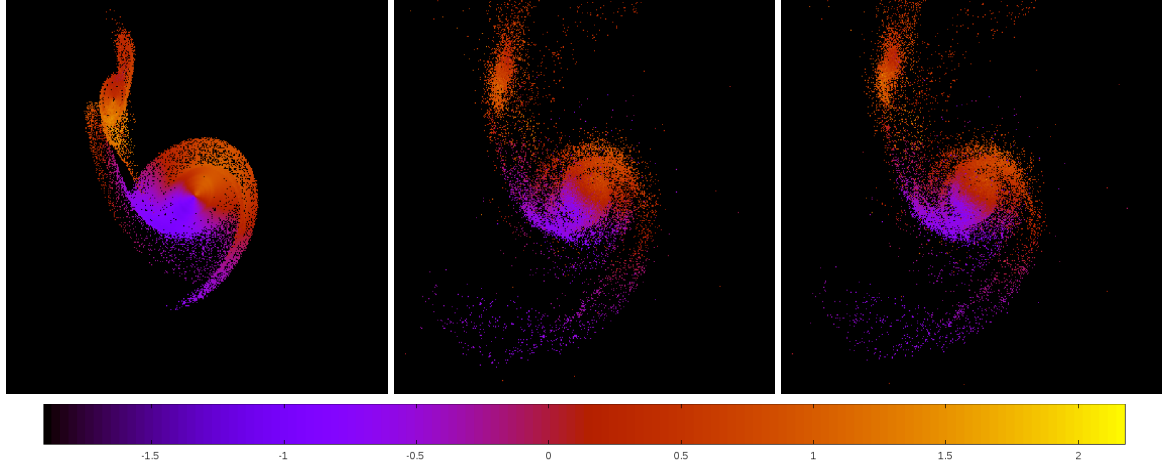


Figure 5.76: Line of sight velocity plots of best SPAM match from Merger Wars (left), initial N-Body match (middle), and best N-Body match (right) for SDSS 587734862680752822

Table 5.26: Orbital Elements & Dynamical Friction for SDSS 587734862680752822

	SPAM Simulation	Initial N-Body Simulation	Best N-Body Simulation
a	-1.292	5.906	7.270
e	4.352	0.477	0.560
r_c	4.332	3.089	3.197
i	61.167°	62.919°	62.456°
Ω	110.735°	108.095°	108.035°
ω	22.342°	279.125°	287.164°
ν	14.210°	93.281°	84.689°
t_n	50	56	55
$\ln\Lambda$	N/A	1.00E-03	1.05E-03

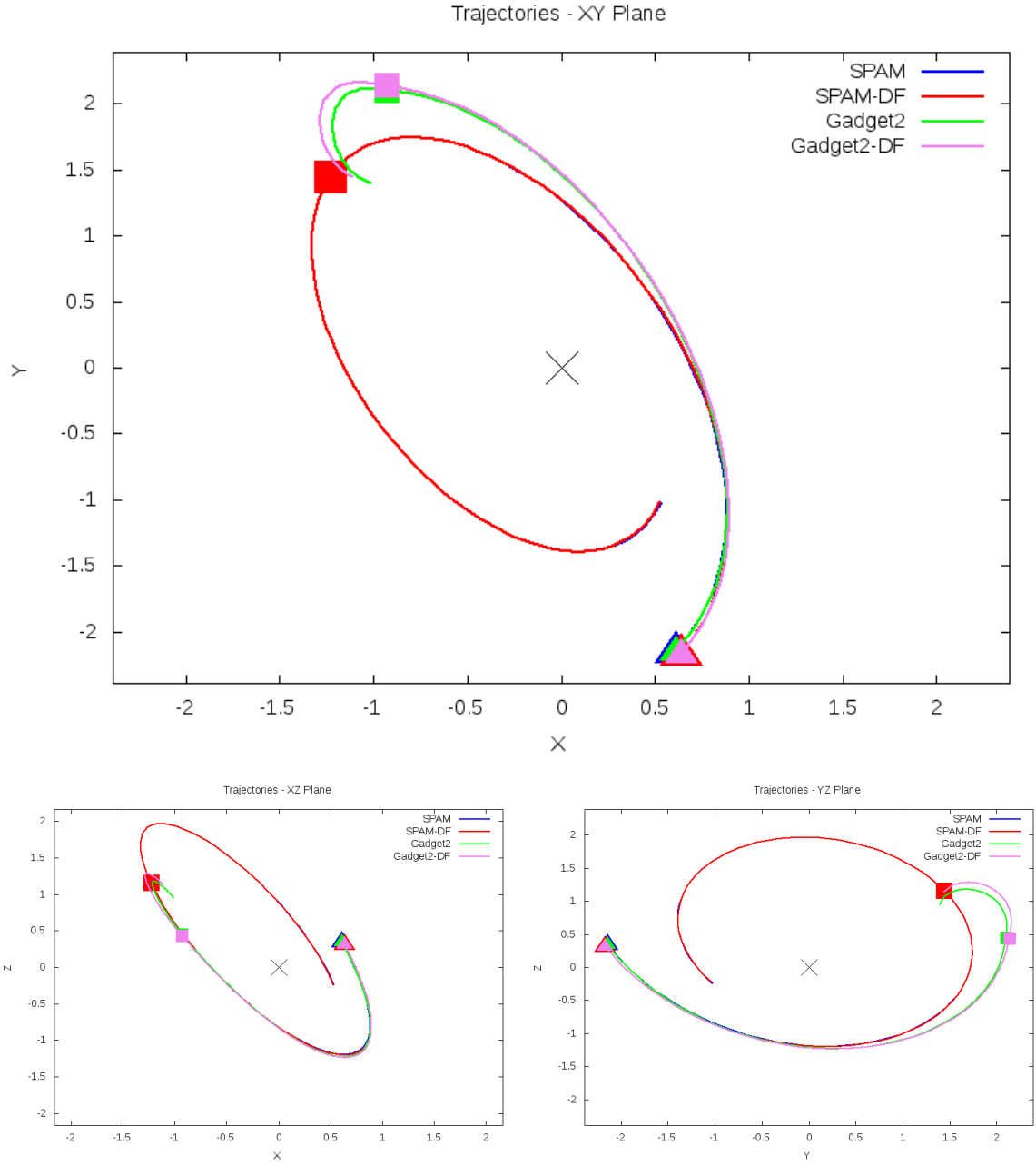


Figure 5.77: Trajectory plots of best SPAM match from Merger Wars, initial N-Body match, and best N-Body match for SDSS 587734862680752822

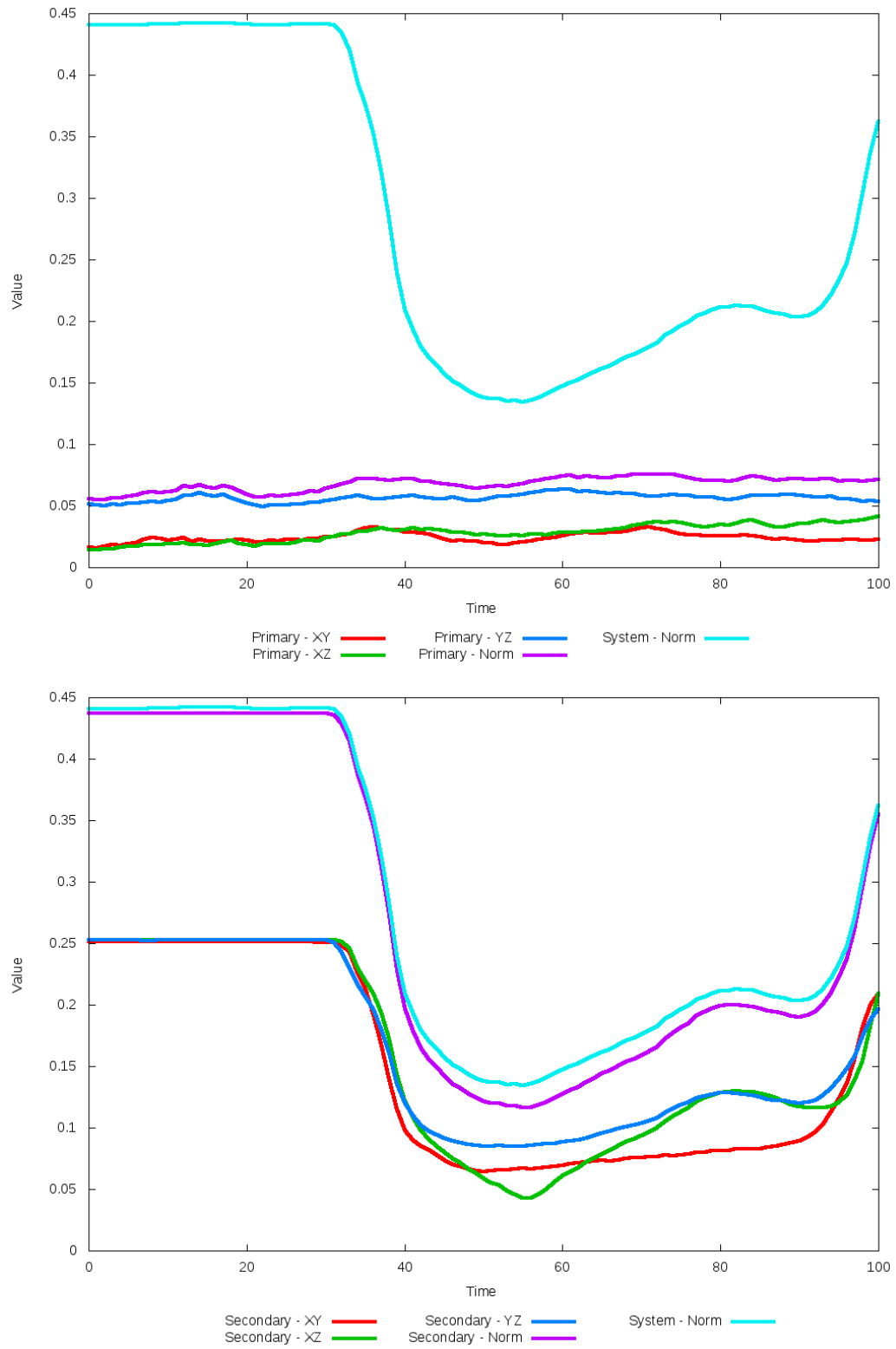


Figure 5.78: All metrics versus simulation time of the best N-Body simulation for SDSS 587734862680752822

5.1.14 SDSS 587735043609329845 (Arp 82)

Arp 82's N-Body simulations show very good agreement positionally with the the SPAM simulation and observational data. However, the optimization method could not find a better choice of dynamical friction than the starting value. Despite the very good positional agreement, the line of sight velocity in the primary galaxy is noticeably greater in the N-Body simulation than the SPAM simulation. The trajectory of the N-Body simulation is much broader and appears more stable than the SPAM simulation's trajectory. The N-Body simulation shows two close approaches to the target position in the SPAM trajectory, as can be very strongly seen in the figures of the metrics used by the optimization routine.

Table 5.27: Identification Information and Merger Zoo summary for SDSS 587735043609329845.

Name	Aliases	RA (hms)	Dec (dms)	Redshift
SDSS 587735043609329845	Arp 82, NGC 2535/2536	8:11:13.5	+25:12:23.8	0.013666

R_x	R_y	R_z	V_x	V_y	V_z
-0.48646	-1.45004	-0.62585	0.40688	-0.53238	0.04629

	Primary Galaxy	Secondary Galaxy
mass	1.48573	0.74812
radius	0.39338	0.19293
ϕ	26.64819°	49.48416°
θ	342.60021°	232.84096°
ϵ	0.3	0.3

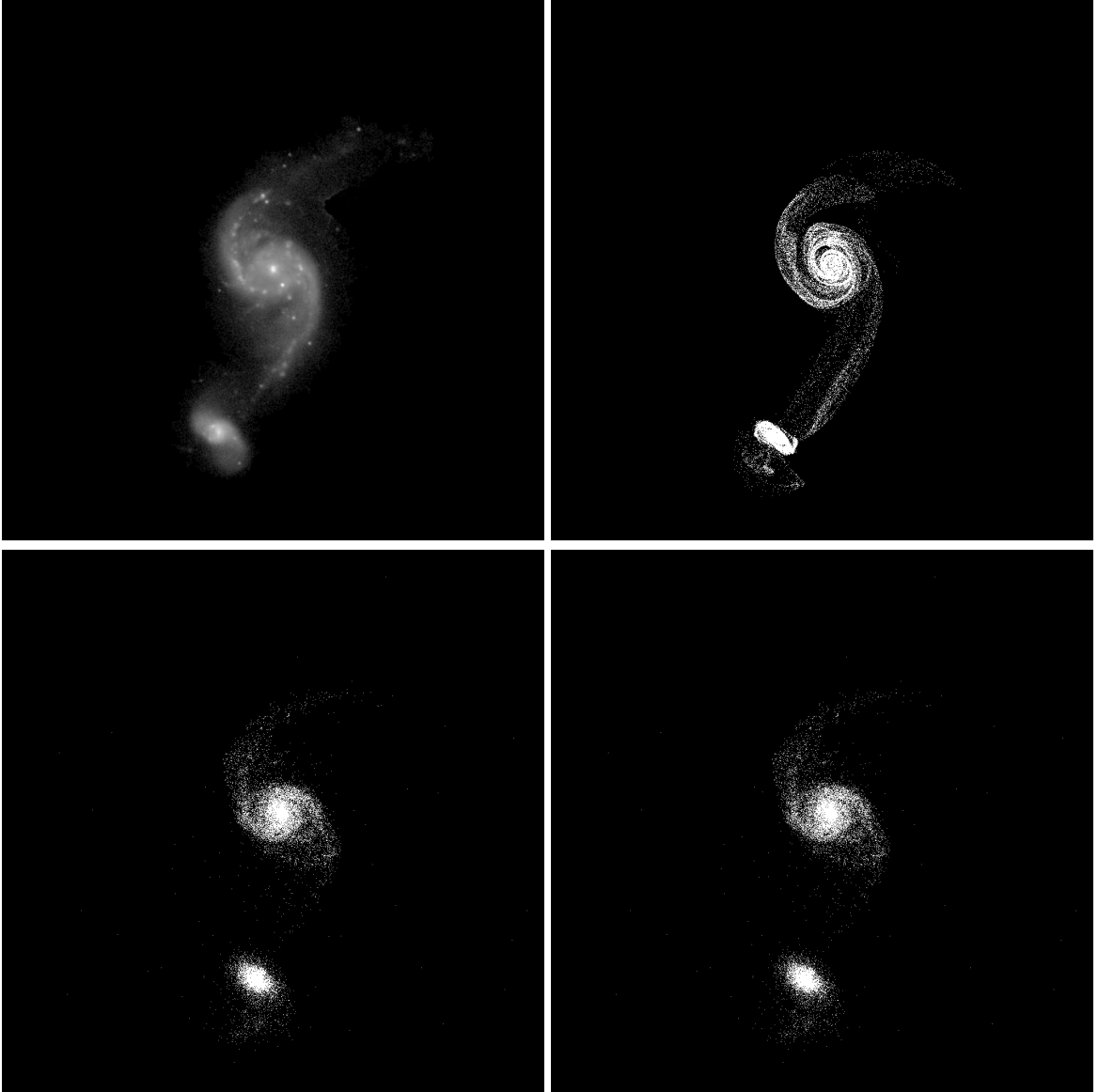


Figure 5.79: Target image (top-left), best SPAM match from Merger Wars (top-right), initial N-Body match (bottom-left), and best N-Body match (bottom-right) for SDSS 587735043609329845

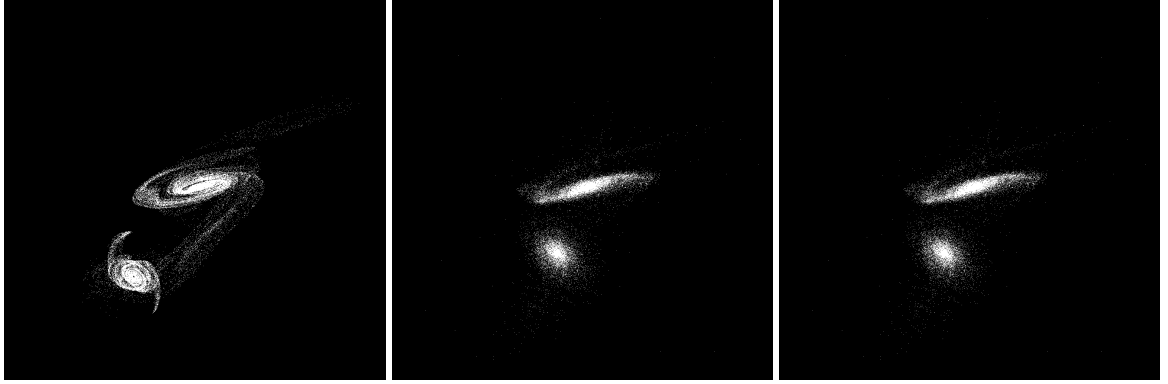


Figure 5.80: XZ projections of best SPAM match from Merger Wars (left), initial N-Body match (middle), and best N-Body match (right) for SDSS 587735043609329845

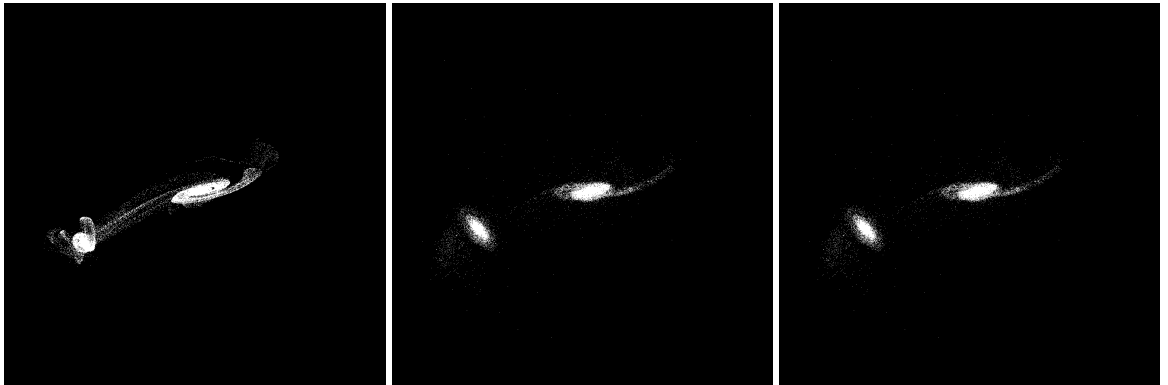


Figure 5.81: YZ projections of best SPAM match from Merger Wars (left), initial N-Body match (middle), and best N-Body match (right) for SDSS 587735043609329845

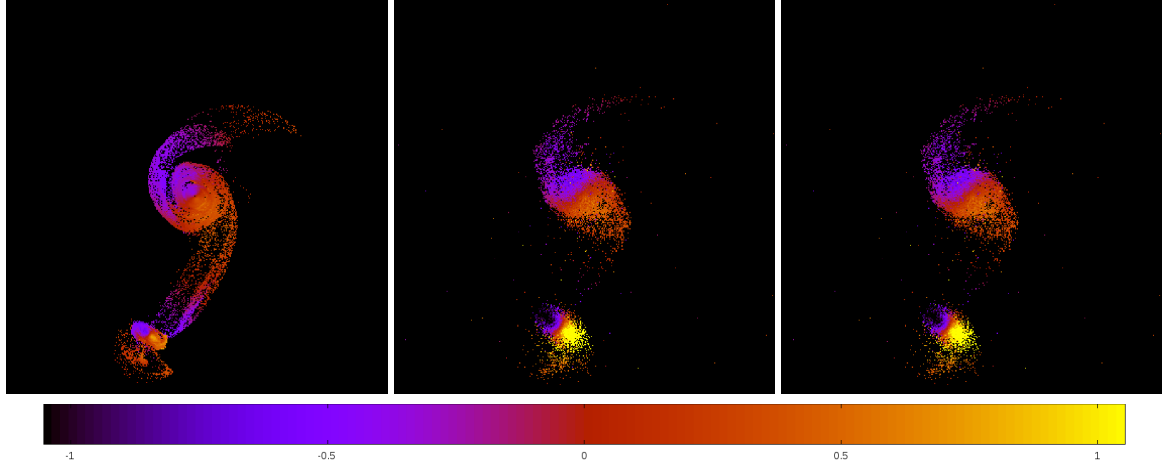


Figure 5.82: Line of sight velocity plots of best SPAM match from Merger Wars (left), initial N-Body match (middle), and best N-Body match (right) for SDSS 587735043609329845

Table 5.28: Orbital Elements & Dynamical Friction for SDSS 587735043609329845

	SPAM Simulation	Initial N-Body Simulation	Best N-Body Simulation
a	6.588	-0.826	-0.826
e	0.655	4.002	4.002
r_c	2.270	2.480	2.480
i	28.593°	27.563°	27.563°
Ω	300.108°	299.857°	299.857°
ω	229.748°	280.374°	280.374°
ν	77.940°	35.634°	35.634°
t_n	50	12	12
$\ln\Lambda$	N/A	1.00E-03	1.00E-03

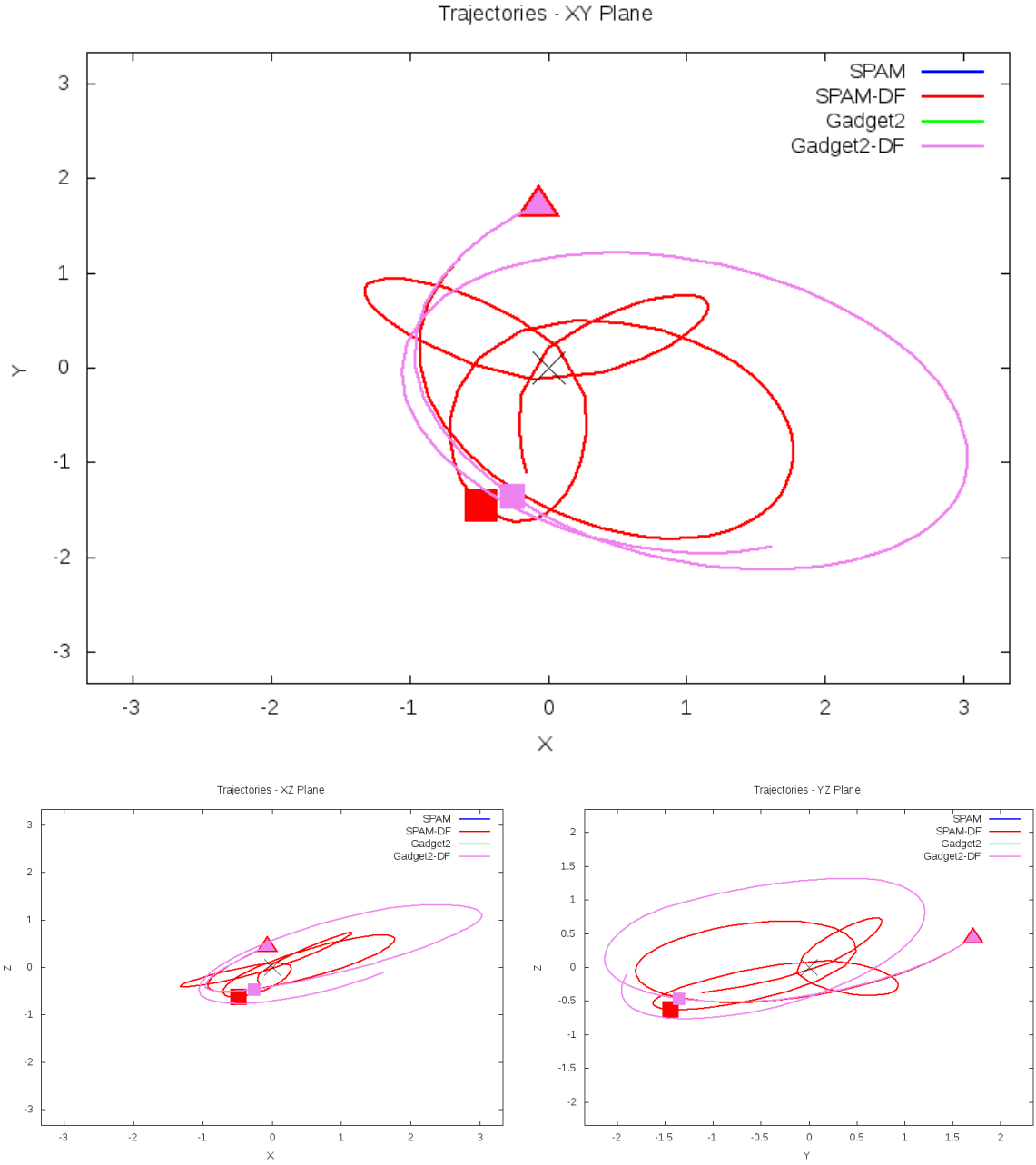


Figure 5.83: Trajectory plots of best SPAM match from Merger Wars, initial N-Body match, and best N-Body match for SDSS 587735043609329845

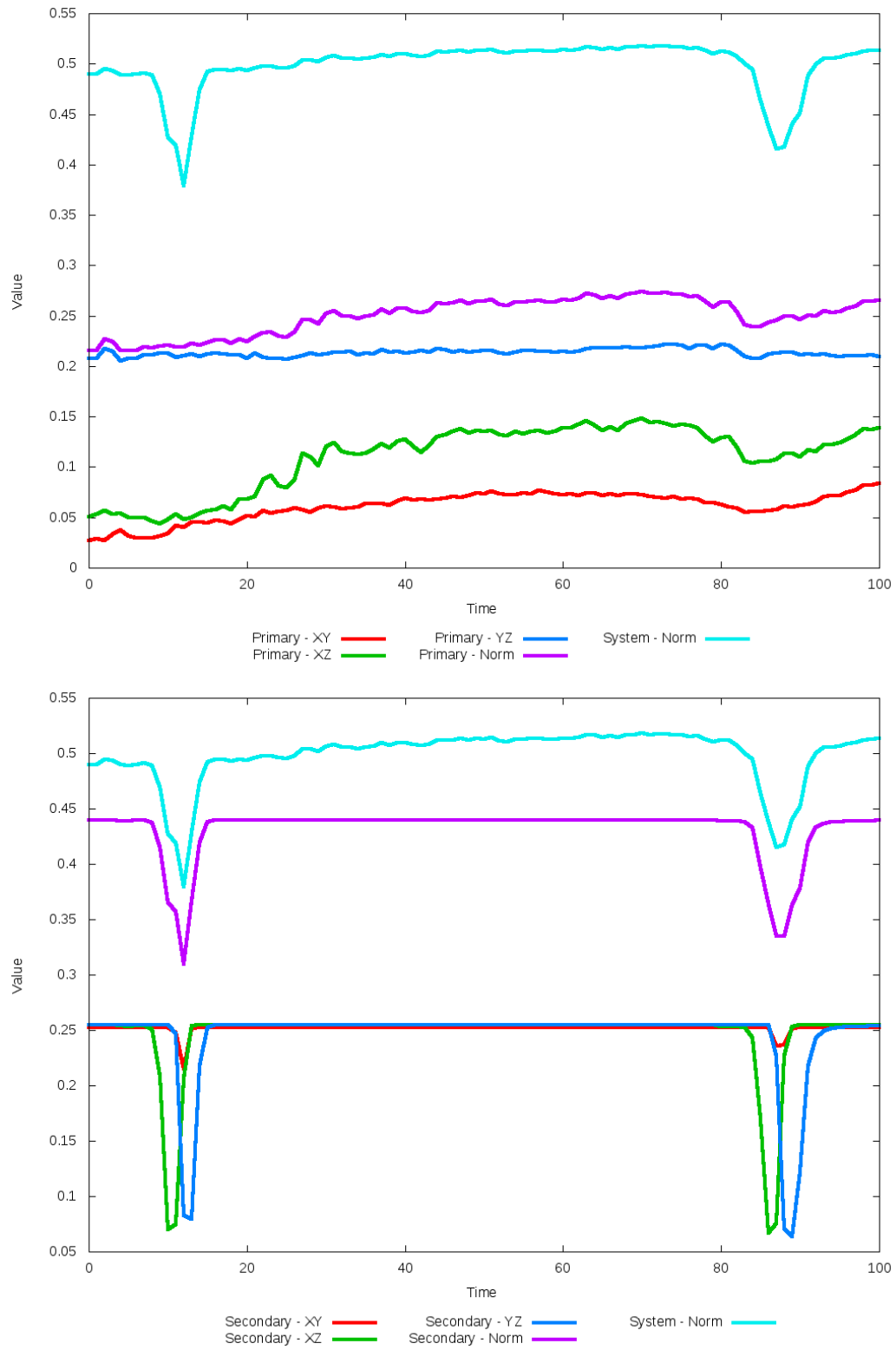


Figure 5.84: All metrics versus simulation time of the best N-Body simulation for SDSS 587735043609329845

5.1.15 SDSS 587735665840881790 (Arp 239)

The optimized N-Body simulation for Arp 239 shows a significant improvement in matching both the observational data and SPAM simulation in the XY projection, but poorly matches in the other projections. The relative positions of the galaxies are in better agreement with the observational data than SPAM. At the time of the best match, the line of sight velocities of the primary galaxy is in good agreement between the SPAM simulation and optimized N-Body simulation. Based on the SPAM simulation trajectories, the galaxies are close to merging while the N-Body simulations show a merger happening sooner as the orbit decays more quickly.

Table 5.29: Identification Information and Merger Zoo summary for SDSS 587735665840881790.

Name	Aliases	RA (hms)	Dec (dms)	Redshift
SDSS 587735665840881790	Arp 239, NGC 5278	13:41:39.3	+55:40:14.6	0.02521

\mathbf{R}_x	\mathbf{R}_y	\mathbf{R}_z	\mathbf{V}_x	\mathbf{V}_y	\mathbf{V}_z
-0.8126	0.26807	1.42974	-0.61636	0.10013	0.34708

	Primary Galaxy	Secondary Galaxy
mass	0.92793	0.18718
radius	0.49658	0.14763
ϕ	58.81685°	94.3125°
θ	235.38311°	335.40372°
ϵ	0.3	0.3

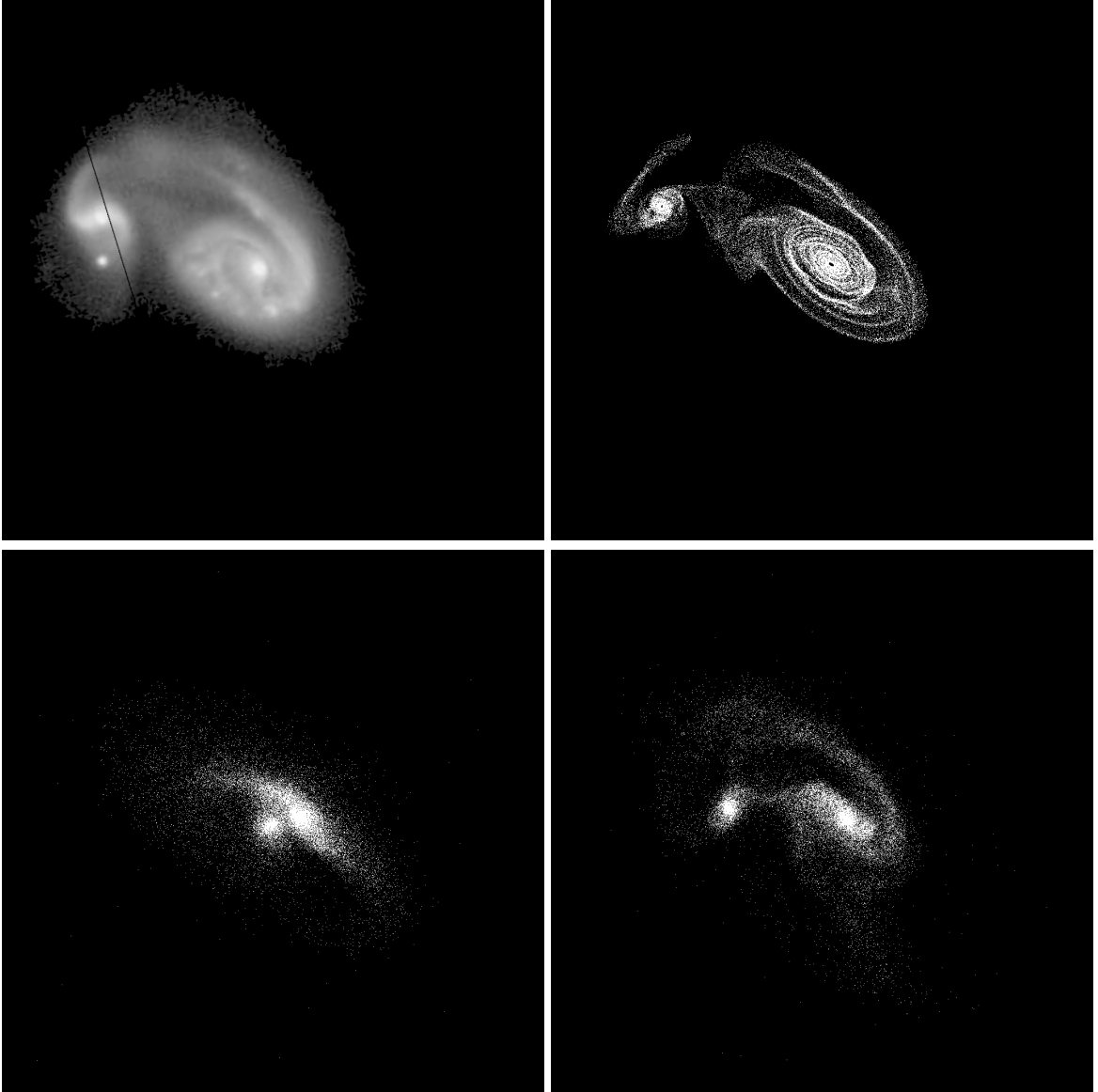


Figure 5.85: Target image (top-left), best SPAM match from Merger Wars (top-right), initial N-Body match (bottom-left), and best N-Body match (bottom-right) for SDSS 587735665840881790

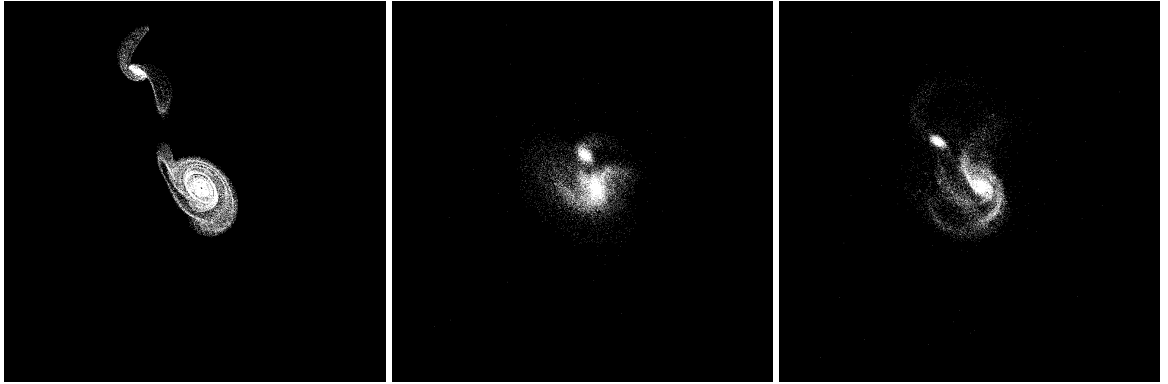


Figure 5.86: XZ projections of best SPAM match from Merger Wars (left), initial N-Body match (middle), and best N-Body match (right) for SDSS 587735665840881790

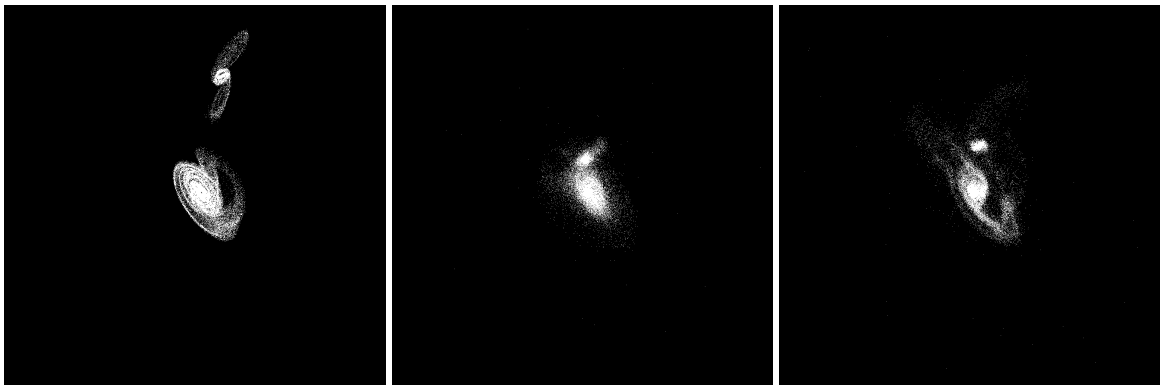


Figure 5.87: YZ projections of best SPAM match from Merger Wars (left), initial N-Body match (middle), and best N-Body match (right) for SDSS 587735665840881790

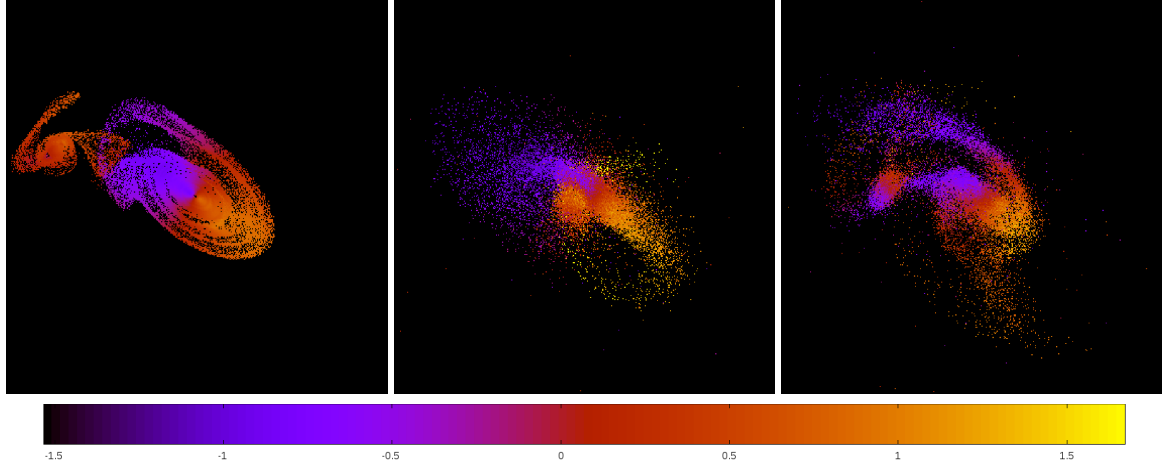


Figure 5.88: Line of sight velocity plots of best SPAM match from Merger Wars (left), initial N-Body match (middle), and best N-Body match (right) for SDSS 587735665840881790

Table 5.30: Orbital Elements & Dynamical Friction for SDSS 587735665840881790

	SPAM Simulation	Initial N-Body Simulation	Best N-Body Simulation
a	-0.963	-0.282	-3.013
e	2.432	2.713	1.380
r_c	1.379	0.483	1.145
i	82.060°	94.983°	85.476°
Ω	355.219°	6.012°	0.195°
ω	39.910°	44.547°	77.152°
ν	80.050°	56.843°	51.523°
t_n	50	48	42
$\ln\Lambda$	N/A	1.00E-03	2.00E-03

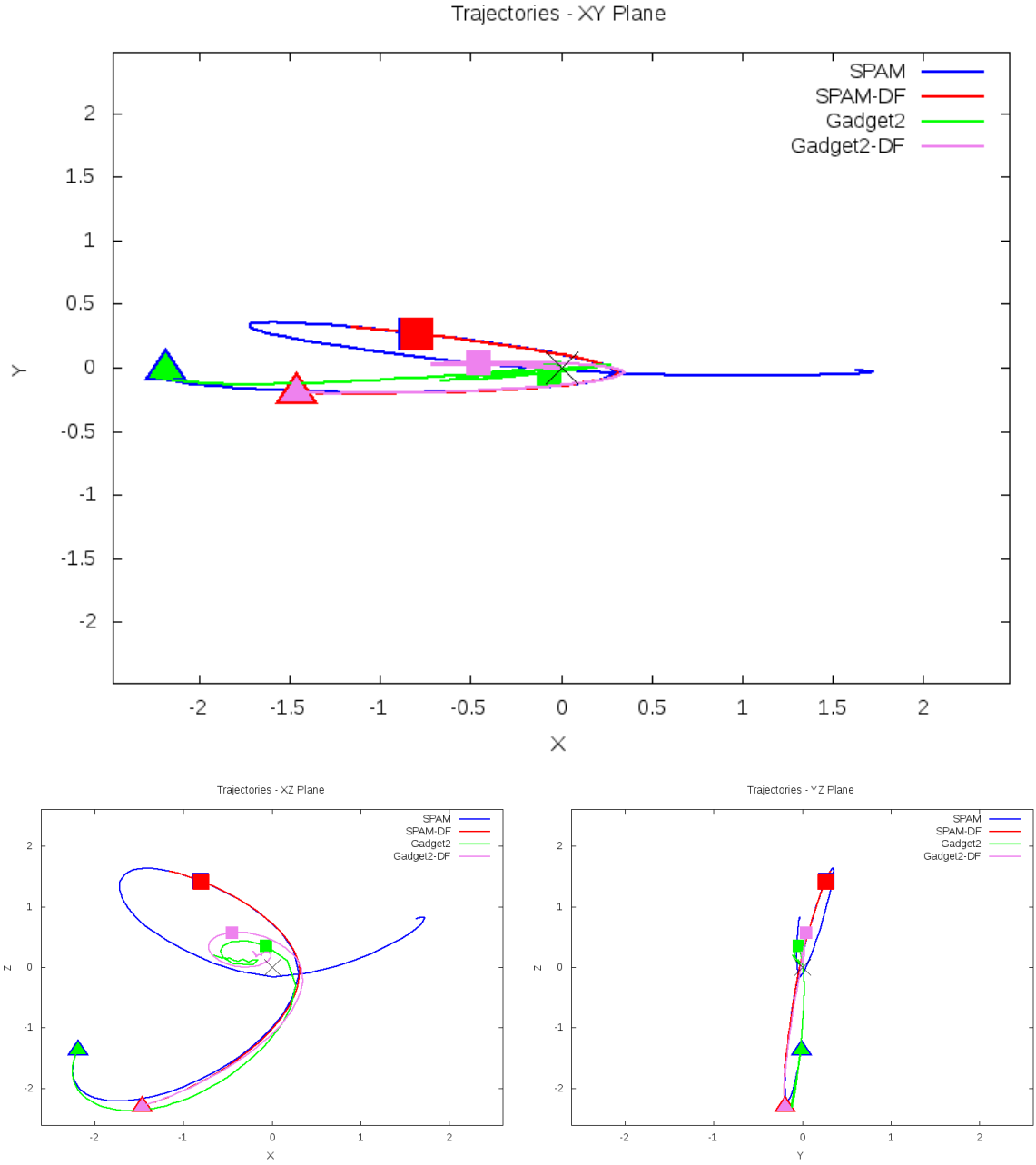


Figure 5.89: Trajectory plots of best SPAM match from Merger Wars, initial N-Body match, and best N-Body match for SDSS 587735665840881790

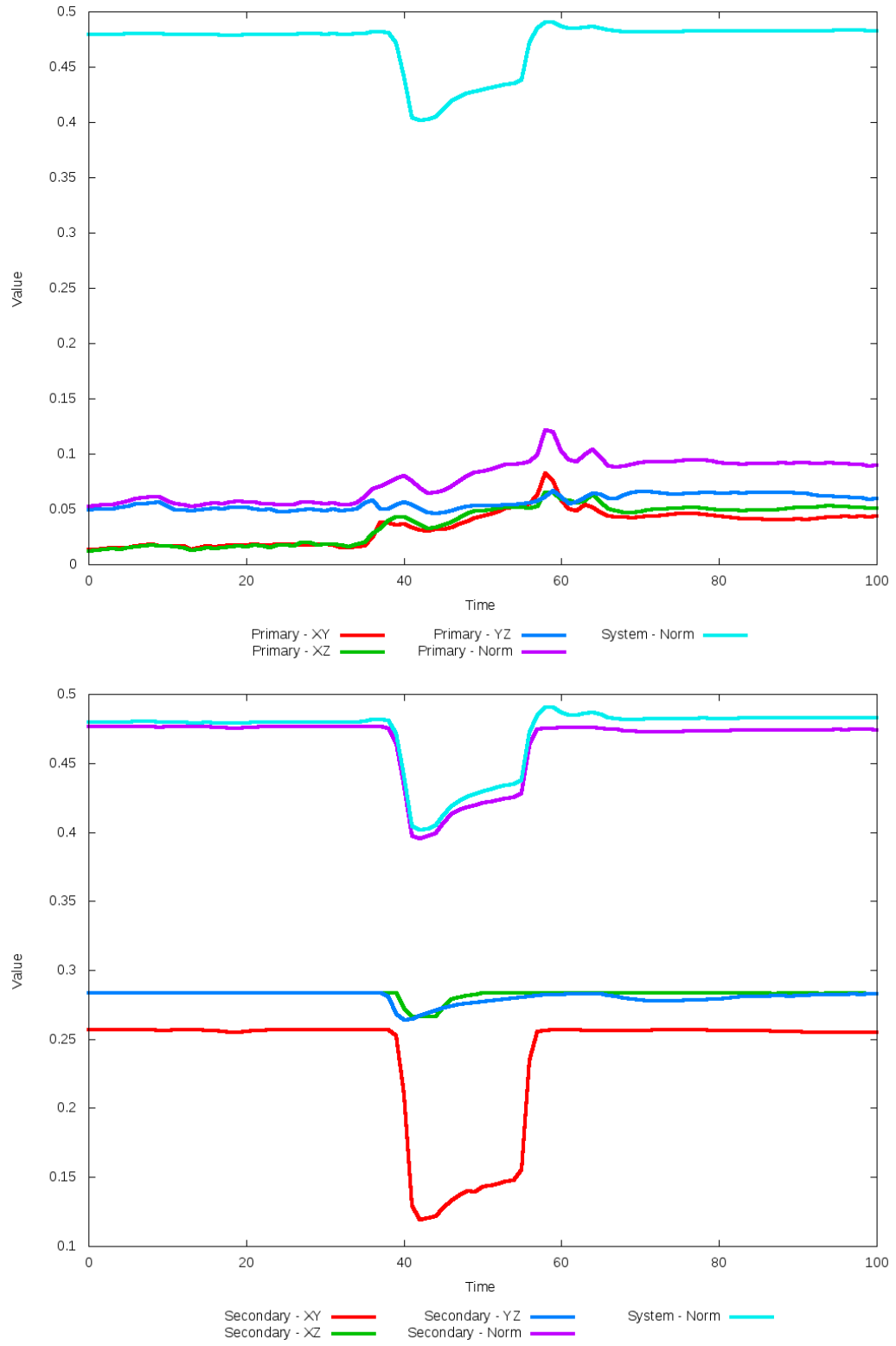


Figure 5.90: All metrics versus simulation time of the best N-Body simulation for SDSS 587735665840881790

5.1.16 SDSS 587736523764334706 (Arp 274)

Arp 274 shows very good agreement between all its models and the observational data. Although the galaxies appear to be relatively close to each other in the XY projection, looking at other projections show they are actually far apart and are in the early stages of an interaction. As such, there are no tidal features. Because the galaxies are not within sufficient distance to each other, dynamical friction does not impact the orbits and trajectories of the simulations. As such, the optimization methodology cannot find any better value for dynamical friction than the starting value.

Table 5.31: Identification Information and Merger Zoo summary for SDSS 587736523764334706.

Name	Aliases	RA (hms)	Dec (dms)	Redshift
SDSS 587736523764334706	Arp 274, NGC 5679	14:35:08.7	+5:21:31.7	0.028867

R_x	R_y	R_z	V_x	V_y	V_z
1.29969	-0.31467	3.70378	1.33823	0.91009	-0.88972

	Primary Galaxy	Secondary Galaxy
mass	0.55893	0.17255
radius	1.18348	0.84617
ϕ	126.88209°	51.3787°
θ	296.58787°	232.55479°
ϵ	0.3	0.3

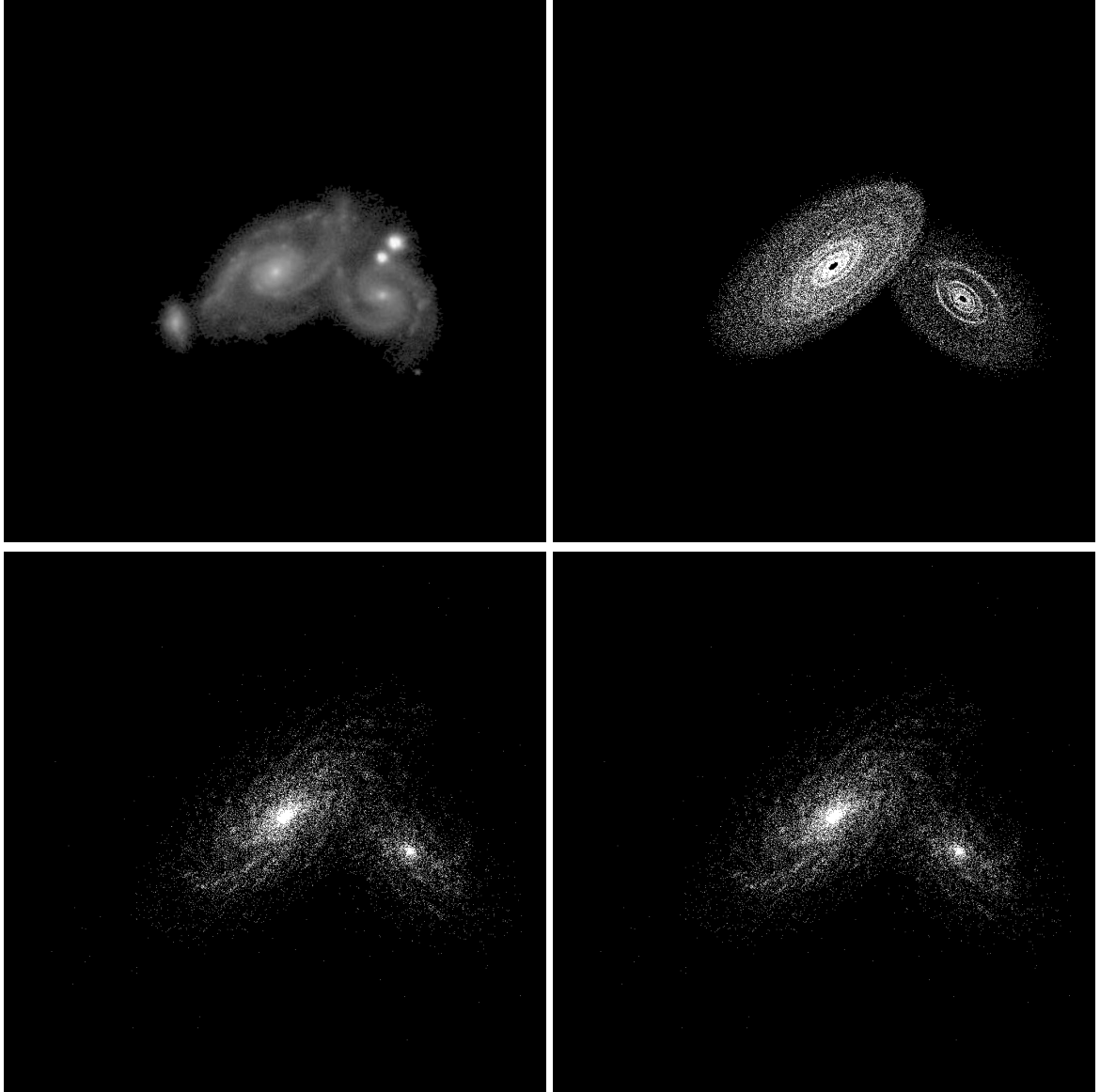


Figure 5.91: Target image (top-left), best SPAM match from Merger Wars (top-right), initial N-Body match (bottom-left), and best N-Body match (bottom-right) for SDSS 587736523764334706

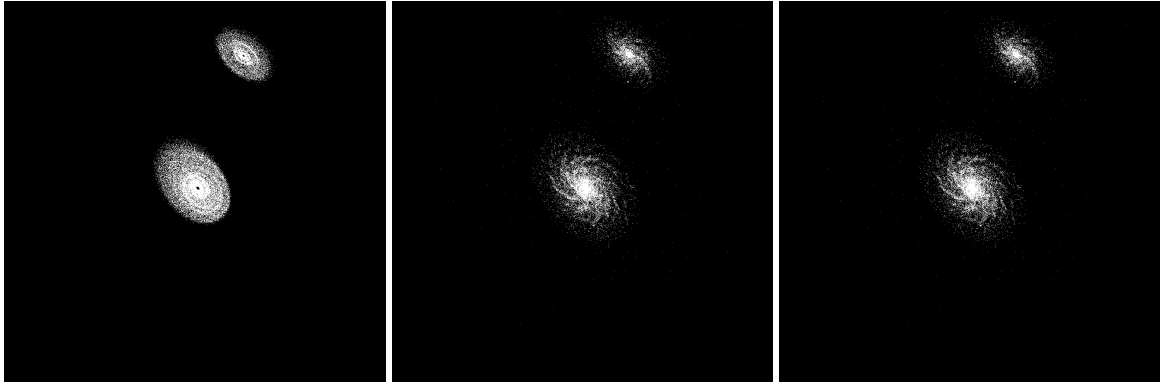


Figure 5.92: XZ projections of best SPAM match from Merger Wars (left), initial N-Body match (middle), and best N-Body match (right) for SDSS 587736523764334706



Figure 5.93: YZ projections of best SPAM match from Merger Wars (left), initial N-Body match (middle), and best N-Body match (right) for SDSS 587736523764334706

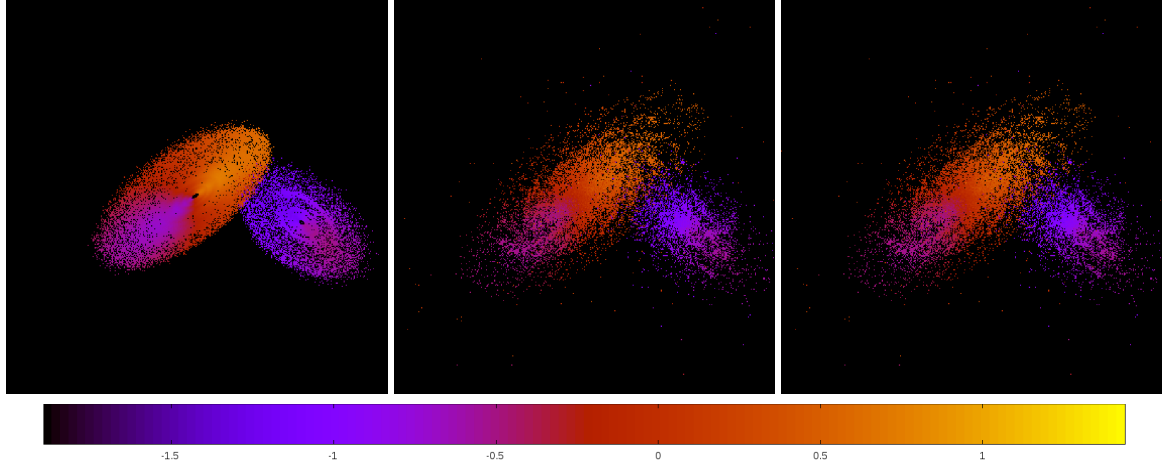


Figure 5.94: Line of sight velocity plots of best SPAM match from Merger Wars (left), initial N-Body match (middle), and best N-Body match (right) for SDSS 587736523764334706

Table 5.32: Orbital Elements & Dynamical Friction for SDSS 587736523764334706

	SPAM Simulation	Initial N-Body Simulation	Best N-Body Simulation
a	-0.079	-0.079	-0.079
e	97.576	97.152	97.152
r_c	7.616	7.629	7.629
i	76.821°	76.799°	76.799°
Ω	206.822°	206.779°	206.779°
ω	119.805°	119.710°	119.710°
ν	345.176°	344.705°	344.705°
t_n	50	50	50
$\ln\Lambda$	N/A	1.00E-03	1.00E-03

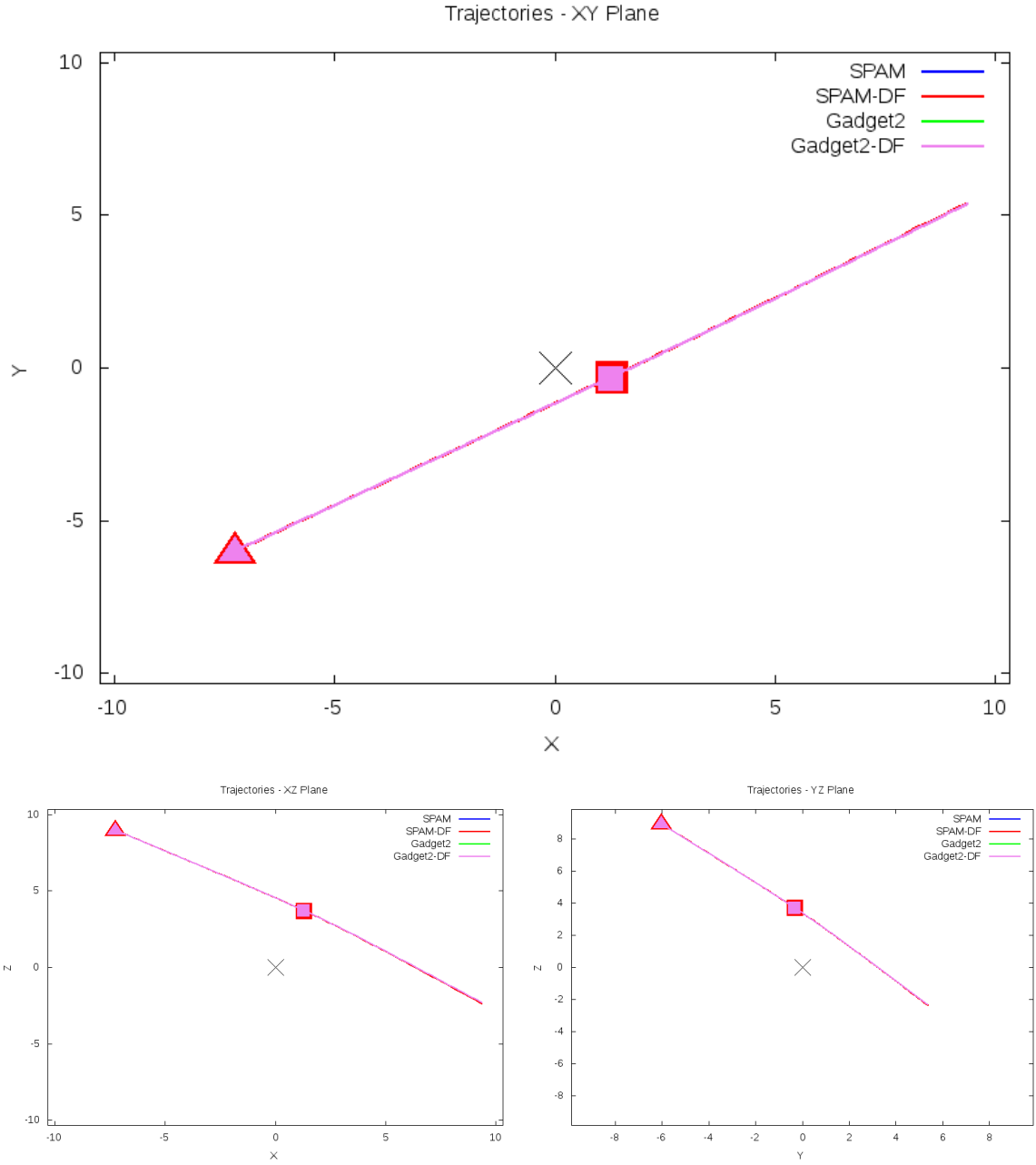


Figure 5.95: Trajectory plots of best SPAM match from Merger Wars, initial N-Body match, and best N-Body match for SDSS 587736523764334706

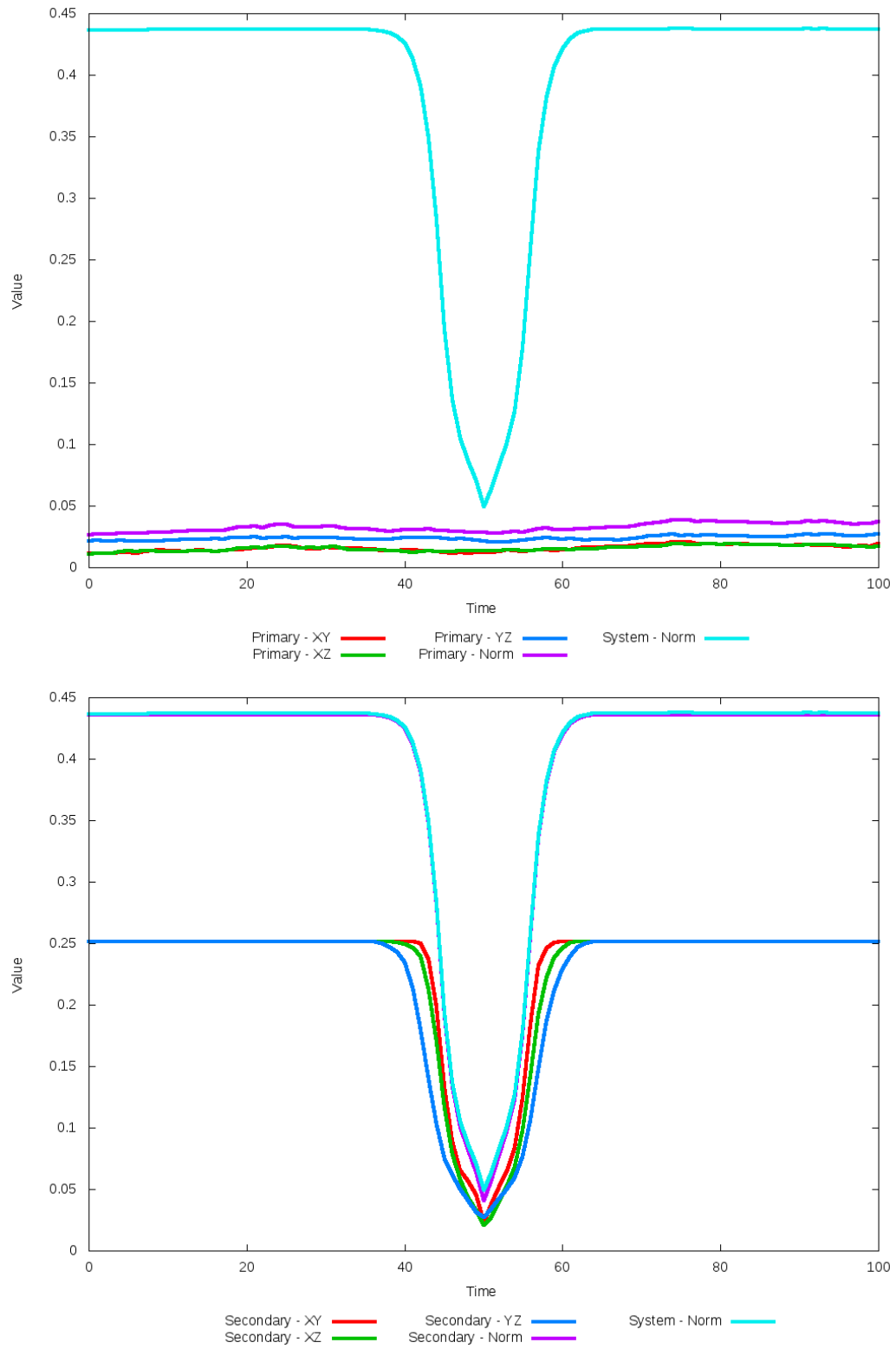


Figure 5.96: All metrics versus simulation time of the best N-Body simulation for SDSS 587736523764334706

5.1.17 SDSS 587736941981466667 (Arp 199)

Arp 199 shows very good agreement between its simulations and observational data. Although the initial and optimized N-Body simulations appear nearly indistinguishable, the optimization routine did make a significant change in dynamical friction. Despite the change, the trajectories did not change by an appreciable amount. The interaction between these two galaxies appears to be weak.

Table 5.33: Identification Information and Merger Zoo summary for SDSS 587736941981466667.

Name	Aliases	RA (hms)	Dec (dms)	Redshift
SDSS 587736941981466667	Arp 199, NGC 5544/5545	14:17:02.5	+36:34:16.6	0.01014

R_x	R_y	R_z	V_x	V_y	V_z
-0.27341	0.18994	0.74436	1.28828	1.04149	0.49963

	Primary Galaxy	Secondary Galaxy
mass	0.17637	0.11239
radius	0.30307	0.3086
ϕ	96.61117°	49.83149°
θ	152.65312°	109.12104°
ϵ	0.3	0.3

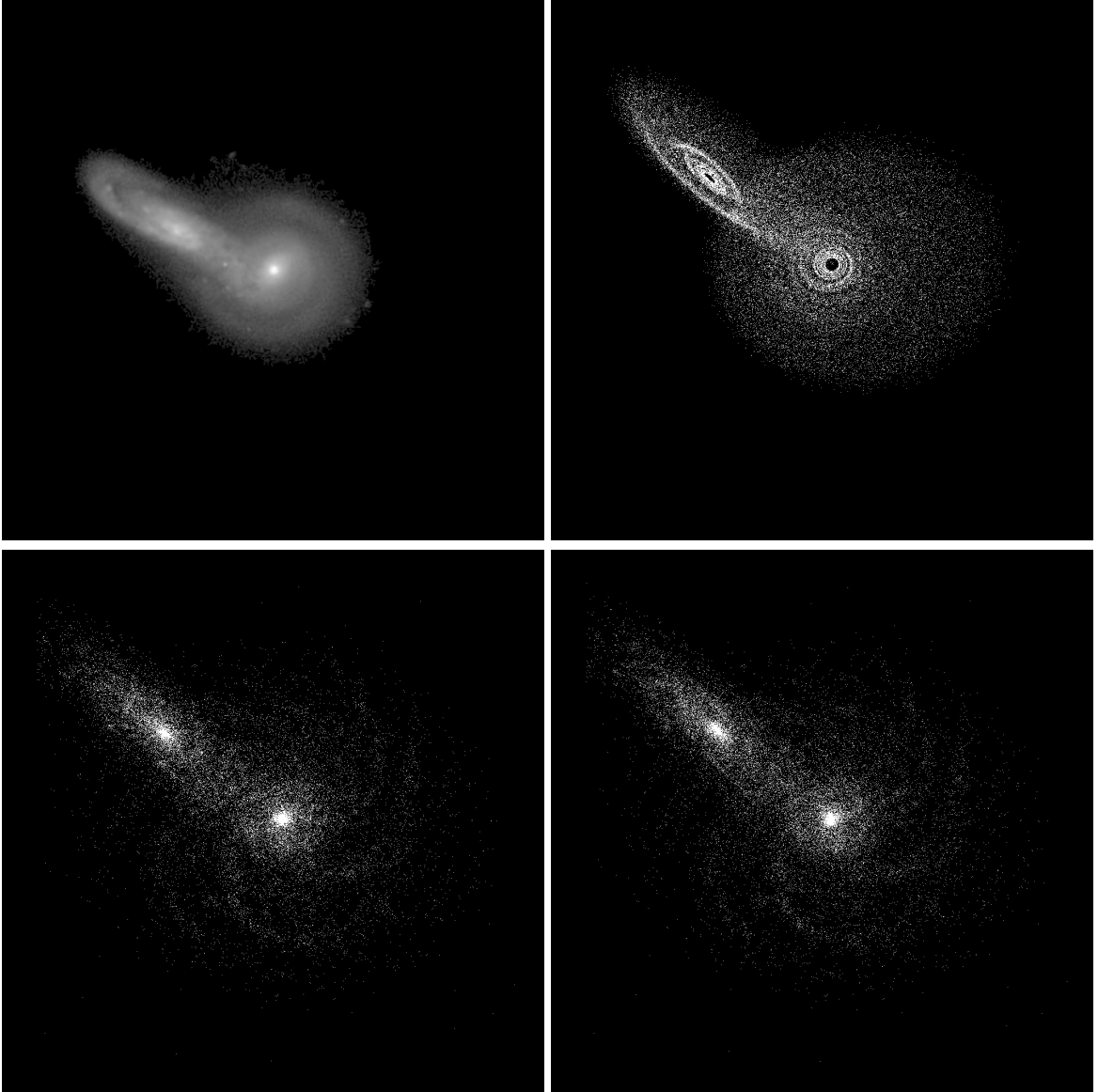


Figure 5.97: Target image (top-left), best SPAM match from Merger Wars (top-right), initial N-Body match (bottom-left), and best N-Body match (bottom-right) for SDSS 587736941981466667



Figure 5.98: XZ projections of best SPAM match from Merger Wars (left), initial N-Body match (middle), and best N-Body match (right) for SDSS 587736941981466667



Figure 5.99: YZ projections of best SPAM match from Merger Wars (left), initial N-Body match (middle), and best N-Body match (right) for SDSS 587736941981466667

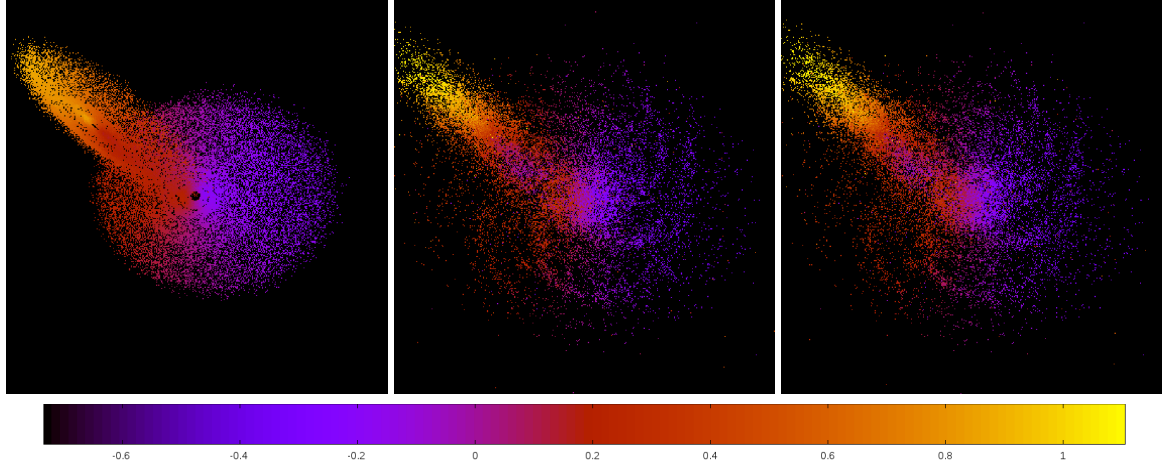


Figure 5.100: Line of sight velocity plots of best SPAM match from Merger Wars (left), initial N-Body match (middle), and best N-Body match (right) for SDSS 587736941981466667

Table 5.34: Orbital Elements & Dynamical Friction for SDSS 587736941981466667

	SPAM Simulation	Initial N-Body Simulation	Best N-Body Simulation
a	-0.049	-0.047	-0.047
e	34.152	34.801	35.432
r_c	1.611	1.605	1.607
i	112.321°	112.418°	112.408°
Ω	211.841°	211.939°	211.944°
ω	71.553°	72.252°	72.198°
ν	9.126°	8.136°	8.958°
t_n	50	50	50
$\ln\Lambda$	N/A	1.00E-03	2.80E-03

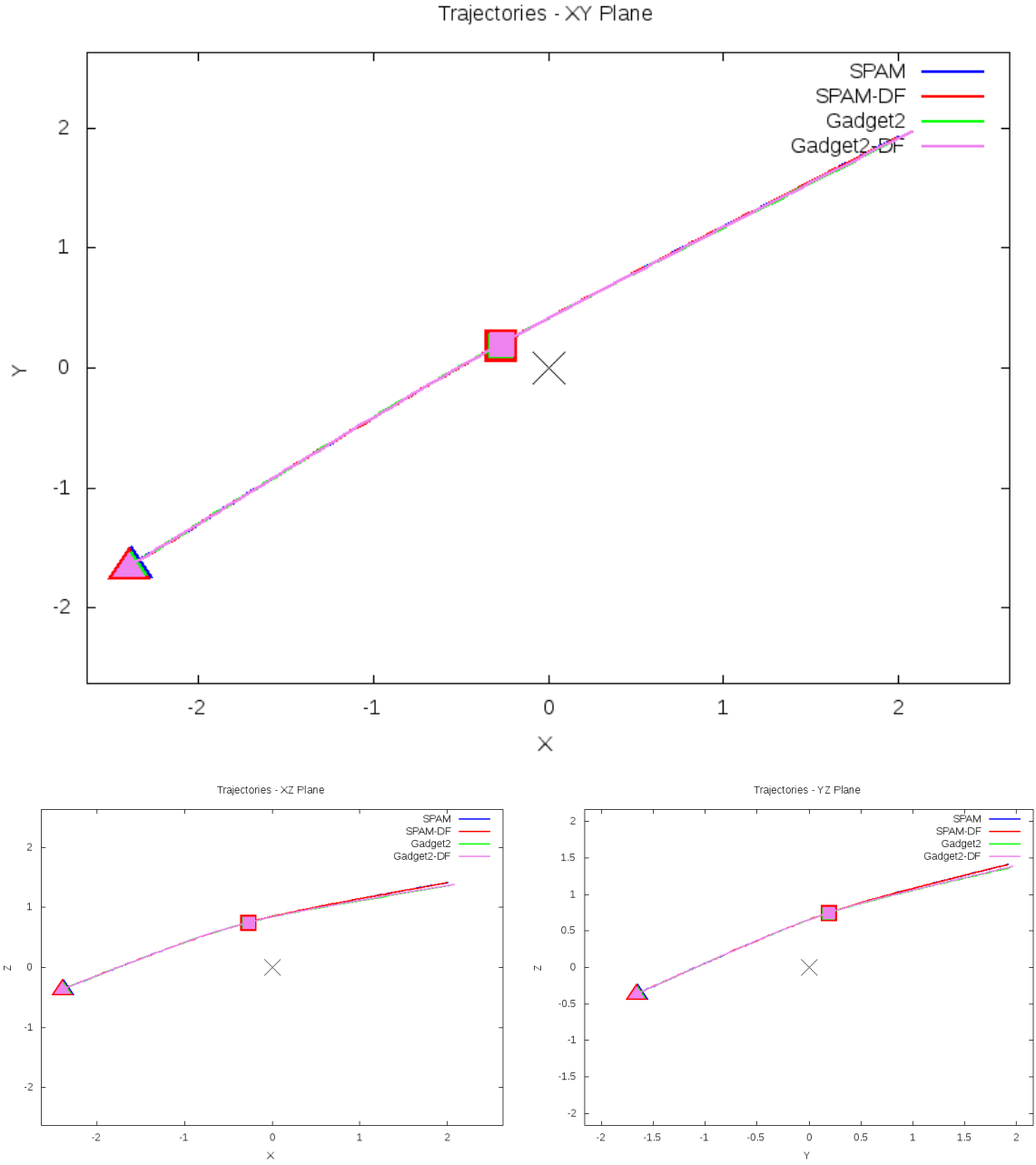


Figure 5.101: Trajectory plots of best SPAM match from Merger Wars, initial N-Body match, and best N-Body match for SDSS 587736941981466667

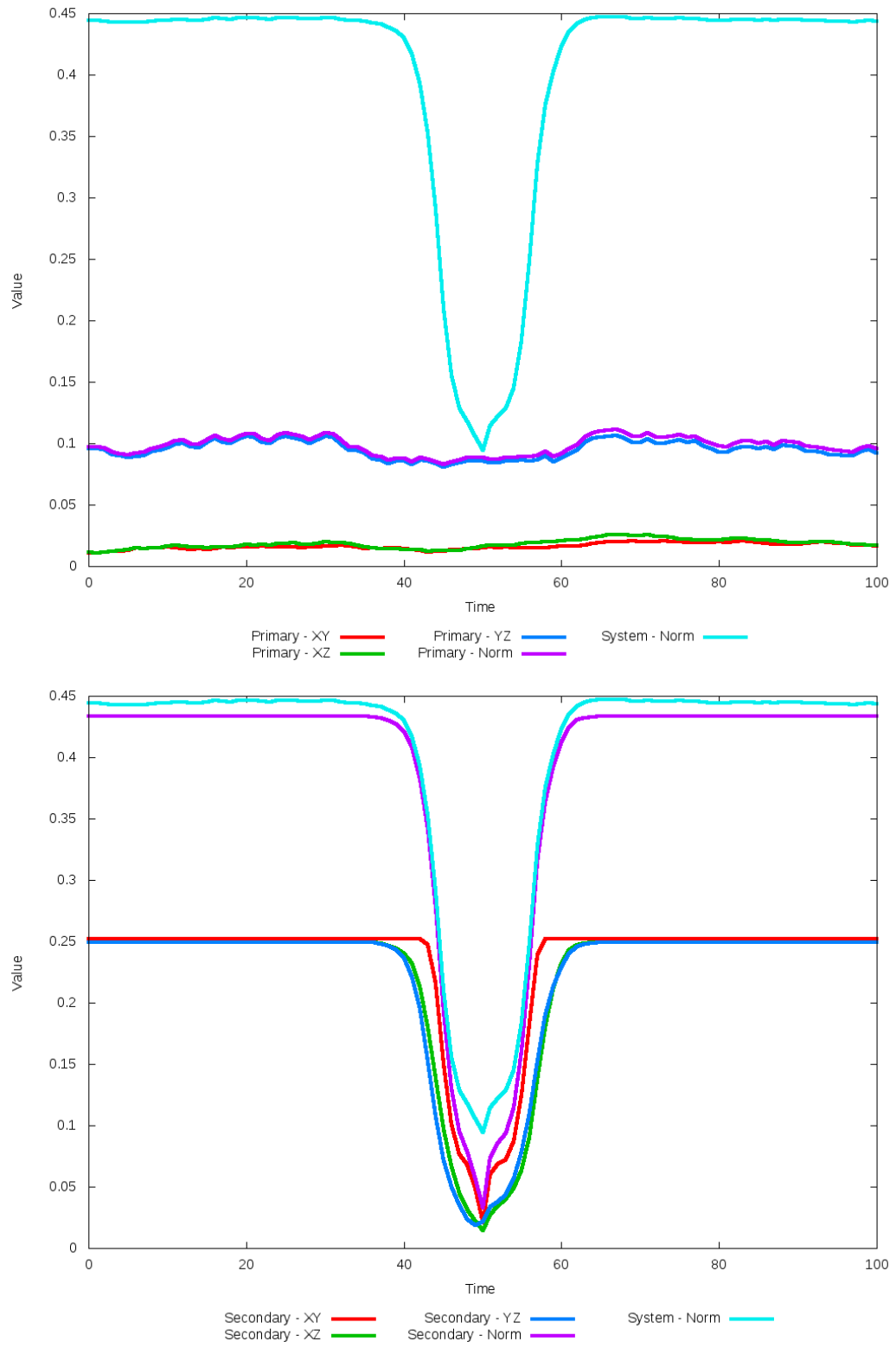


Figure 5.102: All metrics versus simulation time of the best N-Body simulation for SDSS 587736941981466667

5.1.18 SDSS 587738569246376675 (Arp 57)

Arp 57 shows very good agreement between its simulations and observational data. With only a small change in dynamical friction, initial and optimized N-Body simulations appear nearly indistinguishable in all figures. There is however a small change in trajectory between the SPAM and N-Body simulations. Given the hyperbolic trajectories, it is unlikely that these galaxies will interact any further after their weak interaction.

Table 5.35: Identification Information and Merger Zoo summary for SDSS 587738569246376675.

Name	Aliases	RA (hms)	Dec (dms)	Redshift
SDSS 587738569246376675	Arp 57	13:16:47.4	+14:25:39.6	0.060208

\mathbf{R}_x	\mathbf{R}_y	\mathbf{R}_z	\mathbf{V}_x	\mathbf{V}_y	\mathbf{V}_z
-4.62932	-3.48666	8.53665	-1.02385	-0.94978	2.5994

	Primary Galaxy	Secondary Galaxy
mass	1.40808	0.97714
radius	1.1802	0.65139
ϕ	176.93944°	71.08069°
θ	337.85444°	335.44237°
ϵ	0.3	0.3

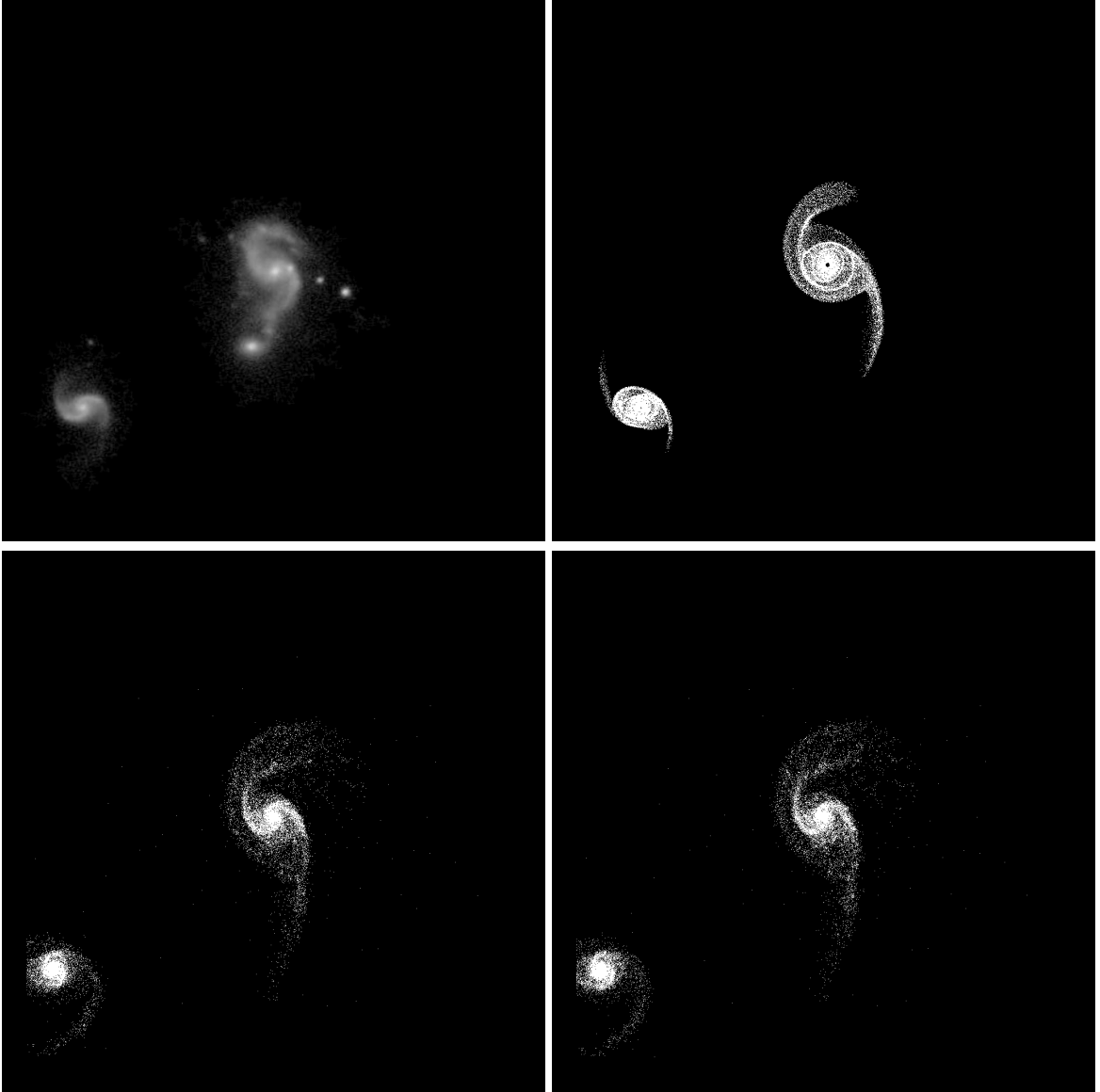


Figure 5.103: Target image (top-left), best SPAM match from Merger Wars (top-right), initial N-Body match (bottom-left), and best N-Body match (bottom-right) for SDSS 587738569246376675

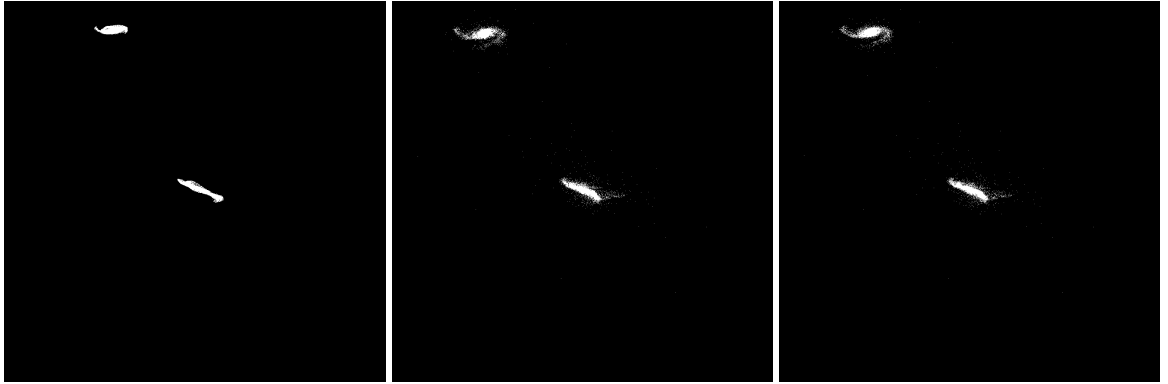


Figure 5.104: XZ projections of best SPAM match from Merger Wars (left), initial N-Body match (middle), and best N-Body match (right) for SDSS 587738569246376675

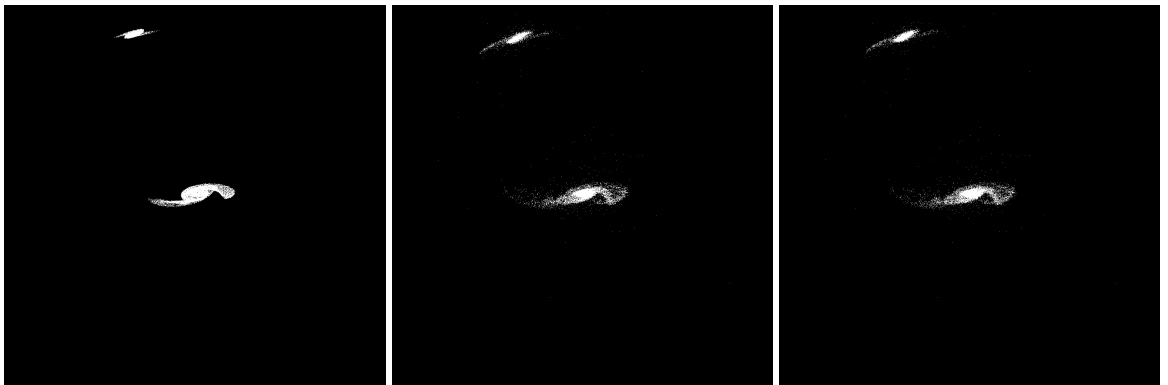


Figure 5.105: YZ projections of best SPAM match from Merger Wars (left), initial N-Body match (middle), and best N-Body match (right) for SDSS 587738569246376675

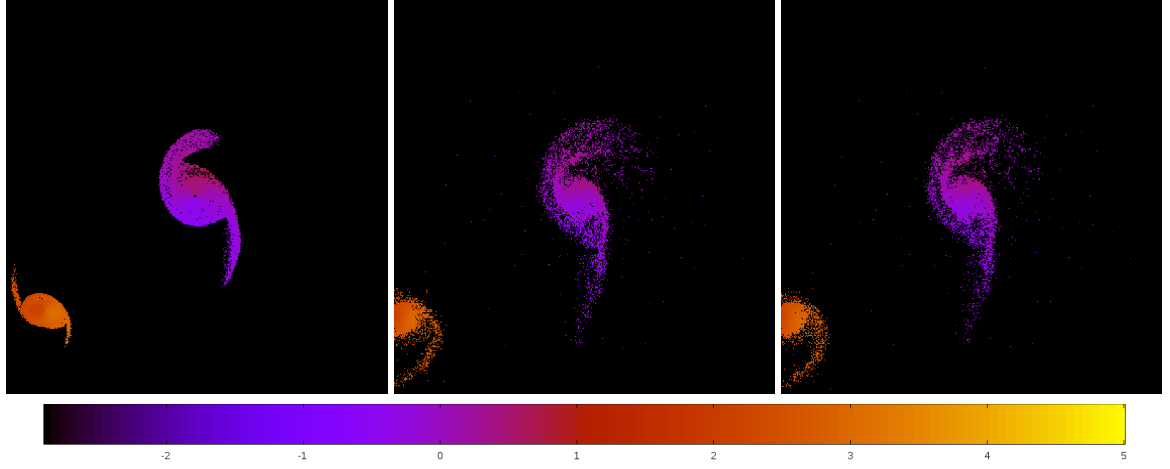


Figure 5.106: Line of sight velocity plots of best SPAM match from Merger Wars (left), initial N-Body match (middle), and best N-Body match (right) for SDSS 587738569246376675

Table 5.36: Orbital Elements & Dynamical Friction for SDSS 587738569246376675

	SPAM Simulation	Initial N-Body Simulation	Best N-Body Simulation
a	-0.134	-0.134	-0.133
e	17.955	18.154	18.294
r_c	2.276	2.302	2.307
i	76.440°	75.680°	75.687°
Ω	196.176°	195.099°	195.128°
ω	331.811°	326.607°	326.583°
ν	86.518°	86.646°	86.660°
t_n	50	51	51
$\ln\Lambda$	N/A	1.00E-03	1.20E-03

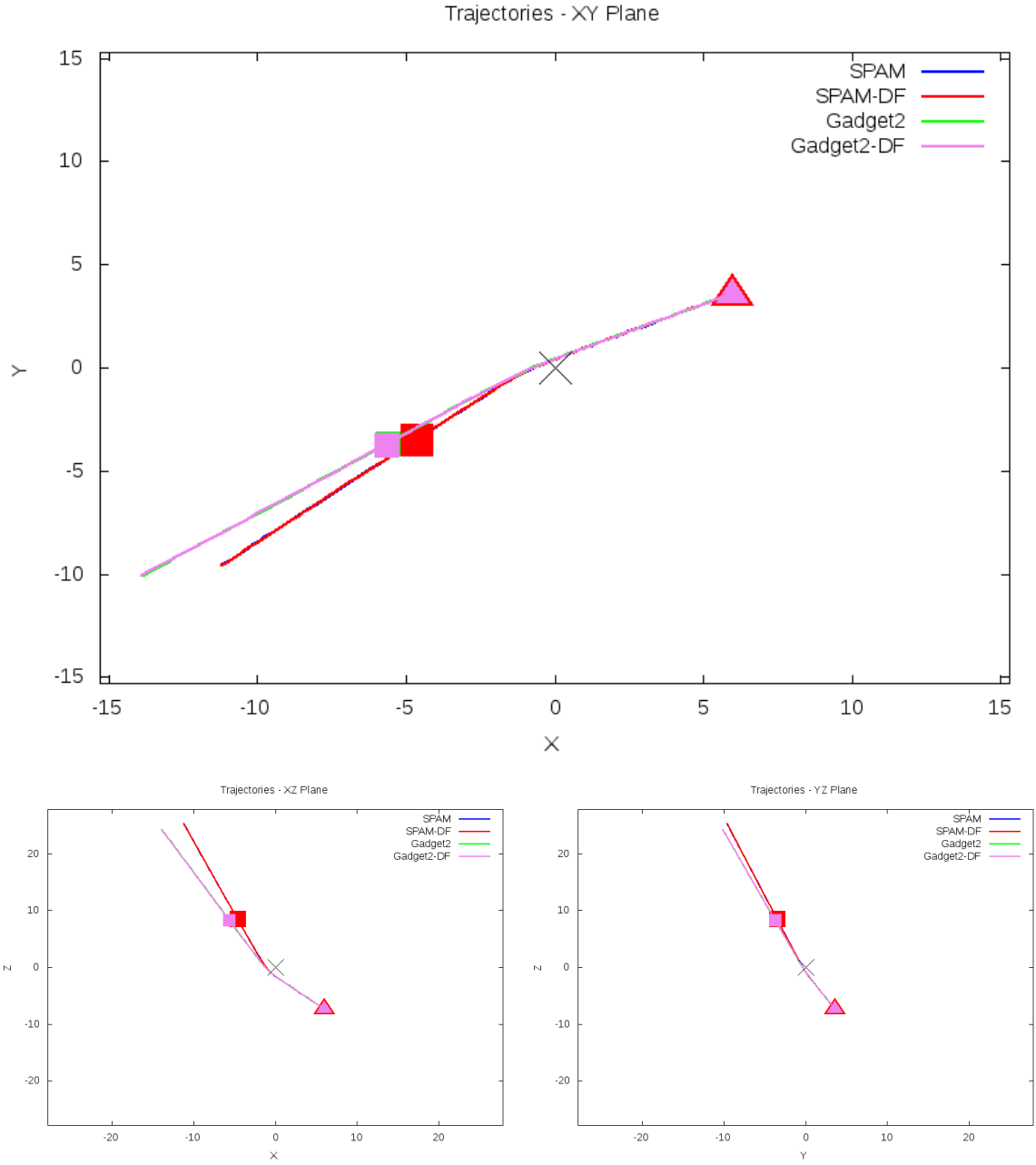


Figure 5.107: Trajectory plots of best SPAM match from Merger Wars, initial N-Body match, and best N-Body match for SDSS 587738569246376675

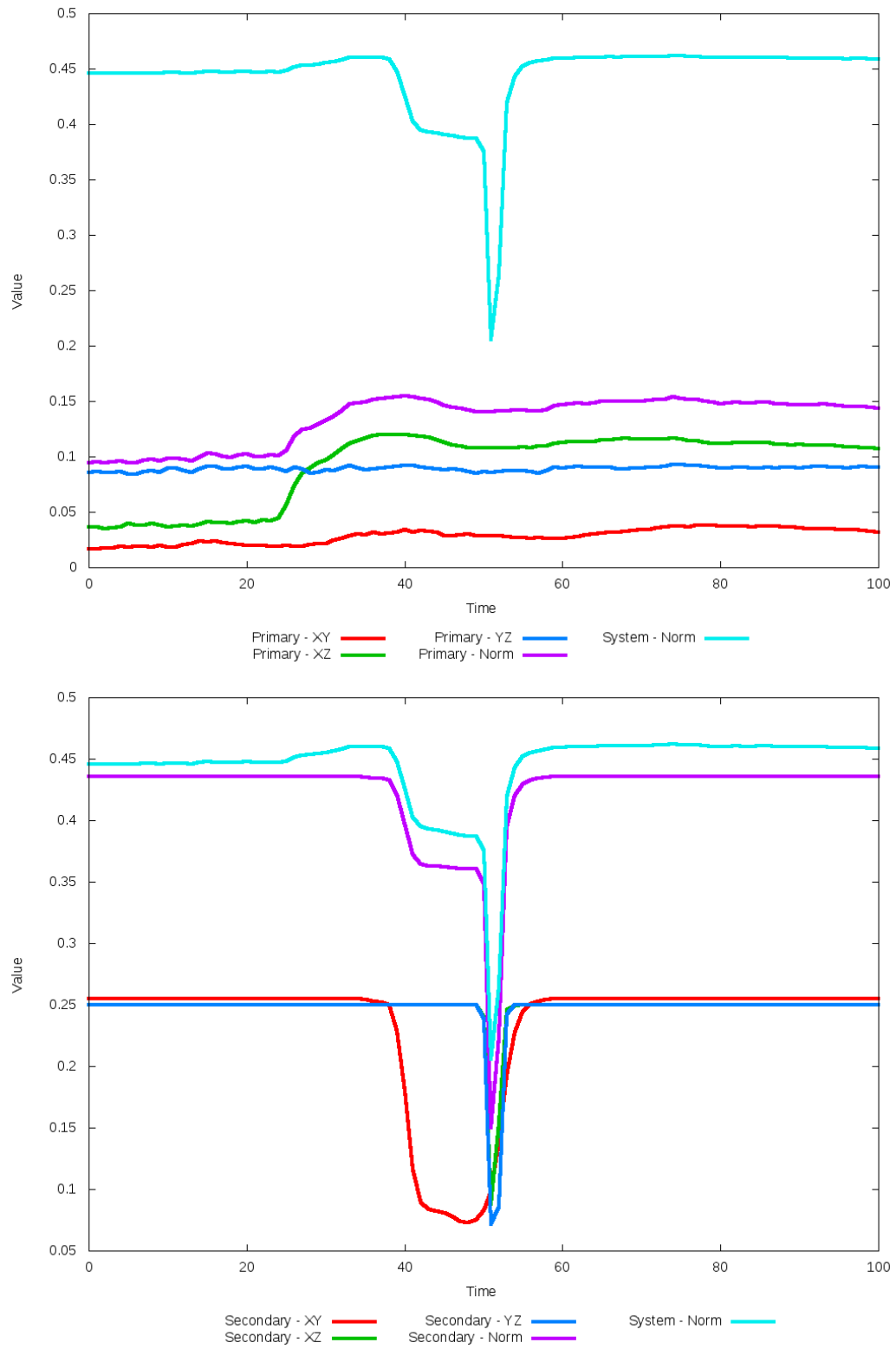


Figure 5.108: All metrics versus simulation time of the best N-Body simulation for SDSS 587738569246376675

5.1.19 SDSS 587738569249390718

This system shows a significant improvement in the positions of the secondary galaxy between the optimized simulation and SPAM simulation. Although there is a bridge between both galaxies in the optimized N-Body simulation, it is more pronounced in the initial simulation. Looking at the trajectories however show a significant change in the XZ and YZ projections, with the optimized simulation very closely matching the SPAM trajectories. Despite the improvement in trajectories, at the time of the interaction, SPAM and the optimized N-Body simulation describe the orbits as hyperbolic and elliptical, respectively. This system also shows that the choice of metric can have a significant impact on the best time to match the target data set - for the optimized dynamical friction, this time varies significantly if using the metric based on the secondary galaxy's XY metric compared to its Norm metric.

Table 5.37: Identification Information and Merger Zoo summary for SDSS 587738569249390718.

Name	Aliases	RA (hms)	Dec (dms)	Redshift
SDSS 587738569249390718	2MASS 13445034+1355178	13:44:50.3	+13:55:16.9	0.082453

R_x	R_y	R_z	V_x	V_y	V_z
-0.82909	2.18149	-1.22409	0.08683	-0.22468	-0.92517

	Primary Galaxy	Secondary Galaxy
mass	0.91339	2.31295
radius	0.73445	1.10831
ϕ	153.56774°	43.83877°
θ	168.63224°	326.12543°
ϵ	0.3	0.3

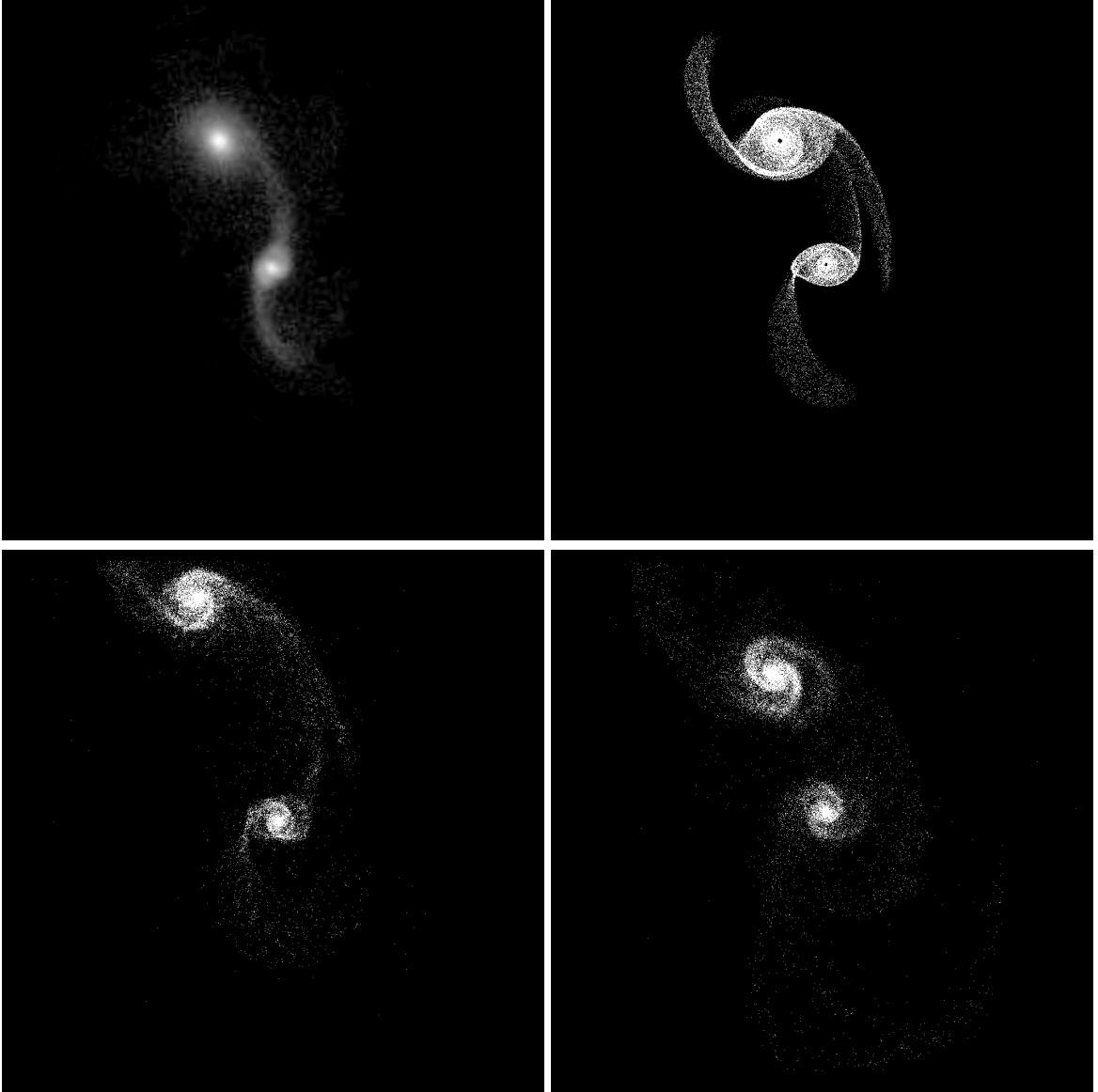


Figure 5.109: Target image (top-left), best SPAM match from Merger Wars (top-right), initial N-Body match (bottom-left), and best N-Body match (bottom-right) for SDSS 587738569249390718

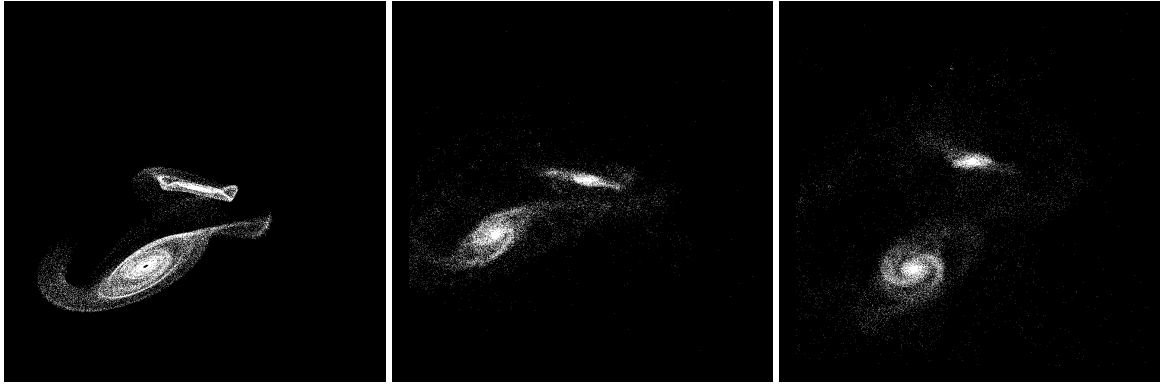


Figure 5.110: XZ projections of best SPAM match from Merger Wars (left), initial N-Body match (middle), and best N-Body match (right) for SDSS 587738569249390718

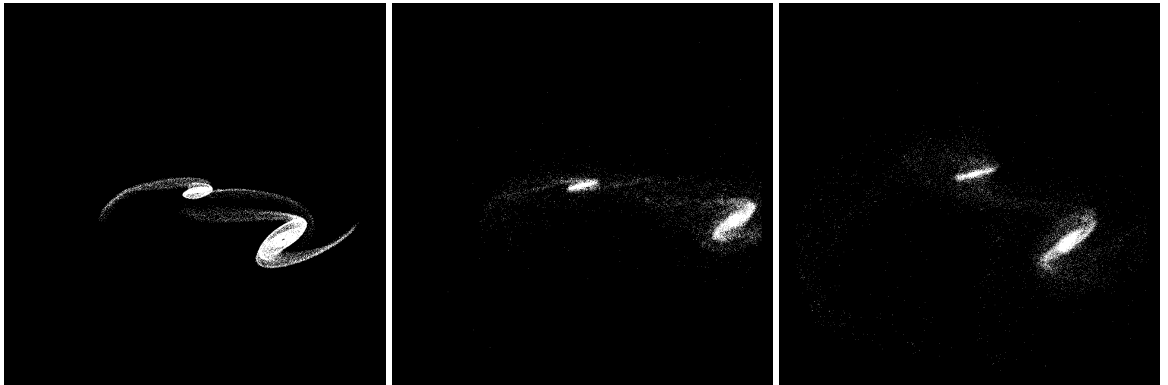


Figure 5.111: YZ projections of best SPAM match from Merger Wars (left), initial N-Body match (middle), and best N-Body match (right) for SDSS 587738569249390718

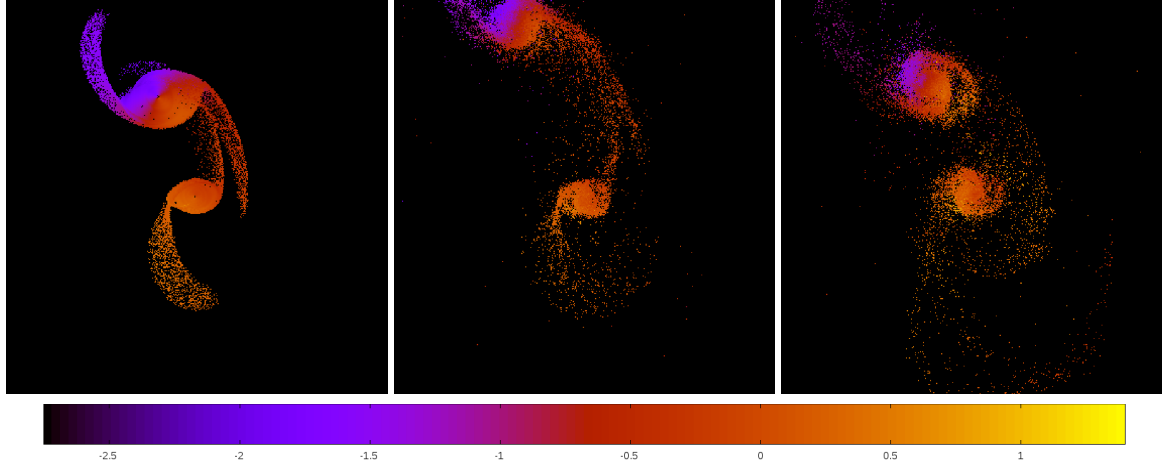


Figure 5.112: Line of sight velocity plots of best SPAM match from Merger Wars (left), initial N-Body match (middle), and best N-Body match (right) for SDSS 587738569249390718

Table 5.38: Orbital Elements & Dynamical Friction for SDSS 587738569249390718

	SPAM Simulation	Initial N-Body Simulation	Best N-Body Simulation
a	-3.140	-1.447	7.573
e	2.619	4.257	0.261
r_c	5.083	4.712	5.600
i	90.073°	89.914°	89.291°
Ω	290.848°	290.649°	290.324°
ω	189.633°	126.805°	191.652°
ν	18.045°	62.127°	11.688°
t_n	50	50	63
$\ln\Lambda$	N/A	1.00E-03	3.00E-04

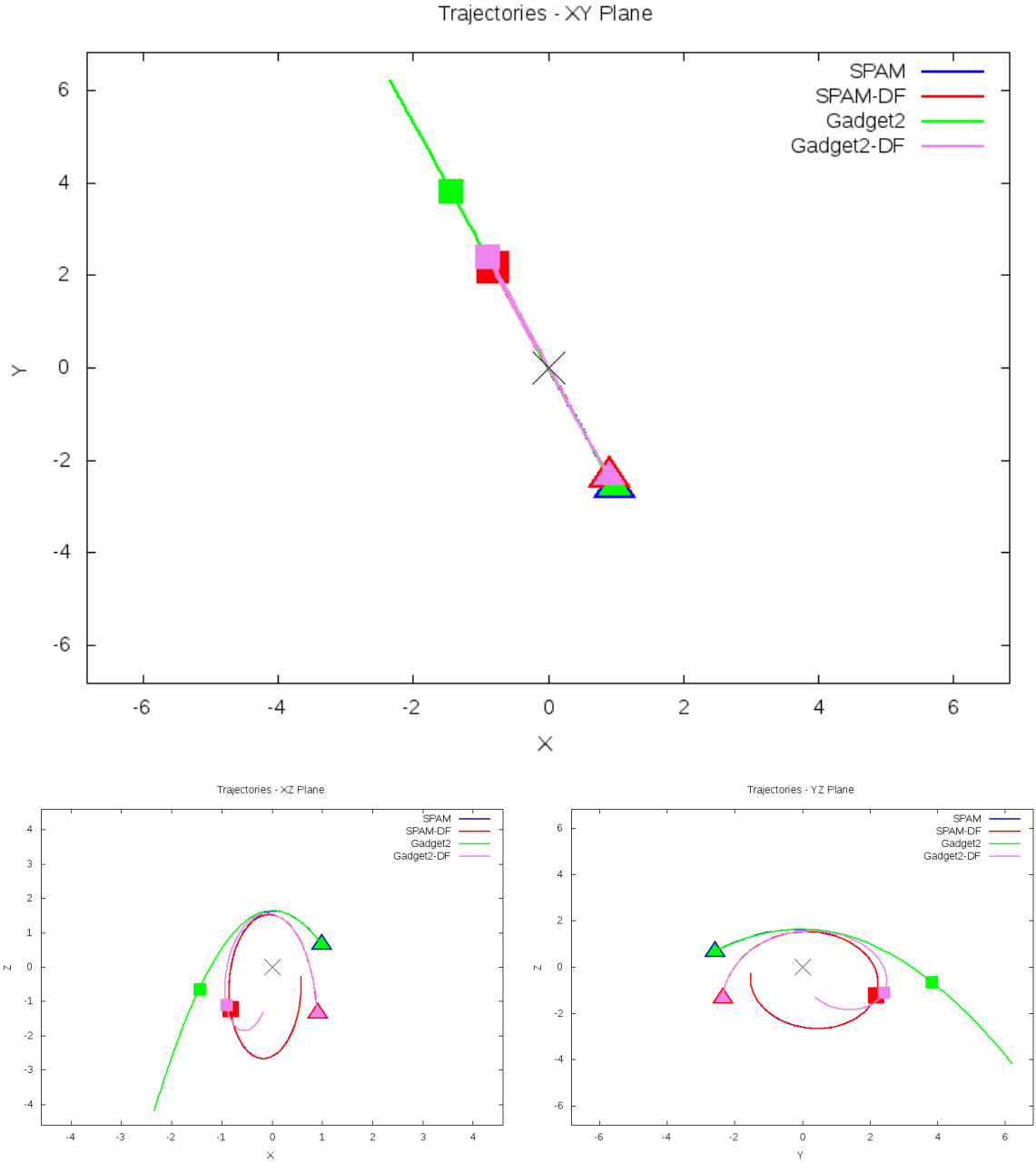


Figure 5.113: Trajectory plots of best SPAM match from Merger Wars, initial N-Body match, and best N-Body match for SDSS 587738569249390718

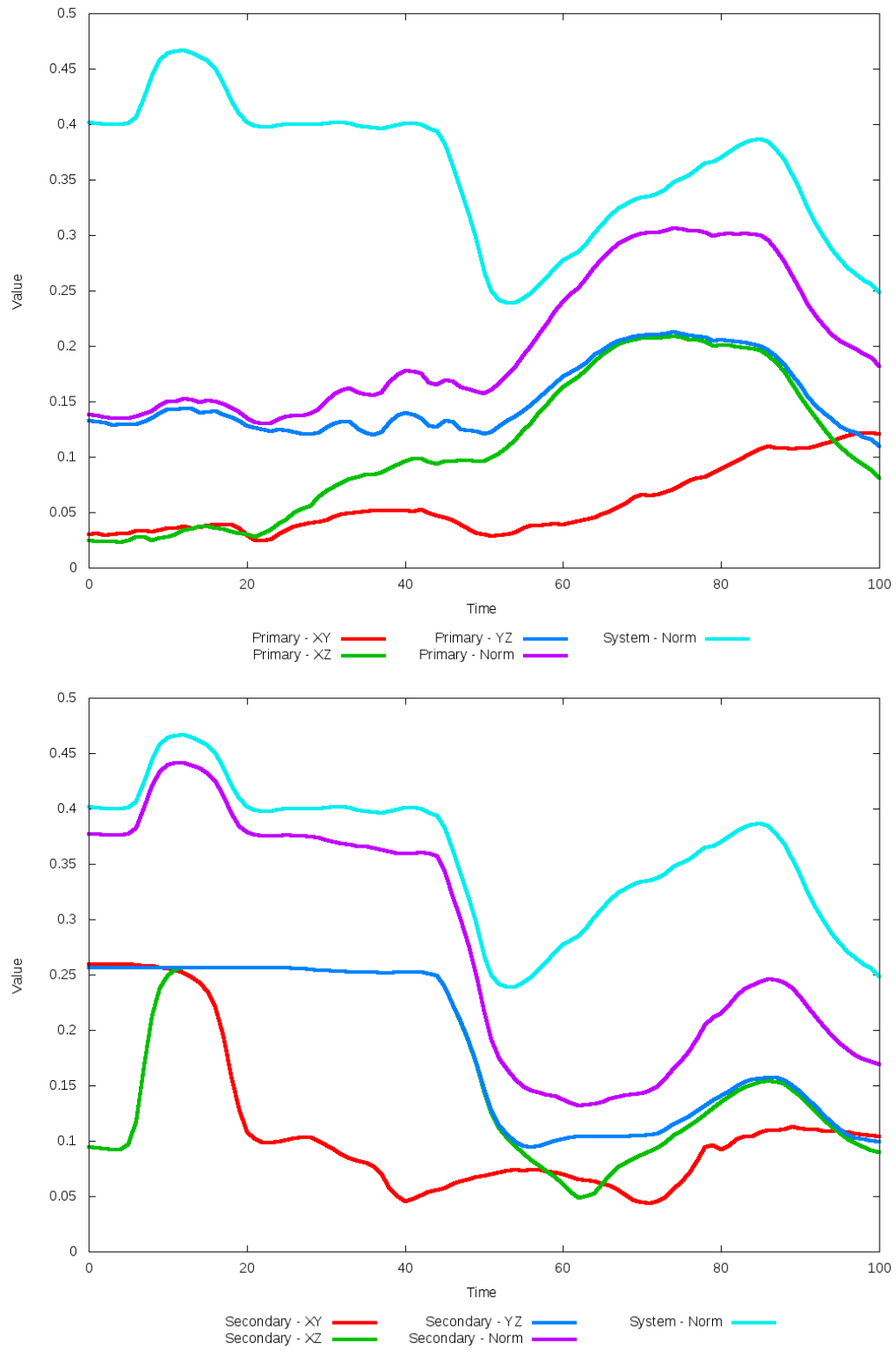


Figure 5.114: All metrics versus simulation time of the best N-Body simulation for SDSS 587738569249390718

5.1.20 SDSS 587739153356095531 (Arp 247)

Arp 247 shows a very good agreement between the optimized N-Body simulation with the SPAM simulation, although the position of the secondary galaxy should be improved when compared to observational data. In the XZ and YZ projections, the match is not as good, showing a significant change in position when compared to the SPAM simulation. The trajectories show the galaxies in the N-Body simulations want to merge much sooner than the SPAM simulations. The optimization routine shows that there are approximately three times at which the secondary galaxy would be a good match with SPAM simulations. The biggest problem with this match was in the Y direction of the secondary galaxy, and the use of a different metric based on the XY projection indicates a better match may be found later during the N-Body simulations.

Table 5.39: Identification Information and Merger Zoo summary for SDSS 587739153356095531.

Name	Aliases	RA (hms)	Dec (dms)	Redshift
SDSS 587739153356095531	Arp 247, IC 2338/2339	8:23:34.0	+21:20:50.3	0.018079

R_x	R_y	R_z	V_x	V_y	V_z
0.47569	-0.71987	-2.73633	0.15406	-0.31429	-0.25394

	Primary Galaxy	Secondary Galaxy
mass	0.74212	0.35877
radius	0.47819	0.22201
ϕ	55.45°	45.65°
θ	319.41176°	335.29411°
ϵ	0.3	0.3

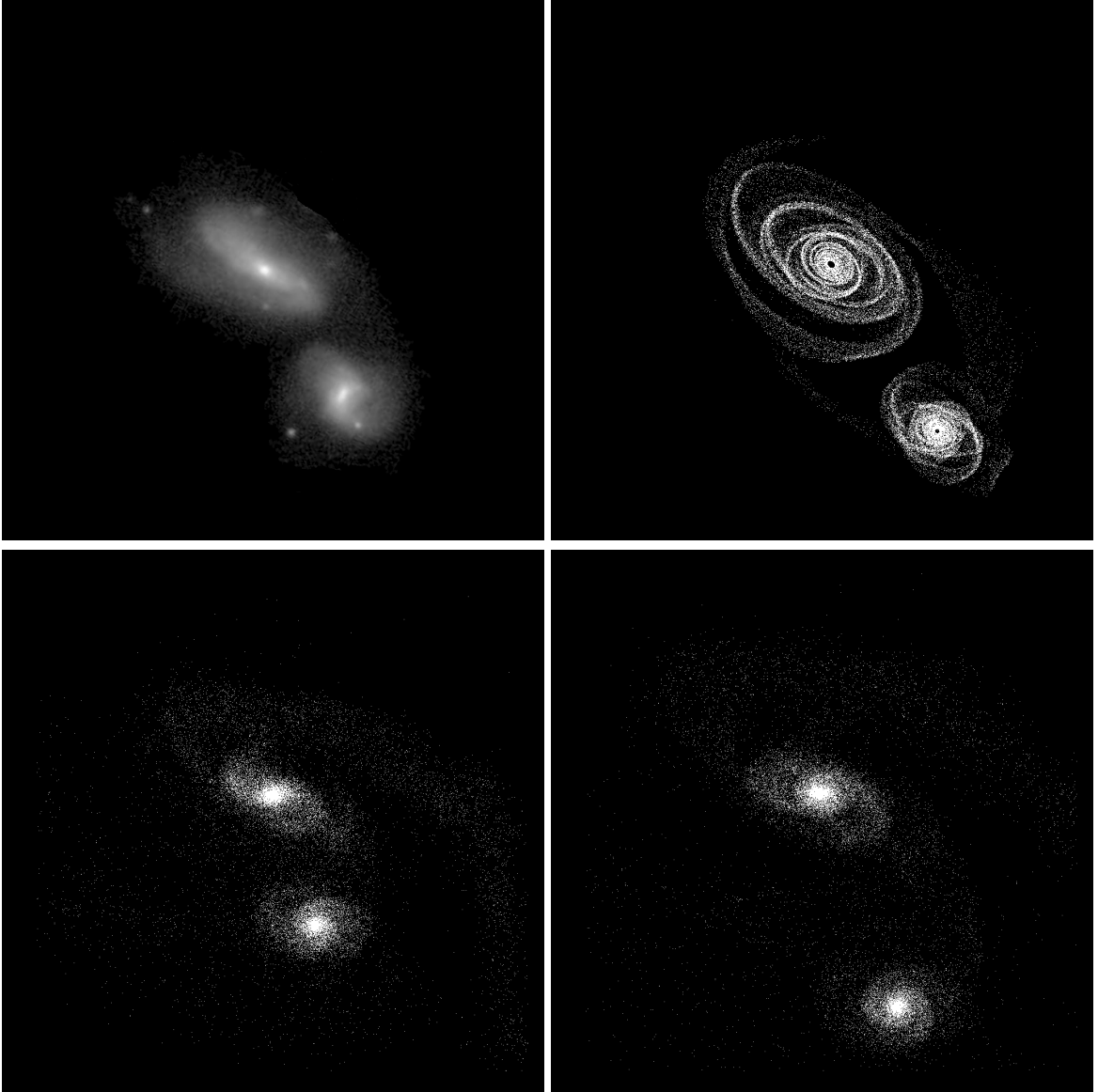


Figure 5.115: Target image (top-left), best SPAM match from Merger Wars (top-right), initial N-Body match (bottom-left), and best N-Body match (bottom-right) for SDSS 587739153356095531

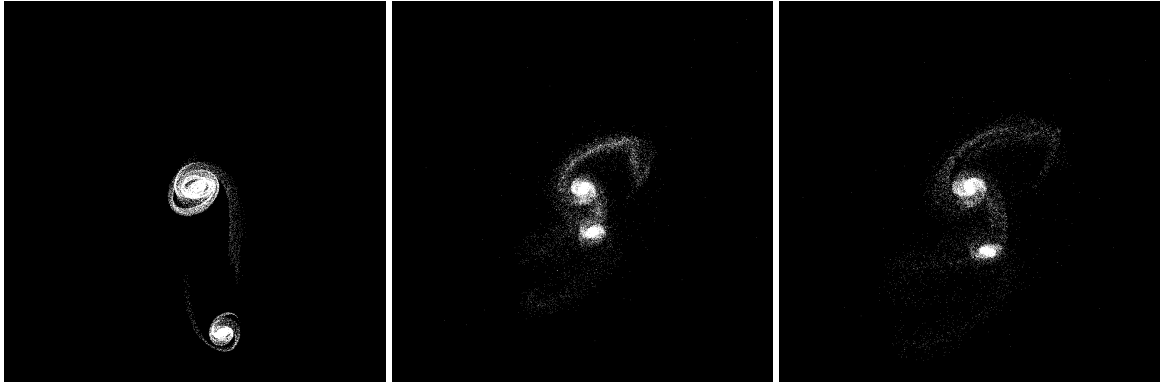


Figure 5.116: XZ projections of best SPAM match from Merger Wars (left), initial N-Body match (middle), and best N-Body match (right) for SDSS 587739153356095531



Figure 5.117: YZ projections of best SPAM match from Merger Wars (left), initial N-Body match (middle), and best N-Body match (right) for SDSS 587739153356095531

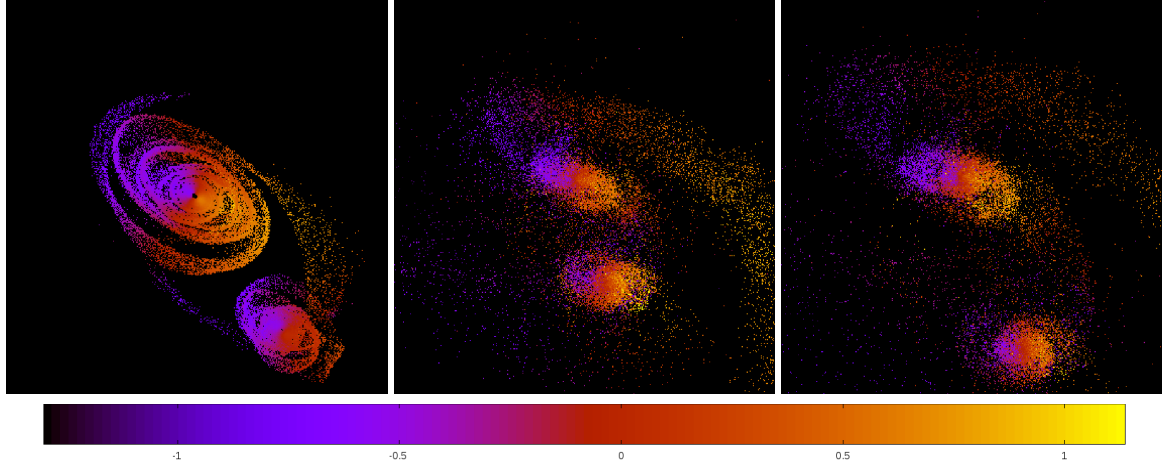


Figure 5.118: Line of sight velocity plots of best SPAM match from Merger Wars (left), initial N-Body match (middle), and best N-Body match (right) for SDSS 587739153356095531

Table 5.40: Orbital Elements & Dynamical Friction for SDSS 587739153356095531

	SPAM Simulation	Initial N-Body Simulation	Best N-Body Simulation
a	-26.271	1.466	3.950
e	1.083	0.325	0.588
r_c	2.185	0.990	1.627
i	92.982°	88.414°	88.340°
Ω	293.947°	288.299°	291.255°
ω	186.258°	134.833°	203.144°
ν	100.995°	163.067°	100.291°
t_n	50	36	39
$\ln\Lambda$	N/A	1.00E-03	2.00E-03

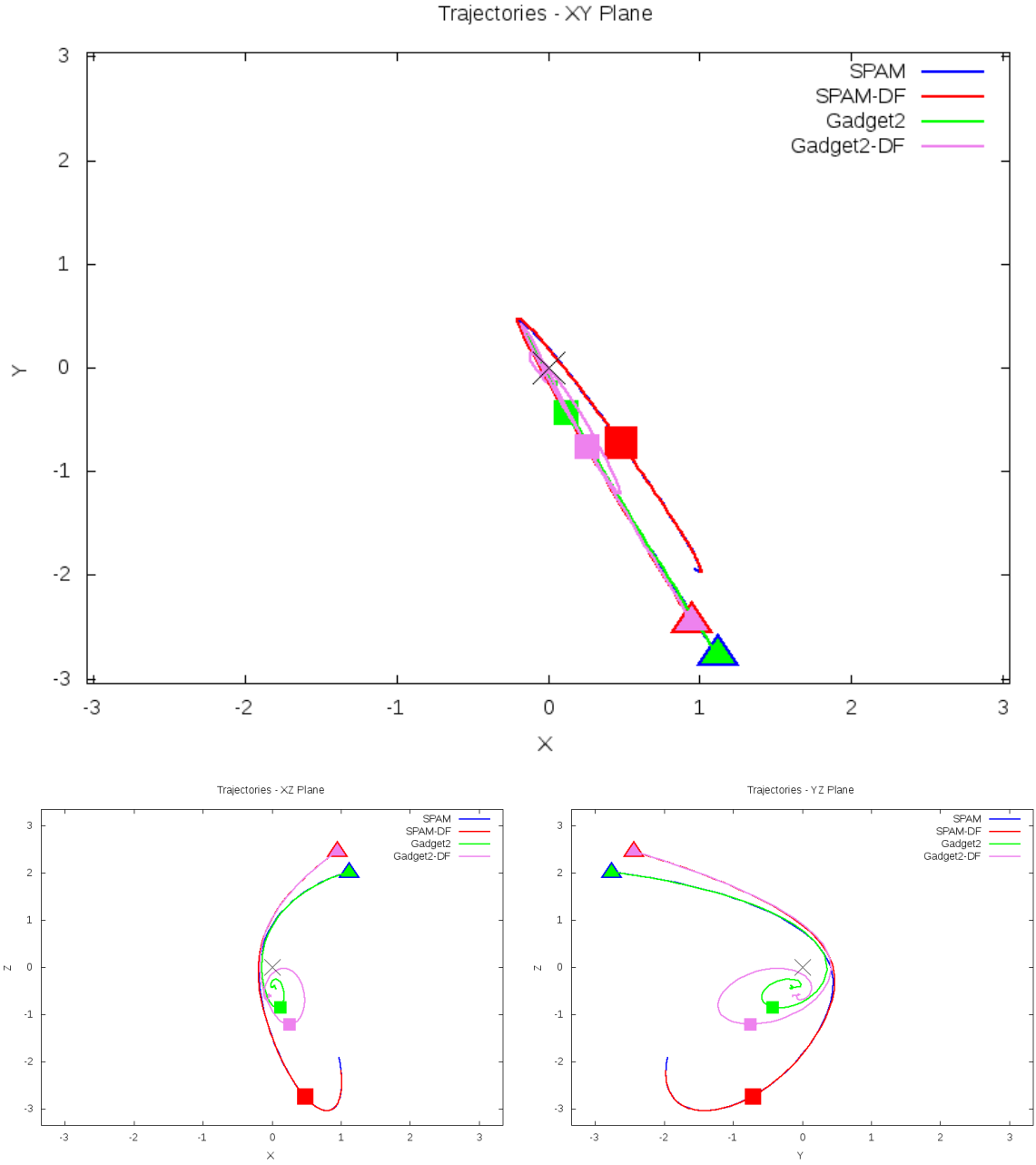


Figure 5.119: Trajectory plots of best SPAM match from Merger Wars, initial N-Body match, and best N-Body match for SDSS 587739153356095531

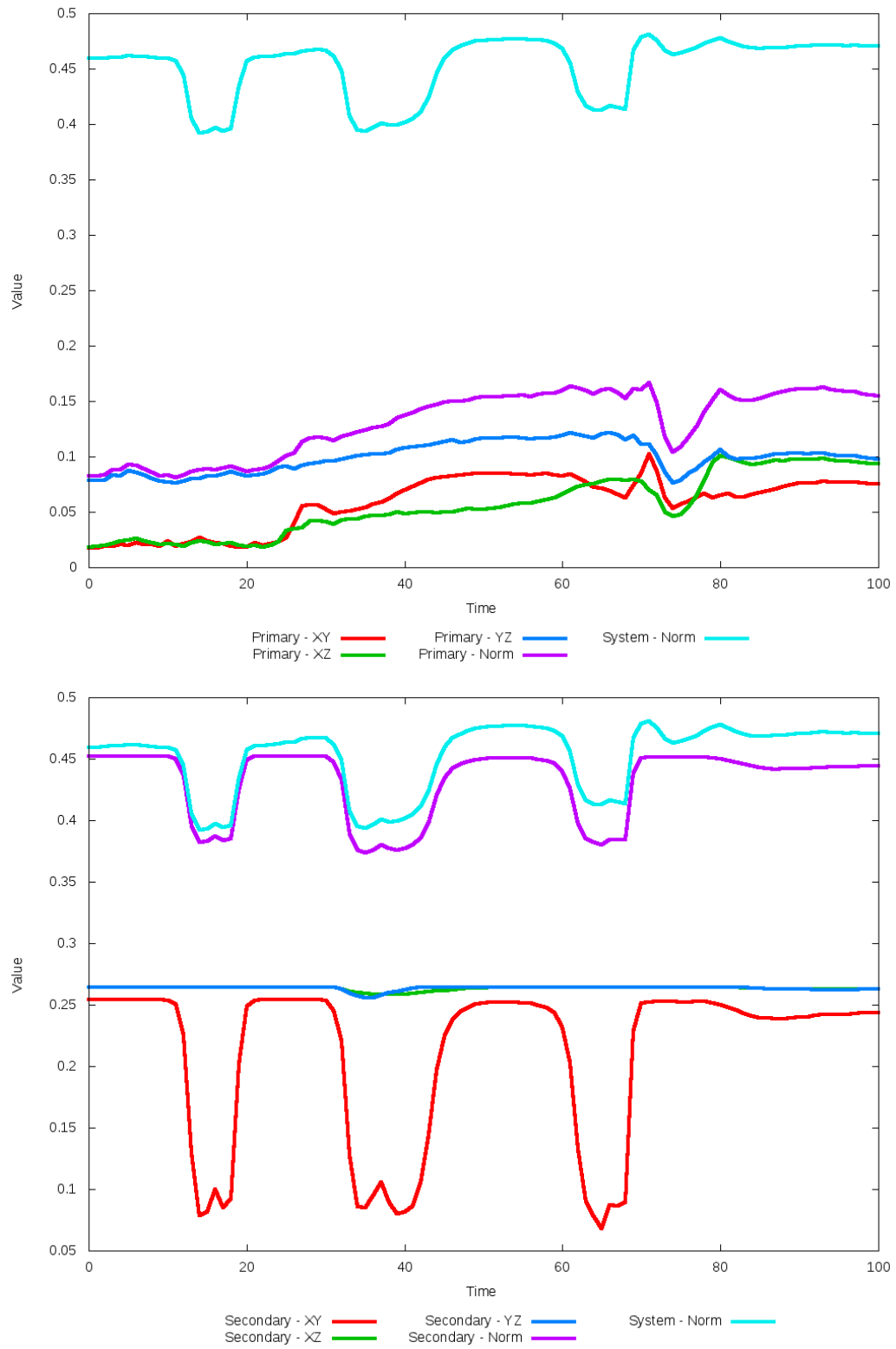


Figure 5.120: All metrics versus simulation time of the best N-Body simulation for SDSS 587739153356095531

5.1.21 SDSS 587739407868690486 (Arp 241)

Arp 241 shows a significant improvement with the optimized N-Body simulation matching the SPAM simulation and observational data. Whereas the initial N-Body simulation appears to quickly exhibit a merger, the optimized simulation's apparent merger happens much later in time. However, the orientation of the tidal features of the primary galaxy are not as well aligned along the Y direction as one would hope to see. The trajectory also changes from being elliptical to hyperbolic as dynamical friction is optimized.

Table 5.41: Identification Information and Merger Zoo summary for SDSS 587739407868690486.

Name	Aliases	RA (hms)	Dec (dms)	Redshift
SDSS 587739407868690486	Arp 241, NGC 5699	14:37:50.4	+30:28:59.5	0.034521

R_x	R_y	R_z	V_x	V_y	V_z
-0.30275	-0.54877	-0.03638	-0.4393	0.47019	0.0

	Primary Galaxy	Secondary Galaxy
mass	0.15827	0.23379
radius	0.24804	0.34462
ϕ	96.07505°	107.19568°
θ	227.47677°	229.43557°
ϵ	0.3	0.3

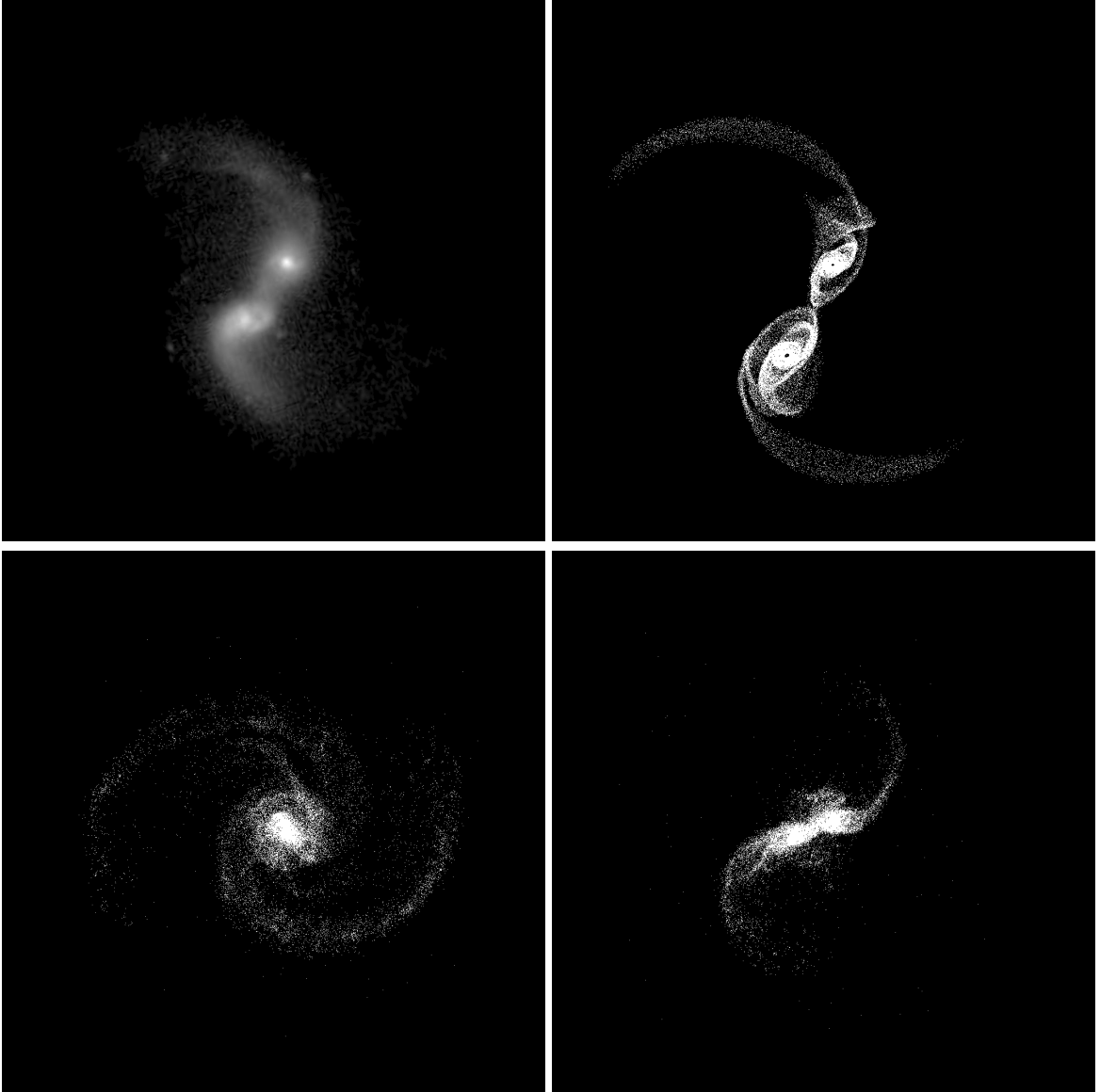


Figure 5.121: Target image (top-left), best SPAM match from Merger Wars (top-right), initial N-Body match (bottom-left), and best N-Body match (bottom-right) for SDSS 587739407868690486

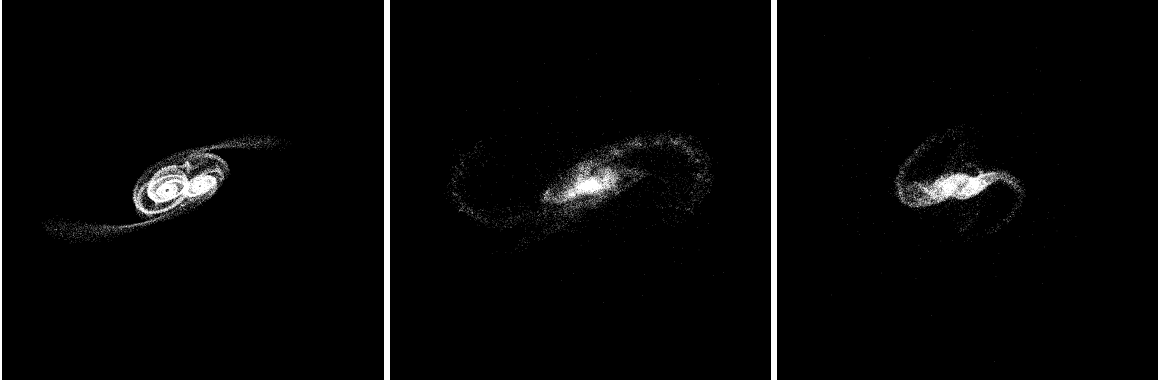


Figure 5.122: XZ projections of best SPAM match from Merger Wars (left), initial N-Body match (middle), and best N-Body match (right) for SDSS 587739407868690486

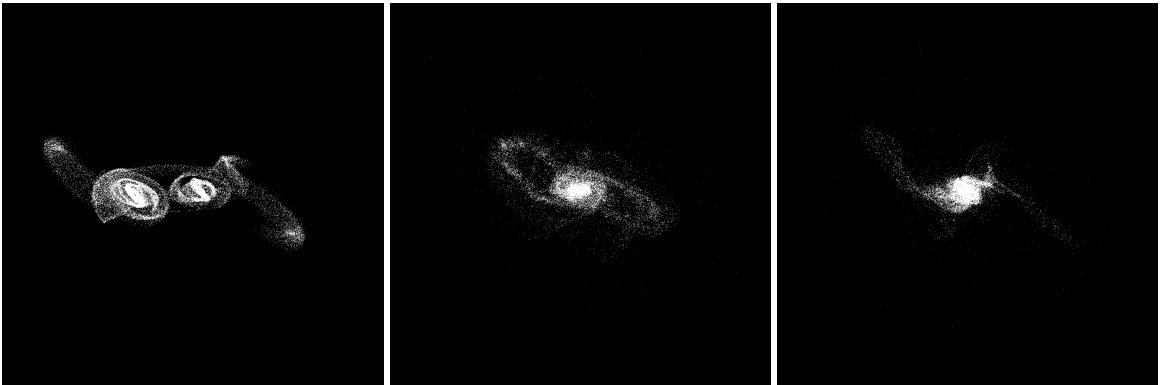


Figure 5.123: YZ projections of best SPAM match from Merger Wars (left), initial N-Body match (middle), and best N-Body match (right) for SDSS 587739407868690486

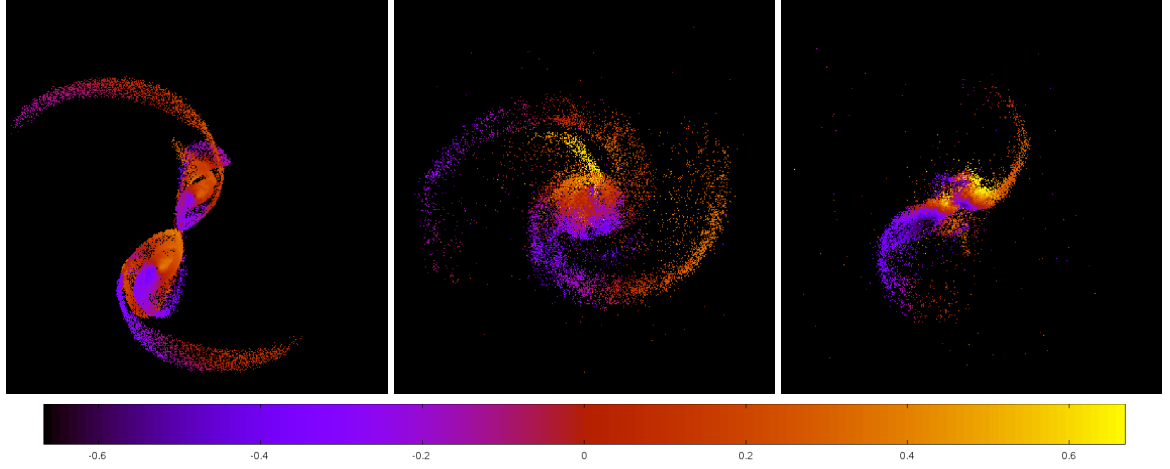


Figure 5.124: Line of sight velocity plots of best SPAM match from Merger Wars (left), initial N-Body match (middle), and best N-Body match (right) for SDSS 587739407868690486

Table 5.42: Orbital Elements & Dynamical Friction for SDSS 587739407868690486

	SPAM Simulation	Initial N-Body Simulation	Best N-Body Simulation
a	-1.712	0.170	-0.652
e	1.681	0.991	1.726
r_c	1.166	0.002	0.473
i	176.506°	161.667°	178.221°
Ω	133.055°	314.831°	43.004°
ω	279.537°	198.167°	235.506°
ν	331.324°	179.955°	315.480°
t_n	50	25	42
$\ln\Lambda$	N/A	1.00E-03	1.40E-03

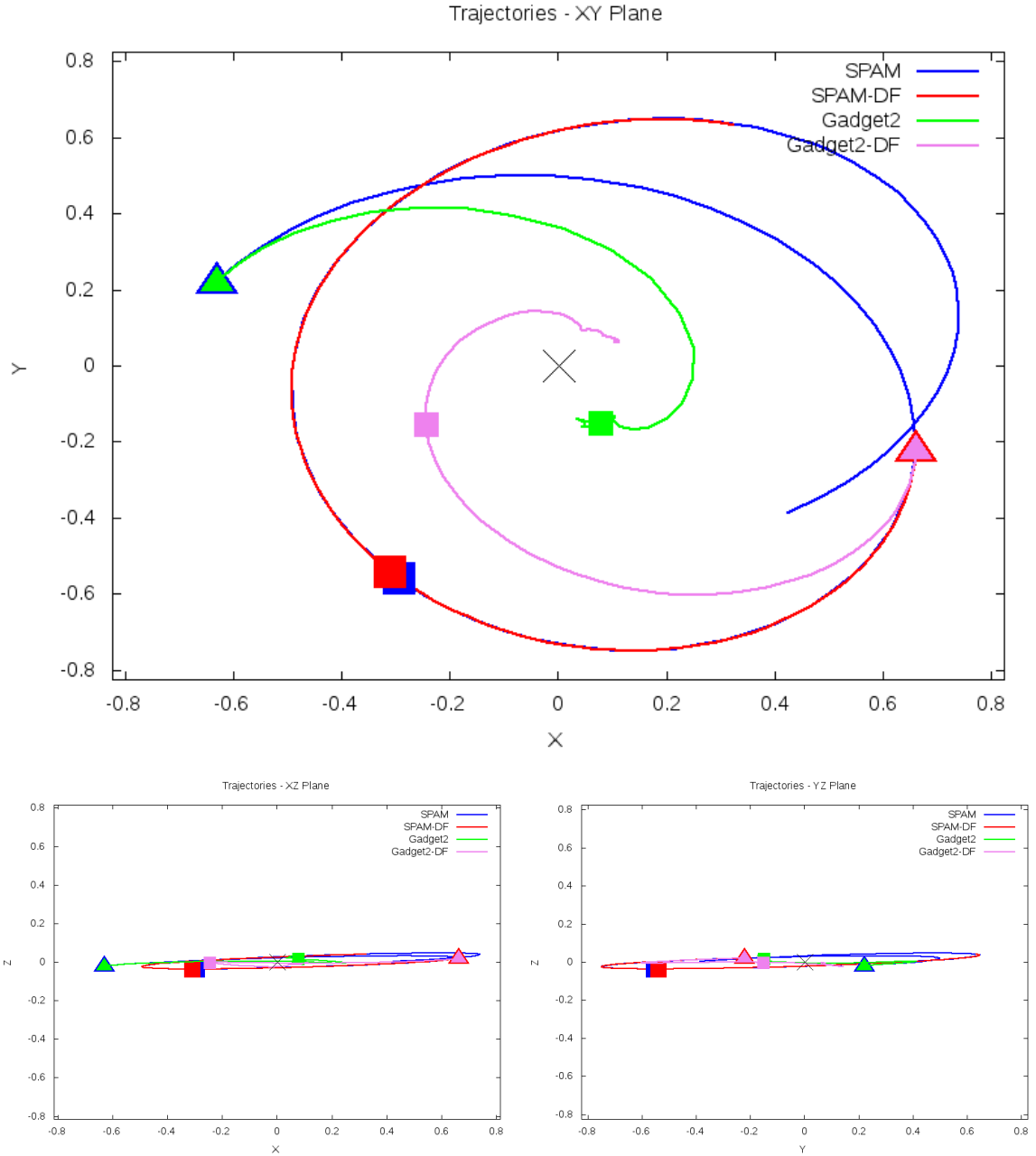


Figure 5.125: Trajectory plots of best SPAM match from Merger Wars, initial N-Body match, and best N-Body match for SDSS 587739407868690486

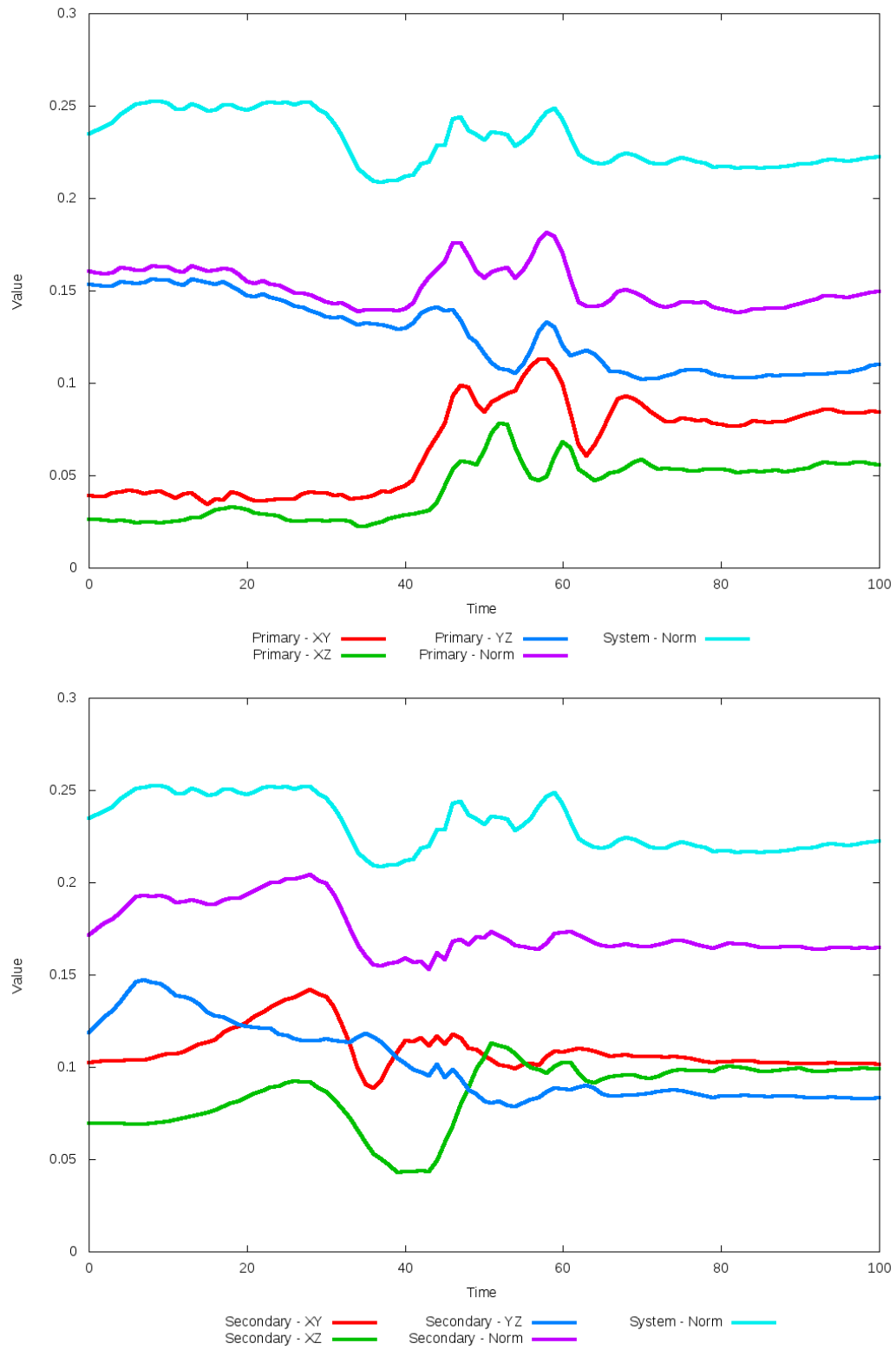


Figure 5.126: All metrics versus simulation time of the best N-Body simulation for SDSS 587739407868690486

5.1.22 SDSS 587739505541578866 (Arp 313)

Arp 313 shows very good agreement between its simulations and observational data. Although the initial and optimized N-Body simulations appear nearly indistinguishable, the optimization routine did make a significant change in dynamical friction. Despite the change, the trajectories did not change by any discernable amount. The interaction between these two galaxies appears to be weak as they pass by each other, unlikely to interact any further.

Table 5.43: Identification Information and Merger Zoo summary for SDSS 587739505541578866.

Name	Aliases	RA (hms)	Dec (dms)	Redshift
SDSS 587739505541578866	Arp 313, NGC 3994/3995	11:57:36.4	+32:16:39.8	0.010854

R_x	R_y	R_z	V_x	V_y	V_z
-0.89489	0.7566	-2.61146	-0.83865	-0.36327	-1.79472

	Primary Galaxy	Secondary Galaxy
mass	0.51513	0.27306
radius	0.30949	0.7403
ϕ	7.91644°	42.80034°
θ	115.71619°	304.2272°
ϵ	0.3	0.3

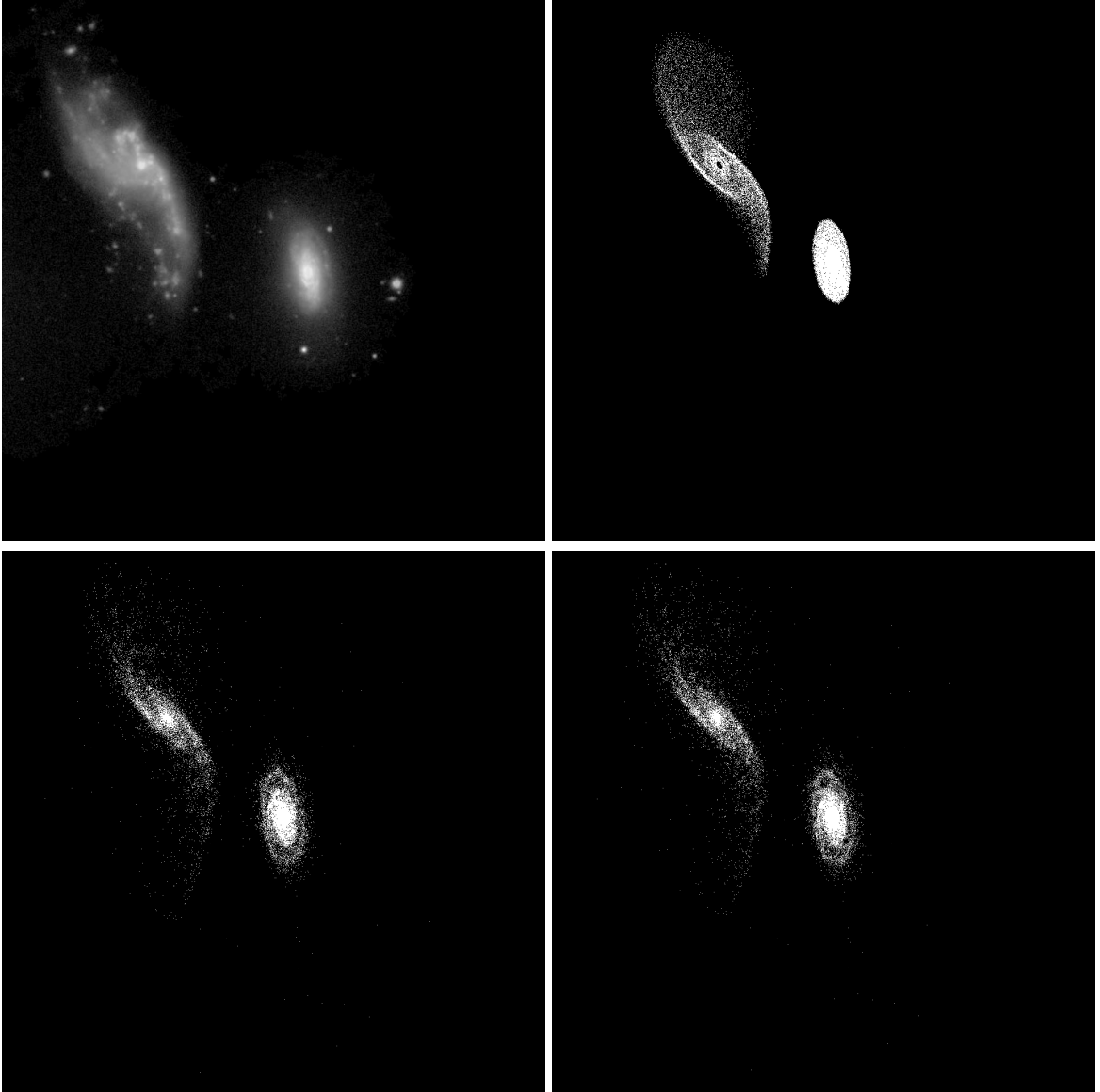


Figure 5.127: Target image (top-left), best SPAM match from Merger Wars (top-right), initial N-Body match (bottom-left), and best N-Body match (bottom-right) for SDSS 587739505541578866

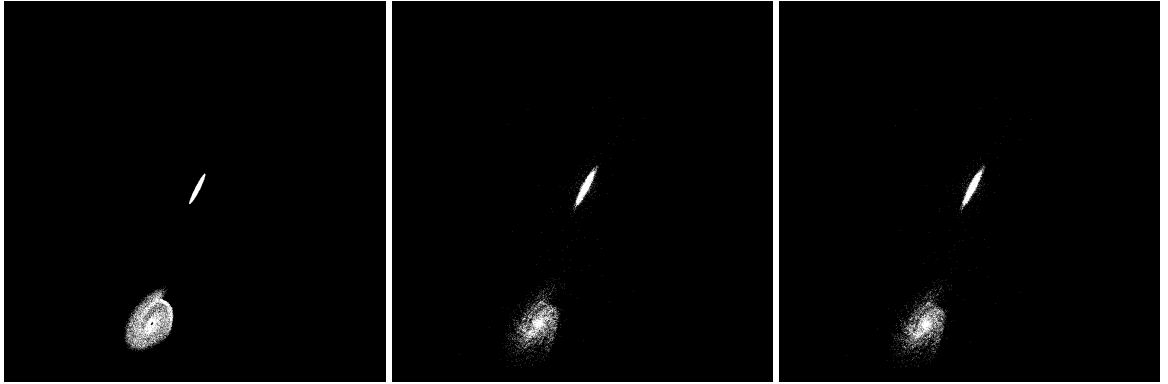


Figure 5.128: XZ projections of best SPAM match from Merger Wars (left), initial N-Body match (middle), and best N-Body match (right) for SDSS 587739505541578866

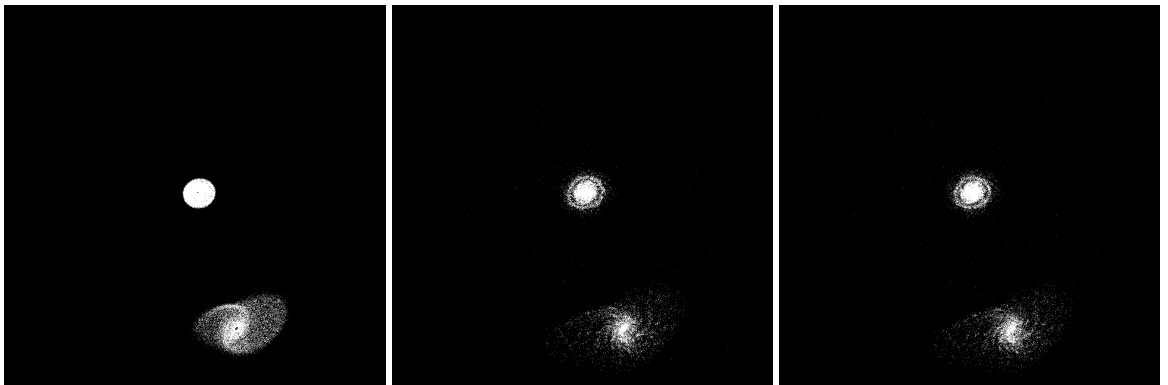


Figure 5.129: YZ projections of best SPAM match from Merger Wars (left), initial N-Body match (middle), and best N-Body match (right) for SDSS 587739505541578866

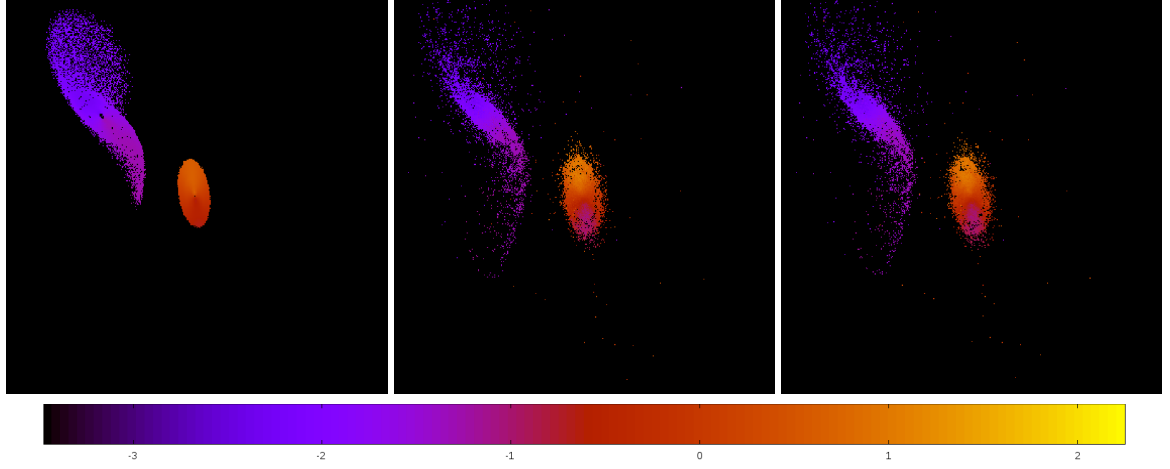


Figure 5.130: Line of sight velocity plots of best SPAM match from Merger Wars (left), initial N-Body match (middle), and best N-Body match (right) for SDSS 587739505541578866

Table 5.44: Orbital Elements & Dynamical Friction for SDSS 587739505541578866

	SPAM Simulation	Initial N-Body Simulation	Best N-Body Simulation
a	-0.091	-0.089	-0.085
e	28.523	28.979	30.127
r_c	2.499	2.486	2.489
i	68.035°	67.821°	67.845°
Ω	255.791°	255.641°	255.689°
ω	194.286°	194.050°	193.954°
ν	65.374°	65.728°	65.858°
t_n	50	50	50
$\ln\Lambda$	N/A	1.00E-03	2.30E-03

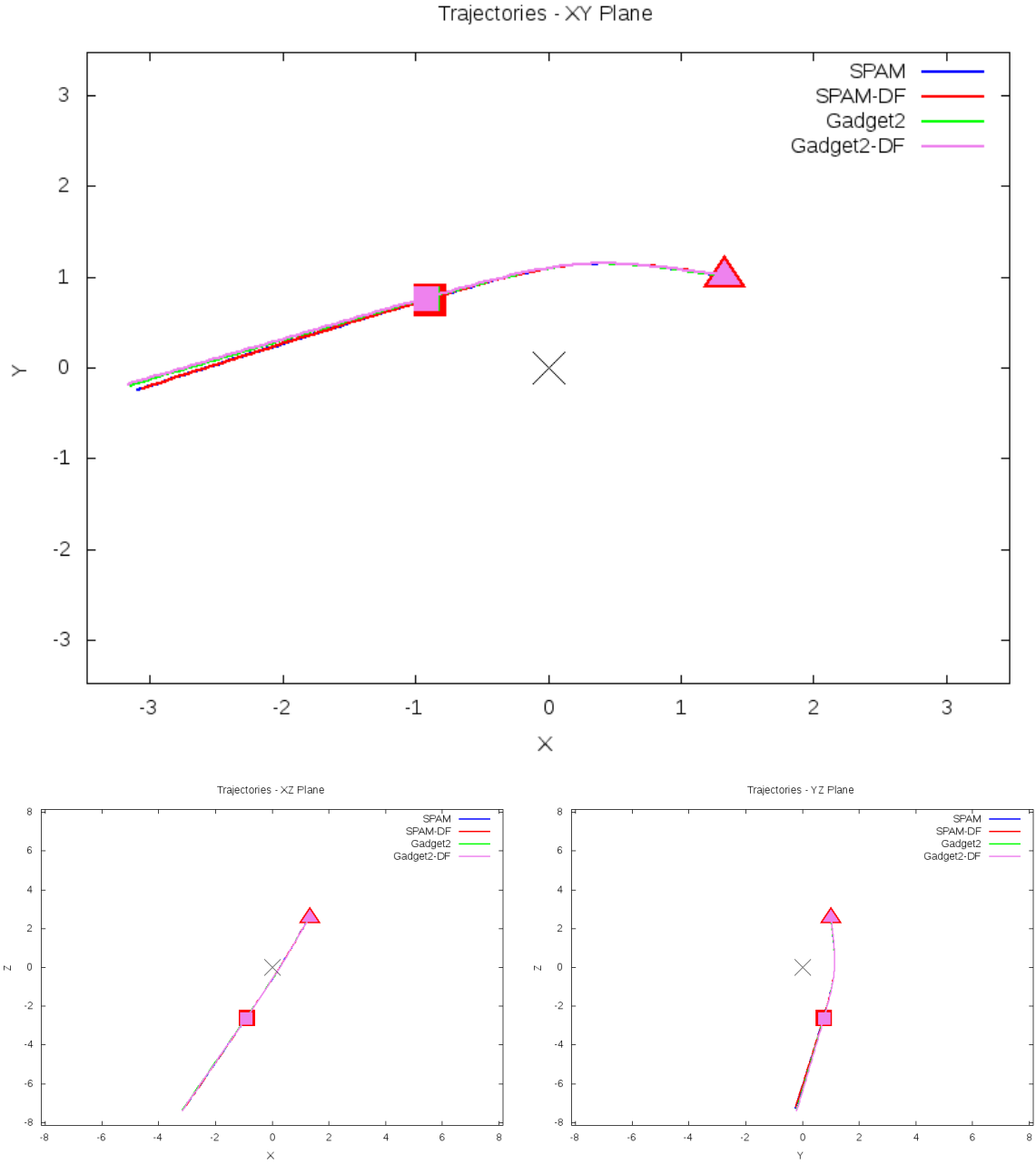


Figure 5.131: Trajectory plots of best SPAM match from Merger Wars, initial N-Body match, and best N-Body match for SDSS 587739505541578866

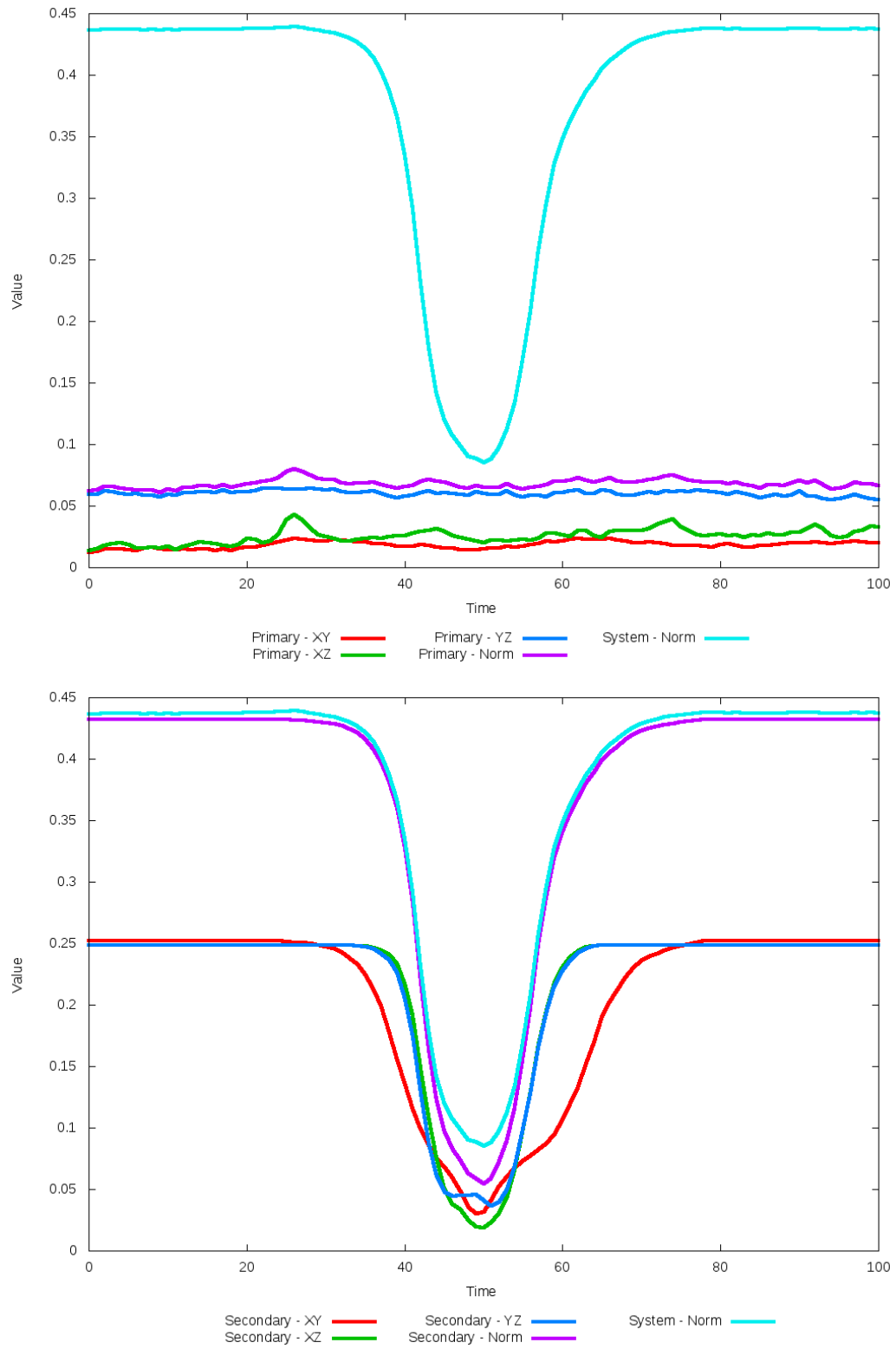


Figure 5.132: All metrics versus simulation time of the best N-Body simulation for SDSS 587739505541578866

5.1.23 SDSS 587739646743412797 (Arp 107)

Arp 107 shows a significant improvement in the positions of the of the galaxies with the optimized dynamical friction when compared to the SPAM simulation and observational data. With the change in dynamical friction, the trajectories of the spam simulations converge on eachother fairly quickly, whereas in the N-Body simulations, the optimized case stays with the SPAM trajectory over a longer period of time before decaying. The more rapid decay in the initial N-Body simulation causes a merger to appear relatively soon during it. The main concern with the optimized N-Body simulation is the very wide and elongated tidal tail. This tail may be reigned if additional physics are utilized, such as gas dynamics.

Table 5.45: Identification Information and Merger Zoo summary for SDSS 587739646743412797.

Name	Aliases	RA (hms)	Dec (dms)	Redshift
SDSS 587739646743412797	Arp 107, UGC 5984	10:52:14.8	+30:03:28.3	0.034597

R_x	R_y	R_z	V_x	V_y	V_z
-1.9621	2.22832	-0.63225	0.00118	0.11473	0.27316

	Primary Galaxy	Secondary Galaxy
mass	0.97107	0.71787
radius	1.09937	0.43672
ϕ	82.03236°	271.02679°
θ	191.07553°	296.26974°
ϵ	0.3	0.3

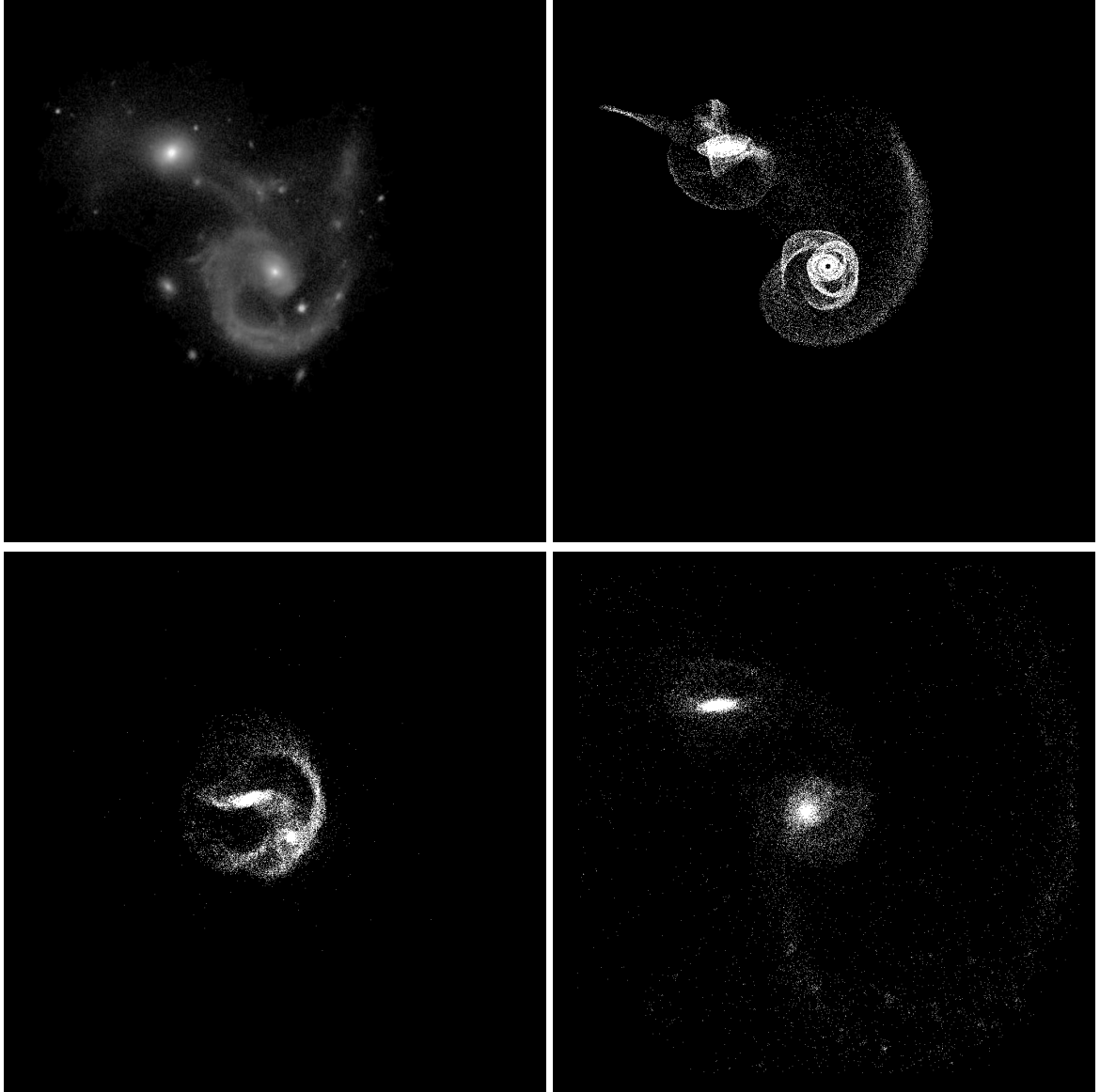


Figure 5.133: Target image (top-left), best SPAM match from Merger Wars (top-right), initial N-Body match (bottom-left), and best N-Body match (bottom-right) for SDSS 587739646743412797

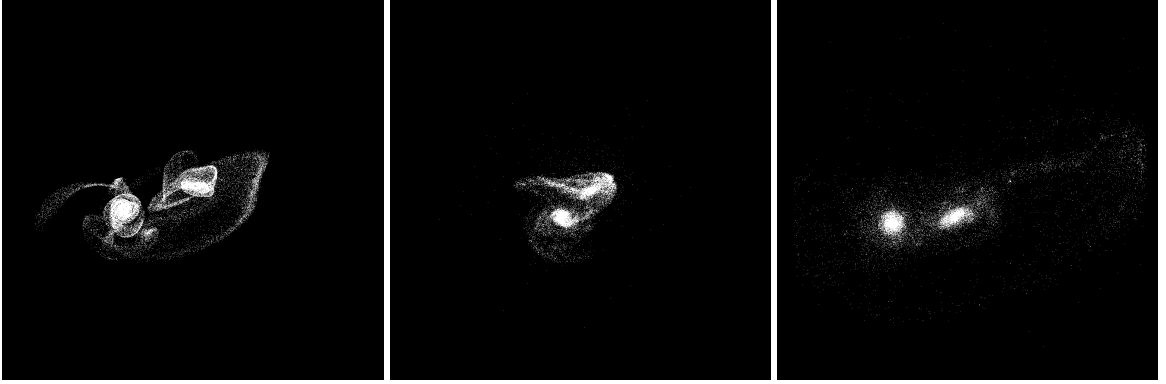


Figure 5.134: XZ projections of best SPAM match from Merger Wars (left), initial N-Body match (middle), and best N-Body match (right) for SDSS 587739646743412797

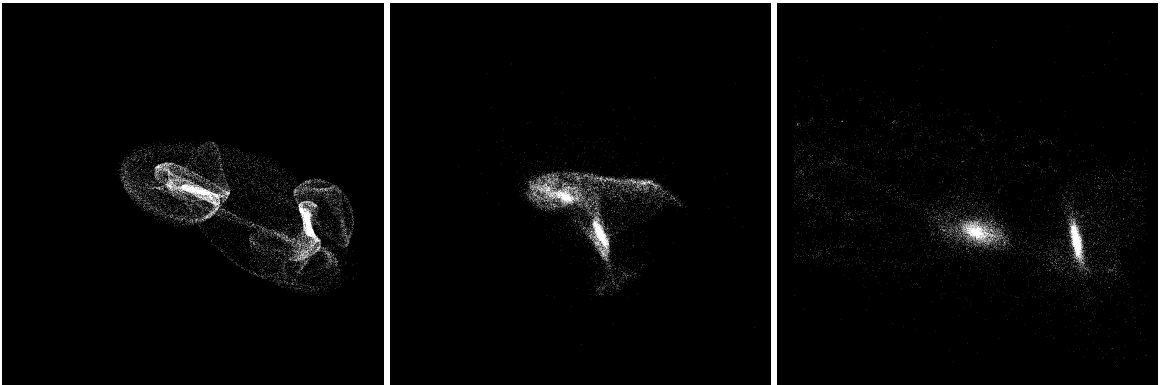


Figure 5.135: YZ projections of best SPAM match from Merger Wars (left), initial N-Body match (middle), and best N-Body match (right) for SDSS 587739646743412797

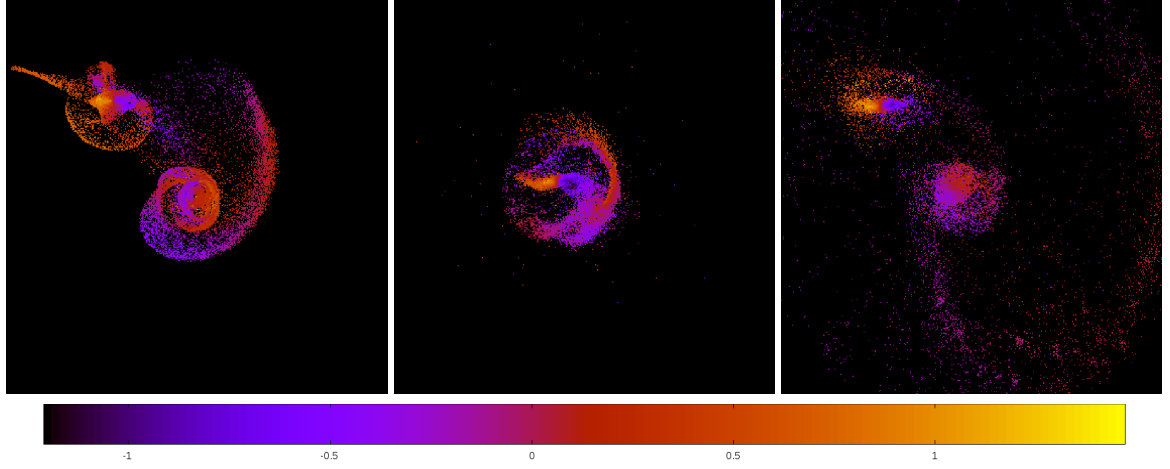


Figure 5.136: Line of sight velocity plots of best SPAM match from Merger Wars (left), initial N-Body match (middle), and best N-Body match (right) for SDSS 587739646743412797

Table 5.46: Orbital Elements & Dynamical Friction for SDSS 587739646743412797

	SPAM Simulation	Initial N-Body Simulation	Best N-Body Simulation
a	4.483	1.890	3.432
e	0.364	0.610	0.945
r_c	2.850	0.738	0.189
i	104.729°	105.662°	99.615°
Ω	128.156°	128.884°	132.458°
ω	176.676°	161.784°	155.625°
ν	170.887°	140.932°	183.039°
t_n	50	27	76
$\ln\Lambda$	N/A	1.00E-03	2.40E-03

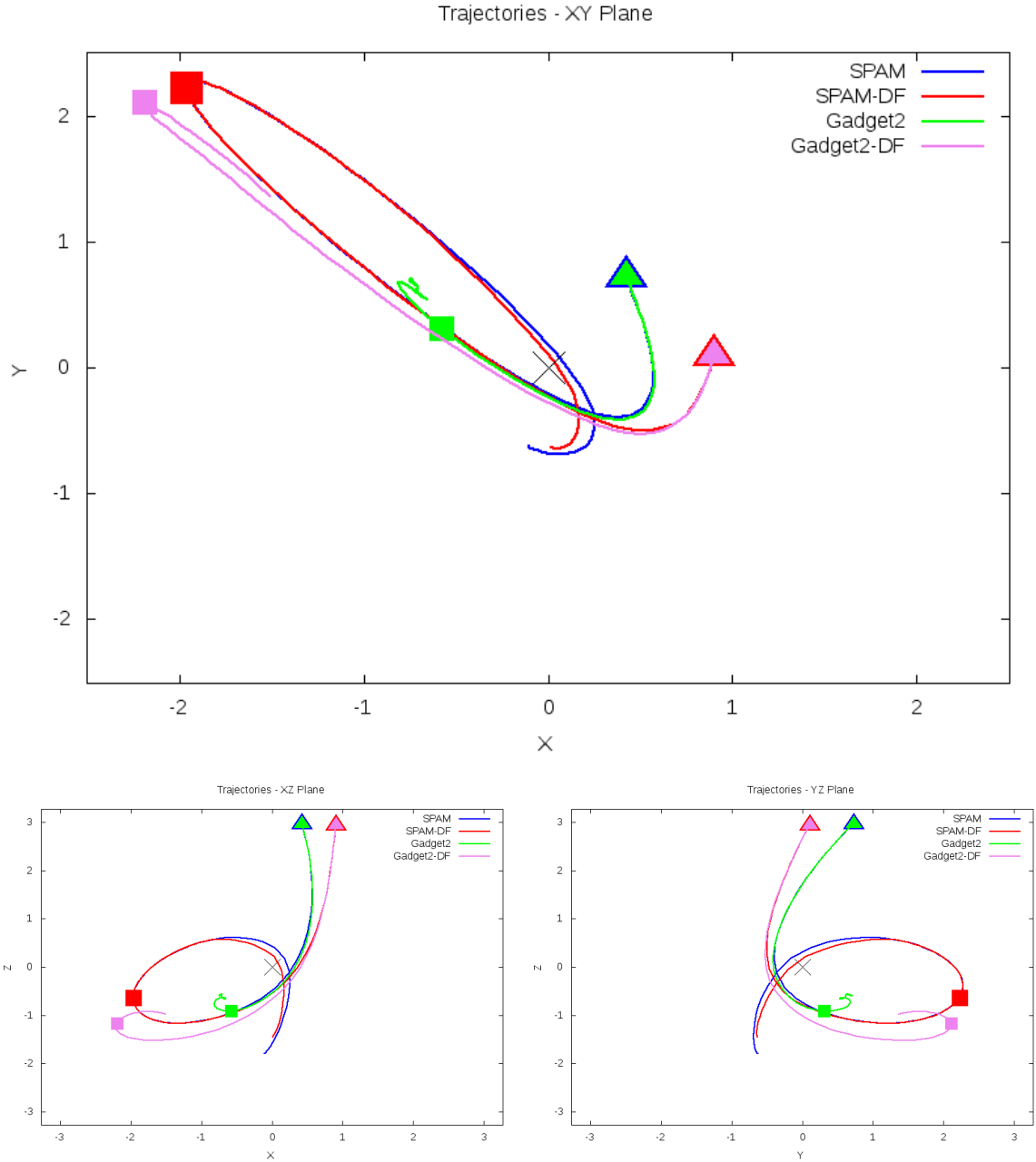


Figure 5.137: Trajectory plots of best SPAM match from Merger Wars, initial N-Body match, and best N-Body match for SDSS 587739646743412797

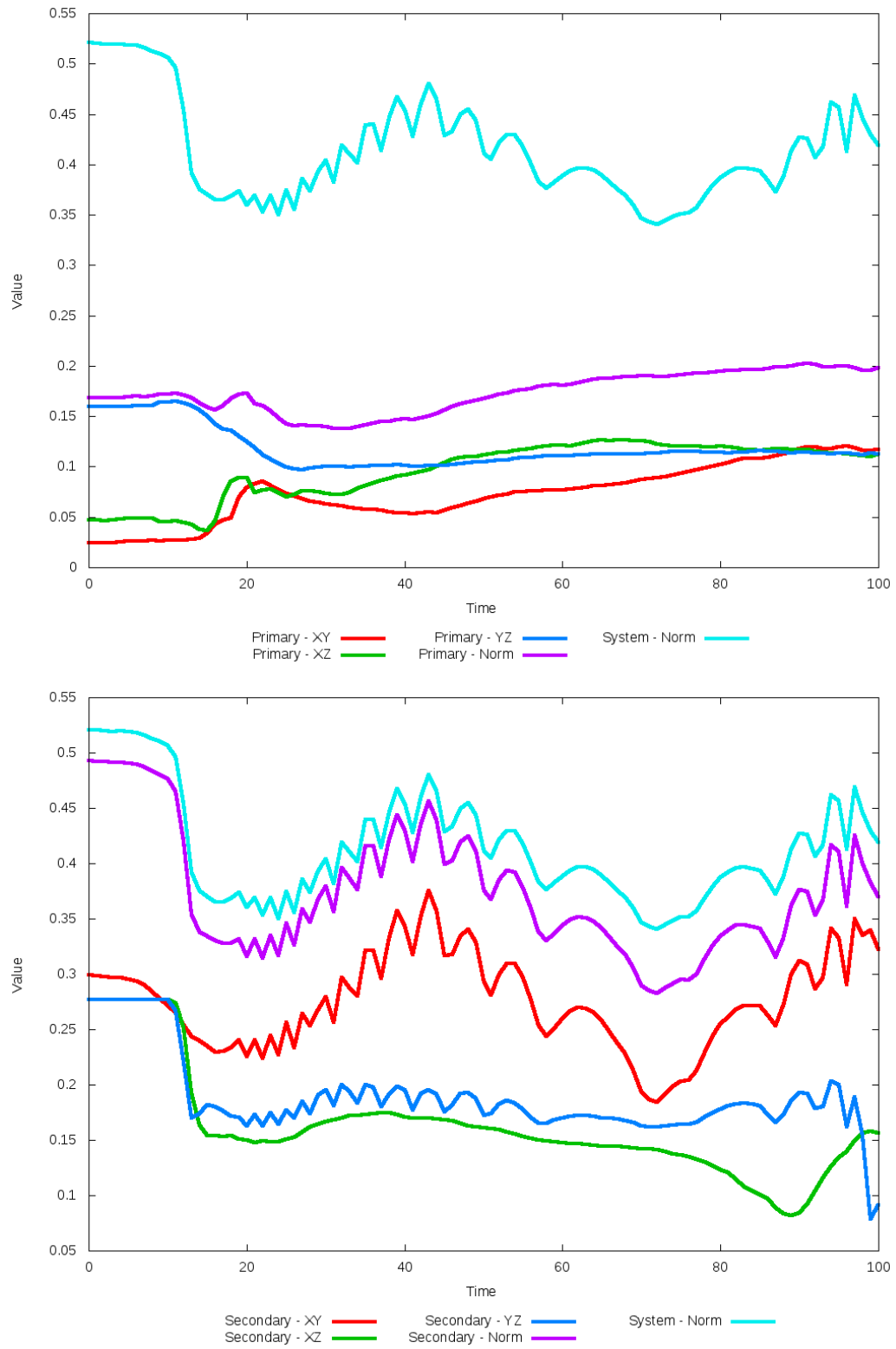


Figure 5.138: All metrics versus simulation time of the best N-Body simulation for SDSS 587739646743412797

5.1.24 SDSS 587739647284805725 (Arp 294)

Arp 294 shows very good agreement between all its models and the observational data. Although the galaxies appear to be relatively close to each other in the XY projection, looking at other projections show they are actually far apart and are in the early stages of an interaction. As such, there are no tidal features. Because the galaxies are not within sufficient distance to each other, dynamical friction does not impact the orbits and trajectories of the simulations. Therefore, the optimization methodology cannot find any better value for dynamical friction than the starting value.

Table 5.47: Identification Information and Merger Zoo summary for SDSS 587739647284805725.

Name	Aliases	RA (hms)	Dec (dms)	Redshift
SDSS 587739647284805725	Arp 294, NGC 3786/3788	11:39:42.4	+31:54:33.4	0.008933

R_x	R_y	R_z	V_x	V_y	V_z
-0.30712	0.91123	-4.13962	-0.72369	-0.3113	-0.14825

	Primary Galaxy	Secondary Galaxy
mass	0.42912	0.66235
radius	0.57938	0.5465
ϕ	70.38163°	178.66037°
θ	59.54056°	109.24137°
ϵ	0.3	0.3

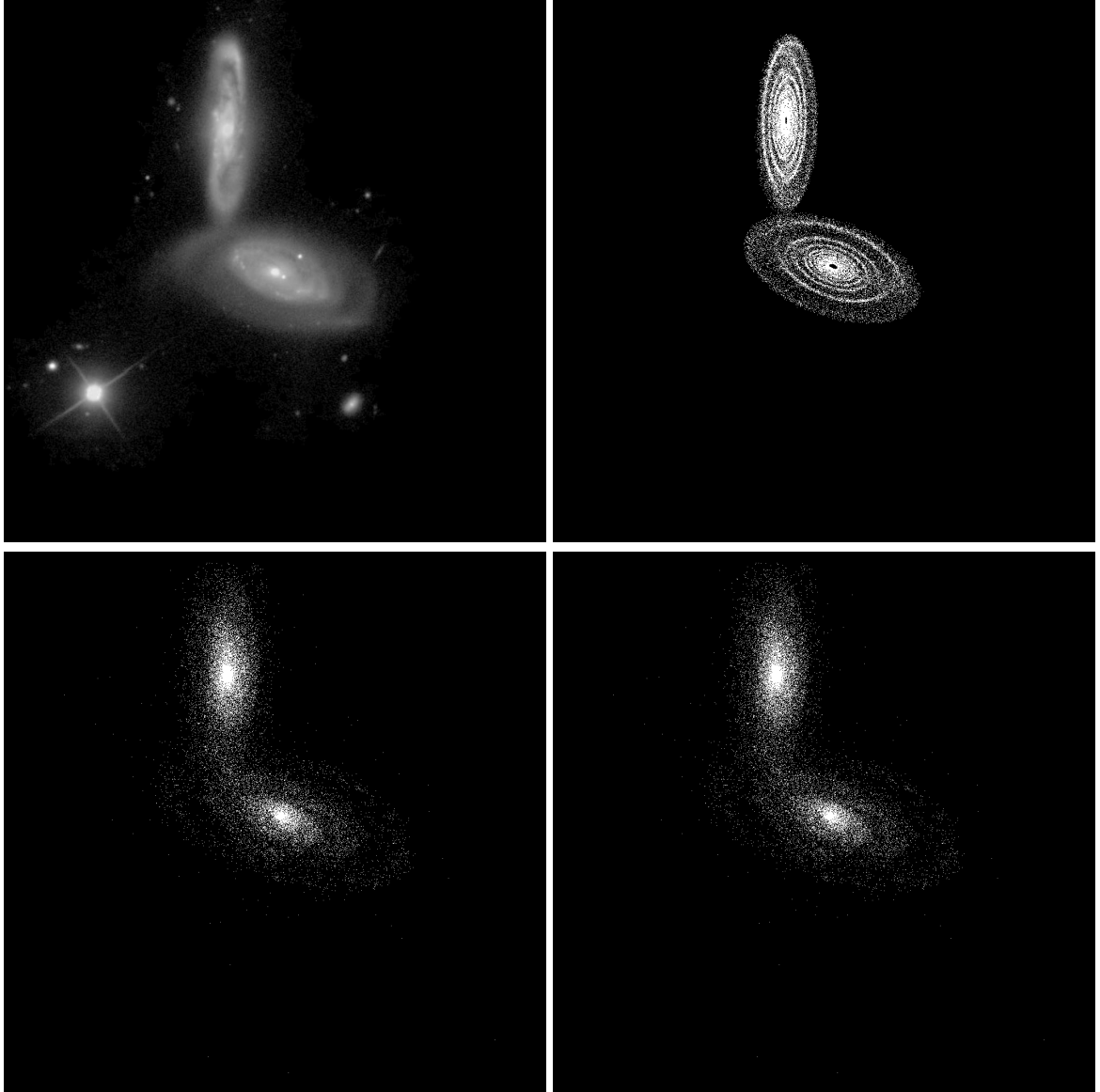


Figure 5.139: Target image (top-left), best SPAM match from Merger Wars (top-right), initial N-Body match (bottom-left), and best N-Body match (bottom-right) for SDSS 587739647284805725

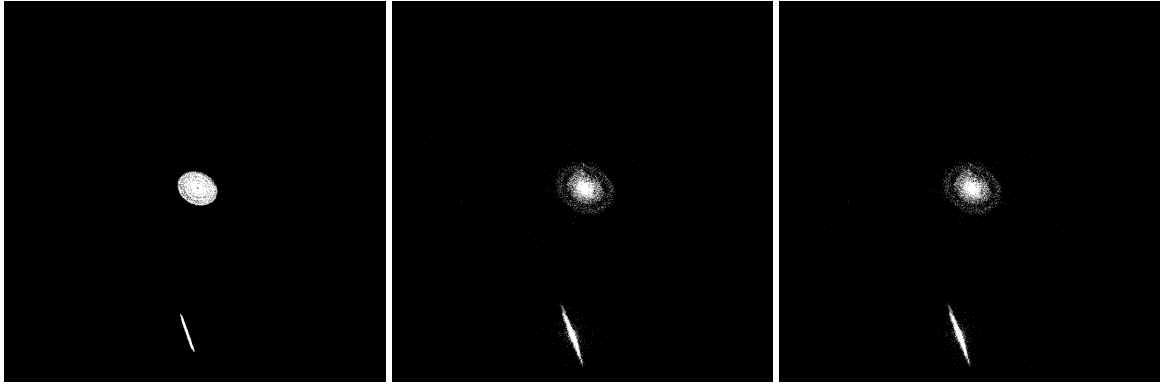


Figure 5.140: XZ projections of best SPAM match from Merger Wars (left), initial N-Body match (middle), and best N-Body match (right) for SDSS 587739647284805725



Figure 5.141: YZ projections of best SPAM match from Merger Wars (left), initial N-Body match (middle), and best N-Body match (right) for SDSS 587739647284805725

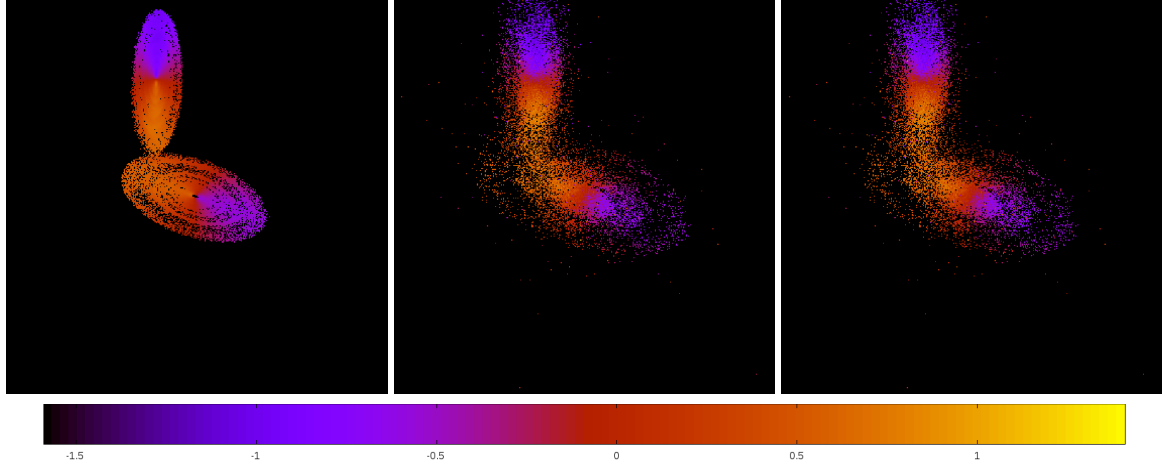


Figure 5.142: Line of sight velocity plots of best SPAM match from Merger Wars (left), initial N-Body match (middle), and best N-Body match (right) for SDSS 587739647284805725

Table 5.48: Orbital Elements & Dynamical Friction for SDSS 587739647284805725

	SPAM Simulation	Initial N-Body Simulation	Best N-Body Simulation
a	-1.001	-1.055	-1.055
e	9.363	9.028	9.028
r_c	8.375	8.472	8.472
i	77.020°	76.865°	76.865°
Ω	205.761°	205.690°	205.690°
ω	258.068°	257.708°	257.708°
ν	10.322°	11.550°	11.550°
t_n	50	51	51
$\ln\Lambda$	N/A	1.00E-03	1.00E-03

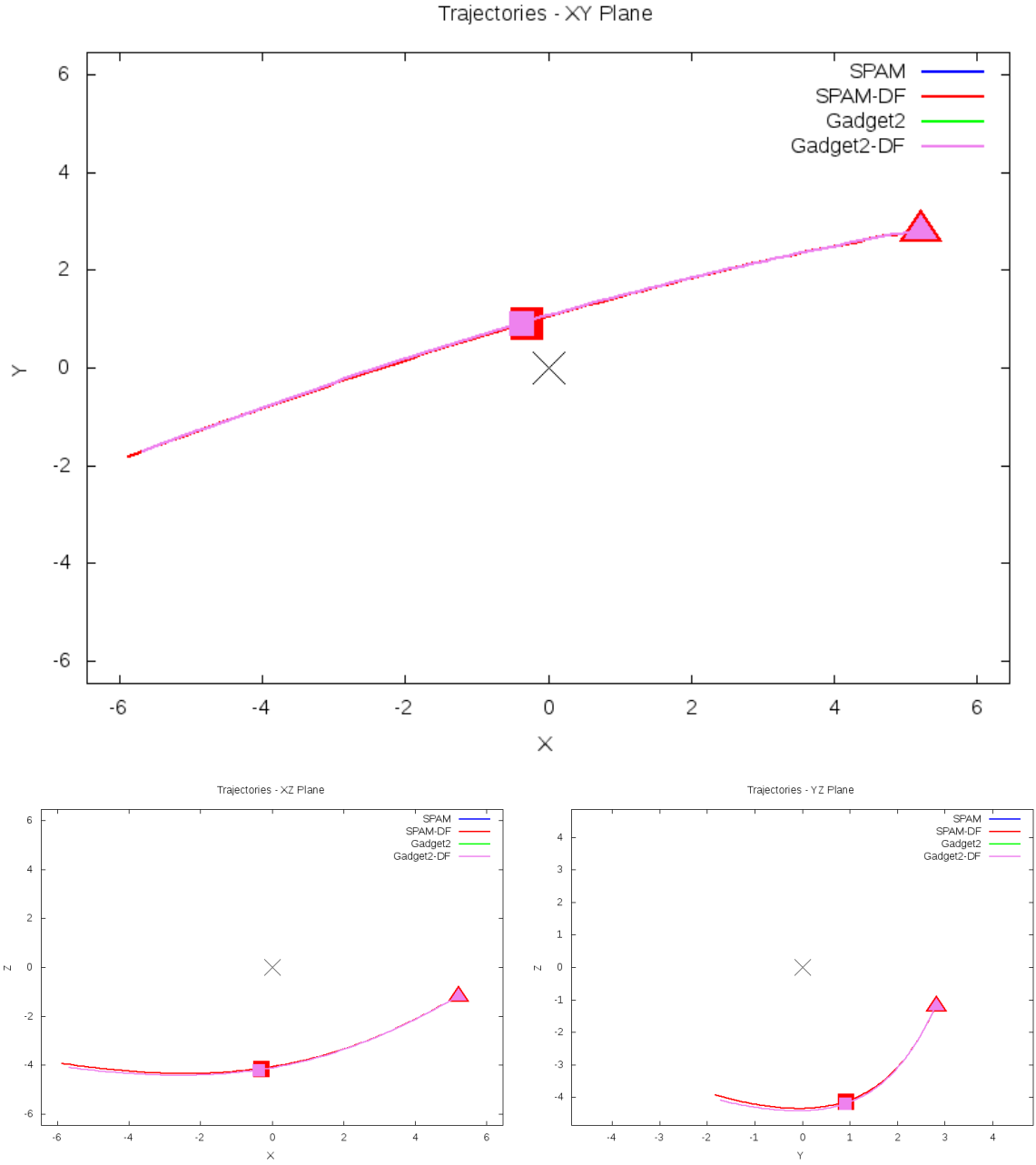


Figure 5.143: Trajectory plots of best SPAM match from Merger Wars, initial N-Body match, and best N-Body match for SDSS 587739647284805725

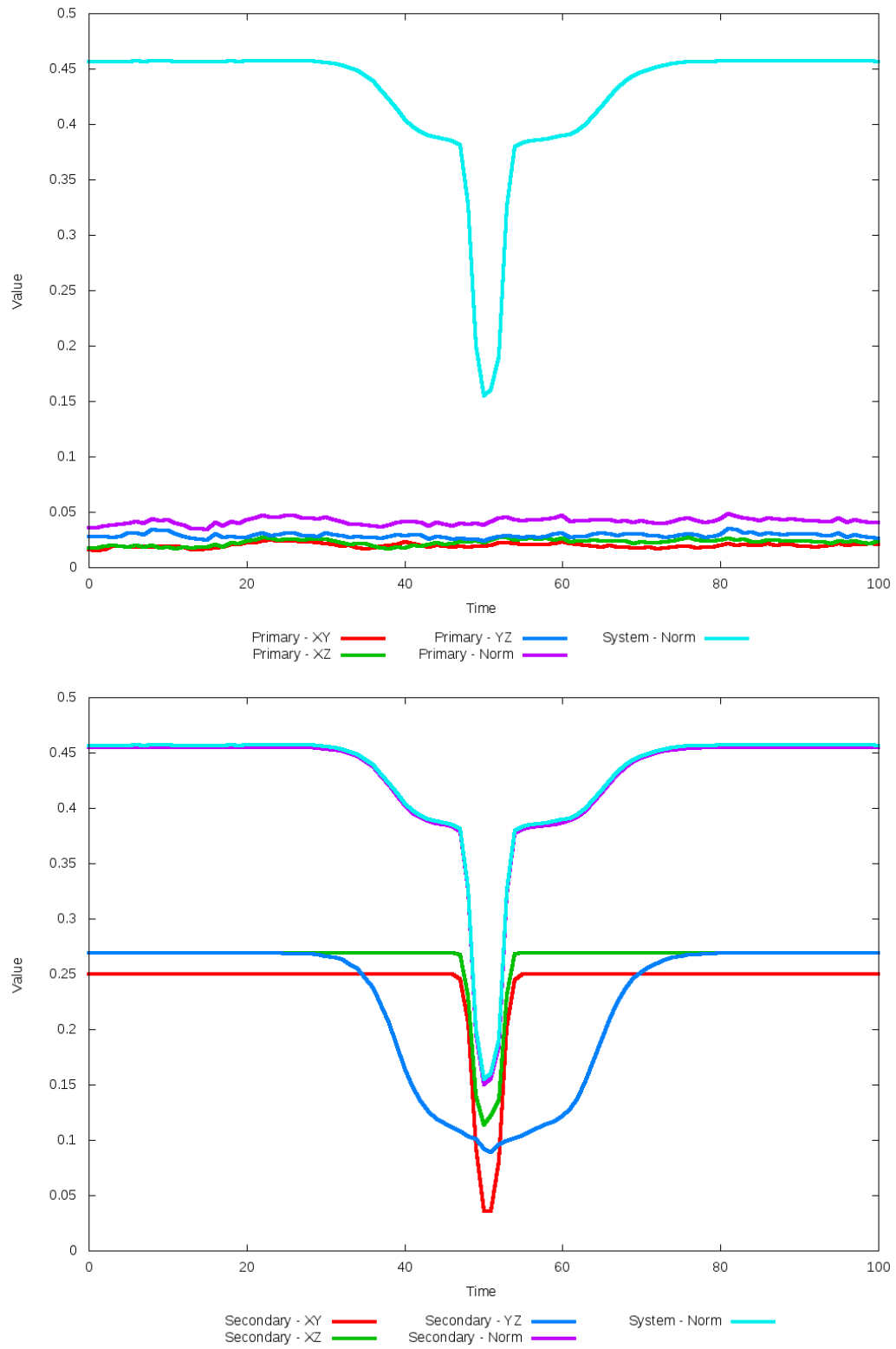


Figure 5.144: All metrics versus simulation time of the best N-Body simulation for SDSS 587739647284805725

5.1.25 SDSS 587739707420967061 (Arp 172)

Arp 172 shows modest improvement matching the SPAM simulation and observational data when dynamical friction is optimized. The tidal features look good, but the orientation and position of the secondary galaxy needs improvement. This is still much better than the initial value of dynamical friction, whose simulation exhibits a merger very quickly. Revisions to the SPAM state vector may alter the orbit sufficiently so they do not decay as rapidly in future N-Body simulations.

Table 5.49: Identification Information and Merger Zoo summary for SDSS 587739707420967061.

Name	Aliases	RA (hms)	Dec (dms)	Redshift
SDSS 587739707420967061	Arp 172, IC 1178/1181	16:05:33.1	+17:36:04.6	0.033687

R_x	R_y	R_z	V_x	V_y	V_z
-0.4413	-1.22532	-2.06561	-0.25131	-0.19632	-0.30839

	Primary Galaxy	Secondary Galaxy
mass	1.82612	1.30459
radius	0.58709	0.53904
ϕ	213.73768°	67.3073°
θ	203.49577°	241.01371°
ϵ	0.3	0.3

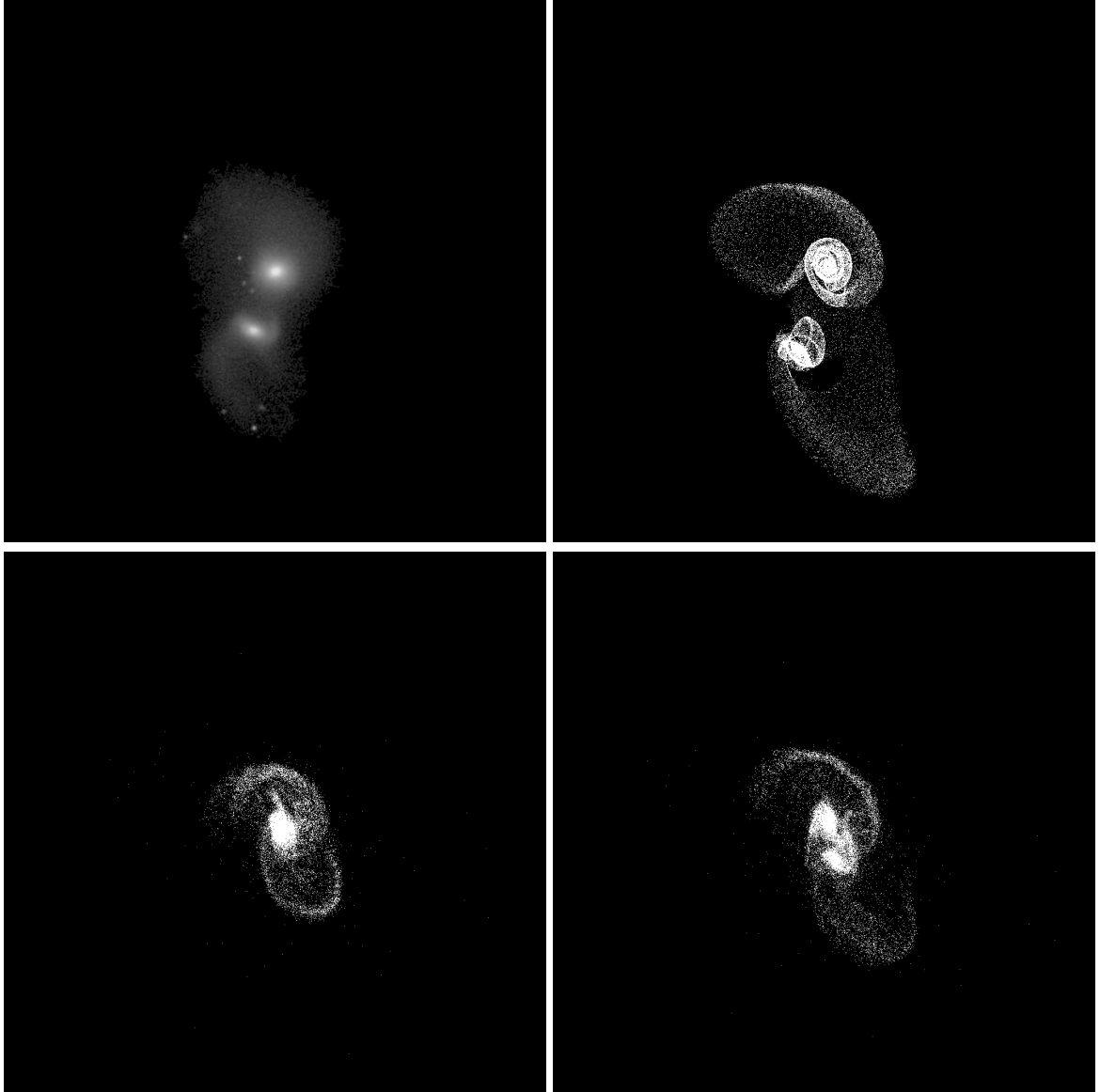


Figure 5.145: Target image (top-left), best SPAM match from Merger Wars (top-right), initial N-Body match (bottom-left), and best N-Body match (bottom-right) for SDSS 587739707420967061

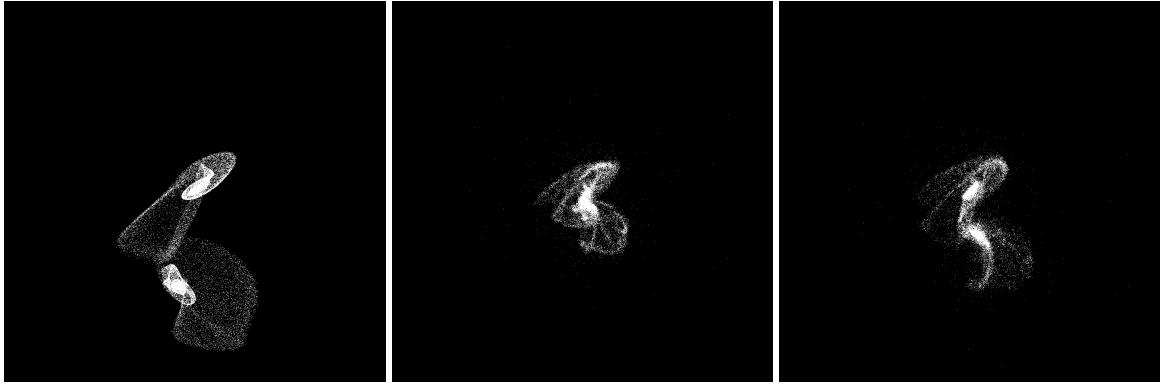


Figure 5.146: XZ projections of best SPAM match from Merger Wars (left), initial N-Body match (middle), and best N-Body match (right) for SDSS 587739707420967061

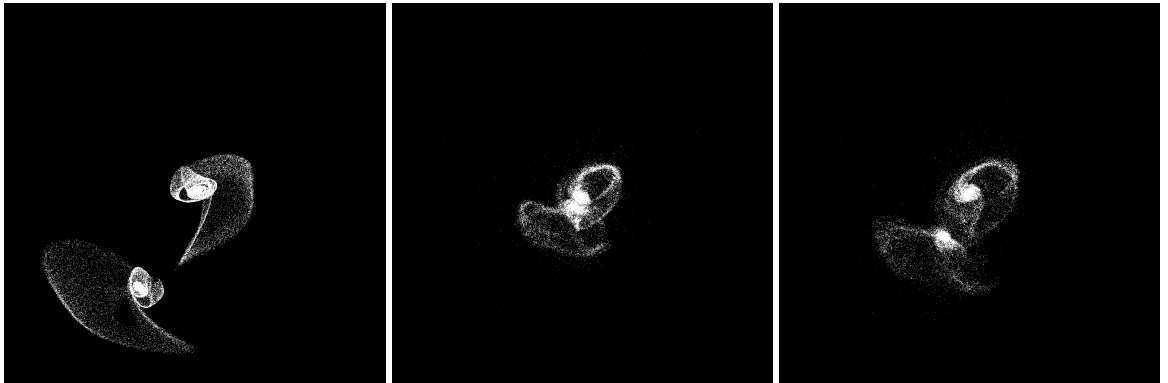


Figure 5.147: YZ projections of best SPAM match from Merger Wars (left), initial N-Body match (middle), and best N-Body match (right) for SDSS 587739707420967061

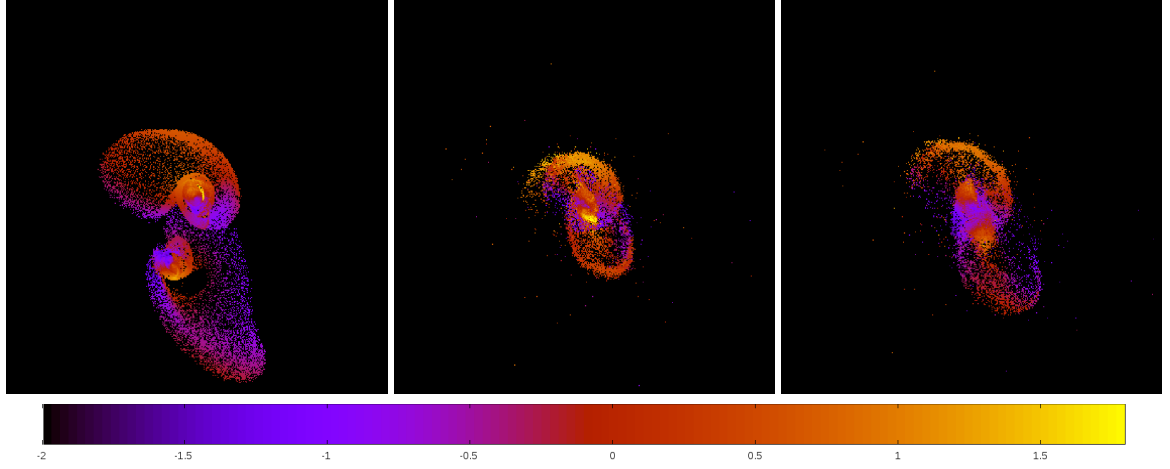


Figure 5.148: Line of sight velocity plots of best SPAM match from Merger Wars (left), initial N-Body match (middle), and best N-Body match (right) for SDSS 587739707420967061

Table 5.50: Orbital Elements & Dynamical Friction for SDSS 587739707420967061

	SPAM Simulation	Initial N-Body Simulation	Best N-Body Simulation
a	3.513	0.769	1.688
e	0.924	0.931	0.873
r_c	0.268	0.053	0.215
i	119.954°	125.036°	123.171°
Ω	184.128°	191.568°	190.351°
ω	116.973°	81.021°	98.816°
ν	165.610°	184.822°	167.974°
t_n	50	34	37
$\ln\Lambda$	N/A	1.00E-03	3.20E-03

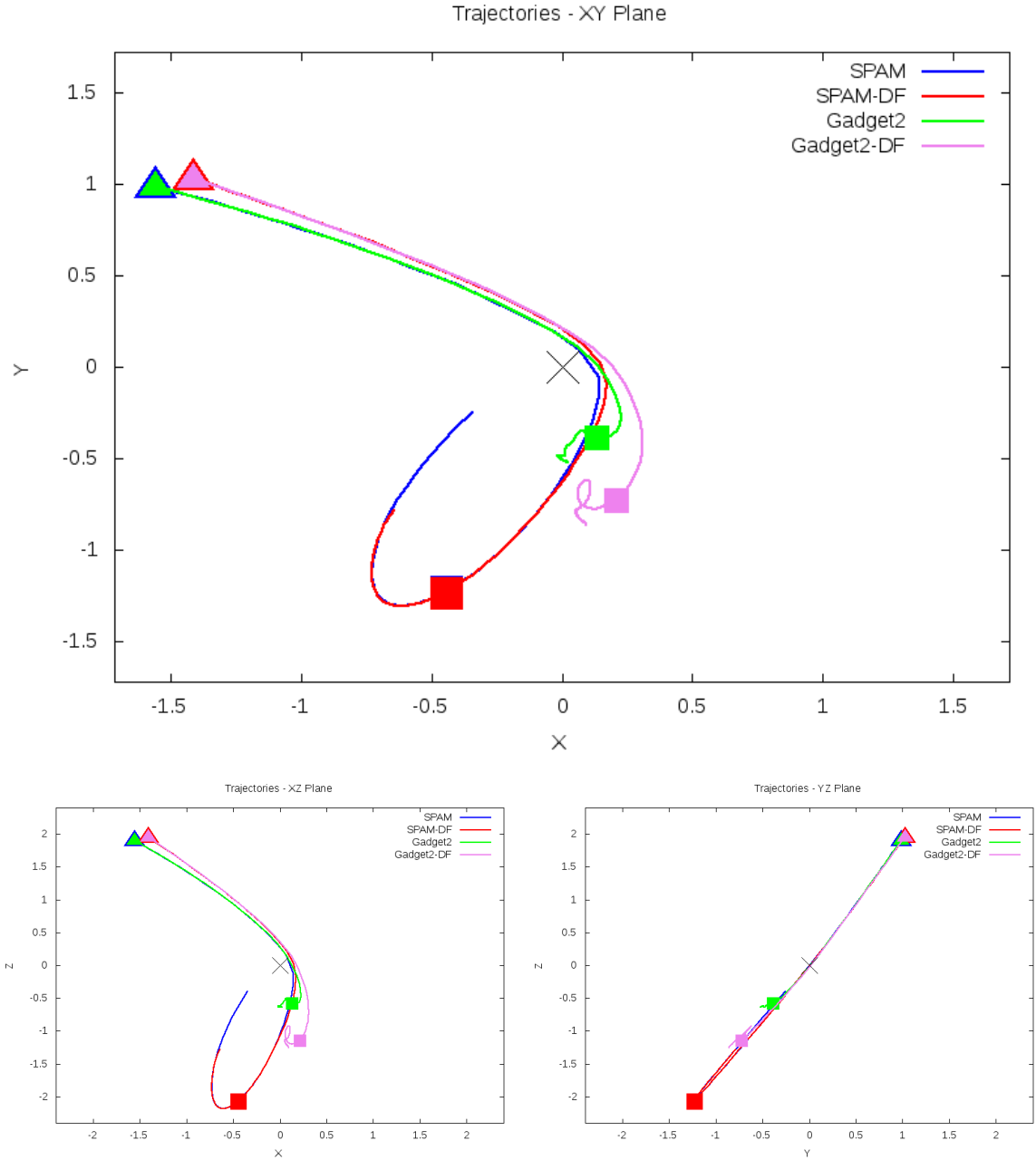


Figure 5.149: Trajectory plots of best SPAM match from Merger Wars, initial N-Body match, and best N-Body match for SDSS 587739707420967061

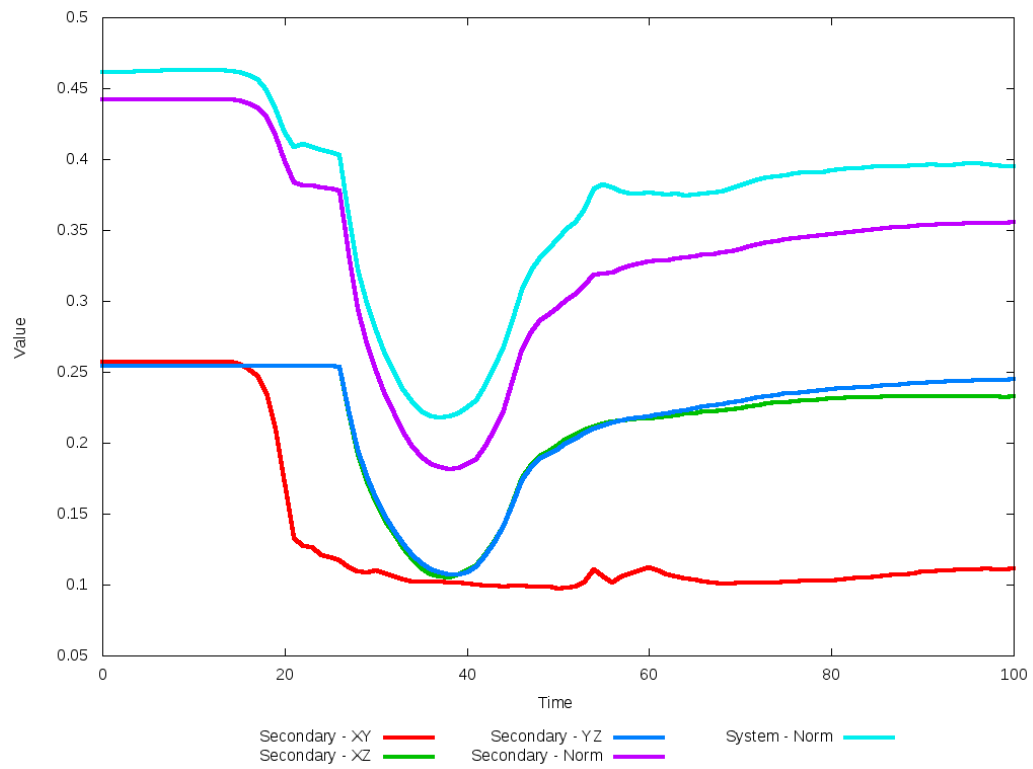
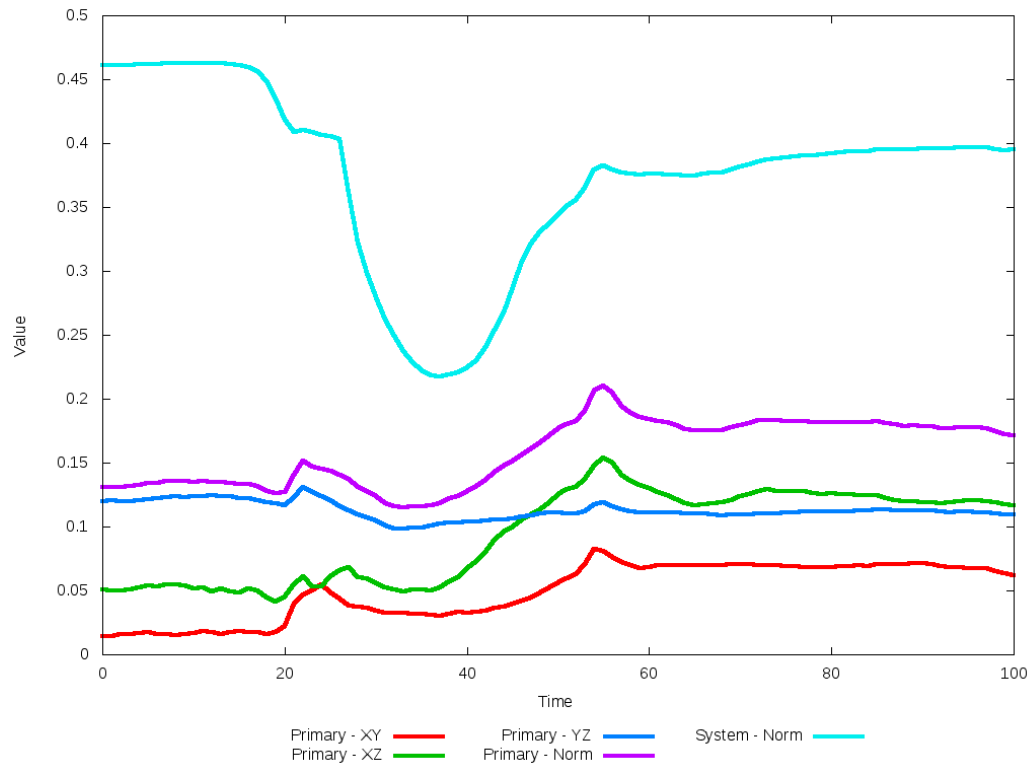


Figure 5.150: All metrics versus simulation time of the best N-Body simulation for SDSS 587739707420967061

5.1.26 SDSS 587739720308818095 (Arp 218)

Arp 218 exhibits good agreement between its N-Body simulations, SPAM simulation, and observational data. In the XY projection, the initial N-Body simulation's tidal features on the primary galaxy are more tightly wrapped around it, which looks closer to what is seen in the SPAM simulation. The trajectories however indicate that the optimized dynamical friction simulation has a more stable orbit and the location of the secondary galaxy is in better agreement. The metric plots show that the quality of fit of the secondary galaxy is relatively unchanged for about 20

Table 5.51: Identification Information and Merger Zoo summary for SDSS 587739720308818095.

Name	Aliases	RA (hms)	Dec (dms)	Redshift
SDSS 587739720308818095	Arp 218, UGC 10084	15:53:36.8	+18:36:34.5	0.049944

R_x	R_y	R_z	V_x	V_y	V_z
2.37024	-1.36863	0.25617	0.43873	-0.34901	-0.15217

	Primary Galaxy	Secondary Galaxy
mass	0.54922	0.13328
radius	0.73772	0.42516
ϕ	148.30063°	49.41001°
θ	231.49951°	261.44764°
ϵ	0.3	0.3

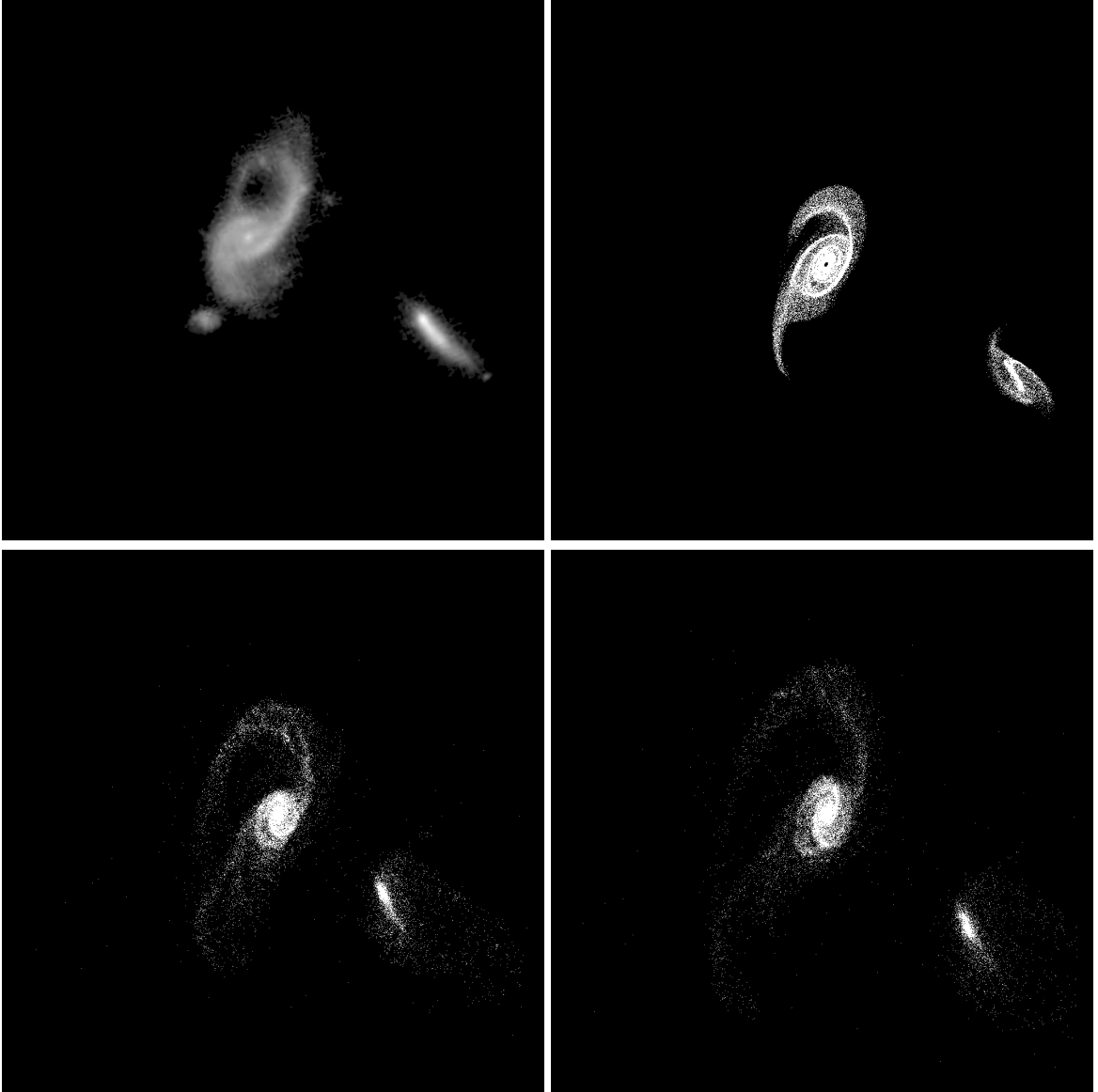


Figure 5.151: Target image (top-left), best SPAM match from Merger Wars (top-right), initial N-Body match (bottom-left), and best N-Body match (bottom-right) for SDSS 587739720308818095

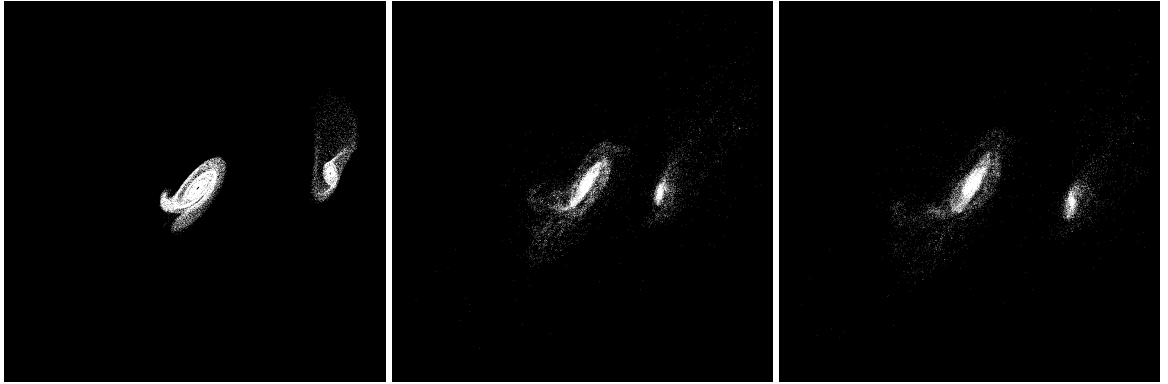


Figure 5.152: XZ projections of best SPAM match from Merger Wars (left), initial N-Body match (middle), and best N-Body match (right) for SDSS 587739720308818095

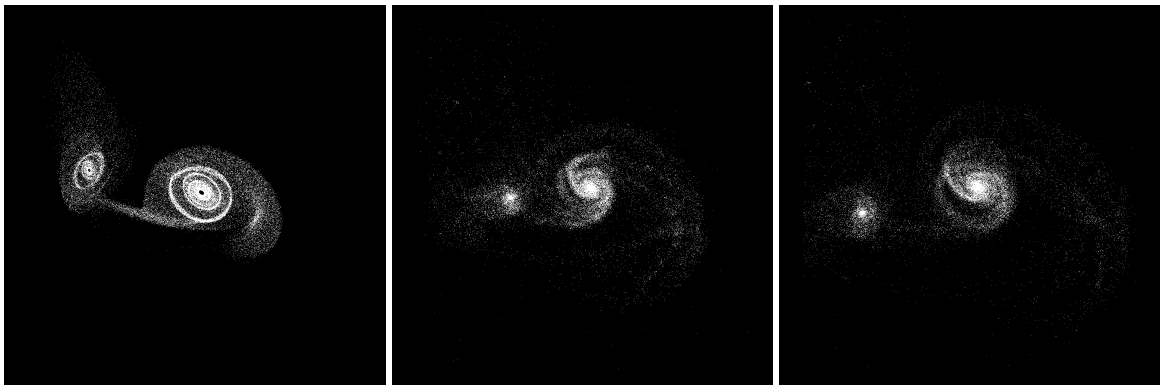


Figure 5.153: YZ projections of best SPAM match from Merger Wars (left), initial N-Body match (middle), and best N-Body match (right) for SDSS 587739720308818095

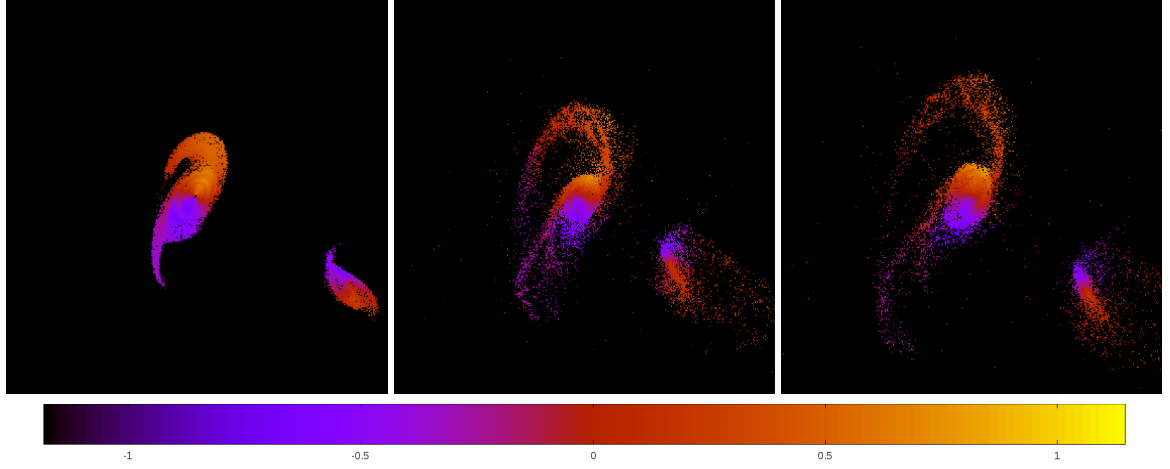


Figure 5.154: Line of sight velocity plots of best SPAM match from Merger Wars (left), initial N-Body match (middle), and best N-Body match (right) for SDSS 587739720308818095

Table 5.52: Orbital Elements & Dynamical Friction for SDSS 587739720308818095

	SPAM Simulation	Initial N-Body Simulation	Best N-Body Simulation
a	-0.822	4.829	9.161
e	3.043	0.784	0.896
r_c	1.678	1.044	0.956
i	112.084°	117.617°	116.953°
Ω	147.821°	145.149°	145.506°
ω	88.639°	46.470°	44.828°
ν	85.497°	128.989°	134.855°
t_n	50	50	64
$\ln\Lambda$	N/A	1.00E-03	2.00E-03

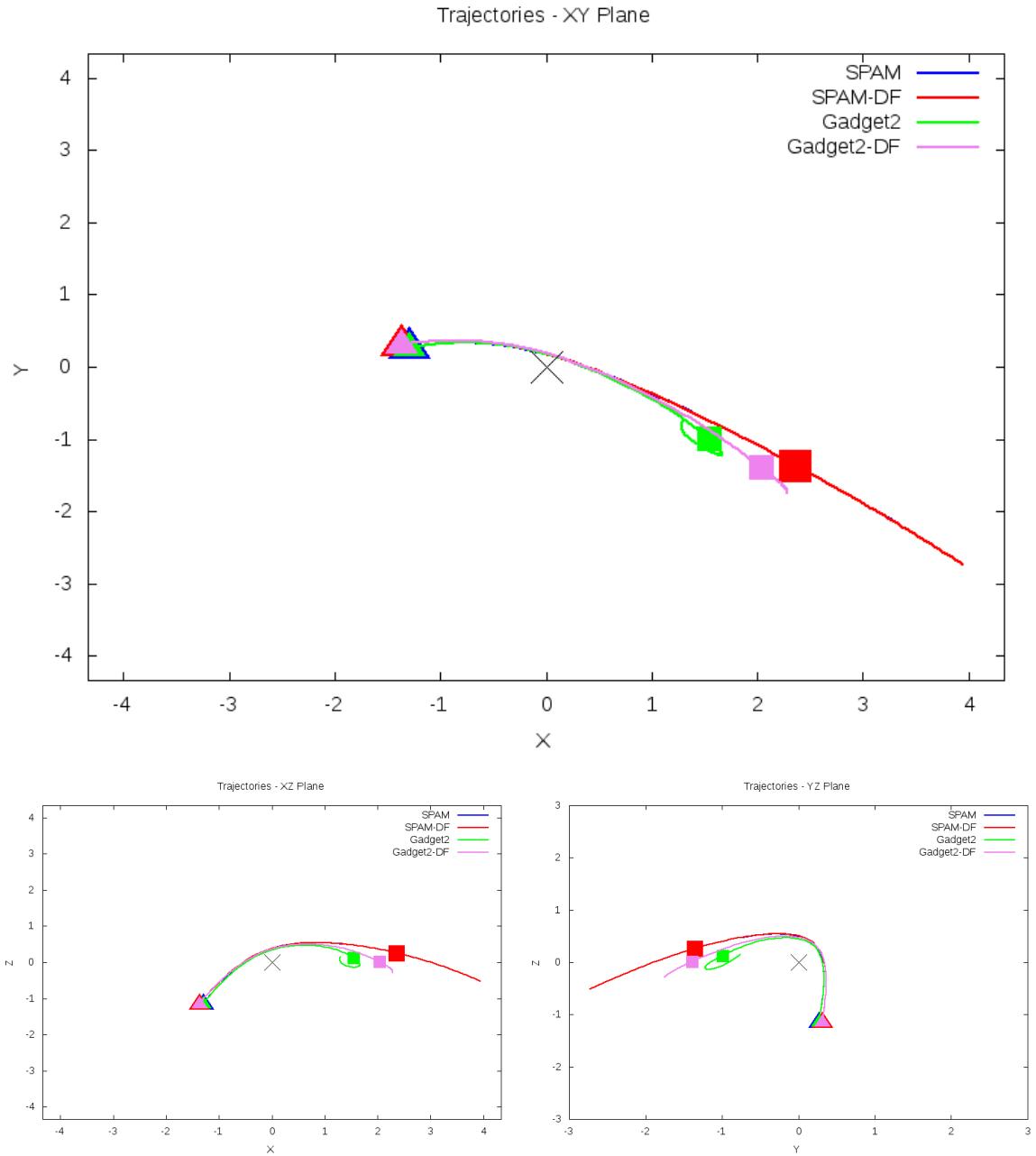


Figure 5.155: Trajectory plots of best SPAM match from Merger Wars, initial N-Body match, and best N-Body match for SDSS 587739720308818095

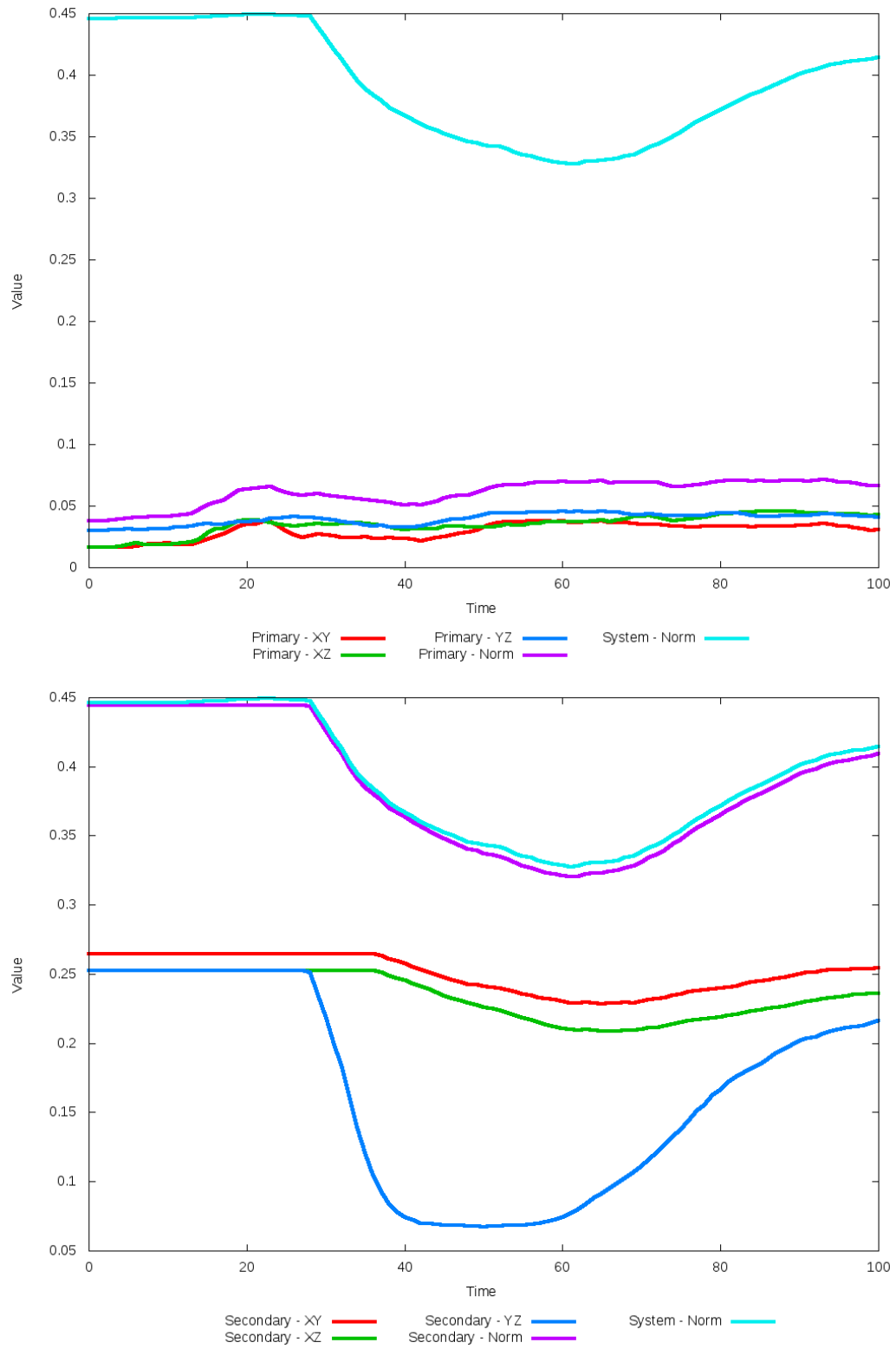


Figure 5.156: All metrics versus simulation time of the best N-Body simulation for SDSS 587739720308818095

5.1.27 SDSS 587739721376202860 (Arp 302)

Arp 302 shows very good agreement between all its models and the observational data. Although the galaxies appear to be relatively close to each other in the XY projection, looking at other projections show they are actually far apart and are in the early stages of an interaction. As such, there are no tidal features. Because the galaxies are not within sufficient distance to each other, dynamical friction does not impact the orbits and trajectories of the simulations. Therefore, the optimization methodology cannot find any better value for dynamical friction than the starting value.

Table 5.53: Identification Information and Merger Zoo summary for SDSS 587739721376202860.

Name	Aliases	RA (hms)	Dec (dms)	Redshift
SDSS 587739721376202860	Arp 302, UGC 9618	14:57:00.6	+24:37:03.3	0.033669

R_x	R_y	R_z	V_x	V_y	V_z
0.18431	-1.70765	4.96754	-1.15744	-1.80231	0.57509

	Primary Galaxy	Secondary Galaxy
mass	0.5629	0.20912
radius	0.94419	0.63482
ϕ	6.239°	36.32914°
θ	283.48382°	345.33778°
ϵ	0.3	0.3

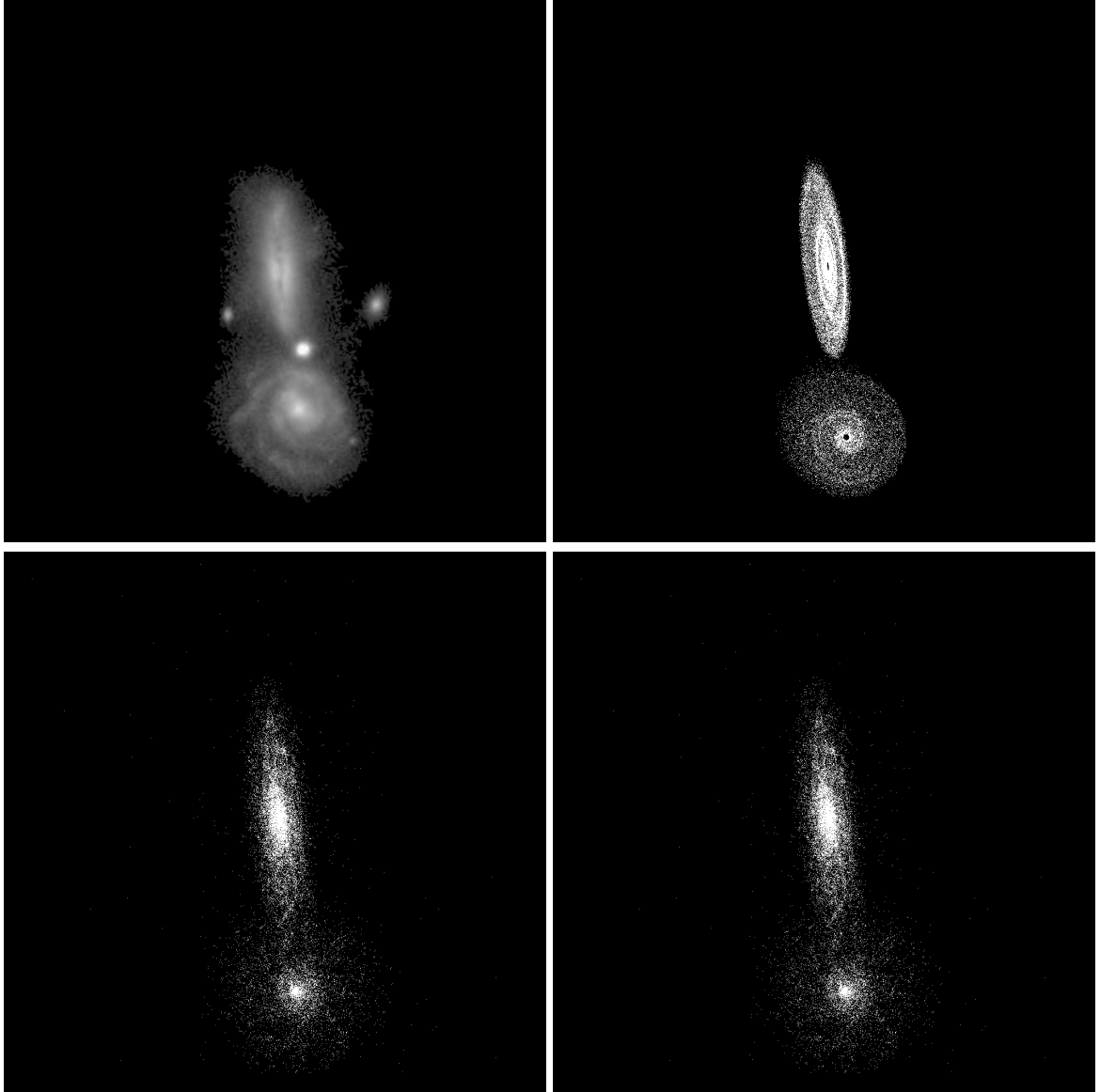


Figure 5.157: Target image (top-left), best SPAM match from Merger Wars (top-right), initial N-Body match (bottom-left), and best N-Body match (bottom-right) for SDSS 587739721376202860

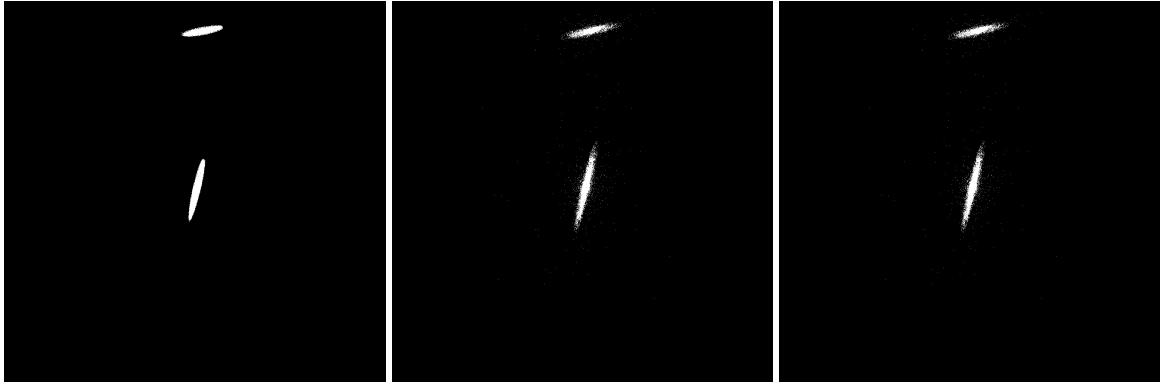


Figure 5.158: XZ projections of best SPAM match from Merger Wars (left), initial N-Body match (middle), and best N-Body match (right) for SDSS 587739721376202860

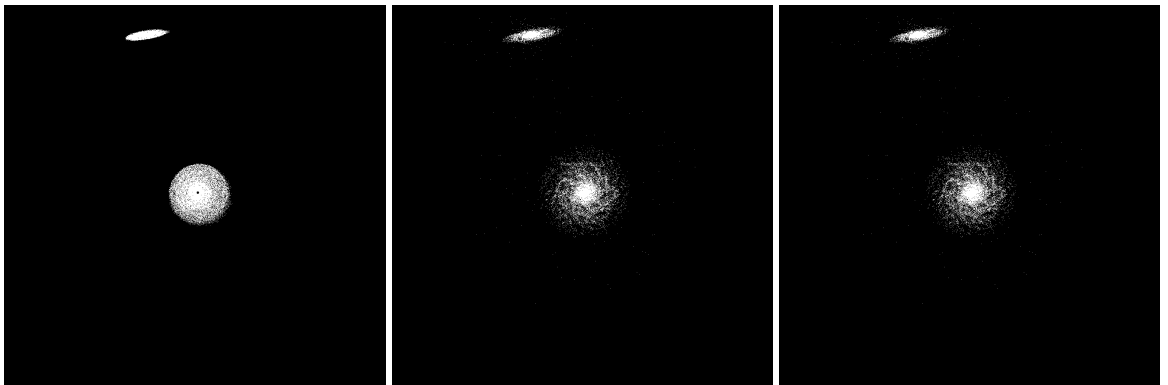


Figure 5.159: YZ projections of best SPAM match from Merger Wars (left), initial N-Body match (middle), and best N-Body match (right) for SDSS 587739721376202860

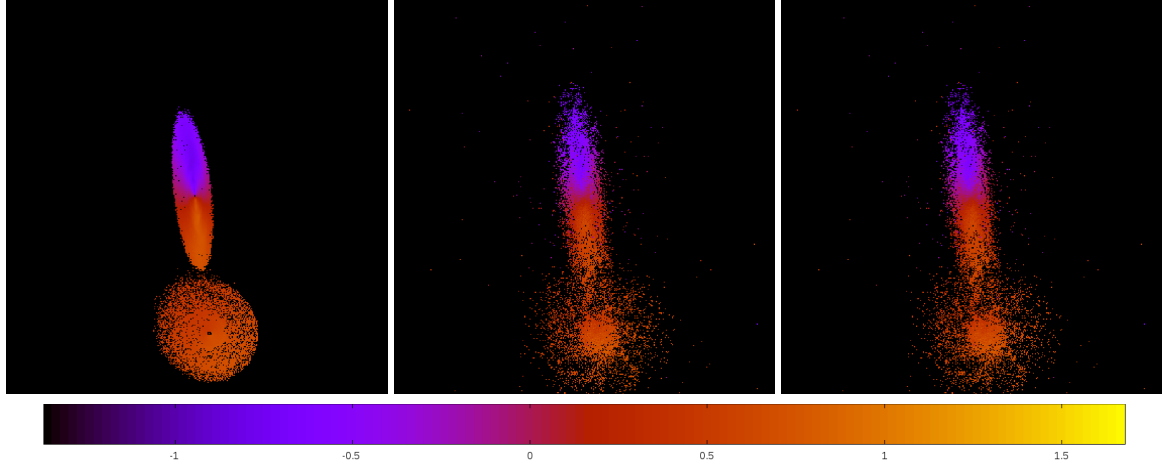


Figure 5.160: Line of sight velocity plots of best SPAM match from Merger Wars (left), initial N-Body match (middle), and best N-Body match (right) for SDSS 587739721376202860

Table 5.54: Orbital Elements & Dynamical Friction for SDSS 587739721376202860

	SPAM Simulation	Initial N-Body Simulation	Best N-Body Simulation
a	-0.063	-0.063	-0.063
e	146.861	146.543	146.543
r_c	9.151	9.142	9.142
i	103.139°	103.203°	103.203°
Ω	53.698°	53.689°	53.689°
ω	74.366°	74.254°	74.254°
ν	29.584°	29.620°	29.620°
t_n	50	50	50
$\ln\Lambda$	N/A	1.00E-03	1.00E-03

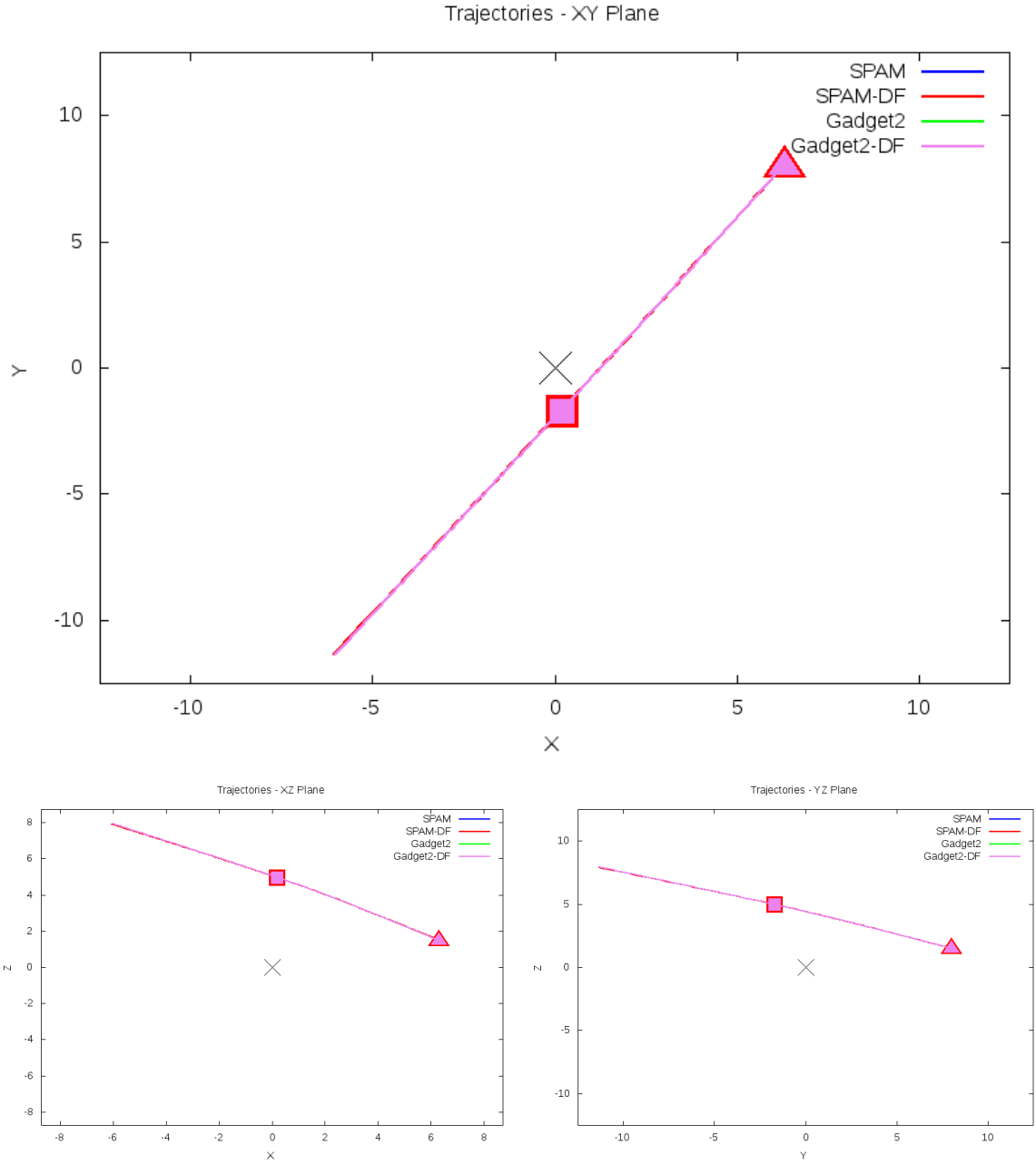


Figure 5.161: Trajectory plots of best SPAM match from Merger Wars, initial N-Body match, and best N-Body match for SDSS 587739721376202860

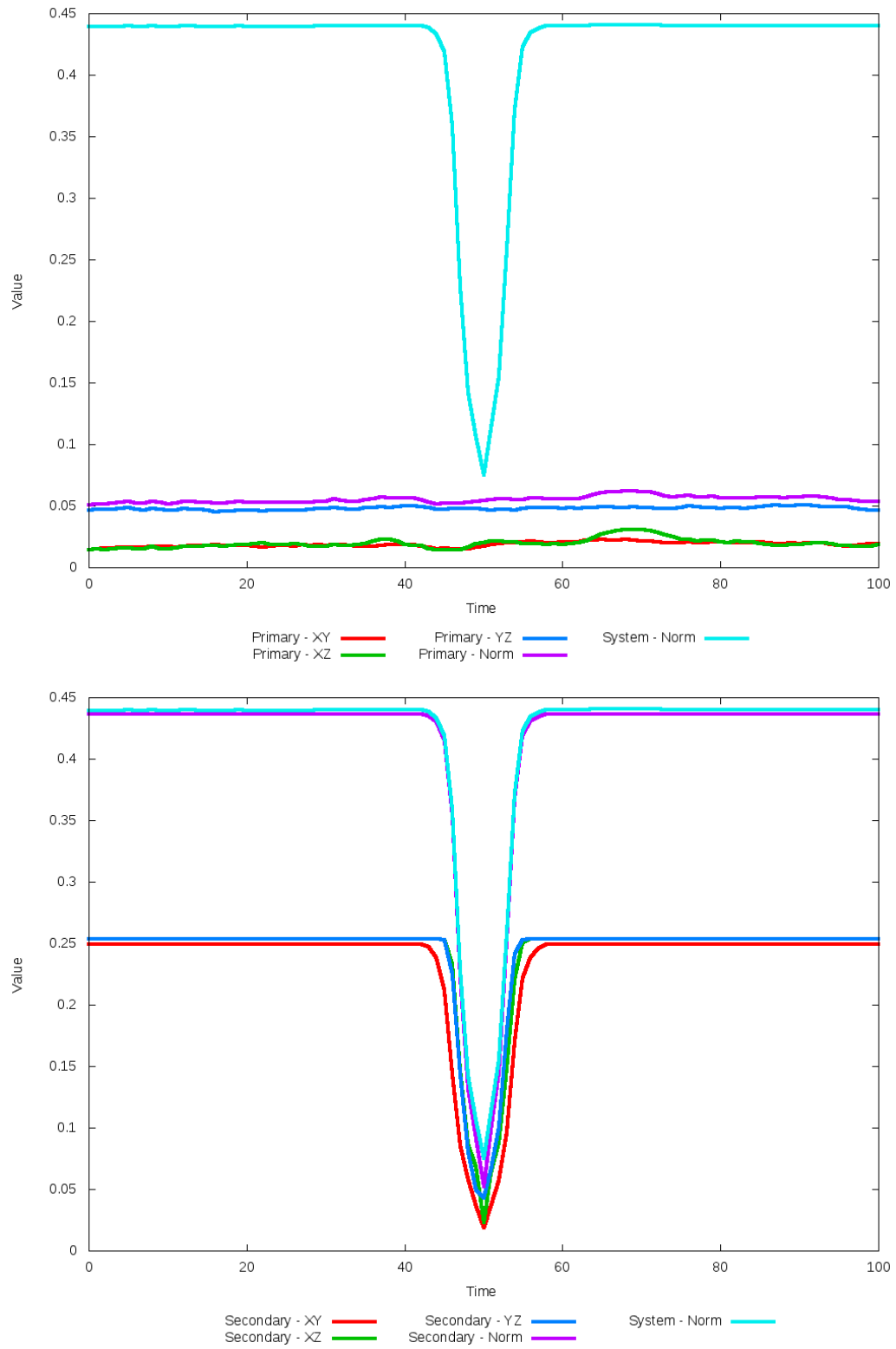


Figure 5.162: All metrics versus simulation time of the best N-Body simulation for SDSS 587739721376202860

5.1.28 SDSS 587739721900163101 (Arp 242)

Arp 242 shows significant improvement matching the SPAM simulation and observational data, despite not seeing a clear separation of the galactic centers of each galaxy in the XY projection. The tails along the Y direction and location of the secondary galaxy are in very good agreement with the SPAM simulation, and the orbits between both cases are elliptical. However, the center of mass of the primary galaxy does not match its galactic center. This can especially be seen in the YZ projection which clearly shows the disk and bulge of the primary galaxy to be shifted to the left of center. Furthermore, the other projection views however show the initial choice of dynamical friction to match better.

Table 5.55: Identification Information and Merger Zoo summary for SDSS 587739721900163101.

Name	Aliases	RA (hms)	Dec (dms)	Redshift
SDSS 587739721900163101	Arp 242, NGC 4676	12:46:10.1	+30:43:52.6	0.022059

R_x	R_y	R_z	V_x	V_y	V_z
-0.43119	-0.92661	-1.79015	0.02476	0.3569	-0.01856

	Primary Galaxy	Secondary Galaxy
mass	0.3307	0.55382
radius	0.71235	0.39054
ϕ	7.45496°	57.96958°
θ	85.87695°	212.74889°
ϵ	0.3	0.3

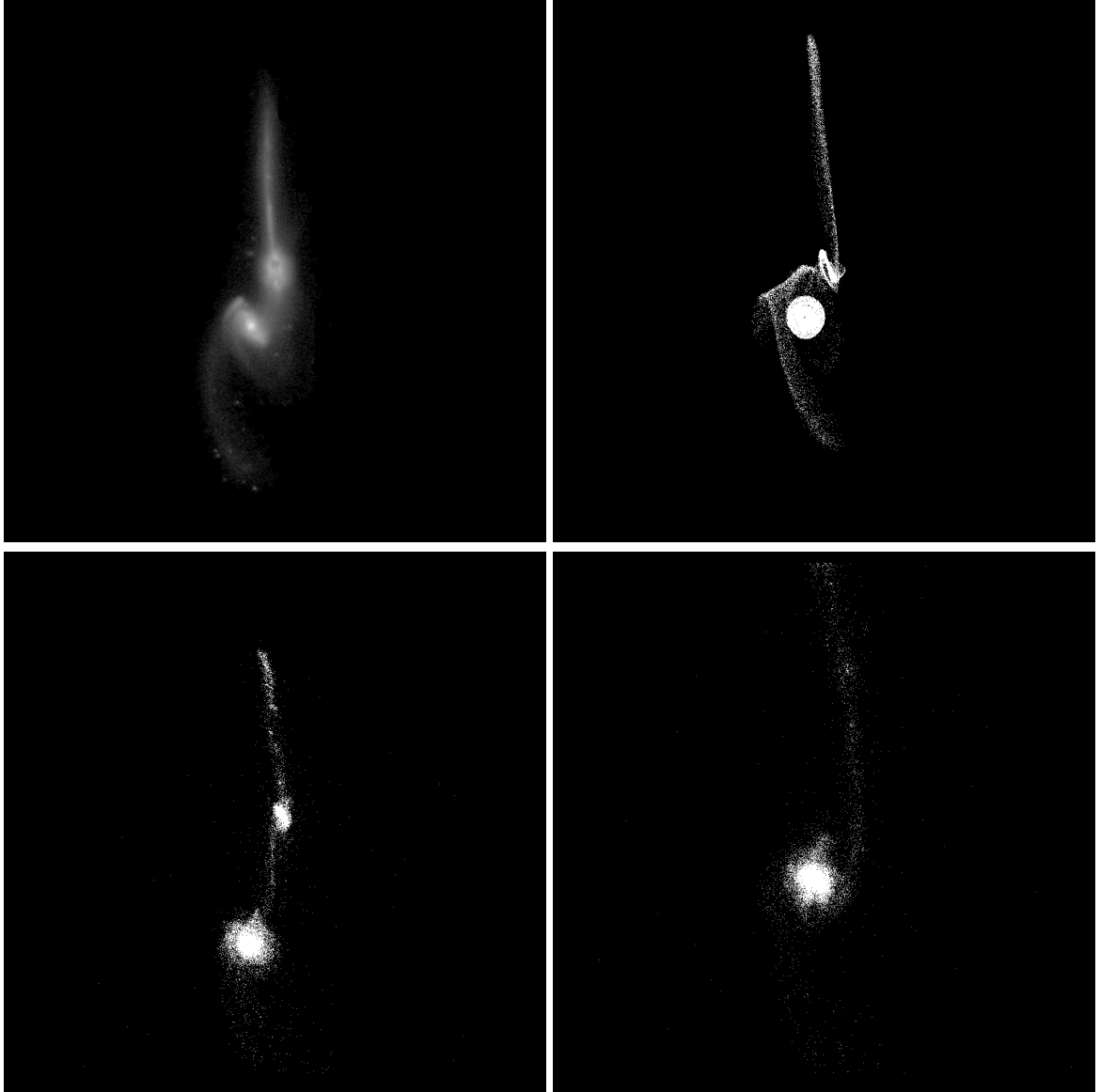


Figure 5.163: Target image (top-left), best SPAM match from Merger Wars (top-right), initial N-Body match (bottom-left), and best N-Body match (bottom-right) for SDSS 587739721900163101

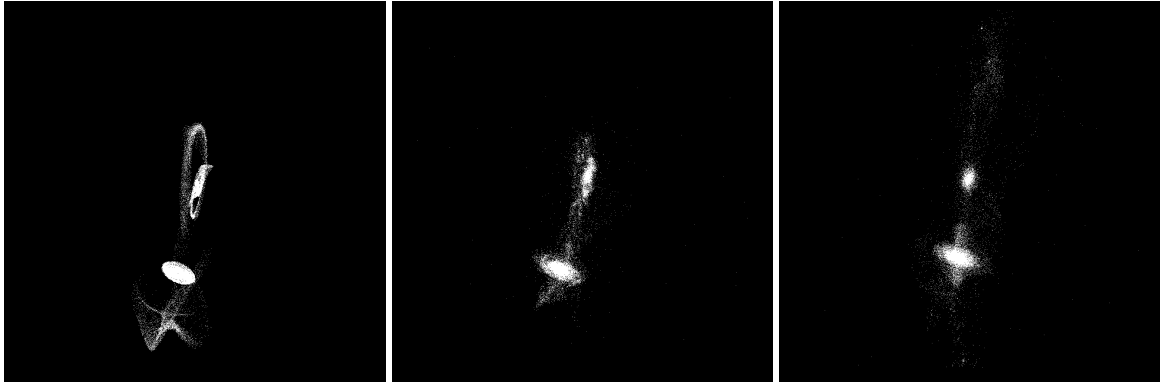


Figure 5.164: XZ projections of best SPAM match from Merger Wars (left), initial N-Body match (middle), and best N-Body match (right) for SDSS 587739721900163101

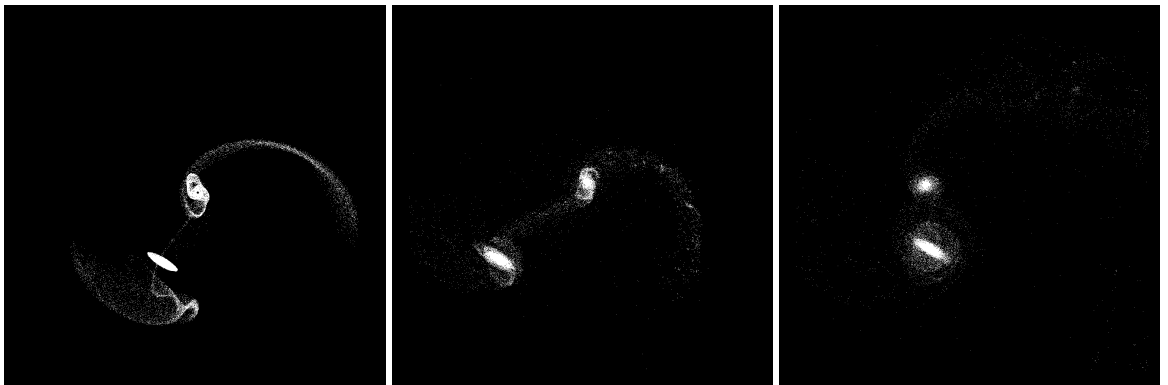


Figure 5.165: YZ projections of best SPAM match from Merger Wars (left), initial N-Body match (middle), and best N-Body match (right) for SDSS 587739721900163101

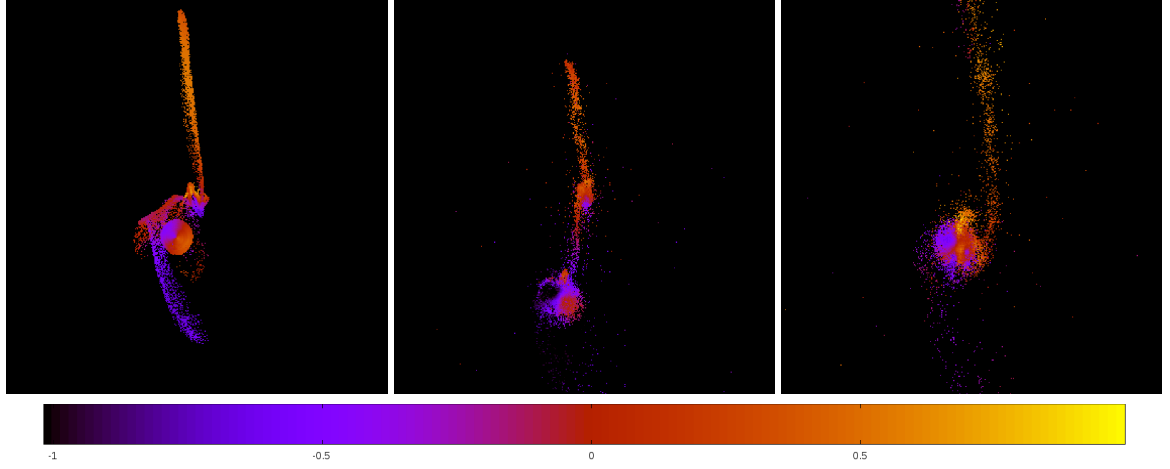


Figure 5.166: Line of sight velocity plots of best SPAM match from Merger Wars (left), initial N-Body match (middle), and best N-Body match (right) for SDSS 587739721900163101

Table 5.56: Orbital Elements & Dynamical Friction for SDSS 587739721900163101

	SPAM Simulation	Initial N-Body Simulation	Best N-Body Simulation
a	5.708	-1.570	1.920
e	0.487	2.900	0.940
r_c	2.925	2.983	0.116
i	101.252°	100.715°	97.385°
Ω	85.440°	84.549°	84.233°
ω	325.789°	146.412°	48.241°
ν	276.520°	69.839°	182.720°
t_n	50	41	65
$\ln\Lambda$	N/A	1.00E-03	5.00E-04

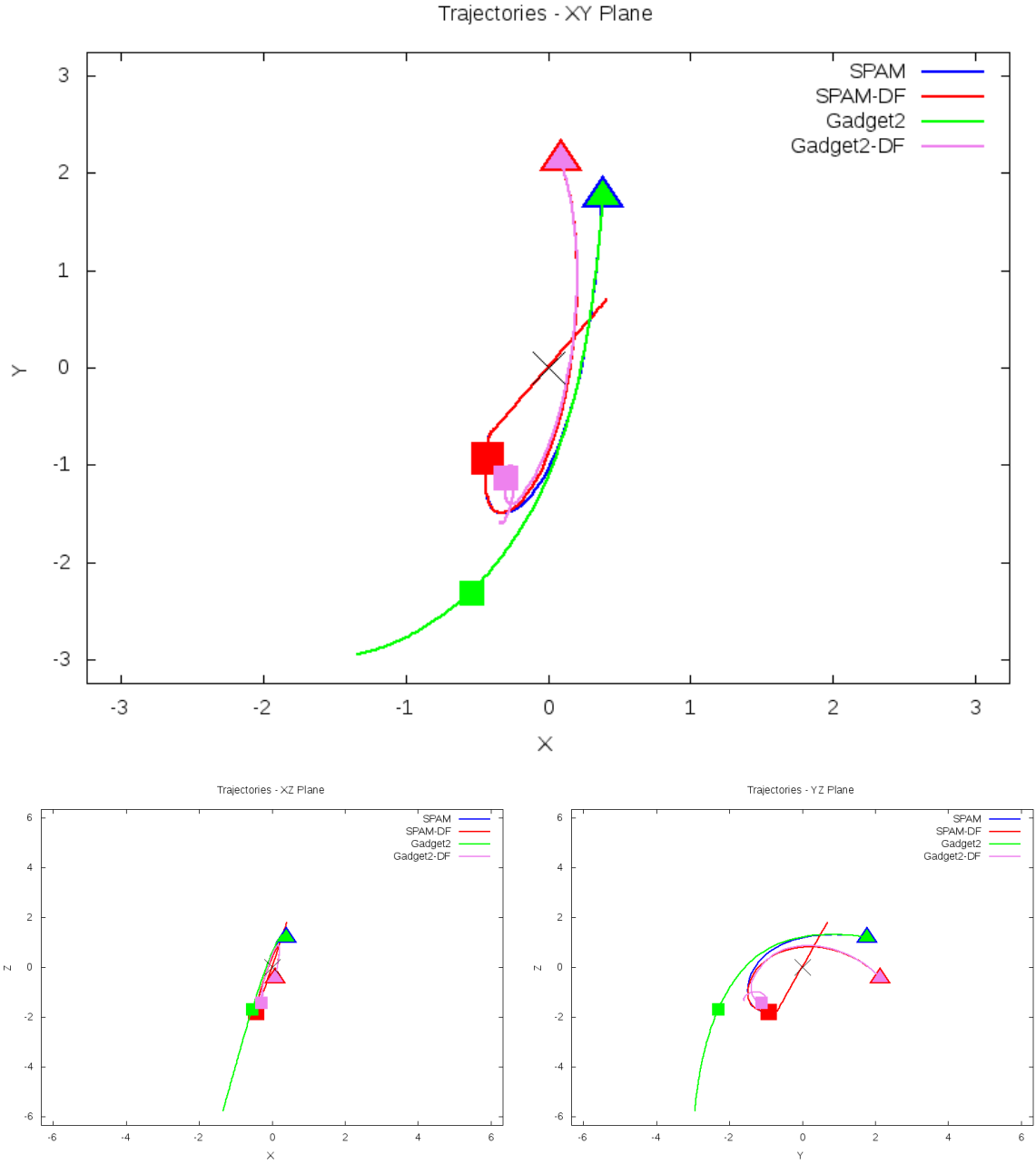


Figure 5.167: Trajectory plots of best SPAM match from Merger Wars, initial N-Body match, and best N-Body match for SDSS 587739721900163101

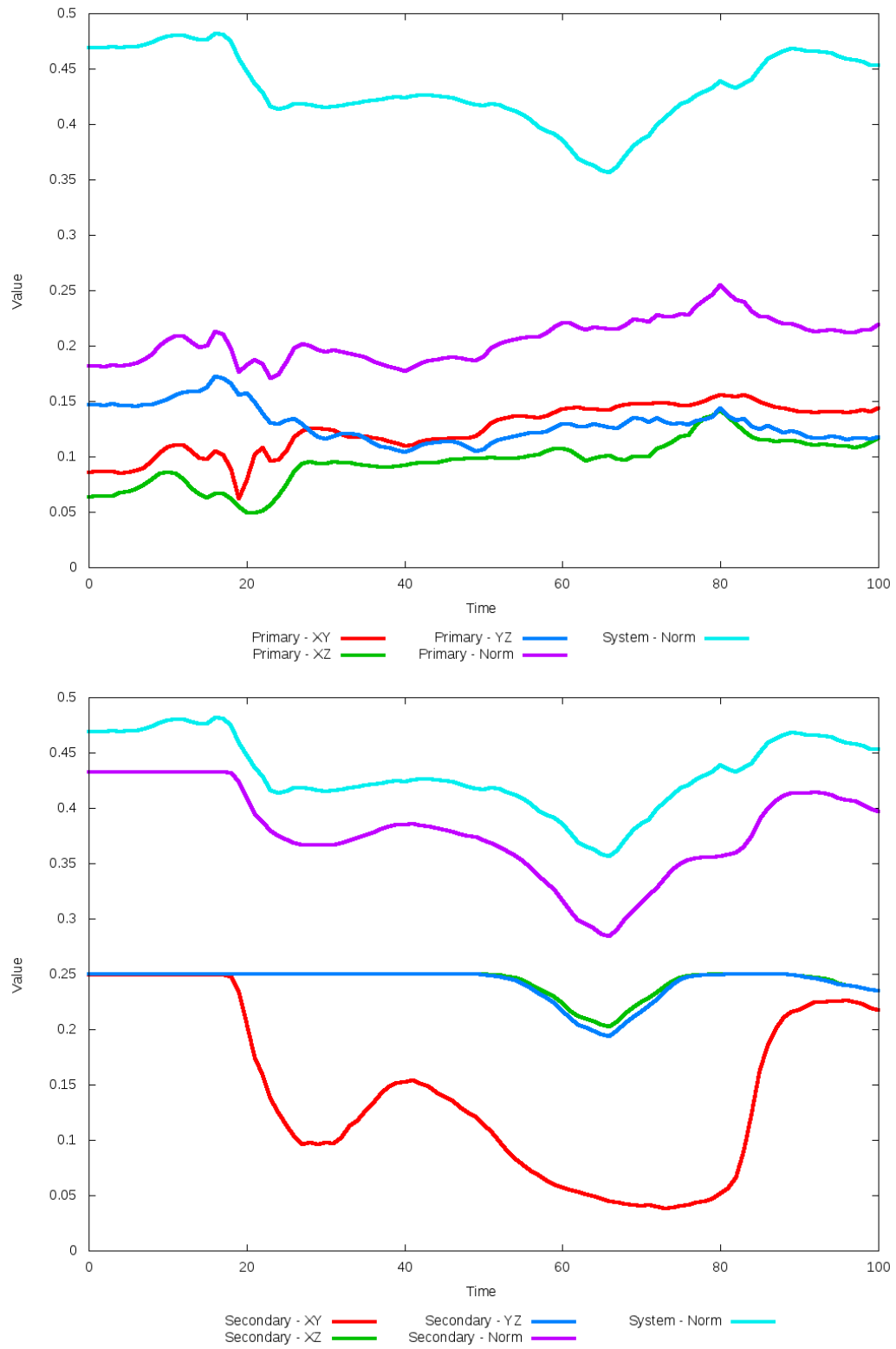


Figure 5.168: All metrics versus simulation time of the best N-Body simulation for SDSS 587739721900163101

5.1.29 SDSS 587739810496708646 (Arp 72)

Arp 72 shows very good agreement between its simulations and observational data. Although the initial and optimized N-Body simulations appear nearly indistinguishable, the optimization routine did make a small change in dynamical friction. With this change however, it appears the unoptimized trajectory when viewed in the XY projection is a slightly better match to the SPAM simulations. In any event, the interaction between these two galaxies appears to be weak as they have passed by each other, unlikely to interact any further.

Table 5.57: Identification Information and Merger Zoo summary for SDSS 587739810496708646.

Name	Aliases	RA (hms)	Dec (dms)	Redshift
SDSS 587739810496708646	Arp 72, NGC 5994/5996	15:46:58.2	+17:53:04.4	0.010974

R_x	R_y	R_z	V_x	V_y	V_z
1.11881	-0.58701	1.7904	0.04865	-0.14019	1.01095

	Primary Galaxy	Secondary Galaxy
mass	0.13149	0.09535
radius	0.61225	0.17248
ϕ	6.80196°	90.49367°
θ	224.25723°	228.89454°
ϵ	0.3	0.3

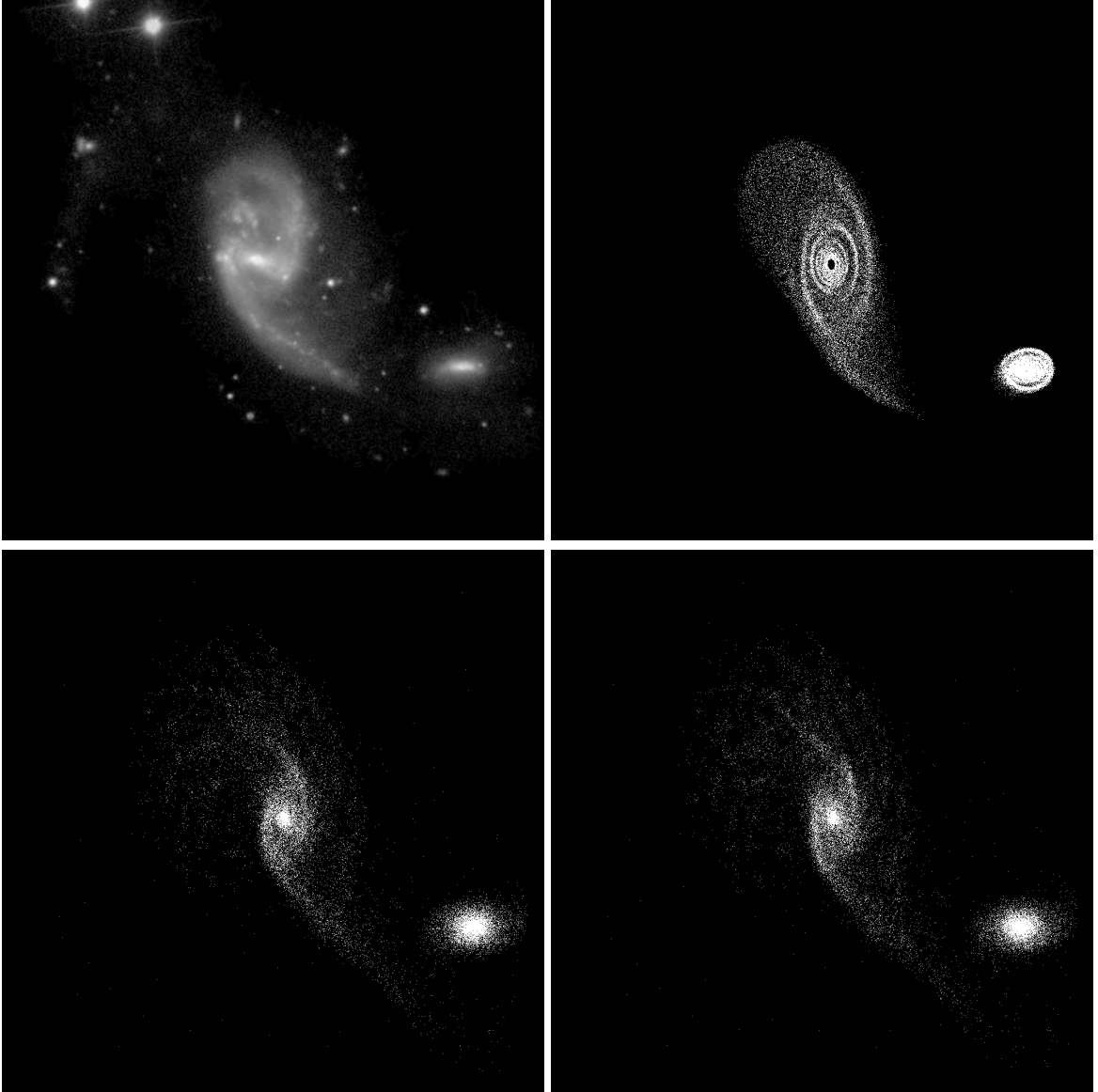


Figure 5.169: Target image (top-left), best SPAM match from Merger Wars (top-right), initial N-Body match (bottom-left), and best N-Body match (bottom-right) for SDSS 587739810496708646

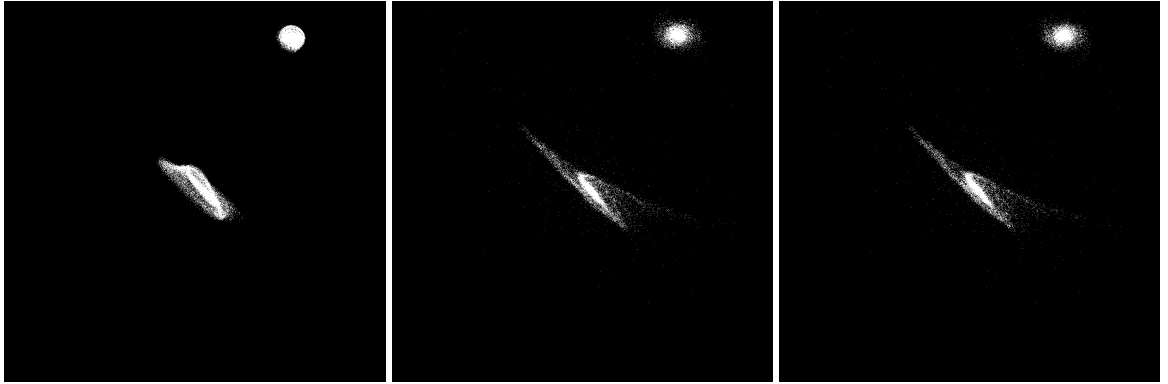


Figure 5.170: XZ projections of best SPAM match from Merger Wars (left), initial N-Body match (middle), and best N-Body match (right) for SDSS 587739810496708646

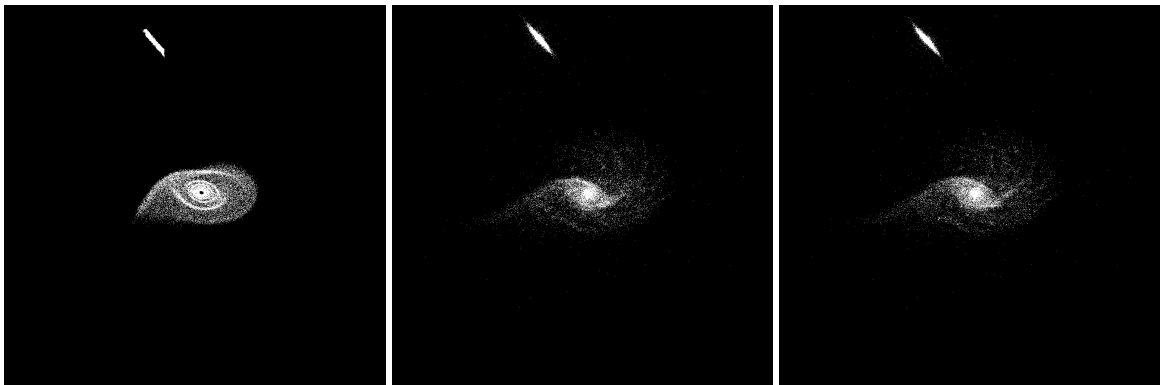


Figure 5.171: YZ projections of best SPAM match from Merger Wars (left), initial N-Body match (middle), and best N-Body match (right) for SDSS 587739810496708646

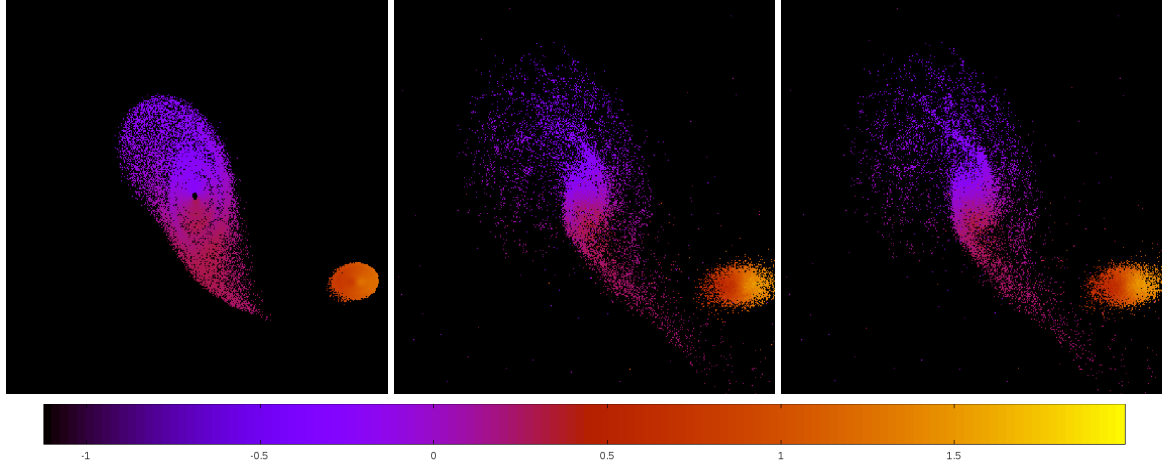


Figure 5.172: Line of sight velocity plots of best SPAM match from Merger Wars (left), initial N-Body match (middle), and best N-Body match (right) for SDSS 587739810496708646

Table 5.58: Orbital Elements & Dynamical Friction for SDSS 587739810496708646

	SPAM Simulation	Initial N-Body Simulation	Best N-Body Simulation
a	-0.111	-0.105	-0.107
e	19.974	20.685	20.396
r_c	2.111	2.077	2.069
i	96.660°	97.218°	97.411°
Ω	341.839°	341.252°	341.286°
ω	352.456°	352.177°	352.260°
ν	62.889°	63.709°	63.651°
t_n	50	50	50
$\ln\Lambda$	N/A	1.00E-03	7.50E-04

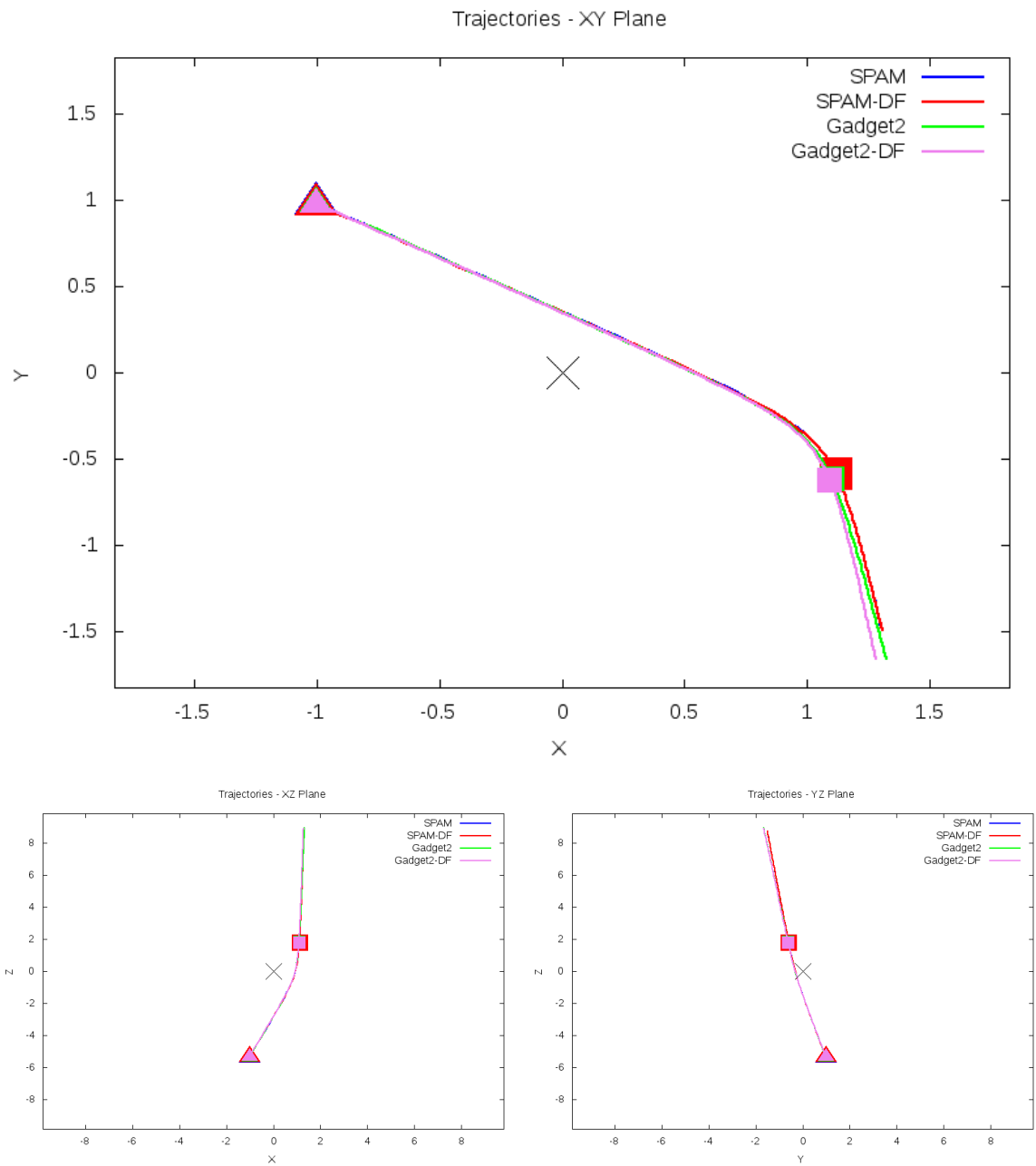


Figure 5.173: Trajectory plots of best SPAM match from Merger Wars, initial N-Body match, and best N-Body match for SDSS 587739810496708646

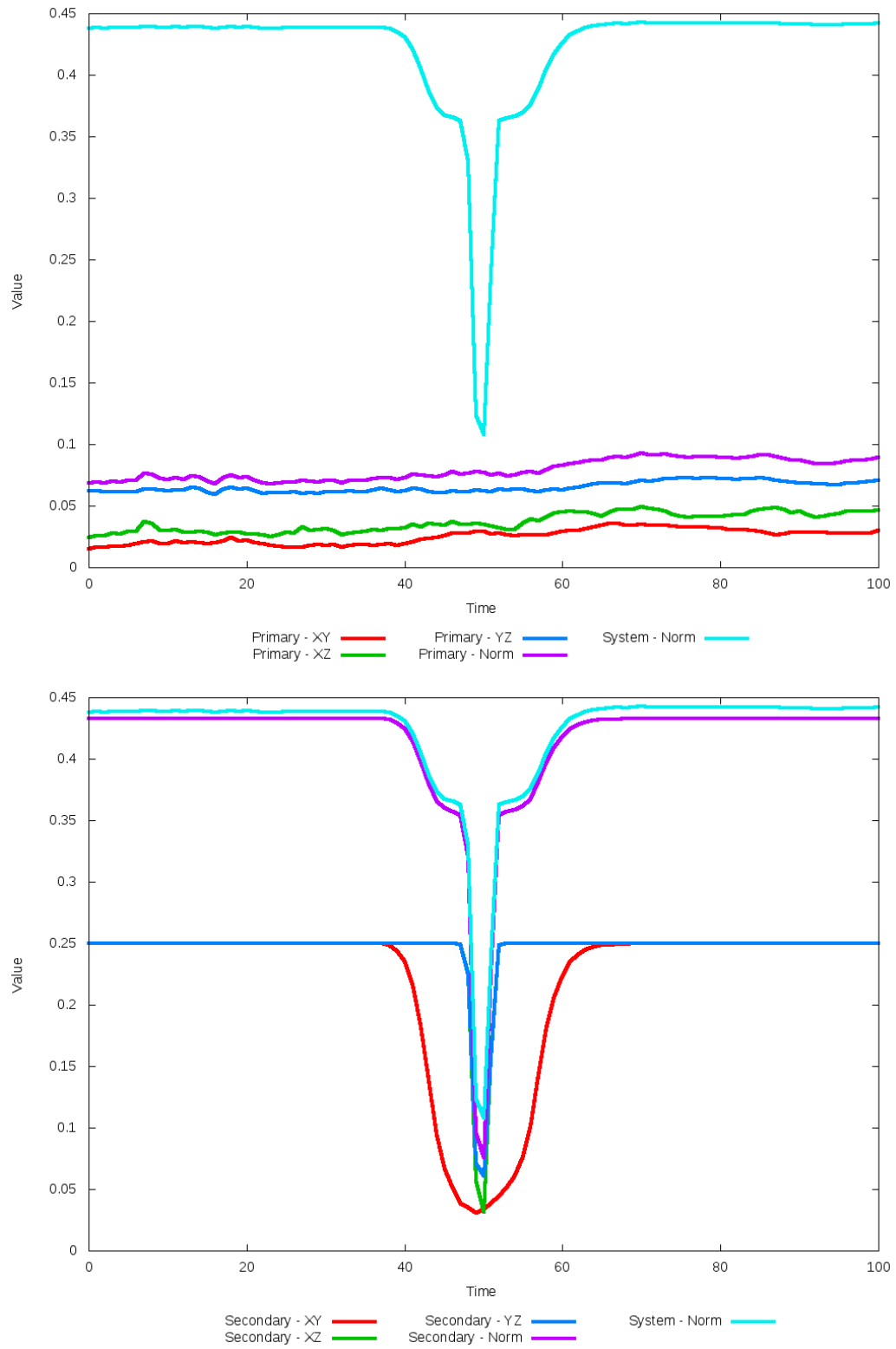


Figure 5.174: All metrics versus simulation time of the best N-Body simulation for SDSS 587739810496708646

5.1.30 SDSS 587739845393580192 (Arp 101)

Arp 101 shows much improvement in the N-Body simulation as dynamical friction is optimized to match the SPAM simulation and observational data. Compared to the initial choice, the distance between the galaxies has increased and the tidal features are not nearly as elongated. Although not a perfect match in the XY projection, the XZ and YZ projections show even better agreement with the SPAM simulation in galaxy placement and morphology. However, the line of sight velocity plots indicate the N-Body simulation is moving away from the observer a little more than the SPAM simulation. The trajectory of the optimized N-Body simulation also better matches that of the SPAM simulations.

Table 5.59: Identification Information and Merger Zoo summary for SDSS 587739845393580192.

Name	Aliases	RA (hms)	Dec (dms)	Redshift
SDSS 587739845393580192	Arp 101, UGC 10164/10169	16:04:31.7	+14:49:08.8	0.015274

R_x	R_y	R_z	V_x	V_y	V_z
0.96821	-2.63044	-2.22943	0.16074	-0.78512	-0.84691

	Primary Galaxy	Secondary Galaxy
mass	0.51707	0.59847
radius	0.43977	0.2968
ϕ	45.10324°	358.74357°
θ	62.33573°	207.08113°
ϵ	0.3	0.3

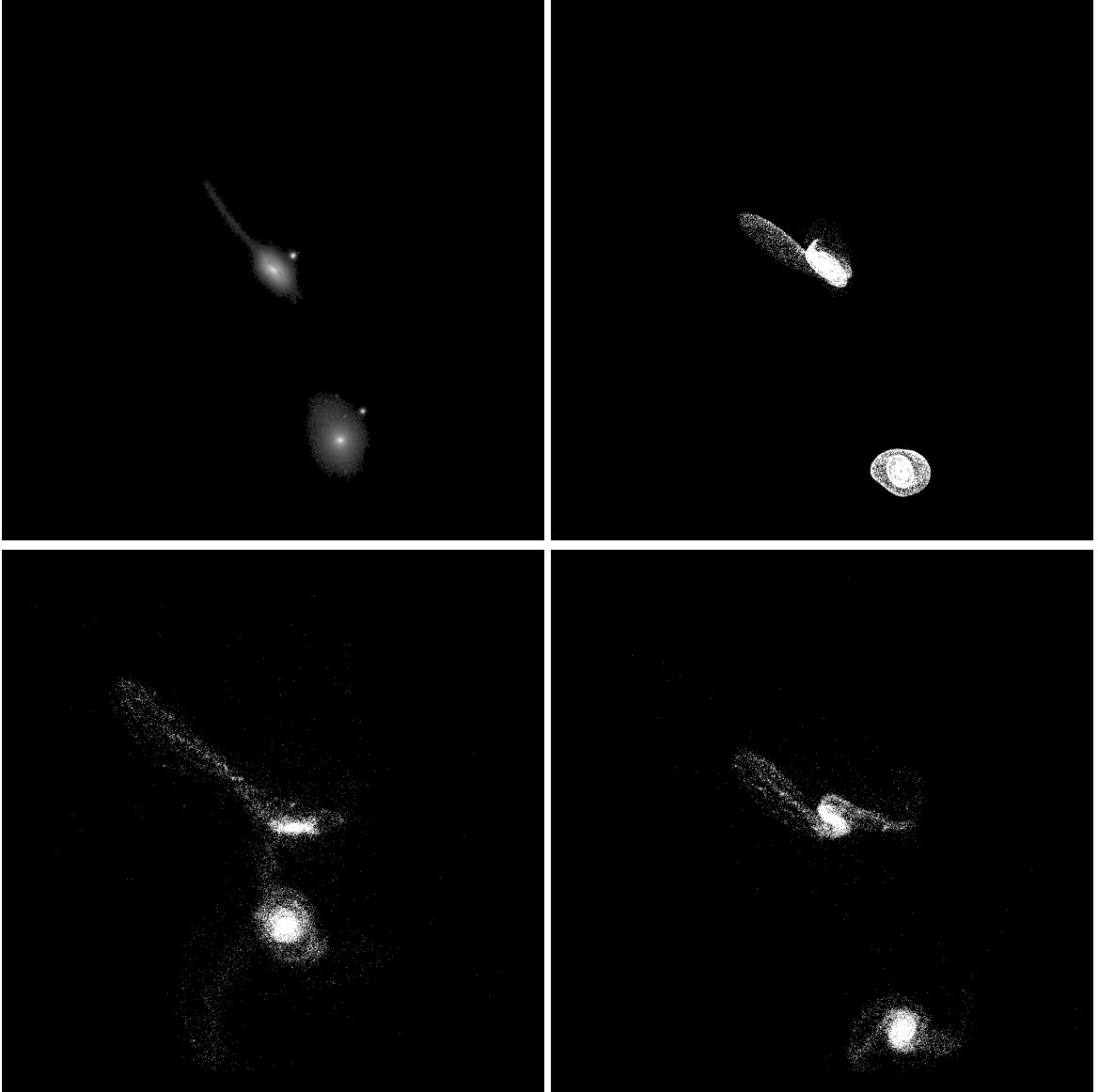


Figure 5.175: Target image (top-left), best SPAM match from Merger Wars (top-right), initial N-Body match (bottom-left), and best N-Body match (bottom-right) for SDSS 587739845393580192

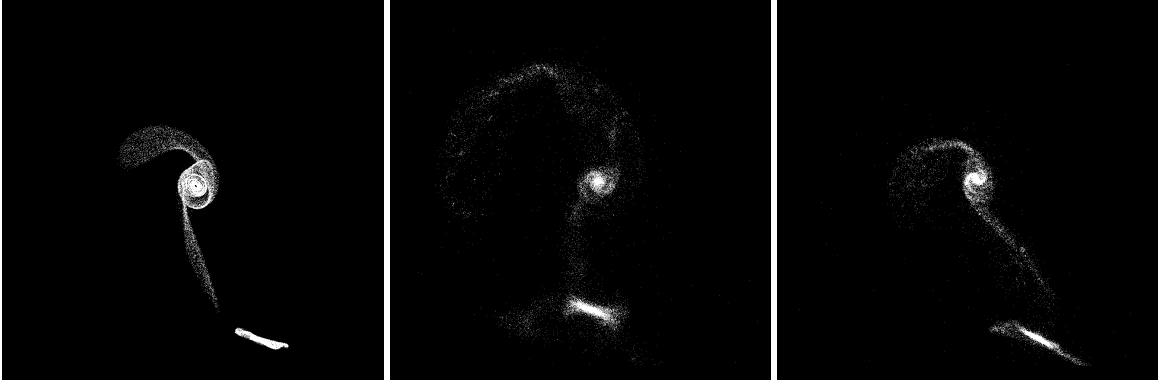


Figure 5.176: XZ projections of best SPAM match from Merger Wars (left), initial N-Body match (middle), and best N-Body match (right) for SDSS 587739845393580192

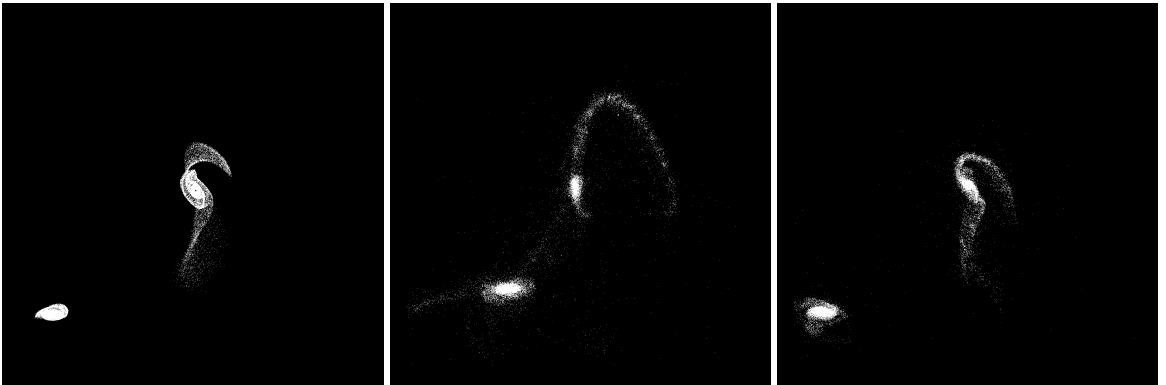


Figure 5.177: YZ projections of best SPAM match from Merger Wars (left), initial N-Body match (middle), and best N-Body match (right) for SDSS 587739845393580192

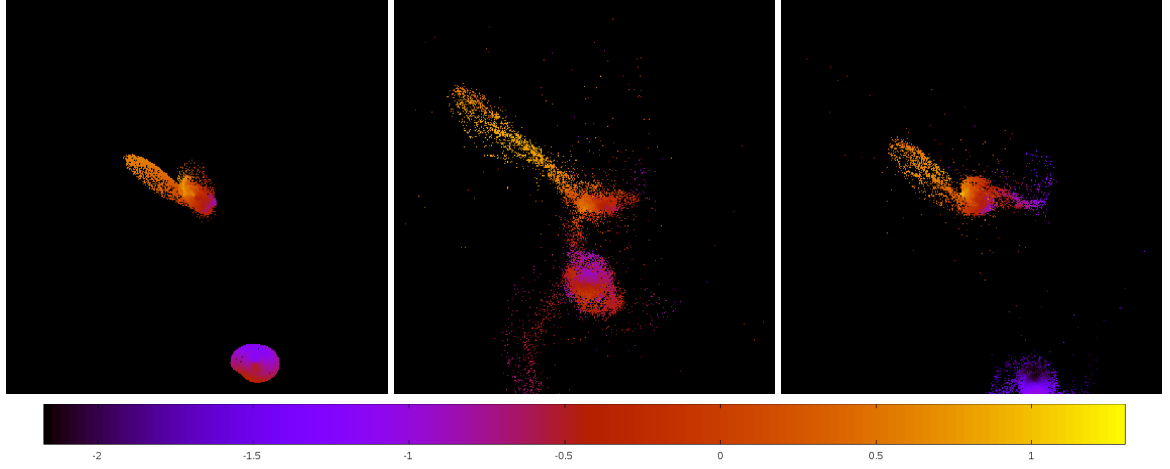


Figure 5.178: Line of sight velocity plots of best SPAM match from Merger Wars (left), initial N-Body match (middle), and best N-Body match (right) for SDSS 587739845393580192

Table 5.60: Orbital Elements & Dynamical Friction for SDSS 587739845393580192

	SPAM Simulation	Initial N-Body Simulation	Best N-Body Simulation
a	-0.461	-4.577	-0.107
e	3.112	1.124	9.981
r_c	0.973	0.568	0.964
i	116.930°	115.752°	117.148°
Ω	134.039°	132.594°	132.986°
ω	126.125°	108.752°	134.969°
ν	98.158°	130.875°	87.376°
t_n	50	49	39
$\ln\Lambda$	N/A	1.00E-03	1.90E-02

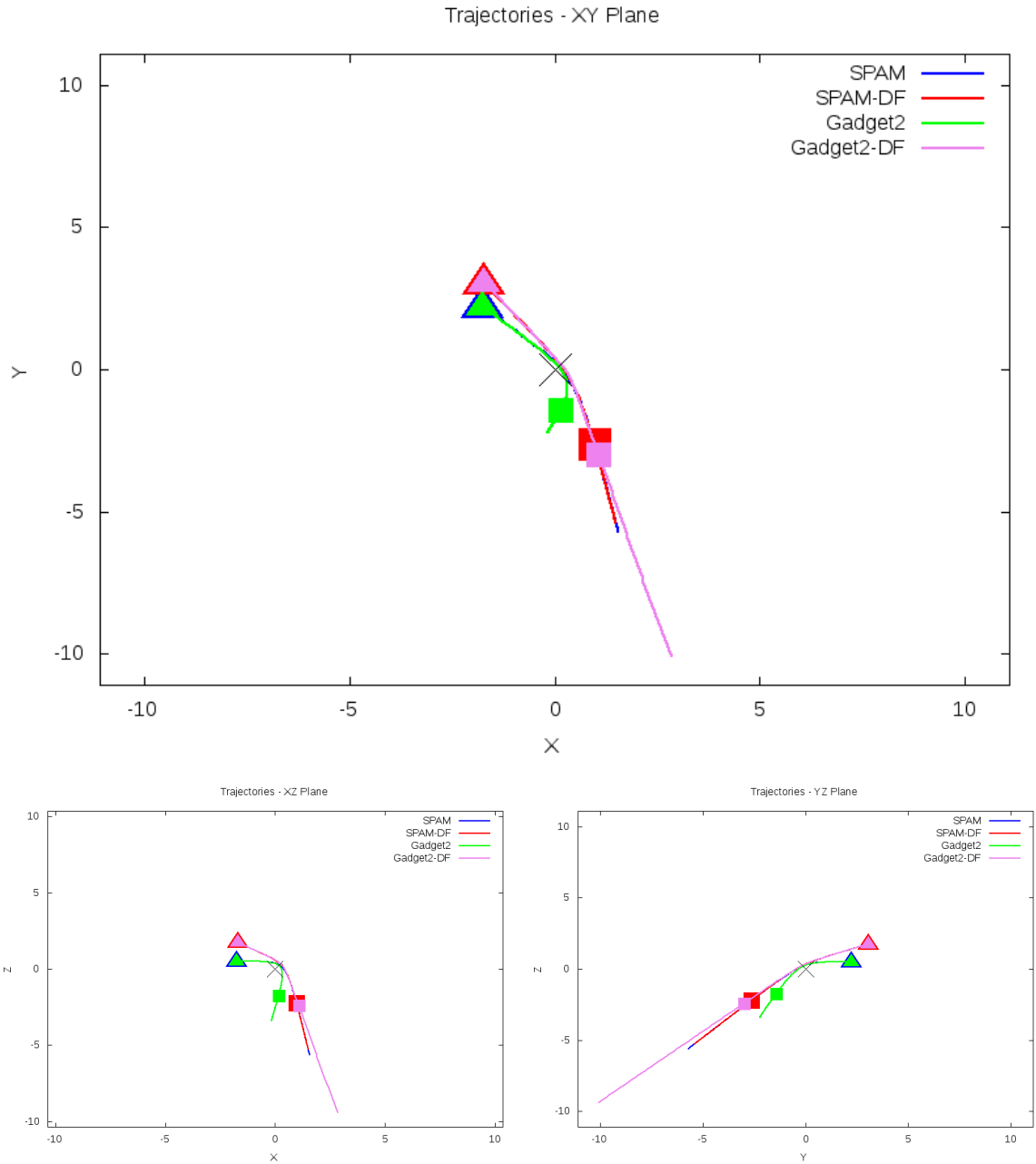


Figure 5.179: Trajectory plots of best SPAM match from Merger Wars, initial N-Body match, and best N-Body match for SDSS 587739845393580192

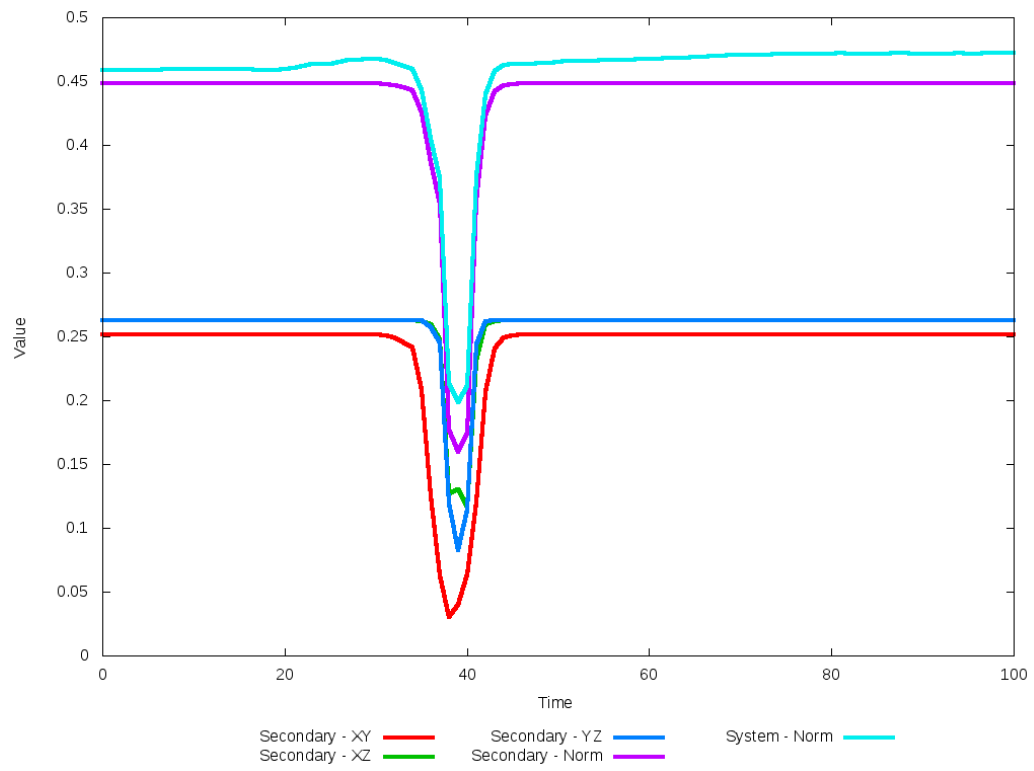
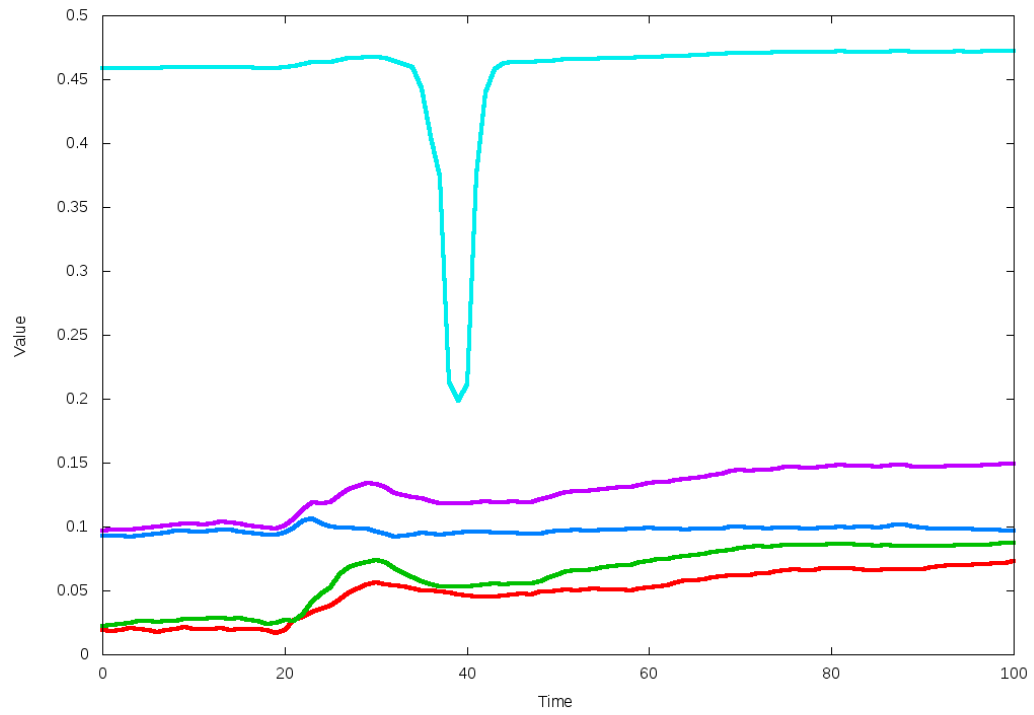


Figure 5.180: All metrics versus simulation time of the best N-Body simulation for SDSS 587739845393580192

5.1.31 SDSS 587741391565422775 (Arp 58)

Arp 58 shows a remarkable improvement in its quality of fit to the SPAM simulation from Merger Wars when dynamical friction is optimized. This improvement came with just a very small change in dynamical friction. The location of the secondary galaxy is consistent with the location of the observational data and SPAM simulation and the morphology is very similar between the primary galaxies. The most significant change however is that the N-Body simulations predict trajectories that will decay sooner than the restricted three-body simulation. A quick observation of the alternative metrics that could have been used by the optimization does show that optimizing along the XZ projection may have found a better match occurring closer to the same time as found by the SPAM simulations.

Table 5.61: Identification Information and Merger Zoo summary for SDSS 587741391565422775.

Name	Aliases	RA (hms)	Dec (dms)	Redshift
SDSS 587741391565422775	Arp 58, UGC 4457	8:31:57.6	+19:12:40.4	0.037222

R_x	R_y	R_z	V_x	V_y	V_z
-1.92706	-1.6735	-1.02462	0.11886	-0.93364	0.06848

	Primary Galaxy	Secondary Galaxy
mass	2.11334	0.35556
radius	1.29023	0.1899
ϕ	173.28798°	45.57512°
θ	44.62654°	230.34231°
ϵ	0.3	0.3

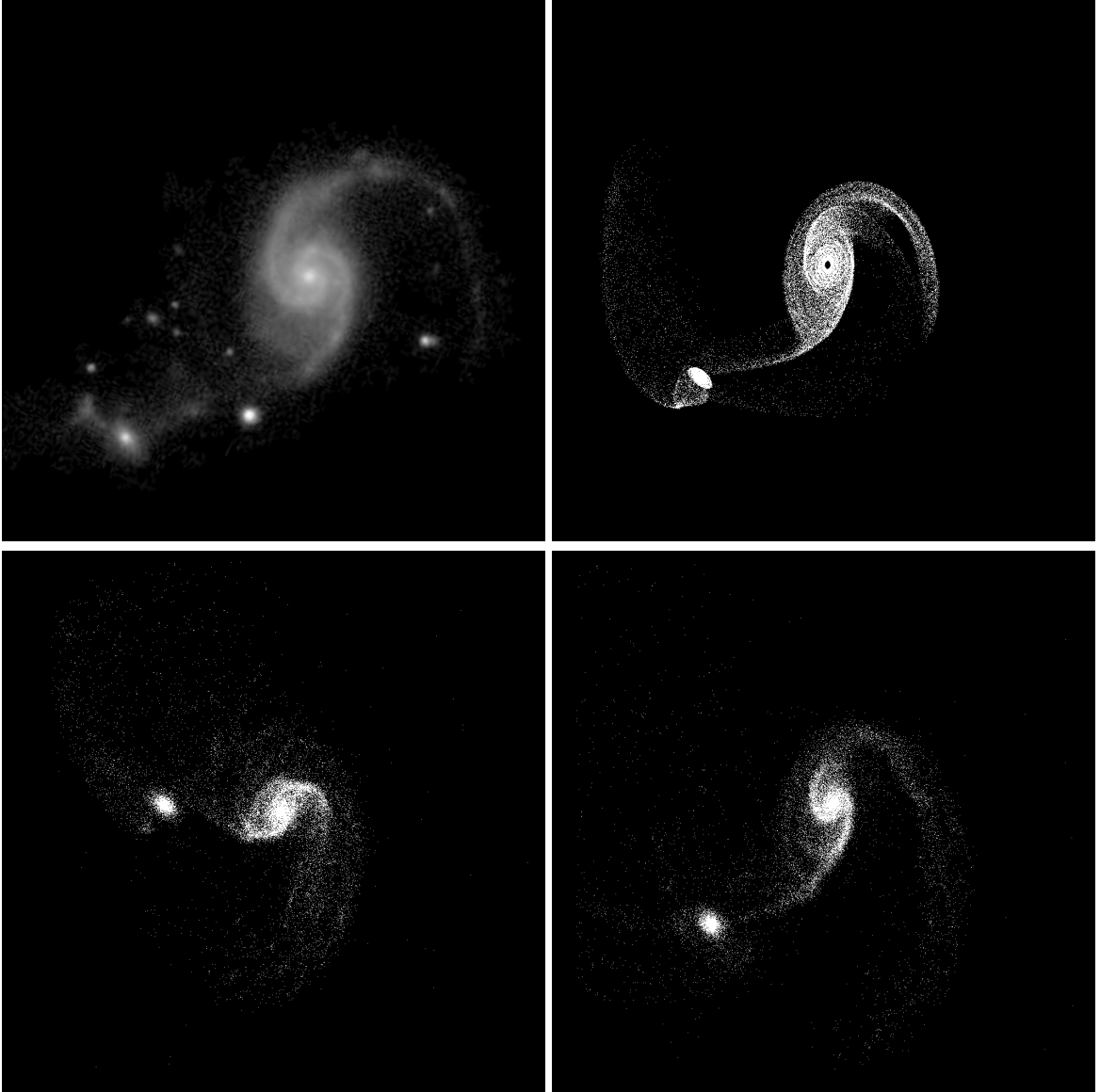


Figure 5.181: Target image (top-left), best SPAM match from Merger Wars (top-right), initial N-Body match (bottom-left), and best N-Body match (bottom-right) for SDSS 587741391565422775

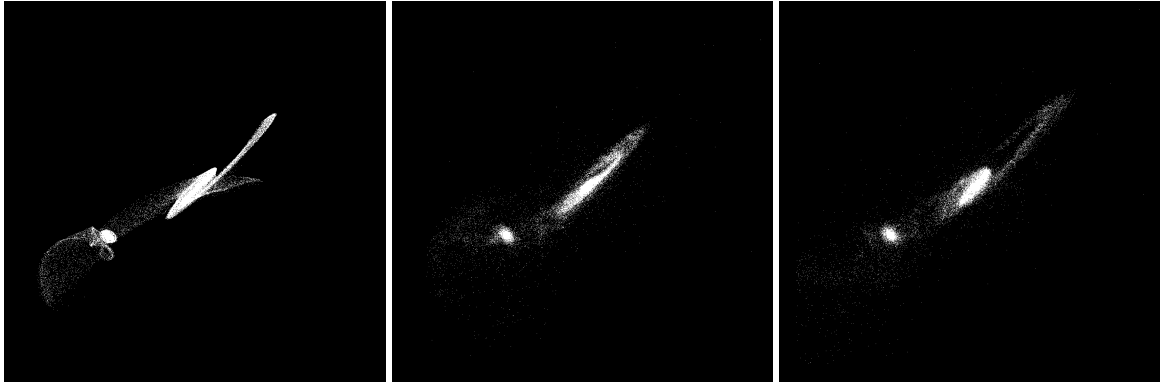


Figure 5.182: XZ projections of best SPAM match from Merger Wars (left), initial N-Body match (middle), and best N-Body match (right) for SDSS 587741391565422775

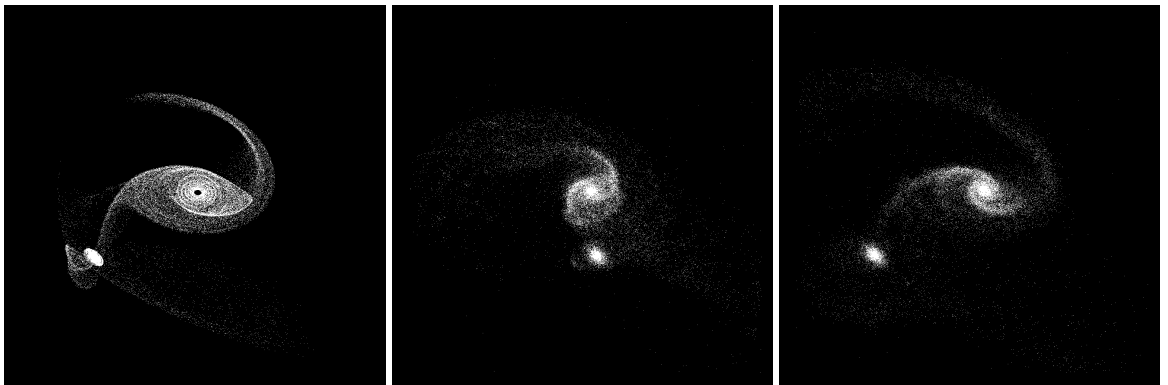


Figure 5.183: YZ projections of best SPAM match from Merger Wars (left), initial N-Body match (middle), and best N-Body match (right) for SDSS 587741391565422775

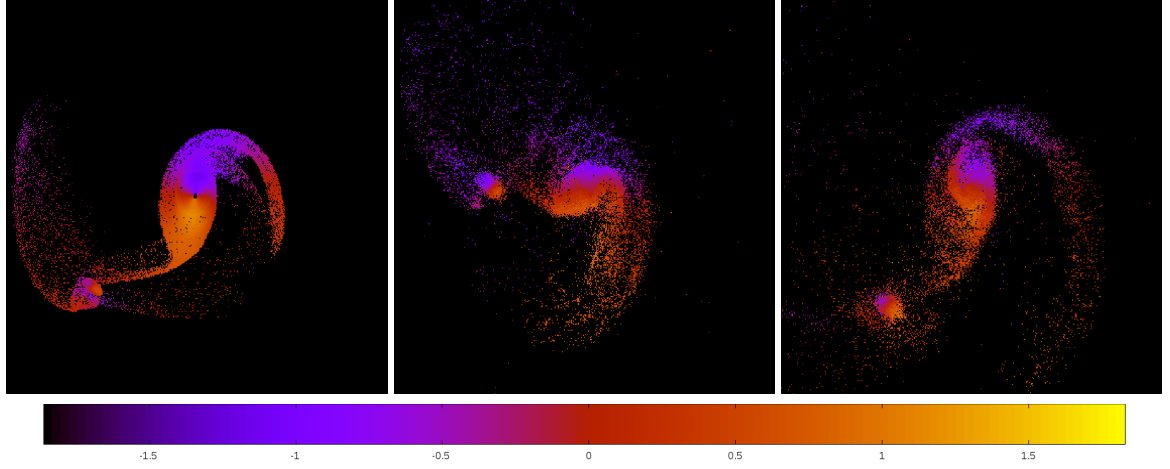


Figure 5.184: Line of sight velocity plots of best SPAM match from Merger Wars (left), initial N-Body match (middle), and best N-Body match (right) for SDSS 587741391565422775

Table 5.62: Orbital Elements & Dynamical Friction for SDSS 587741391565422775

	SPAM Simulation	Initial N-Body Simulation	Best N-Body Simulation
a	-0.910	-0.800	-2.433
e	6.175	5.529	2.983
r_c	4.707	3.625	4.824
i	28.198°	30.522°	30.366°
Ω	269.456°	268.718°	268.160°
ω	274.313°	240.195°	290.720°
ν	33.647°	24.025°	17.299°
t_n	50	42	56
$\ln\Lambda$	N/A	1.00E-03	9.00E-04

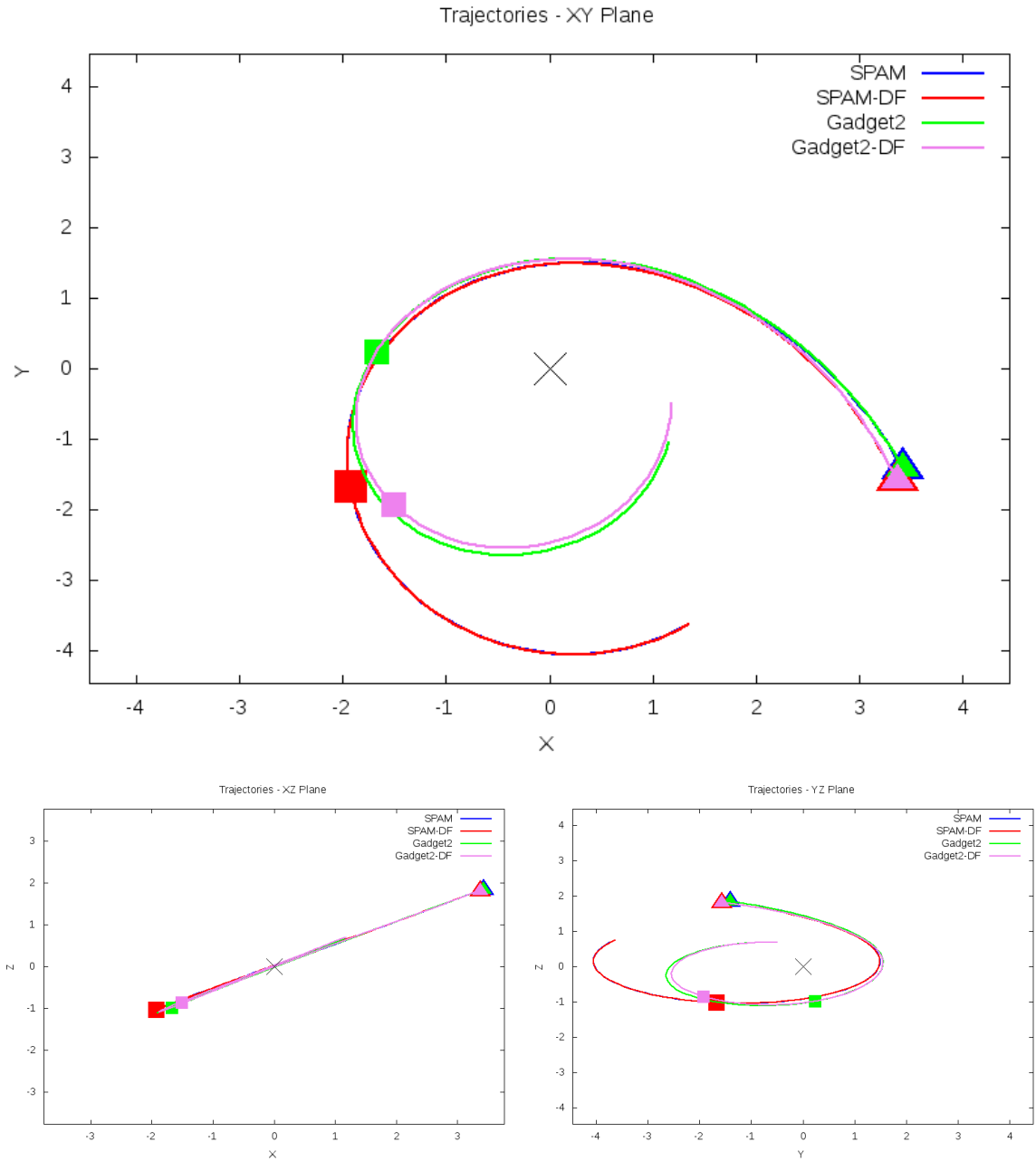


Figure 5.185: Trajectory plots of best SPAM match from Merger Wars, initial N-Body match, and best N-Body match for SDSS 587741391565422775

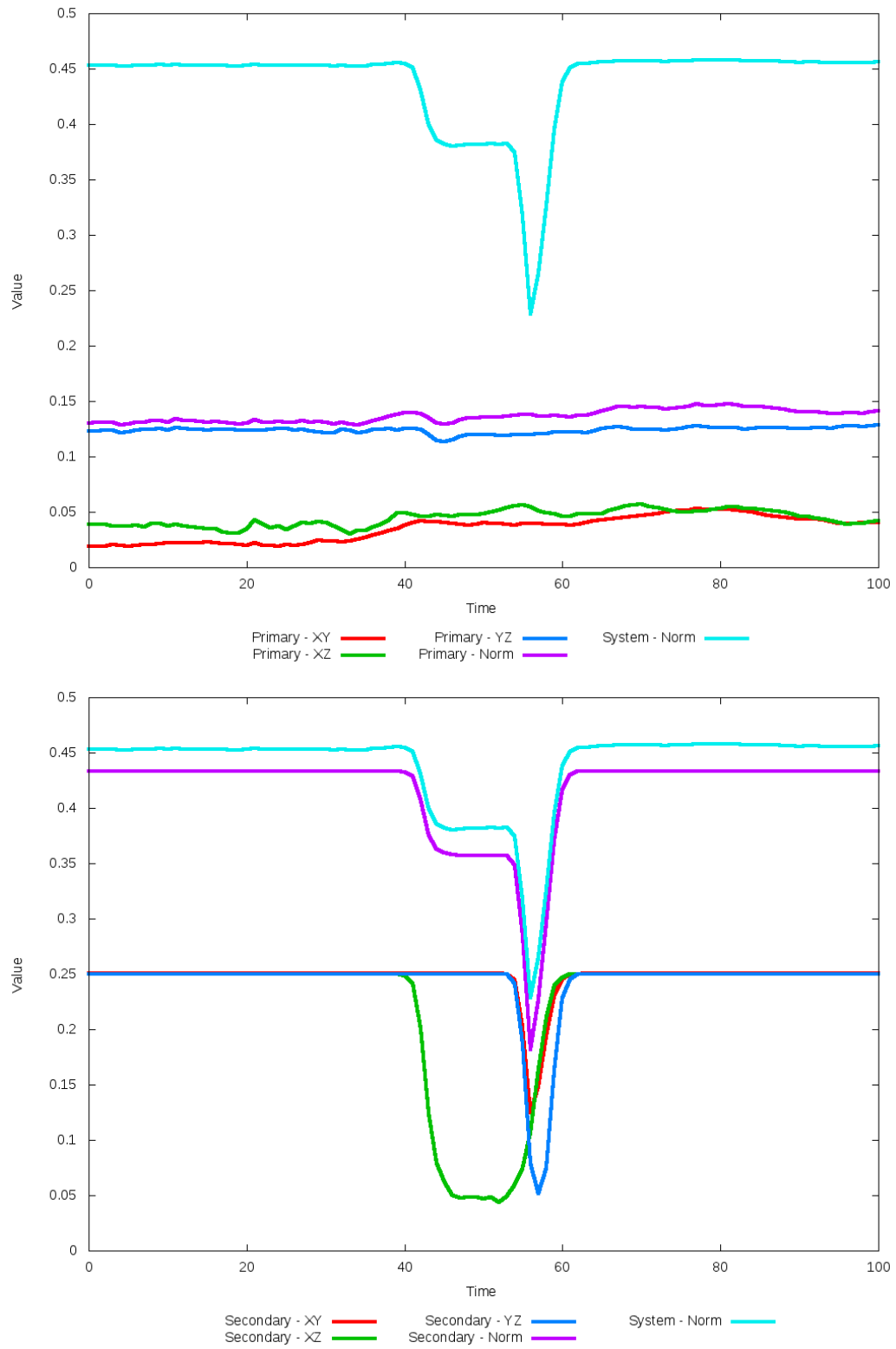


Figure 5.186: All metrics versus simulation time of the best N-Body simulation for SDSS 587741391565422775

5.1.32 SDSS 587741532784361481 (Arp 105)

Arp 105 shows very good morphological agreement between its simulations and observational data, although the position of the secondary galaxy shows much more agreement with the optimized simulation. This can be further seen in their trajectories. Although not a perfect match, the optimized trajectory is much closer to the SPAM simulations near the time of observed interaction. The biggest change between the SPAM simulation and the N-Body simulations is the broader disk seen in the N-Body calculations.

Table 5.63: Identification Information and Merger Zoo summary for SDSS 587741532784361481.

Name	Aliases	RA (hms)	Dec (dms)	Redshift
SDSS 587741532784361481	Arp 105, NGC 3561	11:11:12.9	+28:42:42.4	0.029356

R_x	R_y	R_z	V_x	V_y	V_z
-0.10214	-2.12459	5.33525	0.21877	-0.02317	1.56857

	Primary Galaxy	Secondary Galaxy
mass	0.59529	2.82108
radius	0.61541	0.79173
ϕ	-34.375°	141.75°
θ	306.3354°	0.0°
ϵ	0.3	0.3

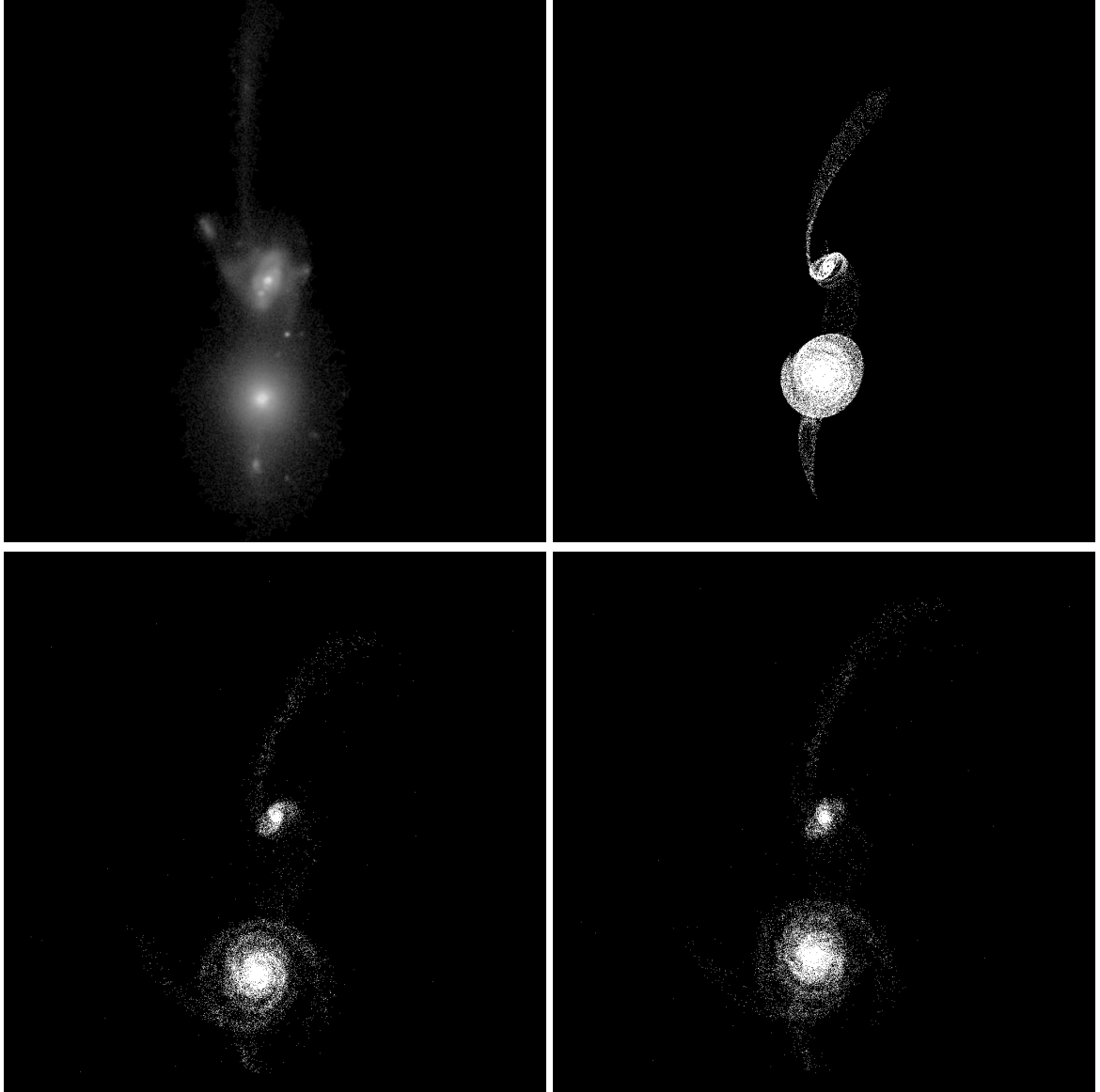


Figure 5.187: Target image (top-left), best SPAM match from Merger Wars (top-right), initial N-Body match (bottom-left), and best N-Body match (bottom-right) for SDSS 587741532784361481

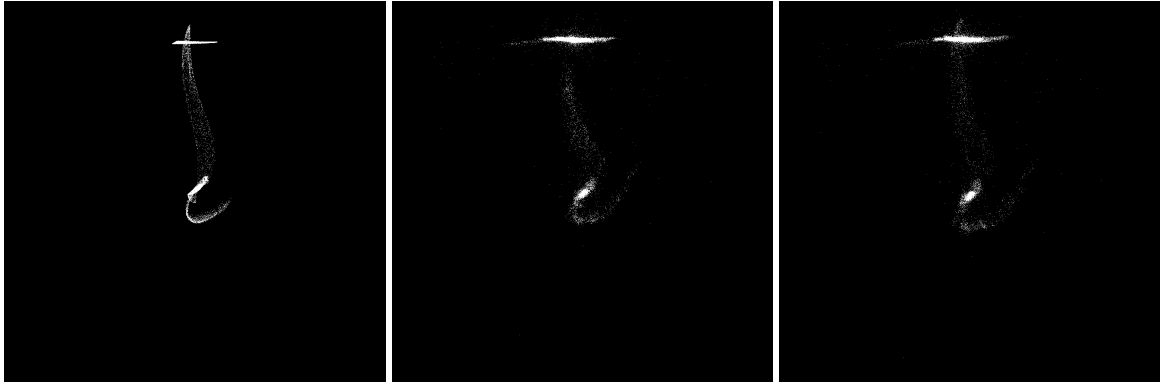


Figure 5.188: XZ projections of best SPAM match from Merger Wars (left), initial N-Body match (middle), and best N-Body match (right) for SDSS 587741532784361481

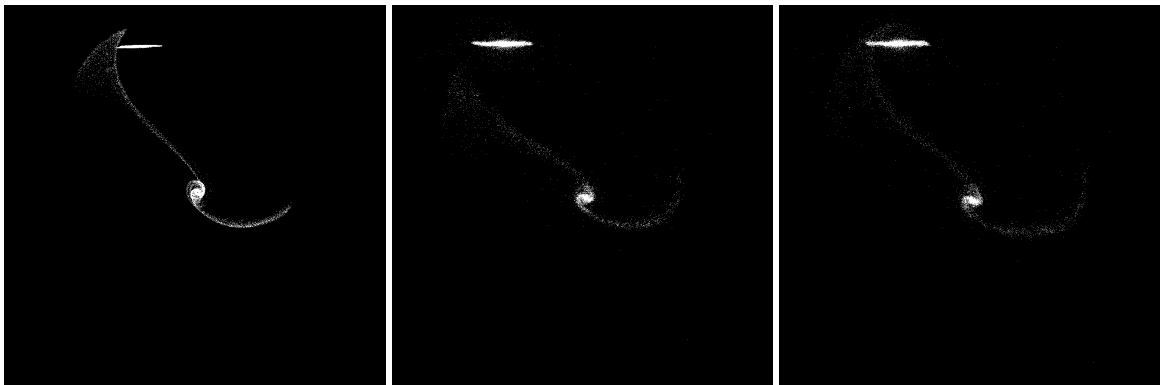


Figure 5.189: YZ projections of best SPAM match from Merger Wars (left), initial N-Body match (middle), and best N-Body match (right) for SDSS 587741532784361481

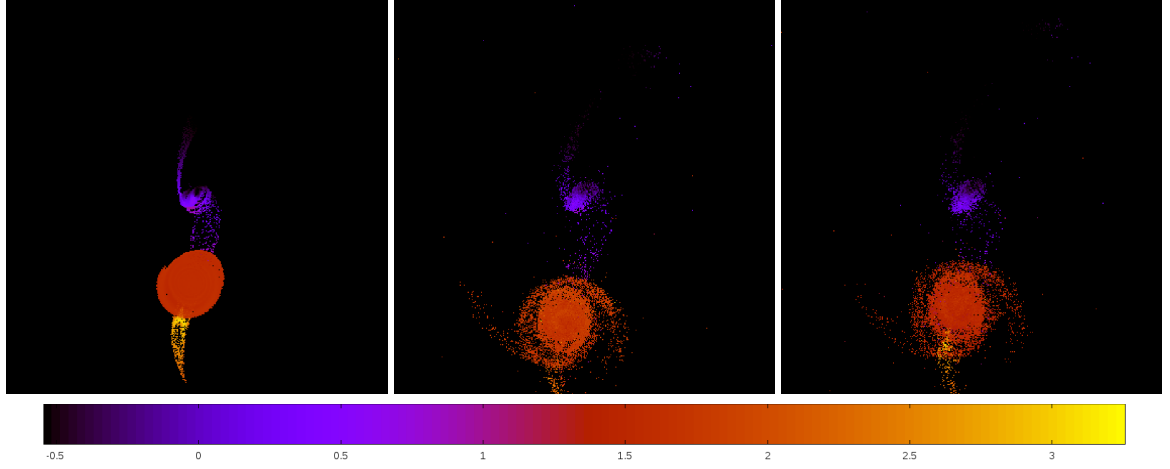


Figure 5.190: Line of sight velocity plots of best SPAM match from Merger Wars (left), initial N-Body match (middle), and best N-Body match (right) for SDSS 587741532784361481

Table 5.64: Orbital Elements & Dynamical Friction for SDSS 587741532784361481

	SPAM Simulation	Initial N-Body Simulation	Best N-Body Simulation
a	-0.421	-0.318	-0.447
e	10.944	12.863	9.497
r_c	4.182	3.774	3.798
i	82.338°	81.075°	80.657°
Ω	247.527°	245.728°	244.873°
ω	357.414°	345.784°	348.278°
ν	72.184°	75.627°	76.163°
t_n	50	49	52
$\ln\Lambda$	N/A	1.00E-03	3.00E-04

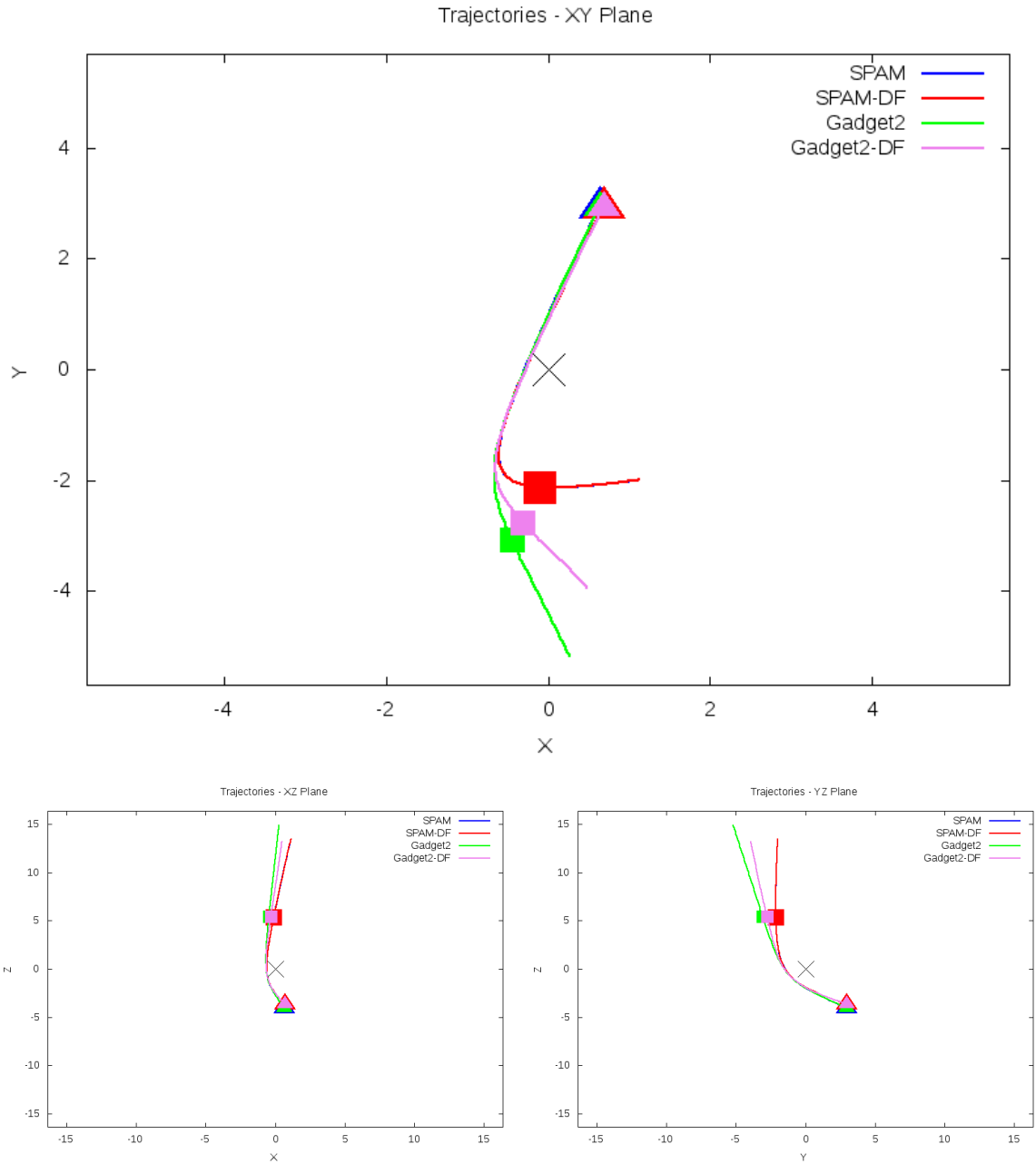


Figure 5.191: Trajectory plots of best SPAM match from Merger Wars, initial N-Body match, and best N-Body match for SDSS 587741532784361481

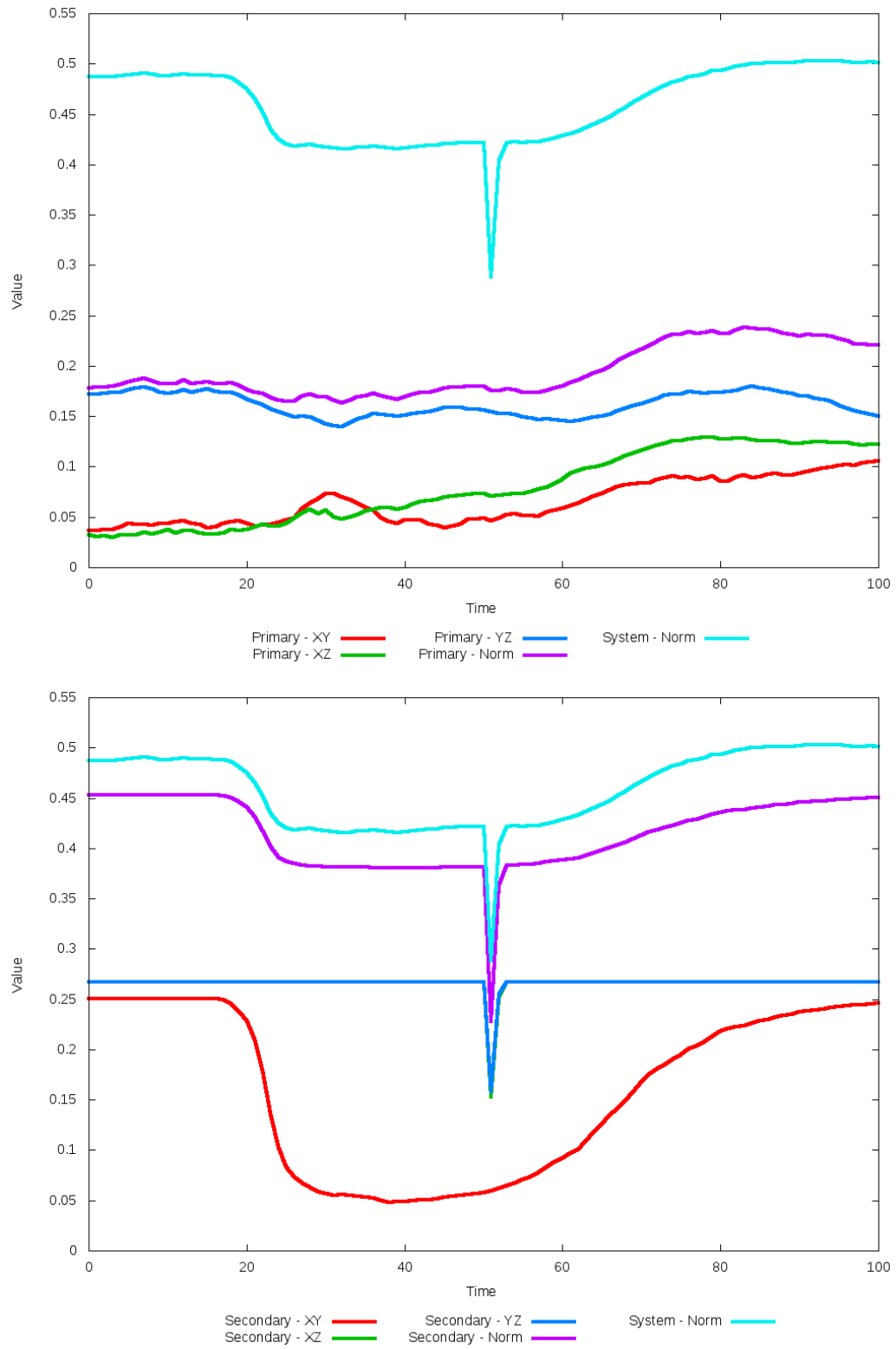


Figure 5.192: All metrics versus simulation time of the best N-Body simulation for SDSS 587741532784361481

5.1.33 SDSS 587741534400217110 (Arp 97)

Arp 97 shows very good agreement between its simulations and observational data. Although the initial and optimized N-Body simulations appear nearly indistinguishable, the optimization routine did make a small change in dynamical friction. With this change, the trajectory of the optimized N-Body simulation is a little closer to the SPAM simulations. Morphologically however, the N-Body simulations both show a better agreement with the observational data than the restricted-three body simulations exhibit. This can be seen by the more distinctive right most spiral arm of the secondary galaxy. In any event, the interaction between these two galaxies appears to be weak as they have passed by each other, unlikely to interact any further.

Table 5.65: Identification Information and Merger Zoo summary for SDSS 587741534400217110.

Name	Aliases	RA (hms)	Dec (dms)	Redshift
SDSS 587741534400217110	Arp 97, UGC 7085A	12:05:45.4	+31:03:31.0	0.023366

R_x	R_y	R_z	V_x	V_y	V_z
-0.03825	1.80871	0.30038	-0.2417	0.18815	0.26631

	Primary Galaxy	Secondary Galaxy
mass	0.09611	0.12302
radius	0.54242	0.24137
ϕ	53.17979°	146.64794°
θ	46.33769°	24.75554°
ϵ	0.3	0.3

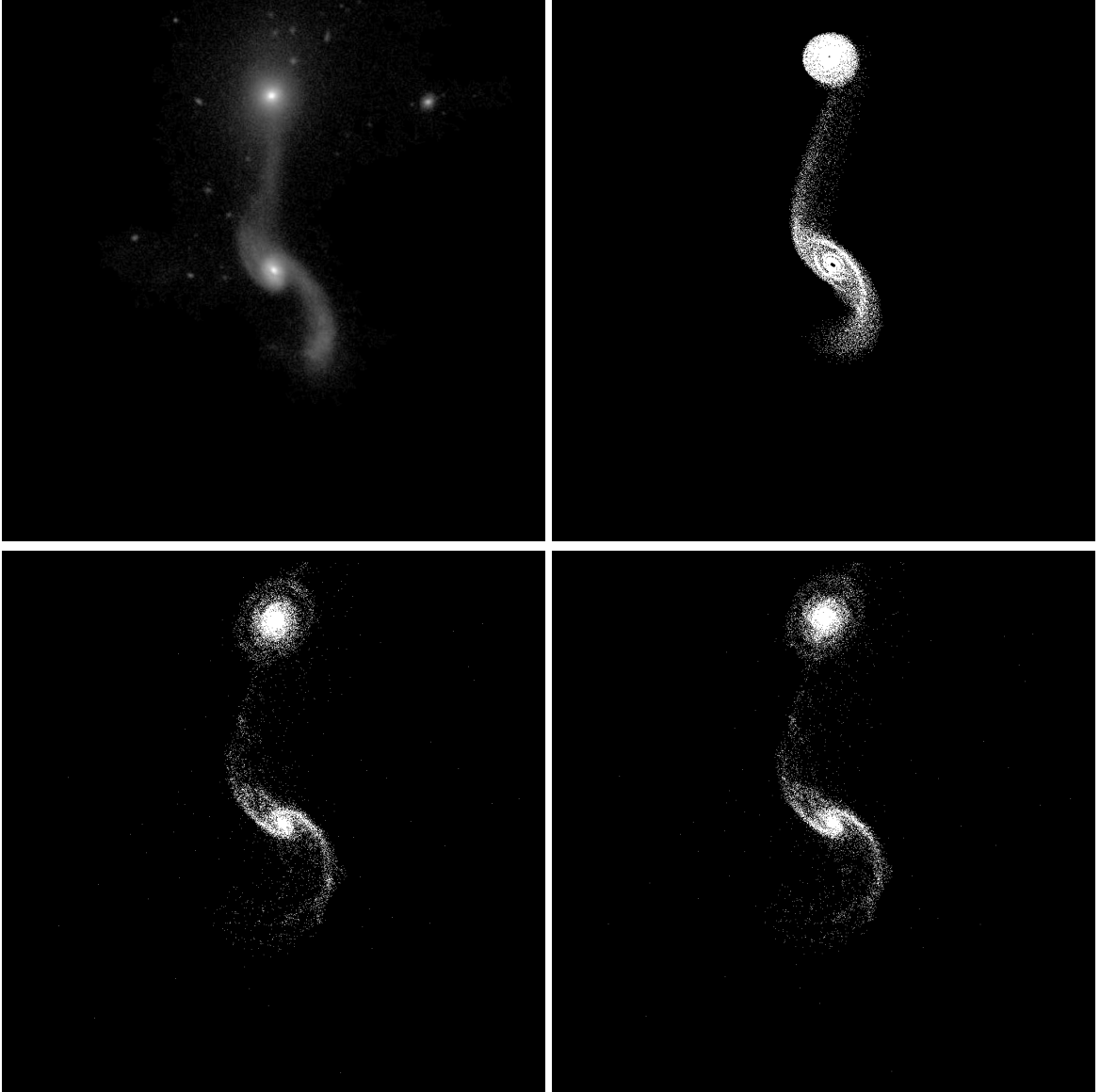


Figure 5.193: Target image (top-left), best SPAM match from Merger Wars (top-right), initial N-Body match (bottom-left), and best N-Body match (bottom-right) for SDSS 587741534400217110

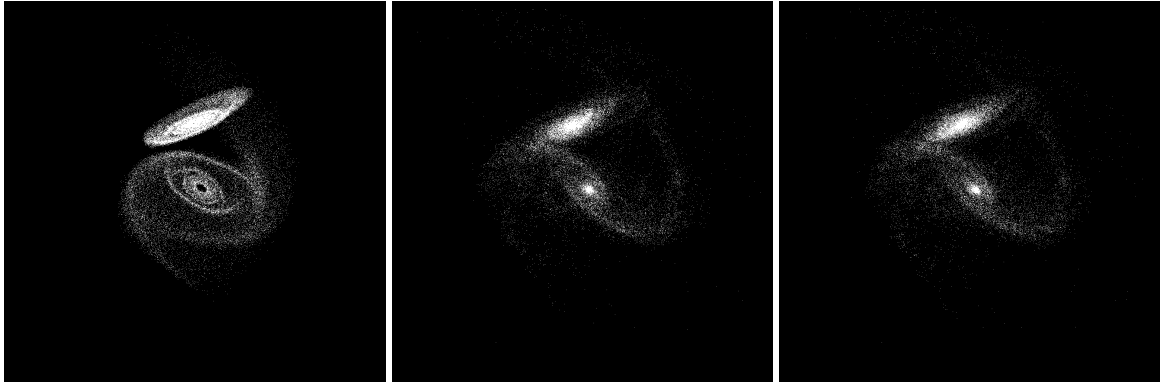


Figure 5.194: XZ projections of best SPAM match from Merger Wars (left), initial N-Body match (middle), and best N-Body match (right) for SDSS 587741534400217110



Figure 5.195: YZ projections of best SPAM match from Merger Wars (left), initial N-Body match (middle), and best N-Body match (right) for SDSS 587741534400217110

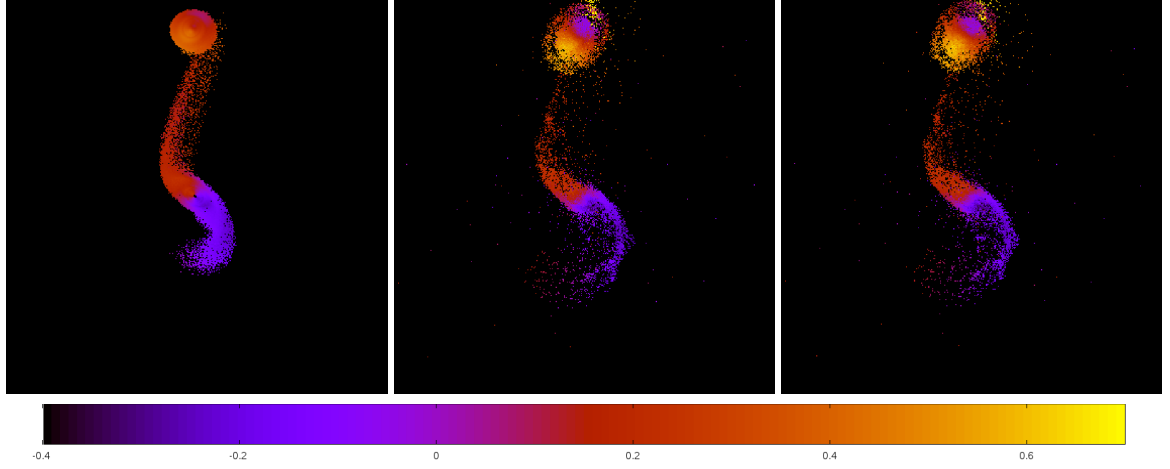


Figure 5.196: Line of sight velocity plots of best SPAM match from Merger Wars (left), initial N-Body match (middle), and best N-Body match (right) for SDSS 587741534400217110

Table 5.66: Orbital Elements & Dynamical Friction for SDSS 587741534400217110

	SPAM Simulation	Initial N-Body Simulation	Best N-Body Simulation
a	-1.001	-0.909	-0.828
e	3.847	4.000	4.315
r_c	2.850	2.726	2.744
i	44.983°	42.772°	43.051°
Ω	81.648°	82.090°	82.150°
ω	329.387°	331.281°	331.026°
ν	43.803°	42.809°	42.954°
t_n	50	49	49
$\ln\Lambda$	N/A	1.00E-03	1.20E-03

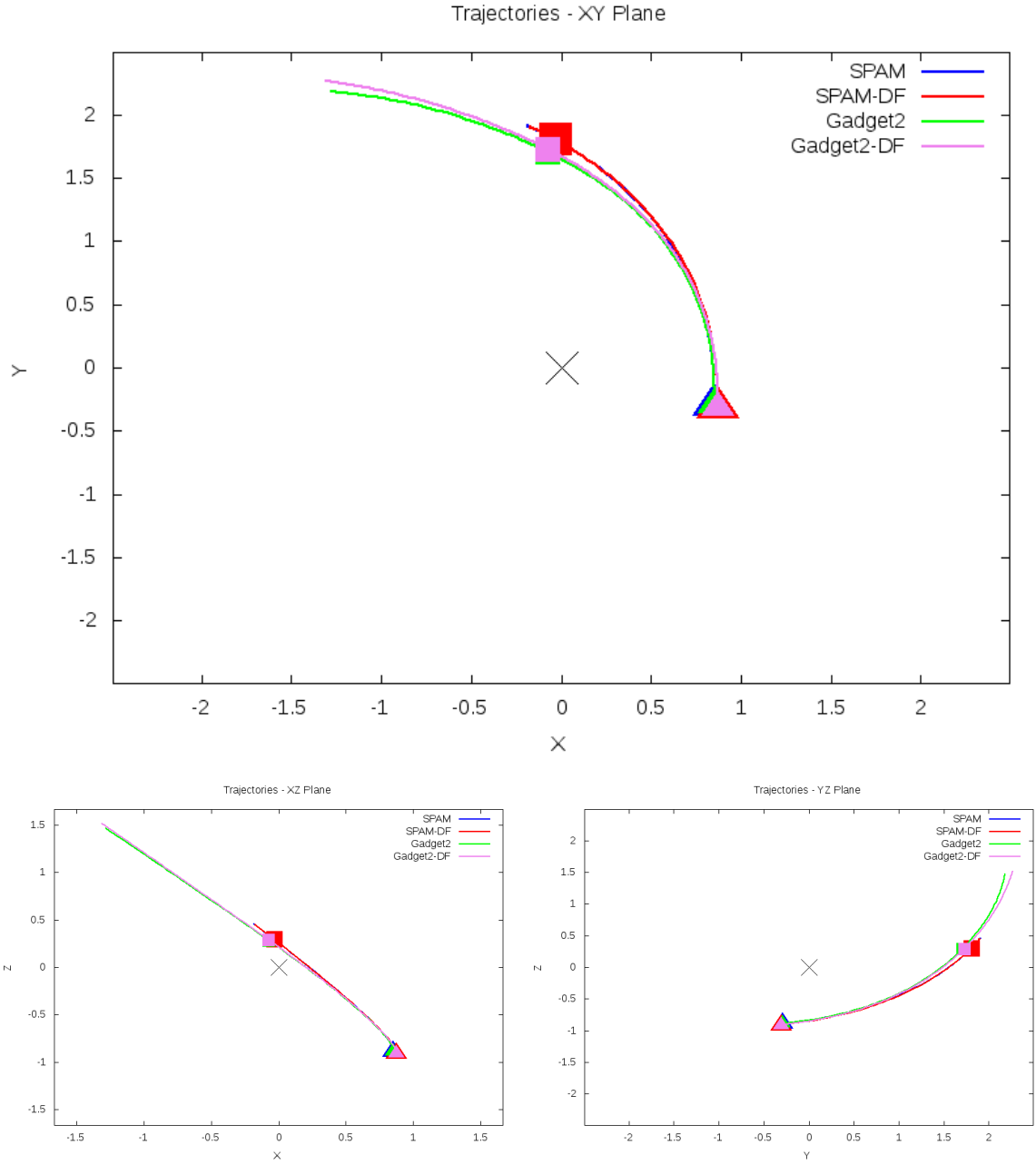


Figure 5.197: Trajectory plots of best SPAM match from Merger Wars, initial N-Body match, and best N-Body match for SDSS 587741534400217110

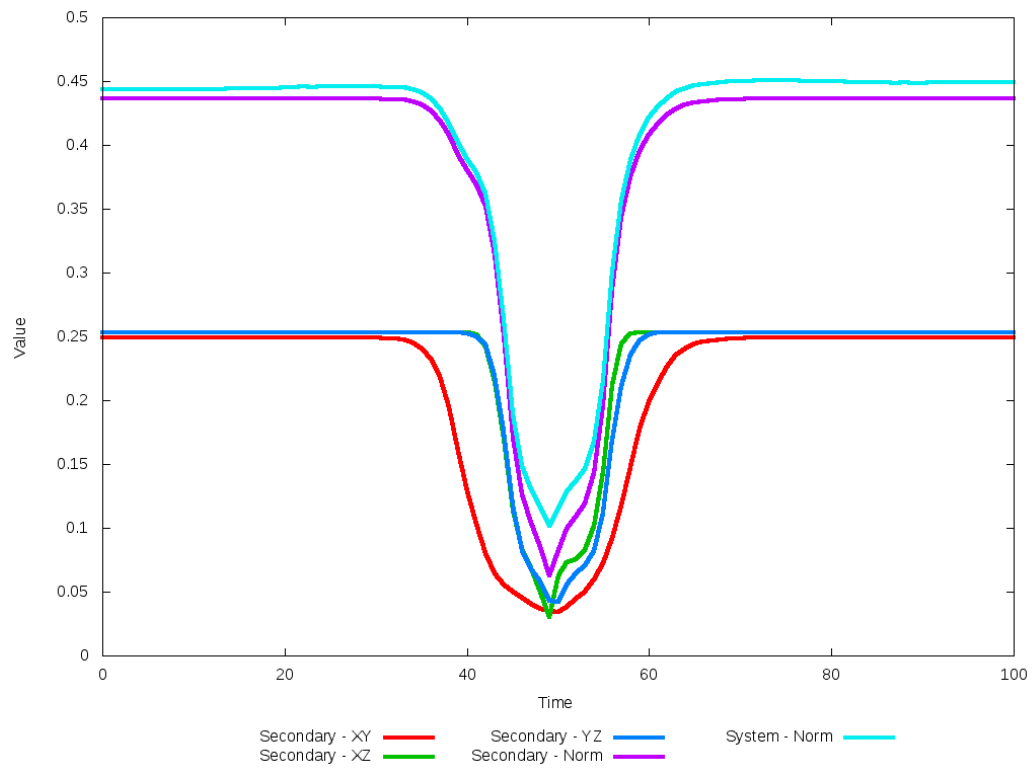
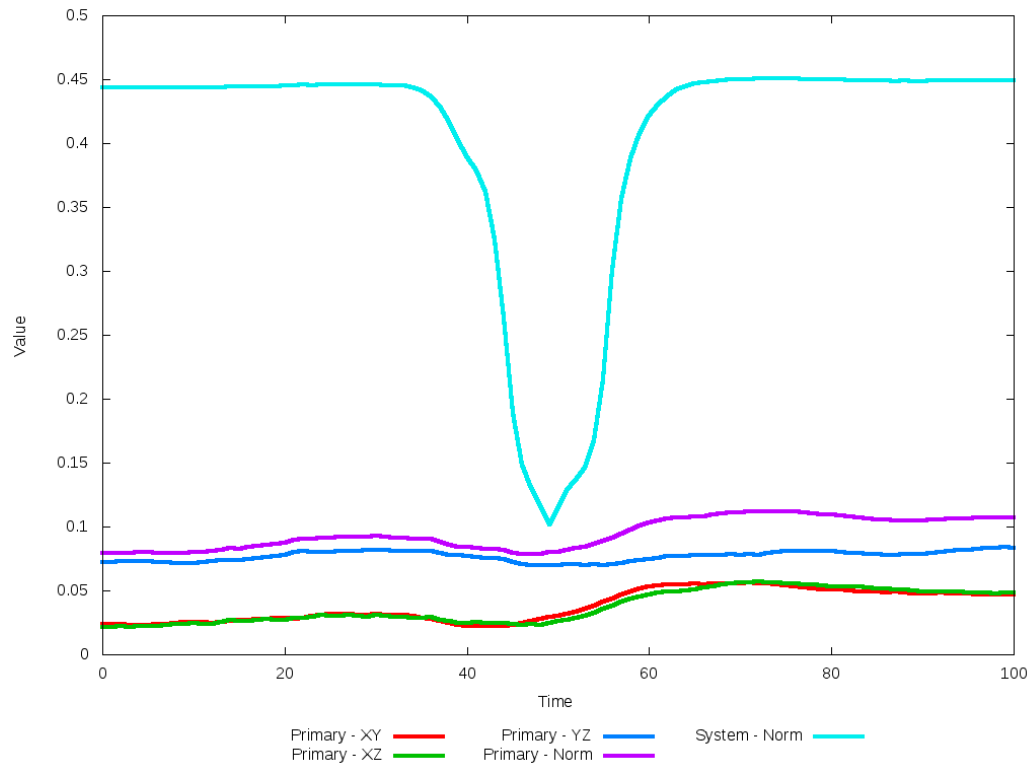


Figure 5.198: All metrics versus simulation time of the best N-Body simulation for SDSS 587741534400217110

5.1.34 SDSS 587741602030026825 (Arp 305)

Arp 305 shows very good agreement between its simulations and observational data. Although the initial and optimized N-Body simulations appear nearly indistinguishable, the optimization routine did make a small change in dynamical friction. With this change, the trajectories of the optimized simulation and the SPAM simulations are nearly indistinguishable. The primary discrepancy between the simulations and observational data is that both that data and the SPAM simulations do not show as broad of tidal features in the primary galaxy as the N-Body simulations show. With additional physics, the N-Body simulations may reduce their appearance. In any event, the interaction between these two galaxies appears to be weak as they have passed by each other, unlikely to interact any further.

Table 5.67: Identification Information and Merger Zoo summary for SDSS 587741602030026825.

Name	Aliases	RA (hms)	Dec (dms)	Redshift
SDSS 587741602030026825	Arp 305, NGC 4016/4017	11:58:45.6	+27:27:07.3	0.011521

R_x	R_y	R_z	V_x	V_y	V_z
2.96778	3.61902	-0.12375	0.30078	0.67945	0.07129

	Primary Galaxy	Secondary Galaxy
mass	0.33782	0.18678
radius	0.70035	0.46849
ϕ	45.8125°	166.875°
θ	286.21118°	234.7826°
ϵ	0.3	0.3

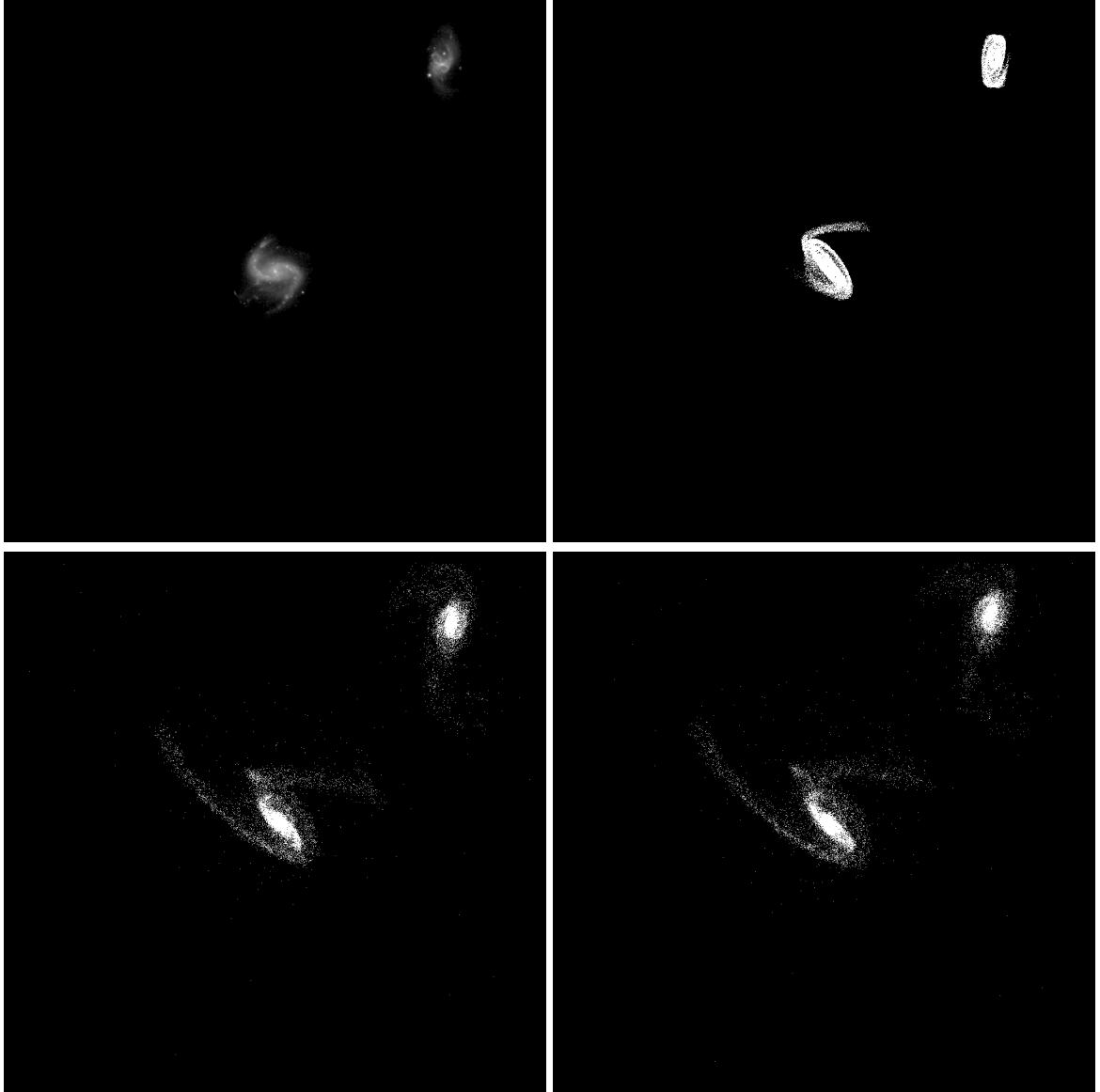


Figure 5.199: Target image (top-left), best SPAM match from Merger Wars (top-right), initial N-Body match (bottom-left), and best N-Body match (bottom-right) for SDSS 587741602030026825

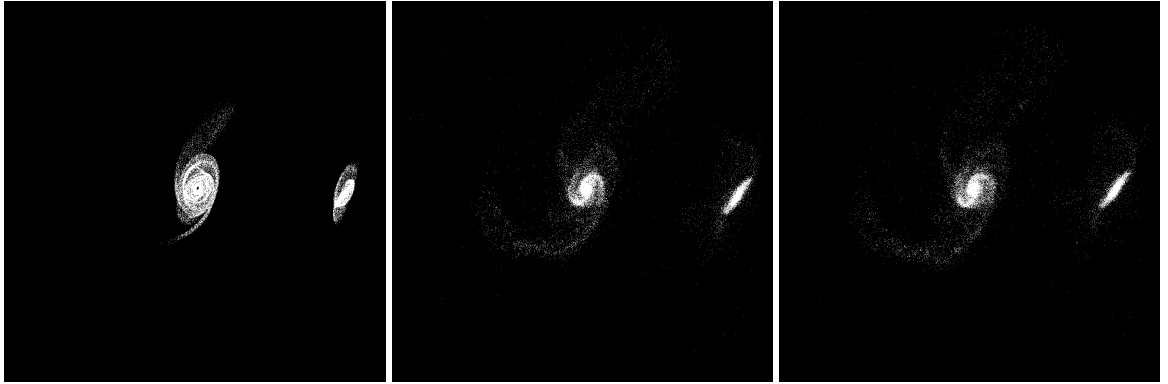


Figure 5.200: XZ projections of best SPAM match from Merger Wars (left), initial N-Body match (middle), and best N-Body match (right) for SDSS 587741602030026825

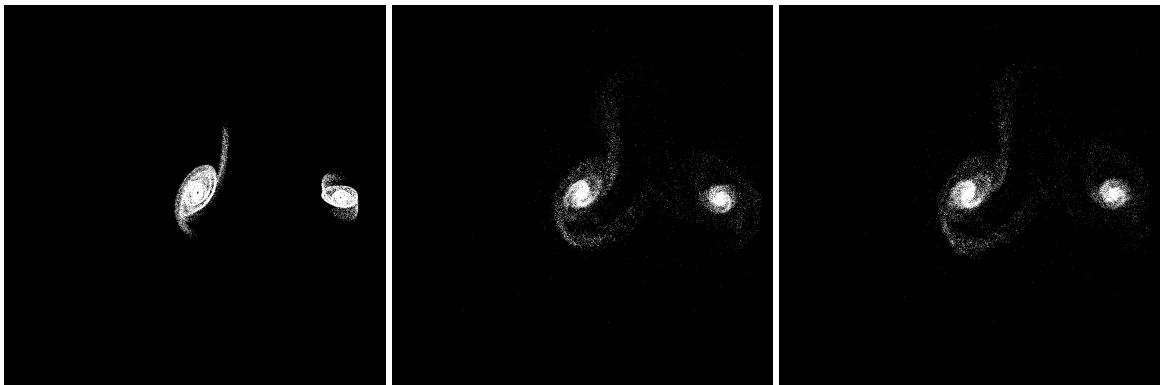


Figure 5.201: YZ projections of best SPAM match from Merger Wars (left), initial N-Body match (middle), and best N-Body match (right) for SDSS 587741602030026825

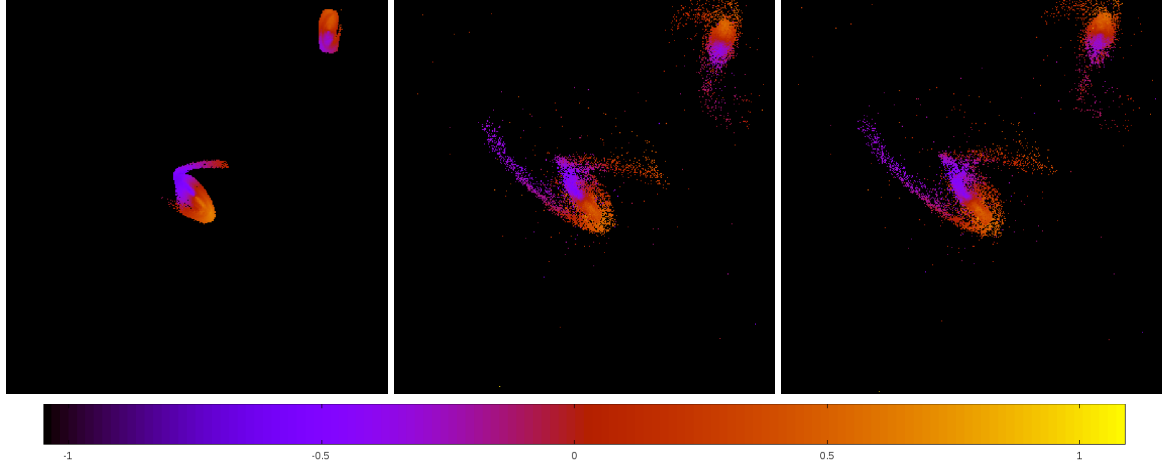


Figure 5.202: Line of sight velocity plots of best SPAM match from Merger Wars (left), initial N-Body match (middle), and best N-Body match (right) for SDSS 587741602030026825

Table 5.68: Orbital Elements & Dynamical Friction for SDSS 587741602030026825

	SPAM Simulation	Initial N-Body Simulation	Best N-Body Simulation
a	-0.476	-0.506	-0.637
e	6.112	5.703	4.807
r_c	2.431	2.378	2.425
i	24.505°	25.677°	24.764°
Ω	53.972°	52.022°	52.013°
ω	274.309°	272.078°	274.312°
ν	82.037°	82.406°	83.375°
t_n	50	50	52
$\ln\Lambda$	N/A	1.00E-03	5.00E-04

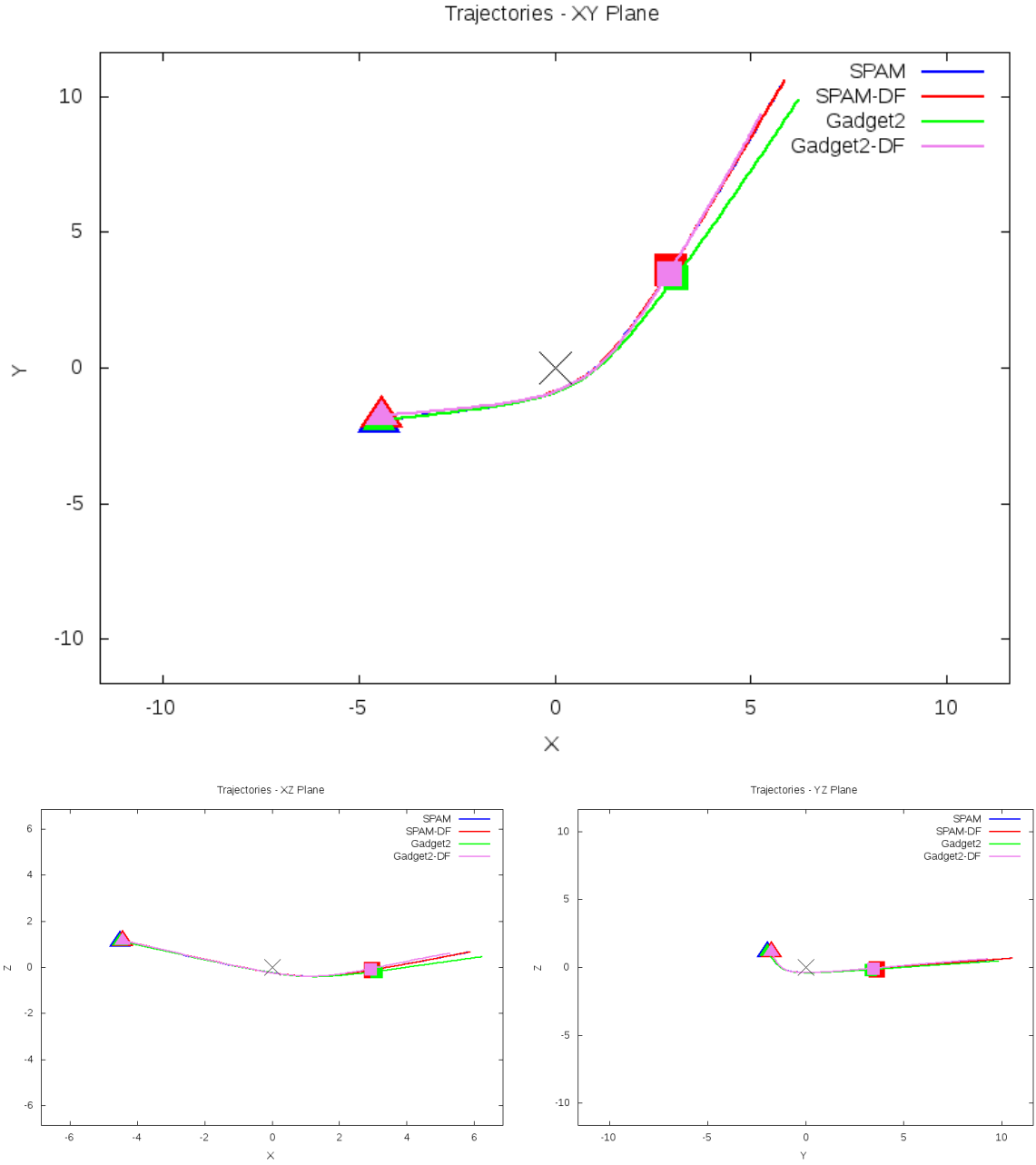


Figure 5.203: Trajectory plots of best SPAM match from Merger Wars, initial N-Body match, and best N-Body match for SDSS 587741602030026825

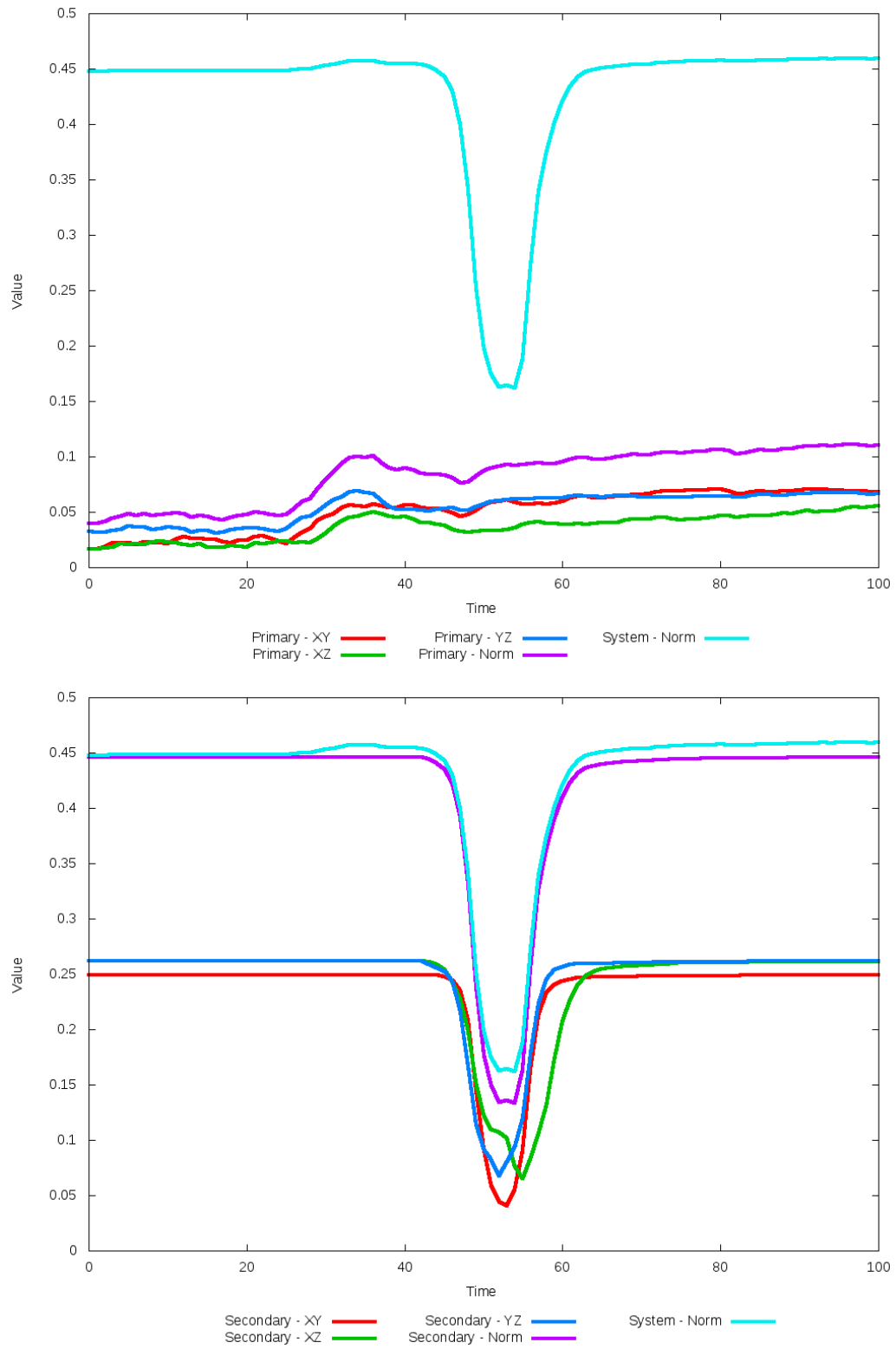


Figure 5.204: All metrics versus simulation time of the best N-Body simulation for SDSS 587741602030026825

5.1.35 SDSS 587741722819493915 (Arp 106)

Arp 106's N-Body simulations exhibit only a moderate quality of fit to observational data and SPAM simulation. Although the primary galaxy morphologically looks good, the location of the secondary galaxy is poorly placed in the N-Body simulations based on the XY projections, plus it lacks strong apparent tidal features. However, observations of the XZ and YZ projections show remarkably better agreement, both in position and tidal features. The dynamical friction found by the optimization routine has it approaching zero, yet that sets the N-Body simulation on an orbit that decays more quickly. It is likely that the optimization routine found a local minima and warrants further review. The state vector provided to our pipeline from Merger Wars should be reviewed for other candidates.

Table 5.69: Identification Information and Merger Zoo summary for SDSS 587741722819493915.

Name	Aliases	RA (hms)	Dec (dms)	Redshift
SDSS 587741722819493915	Arp 106, NGC 4211	12:15:35.8	+28:10:39.8	0.022012

R_x	R_y	R_z	V_x	V_y	V_z
-0.42567	-0.83668	-1.93196	-0.4365	0.00717	-1.09404

	Primary Galaxy	Secondary Galaxy
mass	1.33245	0.1993
radius	0.59839	0.1963
ϕ	108.92933°	39.06386°
θ	319.92442°	160.84304°
ϵ	0.3	0.3

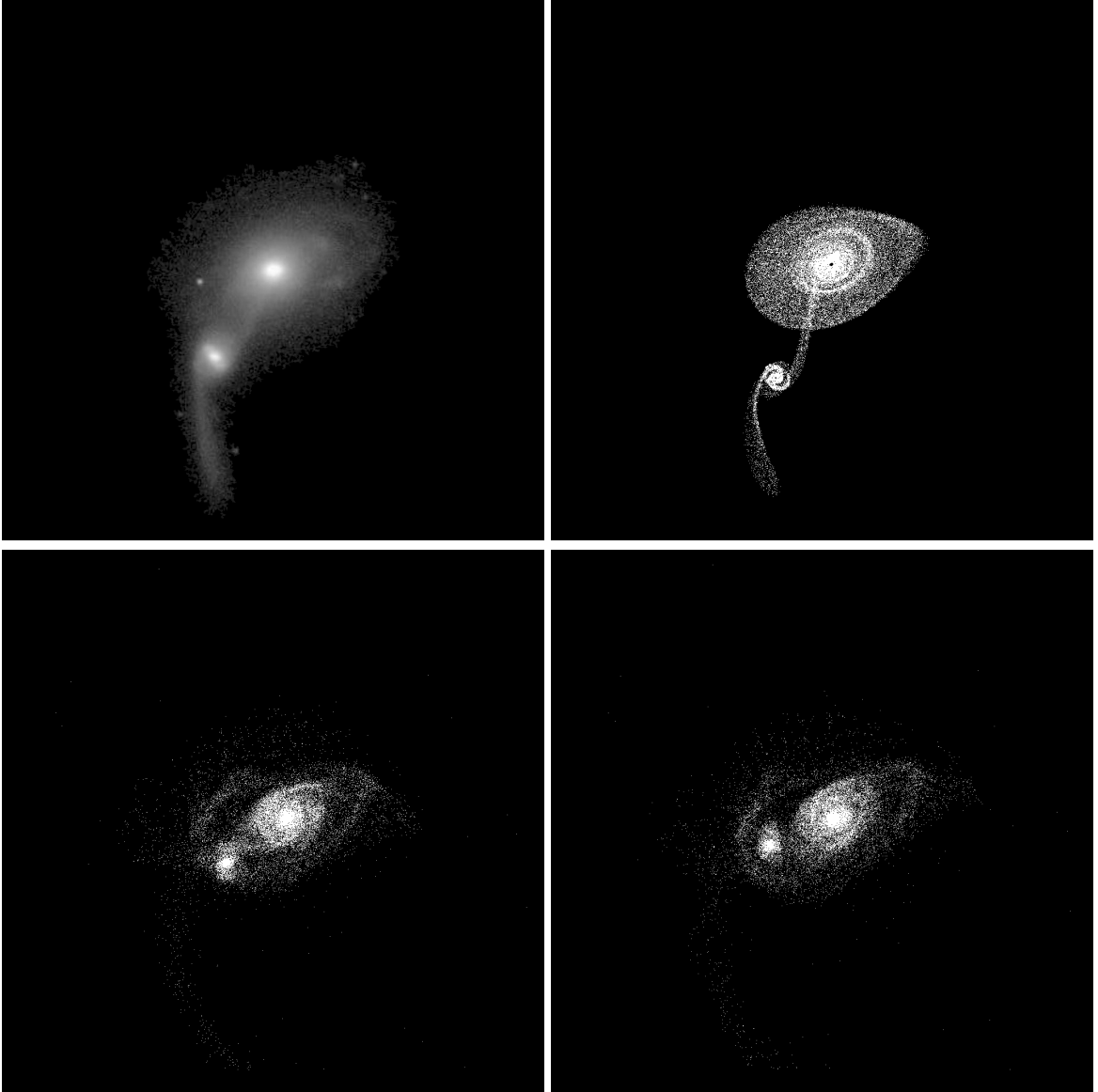


Figure 5.205: Target image (top-left), best SPAM match from Merger Wars (top-right), initial N-Body match (bottom-left), and best N-Body match (bottom-right) for SDSS 587741722819493915

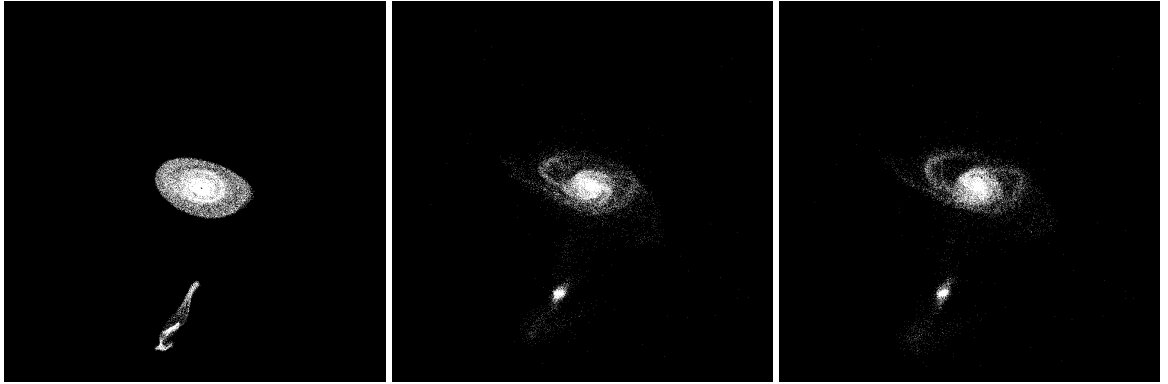


Figure 5.206: XZ projections of best SPAM match from Merger Wars (left), initial N-Body match (middle), and best N-Body match (right) for SDSS 587741722819493915

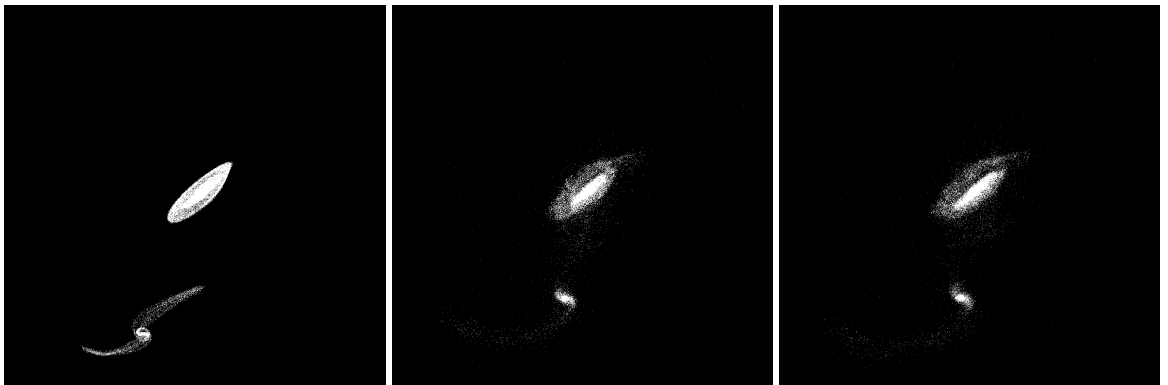


Figure 5.207: YZ projections of best SPAM match from Merger Wars (left), initial N-Body match (middle), and best N-Body match (right) for SDSS 587741722819493915

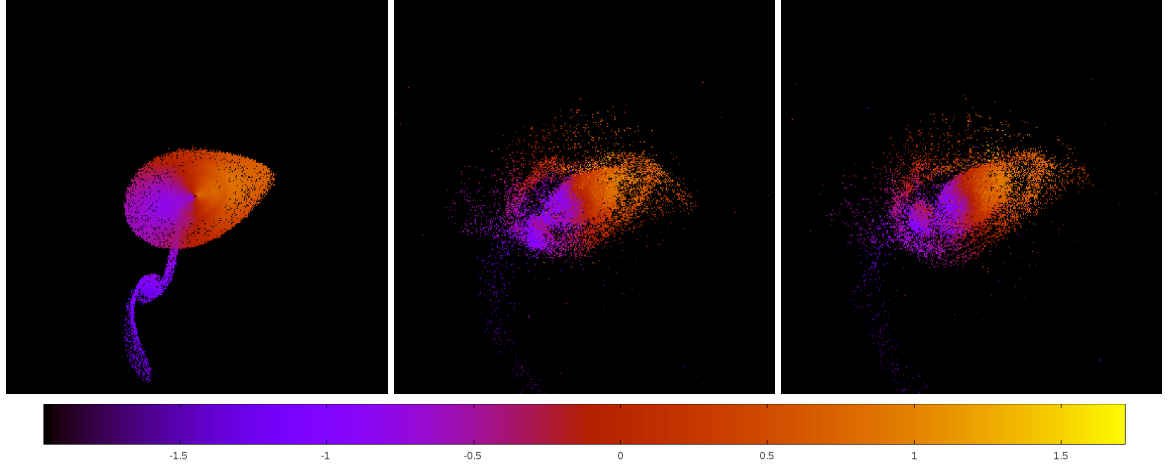


Figure 5.208: Line of sight velocity plots of best SPAM match from Merger Wars (left), initial N-Body match (middle), and best N-Body match (right) for SDSS 587741722819493915

Table 5.70: Orbital Elements & Dynamical Friction for SDSS 587741722819493915

	SPAM Simulation	Initial N-Body Simulation	Best N-Body Simulation
a	-0.283	-0.550	-0.890
e	6.897	3.874	2.817
r_c	1.668	1.580	1.618
i	110.161°	110.517°	110.252°
Ω	112.115°	114.778°	113.674°
ω	180.794°	196.955°	199.766°
ν	72.572°	65.476°	67.001°
t_n	50	47	48
$\ln\Lambda$	N/A	1.00E-03	0.00E+00

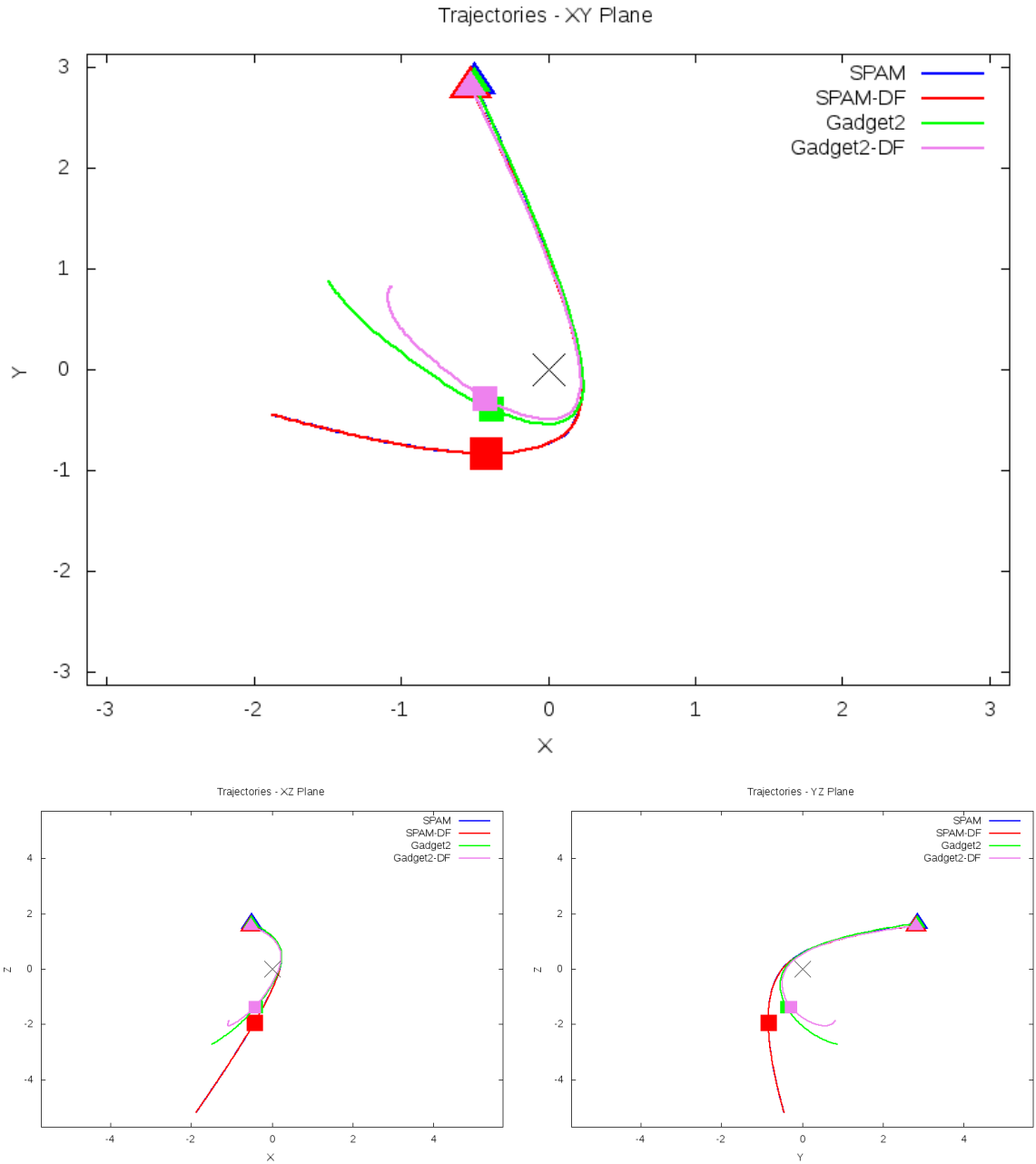


Figure 5.209: Trajectory plots of best SPAM match from Merger Wars, initial N-Body match, and best N-Body match for SDSS 587741722819493915

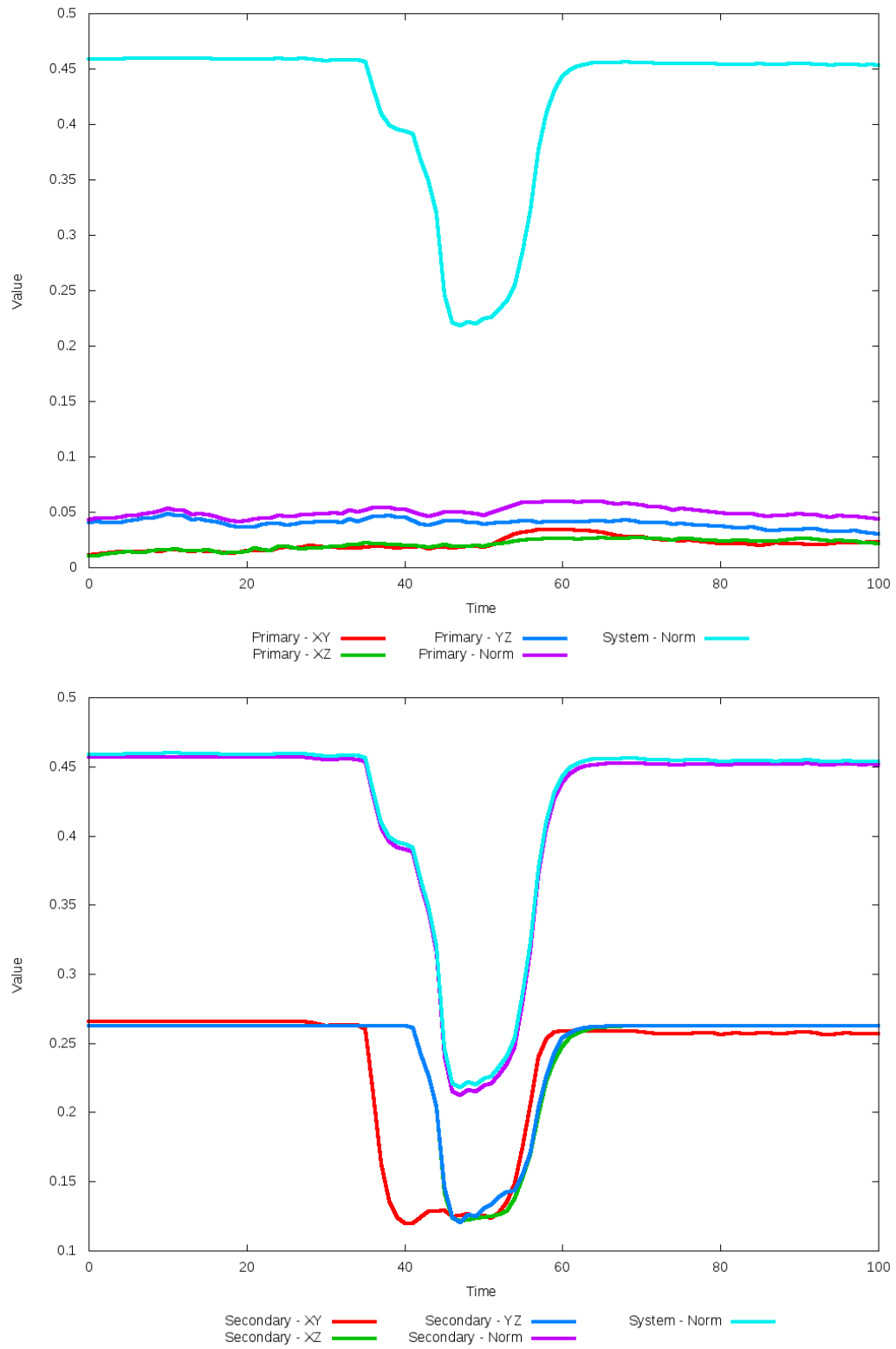


Figure 5.210: All metrics versus simulation time of the best N-Body simulation for SDSS 587741722819493915

5.1.36 SDSS 587741817851674654 (NGC 2802/2803)

NGC 2802/2803 shows very good agreement between its simulations and observational data. Although the initial and optimized N-Body simulations appear nearly indistinguishable, the optimization routine did make a small change in dynamical friction. With this change, the trajectories of the optimized simulation is minutely closer to that of the SPAM simulations. In any event, the interaction between these two galaxies appears to be weak as they have passed by each other, unlikely to interact any further.

Table 5.71: Identification Information and Merger Zoo summary for SDSS 587741817851674654.

Name	Aliases	RA (hms)	Dec (dms)	Redshift
SDSS 587741817851674654	NGC 2802/2803, UGC 4897	9:16:41.4	+18:57:49.3	0.02914

R_x	R_y	R_z	V_x	V_y	V_z
1.06338	1.04559	1.63578	1.00283	0.31386	1.55365

	Primary Galaxy	Secondary Galaxy
mass	0.56343	0.23131
radius	0.9187	0.50148
ϕ	108.04444°	30.31226°
θ	327.91147°	146.78275°
ϵ	0.3	0.3

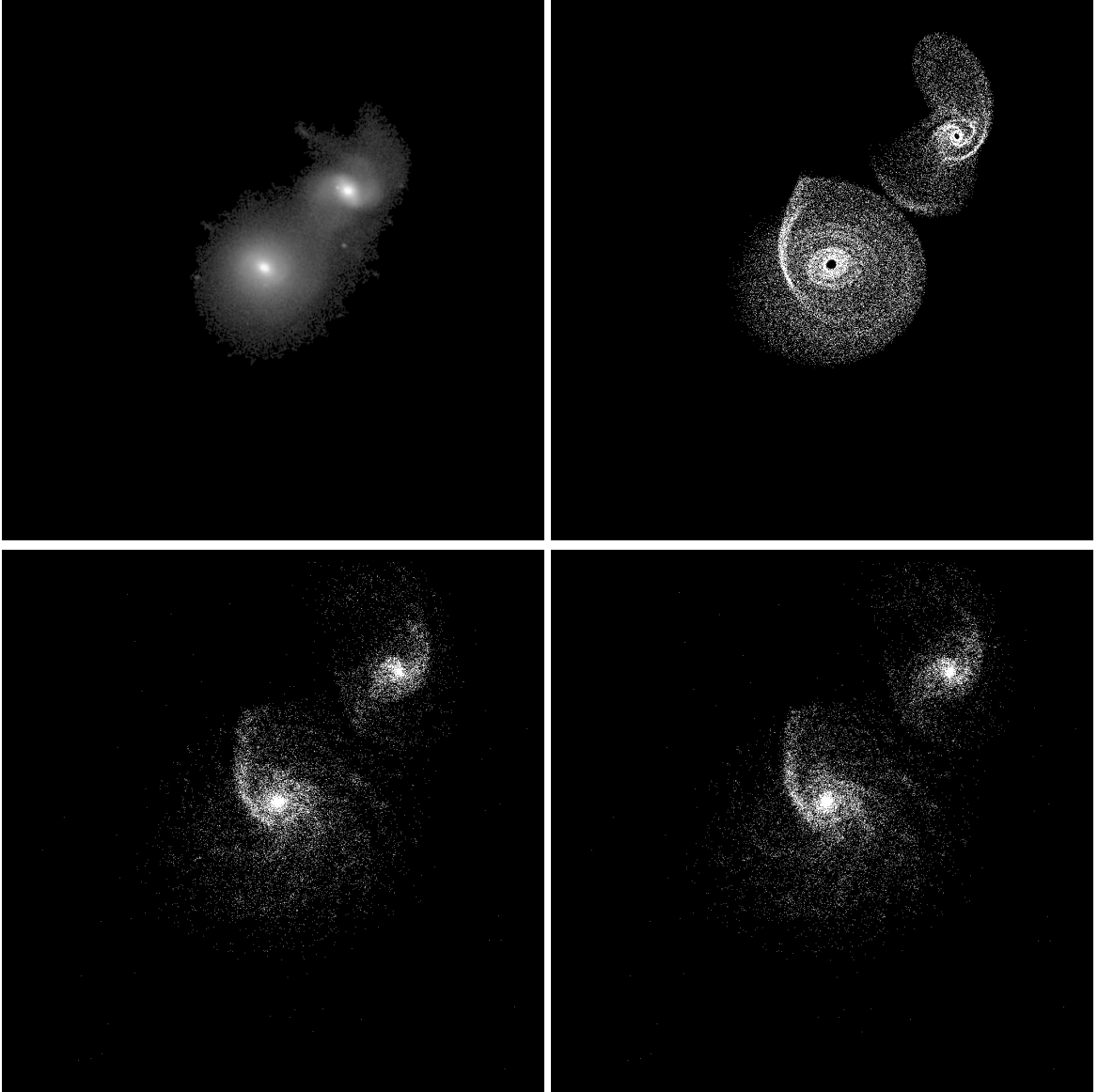


Figure 5.211: Target image (top-left), best SPAM match from Merger Wars (top-right), initial N-Body match (bottom-left), and best N-Body match (bottom-right) for SDSS 587741817851674654

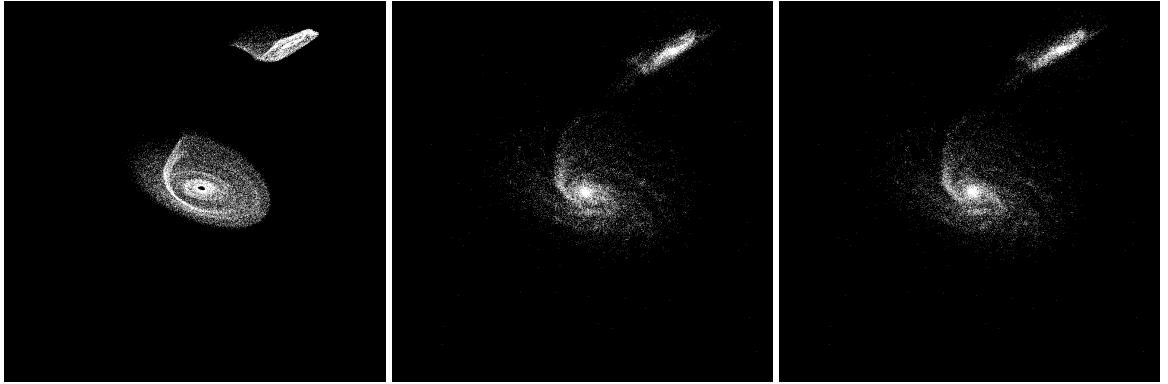


Figure 5.212: XZ projections of best SPAM match from Merger Wars (left), initial N-Body match (middle), and best N-Body match (right) for SDSS 587741817851674654

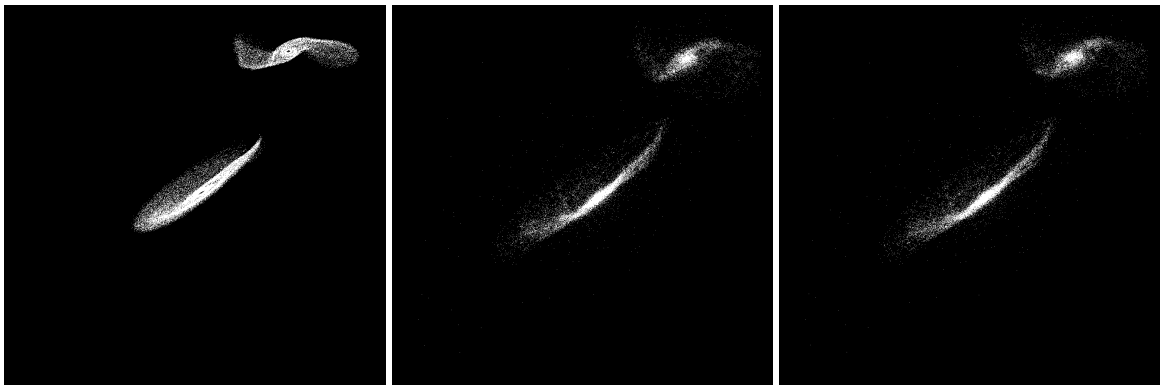


Figure 5.213: YZ projections of best SPAM match from Merger Wars (left), initial N-Body match (middle), and best N-Body match (right) for SDSS 587741817851674654

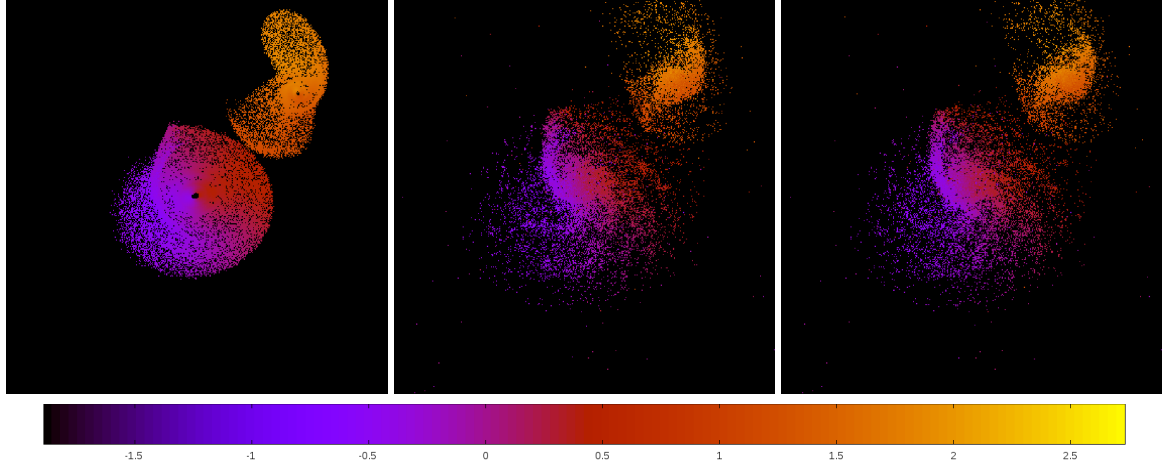


Figure 5.214: Line of sight velocity plots of best SPAM match from Merger Wars (left), initial N-Body match (middle), and best N-Body match (right) for SDSS 587741817851674654

Table 5.72: Orbital Elements & Dynamical Friction for SDSS 587741817851674654

	SPAM Simulation	Initial N-Body Simulation	Best N-Body Simulation
a	-0.097	-0.100	-0.100
e	14.824	14.339	14.390
r_c	1.345	1.334	1.334
i	122.753°	122.626°	122.628°
Ω	89.396°	90.492°	90.454°
ω	346.373°	340.285°	340.285°
ν	75.111°	74.973°	75.249°
t_n	50	50	50
$\ln\Lambda$	N/A	1.00E-03	1.20E-03

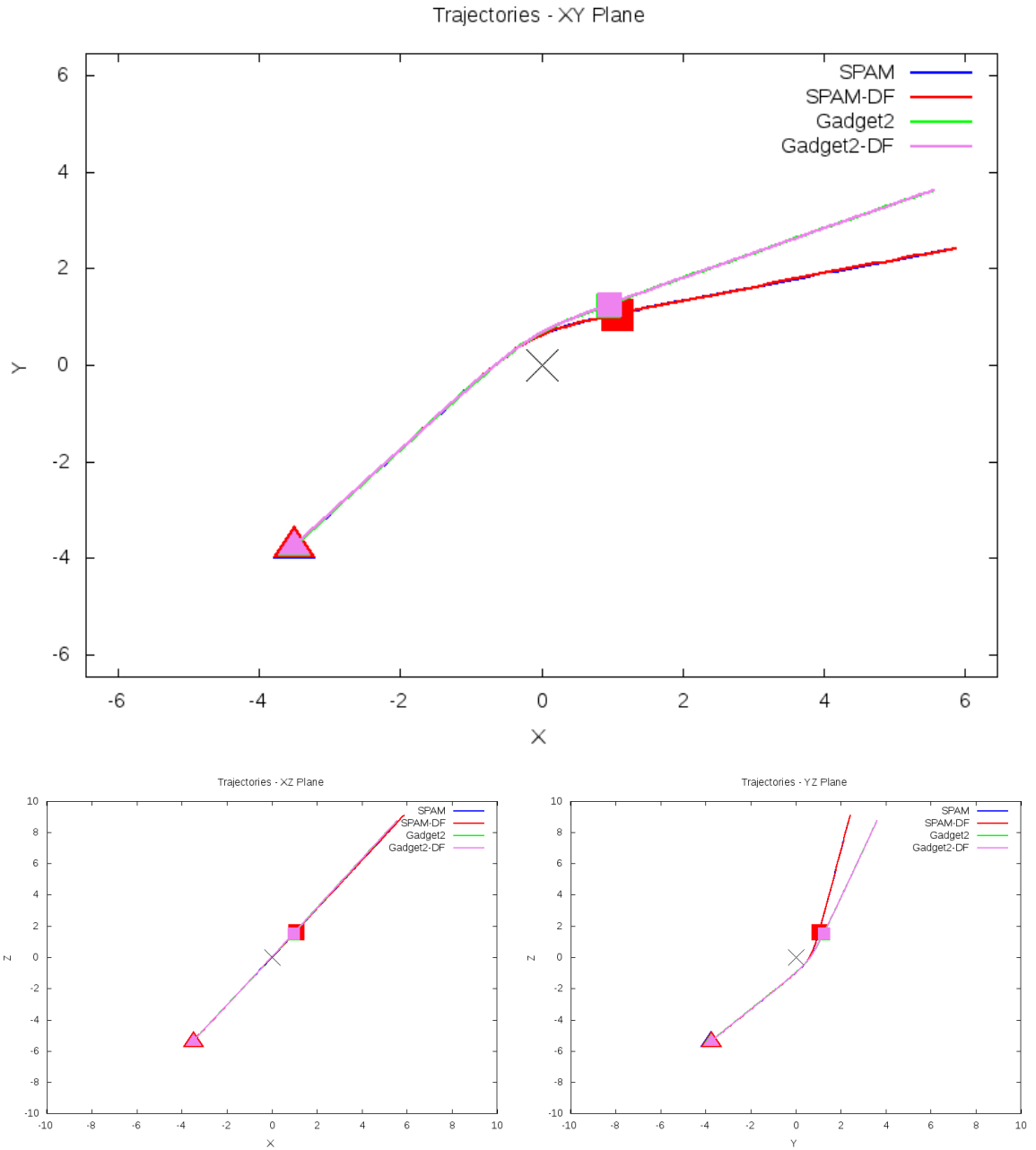


Figure 5.215: Trajectory plots of best SPAM match from Merger Wars, initial N-Body match, and best N-Body match for SDSS 587741817851674654

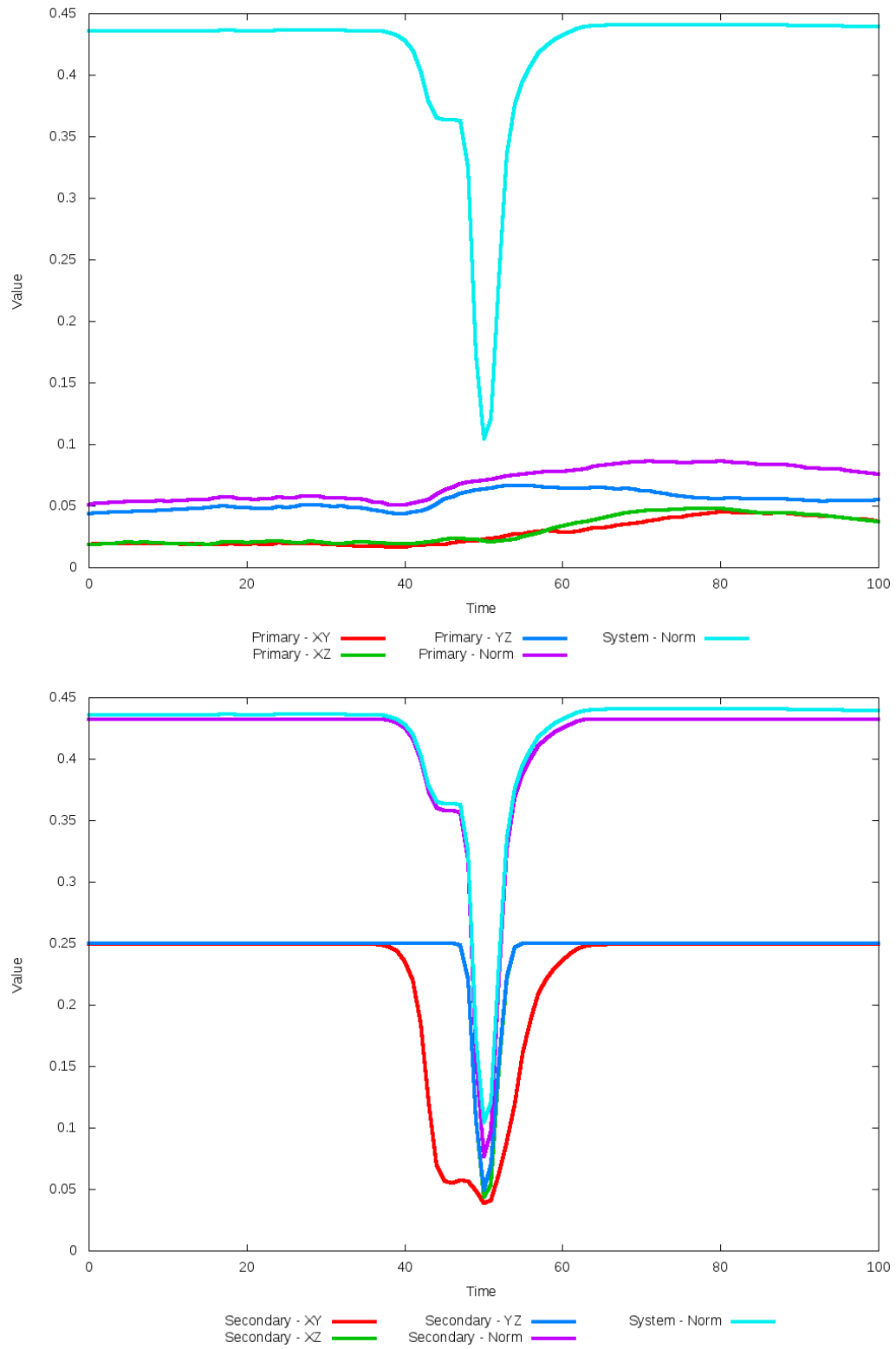


Figure 5.216: All metrics versus simulation time of the best N-Body simulation for SDSS 587741817851674654

5.1.37 SDSS 587741829658181698 (Arp 301)

Arp 301 shows very good agreement between its simulations and observational data. Although the initial and optimized N-Body simulations appear nearly indistinguishable, the optimization routine did make a small change in dynamical friction. With this change, the trajectories of the optimized simulation is minutely closer to that of the SPAM simulations. The primary difference between the N-Body simulations and the observational data is a broader tidal tail in the primary galaxy. In any event, the interaction between these two galaxies appears to be weak as they have passed by each other.

Table 5.73: Identification Information and Merger Zoo summary for SDSS 587741829658181698.

Name	Aliases	RA (hms)	Dec (dms)	Redshift
SDSS 587741829658181698	Arp 301, UGC 6207	11:09:51.4	+24:15:41.8	0.020591

R_x	R_y	R_z	V_x	V_y	V_z
-1.15174	-0.32733	-1.2717	-1.85991	0.14873	-0.01861

	Primary Galaxy	Secondary Galaxy
mass	1.13467	1.49592
radius	0.68248	1.11228
ϕ	9.1875°	78.0°
θ	160.99378°	252.6708°
ϵ	0.3	0.3

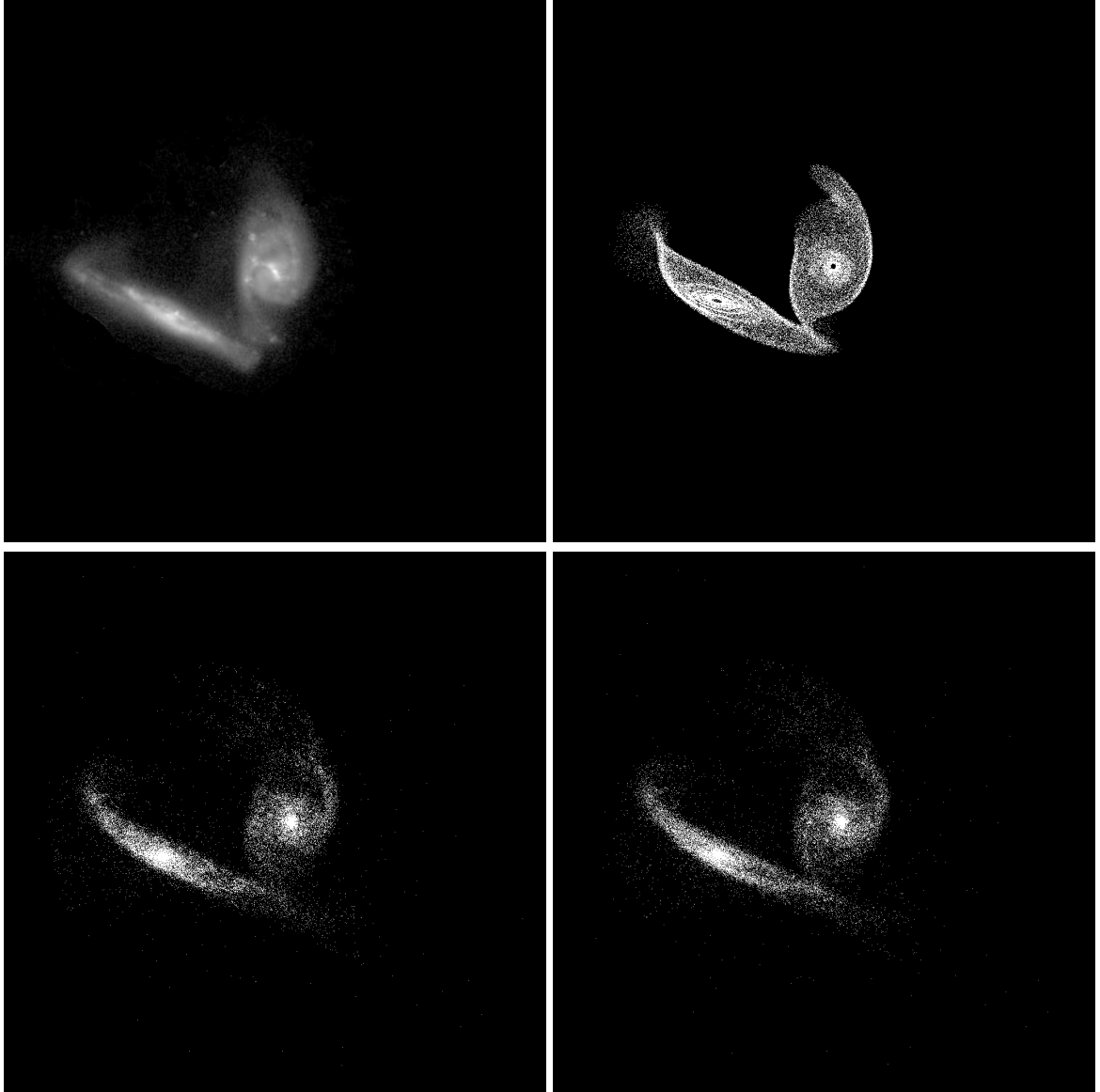


Figure 5.217: Target image (top-left), best SPAM match from Merger Wars (top-right), initial N-Body match (bottom-left), and best N-Body match (bottom-right) for SDSS 587741829658181698

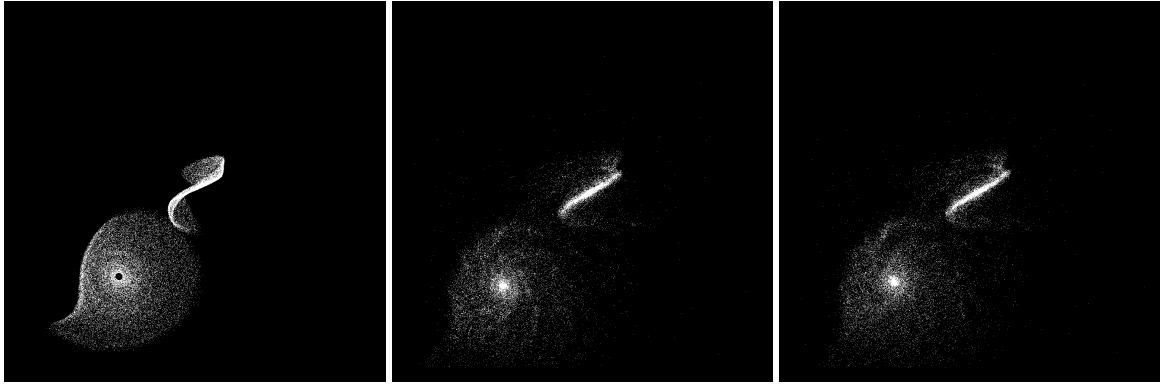


Figure 5.218: XZ projections of best SPAM match from Merger Wars (left), initial N-Body match (middle), and best N-Body match (right) for SDSS 587741829658181698

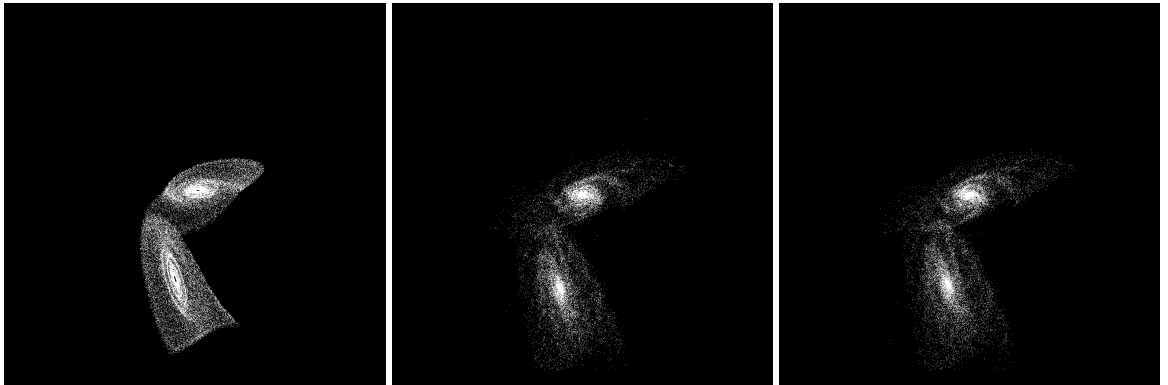


Figure 5.219: YZ projections of best SPAM match from Merger Wars (left), initial N-Body match (middle), and best N-Body match (right) for SDSS 587741829658181698

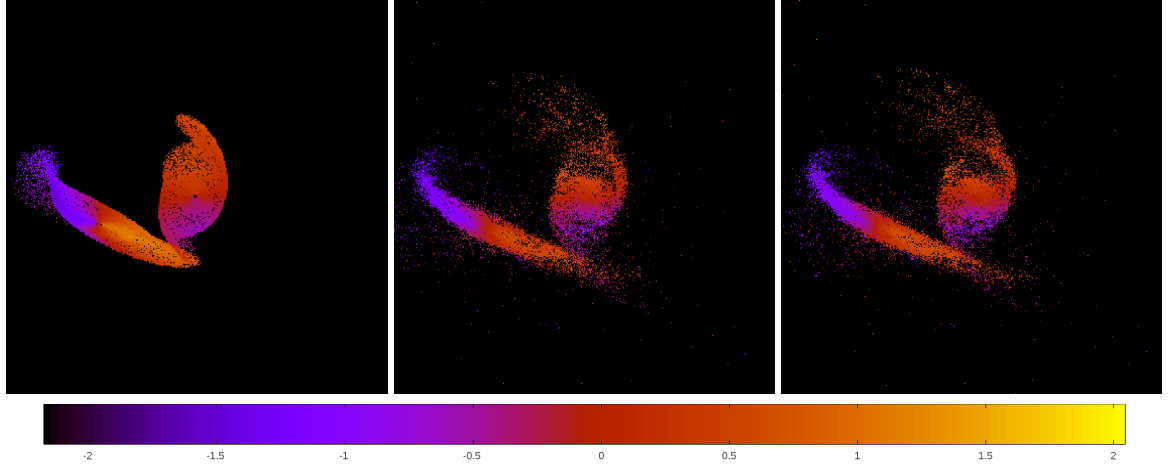


Figure 5.220: Line of sight velocity plots of best SPAM match from Merger Wars (left), initial N-Body match (middle), and best N-Body match (right) for SDSS 587741829658181698

Table 5.74: Orbital Elements & Dynamical Friction for SDSS 587741829658181698

	SPAM Simulation	Initial N-Body Simulation	Best N-Body Simulation
a	-0.470	-0.520	-0.622
e	6.438	5.946	5.116
r_c	2.559	2.573	2.558
i	108.350°	108.447°	108.417°
Ω	175.238°	174.195°	174.182°
ω	263.608°	251.980°	253.209°
ν	46.301°	51.233°	49.249°
t_n	50	51	51
$\ln\Lambda$	N/A	1.00E-03	4.50E-04

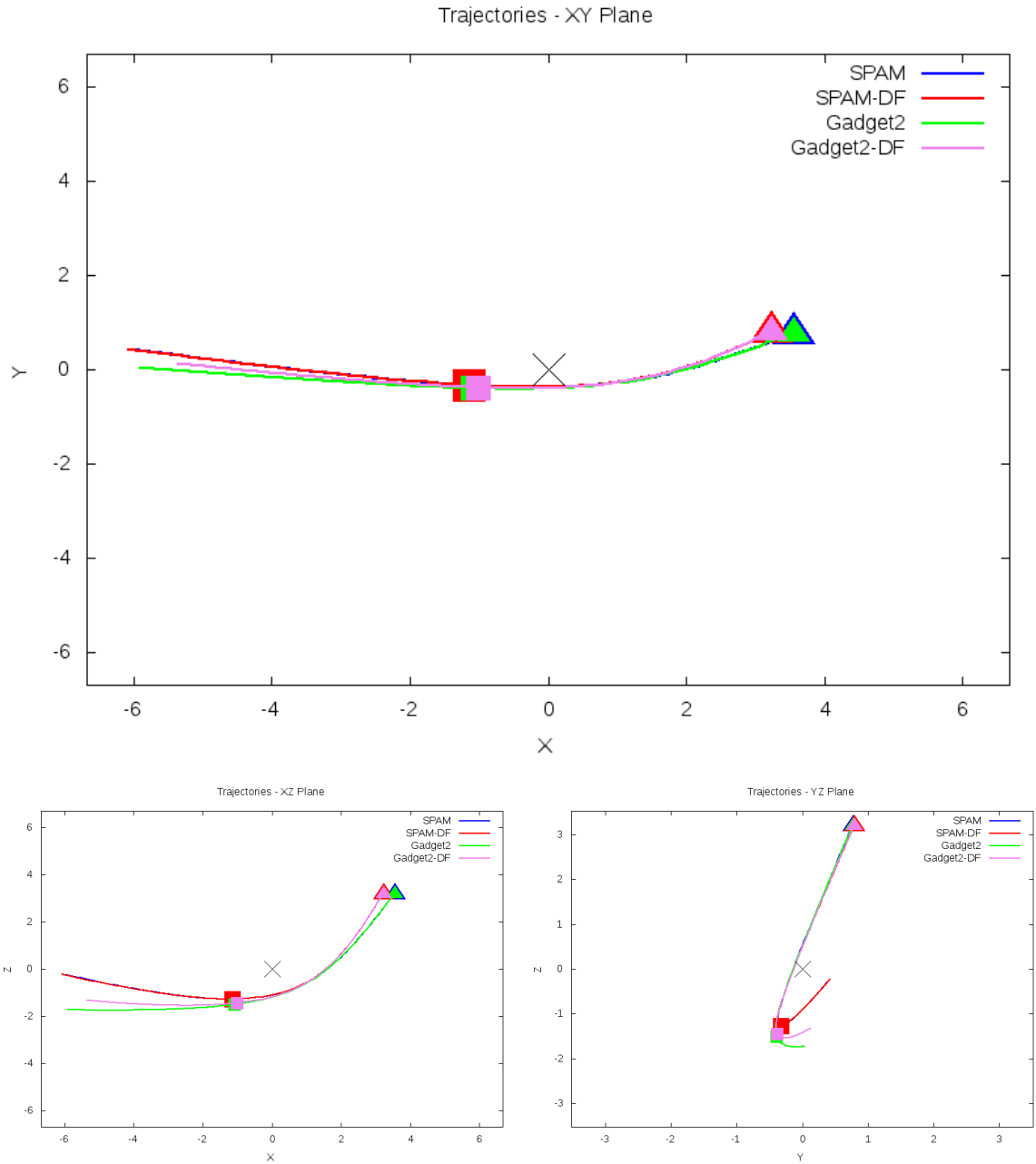


Figure 5.221: Trajectory plots of best SPAM match from Merger Wars, initial N-Body match, and best N-Body match for SDSS 587741829658181698

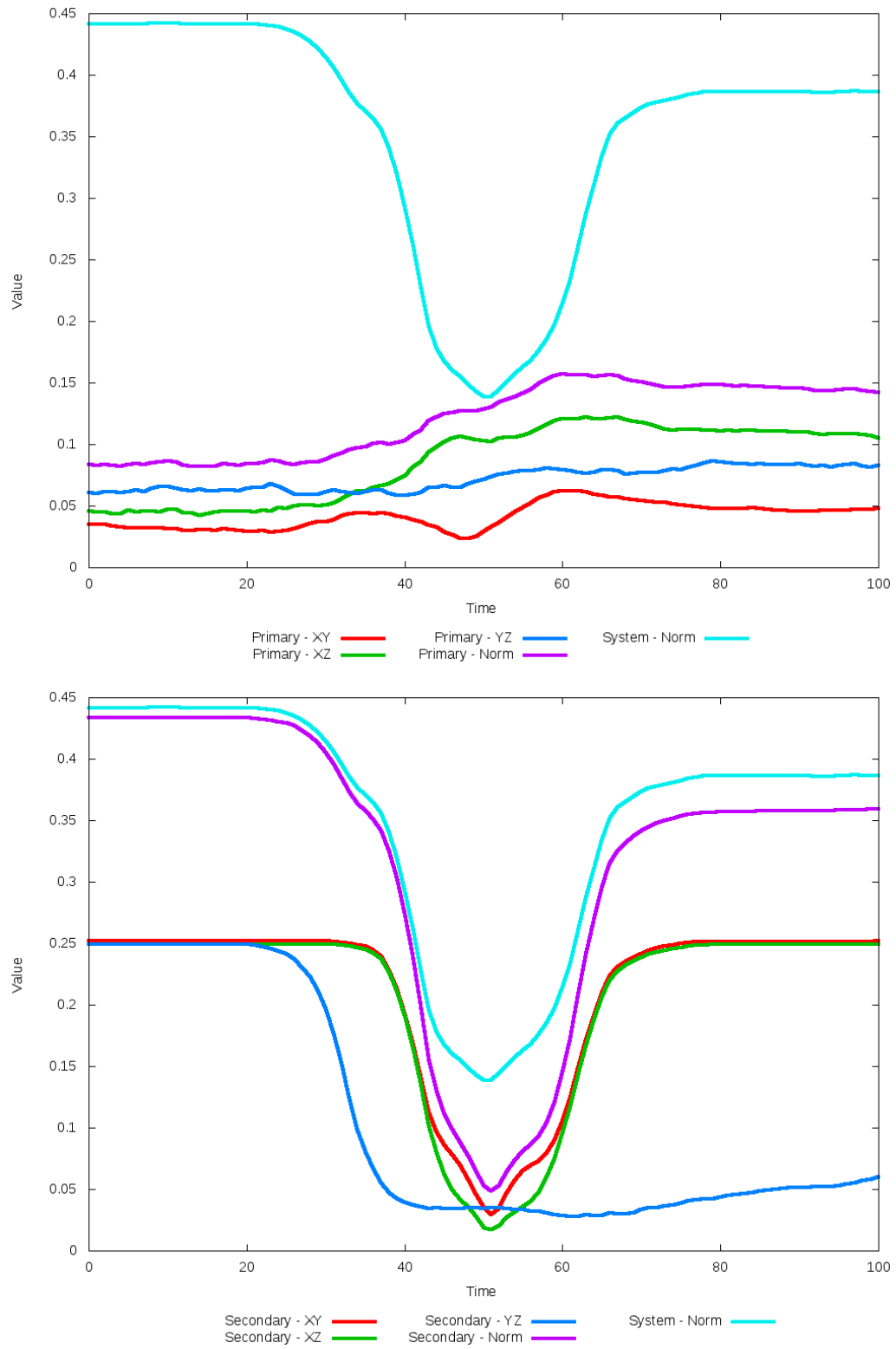


Figure 5.222: All metrics versus simulation time of the best N-Body simulation for SDSS 587741829658181698

5.1.38 SDSS 587742010583941189 (Arp 89)

Arp 89 shows a remarkable improvement in its quality of fit to the SPAM simulation from Merger Wars when dynamical friction is optimized. However, the optimization routine found the best agreement between the N-Body simulation and SPAM simulation with a dynamical friction value of essentially zero. Although the change in dynamical friction did not cause any appreciable change in the starting location of the secondary galaxy, it did change the initial velocity which in turn changed the trajectory, resulting in a very good match. There is however a small discrepancy in the line of site velocity of the end of the left most tail of the primary galaxy whereby SPAM predicts more negative velocities.

Table 5.75: Identification Information and Merger Zoo summary for SDSS 587742010583941189.

Name	Aliases	RA (hms)	Dec (dms)	Redshift
SDSS 587742010583941189	Arp 89, NGC 2648	8:42:39.8	+14:17:08.2	0.006871

R_x	R_y	R_z	V_x	V_y	V_z
-0.98742	-0.65926	-2.46557	0.12428	-0.48102	-0.12119

	Primary Galaxy	Secondary Galaxy
mass	0.51217	0.30955
radius	0.80325	0.31048
ϕ	149.1875°	110.6875°
θ	78.26086°	70.43478°
ϵ	0.3	0.3

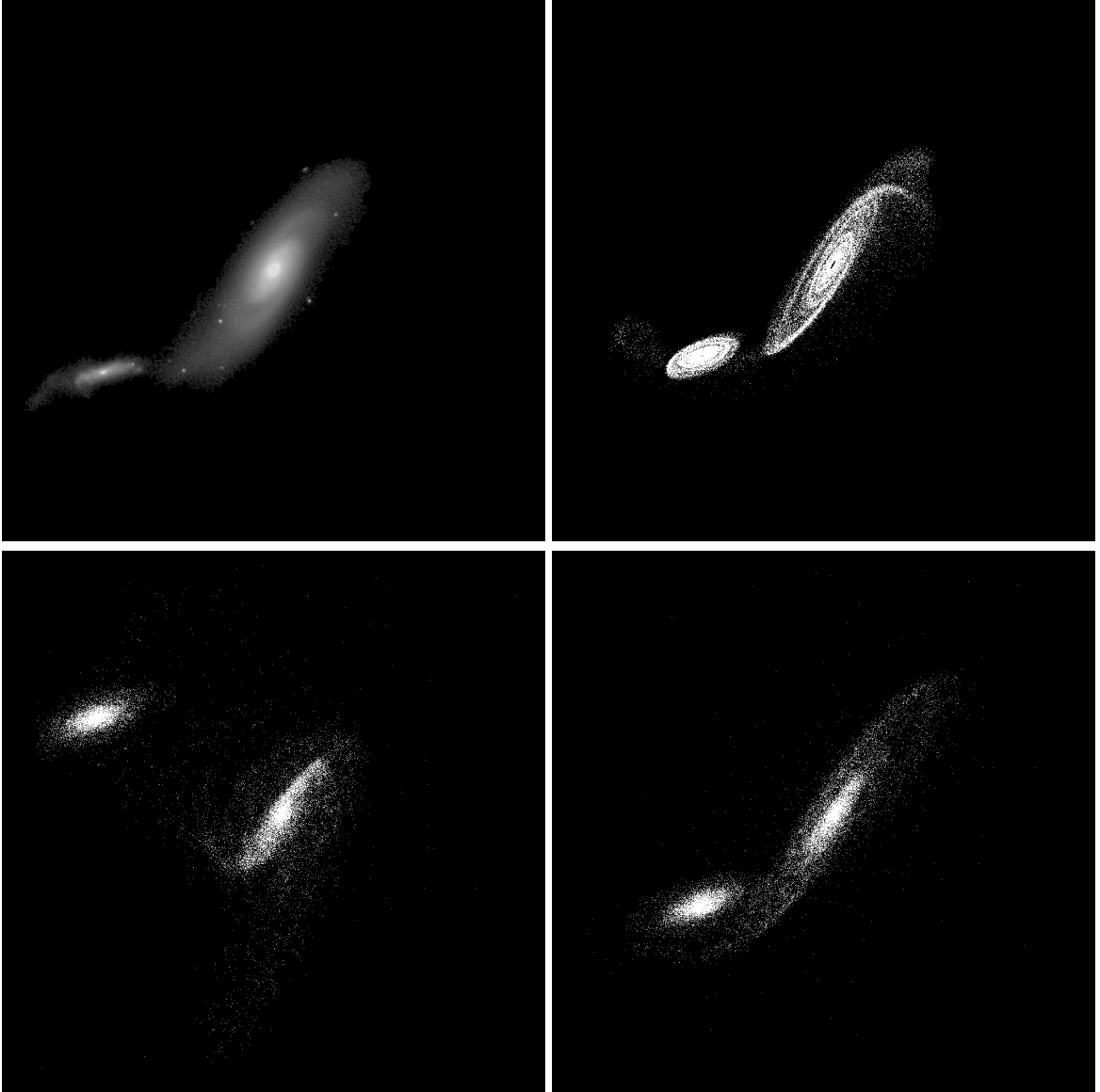


Figure 5.223: Target image (top-left), best SPAM match from Merger Wars (top-right), initial N-Body match (bottom-left), and best N-Body match (bottom-right) for SDSS 587742010583941189

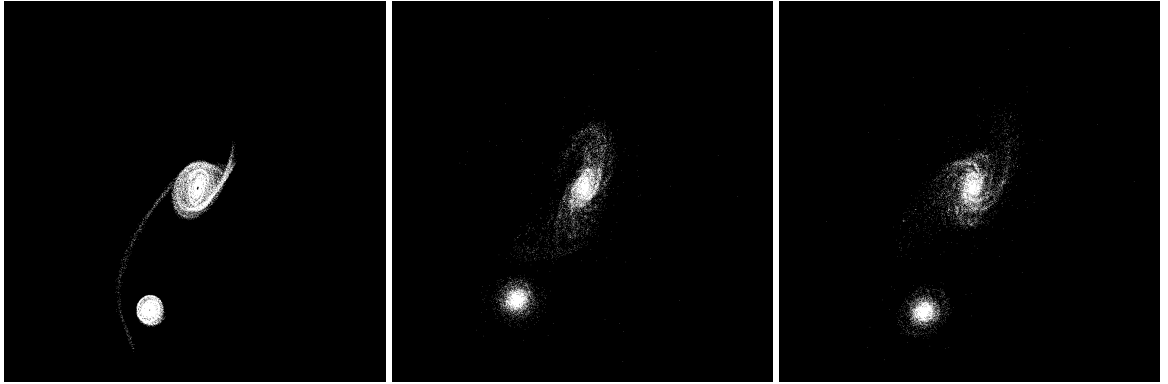


Figure 5.224: XZ projections of best SPAM match from Merger Wars (left), initial N-Body match (middle), and best N-Body match (right) for SDSS 587742010583941189

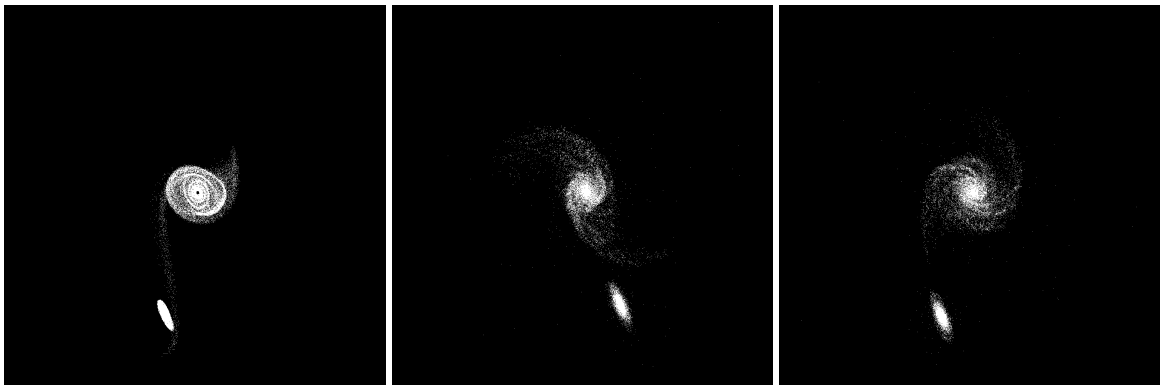


Figure 5.225: YZ projections of best SPAM match from Merger Wars (left), initial N-Body match (middle), and best N-Body match (right) for SDSS 587742010583941189

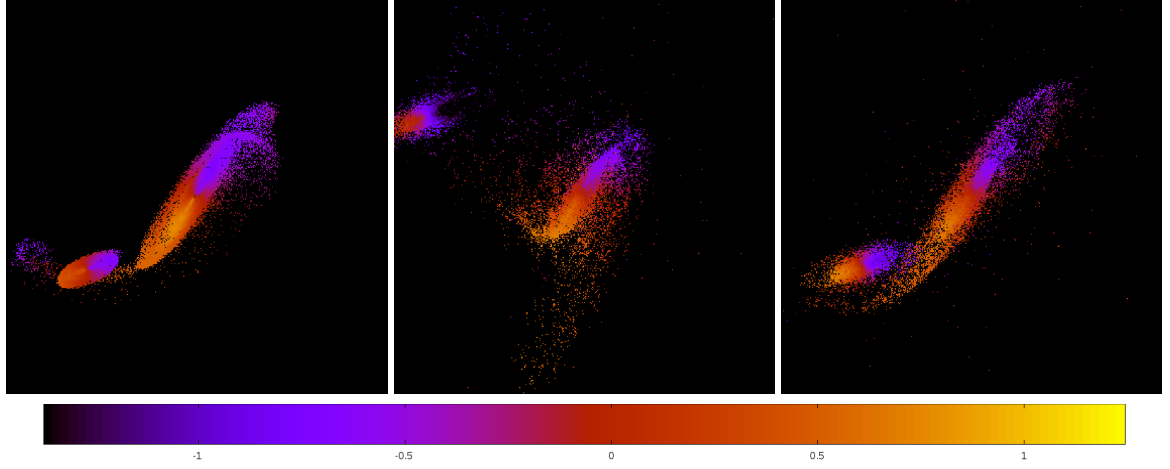


Figure 5.226: Line of sight velocity plots of best SPAM match from Merger Wars (left), initial N-Body match (middle), and best N-Body match (right) for SDSS 587742010583941189

Table 5.76: Orbital Elements & Dynamical Friction for SDSS 587742010583941189

	SPAM Simulation	Initial N-Body Simulation	Best N-Body Simulation
a	-3.202	-0.616	-4.126
e	2.560	7.339	2.202
r_c	4.995	3.907	4.958
i	64.834°	65.062°	65.245°
Ω	291.068°	291.132°	291.506°
ω	246.906°	195.972°	242.536°
ν	28.551°	48.062°	31.855°
t_n	50	35	51
$\ln\Lambda$	N/A	1.00E-03	0.00E+00

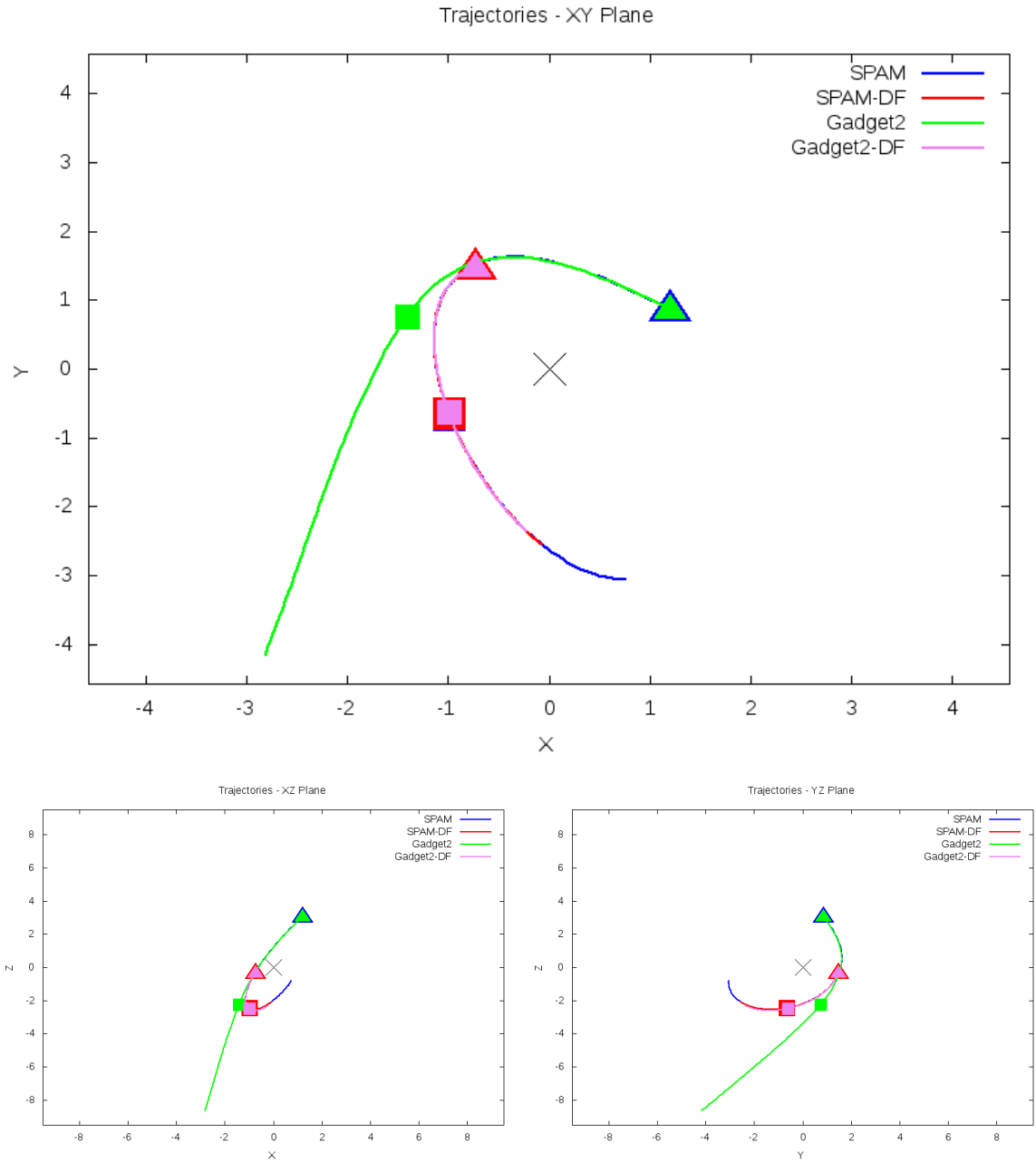


Figure 5.227: Trajectory plots of best SPAM match from Merger Wars, initial N-Body match, and best N-Body match for SDSS 587742010583941189

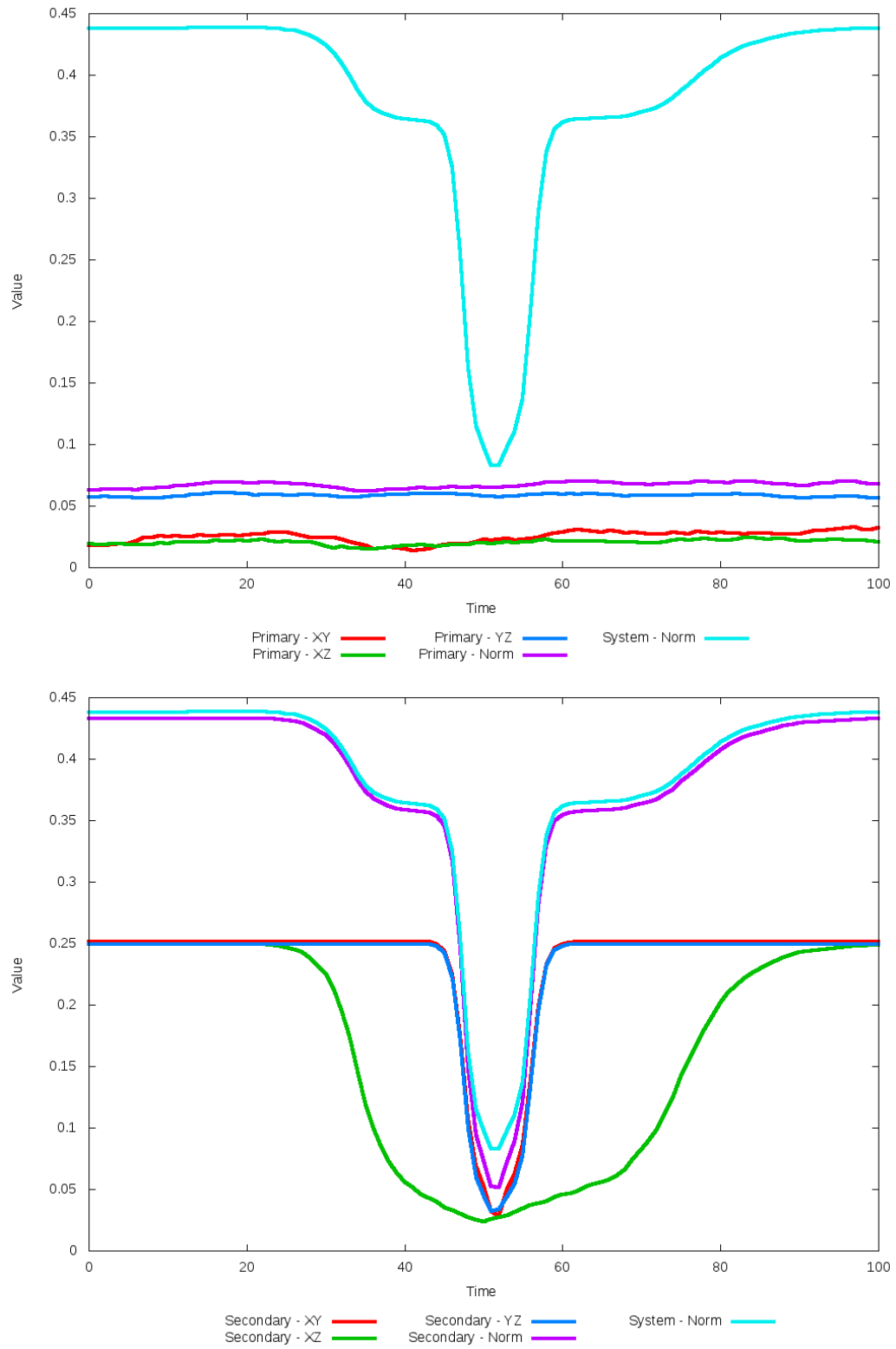


Figure 5.228: All metrics versus simulation time of the best N-Body simulation for SDSS 587742010583941189

5.1.39 SDSS 587742014353702970 (Arp 87)

Arp 87 shows very good agreement between all its models and the observational data. However, all simulations predict broader and more elongated tidal features that may change with the inclusion of additional physics. The optimization routine did find an optimal dynamical friction, although any improvement is very difficult to see in any of the figures, other than the XY trajectory. The choice of optimized dynamical friction found a trajectory that moves the best match slightly further away from the SPAM and initial N-Body trajectory.

Table 5.77: Identification Information and Merger Zoo summary for SDSS 587742014353702970.

Name	Aliases	RA (hms)	Dec (dms)	Redshift
SDSS 587742014353702970	Arp 87, NGC 3808	11:40:44.0	+22:25:45.8	0.023603

\mathbf{R}_x	\mathbf{R}_y	\mathbf{R}_z	\mathbf{V}_x	\mathbf{V}_y	\mathbf{V}_z
-0.23056	1.79463	-2.58944	-0.24992	0.26734	-0.62973

	Primary Galaxy	Secondary Galaxy
mass	0.1458	0.16789
radius	0.53863	0.36106
ϕ	116.68822°	65.78378°
θ	32.04906°	249.07924°
ϵ	0.3	0.3

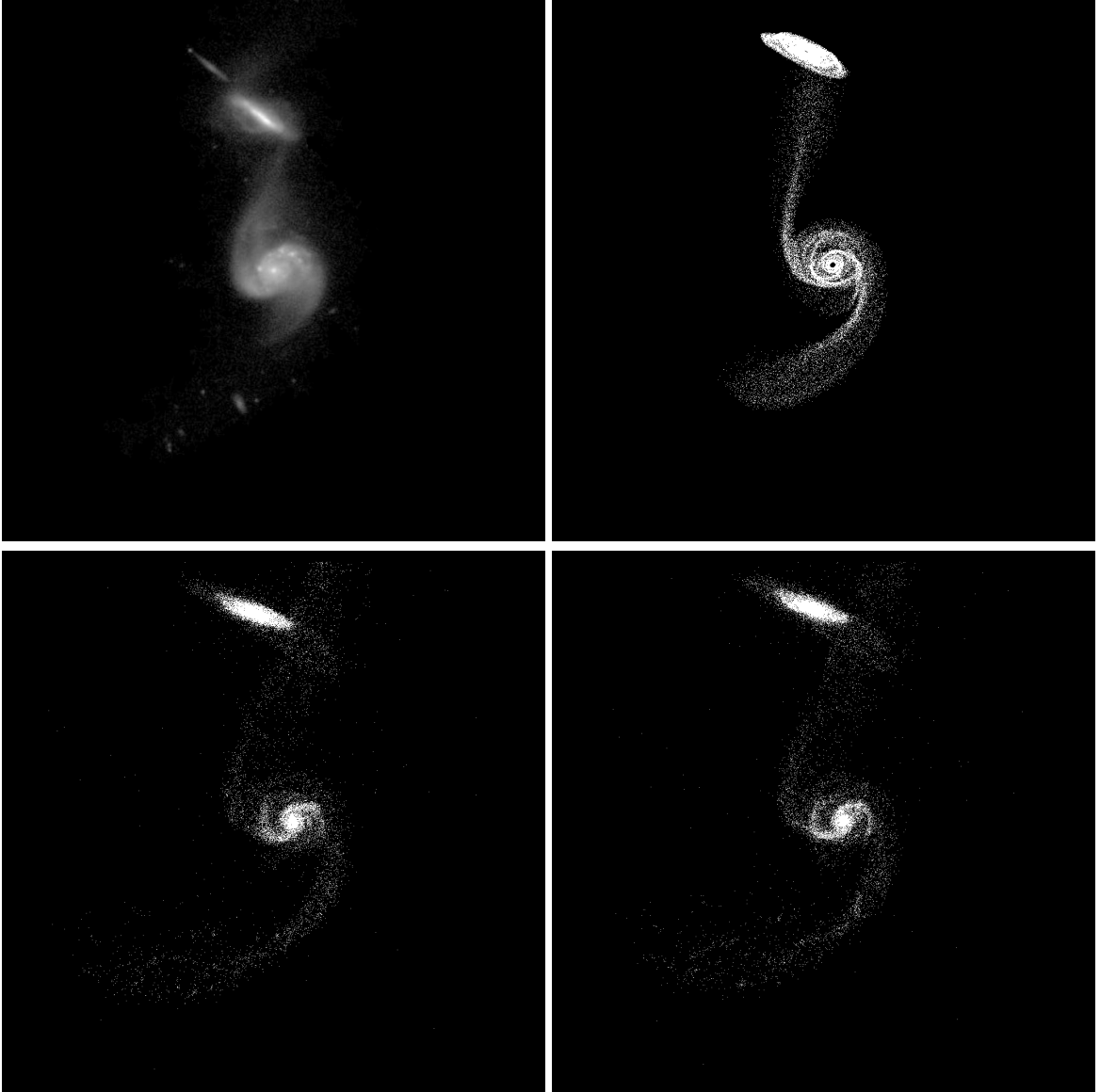


Figure 5.229: Target image (top-left), best SPAM match from Merger Wars (top-right), initial N-Body match (bottom-left), and best N-Body match (bottom-right) for SDSS 587742014353702970

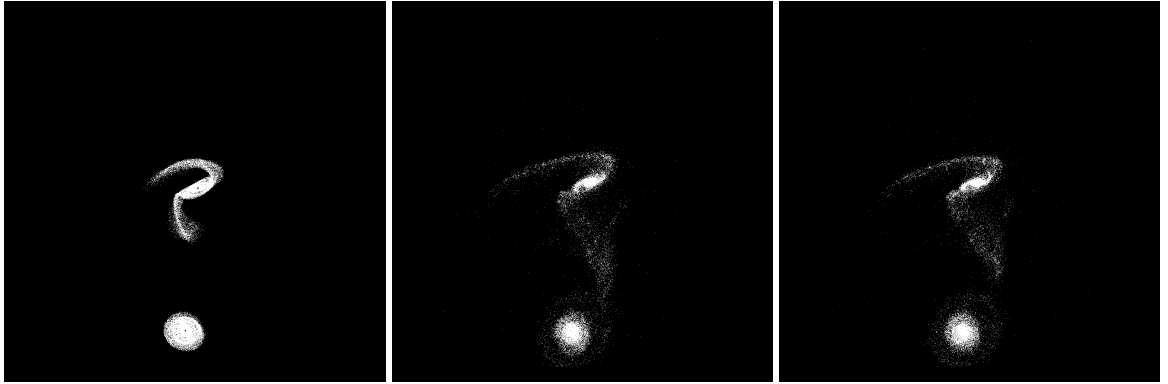


Figure 5.230: XZ projections of best SPAM match from Merger Wars (left), initial N-Body match (middle), and best N-Body match (right) for SDSS 587742014353702970

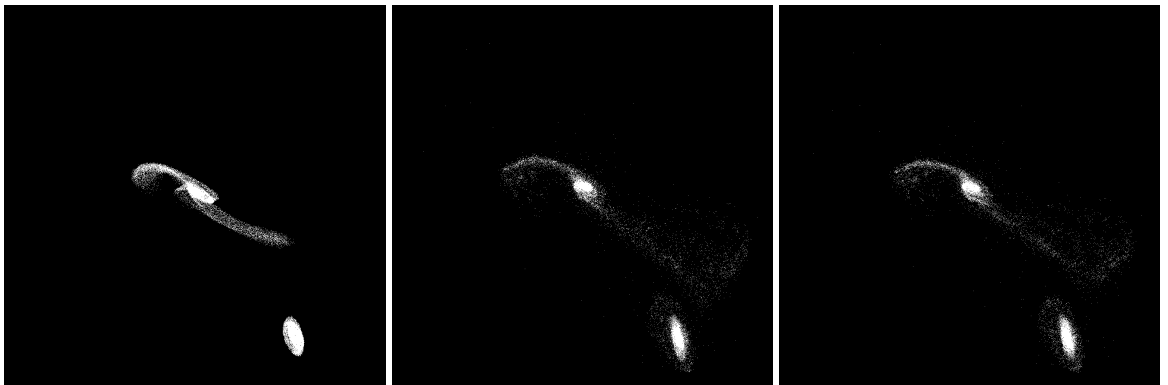


Figure 5.231: YZ projections of best SPAM match from Merger Wars (left), initial N-Body match (middle), and best N-Body match (right) for SDSS 587742014353702970

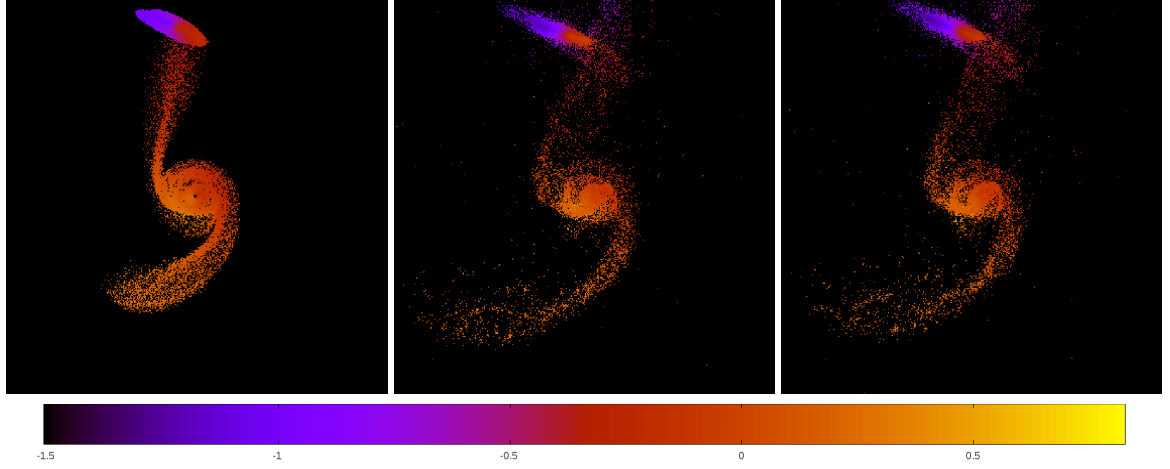


Figure 5.232: Line of sight velocity plots of best SPAM match from Merger Wars (left), initial N-Body match (middle), and best N-Body match (right) for SDSS 587742014353702970

Table 5.78: Orbital Elements & Dynamical Friction for SDSS 587742014353702970

	SPAM Simulation	Initial N-Body Simulation	Best N-Body Simulation
a	-0.324	-0.324	-0.278
e	6.920	6.753	7.686
r_c	1.920	1.861	1.862
i	59.852°	60.713°	61.099°
Ω	221.099°	219.428°	220.466°
ω	173.164°	173.735°	172.567°
ν	78.267°	78.872°	78.248°
t_n	50	50	49
$\ln\Lambda$	N/A	1.00E-03	1.50E-03

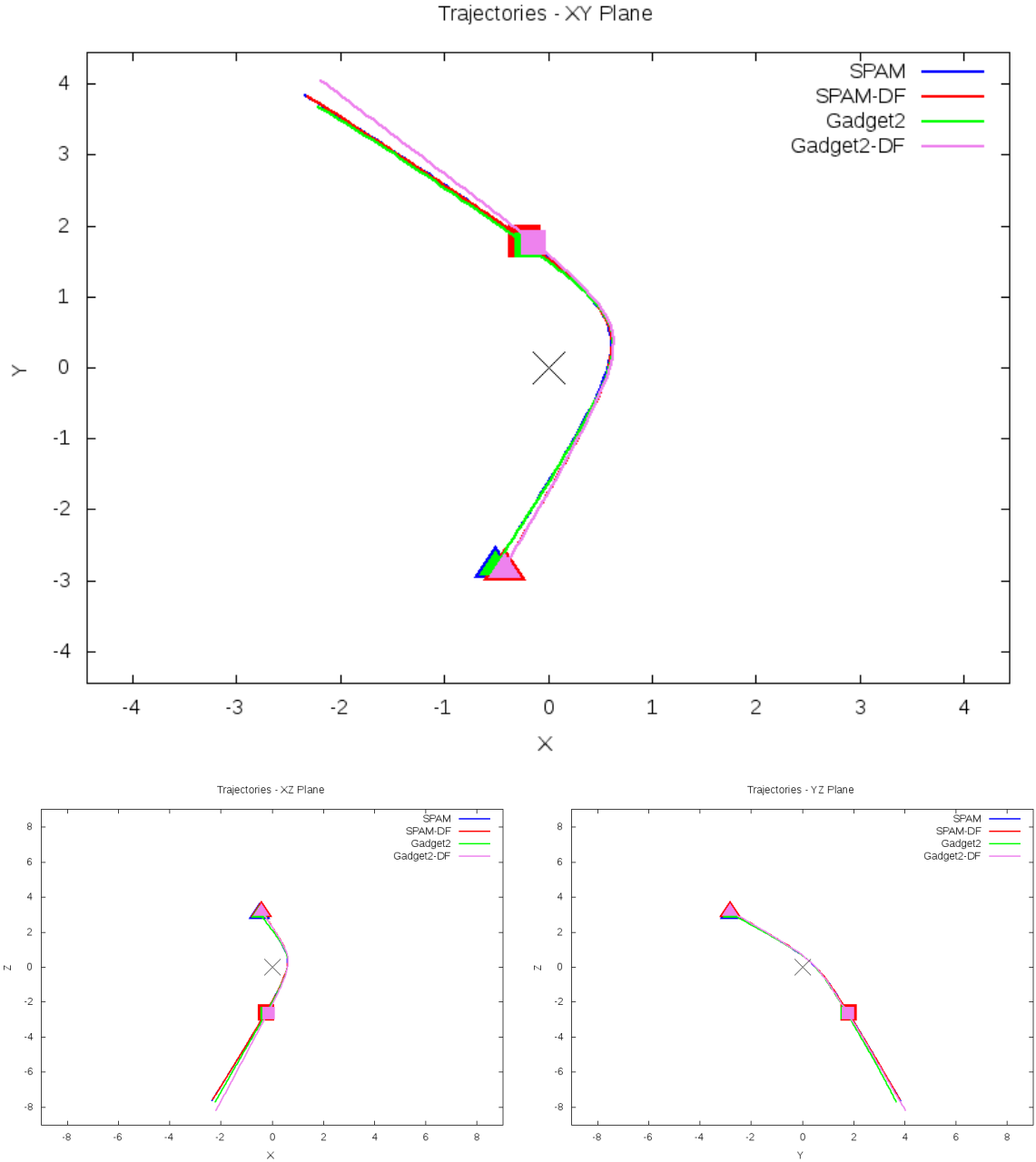


Figure 5.233: Trajectory plots of best SPAM match from Merger Wars, initial N-Body match, and best N-Body match for SDSS 587742014353702970

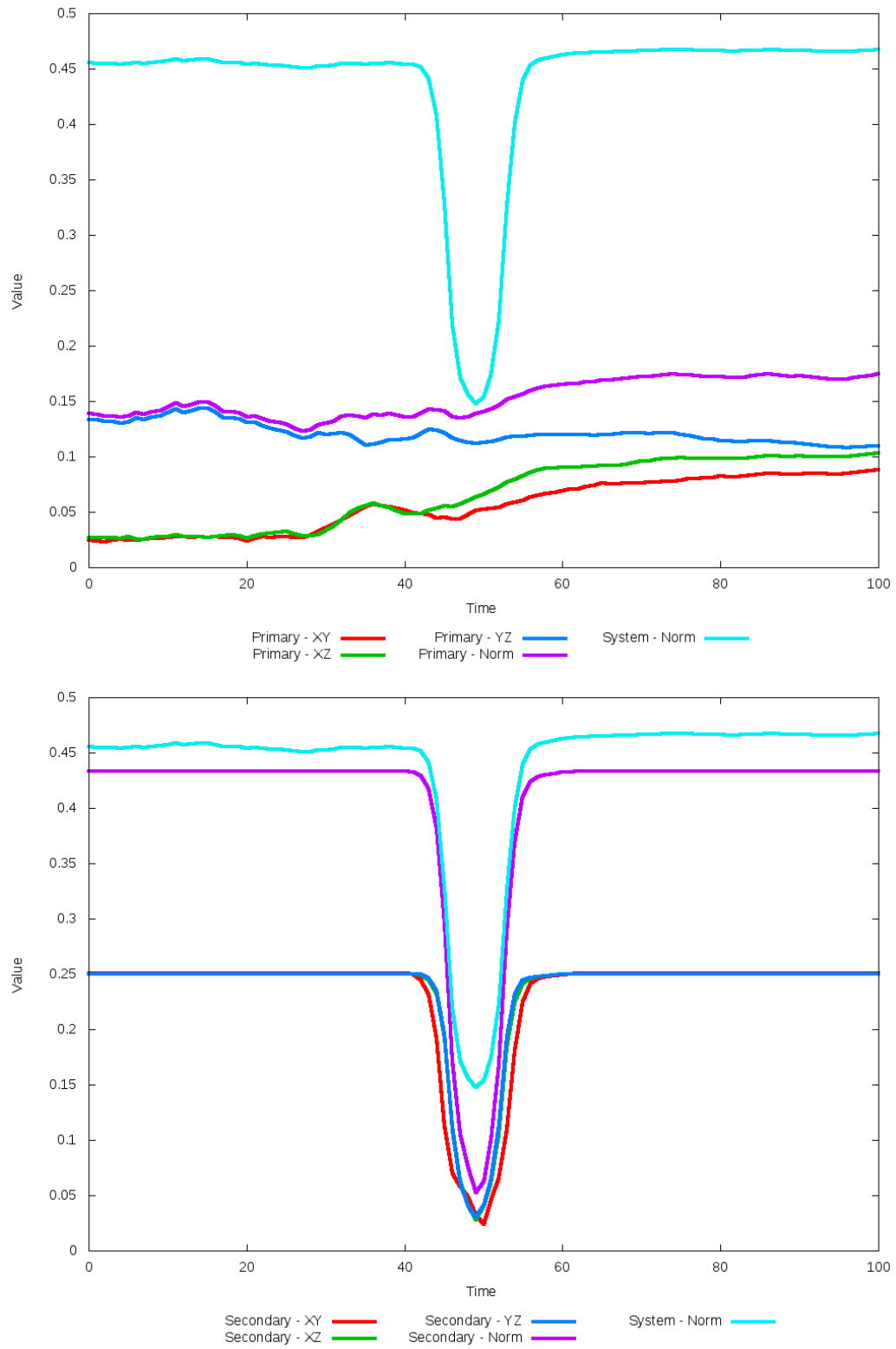


Figure 5.234: All metrics versus simulation time of the best N-Body simulation for SDSS 587742014353702970

5.1.40 SDSS 587742571610243080 (Arp 191)

Arp 191's N-Body simulations show very good agreement positionally with the the SPAM simulation and observational data. However, the optimization method could not find a better choice of dynamical friction than the starting value. The main differences between the N-Body and restricted three-body simulations are broader tidal features of the primary galaxy in the N-Body simulations and a small change in the trajectories in the XY plane.

Table 5.79: Identification Information and Merger Zoo summary for SDSS 587742571610243080.

Name	Aliases	RA (hms)	Dec (dms)	Redshift
SDSS 587742571610243080	Arp 191, UGC 6175	11:07:20.8	+18:25:58.6	0.026548

R_x	R_y	R_z	V_x	V_y	V_z
0.60209	-0.36672	-3.1872	-0.01698	0.20511	-1.60752

	Primary Galaxy	Secondary Galaxy
mass	0.73935	1.22722
radius	0.49155	0.54816
ϕ	101.875°	53.0625°
θ	2.23602°	216.8944°
ϵ	0.3	0.3

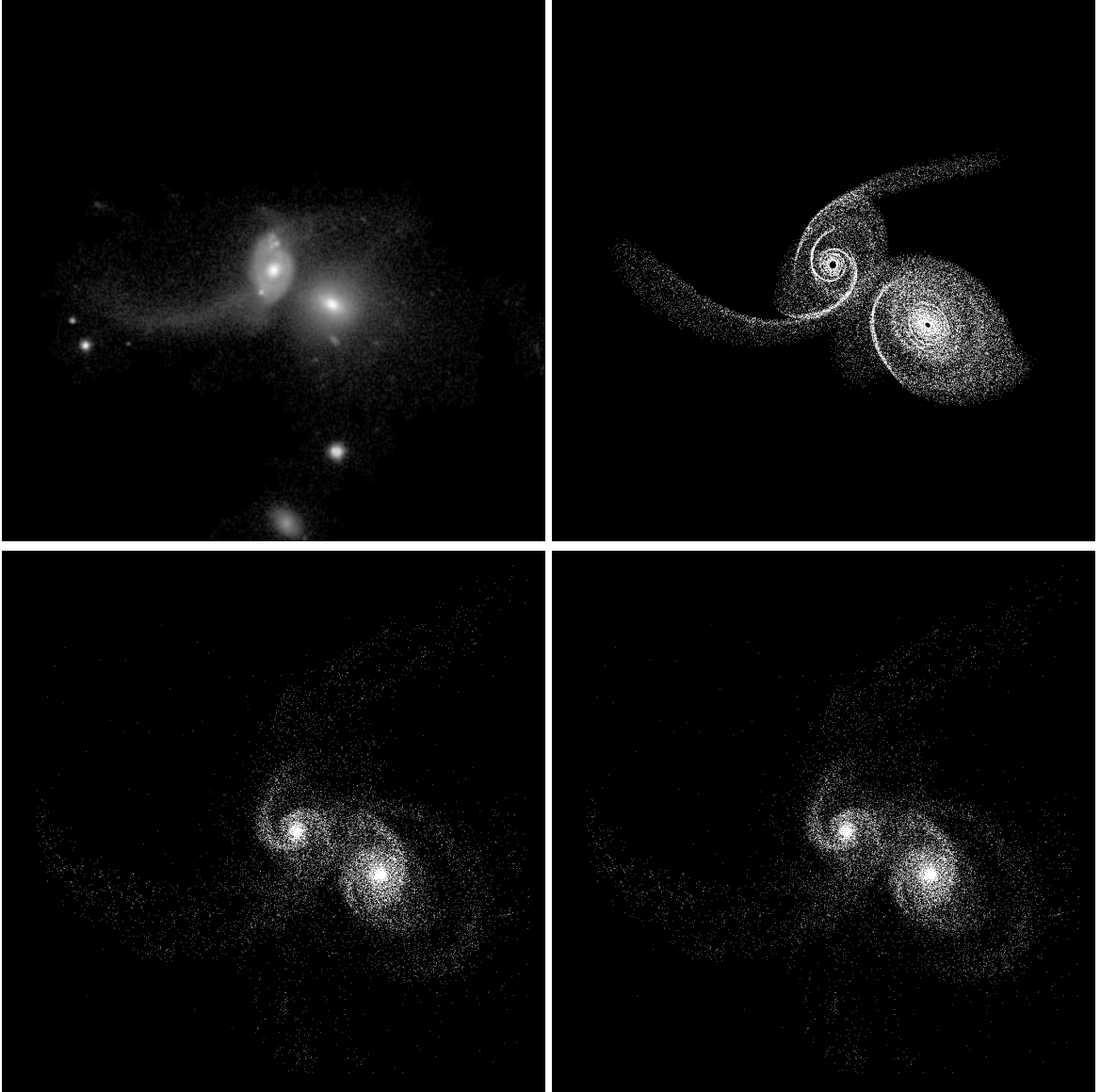


Figure 5.235: Target image (top-left), best SPAM match from Merger Wars (top-right), initial N-Body match (bottom-left), and best N-Body match (bottom-right) for SDSS 587742571610243080

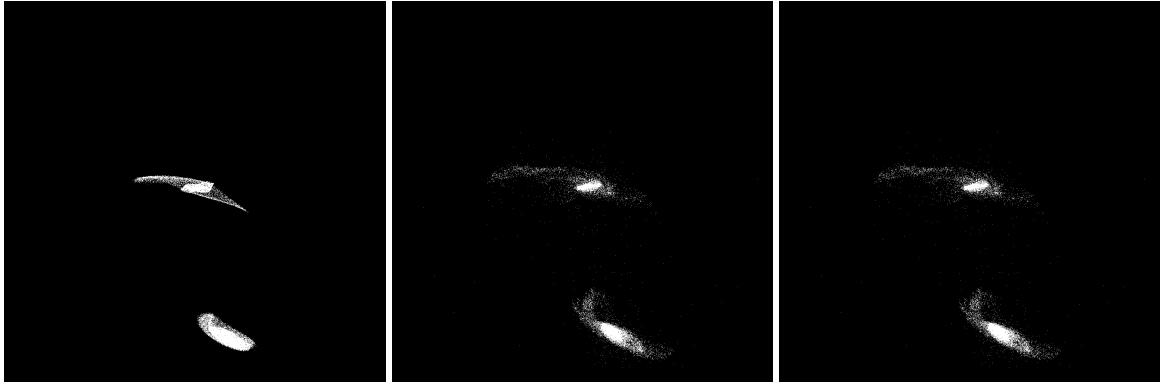


Figure 5.236: XZ projections of best SPAM match from Merger Wars (left), initial N-Body match (middle), and best N-Body match (right) for SDSS 587742571610243080

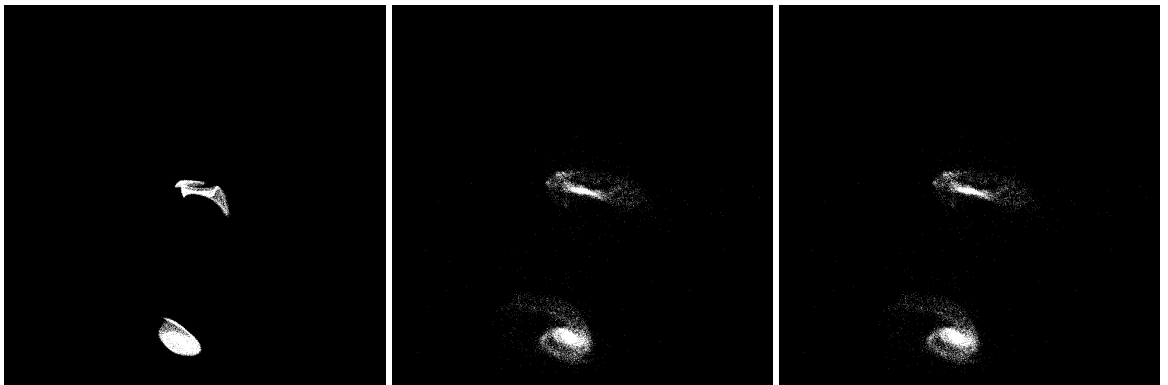


Figure 5.237: YZ projections of best SPAM match from Merger Wars (left), initial N-Body match (middle), and best N-Body match (right) for SDSS 587742571610243080

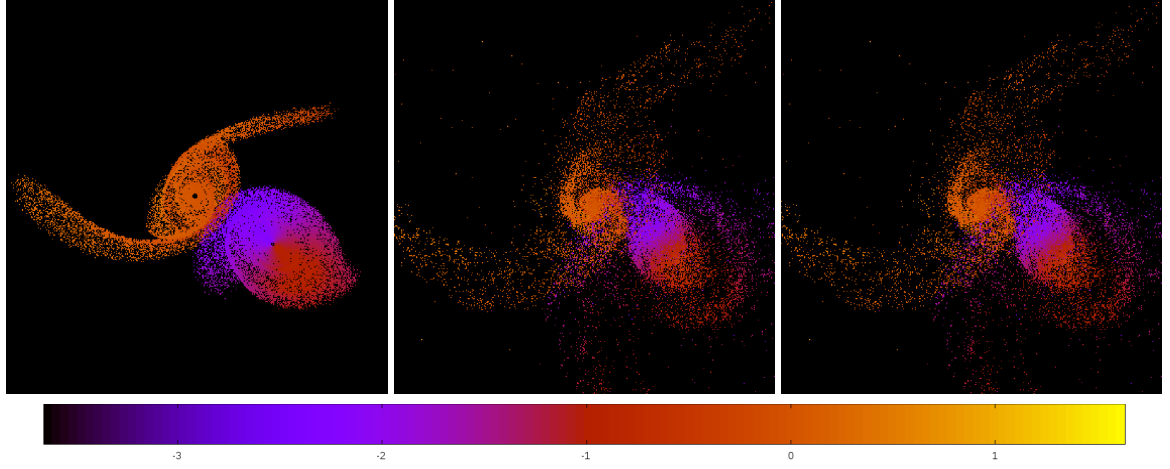


Figure 5.238: Line of sight velocity plots of best SPAM match from Merger Wars (left), initial N-Body match (middle), and best N-Body match (right) for SDSS 587742571610243080

Table 5.80: Orbital Elements & Dynamical Friction for SDSS 587742571610243080

	SPAM Simulation	Initial N-Body Simulation	Best N-Body Simulation
a	-0.394	-0.471	-0.471
e	5.447	4.577	4.577
r_c	1.751	1.686	1.686
i	85.832°	85.090°	85.090°
Ω	129.422°	127.506°	127.506°
ω	175.924°	173.121°	173.121°
ν	82.310°	84.047°	84.047°
t_n	50	51	51
$\ln\Lambda$	N/A	1.00E-03	1.00E-03

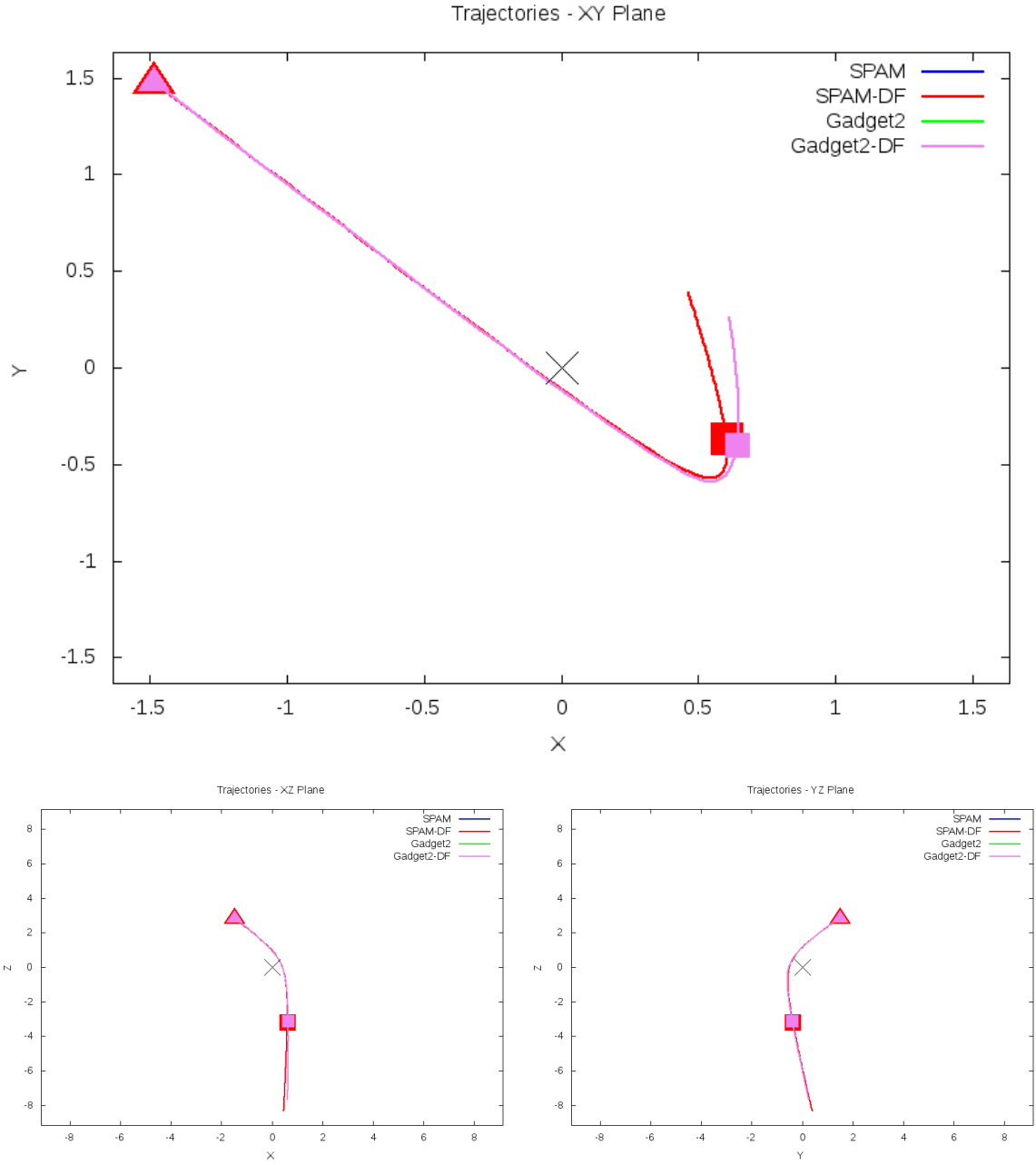


Figure 5.239: Trajectory plots of best SPAM match from Merger Wars, initial N-Body match, and best N-Body match for SDSS 587742571610243080

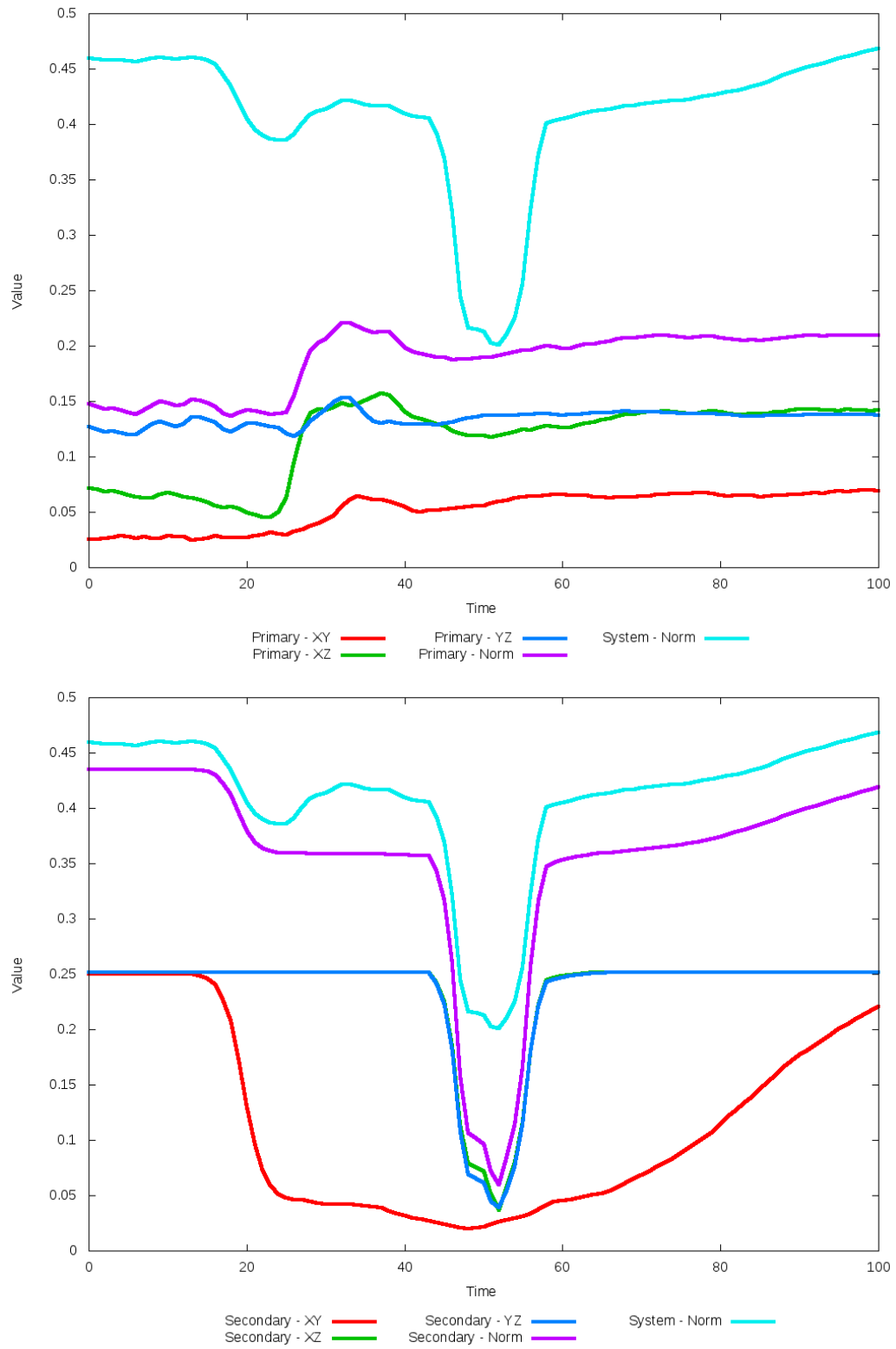


Figure 5.240: All metrics versus simulation time of the best N-Body simulation for SDSS 587742571610243080

5.1.41 SDSS 587745402001817662 (Arp 237)

Arp 237 cannot be well matched with N-Body simulations using our pipeline approach. The observational data shows two galaxies already very close to one another in the middle of a merger process. The SPAM simulations show very rich and fine structure as the tracer particles bounce around. The trajectories of the SPAM simulations show a very high periodicity. Although both SPAM simulations should arrive back at the same point when backwards and forward integrated, numerical precision causes a slight offset. Although the initial N-Body simulation shows some promise of matching early in its trajectory, there isn't a clear separation of the galaxies. An N-Body simulation of this system will require additional physics to be added given the extent of a merger that is underway.

Table 5.81: Identification Information and Merger Zoo summary for SDSS 587745402001817662.

Name	Aliases	RA (hms)	Dec (dms)	Redshift
SDSS 587745402001817662	Arp 237, UGC 5044	9:27:43.4	+12:17:14.1	0.028833

R_x	R_y	R_z	V_x	V_y	V_z
-0.54962	0.12782	0.12509	0.50274	-0.83732	0.28701

	Primary Galaxy	Secondary Galaxy
mass	1.08587	0.45008
radius	0.52331	0.34502
ϕ	86.86455°	55.83273°
θ	348.72428°	148.42085°
ϵ	0.3	0.3

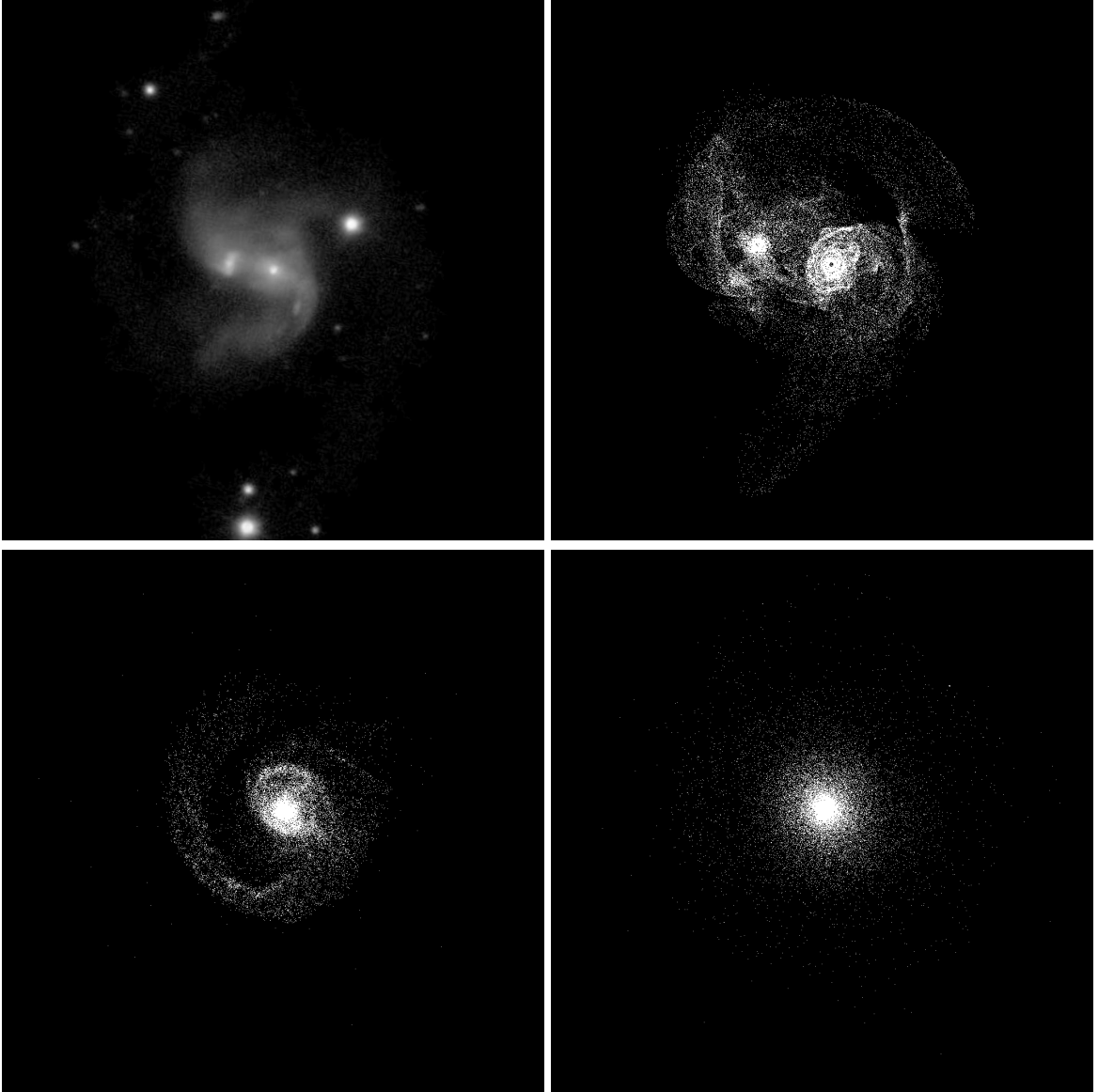


Figure 5.241: Target image (top-left), best SPAM match from Merger Wars (top-right), initial N-Body match (bottom-left), and best N-Body match (bottom-right) for SDSS 587745402001817662

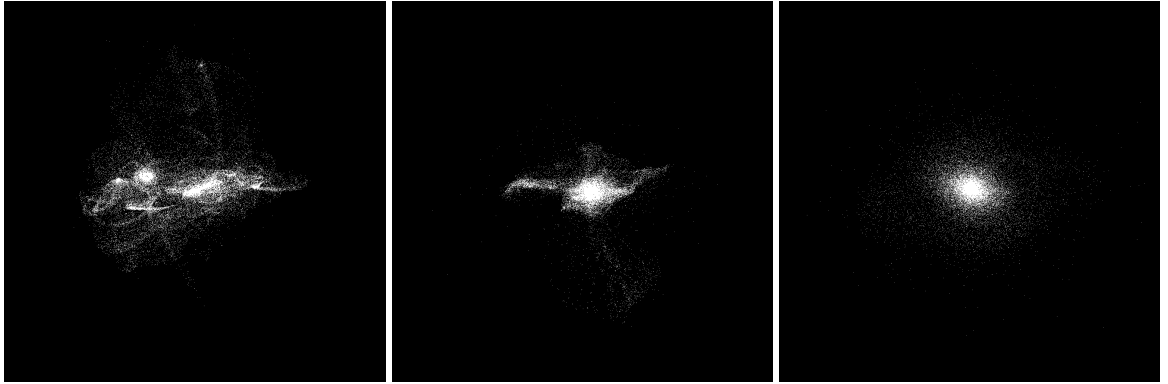


Figure 5.242: XZ projections of best SPAM match from Merger Wars (left), initial N-Body match (middle), and best N-Body match (right) for SDSS 587745402001817662

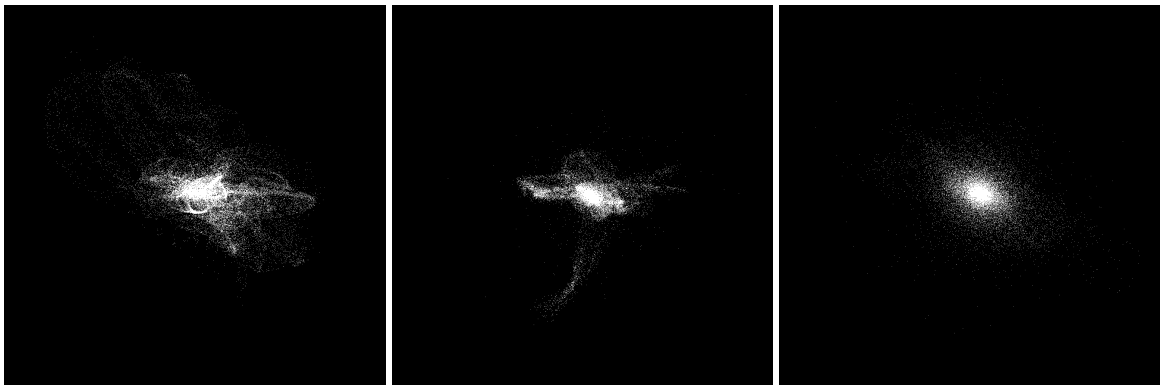


Figure 5.243: YZ projections of best SPAM match from Merger Wars (left), initial N-Body match (middle), and best N-Body match (right) for SDSS 587745402001817662

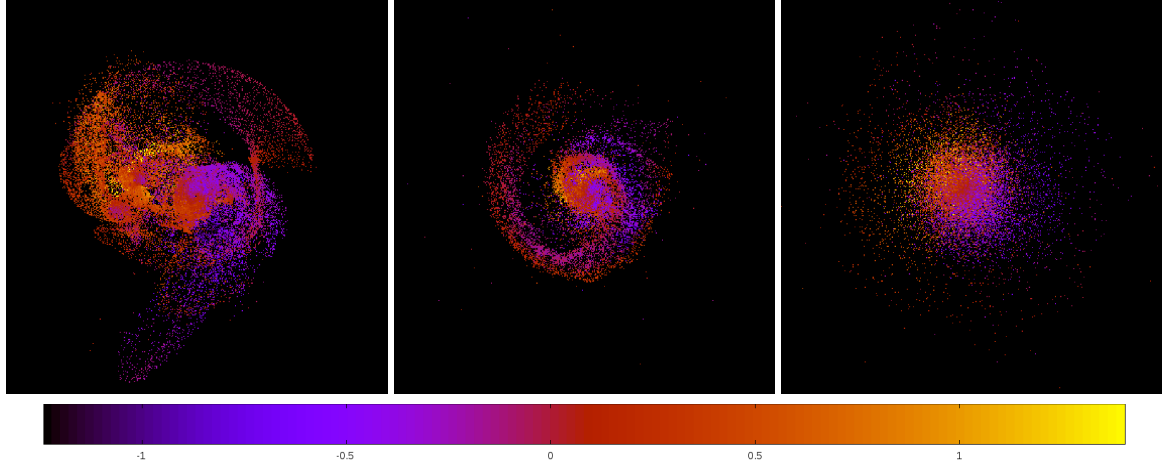


Figure 5.244: Line of sight velocity plots of best SPAM match from Merger Wars (left), initial N-Body match (middle), and best N-Body match (right) for SDSS 587745402001817662

Table 5.82: Orbital Elements & Dynamical Friction for SDSS 587745402001817662

	SPAM Simulation	Initial N-Body Simulation	Best N-Body Simulation
a	6.039	0.157	0.094
e	0.875	0.997	1.000
r_c	0.756	0.000	0.000
i	33.500°	41.214°	31.146°
Ω	147.340°	154.867°	284.319°
ω	98.143°	63.902°	33.969°
ν	283.424°	180.154°	179.996°
t_n	50	15	93
$\ln\Lambda$	N/A	1.00E-03	2.80E-03

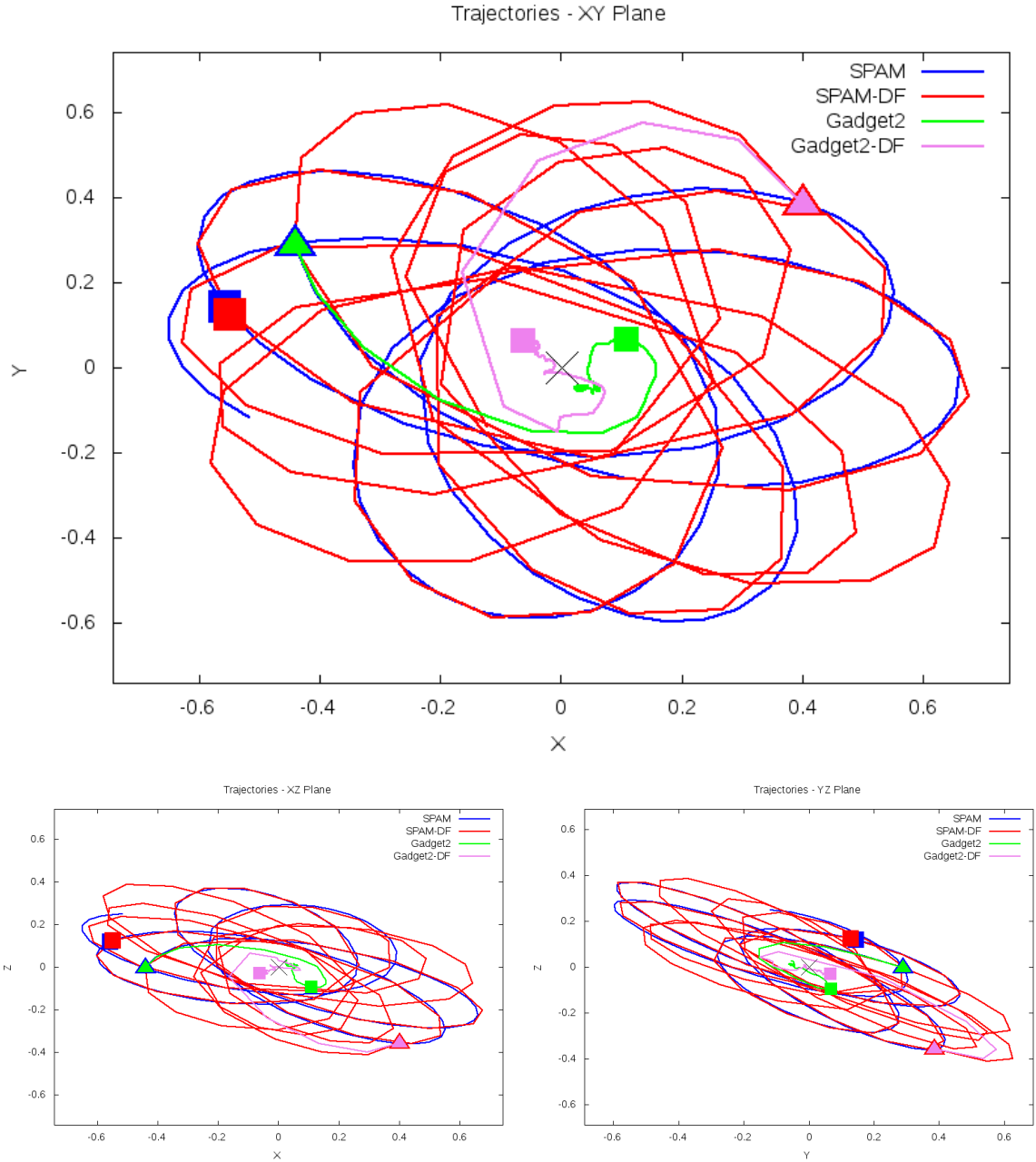


Figure 5.245: Trajectory plots of best SPAM match from Merger Wars, initial N-Body match, and best N-Body match for SDSS 587745402001817662

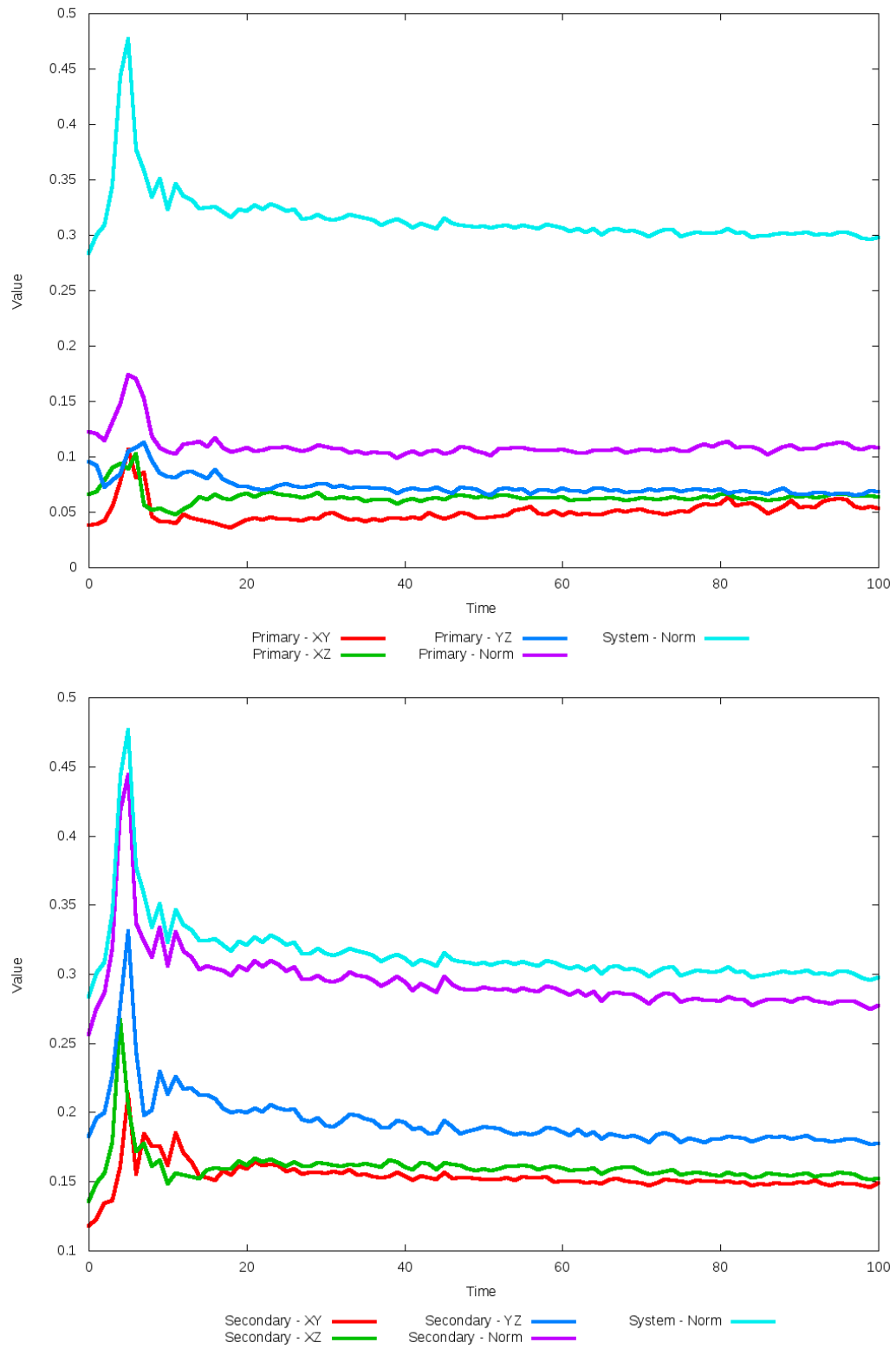


Figure 5.246: All metrics versus simulation time of the best N-Body simulation for SDSS 587745402001817662

5.1.42 SDSS 587746029596311590 (Arp 181)

Arp 181 shows only modest agreement between its optimized N-Body simulation, SPAM simulation, and observational data. In the initial N-Body simulation, the primary galaxy does not appear near the expected origin within the figures. This is due to all three components (halo, bulge, and disk) being used to determine the center of mass, in which the center of the disk and bulge are not centered within the halo. The optimized dynamical friction simulation improves on the placement of each galaxy (although the secondary galaxy could be improved further), it does have broader tidal features than desired. In the XZ and YZ projections however, the placement of the secondary galaxy is poor. The expected line of sight velocity is also much different across the system when compared to the SPAM simulations. The orbits, although close to each other at the time of best match, are markedly different. This system definitely will require more physics to be used, and may also require review of the state vector provided by Merger Wars.

Table 5.83: Identification Information and Merger Zoo summary for SDSS 587746029596311590.

Name	Aliases	RA (hms)	Dec (dms)	Redshift
SDSS 587746029596311590	Arp 181, NGC 3212	10:28:16.6	+79:49:24.5	0.032402

R_x	R_y	R_z	V_x	V_y	V_z
-0.20706	-0.12072	-0.51456	-1.17676	-0.37393	-1.19254

	Primary Galaxy	Secondary Galaxy
mass	0.48543	0.86206
radius	0.10418	0.11542
ϕ	96.0°	65.6875°
θ	127.45341°	221.36645°
ϵ	0.3	0.3

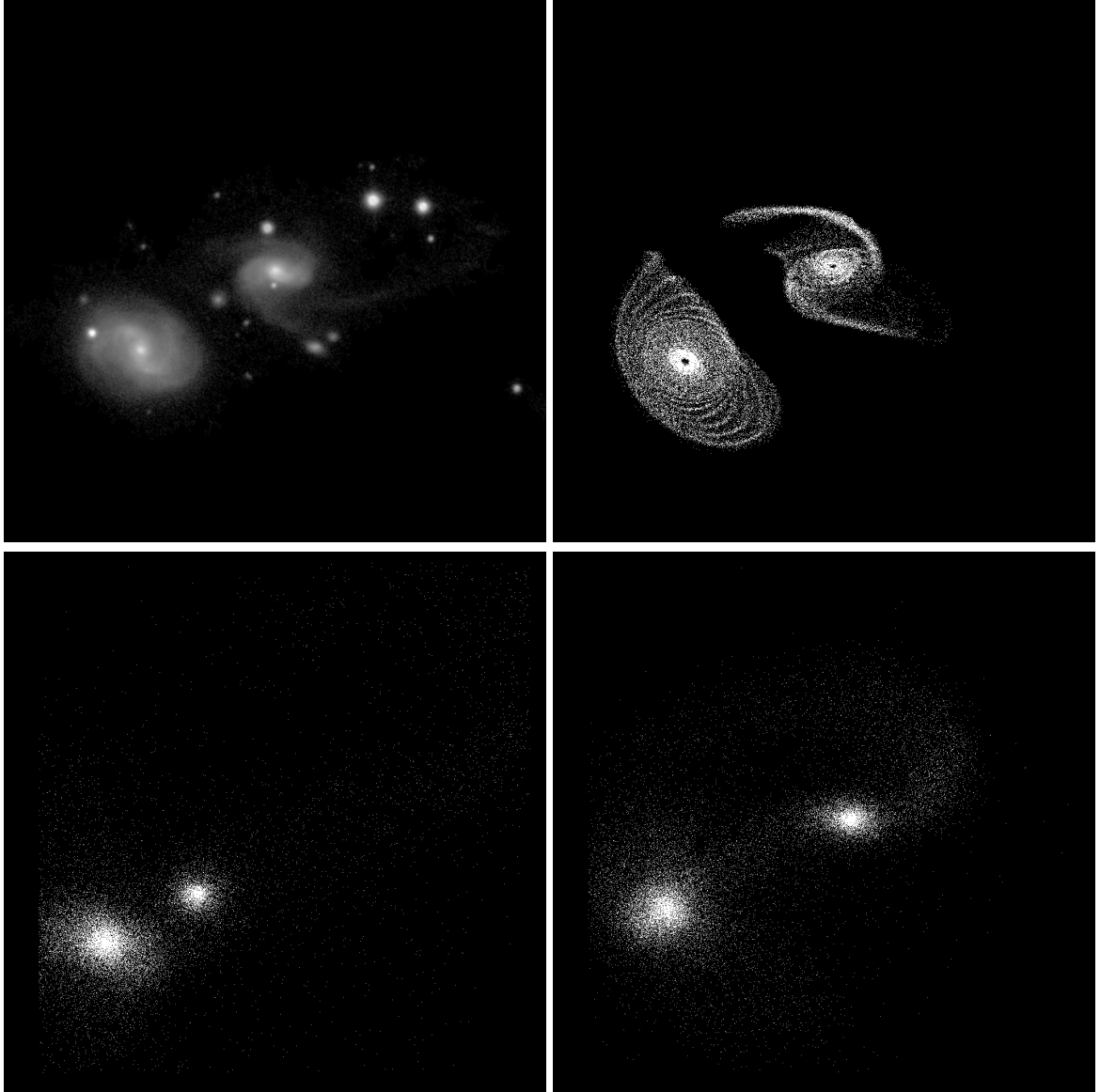


Figure 5.247: Target image (top-left), best SPAM match from Merger Wars (top-right), initial N-Body match (bottom-left), and best N-Body match (bottom-right) for SDSS 587746029596311590

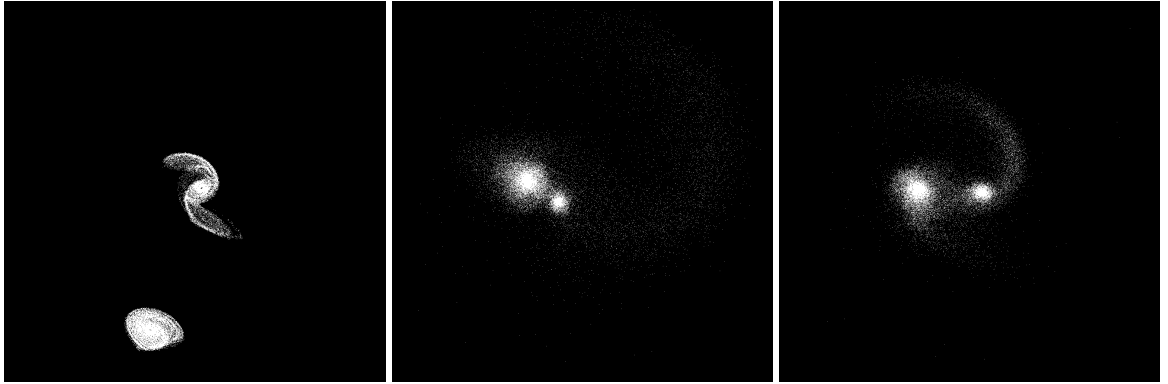


Figure 5.248: XZ projections of best SPAM match from Merger Wars (left), initial N-Body match (middle), and best N-Body match (right) for SDSS 587746029596311590

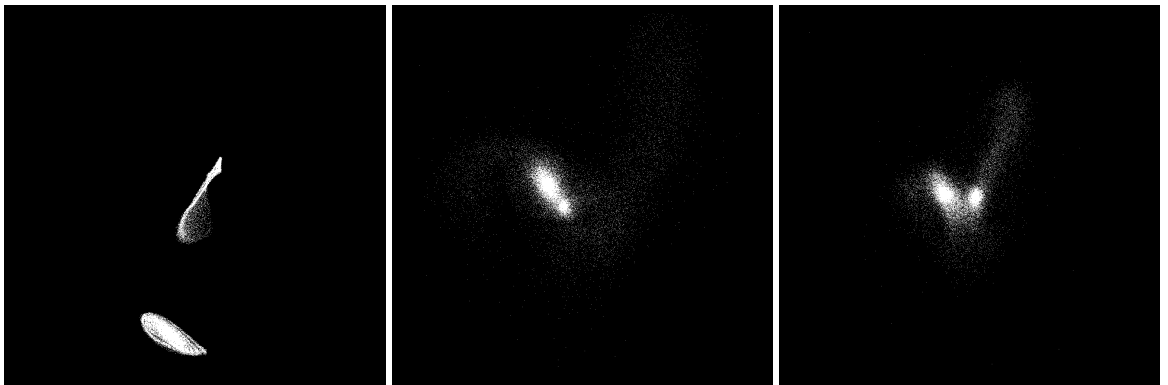


Figure 5.249: YZ projections of best SPAM match from Merger Wars (left), initial N-Body match (middle), and best N-Body match (right) for SDSS 587746029596311590

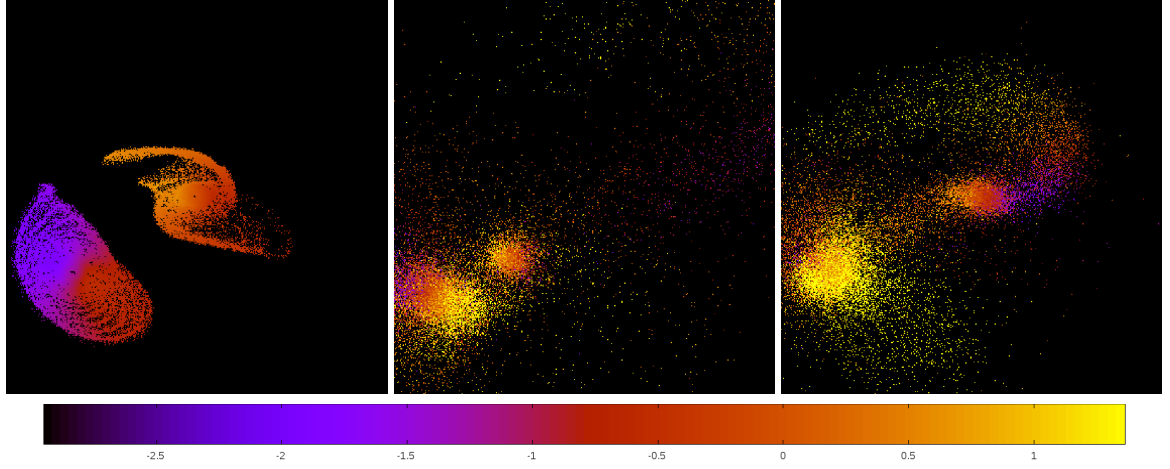


Figure 5.250: Line of sight velocity plots of best SPAM match from Merger Wars (left), initial N-Body match (middle), and best N-Body match (right) for SDSS 587746029596311590

Table 5.84: Orbital Elements & Dynamical Friction for SDSS 587746029596311590

	SPAM Simulation	Initial N-Body Simulation	Best N-Body Simulation
a	-0.318	0.295	1.320
e	1.933	0.956	0.856
r_c	0.297	0.013	0.190
i	100.127°	98.485°	108.801°
Ω	187.694°	215.720°	208.173°
ω	196.000°	181.890°	253.845°
ν	95.560°	183.112°	103.233°
t_n	50	48	49
$\ln\Lambda$	N/A	1.00E-03	5.00E-04

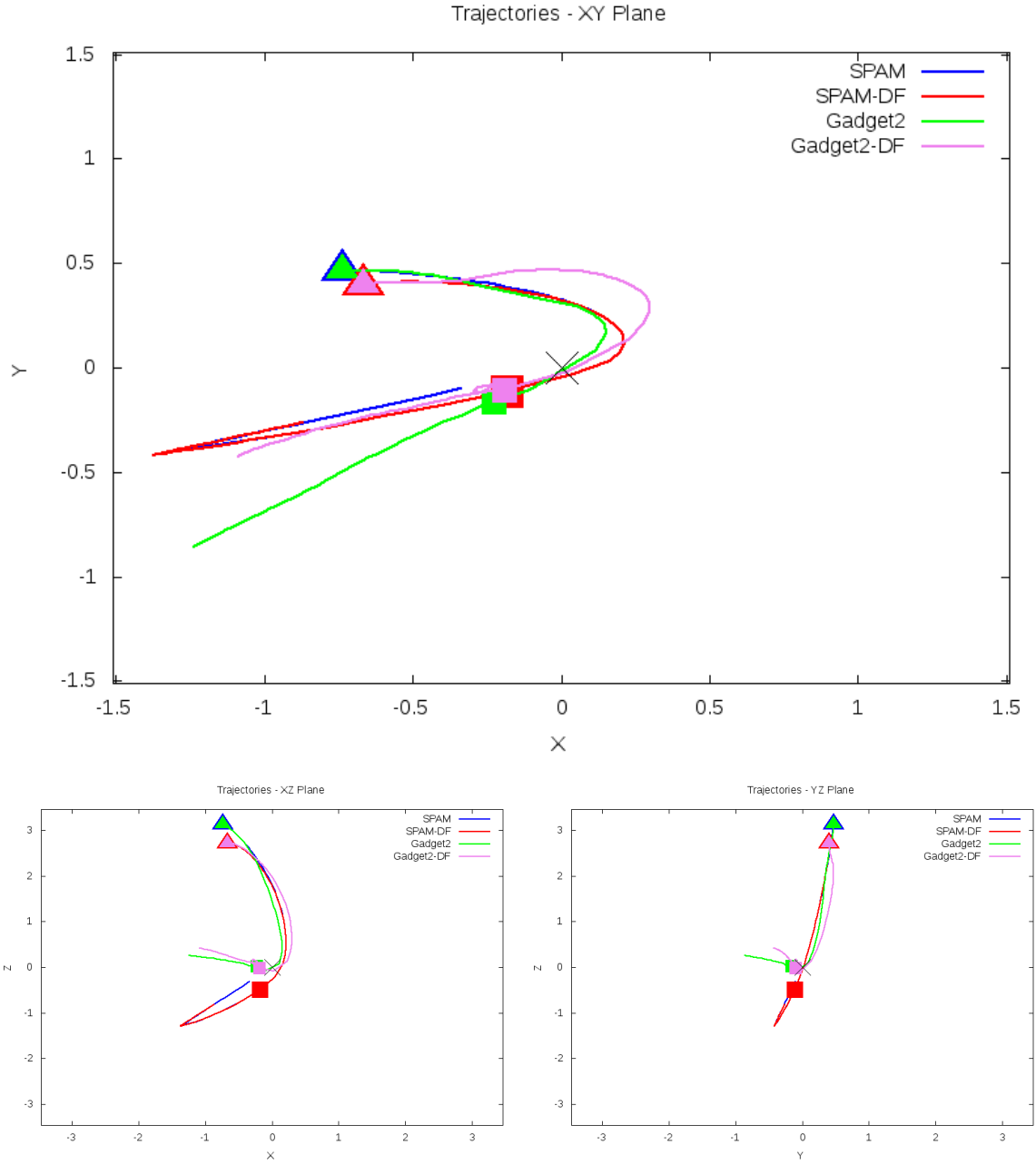


Figure 5.251: Trajectory plots of best SPAM match from Merger Wars, initial N-Body match, and best N-Body match for SDSS 587746029596311590

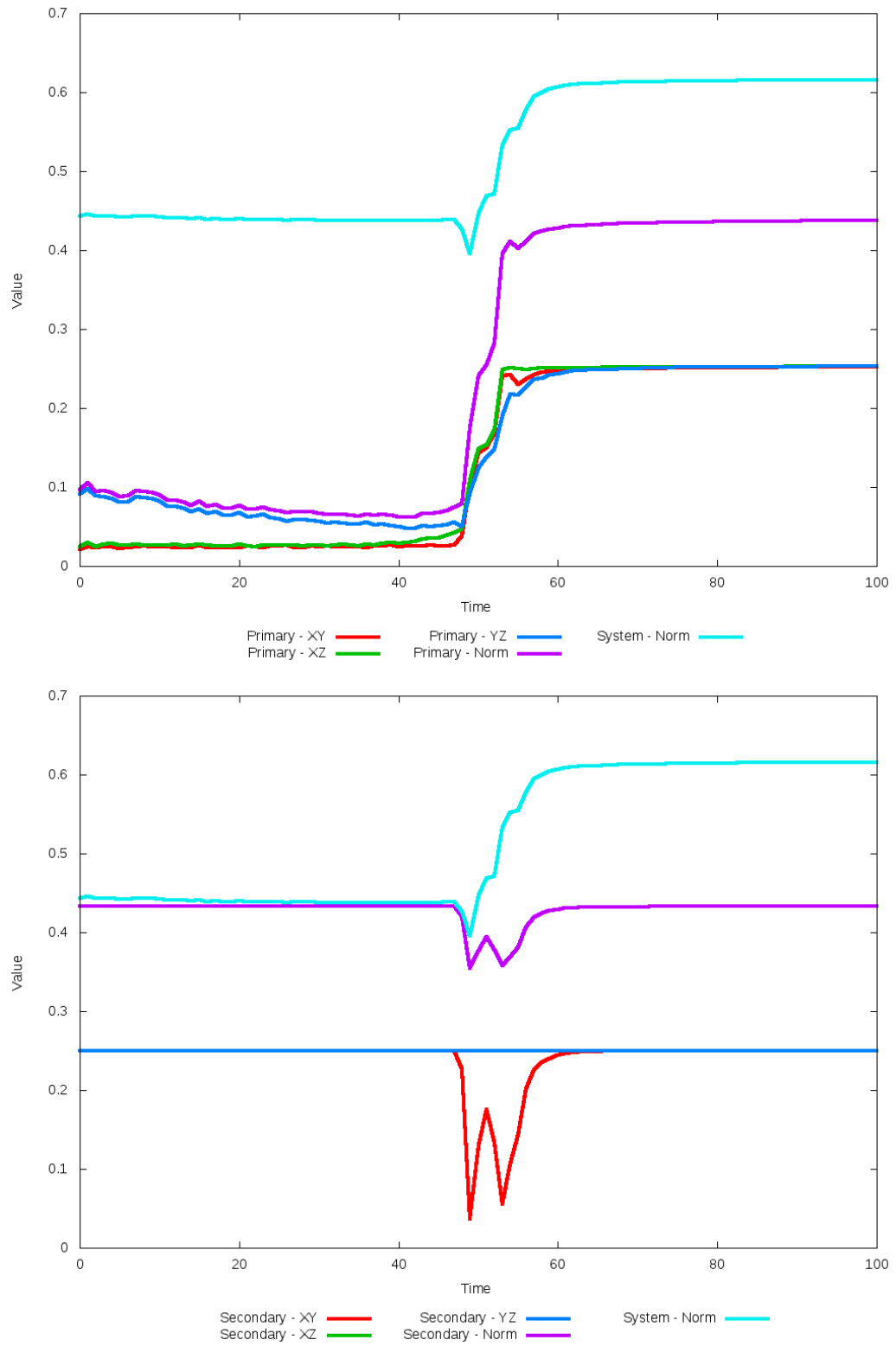


Figure 5.252: All metrics versus simulation time of the best N-Body simulation for SDSS 587746029596311590

5.1.43 SDSS 587747120521216156 (Arp 146)

Arp 146 shows very good agreement between its simulations and observational data, in particular capturing the ring formed by the tails of the secondary galaxy. Although the placement of the secondary galaxy in the optimized simulation matches the SPAM simulation's secondary galaxy better than the initial N-Body simulation, the latter looks to be a better match to the observational data. Both N-Body simulations however exhibit noticeable changes in the line of sight velocity compared to the restricted three-body simulations. In the XZ and YZ projections, the N-Body simulations also capture the same richness in morphology as the other simulations. The trajectories of the SPAM simulations appear hyperbolic while the N-Body simulations appear to be elliptical.

Table 5.85: Identification Information and Merger Zoo summary for SDSS 587747120521216156.

Name	Aliases	RA (hms)	Dec (dms)	Redshift
SDSS 587747120521216156	Arp 146	0:06:44.7	-6:38:12.9	0.07544

R_x	R_y	R_z	V_x	V_y	V_z
1.20338	0.67312	0.64081	0.43046	0.50439	0.43521

	Primary Galaxy	Secondary Galaxy
mass	0.50371	0.60483
radius	0.58896	0.86039
ϕ	72.5°	48.8125°
θ	111.80124°	67.08074°
ϵ	0.3	0.3

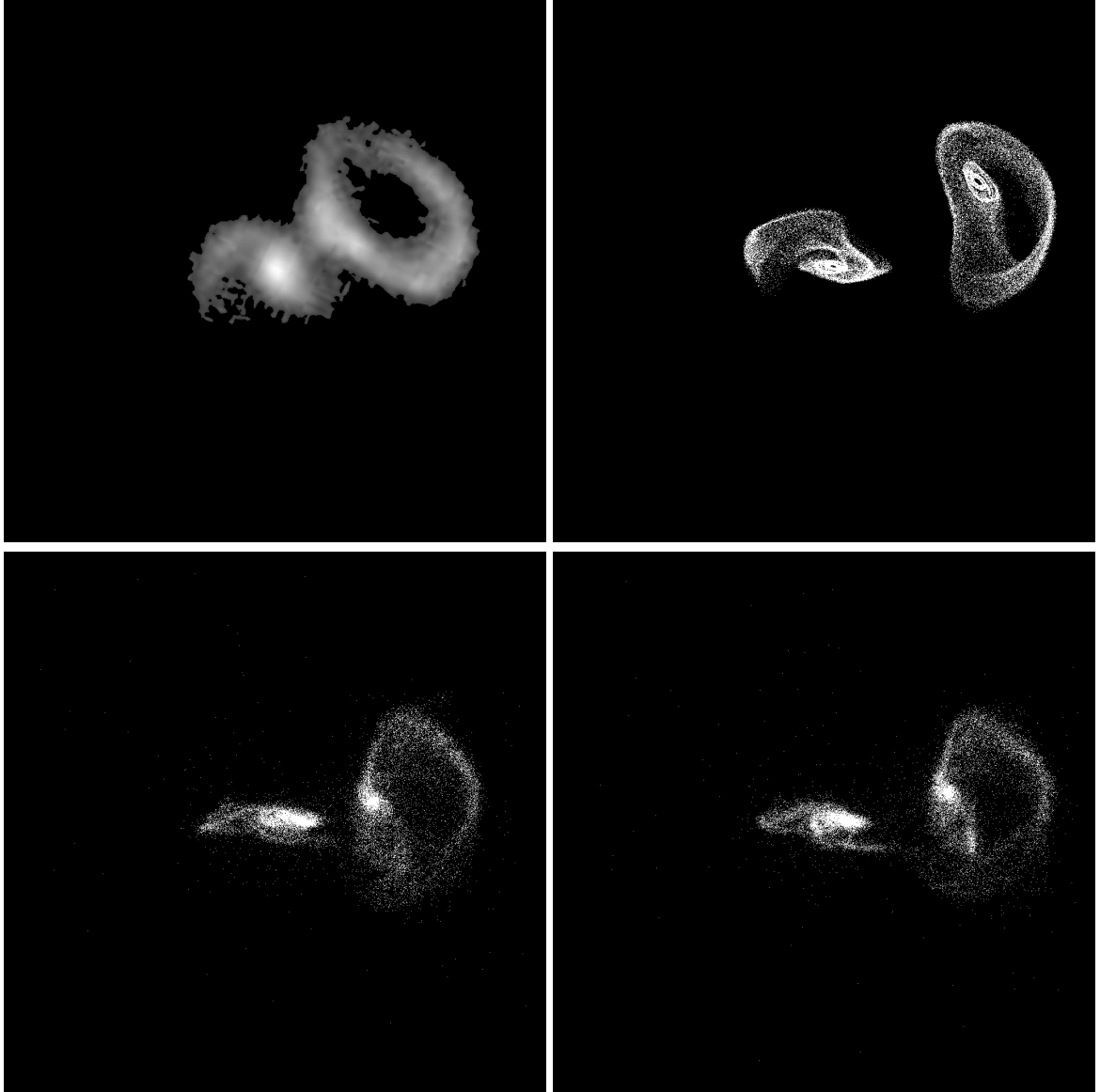


Figure 5.253: Target image (top-left), best SPAM match from Merger Wars (top-right), initial N-Body match (bottom-left), and best N-Body match (bottom-right) for SDSS 587747120521216156

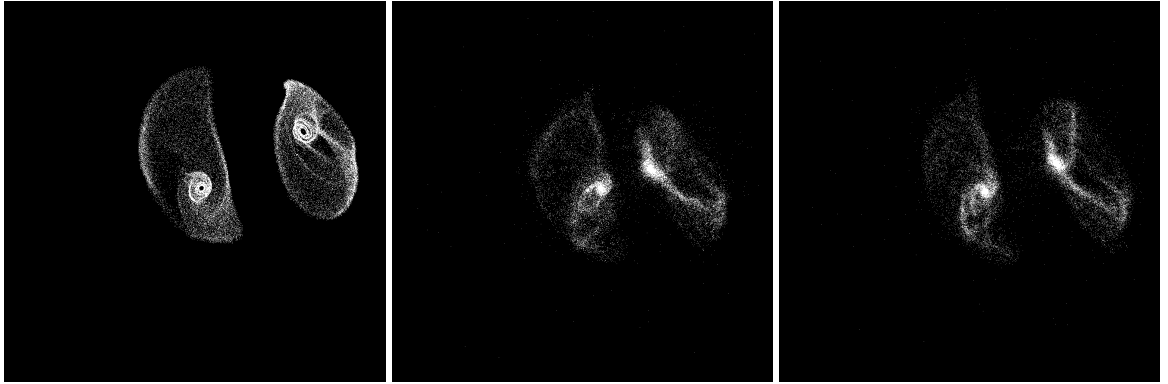


Figure 5.254: XZ projections of best SPAM match from Merger Wars (left), initial N-Body match (middle), and best N-Body match (right) for SDSS 587747120521216156

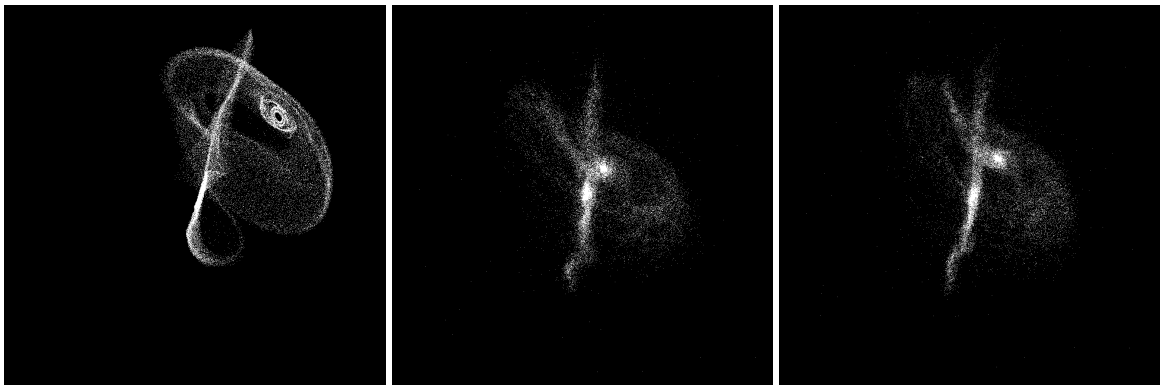


Figure 5.255: YZ projections of best SPAM match from Merger Wars (left), initial N-Body match (middle), and best N-Body match (right) for SDSS 587747120521216156

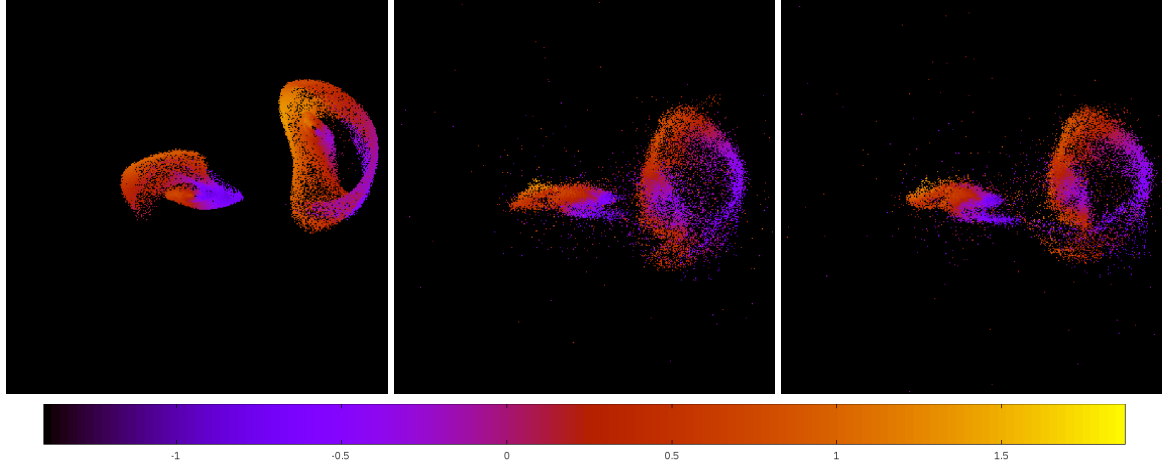


Figure 5.256: Line of sight velocity plots of best SPAM match from Merger Wars (left), initial N-Body match (middle), and best N-Body match (right) for SDSS 587747120521216156

Table 5.86: Orbital Elements & Dynamical Friction for SDSS 587747120521216156

	SPAM Simulation	Initial N-Body Simulation	Best N-Body Simulation
a	-2.152	1.172	3.349
e	1.245	0.883	0.911
r_c	0.527	0.137	0.299
i	38.210°	33.556°	36.548°
Ω	353.038°	352.868°	353.368°
ω	283.536°	206.767°	230.109°
ν	119.612°	168.578°	145.828°
t_n	50	48	47
$\ln\Lambda$	N/A	1.00E-03	2.40E-03

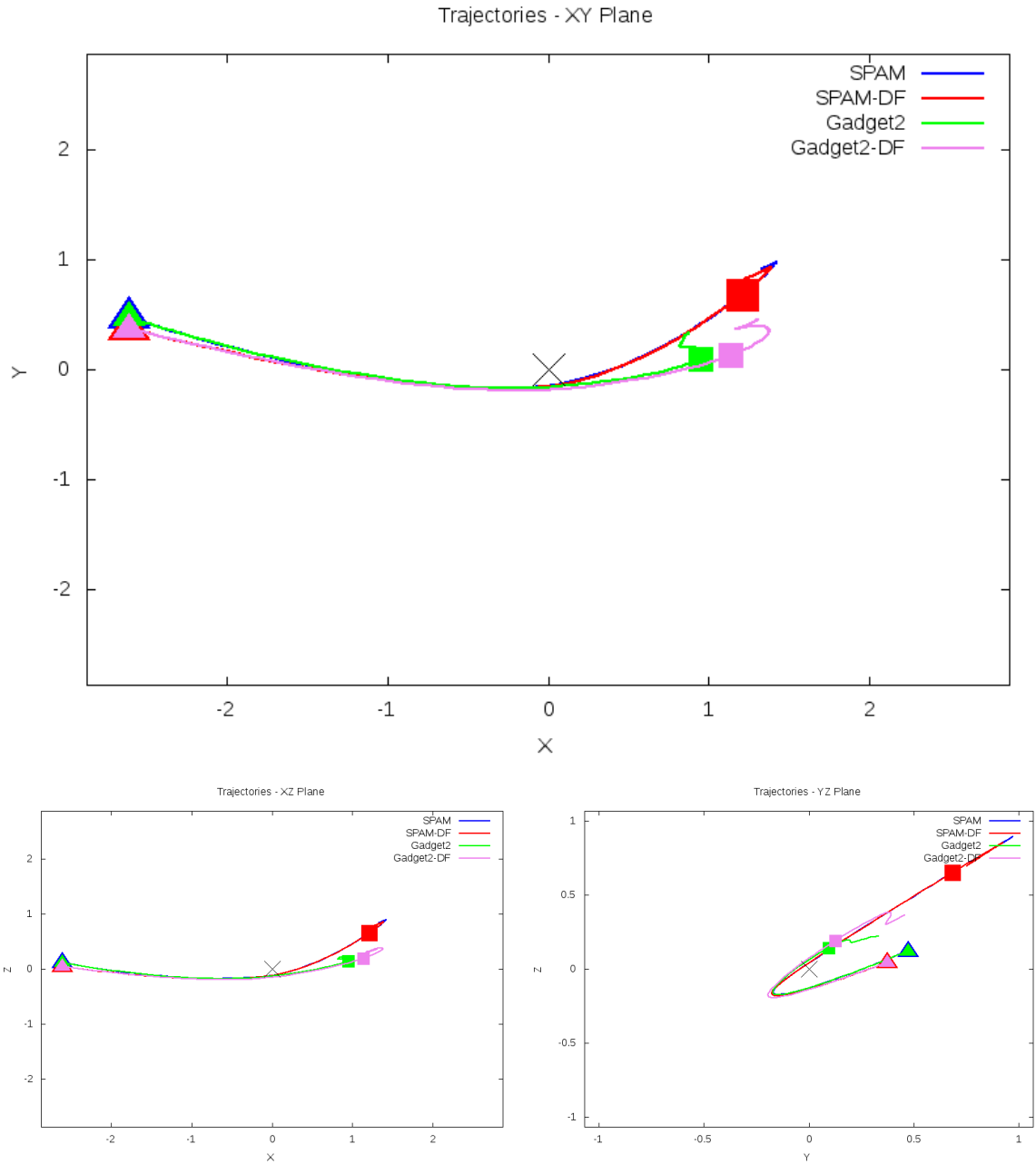


Figure 5.257: Trajectory plots of best SPAM match from Merger Wars, initial N-Body match, and best N-Body match for SDSS 587747120521216156

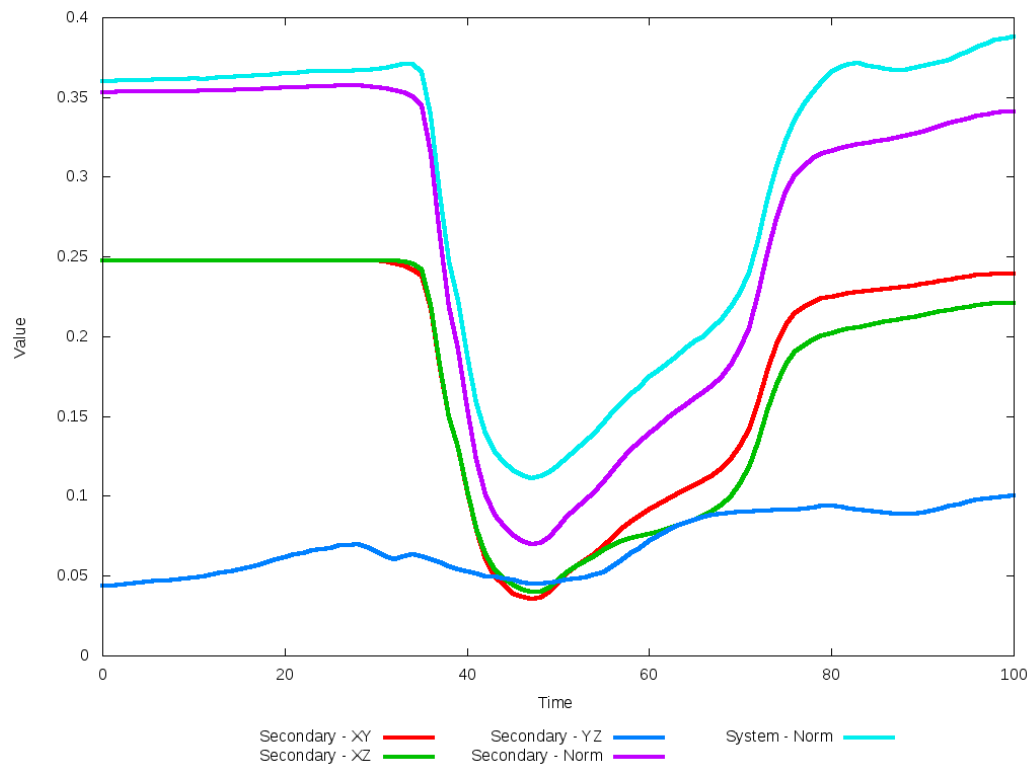
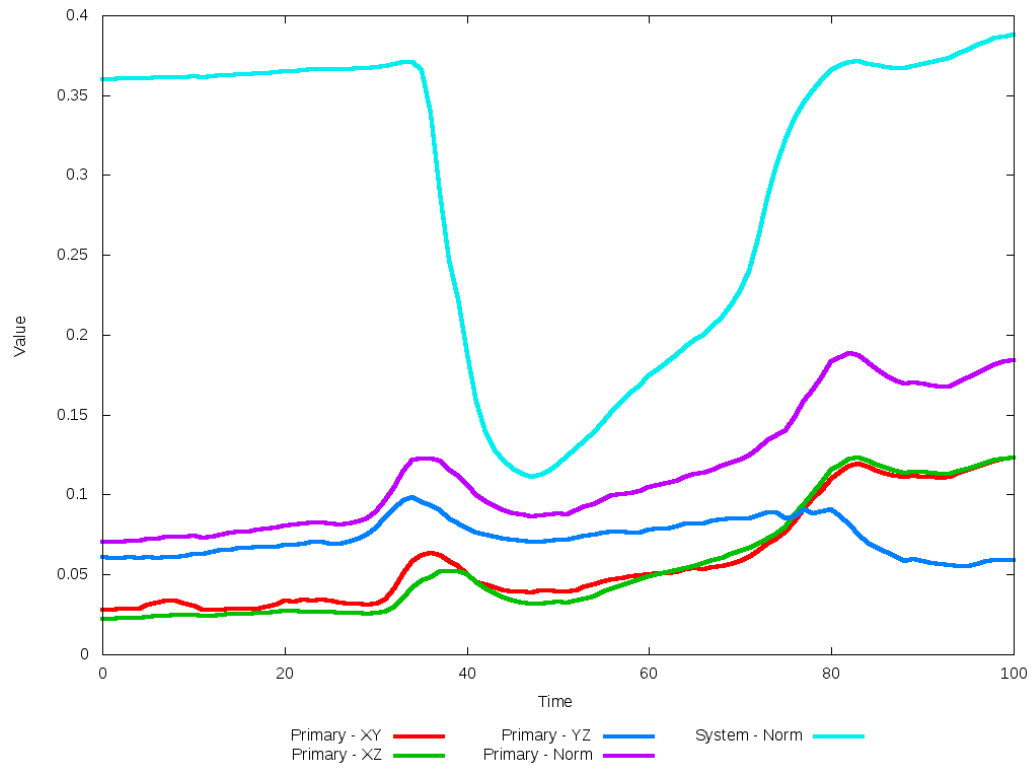


Figure 5.258: All metrics versus simulation time of the best N-Body simulation for SDSS 587747120521216156

5.1.44 SDSS 588007005230530750 (Arp 143)

Arp 143 shows modest positional agreement between its simulations and observational data, with the optimization of dynamical friction improving upon the position of the secondary galaxy and bringing its trajectory closer to the SPAM simulations. However, neither N-Body simulation adequately appear to capture the desired morphology of the secondary galaxy. In particular, the tidal tails of the secondary galaxy are long and thin, extending beyond the primary galaxy. However, with a mass ratio of nearly 3.0, there are three times as many particles in the secondary galaxy to help with visualization. It's possible with more particles, the tails may appear broader.

Table 5.87: Identification Information and Merger Zoo summary for SDSS 588007005230530750.

Name	Aliases	RA (hms)	Dec (dms)	Redshift
SDSS 588007005230530750	Arp 143, NGC 2444/2445	7:46:52.9	+39:01:55.6	0.013503

R_x	R_y	R_z	V_x	V_y	V_z
-0.26053	-1.07287	1.61671	0.31334	-0.12918	0.49763

	Primary Galaxy	Secondary Galaxy
mass	0.41938	0.14077
radius	0.48995	0.51658
ϕ	45.22657°	32.37807°
θ	236.54081°	61.01804°
ϵ	0.3	0.3

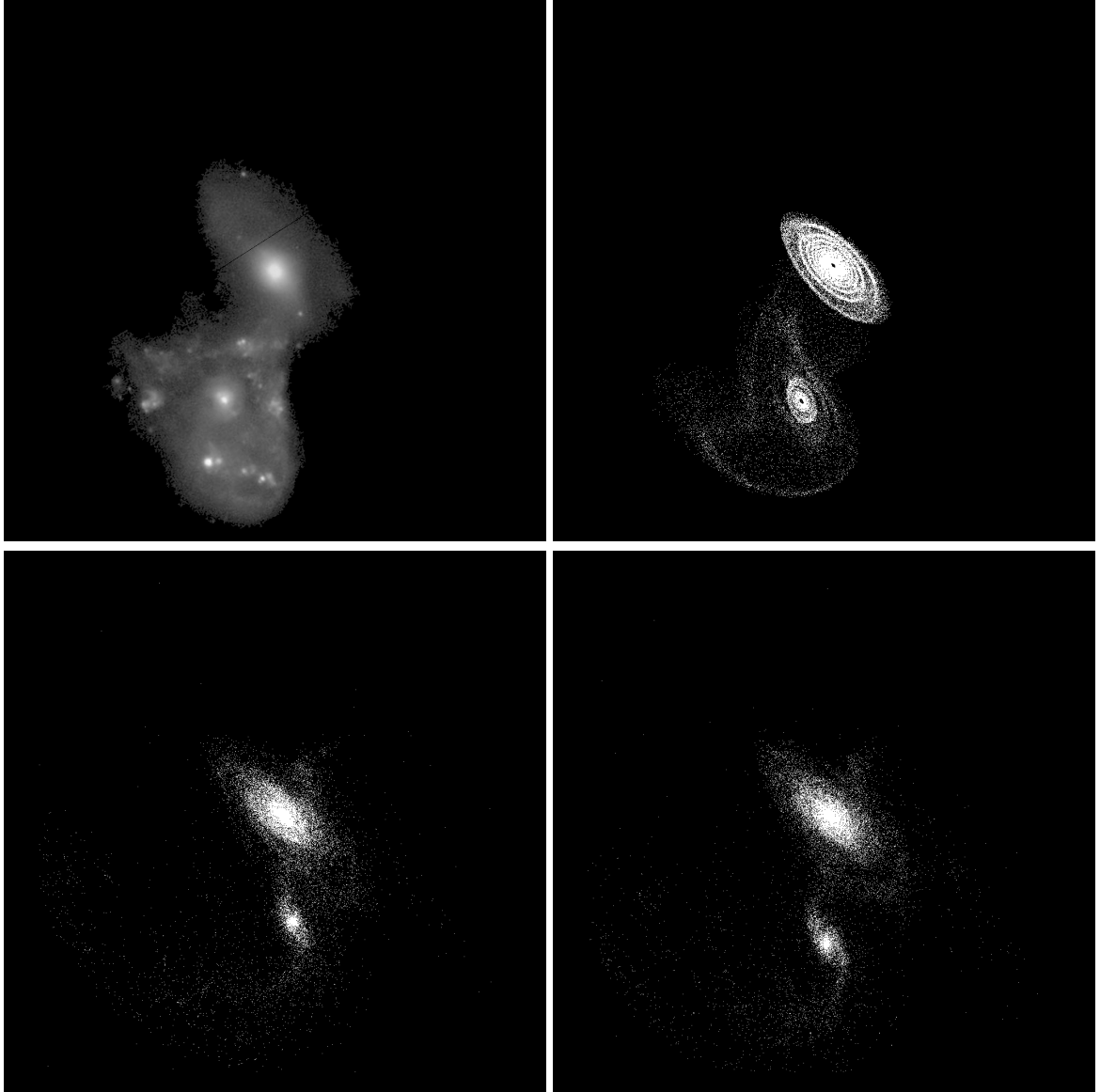


Figure 5.259: Target image (top-left), best SPAM match from Merger Wars (top-right), initial N-Body match (bottom-left), and best N-Body match (bottom-right) for SDSS 588007005230530750

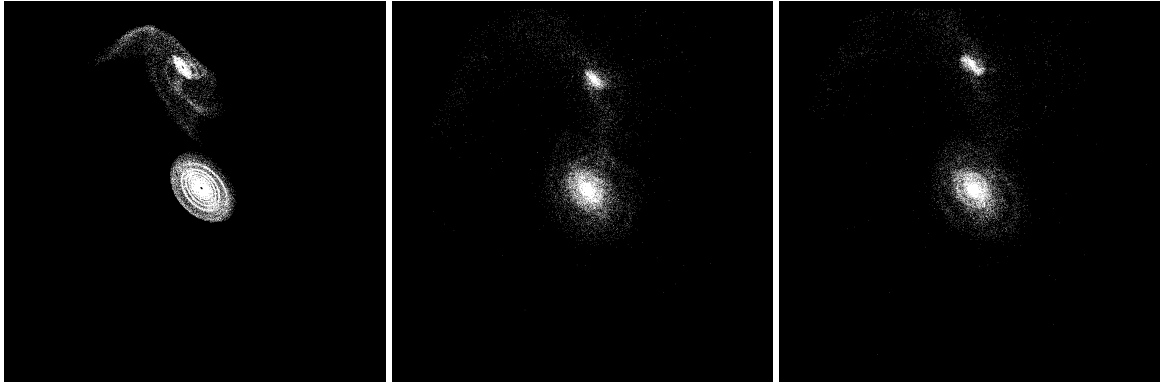


Figure 5.260: XZ projections of best SPAM match from Merger Wars (left), initial N-Body match (middle), and best N-Body match (right) for SDSS 588007005230530750



Figure 5.261: YZ projections of best SPAM match from Merger Wars (left), initial N-Body match (middle), and best N-Body match (right) for SDSS 588007005230530750

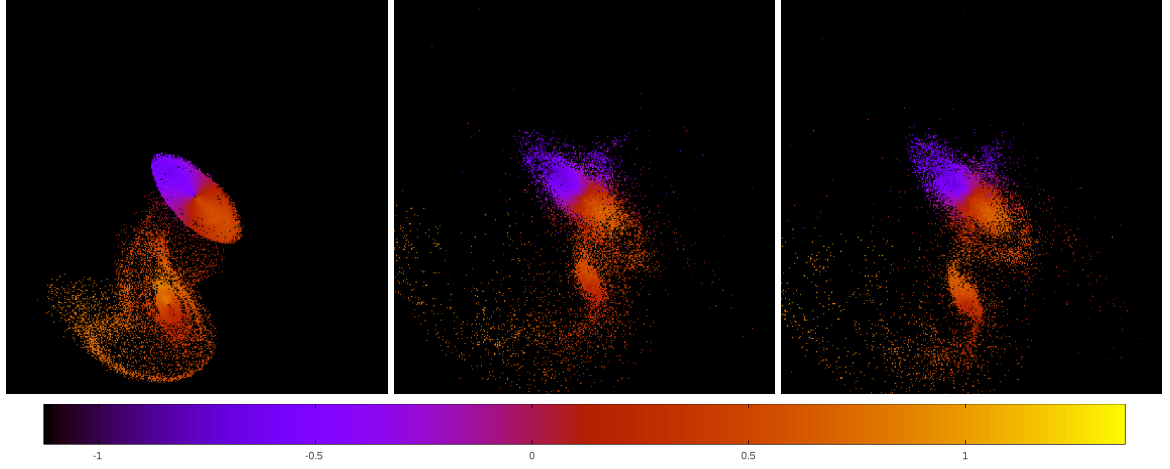


Figure 5.262: Line of sight velocity plots of best SPAM match from Merger Wars (left), initial N-Body match (middle), and best N-Body match (right) for SDSS 588007005230530750

Table 5.88: Orbital Elements & Dynamical Friction for SDSS 588007005230530750

	SPAM Simulation	Initial N-Body Simulation	Best N-Body Simulation
a	-0.827	-2.931	-1.440
e	3.981	1.666	2.477
r_c	2.466	1.953	2.127
i	62.632°	62.493°	62.493°
Ω	207.062°	203.278°	203.115°
ω	10.880°	12.424°	9.124°
ν	57.538°	63.378°	64.055°
t_n	50	50	51
$\ln\Lambda$	N/A	1.00E-03	1.50E-03

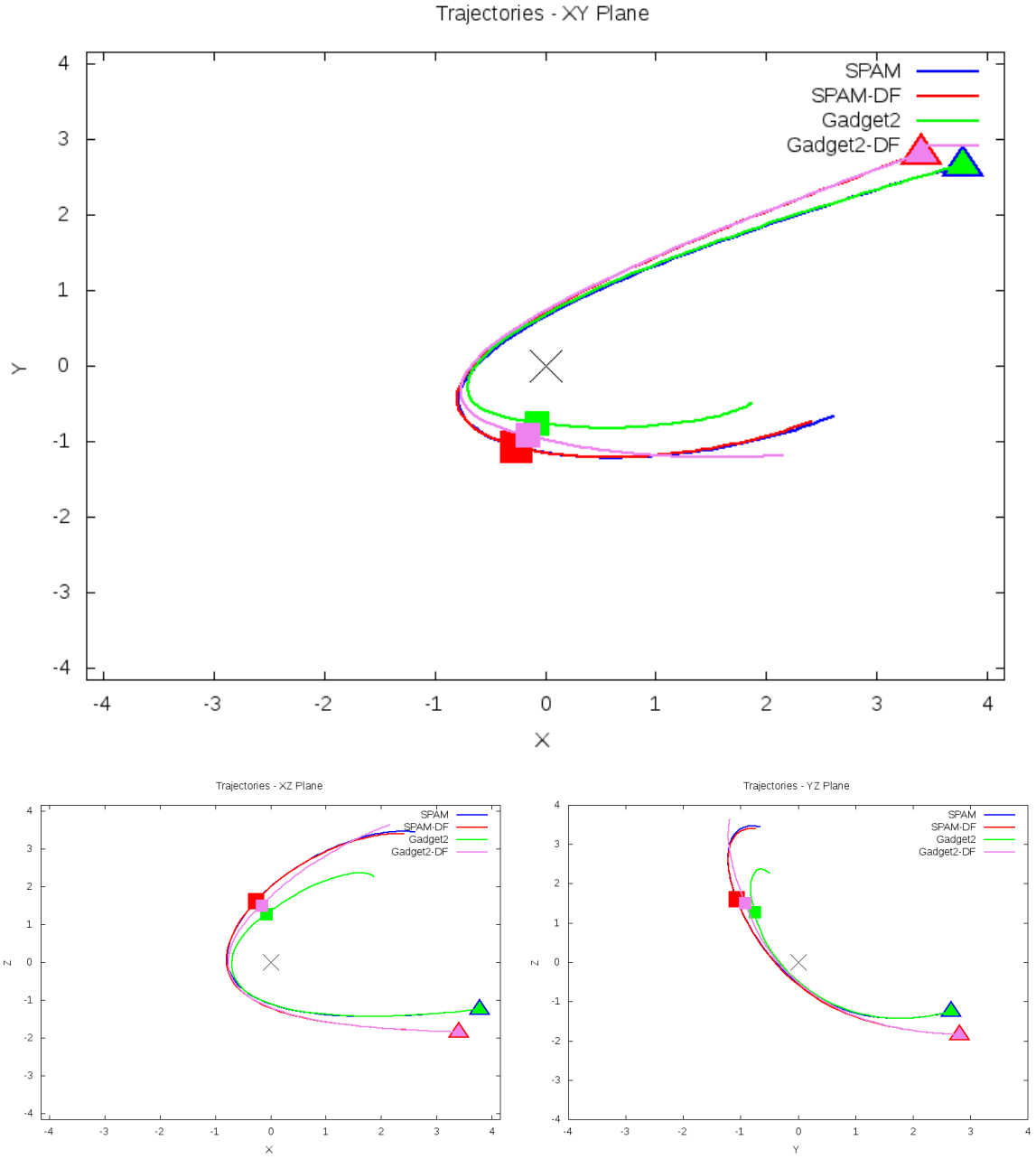


Figure 5.263: Trajectory plots of best SPAM match from Merger Wars, initial N-Body match, and best N-Body match for SDSS 588007005230530750

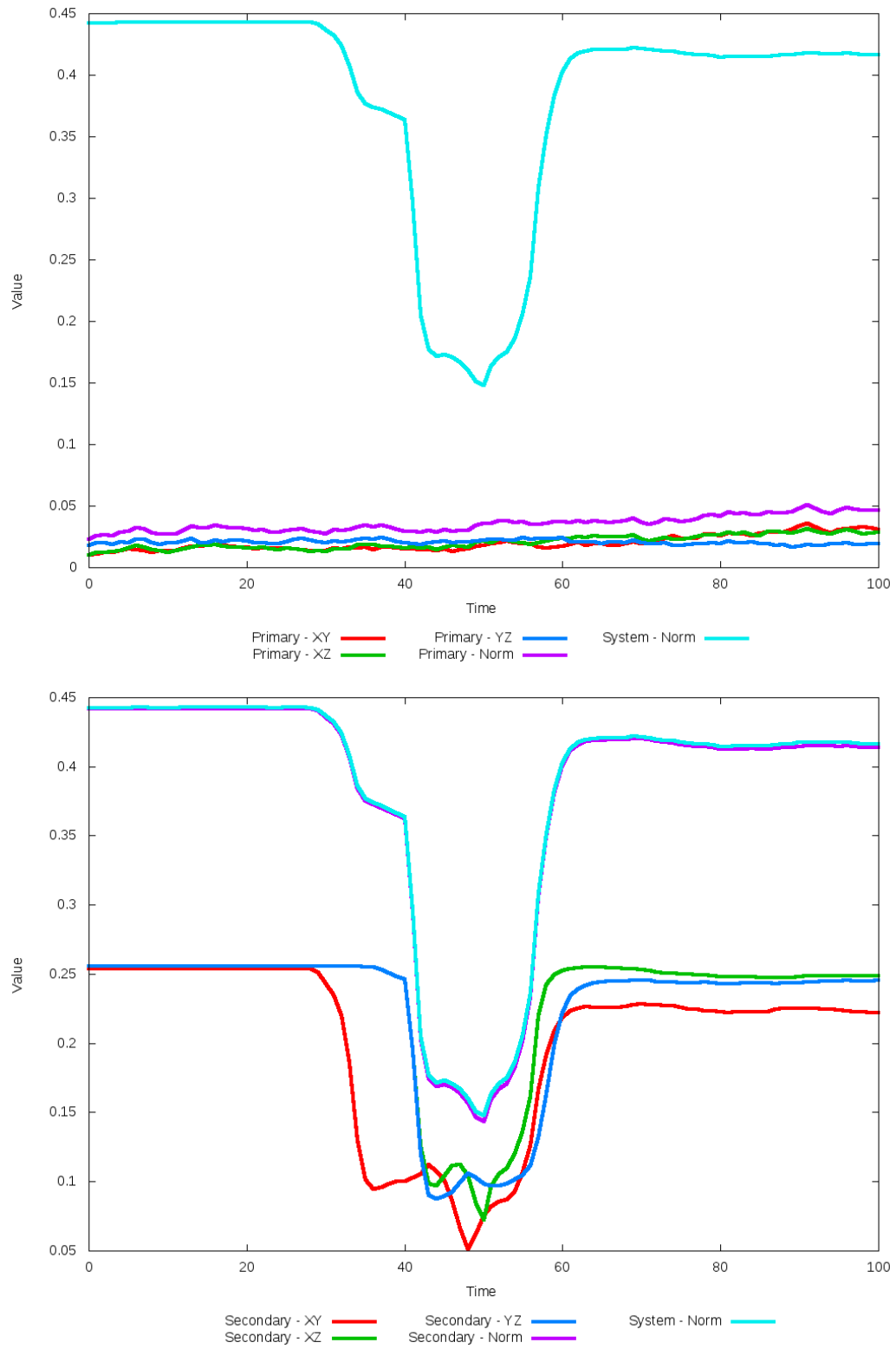


Figure 5.264: All metrics versus simulation time of the best N-Body simulation for SDSS 588007005230530750

5.1.45 SDSS 588011124116422756 (Arp 238)

Arp 238 shows tremendous improvement matching the SPAM simulation and observational data when dynamical friction is optimized. At a quick glance, the initial N-Body simulation looks very similar to the other data sets, albeit rotated approximately 45 degrees counter clockwise in the XY plane. The trajectories paint a different picture, showing the initial simulation's orbit decaying significantly while the optimized simulation's trajectory very closely matches the SPAM trajectories. If the Merger Wars state vector for the system is modified such that SPAM can better match the morphology of the primary galaxy, likely the N-Body simulations should be able to match it too.

Table 5.89: Identification Information and Merger Zoo summary for SDSS 588011124116422756.

Name	Aliases	RA (hms)	Dec (dms)	Redshift
SDSS 588011124116422756	Arp 238, UGC 8335	13:15:31.1	+62:07:45.1	0.030788

R_x	R_y	R_z	V_x	V_y	V_z
0.96515	0.50909	0.06211	1.04124	-1.16798	0.25165

	Primary Galaxy	Secondary Galaxy
mass	1.53689	1.4
radius	0.48536	0.50568
ϕ	117.0625°	116.8125°
θ	131.92546°	228.07453°
ϵ	0.3	0.3

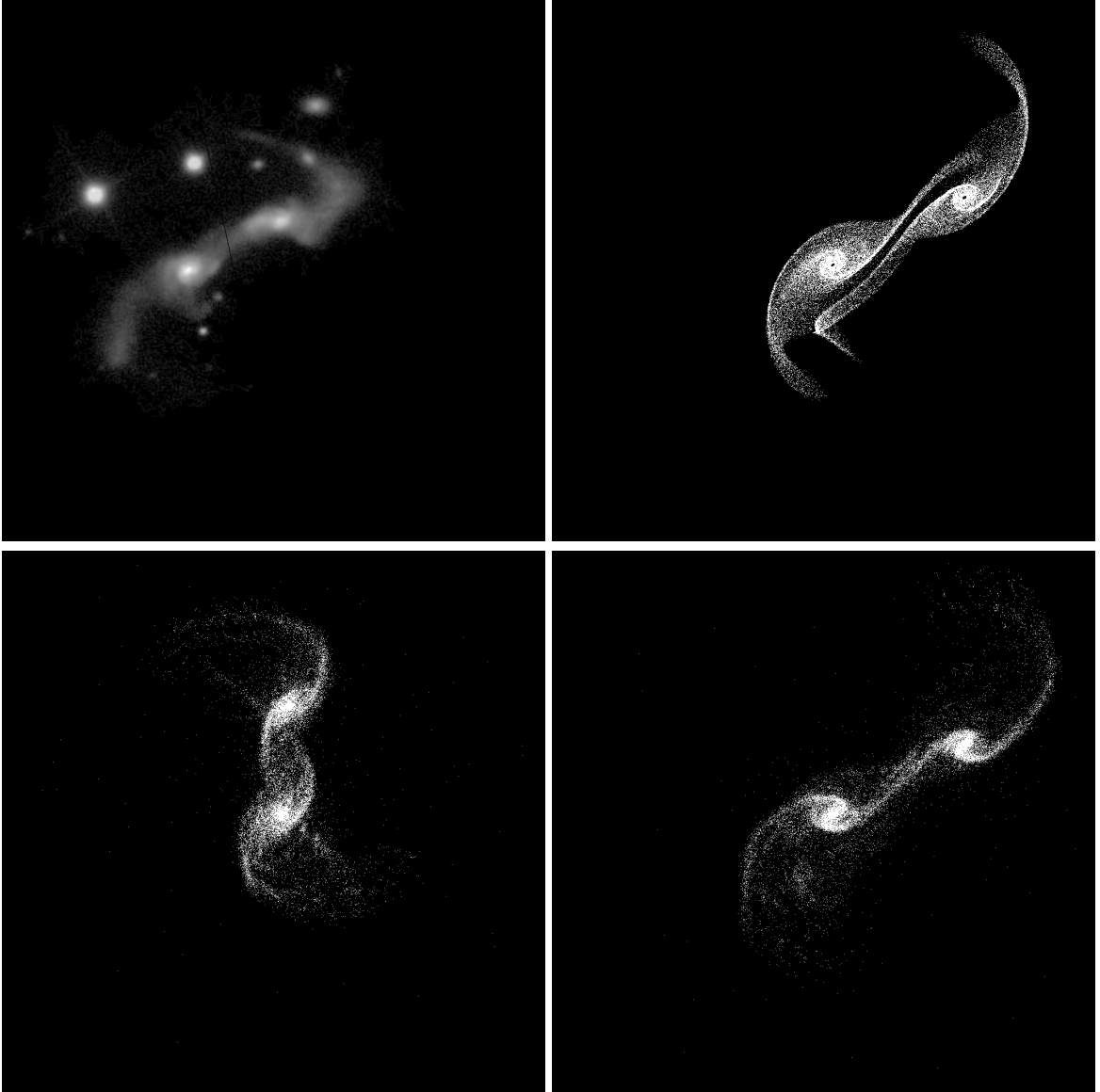


Figure 5.265: Target image (top-left), best SPAM match from Merger Wars (top-right), initial N-Body match (bottom-left), and best N-Body match (bottom-right) for SDSS 588011124116422756

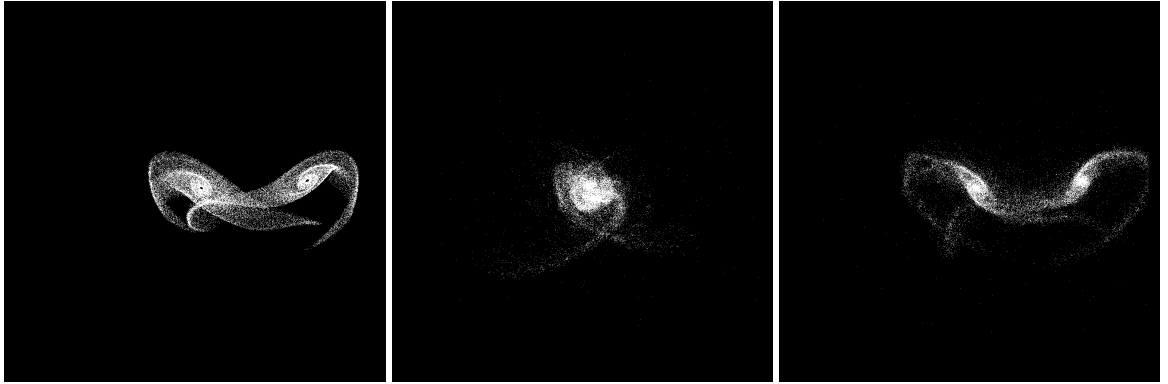


Figure 5.266: XZ projections of best SPAM match from Merger Wars (left), initial N-Body match (middle), and best N-Body match (right) for SDSS 588011124116422756

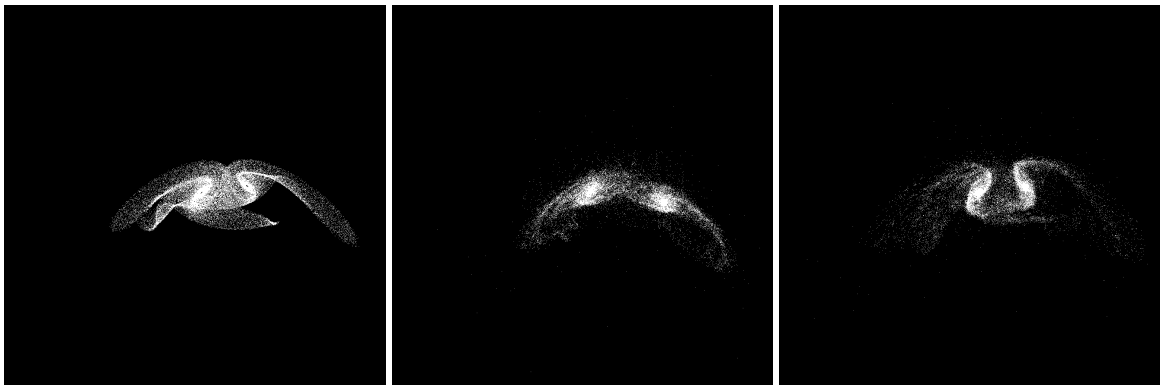


Figure 5.267: YZ projections of best SPAM match from Merger Wars (left), initial N-Body match (middle), and best N-Body match (right) for SDSS 588011124116422756

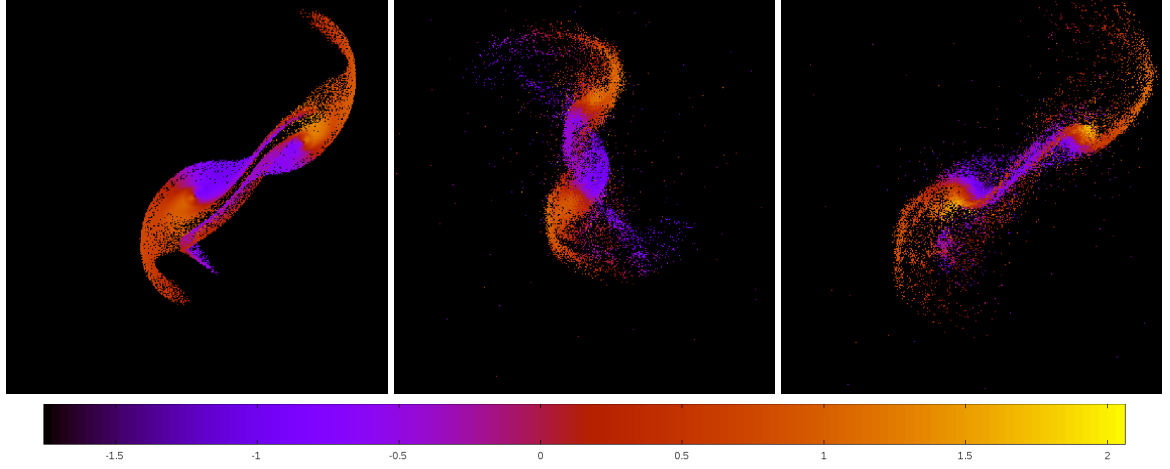


Figure 5.268: Line of sight velocity plots of best SPAM match from Merger Wars (left), initial N-Body match (middle), and best N-Body match (right) for SDSS 588011124116422756

Table 5.90: Orbital Elements & Dynamical Friction for SDSS 588011124116422756

	SPAM Simulation	Initial N-Body Simulation	Best N-Body Simulation
a	-1.282	-0.960	-1.376
e	2.644	2.630	2.486
r_c	2.108	1.564	2.046
i	170.802°	170.238°	170.840°
Ω	48.391°	43.519°	43.270°
ω	2.759°	320.680°	351.284°
ν	19.666°	354.541°	22.469°
t_n	50	32	47
$\ln\Lambda$	N/A	1.00E-03	4.20E-03

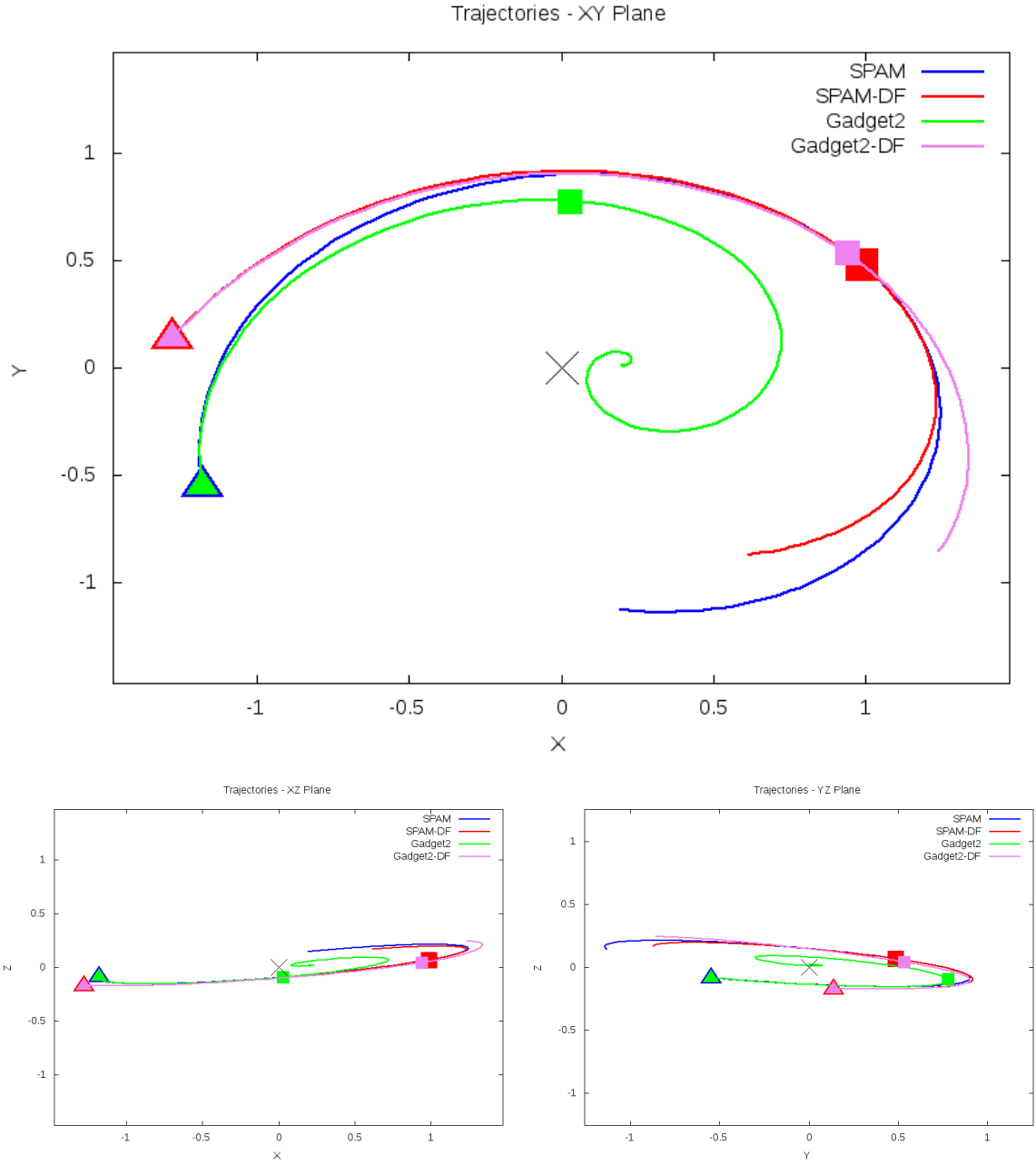


Figure 5.269: Trajectory plots of best SPAM match from Merger Wars, initial N-Body match, and best N-Body match for SDSS 588011124116422756

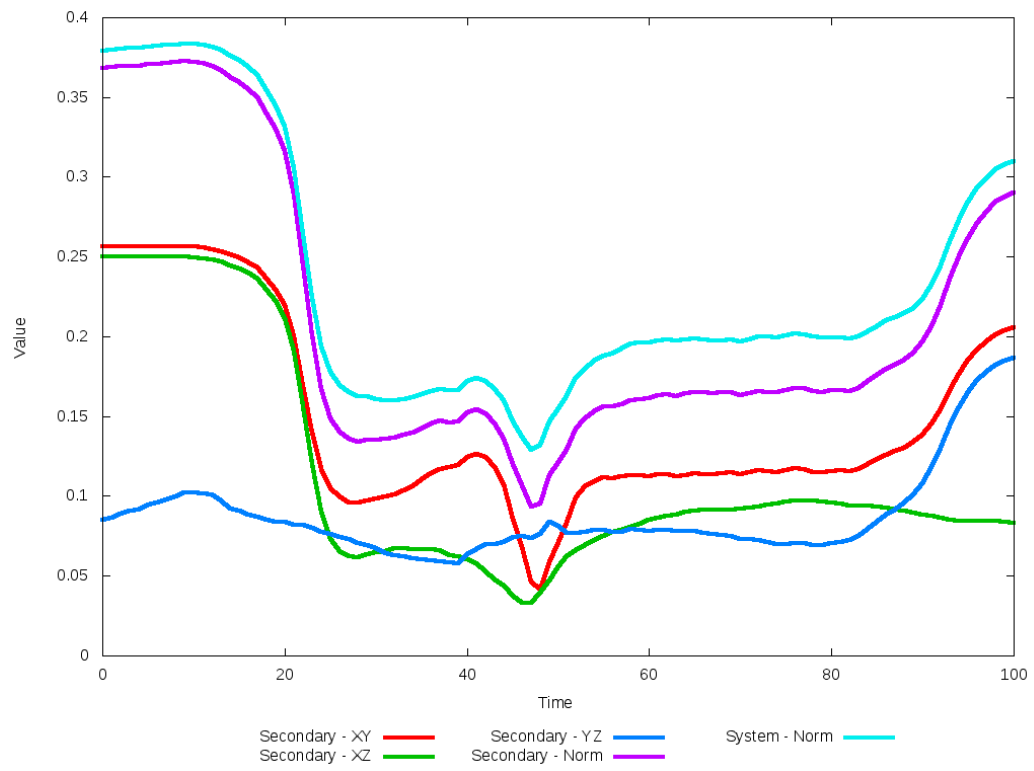
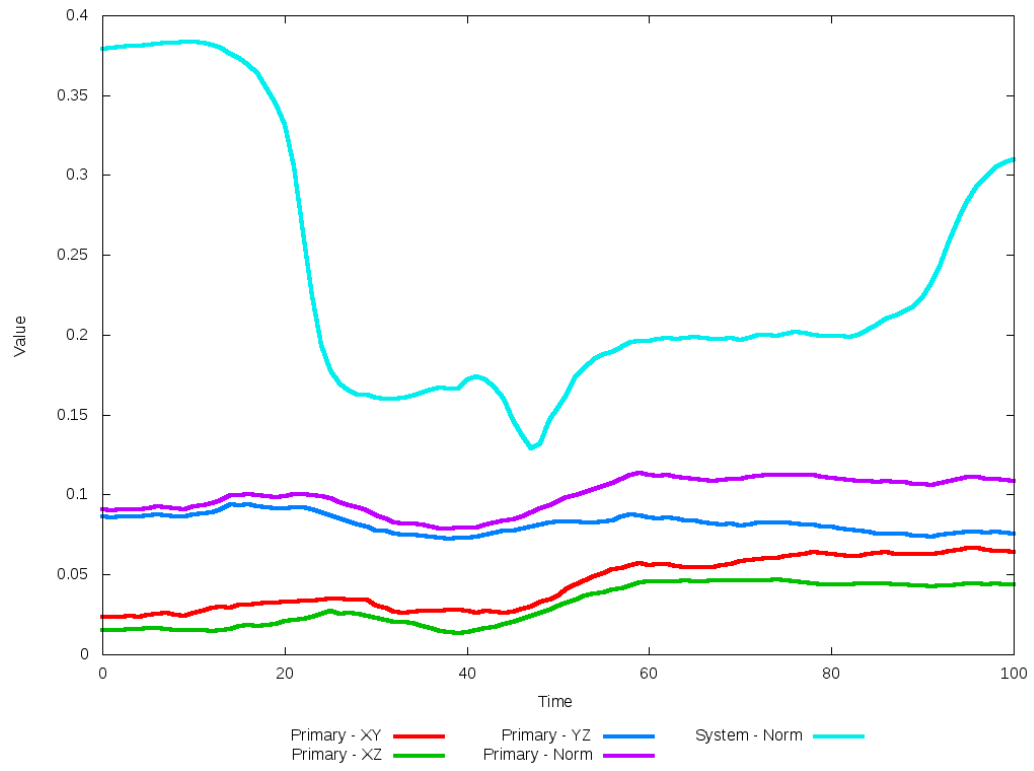


Figure 5.270: All metrics versus simulation time of the best N-Body simulation for SDSS 588011124116422756

5.1.46 SDSS 588013383816904792

This system exhibits only modest agreement between all its simulations and observational data. Morphologically, all look similar with the same spiral arms and tidal features, but the position of the secondary galaxy needs further improvement. In the SPAM simulations, the secondary galaxy appears too far away along the -Y direction, while the N-Body simulations show it too far along the +Y direction. As such, the trajectories of each class of simulation varies significantly once the galaxies come close to each other. This state vector determined by Merger Wars should be revisited to determine if there are alternative orbits to investigate.

Table 5.91: Identification Information and Merger Zoo summary for SDSS 588013383816904792.

Name	Aliases	RA (hms)	Dec (dms)	Redshift
SDSS 588013383816904792	2MASS 12043959+5257265	12:04:39.5	+52:57:25.8	0.080803

R_x	R_y	R_z	V_x	V_y	V_z
0.57769	-0.37316	-1.10901	1.16477	0.09758	-1.35063

	Primary Galaxy	Secondary Galaxy
mass	1.24805	0.59457
radius	0.19797	0.23287
ϕ	85.43445°	97.5088°
θ	317.60473°	4.75135°
ϵ	0.3	0.3

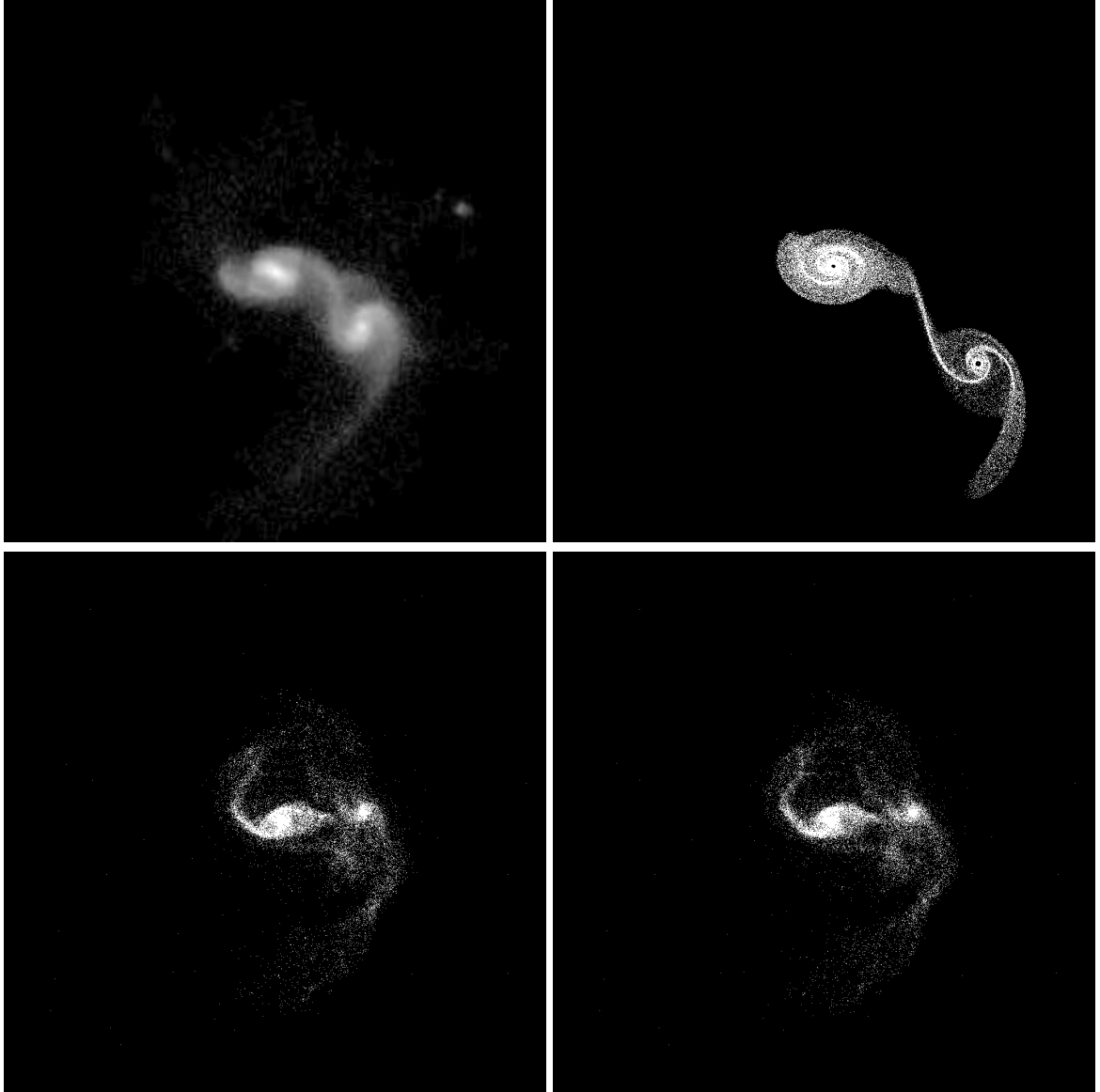


Figure 5.271: Target image (top-left), best SPAM match from Merger Wars (top-right), initial N-Body match (bottom-left), and best N-Body match (bottom-right) for SDSS 588013383816904792



Figure 5.272: XZ projections of best SPAM match from Merger Wars (left), initial N-Body match (middle), and best N-Body match (right) for SDSS 588013383816904792

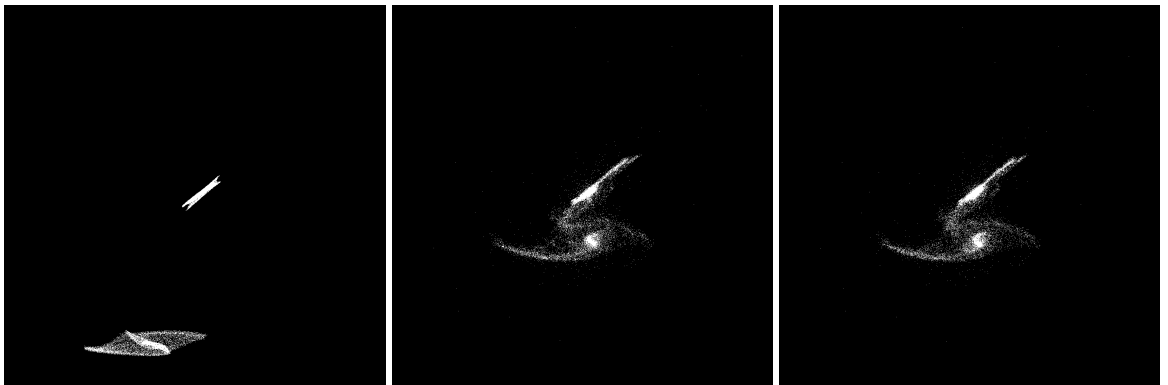


Figure 5.273: YZ projections of best SPAM match from Merger Wars (left), initial N-Body match (middle), and best N-Body match (right) for SDSS 588013383816904792

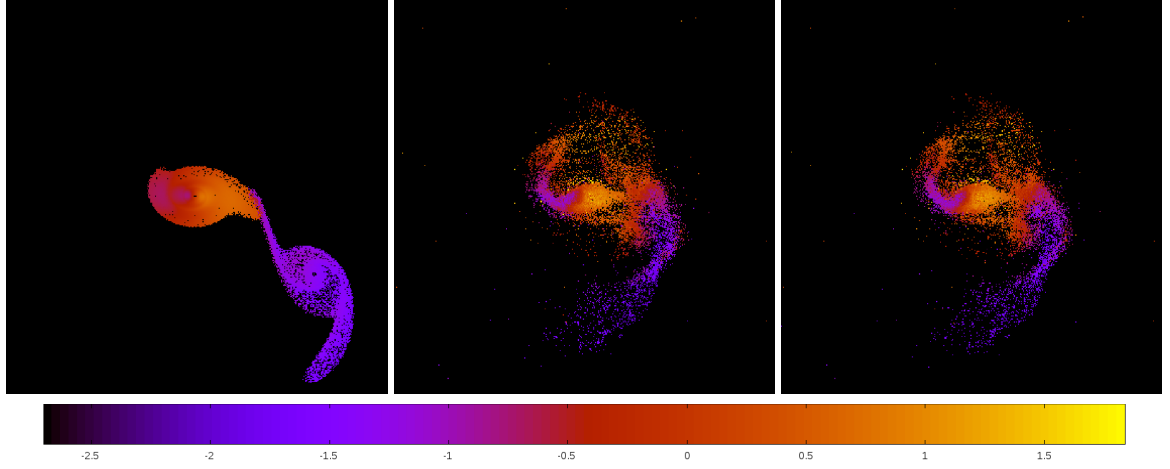


Figure 5.274: Line of sight velocity plots of best SPAM match from Merger Wars (left), initial N-Body match (middle), and best N-Body match (right) for SDSS 588013383816904792

Table 5.92: Orbital Elements & Dynamical Friction for SDSS 588013383816904792

	SPAM Simulation	Initial N-Body Simulation	Best N-Body Simulation
a	-0.313	-0.362	-0.350
e	3.863	2.721	2.790
r_c	0.896	0.623	0.627
i	58.388°	57.687°	57.707°
Ω	50.122°	46.178°	46.194°
ω	193.677°	229.462°	229.376°
ν	80.013°	56.204°	55.867°
t_n	50	34	34
$\ln\Lambda$	N/A	1.00E-03	1.50E-03

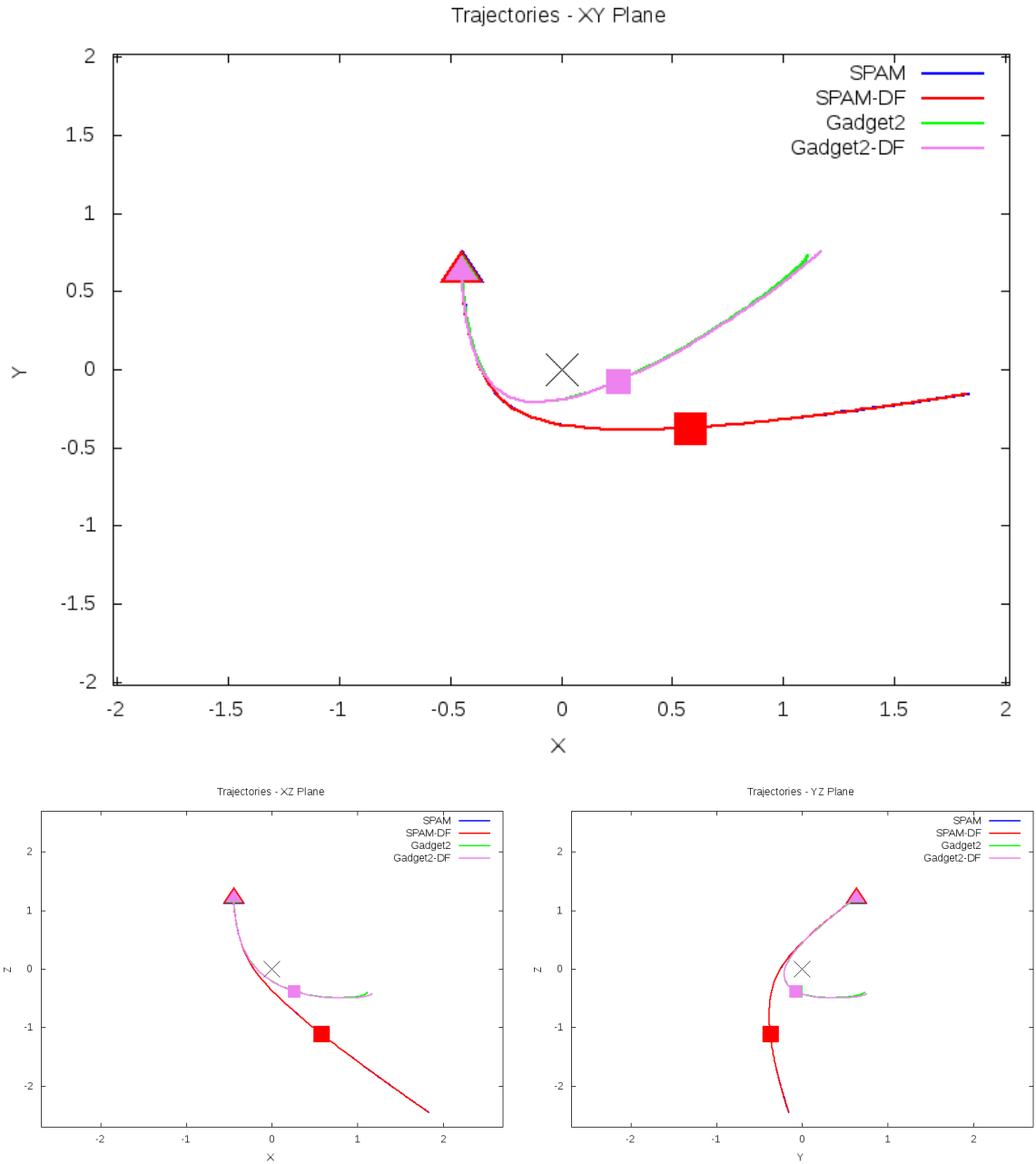


Figure 5.275: Trajectory plots of best SPAM match from Merger Wars, initial N-Body match, and best N-Body match for SDSS 588013383816904792

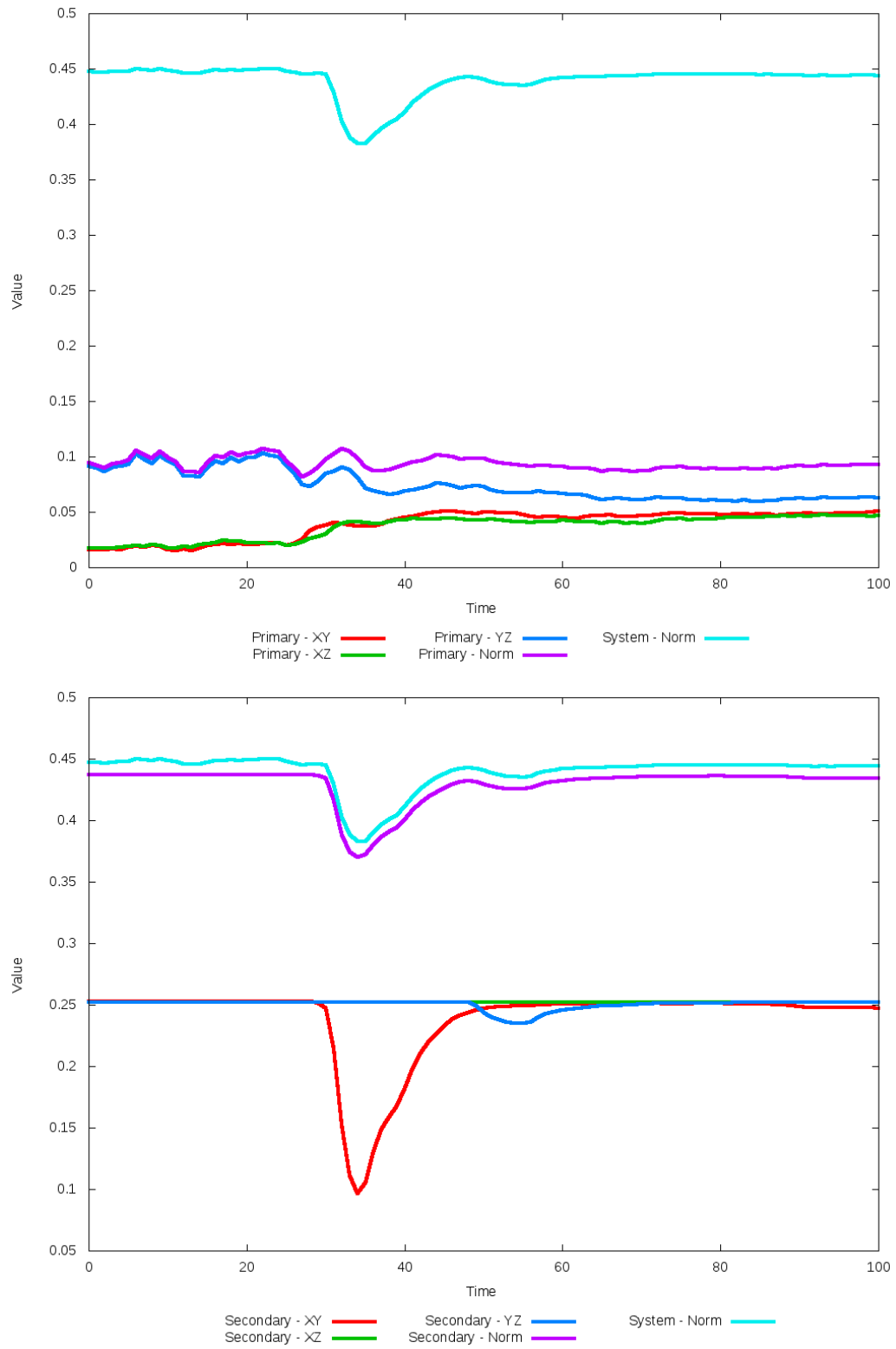


Figure 5.276: All metrics versus simulation time of the best N-Body simulation for SDSS 588013383816904792

5.1.47 SDSS 588017604696408086 (Arp 297)

Arp 297 appears to have achieved a very good agreement between its optimized N-Body simulation, the SPAM simulations, and observational data. Although the spirals are not pronounced in the optimized simulation, the positions of the galaxies are in very good agreement. However, the trajectories show the true story on how his optimized match came to be. In this simulation, with a dynamical friction of zero or nearly zero, the SPAM simulation is already starting relatively close to its predicted apocenter. Because of this, it only backwards integrates a very small amount of time. When the N-Body simulation starts, it only moves for a small amount of time and just so happens to achieve a very good quality of fit thanks to the lack of tidal features to match. Improving the quality of the N-Body simulation will require a manual change to the backwards integration time found by SPAM or a change in SPAM's backwards integration time determination function.

Table 5.93: Identification Information and Merger Zoo summary for SDSS 588017604696408086.

Name	Aliases	RA (hms)	Dec (dms)	Redshift
SDSS 588017604696408086	Arp 297, NGC 5752/5754	14:45:19.6	+38:43:52.5	0.015214

R_x	R_y	R_z	V_x	V_y	V_z
0.77006	-0.18571	-2.39132	0.22907	-0.3688	0.12392

	Primary Galaxy	Secondary Galaxy
mass	0.69896	0.30098
radius	0.71739	0.34935
ϕ	51.4375°	136.0625°
θ	199.00621°	243.7267°
ϵ	0.3	0.3

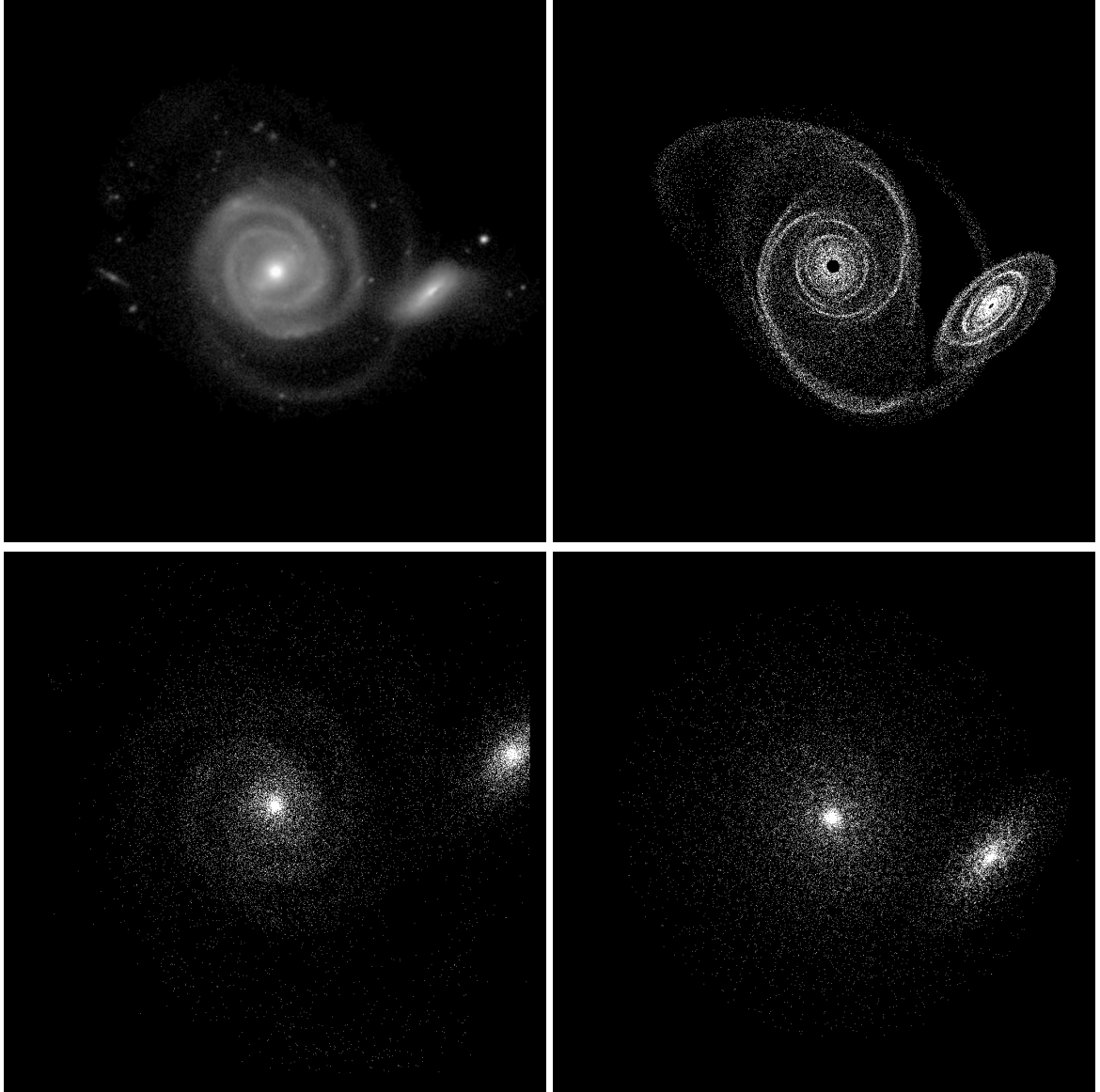


Figure 5.277: Target image (top-left), best SPAM match from Merger Wars (top-right), initial N-Body match (bottom-left), and best N-Body match (bottom-right) for SDSS 588017604696408086

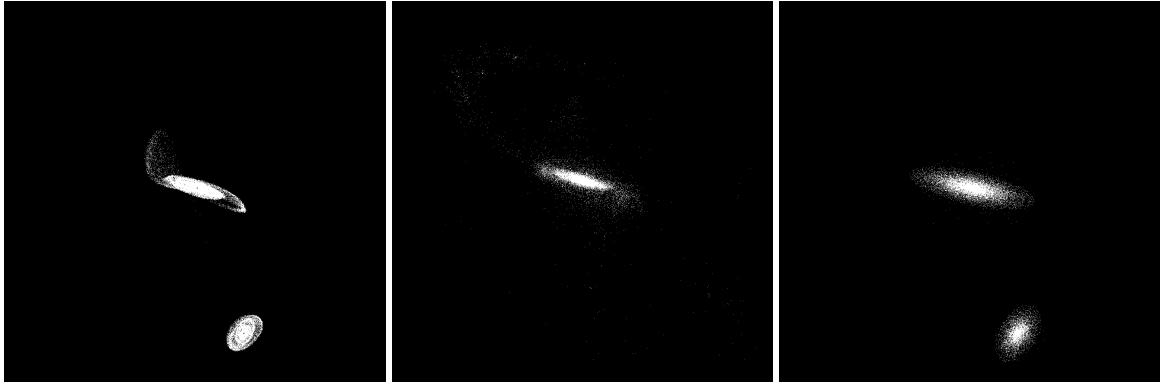


Figure 5.278: XZ projections of best SPAM match from Merger Wars (left), initial N-Body match (middle), and best N-Body match (right) for SDSS 588017604696408086

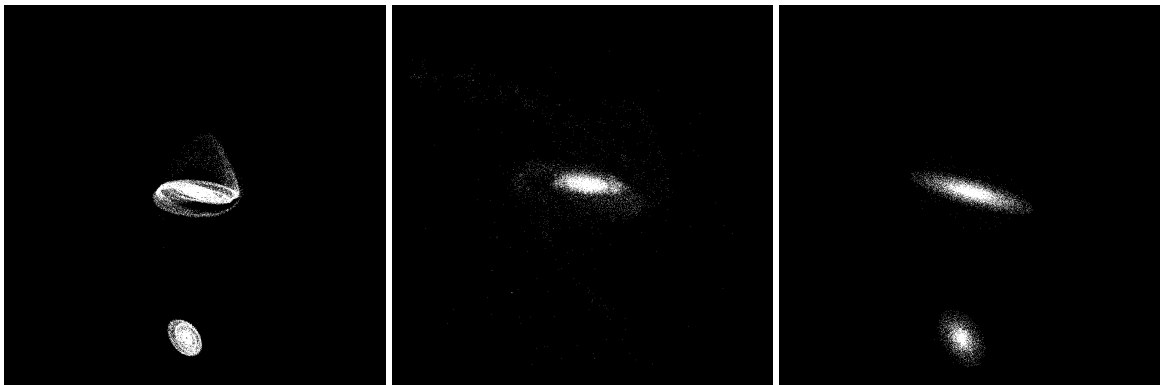


Figure 5.279: YZ projections of best SPAM match from Merger Wars (left), initial N-Body match (middle), and best N-Body match (right) for SDSS 588017604696408086

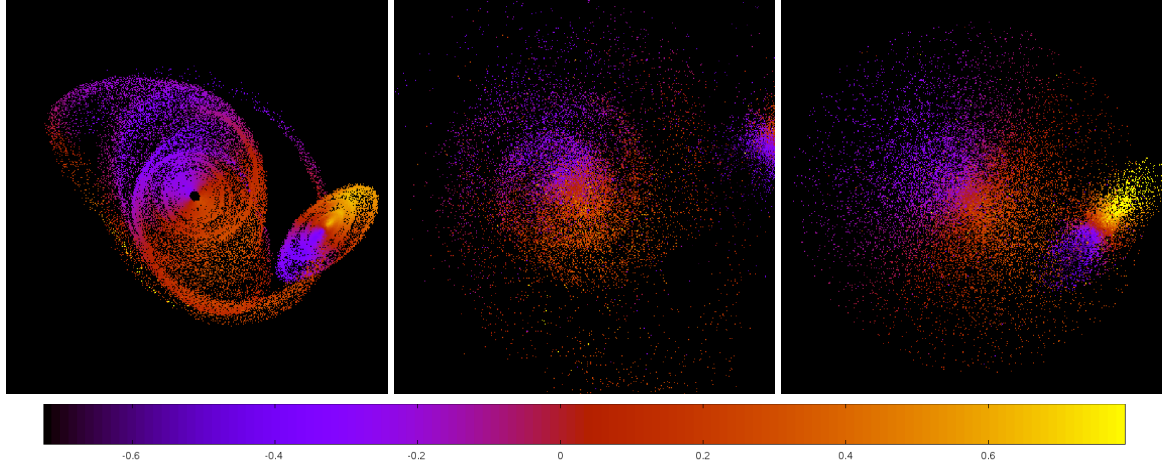


Figure 5.280: Line of sight velocity plots of best SPAM match from Merger Wars (left), initial N-Body match (middle), and best N-Body match (right) for SDSS 588017604696408086

Table 5.94: Orbital Elements & Dynamical Friction for SDSS 588017604696408086

	SPAM Simulation	Initial N-Body Simulation	Best N-Body Simulation
a	-11.431	-10.104	-10.999
e	1.440	1.587	1.457
r_c	5.029	5.929	5.031
i	102.270°	102.168°	102.220°
Ω	305.404°	304.772°	305.635°
ω	288.113°	201.604°	287.820°
ν	355.608°	71.112°	355.806°
t_n	50	70	47
$\ln\Lambda$	N/A	1.00E-03	0.00E+00

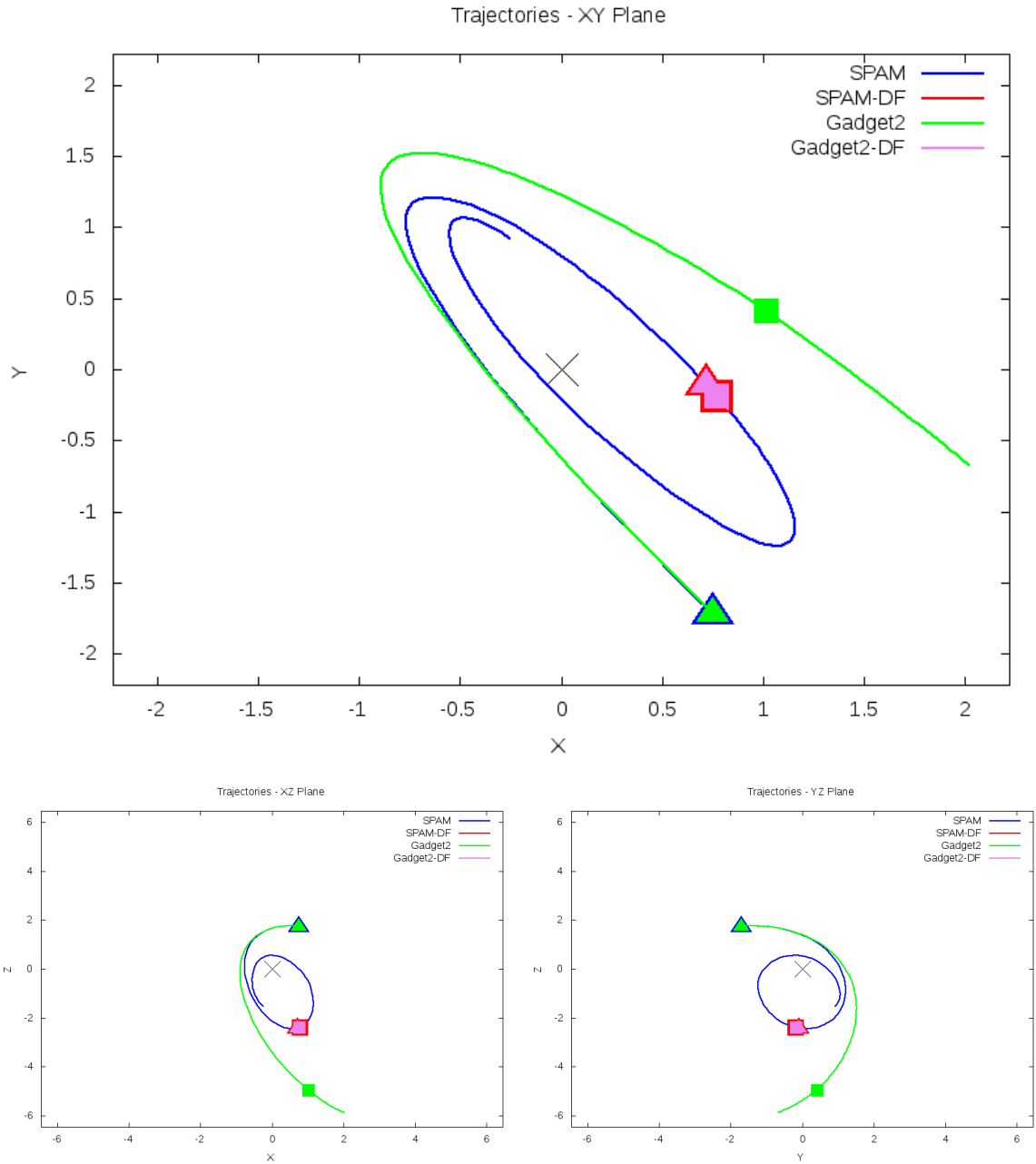


Figure 5.281: Trajectory plots of best SPAM match from Merger Wars, initial N-Body match, and best N-Body match for SDSS 588017604696408086

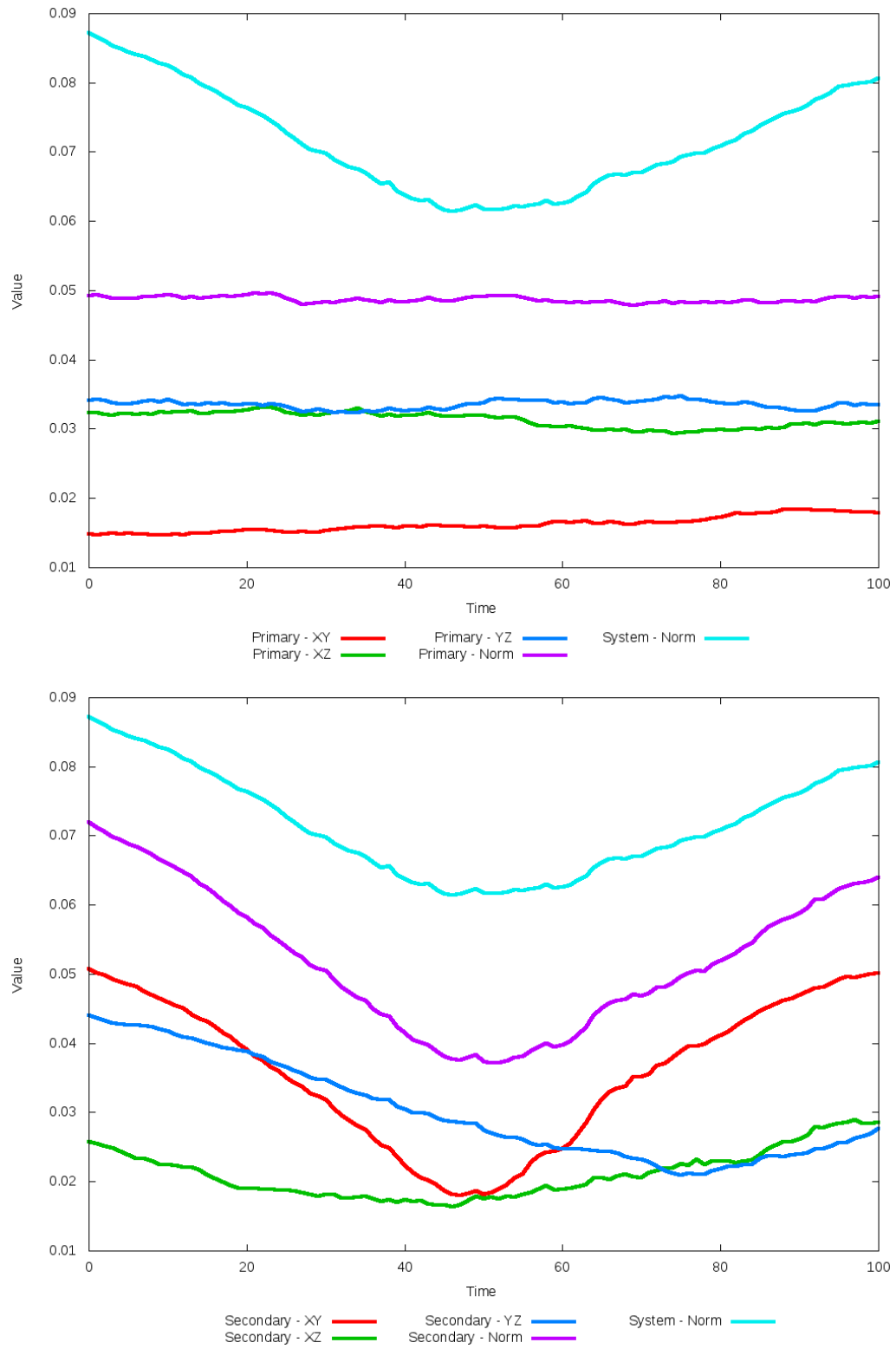


Figure 5.282: All metrics versus simulation time of the best N-Body simulation for SDSS 588017604696408086

5.1.48 SDSS 588017604696408195 (NGC 5753/5755)

NGC 5753/5755 exhibits a much higher degree of interaction between the galaxies in the N-Body simulations than the SPAM simulation and observational data indicate should be present. Both N-Body simulations show spiral features on each galaxy, but they go further by showing very long tails and a galactic bridge between the two. In the XY projection, the initial N-Body simulation's secondary galaxy appears to be better positioned than the optimized case, but the opposite appears true in the other projections. The optimization metric used predicted an overall best match early in the simulation, however if the secondary galaxy's XY metric were used exclusively, it would have found the best match to occur closer to the middle of the simulation time, resulting in a better match. The optimized dynamical friction does show an improvement in matching the orbits in the XZ and YZ planes too.

Table 5.95: Identification Information and Merger Zoo summary for SDSS 588017604696408195.

Name	Aliases	RA (hms)	Dec (dms)	Redshift
SDSS 588017604696408195	NGC 5753/5755, UGC 9507	14:45:18.8	+38:48:20.6	0.032099

R_x	R_y	R_z	V_x	V_y	V_z
-1.65653	-2.3295	-1.43985	-0.3518	-0.50926	-0.03246

	Primary Galaxy	Secondary Galaxy
mass	0.4397	0.2497
radius	0.30783	0.3846
ϕ	141.0625°	110.25°
θ	138.63354°	26.83229°
ϵ	0.3	0.3

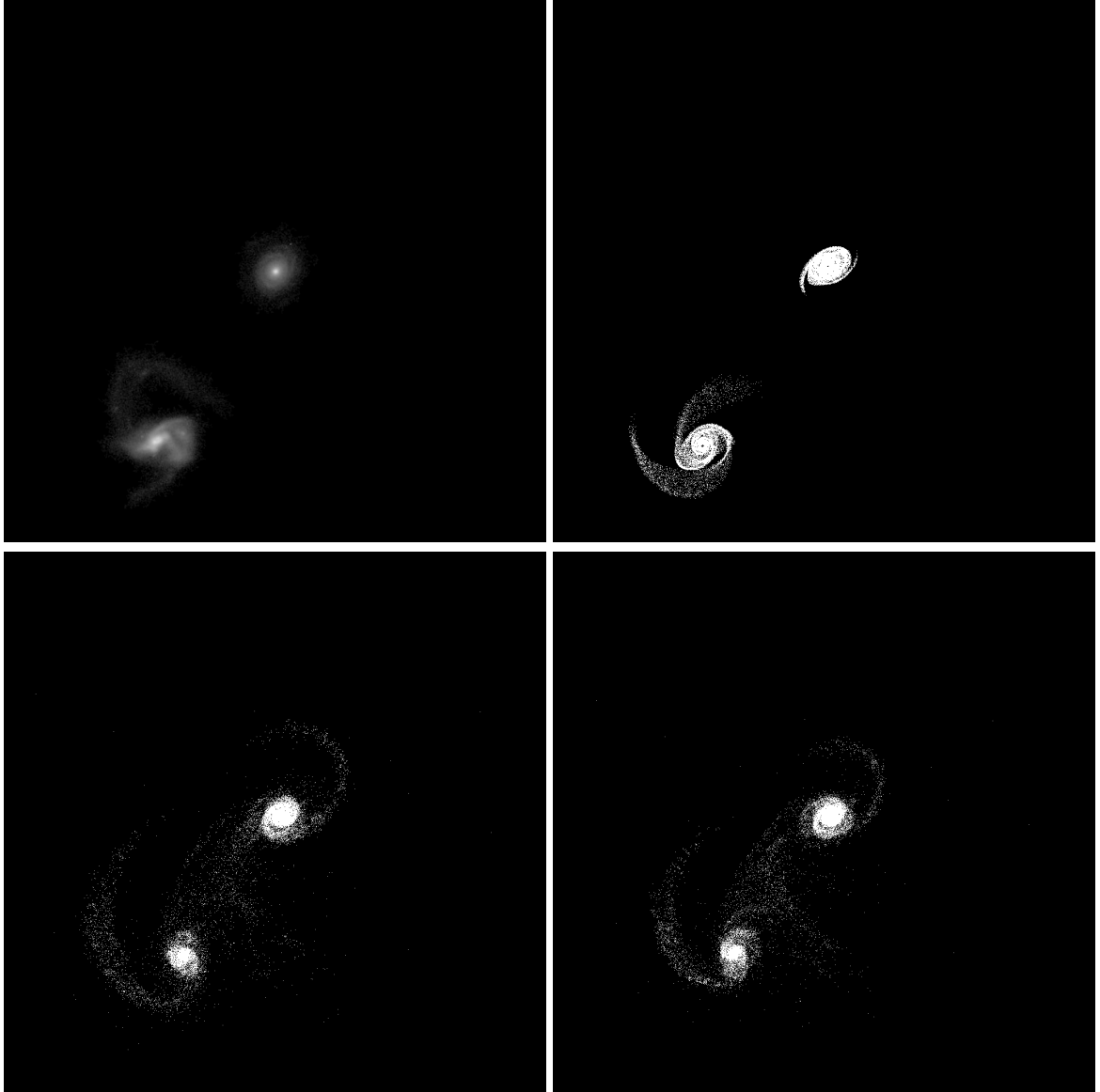


Figure 5.283: Target image (top-left), best SPAM match from Merger Wars (top-right), initial N-Body match (bottom-left), and best N-Body match (bottom-right) for SDSS 588017604696408195

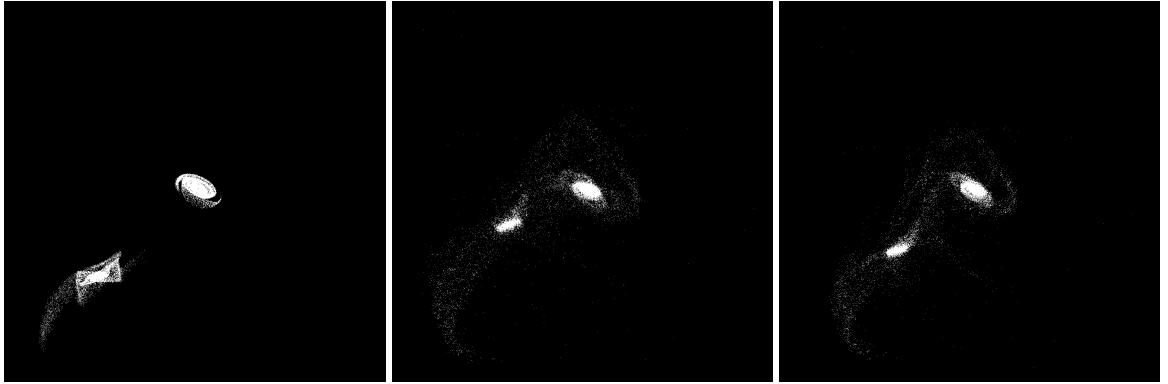


Figure 5.284: XZ projections of best SPAM match from Merger Wars (left), initial N-Body match (middle), and best N-Body match (right) for SDSS 588017604696408195

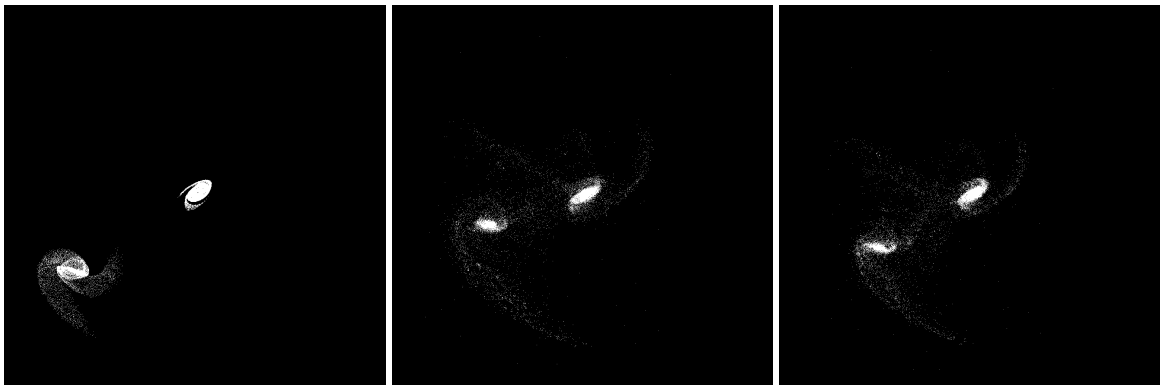


Figure 5.285: YZ projections of best SPAM match from Merger Wars (left), initial N-Body match (middle), and best N-Body match (right) for SDSS 588017604696408195

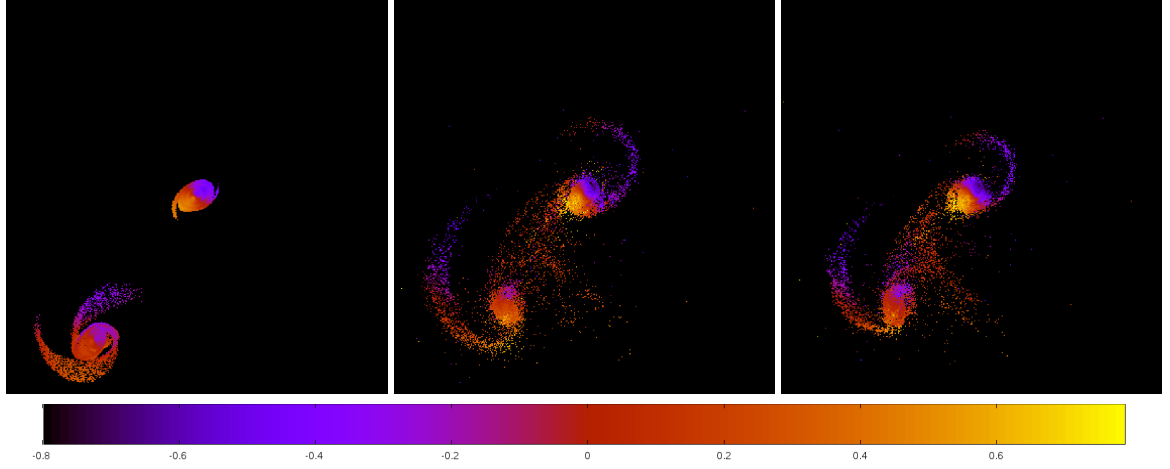


Figure 5.286: Line of sight velocity plots of best SPAM match from Merger Wars (left), initial N-Body match (middle), and best N-Body match (right) for SDSS 588017604696408195

Table 5.96: Orbital Elements & Dynamical Friction for SDSS 588017604696408195

	SPAM Simulation	Initial N-Body Simulation	Best N-Body Simulation
a	-1.119	-1.802	-0.738
e	2.857	1.953	3.377
r_c	2.078	1.718	1.753
i	88.272°	89.682°	90.237°
Ω	235.454°	234.636°	234.363°
ω	248.309°	256.618°	254.285°
ν	84.943°	84.386°	78.056°
t_n	50	41	38
$\ln\Lambda$	N/A	1.00E-03	2.00E-03

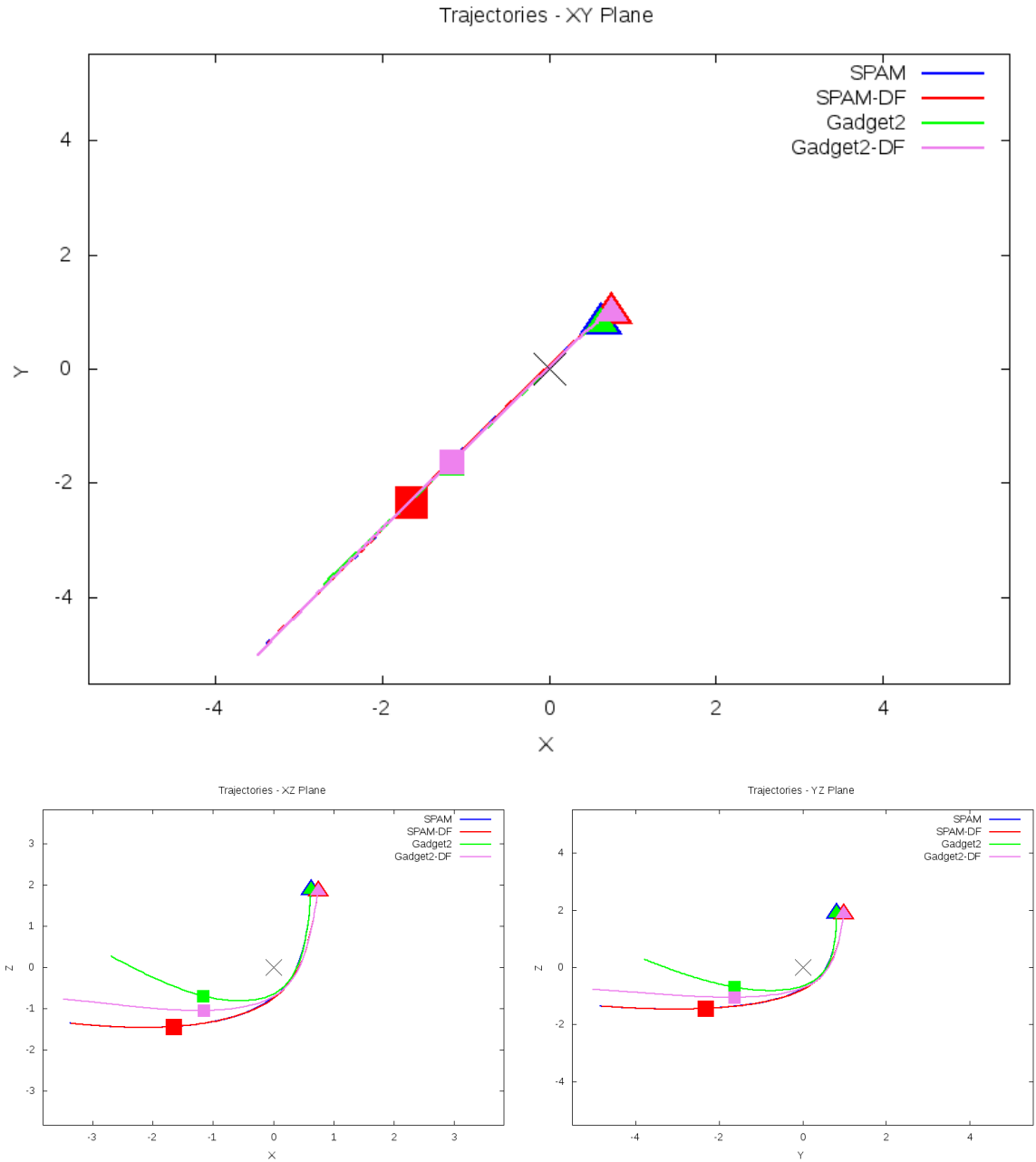


Figure 5.287: Trajectory plots of best SPAM match from Merger Wars, initial N-Body match, and best N-Body match for SDSS 588017604696408195

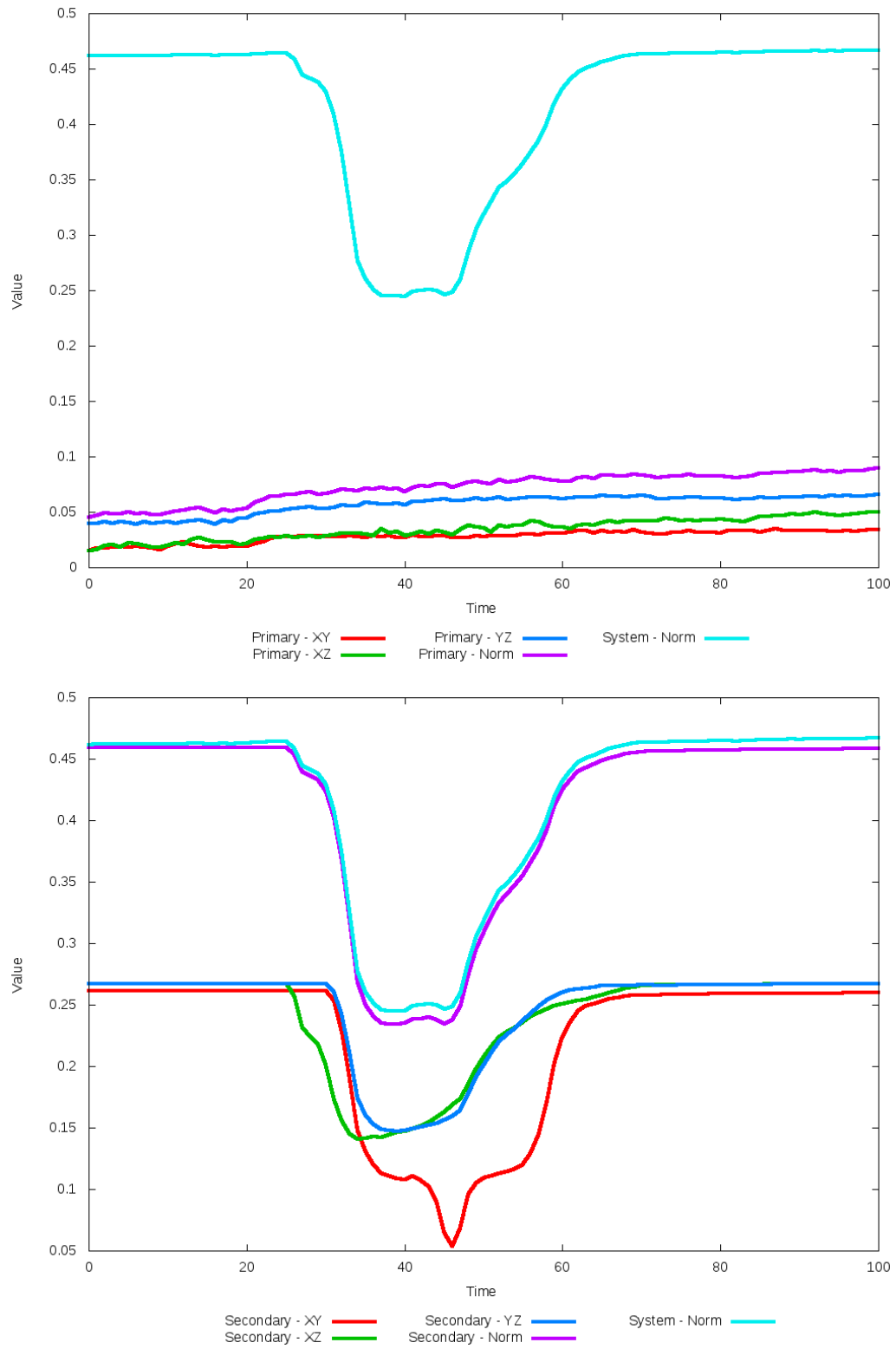


Figure 5.288: All metrics versus simulation time of the best N-Body simulation for SDSS 588017604696408195

5.1.49 SDSS 588017702948962343 (Arp 173)

While the SPAM simulation of Arp 173 matches the observational data very nicely, the N-Body simulations do not. The primary galaxy is very similar between all simulations, exhibiting no appreciable morphology, but the secondary galaxy is greatly out of position. Although the optimized simulation indicates an improvement has been made, it is indiscernable. The trajectories of these simulations show great change to the restricted three-body orbits, with the secondary galaxy appearing to fall apart. It is possible that additional physics may help to hold the galaxy together, but the state vector from Merger Wars should be reviewed to determine if there are alternative candidates to examine.

Table 5.97: Identification Information and Merger Zoo summary for SDSS 588017702948962343.

Name	Aliases	RA (hms)	Dec (dms)	Redshift
SDSS 588017702948962343	Arp 173, UGC 9561	14:51:29.2	+9:20:05.3	0.029441

R_x	R_y	R_z	V_x	V_y	V_z
0.77539	-1.76333	-3.66139	0.4448	0.03362	-0.82359

	Primary Galaxy	Secondary Galaxy
mass	10.87707	0.36014
radius	0.46316	0.45767
ϕ	83.53667°	329.68415°
θ	310.01058°	317.60661°
ϵ	0.3	0.3

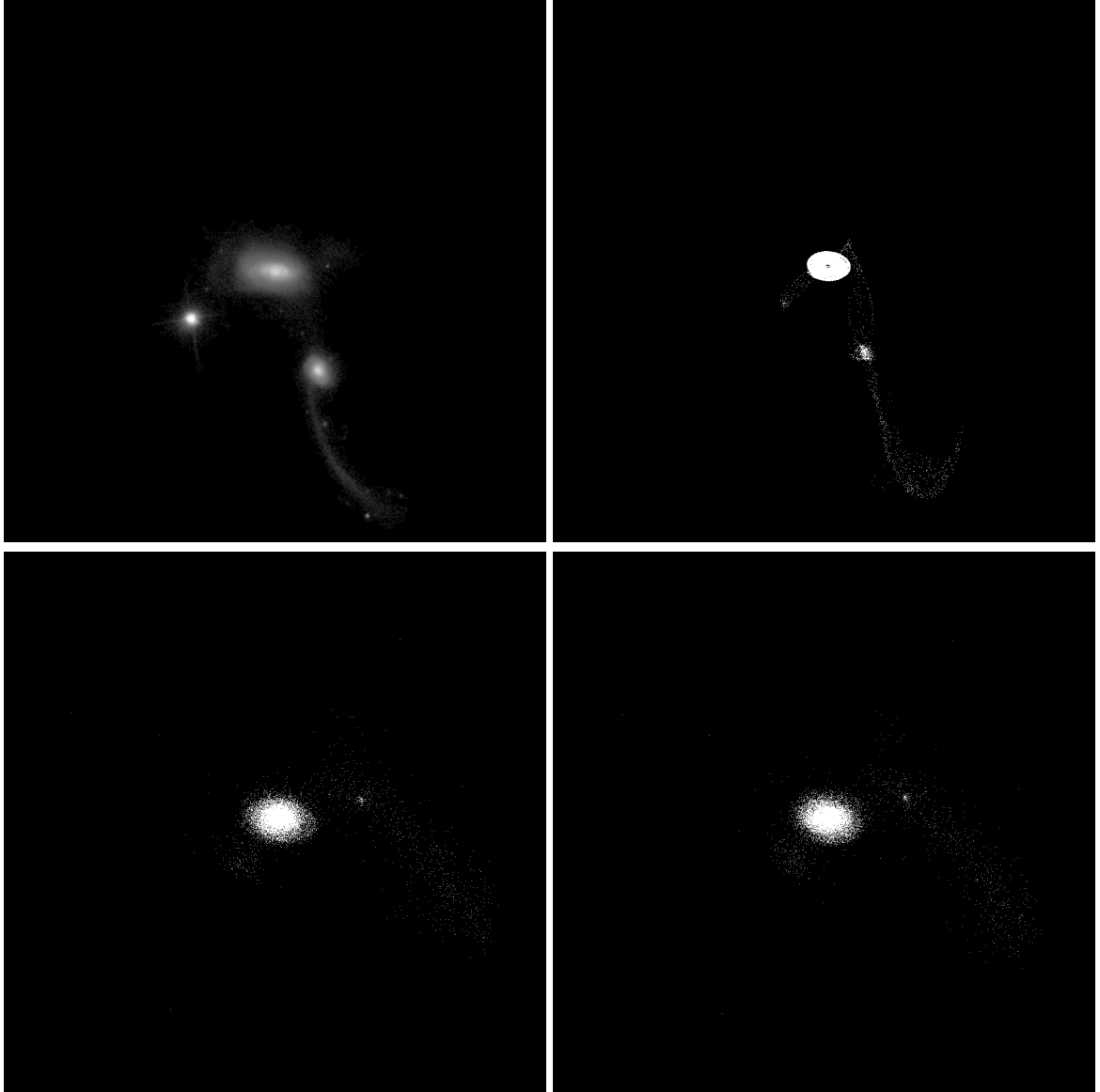


Figure 5.289: Target image (top-left), best SPAM match from Merger Wars (top-right), initial N-Body match (bottom-left), and best N-Body match (bottom-right) for SDSS 588017702948962343

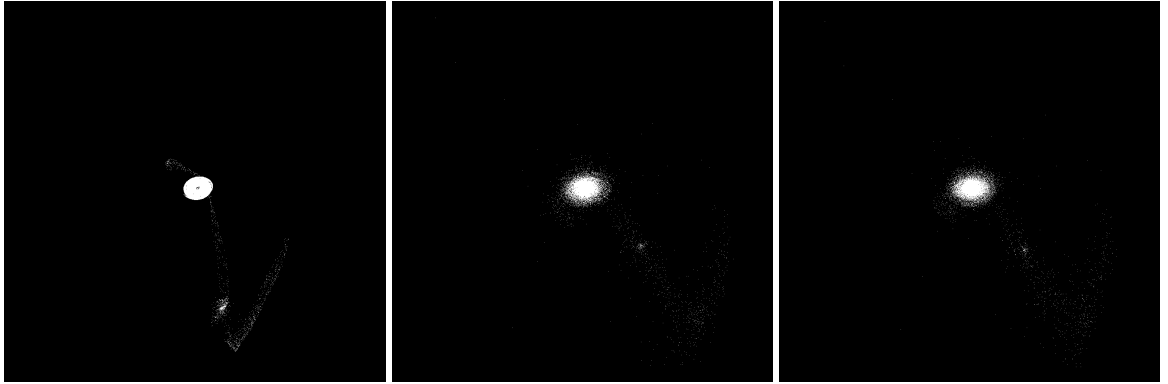


Figure 5.290: XZ projections of best SPAM match from Merger Wars (left), initial N-Body match (middle), and best N-Body match (right) for SDSS 588017702948962343

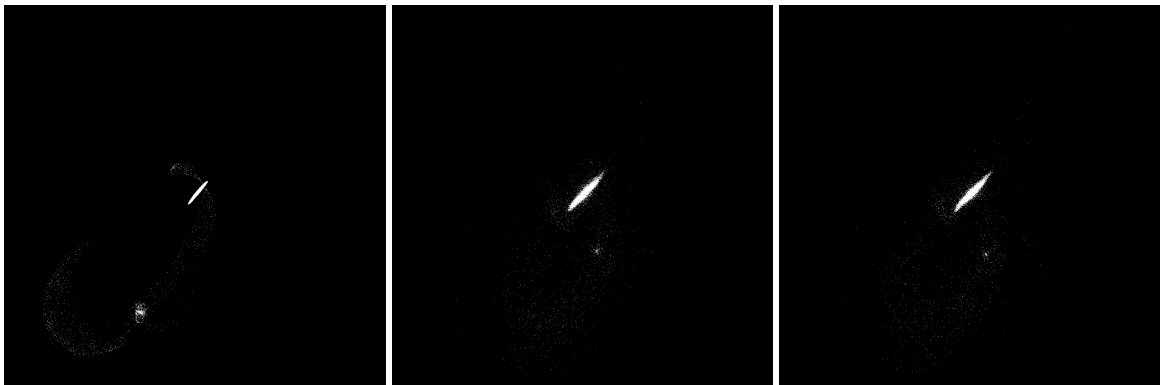


Figure 5.291: YZ projections of best SPAM match from Merger Wars (left), initial N-Body match (middle), and best N-Body match (right) for SDSS 588017702948962343

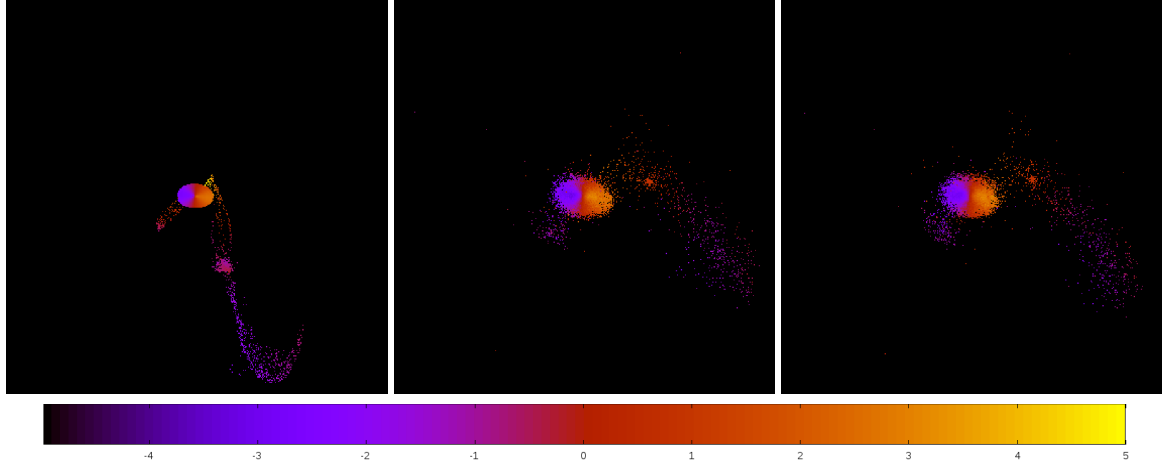


Figure 5.292: Line of sight velocity plots of best SPAM match from Merger Wars (left), initial N-Body match (middle), and best N-Body match (right) for SDSS 588017702948962343

Table 5.98: Orbital Elements & Dynamical Friction for SDSS 588017702948962343

	SPAM Simulation	Initial N-Body Simulation	Best N-Body Simulation
a	-0.964	7.226	7.190
e	5.051	0.728	0.789
r_c	3.905	1.965	1.518
i	66.464°	59.623°	56.918°
Ω	57.854°	41.823°	48.623°
ω	186.479°	171.494°	158.514°
ν	68.268°	121.241°	128.644°
t_n	50	51	50
$\ln\Lambda$	N/A	1.00E-03	1.60E-03

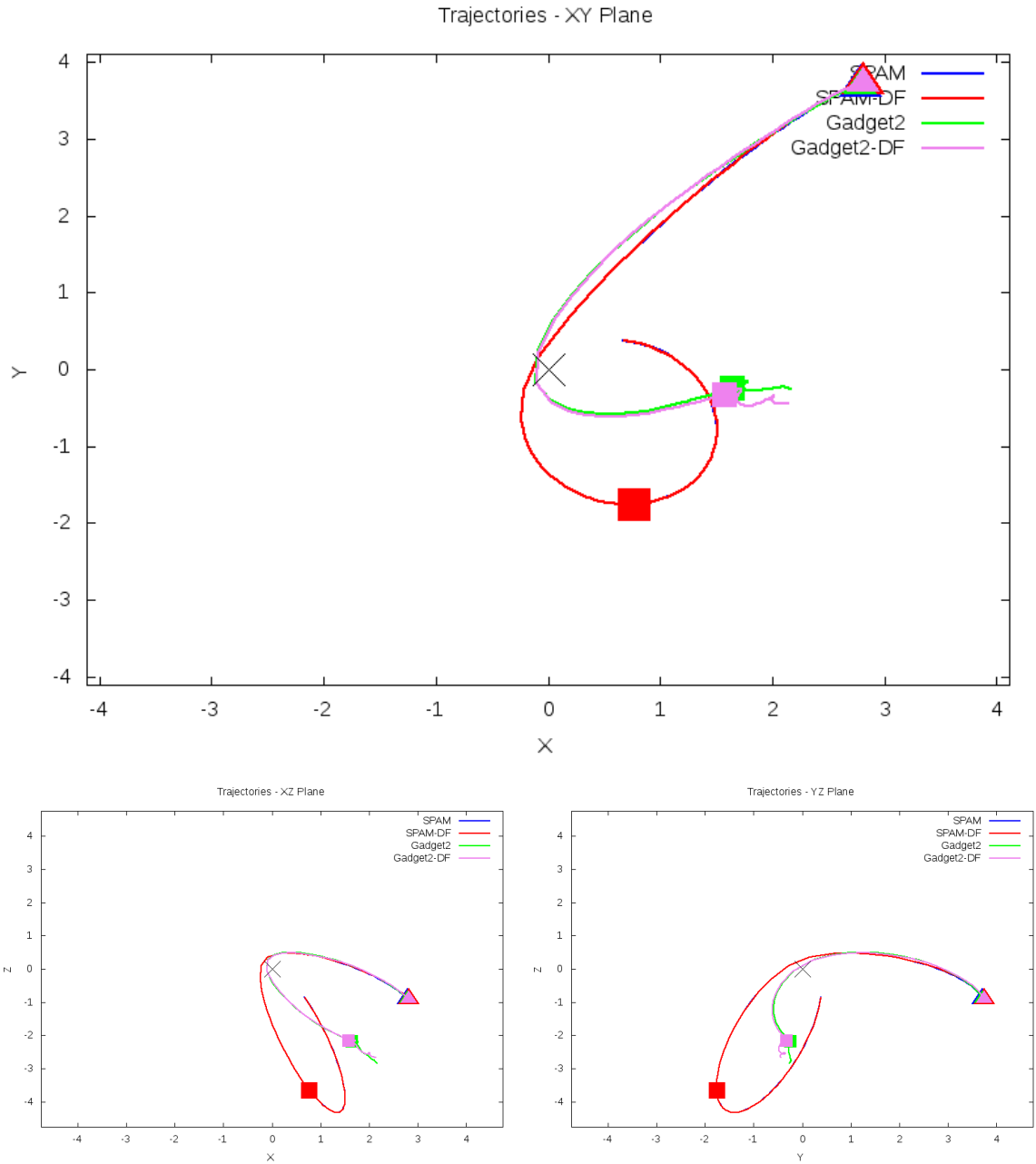


Figure 5.293: Trajectory plots of best SPAM match from Merger Wars, initial N-Body match, and best N-Body match for SDSS 588017702948962343

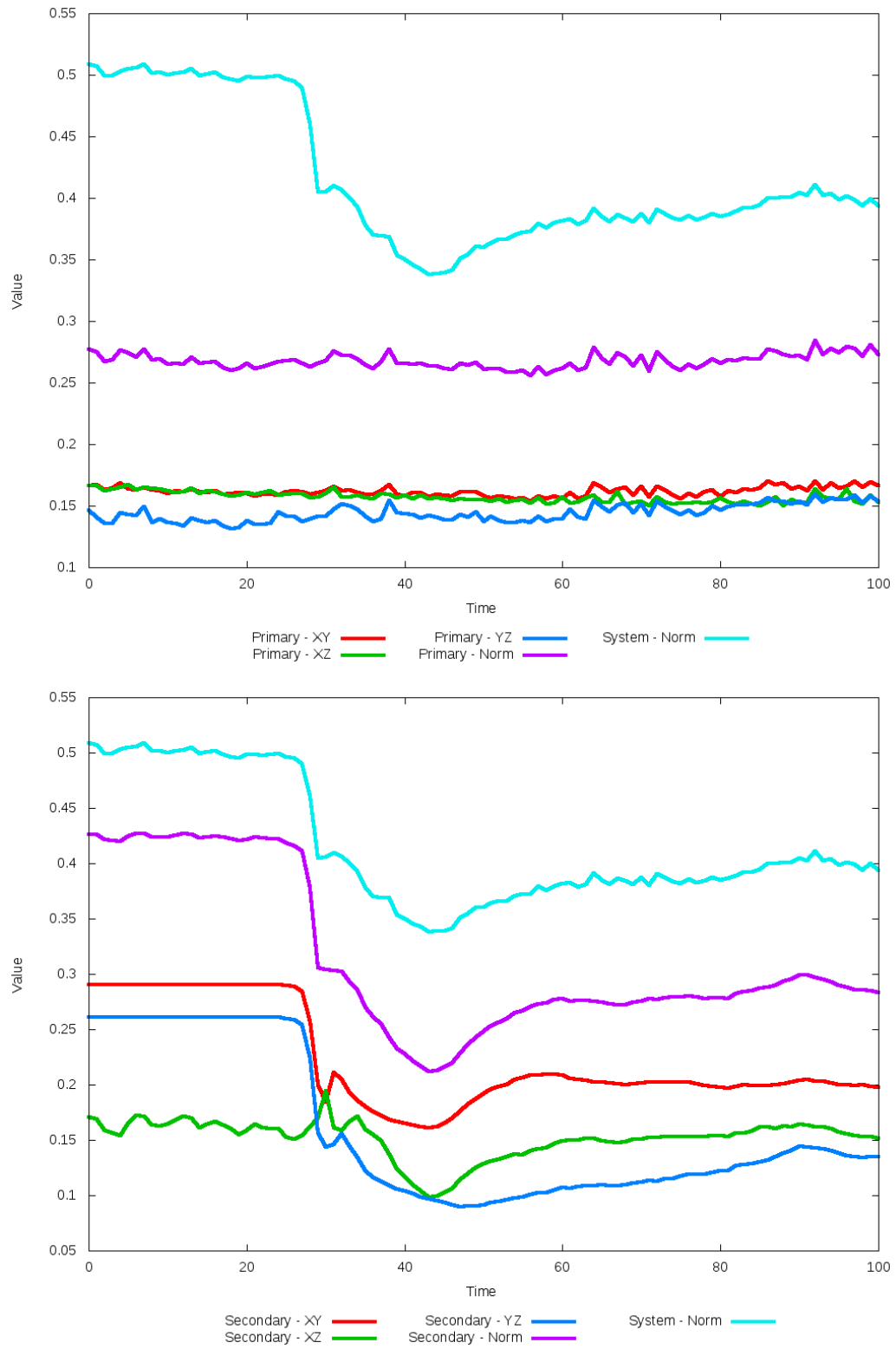


Figure 5.294: All metrics versus simulation time of the best N-Body simulation for SDSS 588017702948962343

5.1.50 SDSS 588017978901528612 (Arp 84)

Arp 84 shows modest agreement between the N-Body simulations with the SPAM simulations and observational data. Neither N-Body simulation captures the location of the secondary galaxy, although they both exhibit the remnants of a tidal tail in the region where the secondary galaxy should be. Both simulations do show similar richness in structure as the SPAM simulations show in the XZ and YZ projections. The trajectories of both N-Body simulations decay quickly, with significantly different orbits at the time of best match. This system will require changes to the state vector used to determine the initial conditions for the N-Body simulations if their orbits are not to decay as much.

Table 5.99: Identification Information and Merger Zoo summary for SDSS 588017978901528612.

Name	Aliases	RA (hms)	Dec (dms)	Redshift
SDSS 588017978901528612	Arp 84, NGC 5394/5395	13:58:37.9	+37:25:28.8	0.011711

R_x	R_y	R_z	V_x	V_y	V_z
0.50703	1.54971	0.15061	-0.14252	0.26477	0.15418

	Primary Galaxy	Secondary Galaxy
mass	0.46797	0.11446
radius	1.14919	0.27229
ϕ	11.0625°	65.5625°
θ	111.80124°	290.68322°
ϵ	0.3	0.3

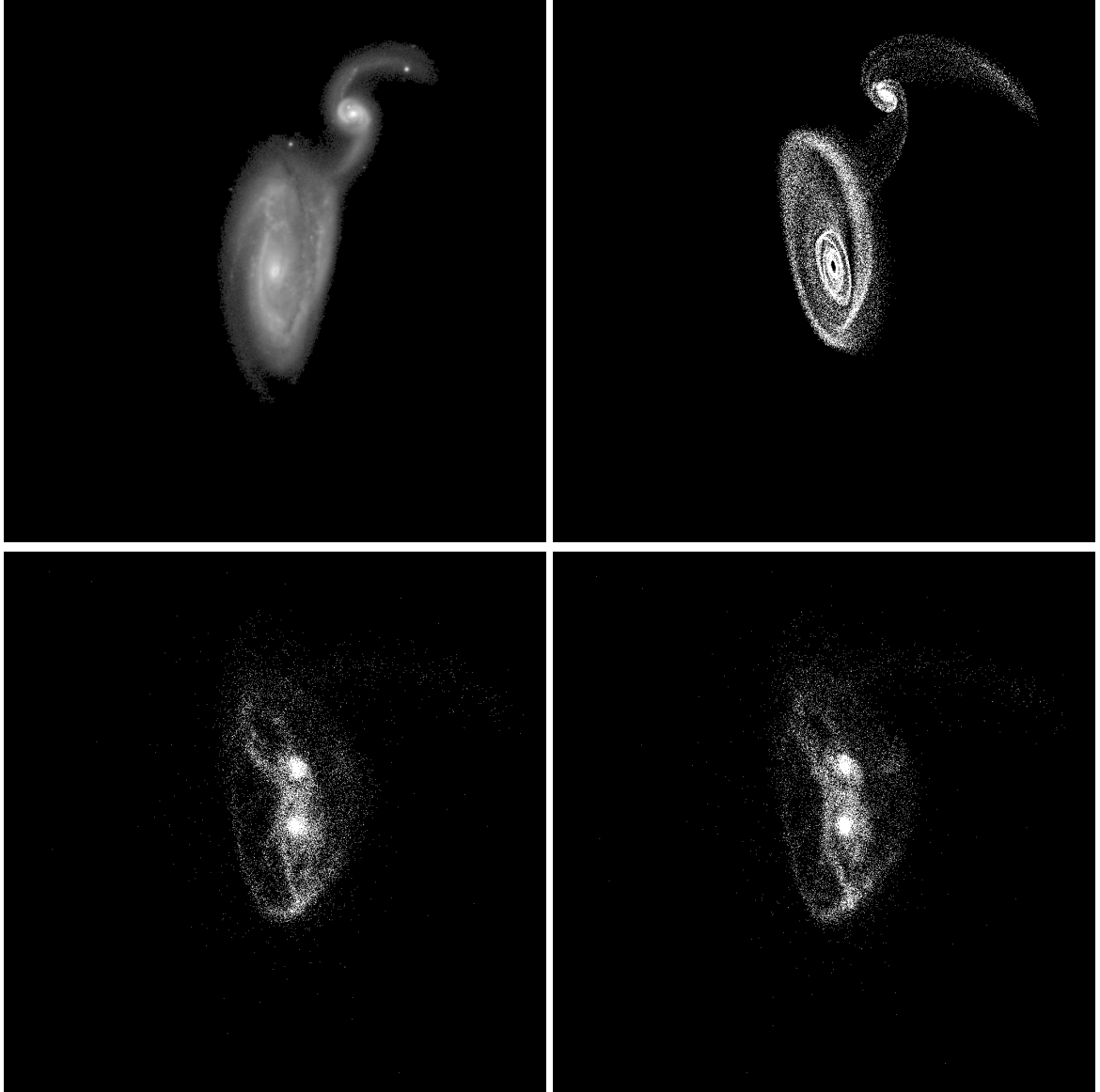


Figure 5.295: Target image (top-left), best SPAM match from Merger Wars (top-right), initial N-Body match (bottom-left), and best N-Body match (bottom-right) for SDSS 588017978901528612

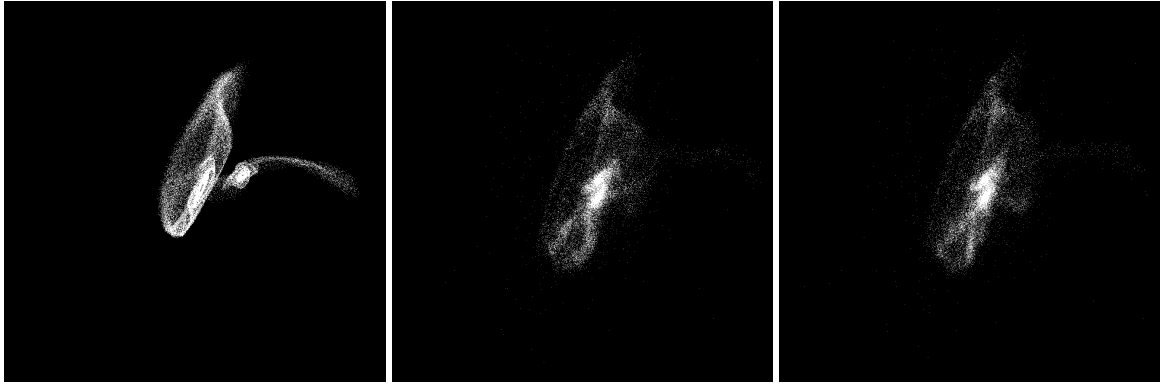


Figure 5.296: XZ projections of best SPAM match from Merger Wars (left), initial N-Body match (middle), and best N-Body match (right) for SDSS 588017978901528612

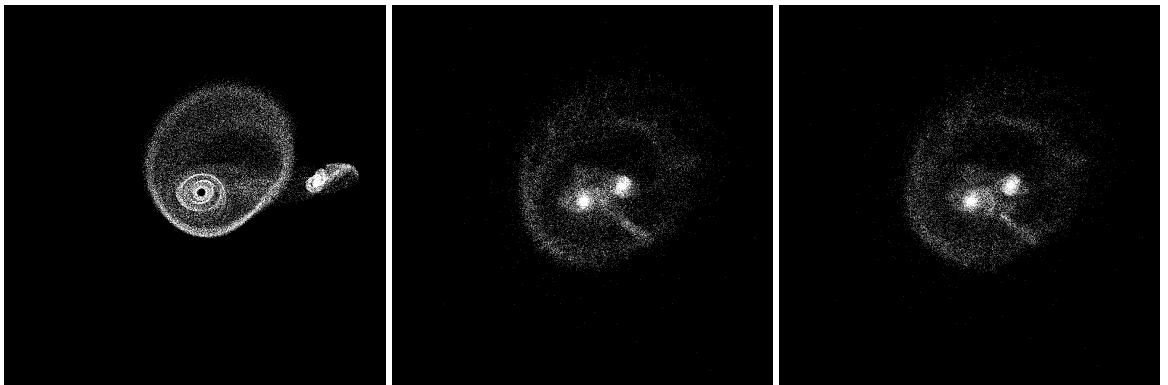


Figure 5.297: YZ projections of best SPAM match from Merger Wars (left), initial N-Body match (middle), and best N-Body match (right) for SDSS 588017978901528612

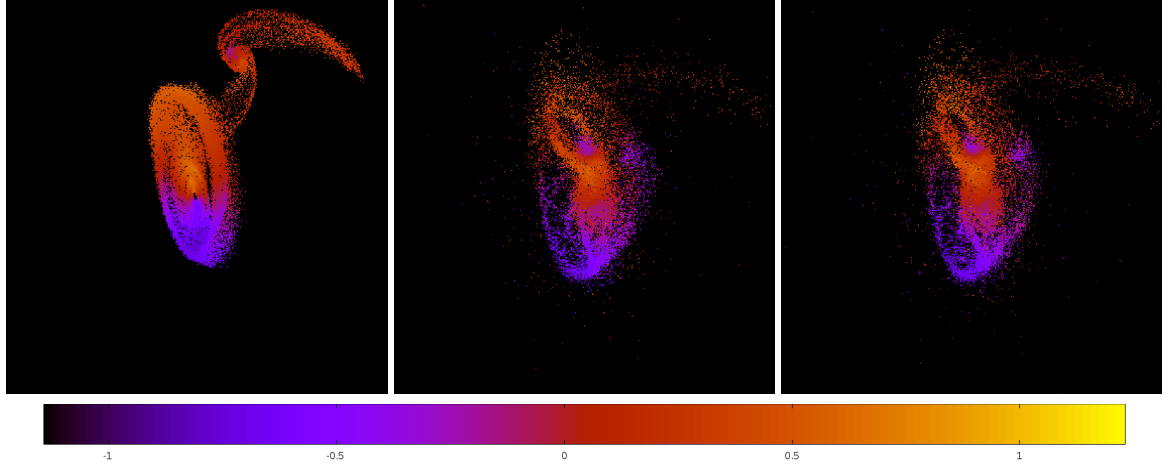


Figure 5.298: Line of sight velocity plots of best SPAM match from Merger Wars (left), initial N-Body match (middle), and best N-Body match (right) for SDSS 588017978901528612

Table 5.100: Orbital Elements & Dynamical Friction for SDSS 588017978901528612

	SPAM Simulation	Initial N-Body Simulation	Best N-Body Simulation
a	-99.872	0.694	0.721
e	1.019	0.828	0.807
r_c	1.892	0.119	0.139
i	32.082°	35.369°	34.844°
Ω	63.410°	60.000°	60.726°
ω	289.378°	175.760°	175.169°
ν	80.596°	198.283°	198.652°
t_n	50	52	52
$\ln\Lambda$	N/A	1.00E-03	1.50E-03

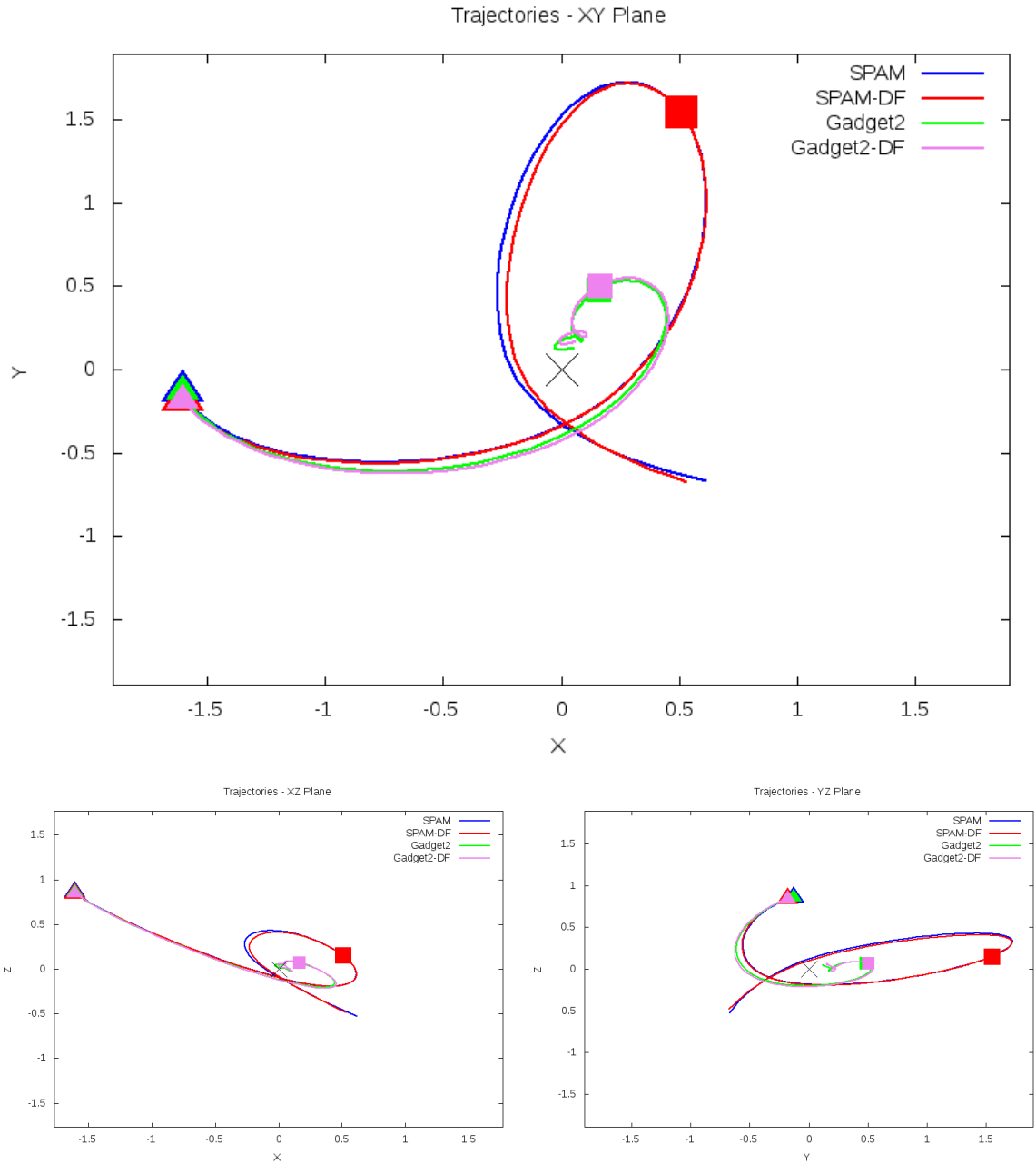


Figure 5.299: Trajectory plots of best SPAM match from Merger Wars, initial N-Body match, and best N-Body match for SDSS 588017978901528612

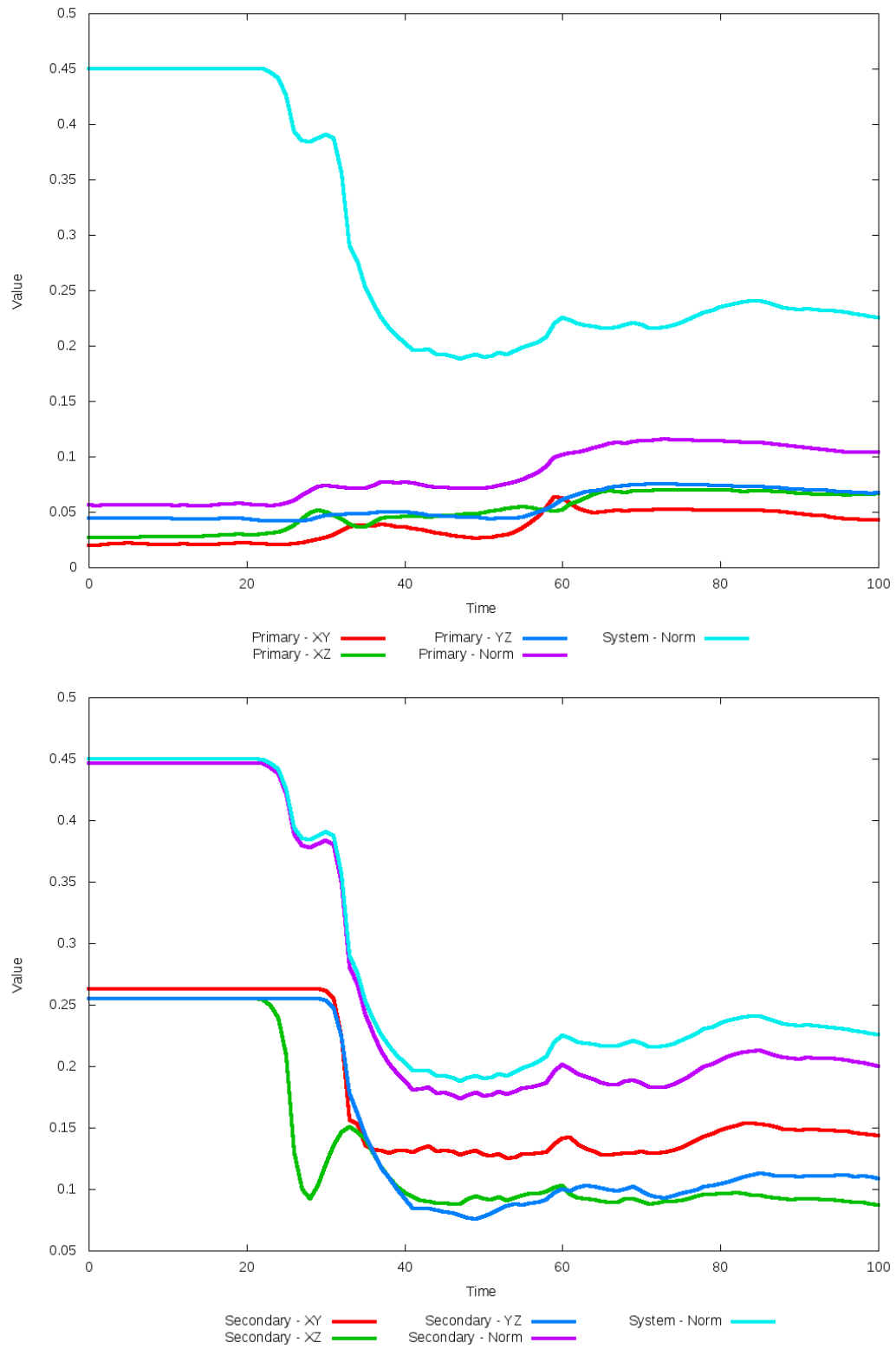


Figure 5.300: All metrics versus simulation time of the best N-Body simulation for SDSS 588017978901528612

5.1.51 SDSS 588018055130710322 (UGC 10650)

UGC 10650 shows a noticeable improvement in the position of the secondary galaxy as dynamical friction is optimized. Although the morphology is relatively good between the N-Body simulations with the SPAM simulations and observational data, the simulations have a significantly larger secondary galaxy than the observational data suggests. As such, that should be reviewed by Merger Wars. Additionally, there is significant differences in the line of sight velocity of the secondary galaxy, and although there is a galactic bridge connecting both galaxies in each simulation, it is very thin in the N-Body simulations.

Table 5.101: Identification Information and Merger Zoo summary for SDSS 588018055130710322.

Name	Aliases	RA (hms)	Dec (dms)	Redshift
SDSS 588018055130710322	UGC 10650	17:00:06.8	+23:07:53.5	0.056835

R_x	R_y	R_z	V_x	V_y	V_z
-0.10914	-1.06691	-1.77066	0.25931	0.18152	0.03363

	Primary Galaxy	Secondary Galaxy
mass	0.38702	0.4096
radius	0.56671	0.46368
ϕ	73.18749°	-63.6875°
θ	346.58385°	187.82608°
ϵ	0.3	0.3

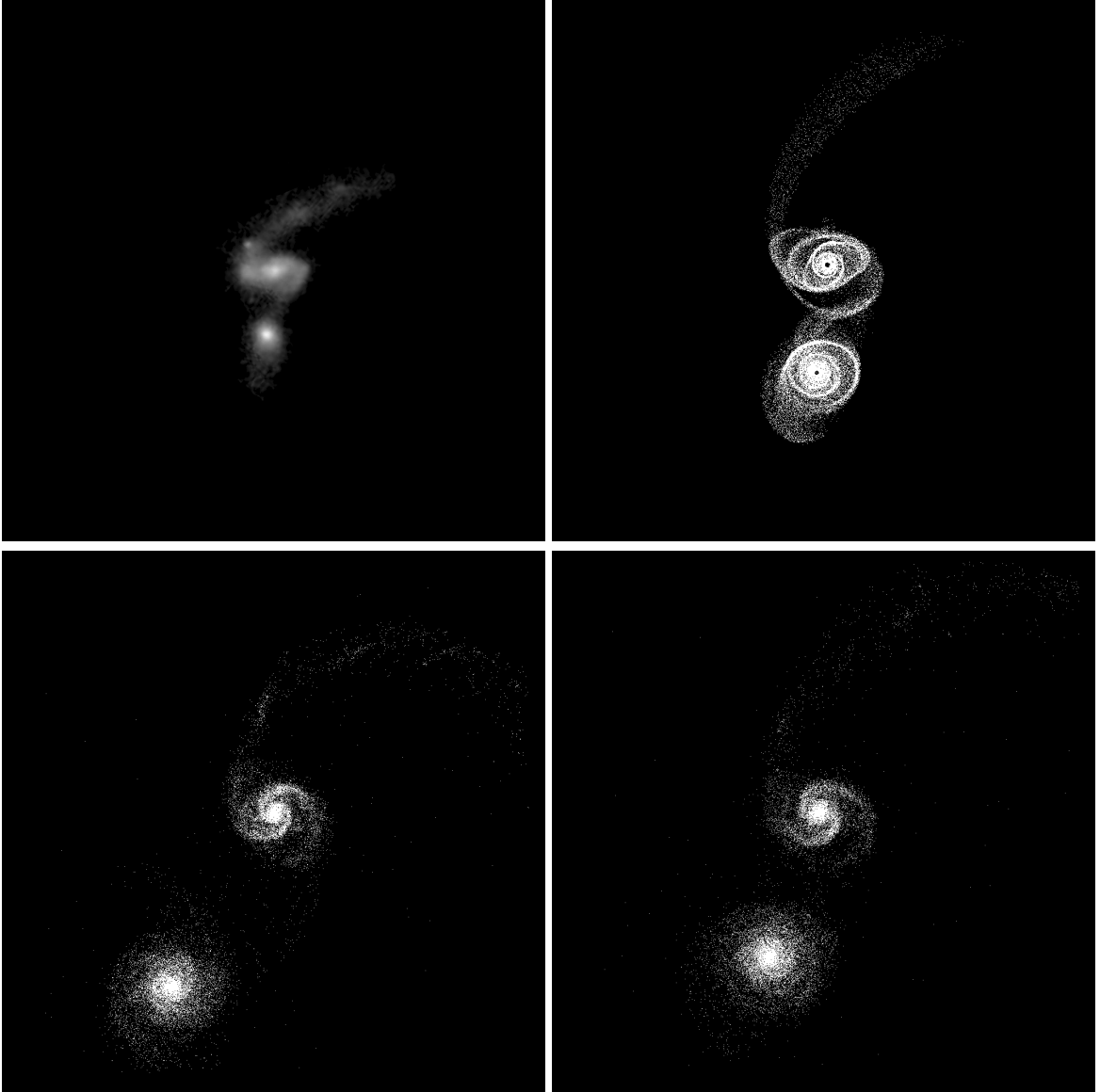


Figure 5.301: Target image (top-left), best SPAM match from Merger Wars (top-right), initial N-Body match (bottom-left), and best N-Body match (bottom-right) for SDSS 588018055130710322

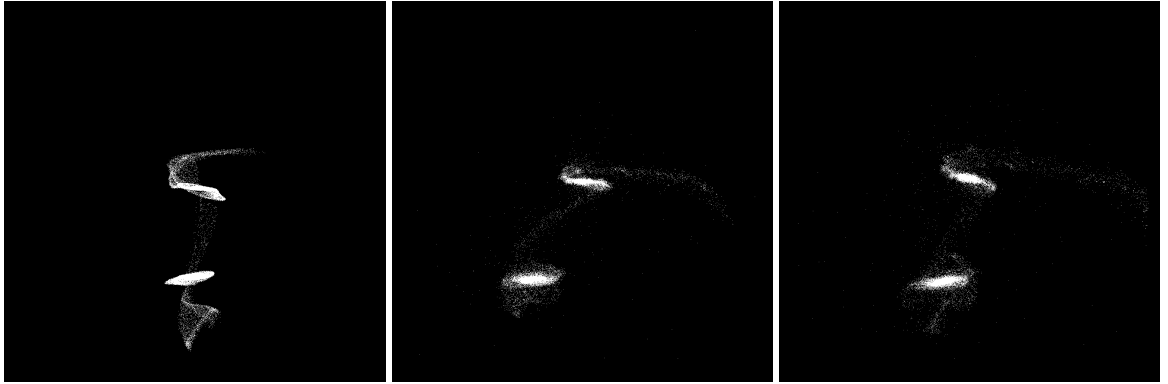


Figure 5.302: XZ projections of best SPAM match from Merger Wars (left), initial N-Body match (middle), and best N-Body match (right) for SDSS 588018055130710322

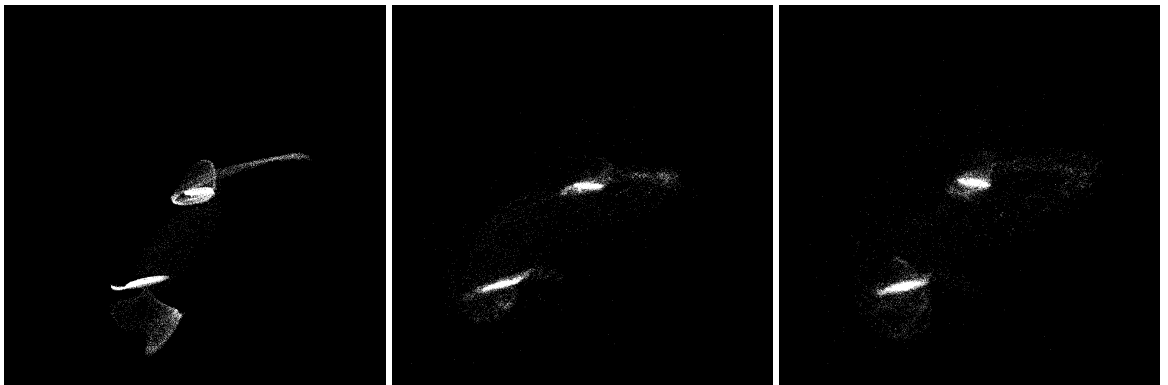


Figure 5.303: YZ projections of best SPAM match from Merger Wars (left), initial N-Body match (middle), and best N-Body match (right) for SDSS 588018055130710322

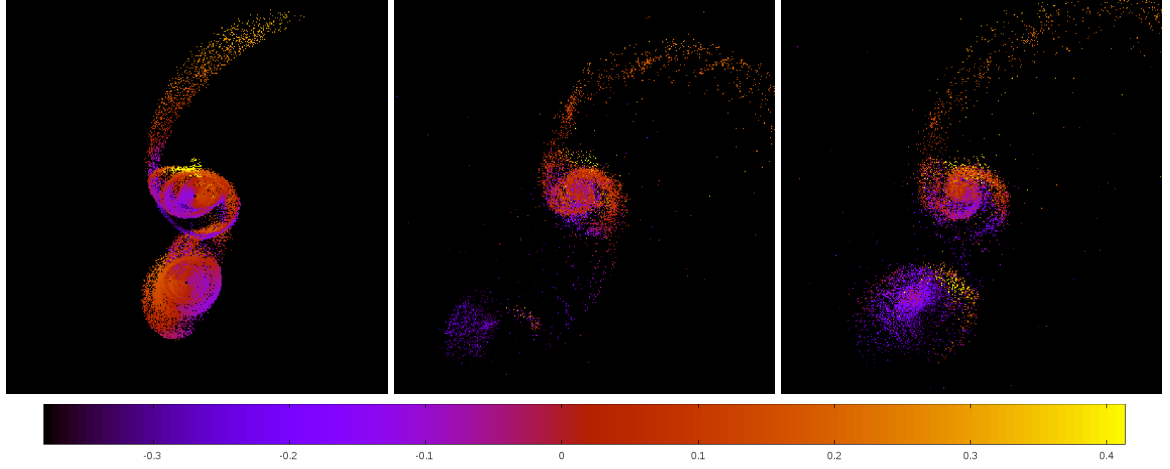


Figure 5.304: Line of sight velocity plots of best SPAM match from Merger Wars (left), initial N-Body match (middle), and best N-Body match (right) for SDSS 588018055130710322

Table 5.102: Orbital Elements & Dynamical Friction for SDSS 588018055130710322

	SPAM Simulation	Initial N-Body Simulation	Best N-Body Simulation
a	4.377	-2.718	11.075
e	0.430	2.081	0.714
r_c	2.496	2.939	3.172
i	64.462°	64.041°	64.833°
Ω	32.083°	31.148°	31.495°
ω	0.185°	157.187°	161.038°
ν	251.249°	70.228°	76.583°
t_n	50	41	47
$\ln\Lambda$	N/A	1.00E-03	7.50E-04

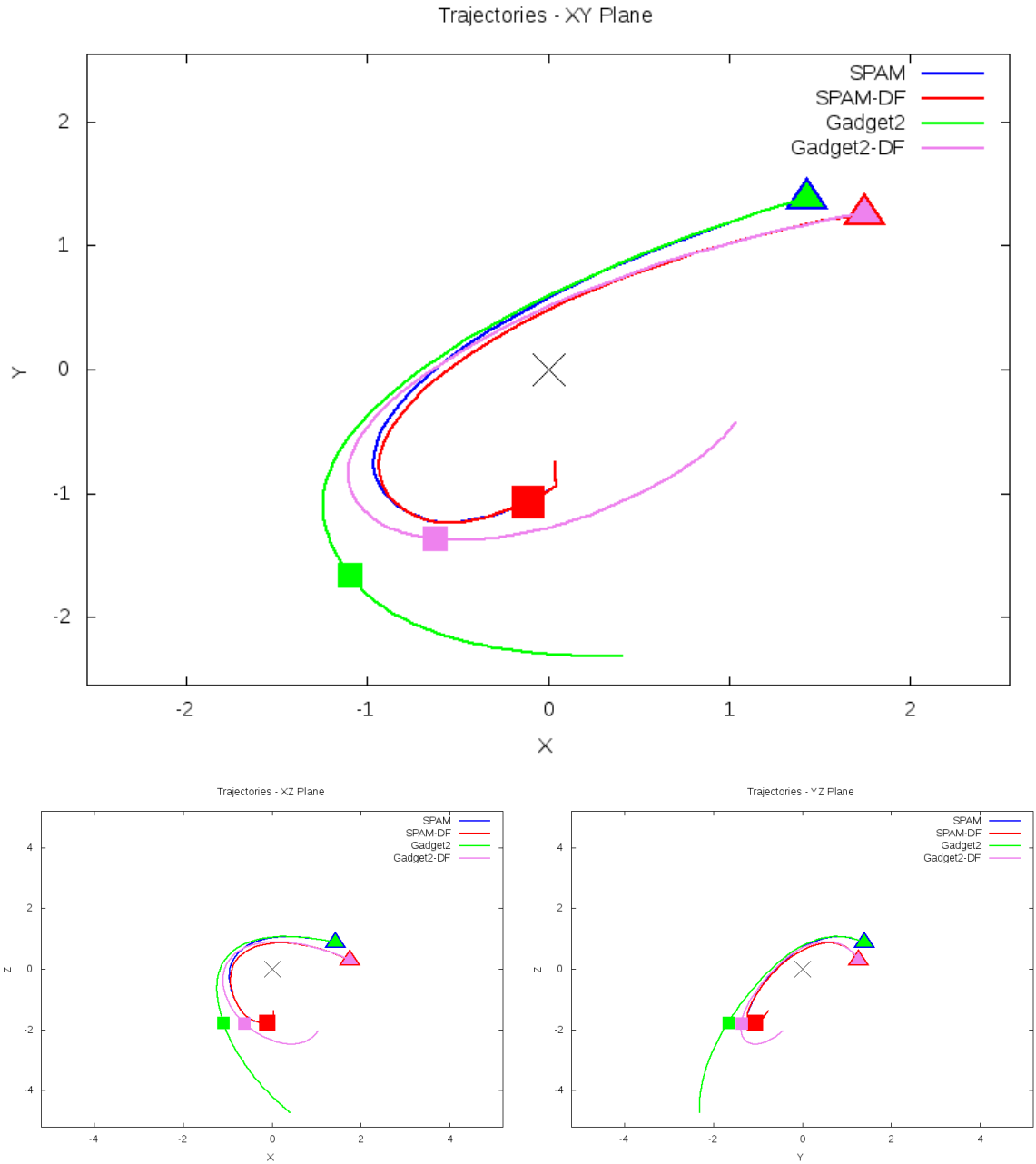


Figure 5.305: Trajectory plots of best SPAM match from Merger Wars, initial N-Body match, and best N-Body match for SDSS 588018055130710322

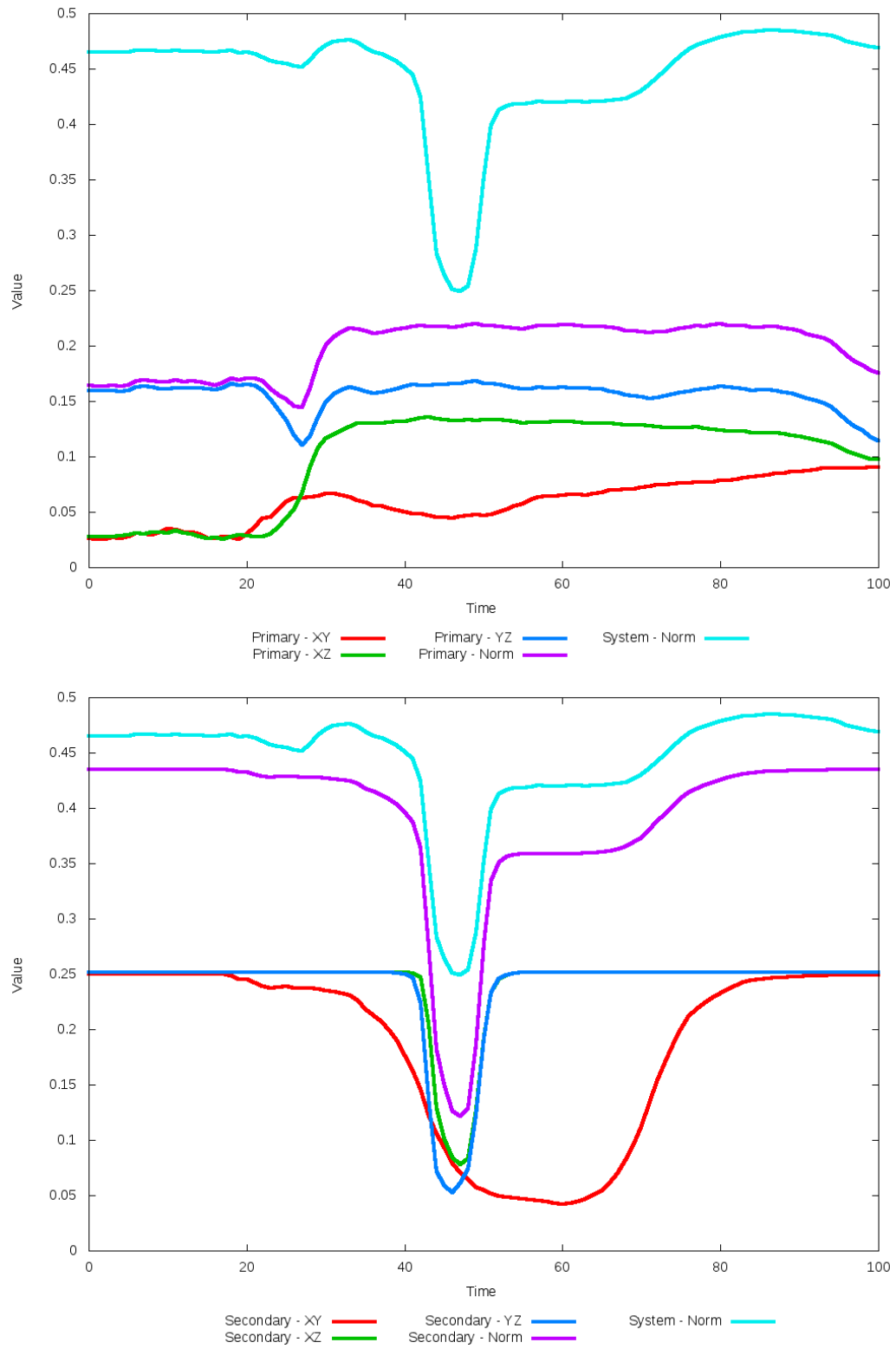


Figure 5.306: All metrics versus simulation time of the best N-Body simulation for SDSS 588018055130710322

5.1.52 SDSS 758874299603222717 (Arp 112)

Arp 112 does not exhibit a very good agreement between the N-Body simulations with the SPAM simulations and observational data. A quick look at the trajectories shows an orbit determined by Merger Wars to have multiple close approaches without a merger, while the N-Body simulations decay into a merger instead. Although the pipeline found a better fit for dynamical friction over the initial value, neither are very good. Given the number of passes in the restricted three-body orbits, the state vector determined by Merger Wars should be reviewed for alternative matches to explore.

Table 5.103: Identification Information and Merger Zoo summary for SDSS 758874299603222717.

Name	Aliases	RA (hms)	Dec (dms)	Redshift
SDSS 758874299603222717	Arp 112	0:01:26.7	+31:26:00.2	0.016048

\mathbf{R}_x	\mathbf{R}_y	\mathbf{R}_z	\mathbf{V}_x	\mathbf{V}_y	\mathbf{V}_z
-0.63148	0.63778	0.26845	-1.00831	-0.19458	0.42192

	Primary Galaxy	Secondary Galaxy
mass	0.90726	0.95484
radius	0.29162	0.27274
ϕ	97.25°	-4.75°
θ	194.53416°	35.77639°
ϵ	0.3	0.3

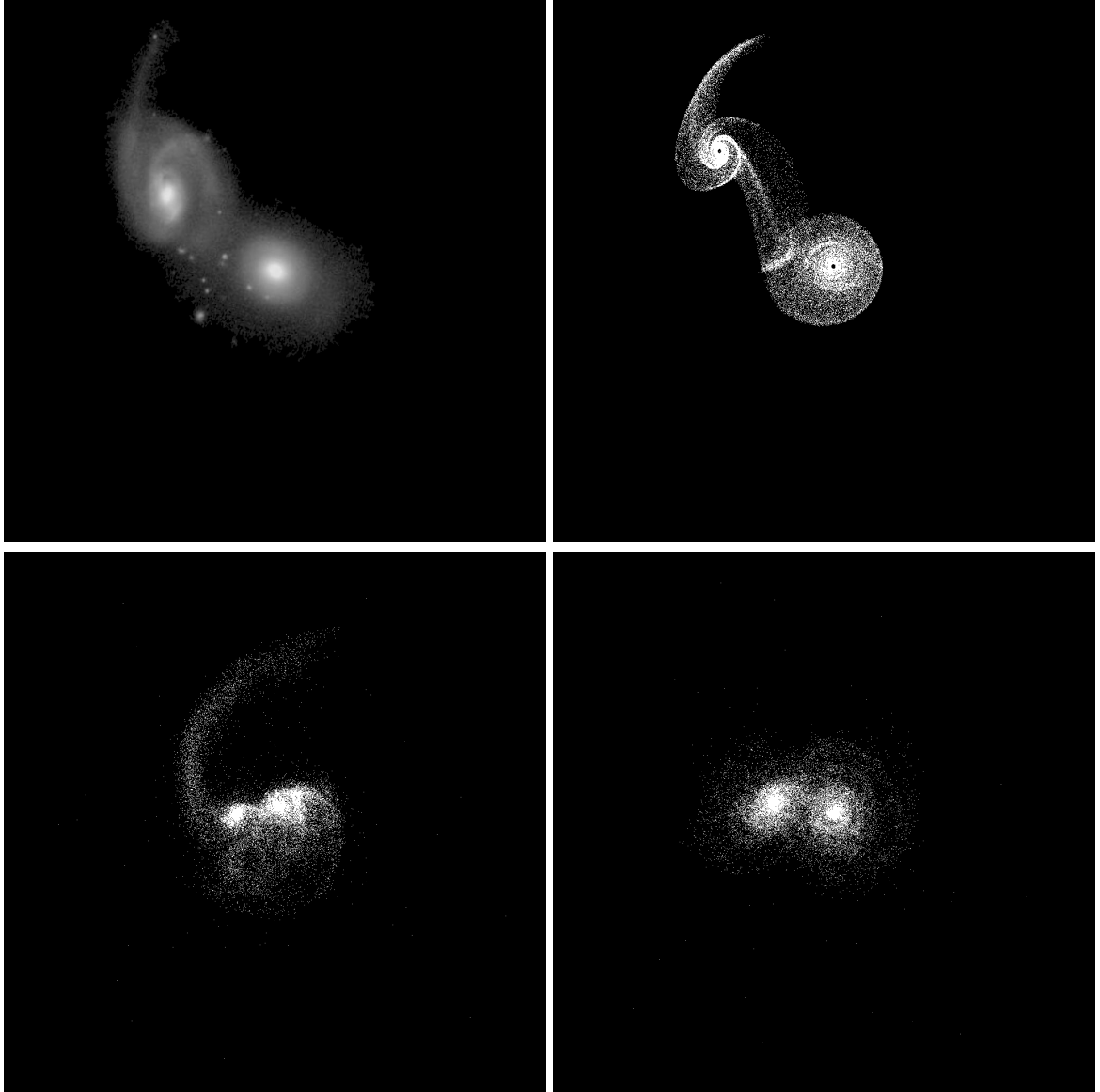


Figure 5.307: Target image (top-left), best SPAM match from Merger Wars (top-right), initial N-Body match (bottom-left), and best N-Body match (bottom-right) for SDSS 758874299603222717

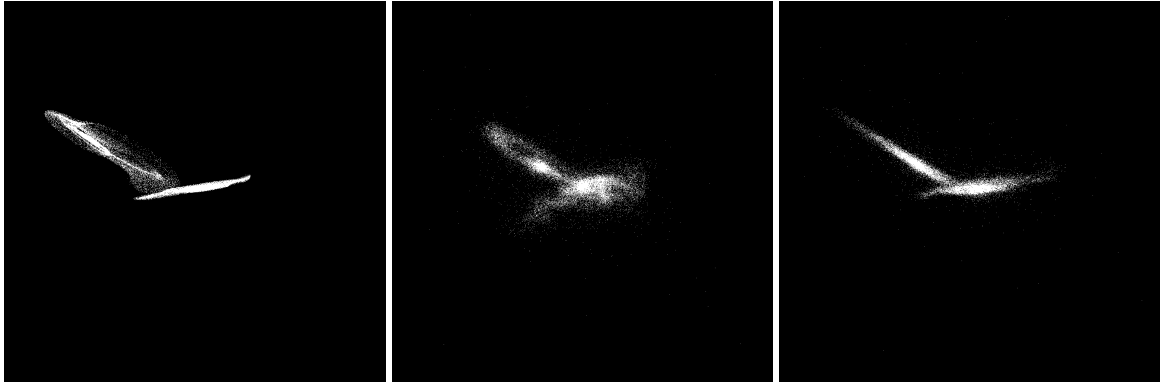


Figure 5.308: XZ projections of best SPAM match from Merger Wars (left), initial N-Body match (middle), and best N-Body match (right) for SDSS 758874299603222717

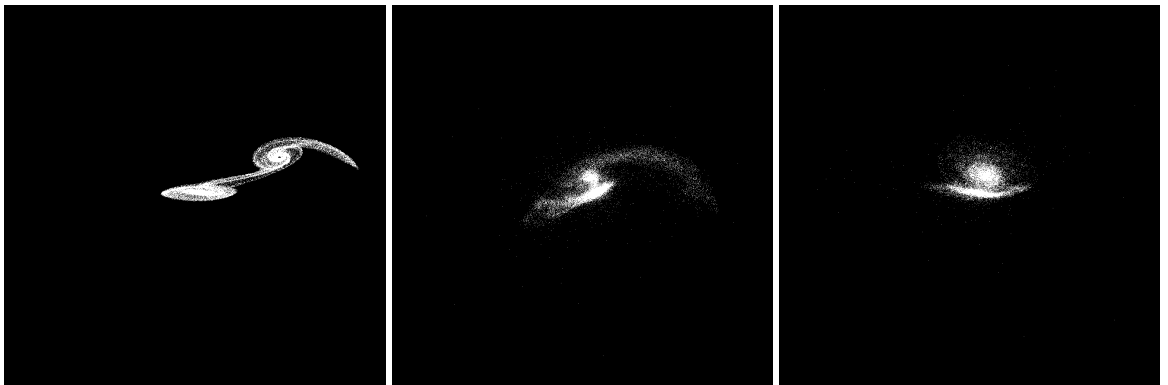


Figure 5.309: YZ projections of best SPAM match from Merger Wars (left), initial N-Body match (middle), and best N-Body match (right) for SDSS 758874299603222717

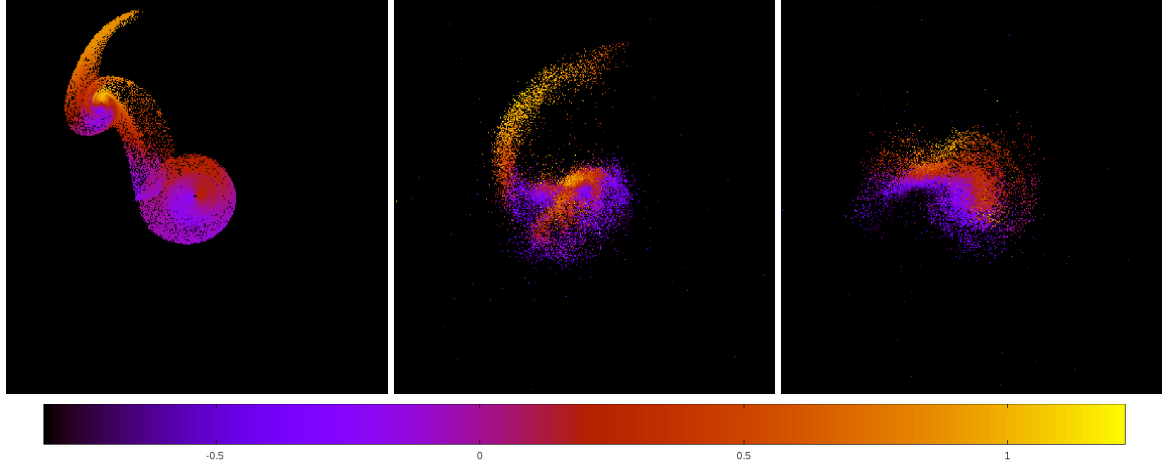


Figure 5.310: Line of sight velocity plots of best SPAM match from Merger Wars (left), initial N-Body match (middle), and best N-Body match (right) for SDSS 758874299603222717

Table 5.104: Orbital Elements & Dynamical Friction for SDSS 758874299603222717

	SPAM Simulation	Initial N-Body Simulation	Best N-Body Simulation
a	-4.511	0.362	-0.325
e	1.287	0.633	2.713
r_c	1.296	0.133	0.556
i	22.760°	23.428°	21.566°
Ω	89.243°	90.088°	89.656°
ω	344.647°	253.899°	125.764°
ν	64.214°	179.217°	309.691°
t_n	50	40	11
$\ln\Lambda$	N/A	1.00E-03	6.00E-04

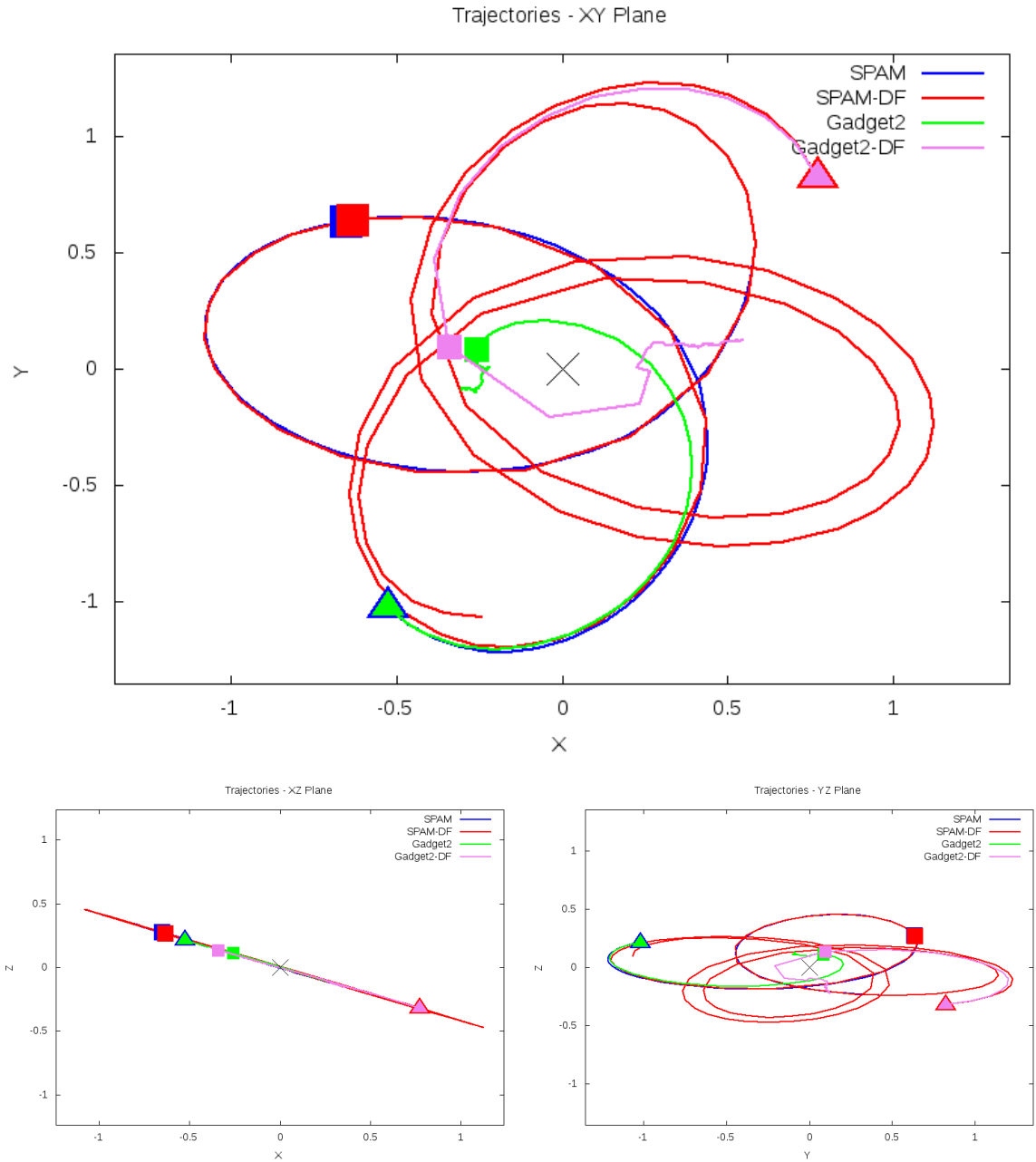


Figure 5.311: Trajectory plots of best SPAM match from Merger Wars, initial N-Body match, and best N-Body match for SDSS 758874299603222717

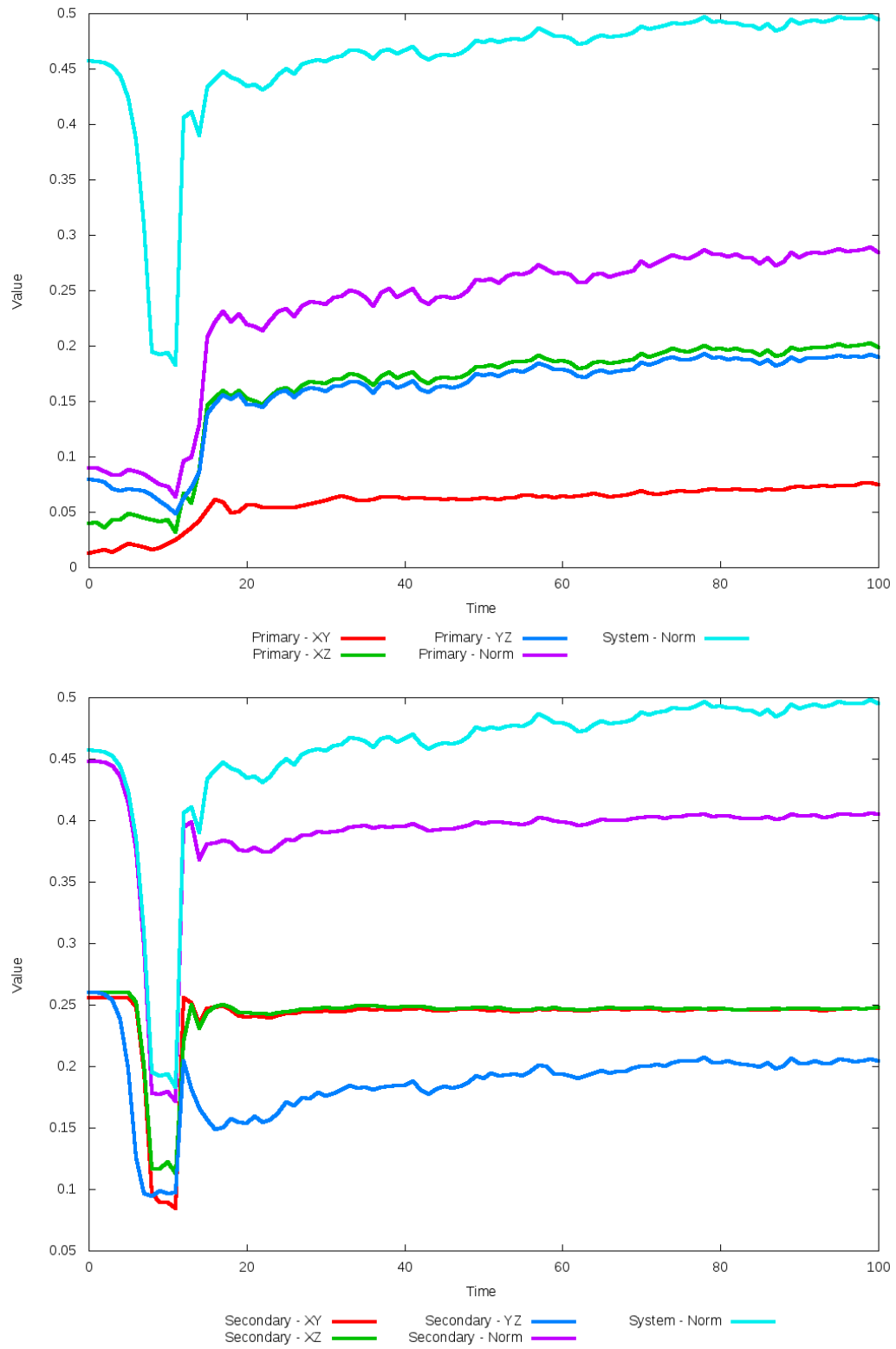


Figure 5.312: All metrics versus simulation time of the best N-Body simulation for SDSS 758874299603222717

5.1.53 SDSS 758877153600208945 (Arp 70)

Arp 70 shows good agreement between its simulations and observational data, and this agreement is improved with the optimization of dynamical friction. The optimization leads to a better placement of the secondary galaxy and a weaker or lessened appearance of a bridge connecting the two galaxies. Although both N-Body simulations show tidal features overlapping each other in the XY projection, it is less pronounced in the optimized simulation. Furthermore, the trajectory of the optimized simulation is in very close agreement with the SPAM simulations.

Table 5.105: Identification Information and Merger Zoo summary for SDSS 758877153600208945.

Name	Aliases	RA (hms)	Dec (dms)	Redshift
SDSS 758877153600208945	Arp 70, UGC 934	1:23:28.2	+30:47:04.0	0.035004

R_x	R_y	R_z	V_x	V_y	V_z
0.61603	-2.03504	-1.99154	0.24821	-0.75856	-0.00241

	Primary Galaxy	Secondary Galaxy
mass	0.60656	0.47041
radius	0.91437	0.5201
ϕ	149.9°	136.1875°
θ	50.4°	38.01242°
ϵ	0.3	0.3

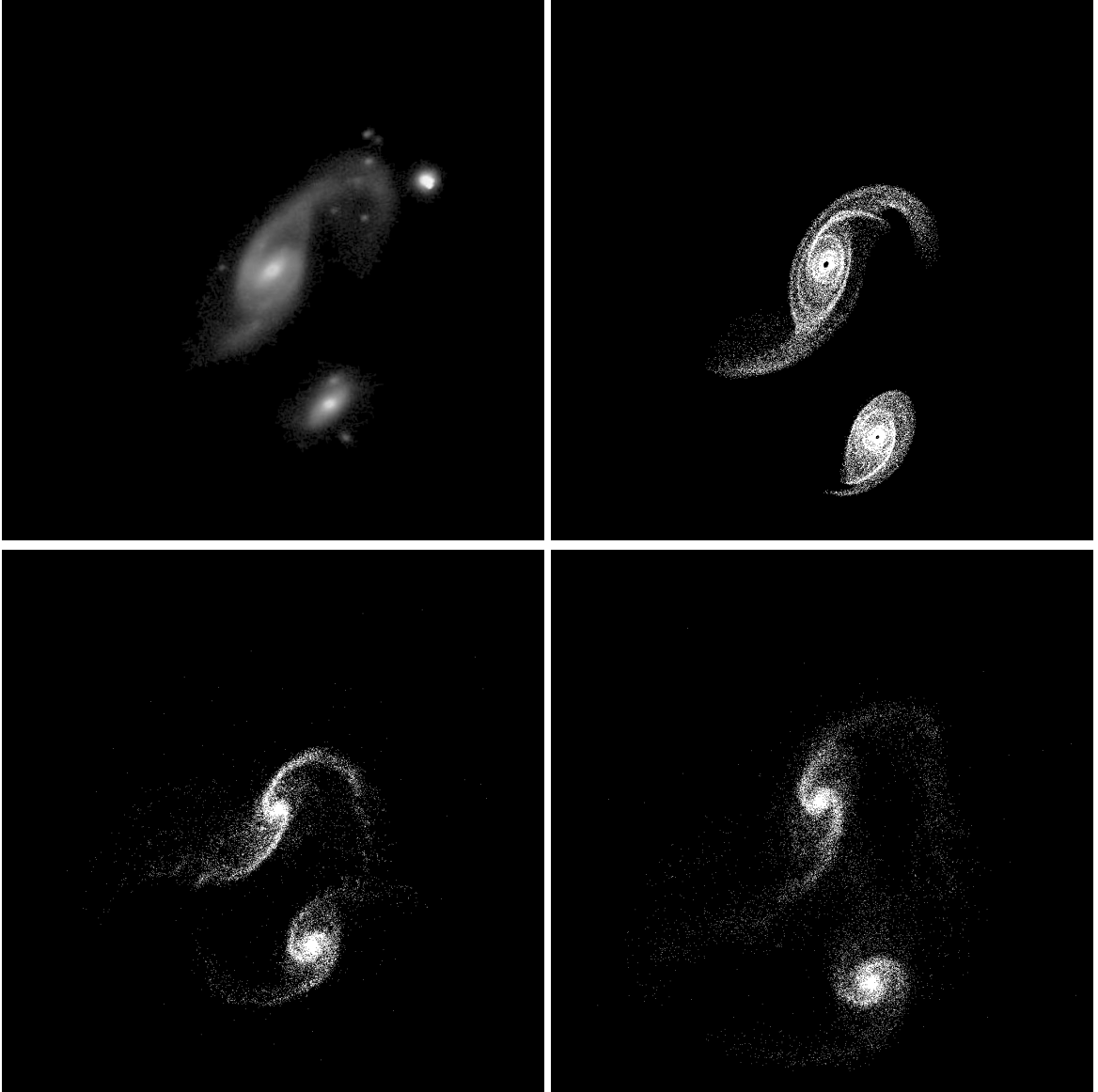


Figure 5.313: Target image (top-left), best SPAM match from Merger Wars (top-right), initial N-Body match (bottom-left), and best N-Body match (bottom-right) for SDSS 758877153600208945

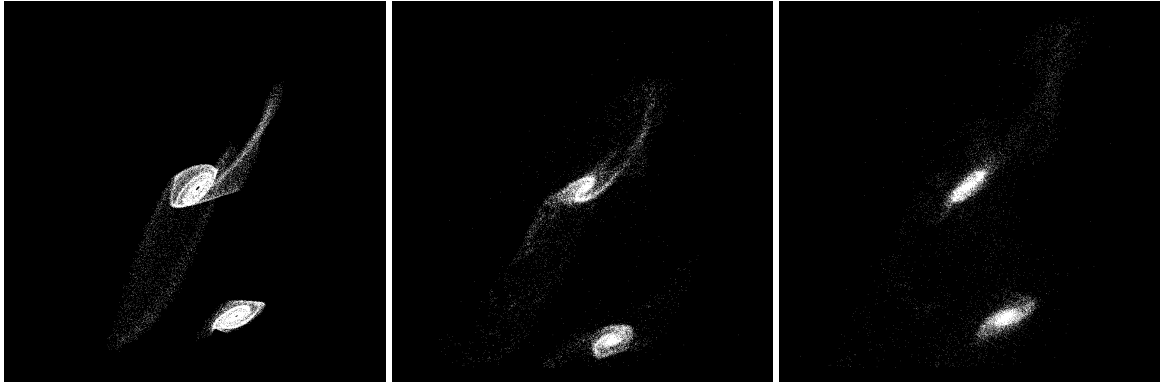


Figure 5.314: XZ projections of best SPAM match from Merger Wars (left), initial N-Body match (middle), and best N-Body match (right) for SDSS 758877153600208945

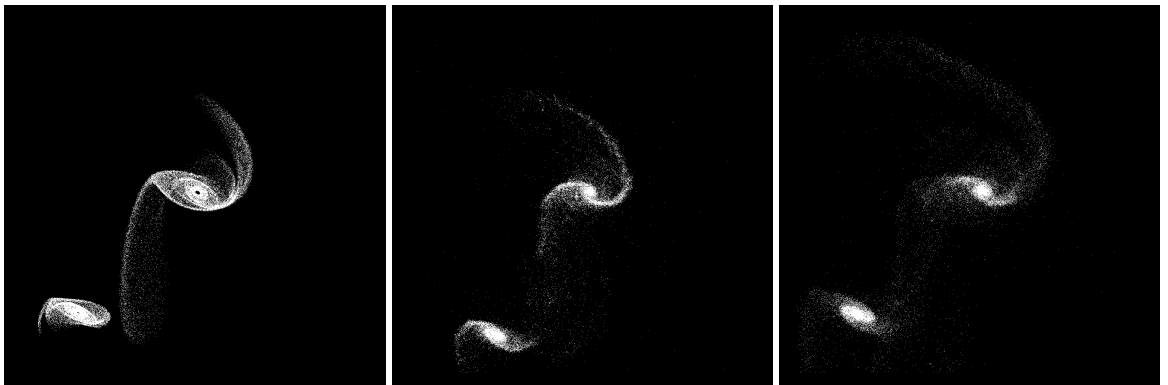


Figure 5.315: YZ projections of best SPAM match from Merger Wars (left), initial N-Body match (middle), and best N-Body match (right) for SDSS 758877153600208945

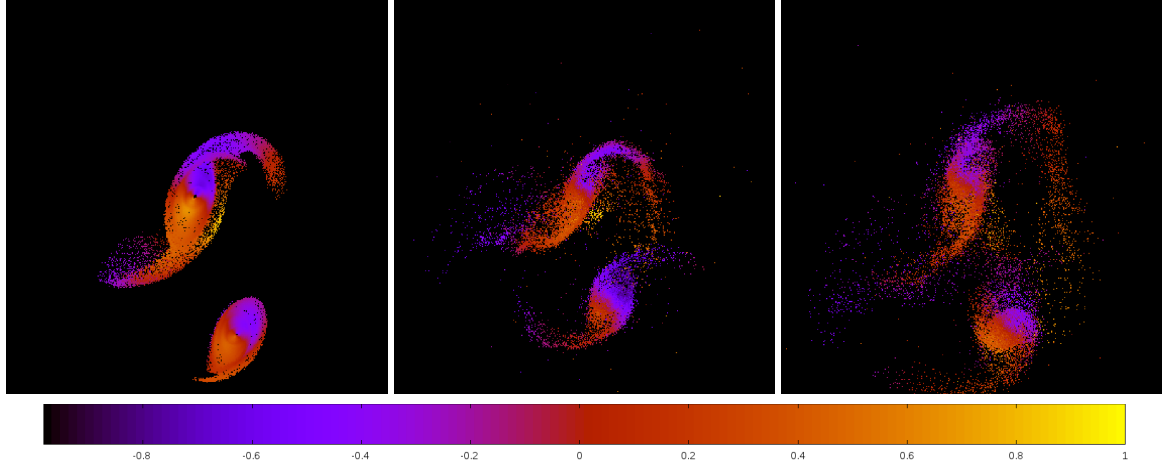


Figure 5.316: Line of sight velocity plots of best SPAM match from Merger Wars (left), initial N-Body match (middle), and best N-Body match (right) for SDSS 758877153600208945

Table 5.106: Orbital Elements & Dynamical Friction for SDSS 758877153600208945

	SPAM Simulation	Initial N-Body Simulation	Best N-Body Simulation
a	-1.159	-0.682	-2.789
e	4.167	5.801	2.287
r_c	3.669	3.272	3.589
i	88.633°	88.665°	89.247°
Ω	288.123°	286.964°	286.056°
ω	259.605°	243.356°	252.367°
ν	57.038°	59.886°	61.101°
t_n	50	43	53
$\ln\Lambda$	N/A	1.00E-03	2.00E-04

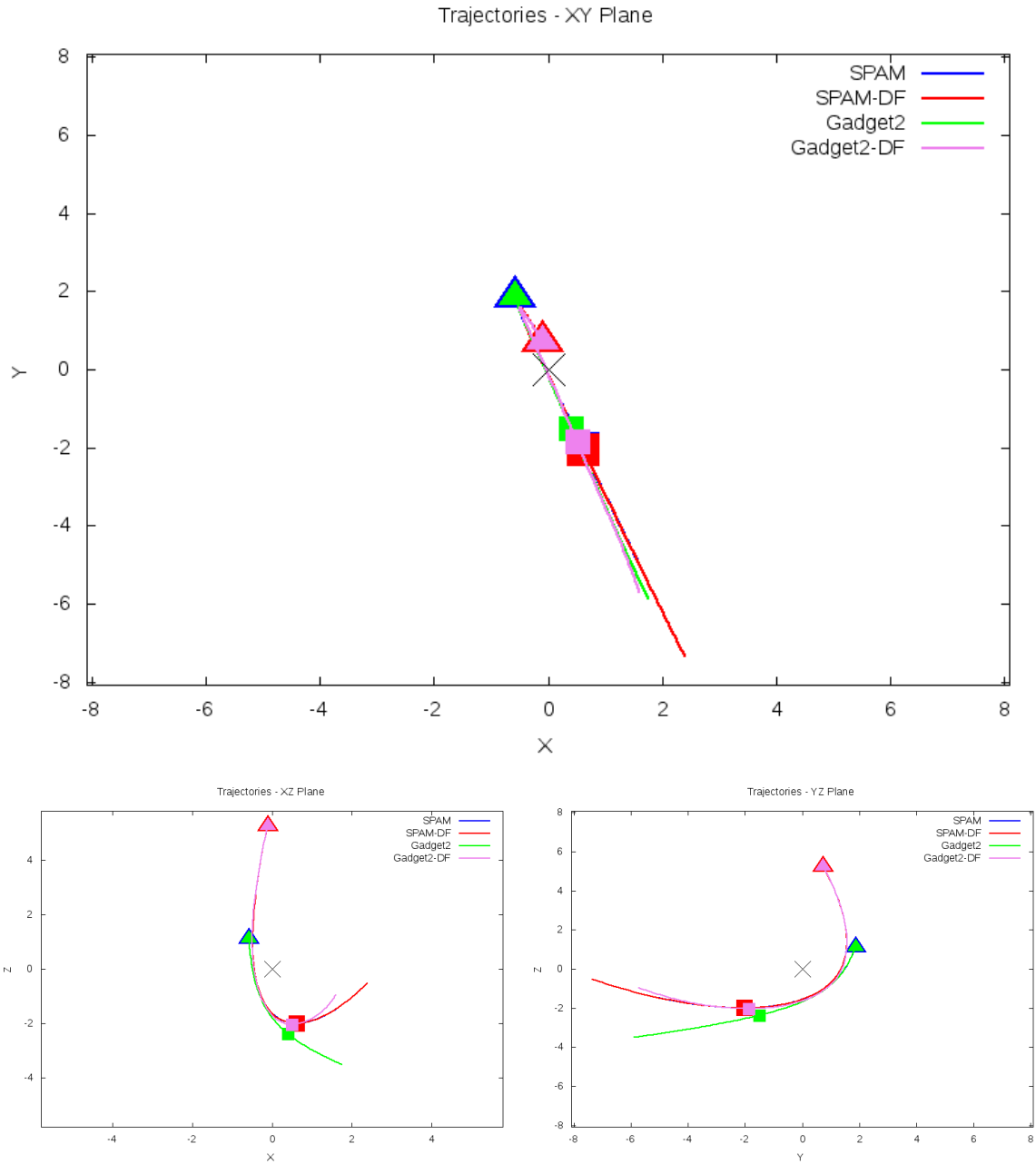


Figure 5.317: Trajectory plots of best SPAM match from Merger Wars, initial N-Body match, and best N-Body match for SDSS 758877153600208945

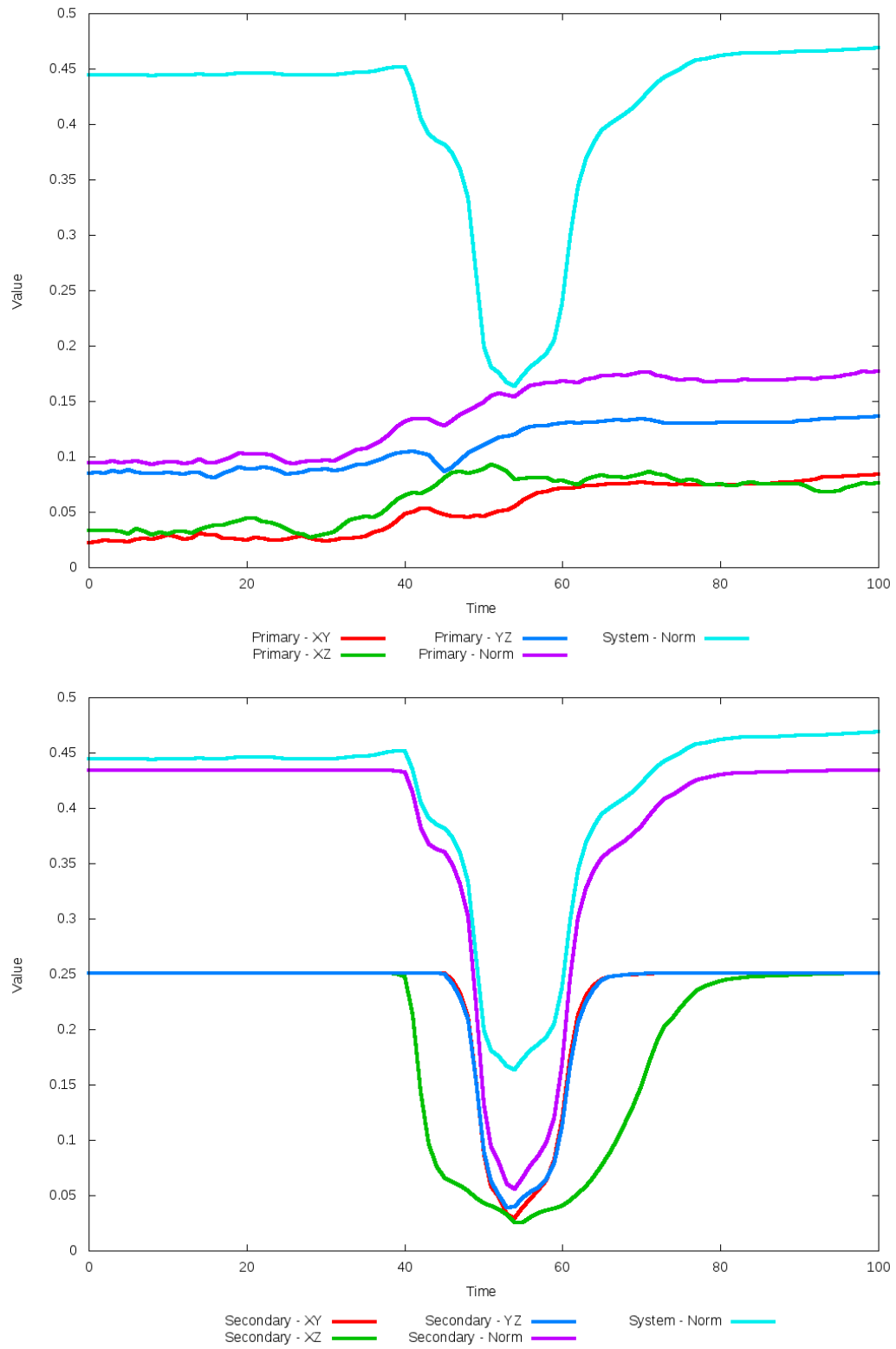


Figure 5.318: All metrics versus simulation time of the best N-Body simulation for SDSS 758877153600208945

5.1.54 SDSS 1237678620102623480

This system exhibits very good agreement between its simulations and observational data. Although both N-Body simulations look very similar, the pipeline's optimization routine found a slight improvement in location of the secondary galaxy by reducing the dynamical friction to nearly zero. This change is a more noticeable in the trajectory figures. Although the simulations all appear simulation, the angles of the orbital elements are significantly different, which indicates they may not have a significant role in the quality of fit for the system.

Table 5.107: Identification Information and Merger Zoo summary for SDSS 1237678620102623480.

Name	Aliases	RA (hms)	Dec (dms)	Redshift
SDSS 1237678620102623480	2MASS 00040703+0320165	0:04:15.4	+3:23:01.8	0.02288

R_x	R_y	R_z	V_x	V_y	V_z
-1.01385	-2.25736	-1.07197	-0.09418	-0.41519	-1.10167

	Primary Galaxy	Secondary Galaxy
mass	0.38946	0.60577
radius	0.69777	0.52425
ϕ	142.48649°	65.29434°
θ	258.15299°	238.65171°
ϵ	0.3	0.3

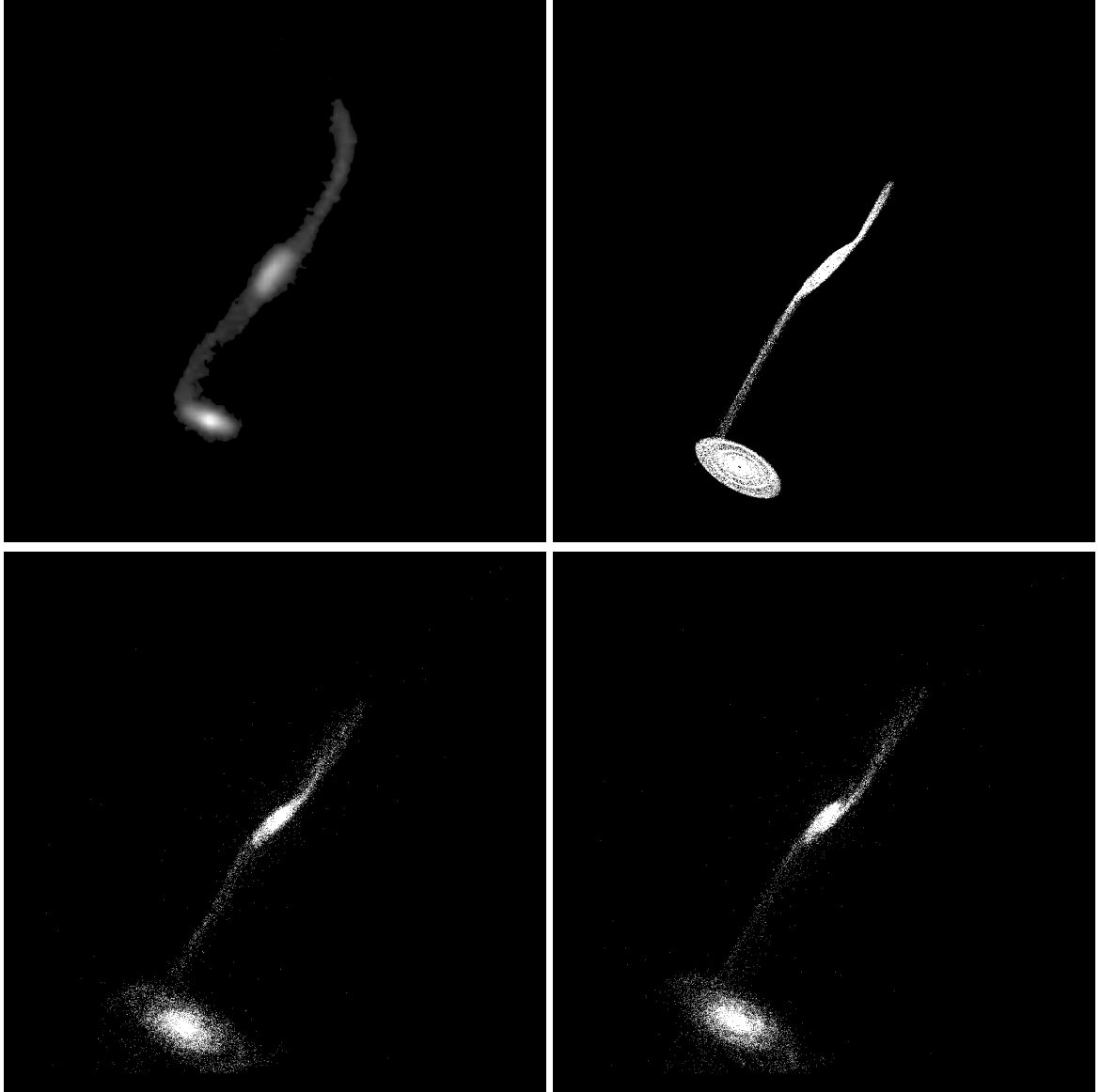


Figure 5.319: Target image (top-left), best SPAM match from Merger Wars (top-right), initial N-Body match (bottom-left), and best N-Body match (bottom-right) for SDSS 1237678620102623480

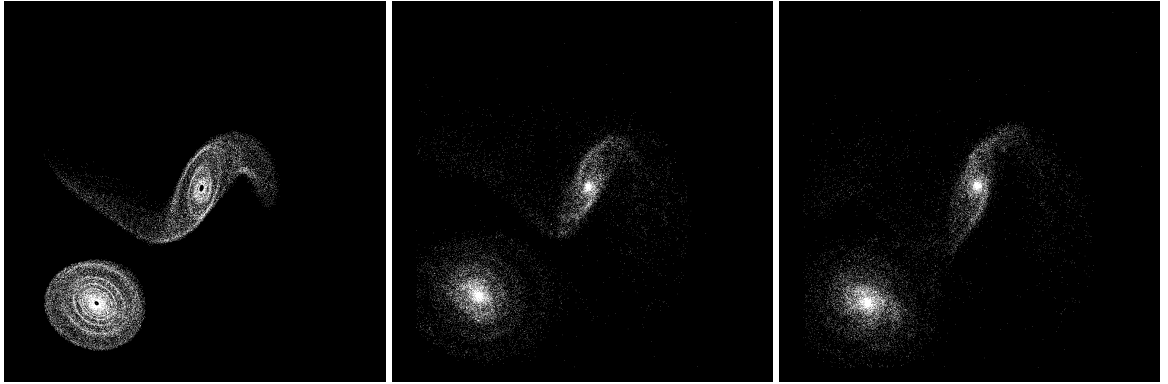


Figure 5.320: XZ projections of best SPAM match from Merger Wars (left), initial N-Body match (middle), and best N-Body match (right) for SDSS 1237678620102623480

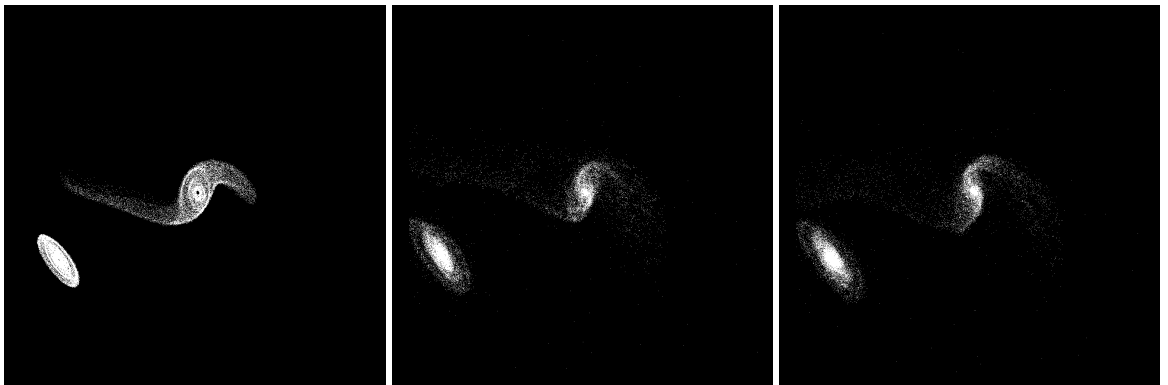


Figure 5.321: YZ projections of best SPAM match from Merger Wars (left), initial N-Body match (middle), and best N-Body match (right) for SDSS 1237678620102623480

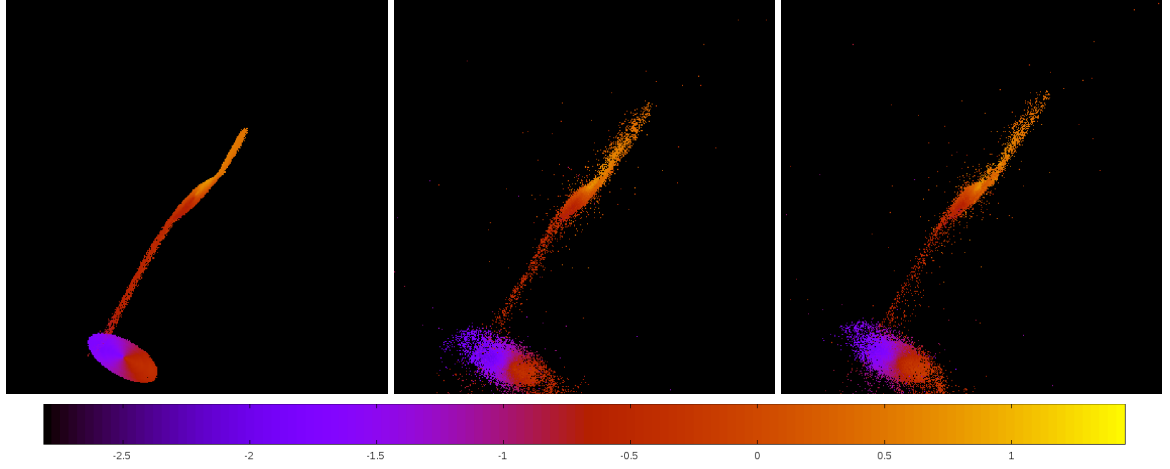


Figure 5.322: Line of sight velocity plots of best SPAM match from Merger Wars (left), initial N-Body match (middle), and best N-Body match (right) for SDSS 1237678620102623480

Table 5.108: Orbital Elements & Dynamical Friction for SDSS 1237678620102623480

	SPAM Simulation	Initial N-Body Simulation	Best N-Body Simulation
a	-0.389	-0.311	-0.450
e	10.713	12.953	9.453
r_c	3.777	3.722	3.802
i	84.780°	85.351°	85.408°
Ω	63.546°	63.551°	63.333°
ω	155.778°	150.960°	153.928°
ν	47.747°	50.124°	48.859°
t_n	50	49	51
$\ln\Lambda$	N/A	1.00E-03	0.00E+00

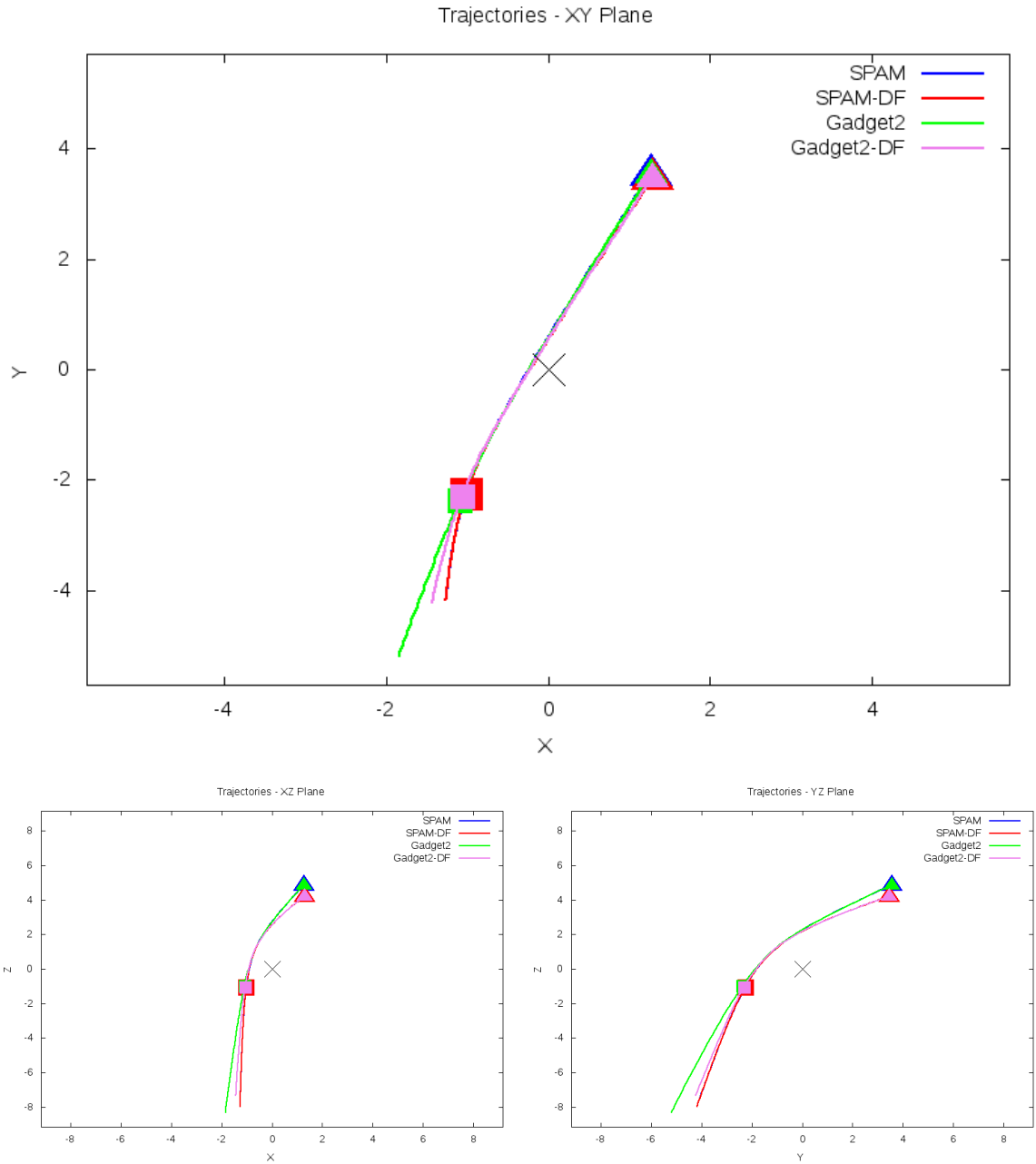


Figure 5.323: Trajectory plots of best SPAM match from Merger Wars, initial N-Body match, and best N-Body match for SDSS 1237678620102623480

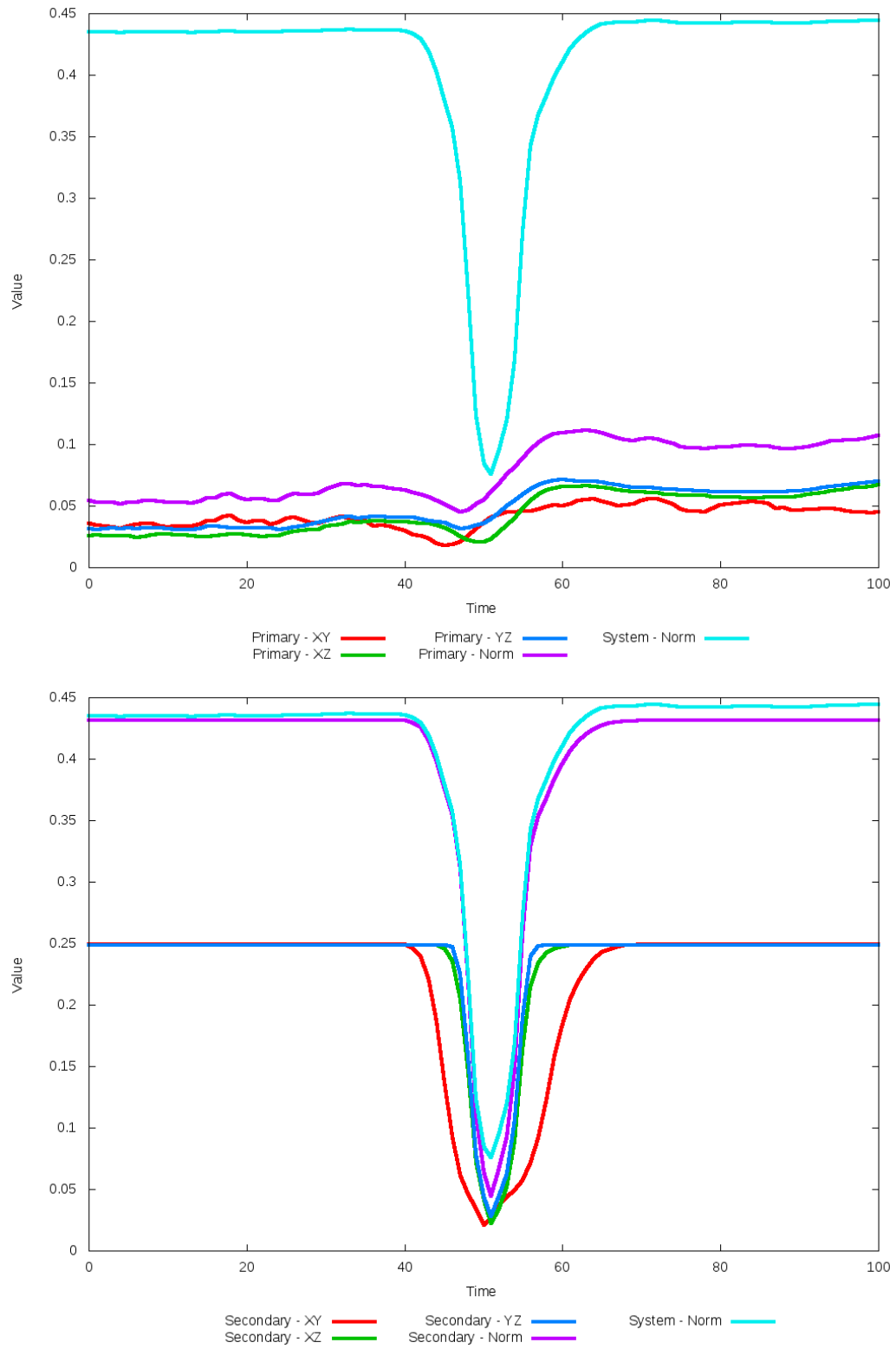


Figure 5.324: All metrics versus simulation time of the best N-Body simulation for SDSS 1237678620102623480

5.2 Pipeline Evaluation

Determining how well our resulting N-Body models match their target systems, be it to observational data or surrogate data from a restricted three-body model, is largely a subjective affair. Of the 54 systems modeled, we can subjectively grade them into one of four ordinal categories. These categories are:

Green – a very good morphological match to the surrogate data and usually the observational data.

Yellow – a decent match to the surrogate data and observational data. These models show promise of fitting better if the restricted three-body model itself was a better match to the observational data or if the pipeline utilized greater temporal resolution through more frequent N-Body output files or increased precision in dynamical friction.

Orange – a poor to fair match to the observational data and surrogate data. These models may exhibit some characteristics of the target system, but need more than just changes in dynamical friction to improve the quality of the match

Red – the N-Body model does not match either target data set; these are very poor matches.

Using this categorization, our pipeline had very good matches to over half of the systems modeled. Including the systems with close matches that would benefit from some additional work brings the number of systems with a decent N-Body model representation to 85%. This once again shows that gravity alone can be used to determine morphologies for many systems. The dataset chosen to develop, test, and evaluate our pipeline was not chosen to show this level of success; the dataset used by our pipeline consisted of systems with restricted three-body models extensively evaluated through the Merger Wars project

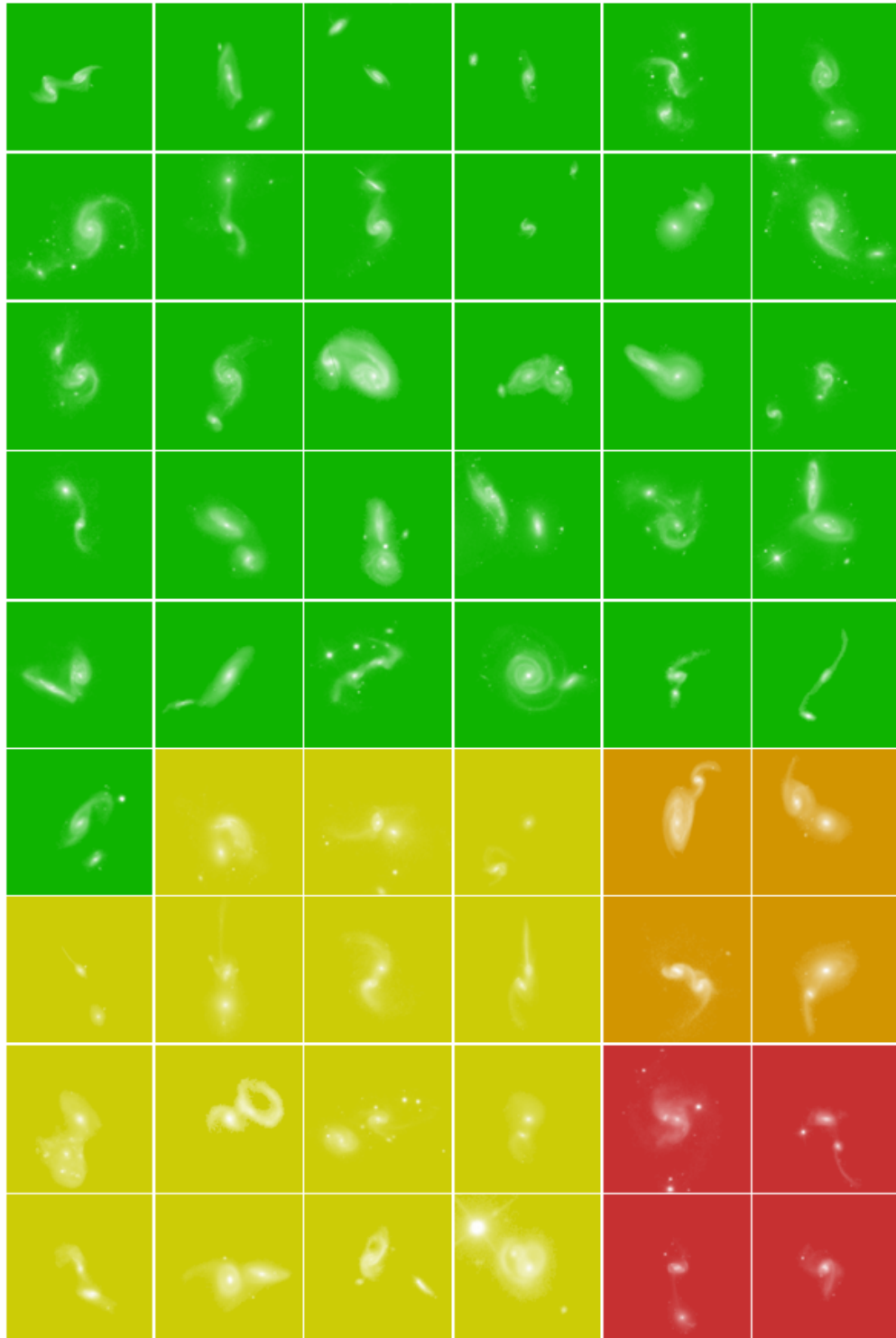


Figure 5.325: Over half of the simulations evaluated yielded N-Body models that were in excellent agreement (green) with the restricted three-body models. Including good matches (yellow) brings the success rate to over 85%.

(Holincheck, 2013). If anything, this should not be surprisingly as our results support the old modeling and simulation adage “garbage-in, garbage-out”.

There were eight systems that did not result in a quality N-Body model match. These systems, identified in orange and red in figure 5.325, were systems with very strong interactions, with the N-Body models often showing a merger has occurred or was imminent. In the restricted three-body simulations with SPAM, mergers are seldom seen. Instead, it is more likely to see tight, binary orbits which are unlikely to be physical when tidal features are present.

Chapter 6: Analysis and Discussion

The prototype pipeline for constructing optimal N-Body models for systems of interacting galaxies has yielded very promising results with roughly 85% of the systems having a good or very good qualitative match to their surrogate data. With this set having been tested, we hope to learn if there are any signs or trends that would indicate under what conditions a system is likely to or unlikely to find a good N-Body model. This N-Body model dataset also allows us to better see some of the limitations of using restricted three-body models to match our target datasets and be used to generate N-Body models. We can use this dataset to have a better understanding of how dynamical friction impacted our ability to find good matches to the target datasets. We set out to demonstrate an automated pipeline focused on the physics of gravity, but there are other physics and phenomena that can and should be accounted for in the pipeline to find the most optimal models of systems of interest.

6.1 Dynamical Friction

Throughout the previous chapter, the dynamical friction as determined during the pipeline's optimization step was reported for each system. This value of dynamical friction is not the absolute optimized value for the system but is only an approximation for two reasons. The first reason is that metrics were only assessed 100 times during each N-Body simulation (this corresponds to the number of output files from the simulation), which for long simulations may not capture the best moment when the simulation may better match the target dataset. This, however, may not have been a bad limitation to impose, as seen when there is a sharp drop in the metrics plotted over time in many of our simulation results. The second reason is that we limited the precision of dynamical friction to three significant

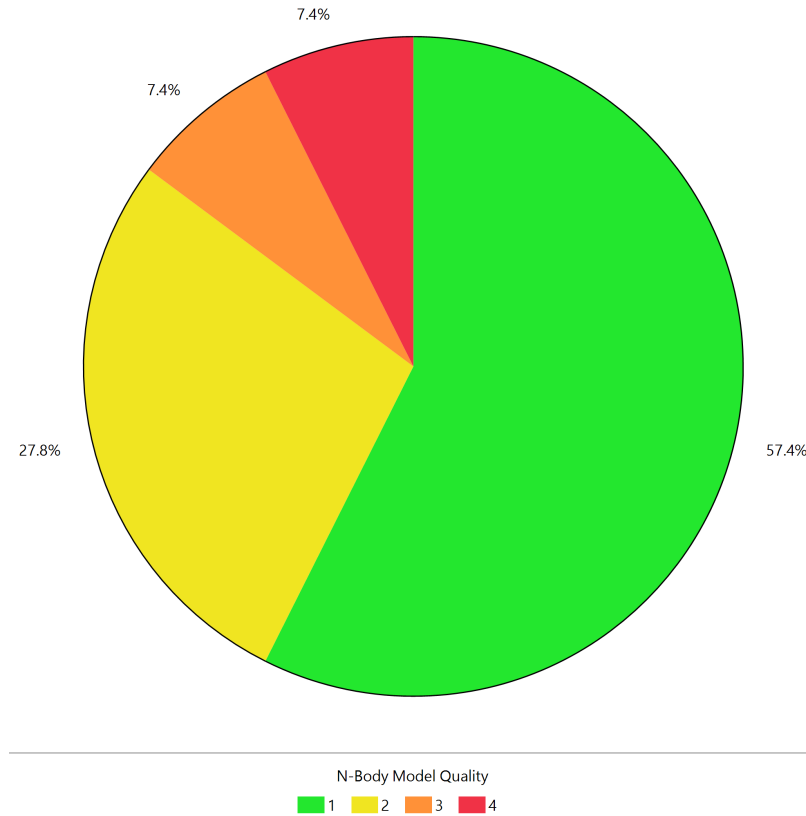


Figure 6.1: The pipeline found very good (green) N-Body matches for over half of the systems modeled while approximately 30% were good (yellow). About 8% of the systems were not very good matches (orange) while another 8% did not match at all.

digits. This was chosen to allow the process to find a better value of dynamical friction in a reasonable number of iterations.

In all, there were eight systems modeled that did not appear to change their value of dynamical friction from the initial starting value of 0.001. Of these, only one system was judged to be very poor, NGC 4320. It should be noted that this system did not actually sample around the starting value to see if it was already optimal. When dynamical friction was sampled around this value to create a finite difference stencil, the initial conditions for the N-Body model did not change. As a result, the metrics evaluated were the same, and the optimization step thought it had reached a minimum. The contribution of dynamical friction as determined by SPAM for this system was appreciable enough to make a change.

This same behavior was seen in three other systems, but they each were judged to be a very good match. It is possible that if a good match is not found when sampling around the starting value of dynamical friction, the system may be in a local minima. To test this, we would have to arbitrarily choose another starting location and see if the initial conditions for the galaxies change.

Surprisingly, there were also eight systems that found their best value of dynamical friction to be 0.0. All but one of these systems were deemed to be a very good match at this value. Without rerunning these simulations, it is unknown whether the resulting value of dynamical friction was chosen due to insufficient numerical precision or if the trajectory of the orbit needs further expansion or contraction compared to greater values (this is illustrated earlier in figure 3.3). Given that our range of dynamical friction varied from 0 to .02 and good matches were found near 0, it is very likely the precision should be increased while searching the allowable range of dynamical friction. The fact that it spans such a small range (i.e. just a couple orders of magnitude) and the tremendous impact it can have on our simulation results supports the finding that dynamical friction is a very sensitive tuning parameter.

Unfortunately, given the range of dynamical friction values found for our best and worst models, the magnitude of this value does not indicate whether or not the corresponding model is a high quality match to the target dataset or not. Ultimately, it is our metrics that should aid in the discovery of the best value of dynamical friction. It is possible that with a significantly larger dataset a trend or correlation may appear.

6.2 Orbital Elements and System Parameters

Along with each system modeled, we calculated the orbital elements of both the best restricted three-body model (SPAM) and best N-Body model (GADGET-2), all of which can

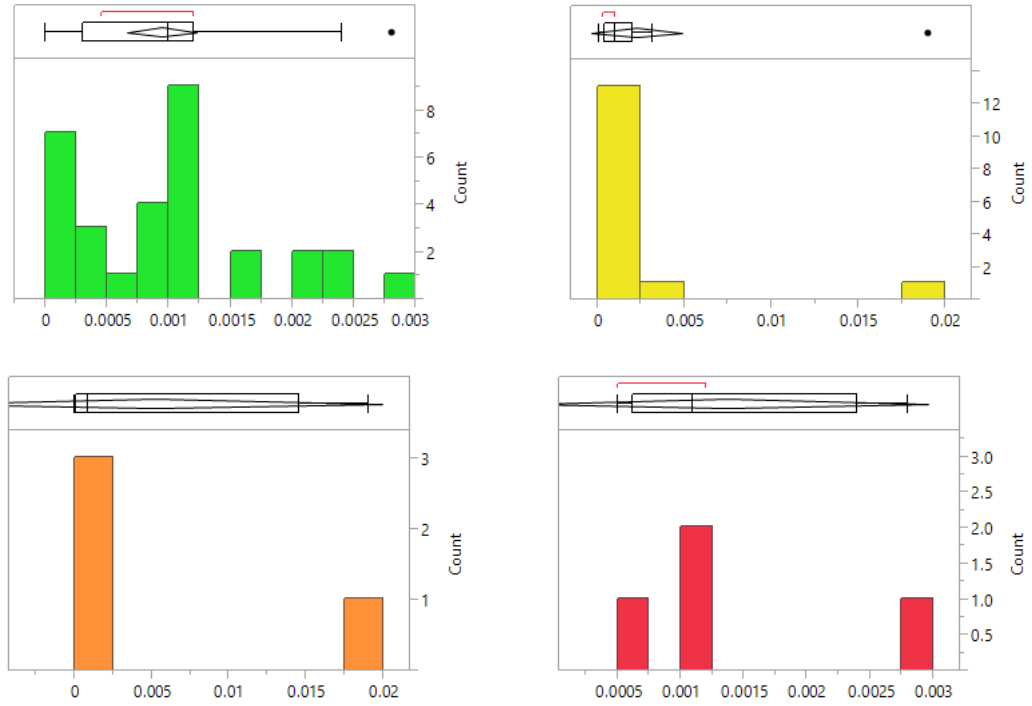


Figure 6.2: Coefficients of dynamical friction chosen by the pipeline varied between 0.0 and 0.02. Their distributions are grouped by their quality as described in figure 6.1.

be found in the results of each system. A few of the orbital elements and quantities derived from them can be telling as to our likelihood of successfully creating a poor, decent, or good N-Body model to match the target dataset. Other elements may be useful for incorporation in calculations of metrics, as they may suggest prior information in a Bayesian relationship. However, most of the elements will not tell us much information.

6.2.1 Indicators of N-Body Model Quality

A good quality N-Body model match to the restricted three-body model should exhibit very similar orbits. However, given that our metrics are designed to find the time at which morphology best matches the target dataset independently of the orbital parameters, it is expected that some of those parameters may not be a perfect match. However, there are

three orbital elements that have shown some noticeable deviation between what was predicted by SPAM and what we found using GADGET-2 which show a strong divergence between their orbit, and these elements may be useful in the future as indicators of trouble matching data, i.e. have poor N-Body model quality. These three elements are the inclination, longitude of the ascending node, and true anomaly.

The inclination as an indicator of model quality is not surprising. The inclination will determine the orientation of the secondary galaxy in the XY plane. A poor match in inclination will likely mean the position of the secondary galaxy will never be in the right position in space to drive down a metric. Figure 6.3 shows the inclination as determined by SPAM versus the determination by GADGET-2. In it, one of the poorest model matches are far from the ideal fitting line (blue), while another poor model has modest deviation, although it falls within the confidence of prediction (light grey region) like other good model matches are, but outside the confidence of fit region (dark grey).

Both the longitude of the ascending node and true anomaly help determine where a body is in time along its orbit. Whereas the inclination showed a very tight correlation between the SPAM and GADGET-2 models, the correlation is not nearly as tight as can be seen by the confidence intervals in figures 6.4 and 6.5.

These two parameters show the poorest models as having some of the highest deviations. This is very clear when looking at the longitude of the ascending node where clearly 3 of the 4 of our worst model matches fall in the middle of the confidence of prediction region or outside of it. There is one good model, however, that also has a large deviation. The true anomaly also shows five of the eight poor models (red and orange) as having large deviations, but there are just as many good models with a large deviation too. Given the proportion of the number of models in their quality groups, large deviations in both of these parameters could be used as evidence by a Bayes classifier that the resulting model may be of poor quality. Because both of these are time related parameters, it is possible that by increasing the frequency of output files during the N-Body simulations, a better

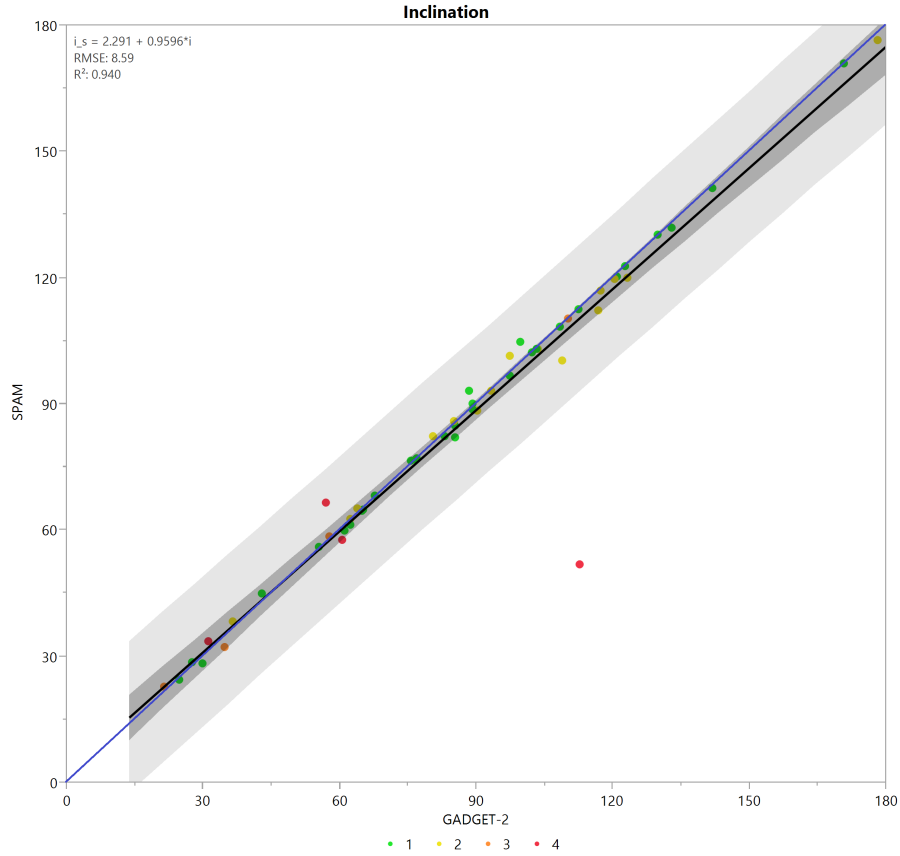


Figure 6.3: The inclination from each system is plotted for the SPAM model against the corresponding GADGET-2 model. Each system is colored by its N-Body model's quality. Most of the models are in excellent agreement with each other, with the the worst models having a strong deviation.

match in time may be found, thereby decreasing their deviations.

The cause of the large deviations in the poor quality models is likely to be dynamical friction. For close encounters using N-body models, the trajectory of the system is greatly altered compared to the parameterized version of dynamical friction in the restricted three-body codes. The true anomaly and the longitude of the ascending node would be greatly affected by this shift. Shifts in the inclination of the system are generally less pronounced unless the secondary galaxy is completely disrupted. When that happens, the approximations used in the three-body model are no longer valid.

On their own, the semi-major axis and the masses of each system do not necessarily

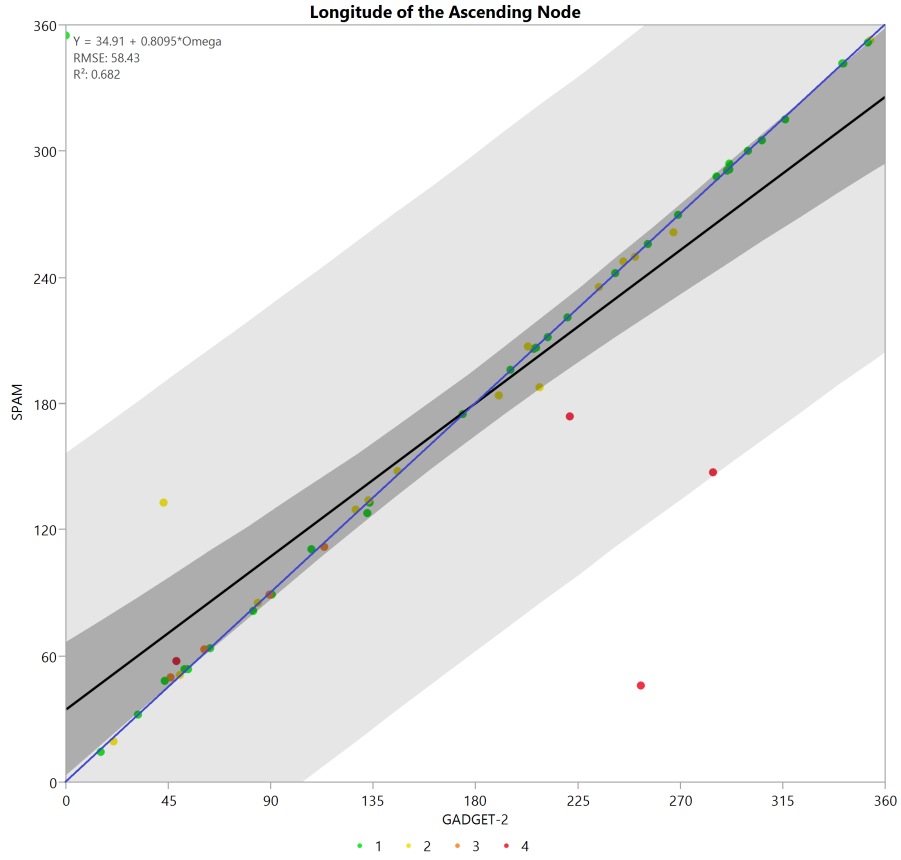


Figure 6.4: The longitude of the ascending node from each system is plotted for the SPAM model against the corresponding GADGET-2 model and colored by its N-Body model's quality. The worst models show significant disagreement between SPAM and GADGET-2.

indicate whether or not we expect to have trouble creating or finding a good N-Body model for our target dataset, but used together to estimate the specific orbital energy of the system does provide some indication whether or not our model will be a quality match. It can be defined using:

$$\epsilon = -\frac{\mu}{2a} \quad (6.1)$$

where μ is the total mass of the system times the gravitational constant and a is the semi-major axis. This quantity describes the total kinetic and potential energy of the system, scaled by its reduced mass. It should remain constant during an entire simulation.

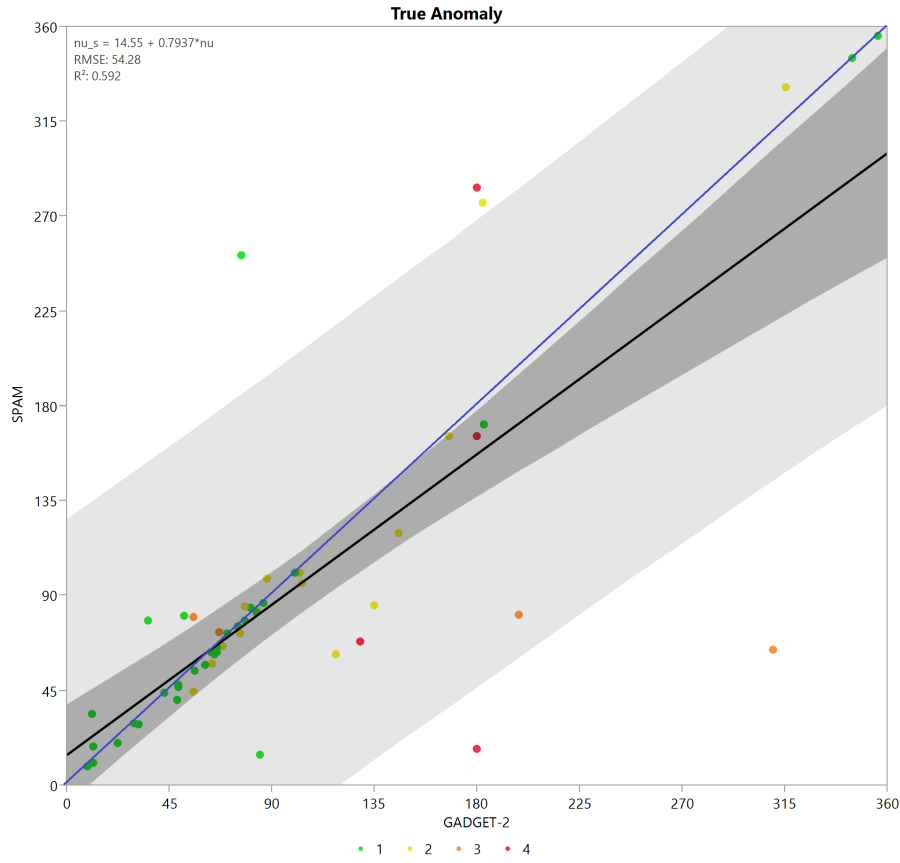


Figure 6.5: The true anomalies from each system is plotted for the SPAM model against the corresponding GADGET-2 model. Each system is colored by its N-Body model's quality. The worst models show significant disagreement between SPAM and GADGET-2, although a couple good models also show a large disagreement.

As seen in figure 6.6, there is generally a linear relationship between this formulation of specific orbital energy as derived from each simulation type. However, all four of our poorest models fall outside the confidence of fit interval, and each has more energy with the GADGET-2 model than SPAM. If we break down the comparison by model quality, we see that the best and good fits are in relative agreement with each other, showing a strong linear relationship. This is not surprising as these models do a good job of matching their orbits. The poorer models do not show as strong of a correlation between the restricted three-body and N-Body models. We can also see the same effect in figure 6.7 when the change in specific orbital energy is plotted. In this figure, the change in specific orbital

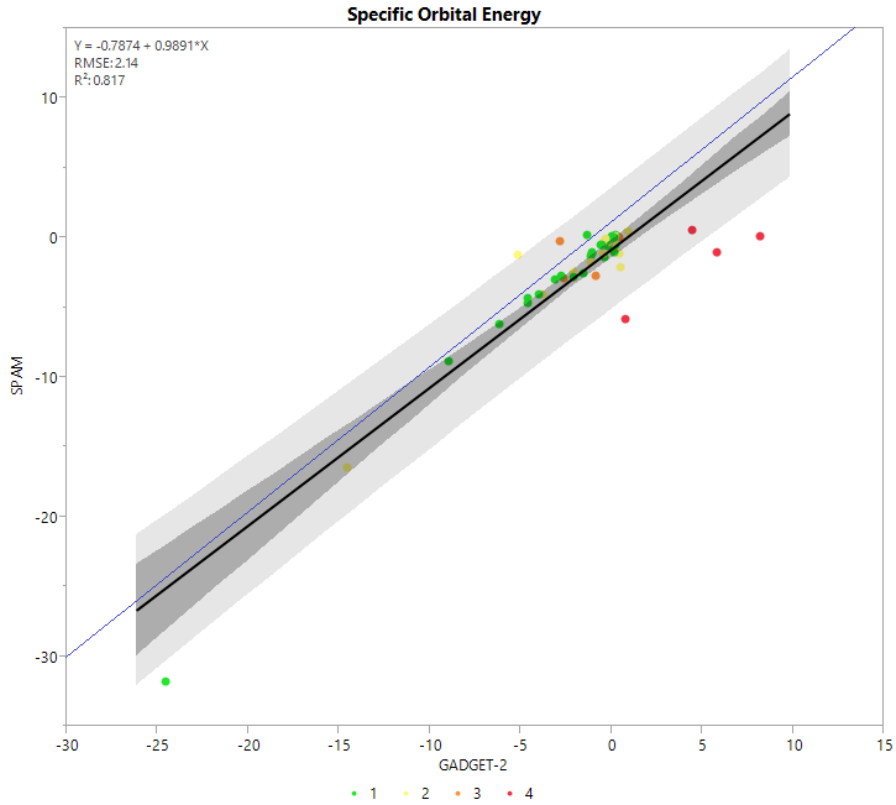


Figure 6.6: The specific orbital energy from each system is plotted for the SPAM model against the corresponding GADGET-2 model and colored by its N-Body model's quality. All four of the worst models have a specific orbital energy that is predicted to be significantly higher with GADGET-2 than SPAM.

energy is plotted (with jittering) for each quality grouping, with matching box plots below them. These box plots show the confidence in the mean, the first and third quartiles, and the span of outliers. Both a scatterplot and box plot are shown to better illustrate the distribution of this parameter. The greatest change in energy appears to be due to the greatest mismatch in orbits, something undesirable in a good match.

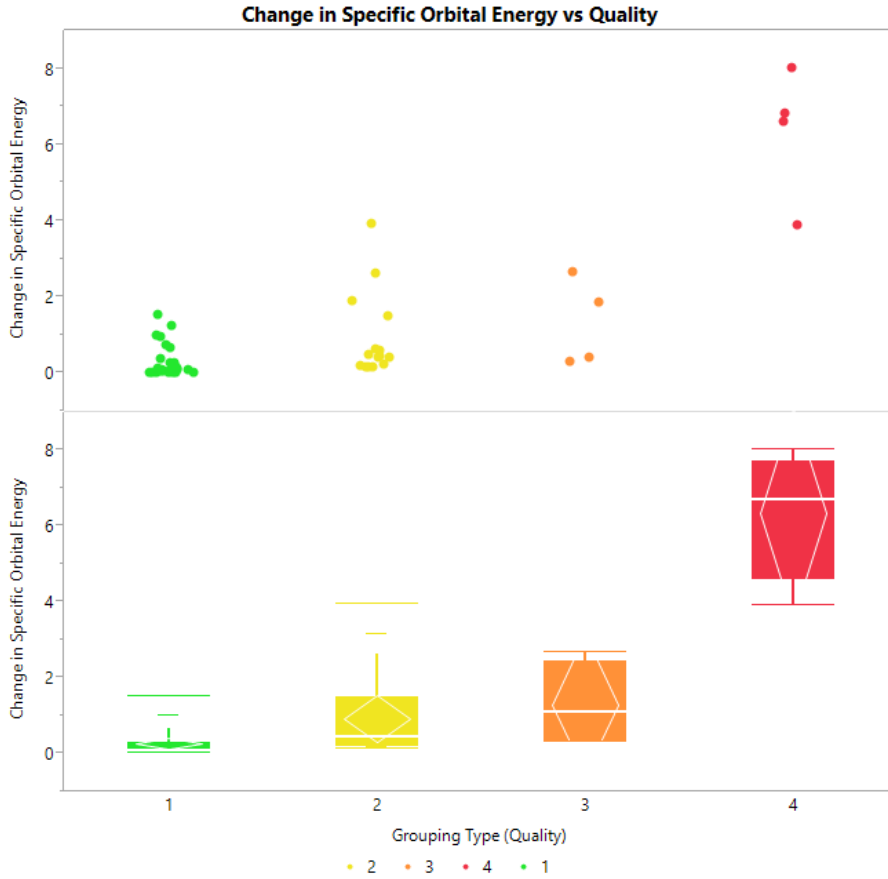


Figure 6.7: The change in specific orbital energy from each system as determined by SPAM and GADGET-2 is plotted by its N-Body model's quality. In general, the mean change in specific orbital energy trends upwards as the model quality worsens.

6.2.2 Indicators of N-Body Modeling Difficulty

While comparison of some of the orbital elements predicted by SPAM to those predicted by GADGET-2 can provide an indication of model quality, other parameters of the system or elements solely from the SPAM simulations can indicate just how difficult it may be to produce any good N-Body model. The two most likely parameters to aid in this determination is the reduced mass and distance of closest approach (pericenter distance for elliptical orbits and focus distance for hyperbolic orbits).

At first, the relationship of distance of closest approach may not appear to be a strong indicator because there is a strong correlation between the value predicted by SPAM and

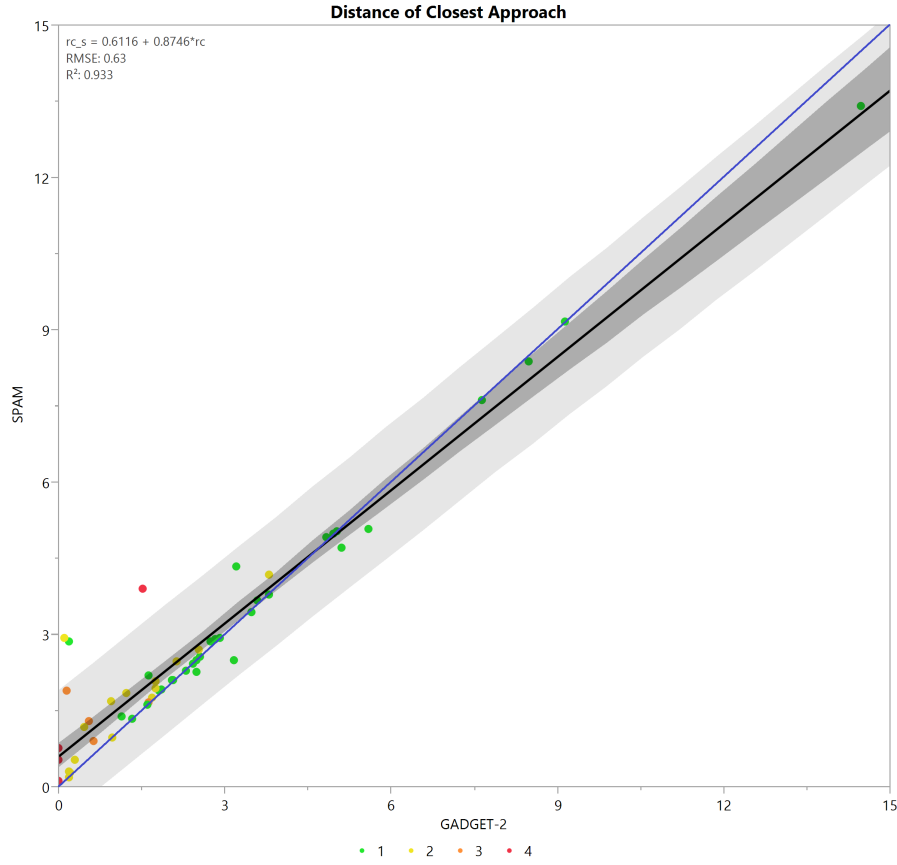


Figure 6.8: The distances of closest approach from each system is plotted for the SPAM model against the corresponding GADGET-2 model. Each system is colored by its N-Body model’s quality. All of the poor models have a distance within 2.0.

GADGET-2, as seen in figure 6.8. However, plotting each grouping of quality type as seen in figure 6.9 makes it very clear that the worst models all have a very small distance of closest approach as computed from the SPAM models. This is not surprising, given that three of the worst model fits came from Arp 104, Arp 237, and NGC 4320, each of which exhibited multiple close approaches or periods. The other very poor system, Arp 173, did not have multiple close approaches, but did have a very tight, circular orbit. In the N-Body simulations, the orbits of the galaxies decayed into one another and merged.

The behavior seen in our N-Body models indicates that the physics of SPAM are not sufficient for these systems. Mostly likely SPAM is not modeling a realistic potential for

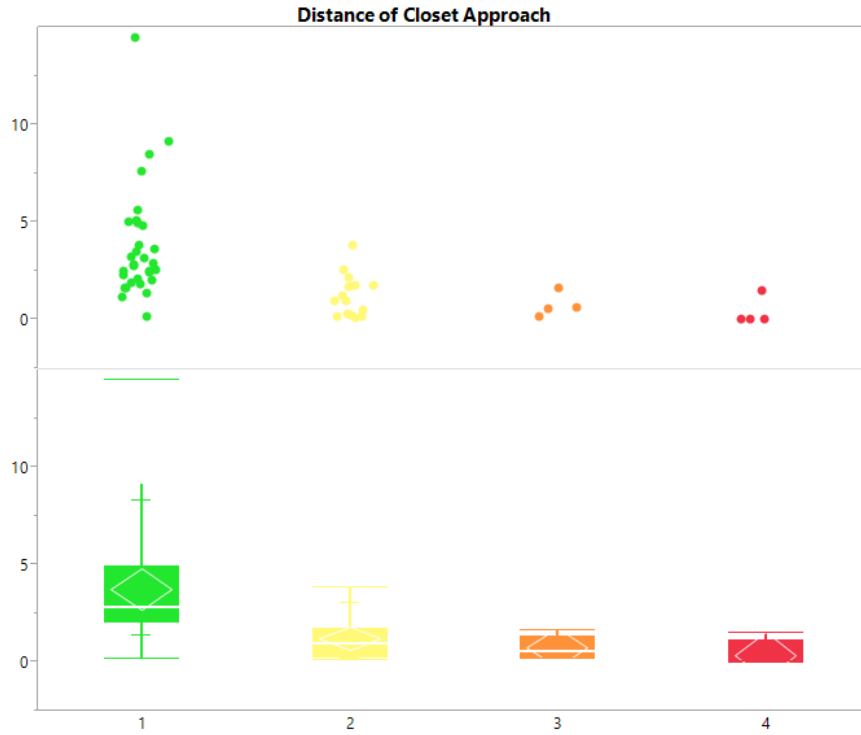


Figure 6.9: The distances of closest approach from each system is plotted for the SPAM model and grouped by its N-Body model's quality. As the mean distance decreases, so does the quality of the models.

the system when the galaxies are supposed to be close together. Recall that SPAM does use a three component potential based on the Hernquist three component galaxy model. However, this potential as defined at the beginning of the simulation does not change as the massless particles trace the morphology of the evolving system. As the galaxies come close to each other, their potential fields should change considerably, starting when their halos begin to overlap. The potential, therefore, is non-physical at these close distances, calling into question the validity of those restricted three-body state vectors.

The mass of the system may actually give some indication of how difficult it may be to obtain a good N-Body model. On their own, the masses of each galaxy do not indicate a trend in the quality of our resulting models. The categories for model category all contain masses that generally span the same range of values. However, the reduced mass of the

system, as seen in figure 6.10, shows a trend whereby increasing reduced mass decreases model quality. This holds even though the best quality models do have a handful of systems with some large reduced masses and some of the poorer models have small reduced masses.

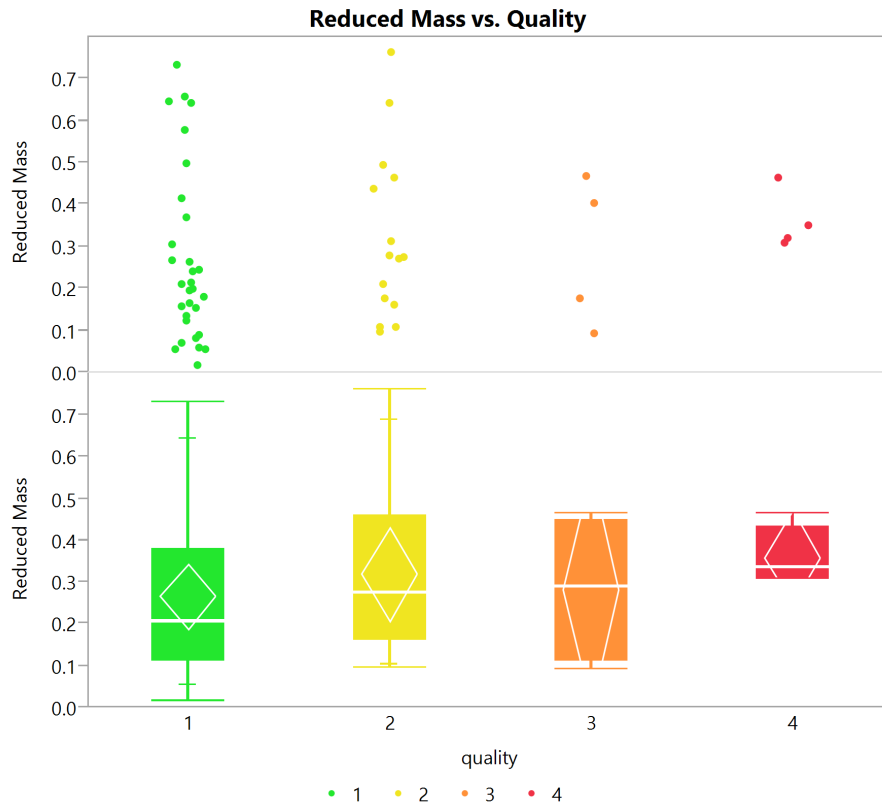


Figure 6.10: The reduced mass from each system shows a trend where systems with larger reduced masses are more likely to have poorer N-Body models.

This observation may have some relationship on numerical accuracy of the simulations as the number of particles used for each system was held constant, whereby systems with larger reduced masses had a greater amount of mass per particle than systems with a lower reduced mass. For these larger particles, the softening lengths did not change as a function of mass, only as a function of the number of particles used. Generally however,

softening lengths were chosen that should be sufficient for a wide range of simulation reduced masses. Furthermore, just because a reduced mass is high, does not necessarily mean both systems have large masses. Unfortunately, the mass ratios of the systems do not indicate any such trend as the reduced mass does.

As discussed earlier, the potential of the restricted three-body simulation does not change during the system evolution in time. The larger reduced masses of the systems indicates stronger gravitational attractions that may alter the potential beyond each galaxy greater than the current limitation SPAM models. That is consistent with the observation when the distance of closest approach becomes smaller, also increasing gravitational attraction.

6.2.3 Other Elements and Parameters

The three remaining orbital elements, the semi-major axis, eccentricity, and argument of periapsis, on their own do not indicate whether or not a model will be troublesome to create or match a target dataset.

Eccentricity shows a very strong correlation between the SPAM and GADGET-2 models. The deviations are greatest at the small values of eccentricity, but those deviations are made up of all model quality types. As such, there is nothing to be learned from this element on its own.

The argument of periapsis has only a modest correlation between the SPAM and GADGET-2 simulations at best. Although figure 6.12 shows the ideal reference line (blue) cutting straight through high quality models (green) nearly exclusively, there are many models of each quality type within and outside the confidence of prediction.

If we look at the change in the argument of periapsis for each model quality type, a trend in the mean values of each group emerges. In general, the poor models have the largest changes in this value. While the change in specific orbital energy may be useful as an indicator if those deviations are large, there are too many outliers in the change of

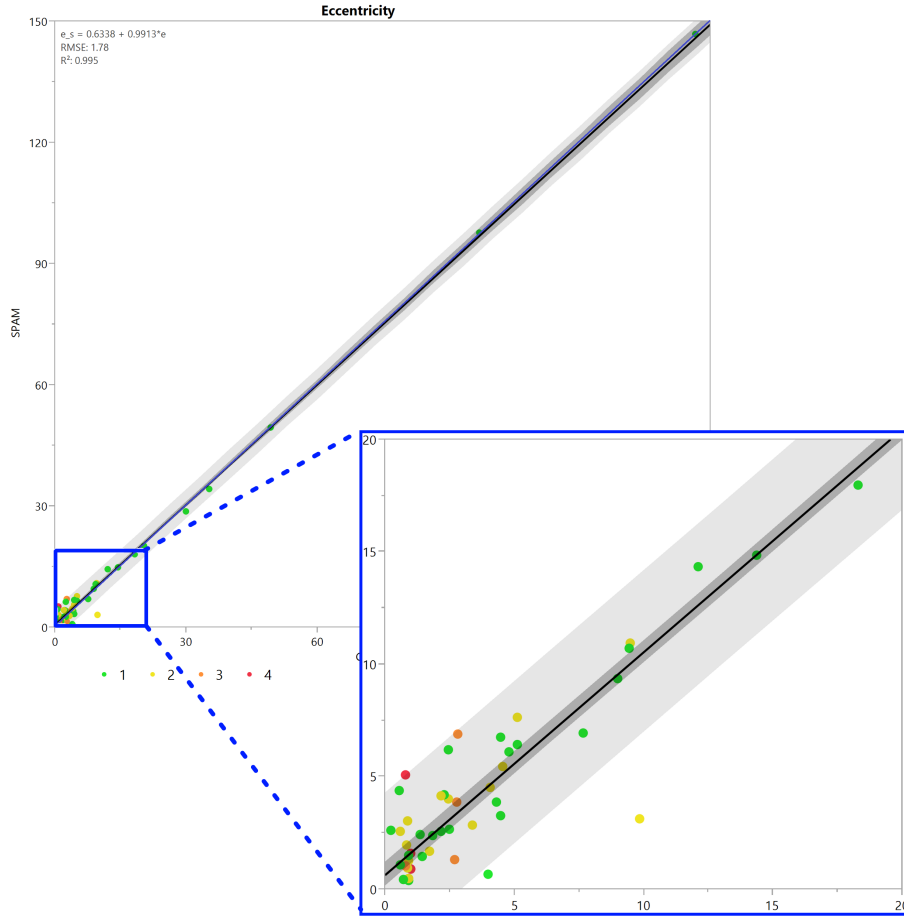


Figure 6.11: The eccentricity from each system is plotted for the SPAM model against the corresponding GADGET-2 model and colored by its N-Body model's quality. Even at low values of eccentricity, there is not a correlation or trend in the data as it relates to model quality.

argument of periapsis. This frequency of outliers, particularly in the best model grouping, does not provide a convincingly suggest that this parameter should be used as an indicator of model quality.

Strictly speaking, the orbits of our systems were either elliptical or hyperbolic. Well over half of them were hyperbolic (having a negative value for the semi-major axis), showing a passing interaction but not a merger occurring. By and large, these hyperbolic orbits had good model fits. There were a number of systems that SPAM predicted would be elliptical, but the N-Body Models predicted them to become hyperbolic as dynamical friction

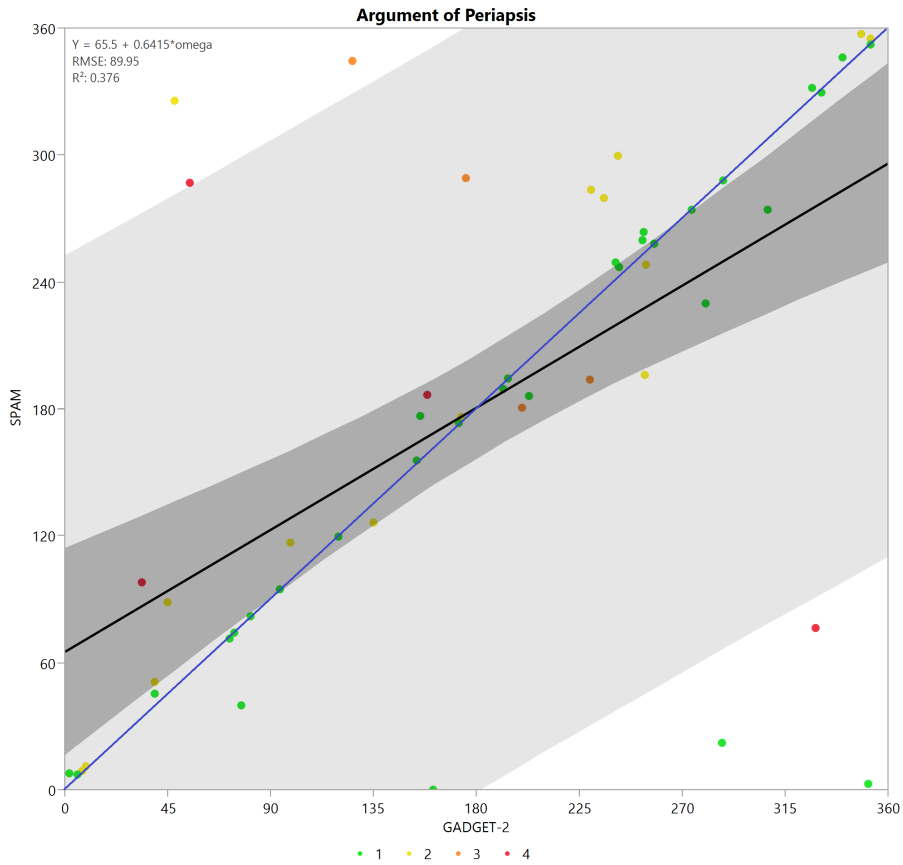


Figure 6.12: The argument of periapsis from each system is plotted for the SPAM model against the corresponding GADGET-2 model and colored by its N-Body model's quality. There is an overall poor agreement in this parameter between the SPAM and GADGET-2 models.

changed, leading to a new orbit for the system to use in the N-Body model. The change in orbit types helps to explain why the semi-major axis does not have a strong correlation between the two modeling types, as it will flip signs (and likely magnitude) as the orbit types change.

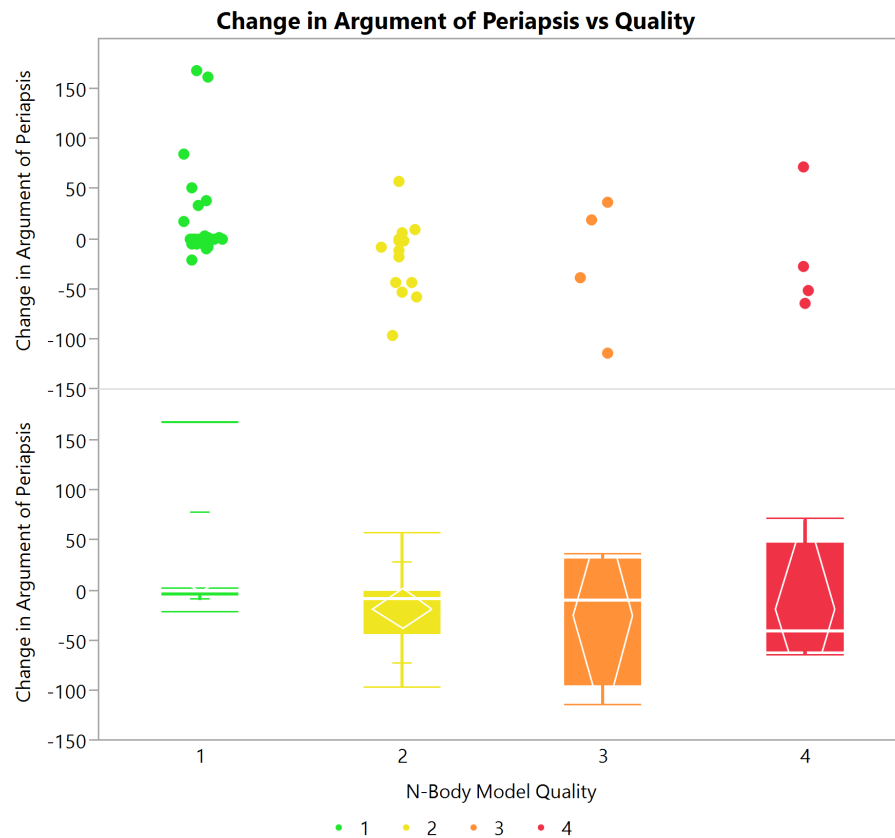


Figure 6.13: The change in the argument of periapsis from each system is plotted by its N-Body model's quality. Although the change in the argument of periapsis has larger means for the poor models, the number of outliers in the good model distribution does not make this value a good use of an indicator.

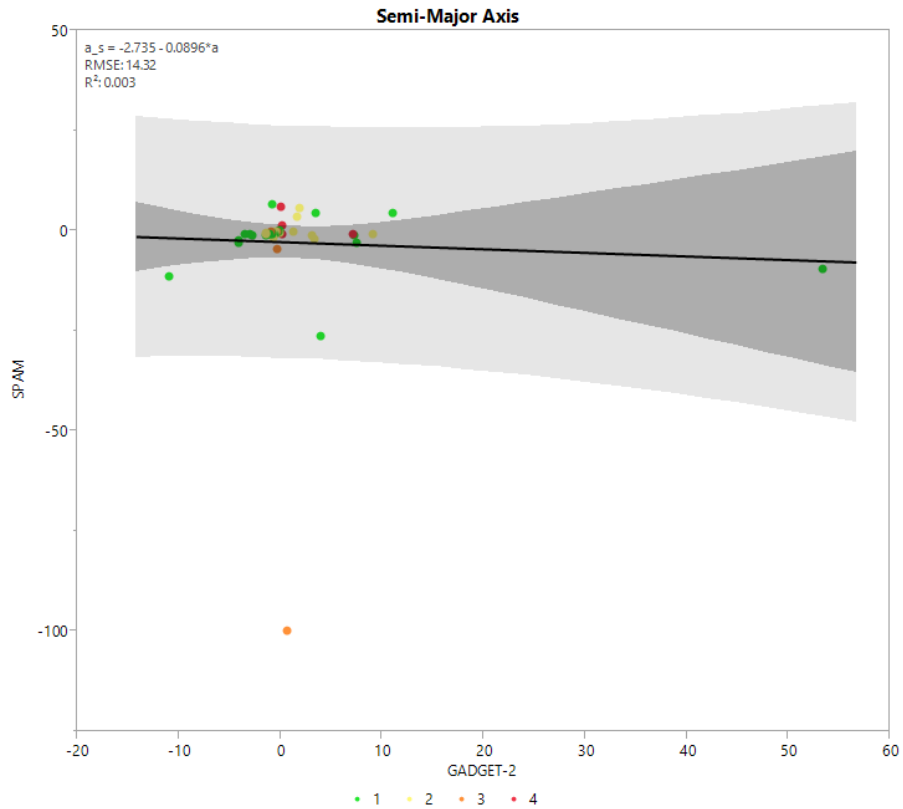


Figure 6.14: The semi-major axis from each system is plotted for the SPAM model against the corresponding GADGET-2 mode and colored by its N-Body model's quality. There is an overall poor agreement between the SPAM and GADGET-2 models in their predicted semi-major axes.

Each of our quality groups had the same number of models that started out as elliptical in SPAM and remained that way after the best GADGET-2 Model was found. This is not surprising as the worst systems are predicted to merge by GADGET-2, which would result in a bounded, tight orbit. This is in contrast to hyperbolic orbits which are unbounded, showing the systems to eventually grow far apart from one another. Unfortunately, there are not enough samples in the poor quality models to know if elliptical or hyperbolic systems definitively will be easier to match or not.

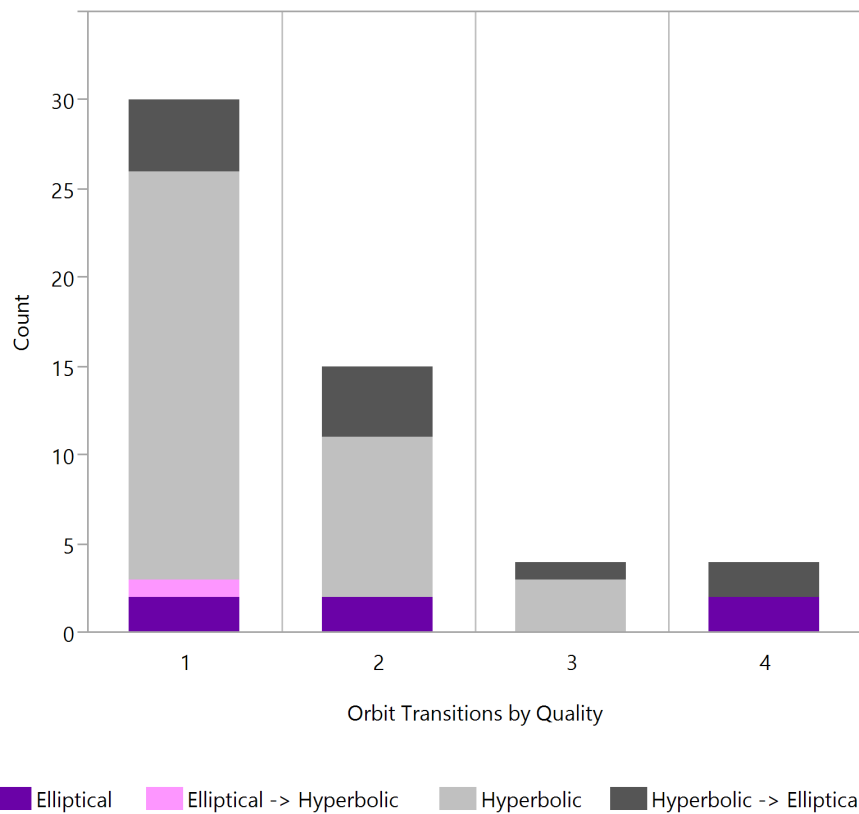


Figure 6.15: Most of the orbits in our dataset were hyperbolic. As dynamical friction changed, the orbit type predicted by SPAM was not the same type as the resulting best GADGET-2 N-Body model.

6.3 Velocity Profiles

A criticism of restricted three-body models is that they cannot predict the velocity profiles that could be seen in N-Body models. In our simulations, approximately 85% of our optimized GADGET-2 models had remarkably similar line of sight velocities when compared to the SPAM models. This 85% should not be confused with the number of models we deemed to be good morphological matches, it just happens to be the same quantity given by our system sample size. Generally we looked at the velocity along the line of sight by seeing how it compared between the models along the disc and tidal features of each galaxy. This is a qualitative assessment when the morphologies are not the same, but quantitative when the morphologies are the same, in which case we can more directly compare velocity magnitudes.

It is not surprising that some of our bad morphology matches, such as Arp 104 and NGC 4320, have very poor velocity matches. With very bad morphologies from systems that appear to be merging in the N-Body simulation but not in the restricted-three body simulation, there is no way to separate the primary from the secondary galaxy. In these systems, the span of velocity magnitude is similar, but the region of space covered is widely different.

There are a few very good morphological matches that do not have as good of velocity matches in their secondary galaxies, such as Arp 82, Arp 97, and UGC 10650. In these systems, the velocity spans a wider amount, as do their true anomalies and arguments of periapsis. One of the systems, Arp 181, was determined to be a decent morphological match, but the velocity profiles of both its primary and secondary galaxies are widely different from the SPAM simulation. Another system, Arp 241 showed decent morphology matching, but the best match was not oriented in the same way as the SPAM simulation showed. Some might want to use rotate the N-Body model until there was a good match, and use whatever the corresponding rotated initial conditions of that orbit and call it a match. This is similar in practice to what is done using Identikit. However, if rotating the

view to find a good match is used, the velocity profile will not be as good of a match as one would like, with significantly greater velocities appearing in the N-Body model.

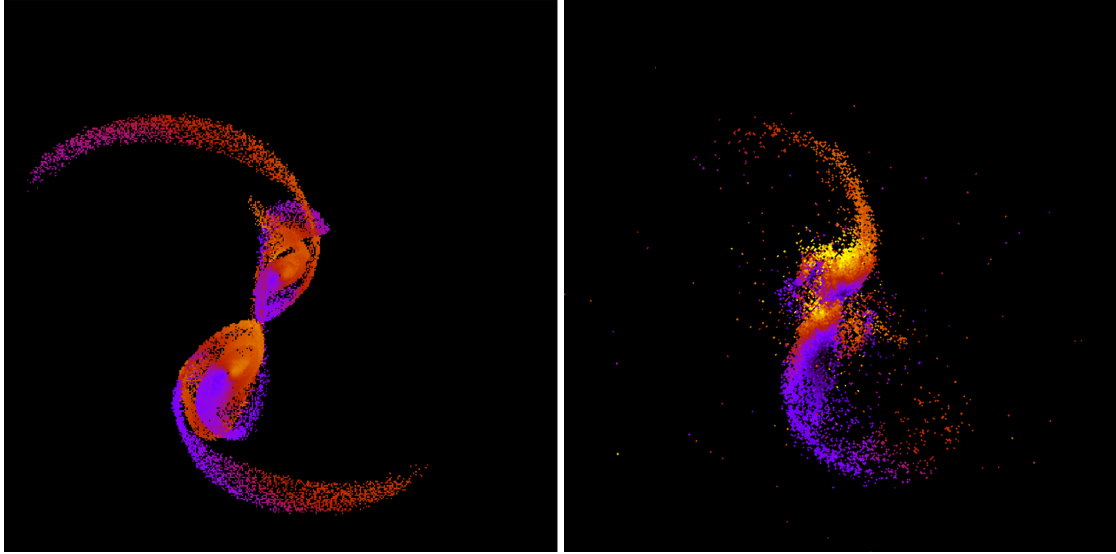


Figure 6.16: If the line of sight velocity plot from the GADGET-2 model (right) of Arp 241 is rotated approximately -40° , it would be a noticeably better morphological match to the SPAM simulation (left). However, the velocities would still be higher near the center of the system in the GADGET-2 model than the SPAM model predicts.

This discussion on line of sight velocity comparisons must be caveated, though, that we are not suggesting that the velocity of the surrogate data predicted by SPAM is correct, only that the N-Body models in general have very good agreement. Should the restricted three-body modeling finding methodology be enhanced to also fit to velocity of the observable data, then we should be able to use it to compare to our N-Body models in other metrics.

6.4 Including Gas Dynamics

Unless the galaxies to be modeled in a system are old enough to have consumed all of its gas in star formation, then some degree of gas should be included in our models. Barnes and Hernquist (1992) succinctly describe the impact that gas has on galaxy evolution by

its feedback to supernovae through heating and cooling and star formation, not just at the center of galaxies but along the outer rims of discs and the ends of tidal tails where shocks may occur. Gas within galaxies is generally modeled today by means of smooth particle hydrodynamics (SPH) or particle in cell methods. Both have their own challenges to implement, such as resolution, computationally efficiency, and numerical accuracy. GADGET-2 and MASS99 both support SPH, making that the tentatively preferred technique to work with. By including gas dynamics, we can add additional physics to models to make them more complete.

To illustrate some of the impact gas can have on the evolution of N-Body models for systems of interacting galaxies, we looked at Arp 58. This system has already shown tremendous improvement when tuning the choice of dynamical friction used by SPAM. We began by converting 10% of the disc's mass to gas and distributed the gas along the disc's rotational plane for each galaxy¹. The gas was given a small amount of angular momentum to spin with its disc, and it did not have any orthogonal velocity to this rotation (i.e. all gas motion was in the plane of the disc). We also provided the gas with a very small amount of initial thermal or internal energy. Dynamical friction was not changed from what was found earlier.

The inclusion of gas in Arp 58 continues to show an improvement in the quality of the morphological match to our surrogate data, as well as an improvement in matching the orbit of the SPAM simulations, as can be seen in figure 6.17. From a visual inspection, the inclusion of gas does not change the overall morphology of the system, but definitely sharpens its features. For this system in particular, the gravity only simulation found a very good match, but the tidal features were broader, particularly for the primary galaxy. Gas has sharpened the tails significantly, which is in better agreement with both SPAM and the observational data. The position of the secondary galaxy as seen in figure 6.18 shows an improved match in space and time. In regions where the gas is compressed, we

¹It is estimated that most galaxies observed today have no more than 10% of their visible mass in the form of gas (Barnes and Hernquist, 1992).

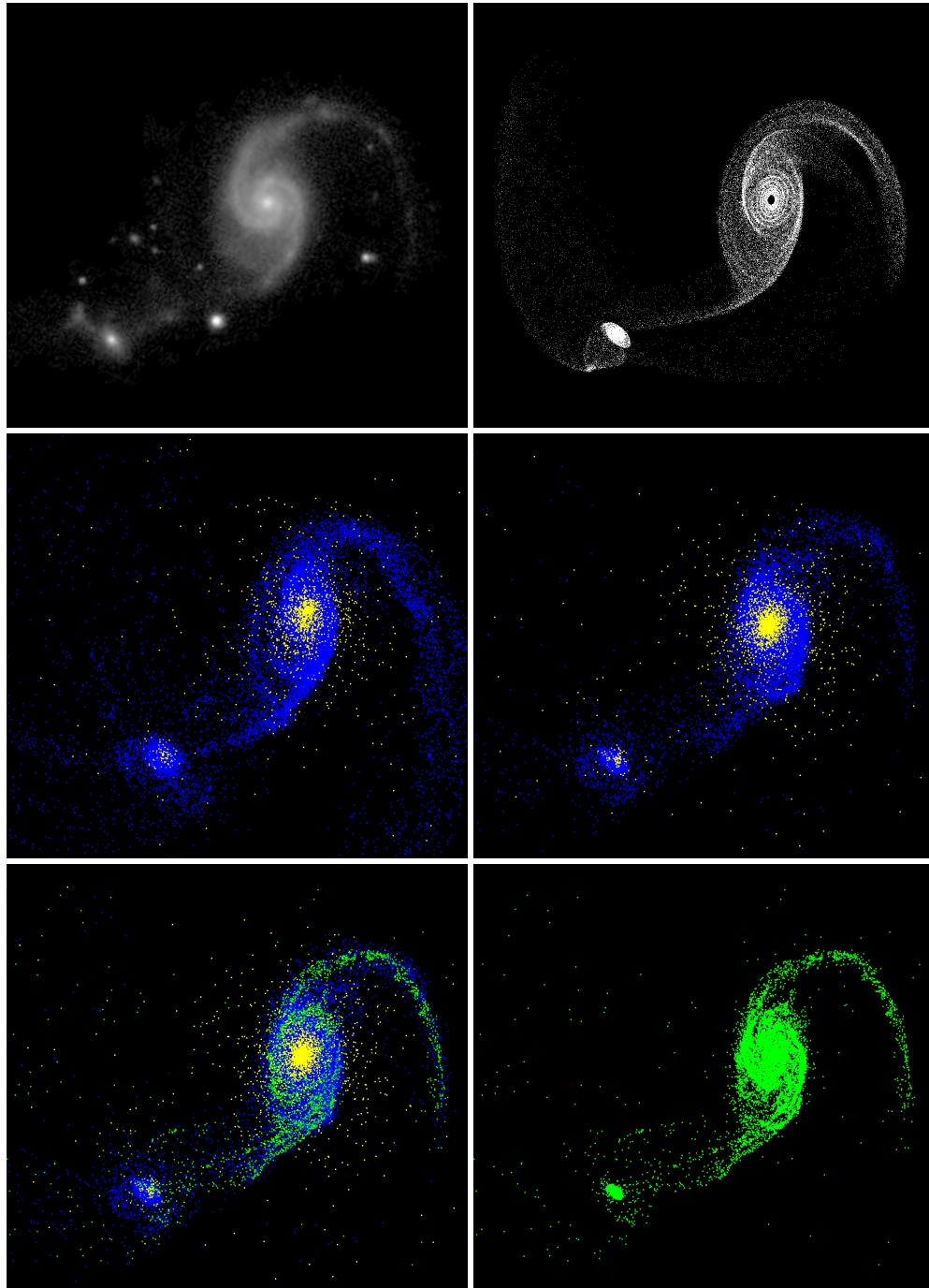


Figure 6.17: The introduction of gas dynamics to an N-Body model can sharpen tidal features. The top row shows a real image and SPAM simulation for Arp 58. The middle row shows the disk particles (blue) and bulge particles (yellow) for our gravity only optimized N-Body model (left) and the same model with gas added (right). The bottom row shows the simulation with gas added, visualized with the gas (green) on the left and only gas on the right.

would expect new stars to form. These young stars would have high luminosities and a significantly affect the appearance of this tidal feature compared to the stars from the disk alone. In general, the arms in spiral galaxies and many of the associated tidal features are most closely associated with the locations of the most recently formed stars (Schombert et al., 1990).

One of the interesting aspects of this project is that the test particles from the restricted three-body code tend to be more narrowly confined in tidal features than those seen in the disk particles from the full N-Body runs. The test particles in the restricted three-body code are dynamically cold in their initial disks. Initially, they are given perfectly circular orbits with no random components of velocity. However, the disk particles are dynamically warmer than the restricted three-body code. Particles from the N-body runs must be initialized with some random motions to prevent large scale instability across the disks. Although the N-Body particles have self-gravity, the low dynamical temperature of the restricted three-body code tends to produce tidal features that are much sharper than those created from a full N-Body run. When gas is introduced into the simulation, its dissipation leads to a dynamically cold distribution and very narrow tidal features that more closely reflect real system.

The same metrics used to compute the quality of fit earlier in the pipeline have been computed using the new disc particles alone, the gas alone, and both the disc and gas particles together. Fortunately, applying the metric to either combination of particles finds the best match at the same point in time, indicating that both the disc and gas particles generally exhibit the same morphology. The overall improvement of our N-Body model helps to support the notion that morphology is still very strongly impacted by the choice of dynamical friction used to get initial conditions from the restricted three-body simulation, but other physics can still tune the model.

Although this demonstrates that it is possible to incorporate gas into our pipeline methodology to autonomously find optimized N-Body models for systems of interacting

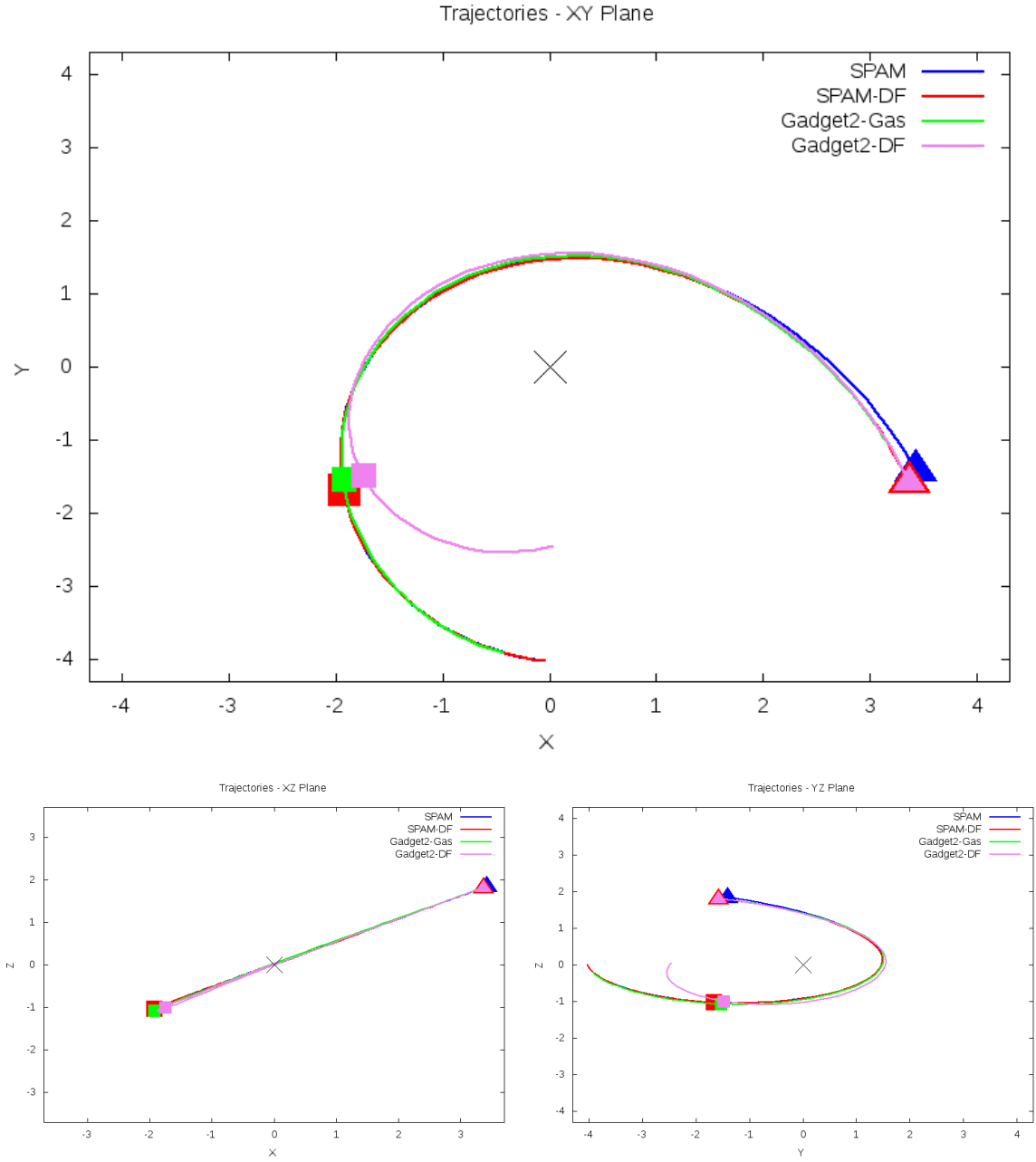


Figure 6.18: Trajectories of Arp 82 from SPAM simulations and the optimized N-Body models with and without gas.

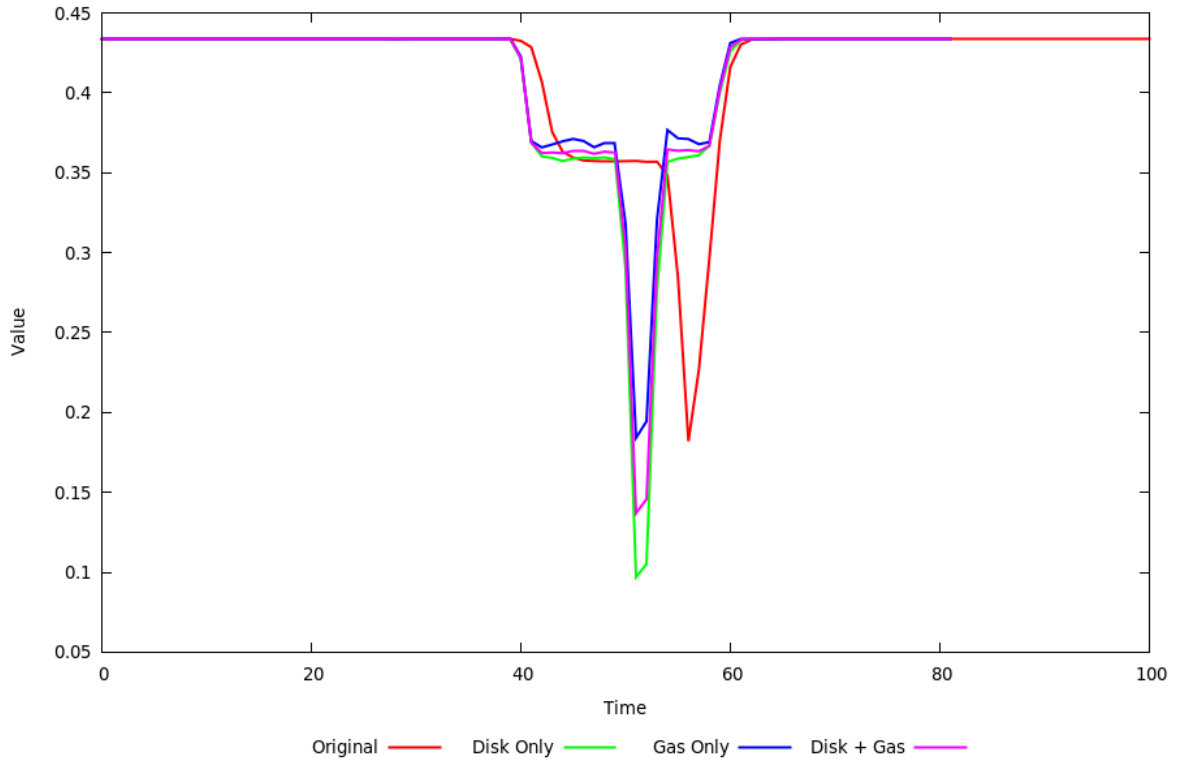


Figure 6.19: The metrics defined for our pipeline not only change the trajectory, but also change the time for the best match to the target dataset, as seen by the secondary galaxy morphology in all three dimensions metric.

galaxies, no such automation has been added to this pipeline and is left for future inclusion. Incorporating gas in an automated fashion without the need for user intervention requires a few components or details to be worked out.

Two questions which arise regarding the first component is how much gas should be included and how is it distributed? Currently, the restricted three-body state vectors do not provide any information to suggest answers to these questions. Additional observational data can be used to estimate the fraction of gas to use, or it can be parameterized like dynamical friction is in the optimization step of our pipeline. In the MASS99 progenitor galaxy model, gas is distributed in the same fashion as the disc particles are. This may be sufficient for galaxies at an early stage, but there may be limits to how well it will work over a wide variety of galaxies. The gas generally needs some thermal energy so

that it can collisionally interact with other particles. In our test, we were able to have a stable evolution of gas by initially heating the gas to a very small amount, near 0 degrees Kelvin. We believe that there is some scaling to go from observational data implying gas temperatures to internal energy of the gas for an SPH simulation.

Lastly, using SPH on other systems will require some investigation into the development of good recipes for determining numerical stability and accuracy. These include defining kernel sizes and densities based on the size of the galaxy and number of particles in the simulation, artificial viscosity, and time step sizes. Simple but effective recipes were used for the gravitational components of the N-Body simulations, and we suspect the same can be found for SPH. We also suspect that an enhanced pipeline that can include gas in the models may need to optimize the amount of gas present in the system and its initial temperature.

6.5 Other Future Work

In the restricted three-body to N-Body optimization pipeline presented in this dissertation, dynamical friction was the primary variable altered from the restricted three-body model. Although it often led to significant changes in the orbits and morphologies of the galaxies modeled, it could not always lead to the best matches to our target surrogate datasets.

6.5.1 Optimizing Additional Model Parameters

Aside from the cases where the SPAM model may have led to the identification of non-physical models, morphologies could be improved with small modifications to the other variables in the restricted three-body state vector. Examples of variables to modify include the disc radii and orientations, and relative location and velocities of the secondary galaxy. In spirit of a multi-method-modeling paradigm, no parameter from the restricted three-body model should necessarily be taken as fixed or perfect, but instead should only be

indicative of local extrema. If uncertainty or other measure of the variance of these parameters as it relates to the quality of fit to the target system is provided, then that measure could be used to determine the breathe of the parameter space for the N-Body model. Our pipeline has demonstrated searching over one variable (e.g. dynamical friction) during its optimization phase, but there is no reason the same Newton method approach cannot be extended multiple dimensions.

6.5.2 Metrics for Optimization

Optimizing in one or many dimensions requires a measure or metric of the system to determine how well it matches. Although we have defined nine metrics², they only focused on the morphology and relative separation of the galaxies in each system. Observational data can allow us to develop metrics against other variables, such as the line of sight velocity (V_z), brightness, luminosity, and star formation rates. All of these are variables at the surface of the system facing the observer. Surrogate datasets also allow us to find matches throughout the system in all spatial directions. Of course, there is the question of how well the data inside the systems matches reality, but since the systems modeled are fundamentally three-dimensional in space, their exact morphologies are determined in the same space. In fact, the two dimensional matches almost anyone makes from any model to a real system are really just the projection of the system onto the observer's field of view and do not take into account depth. This is not exactly true, however, if detailed redshift data is available that varies across the galaxies of interest in sufficient resolution to match the depth of portions of the galaxy in the observers field of view.

Development of other metrics that combine other variables, such as velocities, is left for others to incorporate into this or another similar pipeline. If additional variables are used, ideally they would be incorporated in the restricted three-body and N-Body portions of the pipeline. We have included tools for binning and integrating velocity in similar manners

²Only one metric was used in the determination of our results of the 54 systems studied.

as positional information is integrated in our morphological based metrics.

6.5.3 Comparisons using Observational Data

This pipeline focused on comparisons against surrogate data and not on the real target system. The use of surrogate data allows us to conveniently inspect aspects of the real system that we could not do with today's methods of observations. Of course, one must make the assumption that the surrogate data is itself a validated representation of the system and assume some degree of uniqueness of its solution. However, there may be a need to develop metrics that are based not on the surrogate data, but the observational data instead. Pixels can be read from images in a similar way that particles can be read from the surrogate datasets. However, given the more continuous nature data presented in images, it may be better to use the pixels to only map the edges of morphological features (thus allowing the areas to be computed). Alternatively, the pixels can be used to infer values of integrated quantities, such as brightness, over the galaxies.

Although binning and integrating particles can be a useful technique (as is the case in determining the velocity along the observer's line of sight), alternative representations of the N-Body simulations may be useful for better comparisons. An example of this is volume rendering of meshless particles. In anticipation of needing to use other metrics beyond morphology to optimize N-Body models automatically, we developed a general purpose meshless volume renderer using VisIt (see appendix A for detailed information on the approach and implementation). Typically volume rendering is used as a way to peer inside a three-dimensional dataset. Volume rendering also allows for a natural way to take discrete points and smear them into a continuum and show an integrated effect as particles or objects stack in front of each other. This offers a way to create visualizations from an N-Body dataset that can be used in images with pixels that better mimic the pixels in observational images. We believe this will be crucial in developing quality metrics to compare observational data to N-Body modeled data.

6.5.4 Alternative Progenitor Galaxies

There are other progenitor galaxy models to choose from other than the Hernquist model from MASS99 used in our pipeline. Although this pipeline allows the user to specify his or her own progenitor model to scale, displace, and rotate (if provided in the MASS99 or GADGET-2 compatible format), it does not create models for elliptical galaxies or other configurations. This is partly due to the restricted three-body portion of the pipeline only supporting spiral type galaxies. Although many of the systems appear to consist of spiral type galaxies, some are not nearly as obvious. The pipeline in its entirety should allow for finding models of multiple types of galaxies, both in the restricted three-body portion and the N-Body portion. This can be implemented by adding the galaxy type of each galaxy to the state vector determined by the restricted three-body model. Of course, this will require the restricted three-body portion of the pipeline to support additional galaxy types.

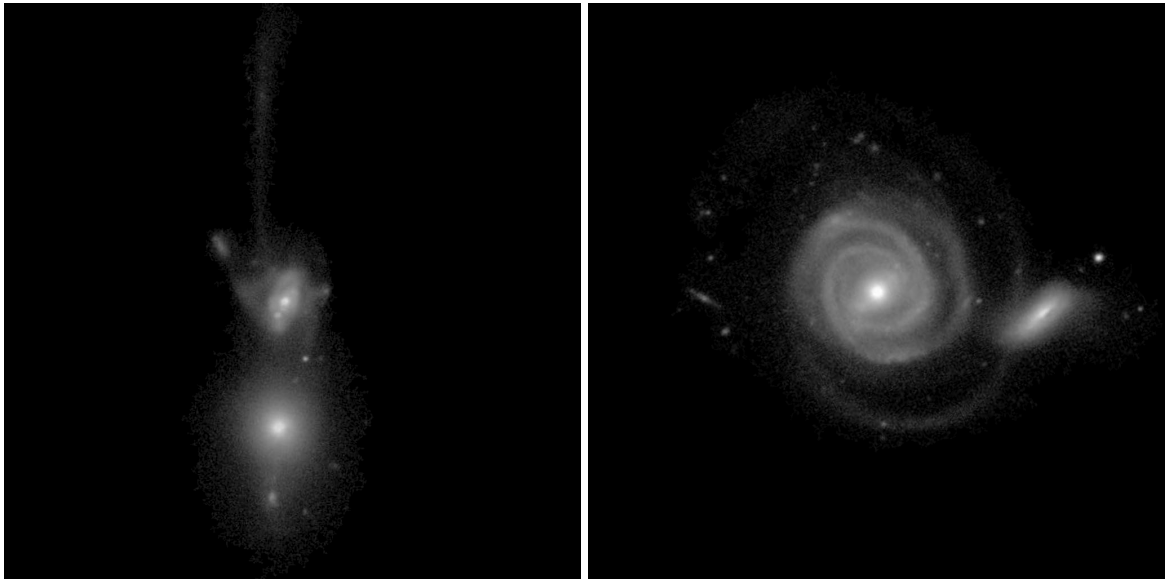


Figure 6.20: Not all galaxies should be modeled as a spiral-type galaxy. Some systems such as Arp 105 (left) may consist of both a spiral and elliptical galaxy while other systems such as Arp 297 (right) clearly contain spiral or disc based galaxies.

Chapter 7: Conclusion

Understanding the evolution of galaxies and their complex interactions with one another is essential to understanding the origins and destination of the universe. For many years, astronomers have developed theories to explain the behaviors of and physics within observable galaxies and mergers, but they have been unable to test and apply these theories systematically to hundreds of thousands of galaxies. Huge datasets, such as the Sloan Digital Sky Survey, offer a well of data from galaxies and mergers that can be used to validate models and theories. However, most models of galaxies are computationally expensive, making it very difficult to model more than just a handful of galaxies with high resolution.

The pipeline prototyped in this effort has demonstrated the abilities to convert a computational inexpensive restricted three-body model of a system of two interacting galaxies into a full N-Body model and to improve upon that model through automation. The 54 systems modeled represent the largest collection of N-Body models representing real systems that has been published to date. Although most of the systems modeled resulted in N-Body models that are either a very promising or a very good match to their target systems, eight systems did not result in a quality match. These poor models are not useful for any in depth study of their target systems. Even without those models, the 46 systems with good and useful models still represent the largest sample of unique models applied to real systems. This is in contrast to other large studies of interacting systems using N-Body models where a variety of N-Body models were run independent of a target system, and those models were matched assigned to systems if they happened to be a reasonable match (Hammer et al., 2009). Once the pipeline was established, an average of 20 N-Body models were generated in search for an optimal match to a surrogate data set provided by a restricted three-body model. The conservative settings chosen by the pipelines automated

process for the N-Body codes of MASS99 and GADGET-2 generally took between 24 and 48 hours using a single computational node with 8 cores to determine the best N-Body model for a real system of interest. This is a relatively small amount of computational resources required to yield a good N-Body model for a system of interacting galaxies 85% of the time.

7.1 The Pipeline for Constructing Optimized N-Body Models

We have prototyped the pipeline for creating optimized N-Body models of systems of interacting galaxies as proposed in figure 1.4. Development of the prototype system was done in such a way as to not limit a user to very specific codes and optimization routines. The only limitation of this implementation is the use of SPAM as a restricted three-body model. This is not to imply that SPAM must be the restricted three-body model used to generate a state vector describing a restricted three-body model that describes a target system, but it is the only one we use to backwards integrate a restricted three-body model to determine initial conditions for the N-Body models.

The software developed to implement the pipeline is extensible, having used Perl and Python scripts to handle the automation. These scripts allow the user to pick a N-Body code such as MASS99 or GADGET-2, choose to provide a progenitor galaxy model or rely on MASS99 to generate one, and specify a restricted three-body state vector. The pipeline will scale, rotate, and displace the galaxies of a system and conduct multiple N-Body simulations. If the user wants to make changes to how the N-Body codes are run, settings for them are all captured in a single Perl script organized by N-Body code. Multiple metrics have been defined to judge how well a model matches a target data set. Although matching real data should be objective of any metric used, our metrics solely score the morphology and relative locations of the galaxies modeled as compared to a surrogate data set produced by SPAM. A Newton optimization method has been used to assist in the

automation of choosing new values of dynamical friction to use when attempting to find an optimal N-Body model.

Along the way, new tools have been created for GADGET-2 to allow for the rapid and efficient post processing and manipulation of GADGET-2 snapshot files. This includes the ability to scale, rotate, and displace galaxies, as well as combine multiple galaxy models into one large system. Additional tools have been develop to compute orbital parameters, compute line of sight velocities, and generate images. The pipeline has also established an easy way to generate initial conditions for galaxies by using MASS99's multiple progenitor galaxy generators by means of a settings file and optionally state vector representing the bulk characteristics of a system at a time of interest (typically provided by a restricted three-body model although not required). The tools allow the user to begin simulations anywhere within the N-Body pipeline too. This means that anyone can do single simulations of a standalone galaxy using SPAM, MASS99, or GADGET-2, a system of two galaxies using the same tools, or evaluate metrics without the need for conducting an entire optimization process.

7.2 Enhancements to the Pipeline

The pipeline developed focuses on the use of spiral galaxies and evolves them using gravity. Our results show that most morphology in a system of interacting galaxies can be explained by gravity on its own. This is particularly true in systems that have a small or mild interaction. For systems undergoing more severe interactions, additional physics such as gas dynamics and star formation are needed to resolve finer structures and brighter tidal tails. We have definitively shown that it is possible to reliably automate the creation of gravity based N-Body models, but have not demonstrated the ability to readily incorporate these other phenomena. Most N-Body codes available today use meshes or smooth particle dynamics to model gas and its associated physical processes. Extending

the pipeline should be feasible to add support for either technique, although great care will be needed to ensure these enhanced models are stable and still physical. This is challenging as currently available restricted three body models do not provide estimates for the added energy that may be required for gas or how it should be distributed.

Determining the optimal N-Body model should not rely on morphology alone. In the prototype pipeline presented, velocity information is only used to see if there are any glaring discrepancies between the restricted three-body and N-Body models. The systems modeled using N-Body codes were based off of restricted three-body models that were not matched along the line of sight velocity of their target system. Without confidence in the restricted three-body models fitness quality to velocity, it is premature to match our N-Body models to their velocity data. However, when the restricted three-body portion of the pipeline is enhanced to use velocity information in computing fitness values, the N-Body portion of the pipeline should follow suit and utilize that too. The same is true when observational data beyond morphology is available for these types of systems. In either case, this will require the development of new or enhanced metrics. These metrics and the current metrics can be used to enhance the optimization portion of the pipeline to revise other parameters of the system, such as initial system orbital parameters. Even without enhancements, this pipeline can be used to construct high quality N-Body models for systems of interacting galaxies with high success within hours automatically without need for operator intervention.

7.2.1 Targeted Efforts for Future Work for the Entire Pipeline

Throughout this dissertation, including the preceding section, a number of suggestions have been made to improve our models and the pipeline. Of all of them, there are three that are strongly recommended that will impact the entire pipeline. Velocity data and matching should be incorporated, not just in the N-Body metrics, but in the restricted three-body modeling and matching process. It is not useful to approach one half of the

entire pipeline and not the other. This will require additional work to obtain velocity data at the beginning of the pipeline process and is made more difficult if velocity data is not available for systems of interest. Another area is the incorporation of gas dynamics. As shown in Chapter 6, the introduction of gas is very important to ensure sharp tidal features are modeled. It's the density of gas in these features that will enable better comparisons of star formation rates with observational data. However, gas is not considered in the restricted three-body portion of the pipeline in any capacity. In some way, that portion needs to provide some estimate of the gas's mass, distribution in space, or energy. If the restricted three-body model cannot explicitly provide guidance, then mapping features of the restricted three-body simulation to gas during the best match process is required.

The one remaining task is to fully automate the entire pipeline from start to finish. The restricted three-body portion of the pipeline contains a graphical user interface to allow a user to find a system of interest and begin making initial assignment of parameters to it. Whereas the original pipeline developed by Holincheck relied on citizen scientists to assist in the model matching process, automation will require replacing this step with machine learning. Fortunately, much work has continued in this regard which exploits machine learning using human behavior and decision making from Merger Wars as a training dataset. Once complete, the N-Body portion of the pipeline will need to be coupled to the restricted three-body portion using the codes already developed or to be enhanced.

Appendix A: A General Purpose Volume Renderer for Meshless Data

A.1 Abstract from Submitted Draft to Astronomy & Computing

Telescopic images provide the primary means of qualitatively validating numerical models of interacting and colliding galaxies. Approximations of galactic structure are often made by using macro-particles in N-Body gravity codes which are meshless by their very nature. Visualization therefore is a necessary component of model analysis and validation. Although the simple plotting of points can provide a good representation of the physical system, it fails to capture the semi-continuous reality of the system. A general purpose volume renderer is discussed and implemented in the VisIt visualization software framework to create a continuum-like representation of the data while still maintaining the simulation's meshless nature. This feature is freely available to all users of the open-source VisIt software and supports volume rendering of any unstructured or meshless datasets.

A.2 Introduction

Volume rendering is a powerful visualization technique allowing a user to peer through a complex, three dimensional dataset. Traditionally a three dimensional structure is decomposed into a series of planes stacked on top of one another, with each pixel's alpha channel (transparency or opacity) scaled to some feature of the dataset. In this way, features of high density or importance become more opaque while less important features remain transparent; this stacking of planes allows the user to see features in the data otherwise hidden by the opaque surfaces.

There are many ways to go about volume rendering, such as splatting (Westover, 1990), ray tracing, 3D texturing, and more recently Fourier Volume Rendering (Corrigan et al.,

2009). In most applications, such as in the medical community, data is uniformly sampled, allowing the user to have each pixel unbiased compared to the next. Things can be more challenging in other structured datasets that do have a volume, when cells, elements, zones, or faces vary in size with neighboring features. In those cases, the user has to take care of using techniques that will smoothly vary the transparency from one object to the next. It is common for many techniques to resample the dataset onto a regular grid, giving more or less objects to define transparencies for. This is not without problems however as it can impact the resolution of the dataset and possibly smear data outside its physical manifold.

Lighting a 3D model also requires a visualization engine to compute gradients throughout the dataset to properly account for the transparency of pixels to others. Since gradients may not exist in a dataset to be plotted for every variable of interest, they may need to be approximated. By remapping or resampling a dataset to a uniform, Cartesian grid, gradients can be and often are approximated easily using finite difference stencils.

A.3 Motivation

The comparison of real images of galaxies requires advanced visualization techniques, such as volume rendering to quickly and easily approximate their appearance. Most computational models of galaxies are some variant of an N-Body method, in which stars or pseudo-stars are modeled as discrete points or particles with mass, velocity, and other properties. Typical visualizations of these points results in a speckled cloud with the data drawn as points which may or may not vary in size. When they do vary in size, normally the point or glyph used is a single, solid color, even though light from stars drops off as $1/r^2$. Most images of galaxies (before being faux colored to show different elements and temperatures in them) have bright and dark spots, and some smoothly varying features, such gases that fill the space between stars and the combined brightness of stars. A more

accurate way to draw the particles from N-Body simulations of galaxies would be if the glyphs were drawn as a radial gradient of color and have transparency to see other particles that overlap.

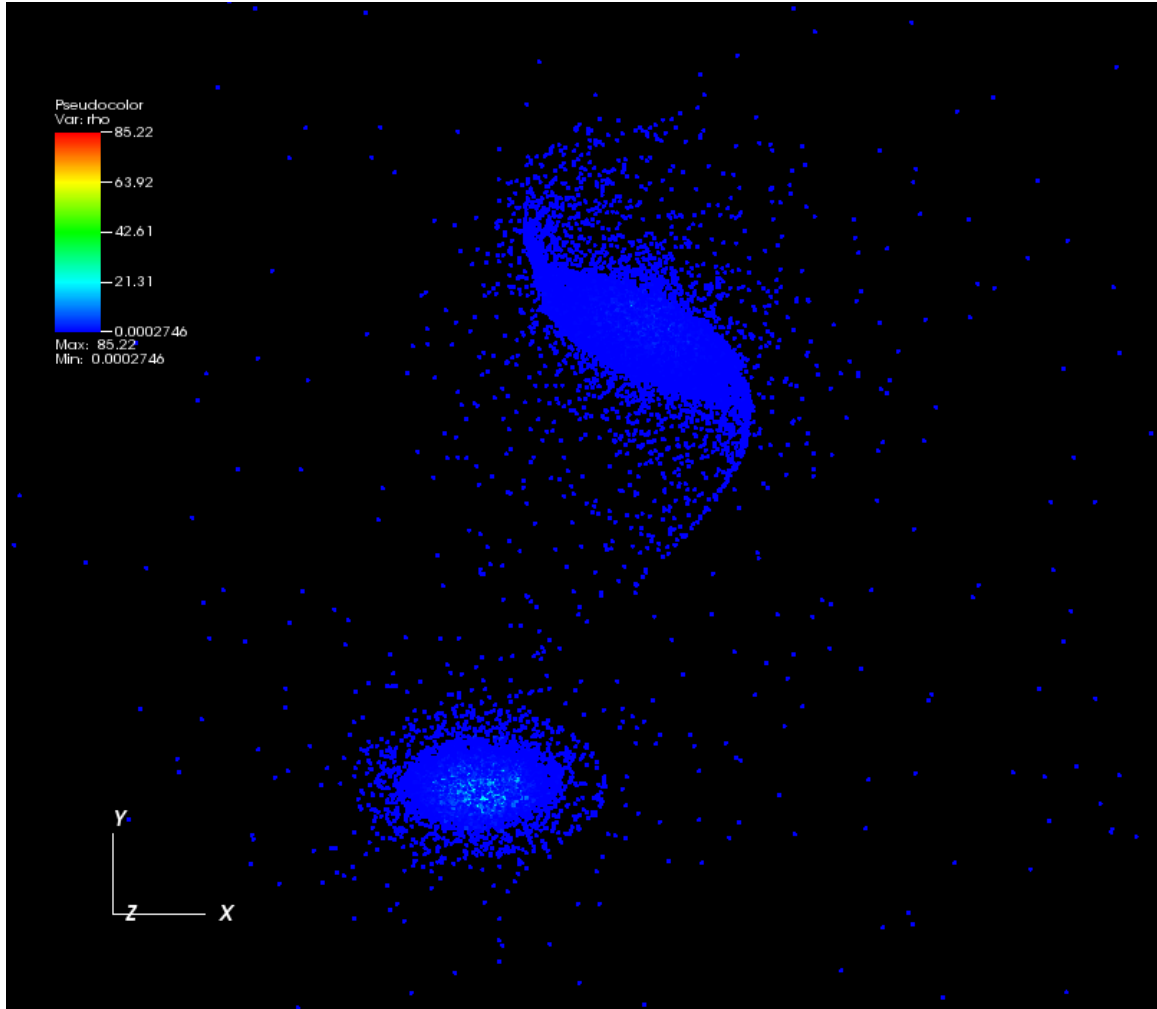


Figure A.1: Simple plotting of macro-particles from an N-Body gravity code shows overall features, and particles fill the screen. NOTE – this and subsequent images are not visualizing dark matter that was included in the simulation.

GADGET-2 (Springel, 2005) and MASS99 (Antunes and Wallin, 2007) are examples of N-Body codes used to model the behavior of one or many galaxies interacting with one another. These codes use hierarchical trees to model gravitational interactions. Gases may

be modeled in both these codes using smooth particle hydrodynamics (SPH) (Gingold and Monaghan, 1977). However, even with the use of SPH for gas, it is still modeled as a cloud of particles without any definite shape (mass and density are computed for each particle, inferring that a volume does exist and is calculated).

Ongoing research in the Galaxy Zoo/Wars project iterates on finding approximate values for features that describe multiple galaxies interacting with each other, such as age, total mass, size, inclination, type, and many others. In this process, the final location and configuration of the galaxy is chosen. The galaxies' positions are integrated backwards in time. The galaxies are forward calculated using these parameters to find the tidal features and velocity field that form from the system (Holincheck and Wallin, 2015). A citizen scientist compares the resulting images from a series of configurations to choose which model best resembles an image from a telescope. These images are similar to those in A.1. Volume rendering a set of points allows for the illusion of volume and smoothly varying properties across an image, particularly with regards to N-Body gravity models. By using volume rendering as opposed to a scatter or pseudo-color plot, the model images should be more relatable to an actual image, and the best candidate parameter sets chosen. This process aids in the understanding of the evolution of interacting galaxies.

A.3.1 Why VisIt?

Under the Accelerated Strategic Computing Initiative (ASCI), the United States Department of Energy invested millions of dollars in modeling, simulation, and computing programs, with a significant emphasis on large scale supercomputing. To aid in the visualization of a variety of hydrodynamics, magneto-hydrodynamics, electrodynamics, radiation transport, and many other physical processes, a massively parallelized visualization platform was created; to “visualize it”, VisIt was created at Lawrence Livermore National Laboratory. It is an open source visualization platform built on top of KitWare's open source VTK framework, and is available in binary and source code forms at <http://visit.llnl.gov>.

The software is designed to enable remote visualization, whereby the visualization engine runs across many computational nodes where the data resides and construct the image on a client engine on the user's computer. The software can also operate on a single node where both the data and user reside.

VisIt supports a wide range of visualization capabilities and an even greater range of scientific and general purpose file types. It natively supports such file formats as HDF4/5, SILO, CGNS, KML, STL, NASTRAN, XDF, and dozens more for a wide variety of data models, to included structured and unstructured meshes. Supported visualization techniques include pseudo-coloring (coloring and/or shading the surfaces of cells), volume rendering, parallel plots, meshes or wireframes, histograms, vector plots, scatter plots, and many more. Its easy to use interface allows the user to apply operators on a plot type to control the selection of data, the transformation of data (such as rotation or scaling), and slicing or inspection of data among many others. Additional features can be added as plugins to add a new capability or enhance an existing capability (Childs, 2011).

The VisIt software includes a robust volume renderer engine which is dataset agnostic, supporting SLIVR, raytracing, and splatting techniques. All of these techniques ultimately require some form of volume to either propagate a line of sight to accumulate color and opacity, or need to accumulate color and opacity by drawing areas. To support a wide range of data formats, this is achieved by mapping the dataset to a uniform, structured Cartesian grid where the user has control over the number of points and stride to use. Depending on the options chosen, most meshes can have very useful volume renders created from them. Unfortunately, until recently renders of meshless datasets could not be visualized properly, as naively mapping a meshless dataset to any Cartesian grid leads to inappropriate interpolation between points.

Thanks to VisIt already supporting a wide range of scientific data formats, being open source, and extensible through plugins, it makes for an excellent platform to add new visualization capabilities that can reach an extremely large audience around the world. By

leveraging the existing source code from the splatting technique in the existing volume renderer, an improved or enhanced volume renderer could be created to support meshless data structures.

A.4 Algorithm and Approach

Any approach to volume rendering presents some difficulties for unstructured meshes, particularly if the mesh is technically meshless, that is there are no explicit links between nodes or points. Every object being rendered must have a well defined volume. In unstructured meshes, this volume can be difficult to define, posing one of three challenges:

1. If the data is cell centered, the actual cells or projections of the cells can be drawn to the screen and color coded. Unfortunately, this will not allow colors to smoothly vary across cell boundaries. In particular, the resulting visualization can give deceptive results if there is a mismatch between the resolution of the unstructured data and another structured grid it may be projected onto.
2. If the data is node centered, it is difficult to define accurately what the simple area of influence that node has with its neighbors, especially if the data is meshless. This too may be made more difficult when the data needs to be projected onto a plane. Gaussian quadrature rules are often used to weight a value at a node across cells. The same resolution matching concerns with cell-centered data is here too.
3. Meshless data does not have connectivity to contend with, but it too needs to have an area of influence or neighborhood of points to work with. A description of that neighborhood size may or may not be within the dataset. If this size is not available (as is the case with most N-Body galaxy simulations), it needs to be estimated, or a single value defined. If using a single value, all particles would be treated the same, regardless if they should have the same opacity or brightness.

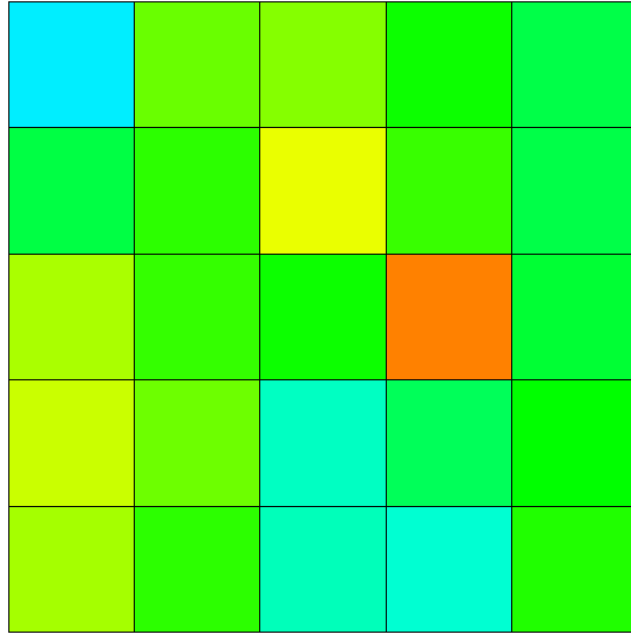


Figure A.2: A simple cell-centered dataset (noise.silo, included with VisIt). The shaded cells do not vary smoothly across the domain.

In the general purpose volume renderer created within the VisIt framework, any unstructured mesh is treated as a meshless data structure. Either cell centers or nodes are treated as the points in a meshless dataset. Throughout the rest of this paper, references to points will refer to the objects with data in a meshless dataset while nodes will refer to a mesh data structure. VisIt's built in Delaunay Triangulation operator (based on the underlying VTK framework of which VisIt is built) performs Delaunay Triangulation to create a tetrahedral mesh, where by all the points from the unstructured mesh become the nodes in the tetrahedral mesh. This intermediate mesh is not visualized and data is not truly mapped to it. Instead, the set of points around each point is inspected to record the maximum distance between them. Half of this distance, i.e. radius, is used to approximate the volume of interest in 3D (or area in 2D). Once these values are determined, the intermediate mesh is destroyed.

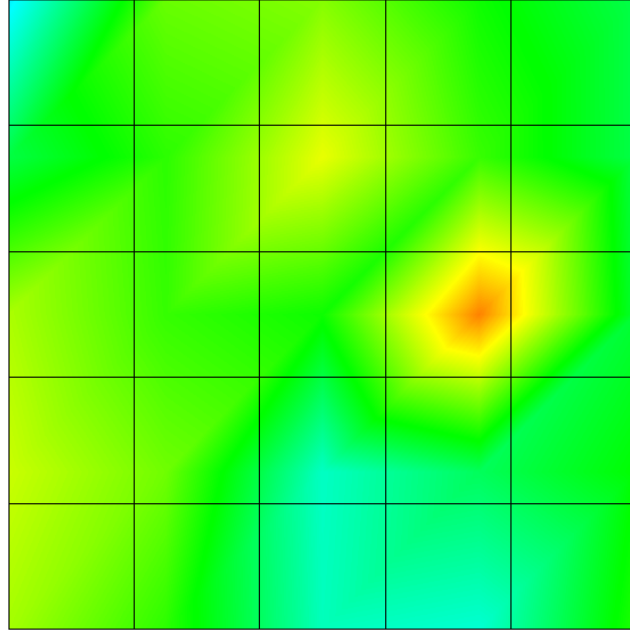


Figure A.3: A simple node-centered dataset. The color varies smoothly, but may show dependence on mesh resolution and topology. In an irregular or unstructured mesh with small and large cells, a node may have far more influence across the domain than originally planned if sufficient mesh resolution was not used.

To better see complex features in a dataset, particularly with volume rendering, cameras must be defined to create lighting and shadowing. These light sources require gradients to be computed at all points. Unfortunately, gradients for every property to be volume rendered are unlikely to be part of a dataset. For every point i needing a gradient, a commonly used smooth particle hydrodynamics gradient function is called to compute over the set of points surrounding it (Monaghan, 1992). In equations A.1 - A.4, s is a scaling factor for convenience, h is the smoothing distance or interaction length, k is the kernel, r is the radius originating at point i , while $r_{i,j}$ is the Cartesian component of the radius vector from point i (Monaghan, 1992). Although un-normalized, VisIt will automatically normalize the set of gradients before the data is needed to process lighting.

$$s_i = \left| \frac{r_i}{h_i} \right| \quad (\text{A.1})$$

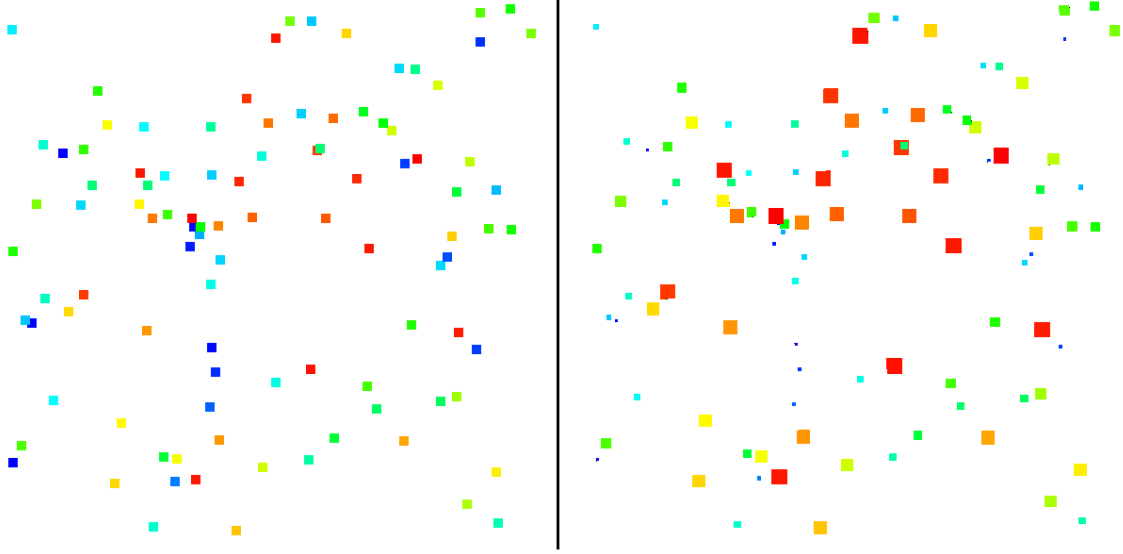


Figure A.4: A meshless dataset. The points are equally sized on the left, while they have been scaled based on a parameter in the dataset on the right. With scaling, the points may not fill up enough of the physical space they are designed to do, at least not without obscuring other important points in the dataset.

$$0 \leq s_i \leq 1, k_i = \frac{r_{i,j} \left(-3s_i + \frac{9}{4}s_i^2 \right)}{r_i h_i} \quad (\text{A.2})$$

$$1 < s_i \leq 2, k_i = -\frac{3}{4} \frac{r_{i,j} (2 - s_i)^2}{r_i h_i} \quad (\text{A.3})$$

$$s_i > 2, k_i = 0 \quad (\text{A.4})$$

With gradients computed and approximate sizes for the volumes chosen, each point is splatted to the screen as a two dimensional disc. This disc has radius equal to half the maximum interaction distance estimated earlier from the Delaunay Triangulation phase, and it is oriented to always be perpendicular to the viewer. The disc's opacity decreases radially to zero, with its maximum value controlled by a user controllable function within VisIt. This is because integrating along a ray from the viewer's eye through the sphere will

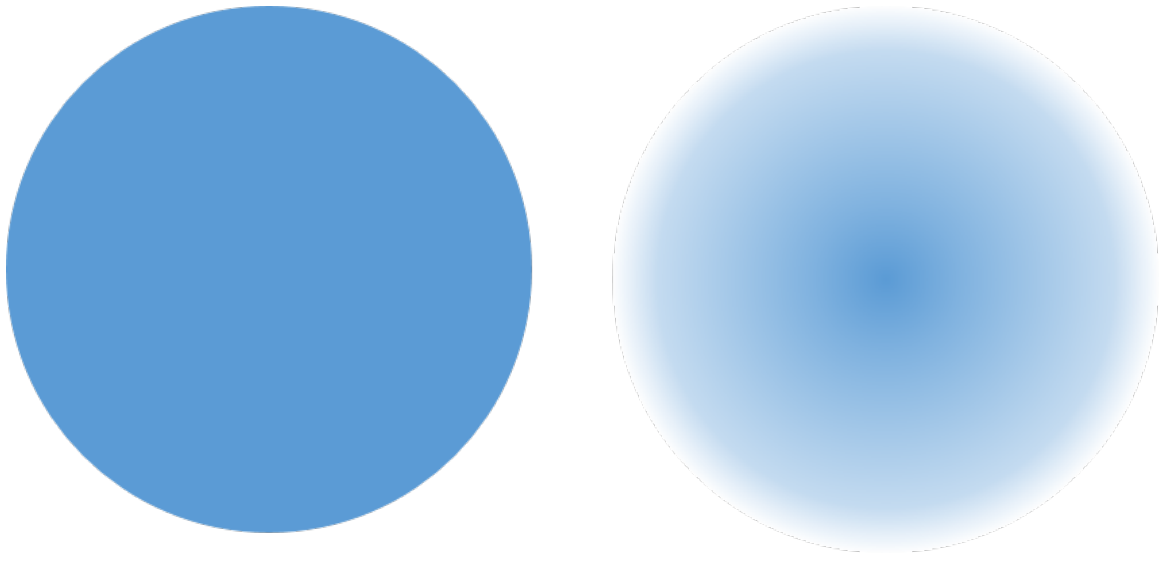


Figure A.5: Splatting as a disk (left) is fast and simple, but indicates the intensity of the property being visualized is constant, whereas a radial gradient (right) indicates the intensity does decrease the further it is from the center.

be largest through the center of the sphere and smallest at the outer most edge. Splatting in this way is significantly different than simple splatting of a point without a gradient.

A.5 Challenges

Although the approach chosen to implement a meshless, volume renderer appears to be simple by essentially treating meshless datasets like an SPH simulation and splat the points, there were many challenges to overcome.

Using the idea of drawing stars as a motivation for volume rendering meshless datasets, the desire was to draw a sphere that was translucent and decayed radially. Although the brightness of a star may decay radially over an infinite radius, for computational efficiency, this needs to be truncated at some radius, as described in the previous section. The VTK platform VisIt is based on uses OpenGL to display images on the screen. Although OpenGL supports drawing points with a fixed radius, it doesn't allow them to fade with radius, as one would expect a shining light to do. More specifically, it doesn't

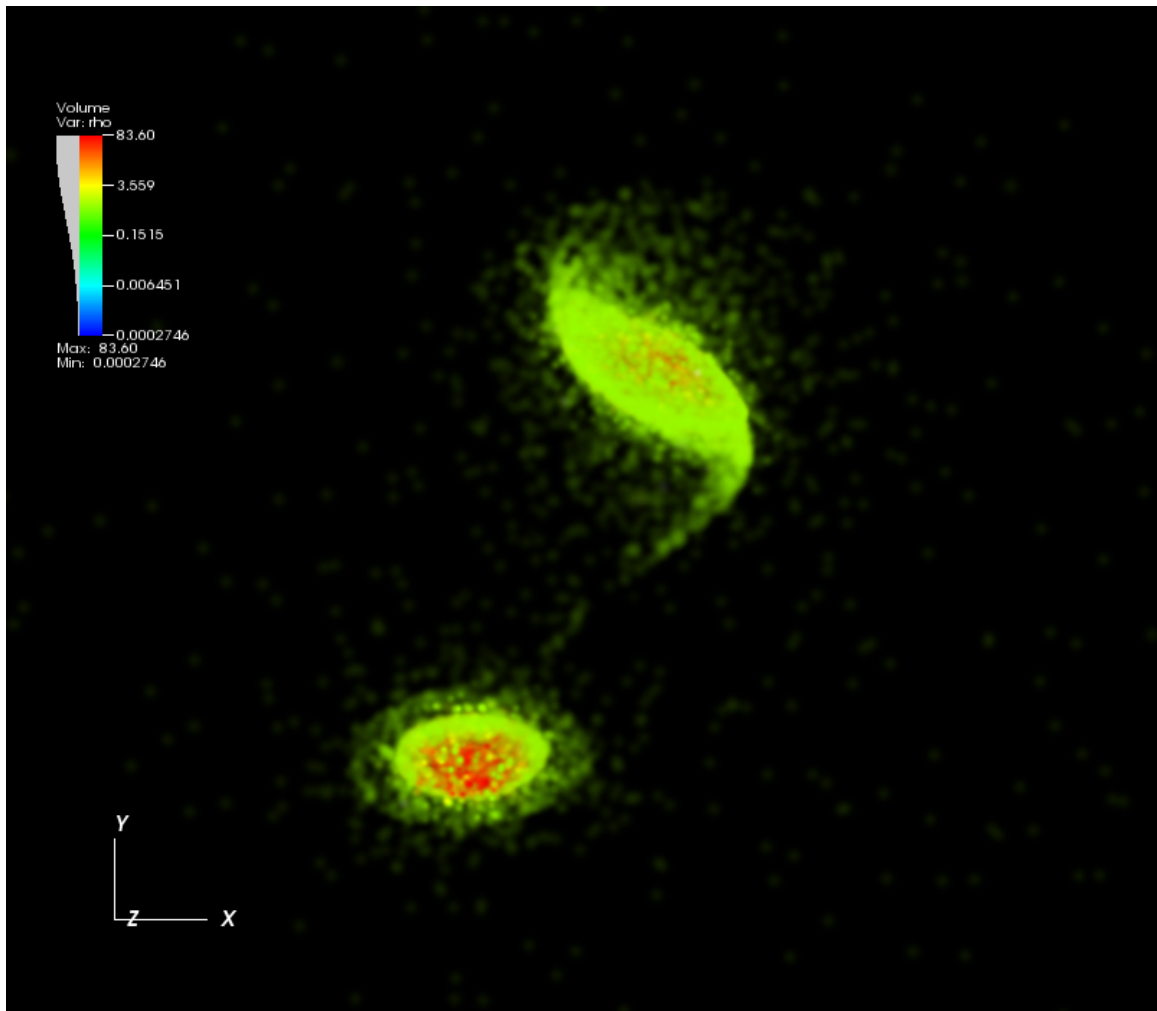


Figure A.6: Once complete, a volume-rendered gravity simulation of galaxies shows depth, volume, and features closer to what would be seen from a telescope.

offer an easy way to do true Gaussian splats. Instead by drawing quadrilaterals, in particular squares, using the function “`glColor4fv(color)`” where ‘color’ has the RGB color of the splat to draw with the alpha channel set to an appropriate value. However, instead of just drawing a square with some transparency, the image is drawn with a radial gradient as seen in A.5, giving a soft, circular shape. For more of a glowing effect, the splats could be drawn using the function `gl.enable(GL_BLEND)`. If desired, a Gaussian kernel could be computed for each splat to have a different decay mechanism, i.e. Gaussian splatting. Unfortunately, with different parameters and formulations possible, there’s no indication

which would be most beneficial to a wide range of meshless datasets. The approach taken in this project using the *glColor4fv* function is general enough for all datasets which may use this splatting technique.

Determining the number of points in a local region can be very time consuming computationally. During development of this plugin for VisIt, there were three competing strategies to estimate the volume of influence for each point. The first option is to require the user to define what this area is. This has two significant benefits – decreased runtimes versus some form of calculation and the area of influence would be known exactly. Unfortunately, this is information that may not be saved or written to a dataset, assuming it exists at all. On the other extreme, comparisons of each point could be convolved with one another to find the nearest ‘n’ points, and use that set to estimate a distance. Naively, this would have $O(N^2)$ complexity. The third way is to use a more sophisticated approach of estimating the area of influence of each point that should be able to have a lower level of numerical complexity, such as $O(N \log(N))$. Initially a tree approach was investigated to group points into regions, and set areas of influence equal to those areas. This approach had three problems: how to define a region size, how to avoid having an irregular set of points from having groups with the same interaction size, and how much development would be needed. During preliminary discussions with the VisIt developers in the Department of Energy, it was strongly encouraged that the volume rendering technique pursued in this report be a set of enhancements to the existing Volume Renderer plugin within it in an effort to minimize code changes. To keep the inputs to the algorithm as minimal as possible, it was chosen to avoid using naive techniques (for numerical complexity), and advanced techniques such as trees. As a compromise, VTK’s built in Delaunay Triangulation algorithm with complexity of $O(N^2)$ was chosen as it would naturally define a region of influence for each node through cell connectivity. Although there is no guarantee that this approach will not create any distorted, high aspect ratio cells, it does not require any additional user input and could be implemented with a few lines of code. This has a significant

advantage as it allows for easier maintenance of the capabilities by the VisIt developers going forward. It also has the advantage of having less numerical complexity than a naive or brute force approach.

Implementing a general purpose, unstructured volume renderer within VisIt is not sufficient alone to generate images of galaxies that resemble what can be seen by telescopes. In many N-Body gravity codes, the gravitational force is computed on a discrete basis, and in turn, particles move in the simulation. As a consequence, density is not computed in MASS99 and other similar models when a continuum is used. Visualization of the mass alone (figure A.7) proved not to be useful, as the image was entirely one color because most of the particles had the same mass. The interaction length of the particles was also very large. This could be controlled to an extent by artificially scaling the opacity by an arbitrary factor, but it's not ideal. Instead, the simulation's output or dump files were read back into a modified version of the MASS99 code. In the modified version, particles were read back into a tree structure, but then the tree was converted to an SPH version used to model gas. This conversion makes the code believe the galaxy macro-particles are now gas particles, defining a continuum that will compute a density. The tree is walked to determine an appropriate interaction length such that all particles interact with approximately the same number of particles, and density is computed in a second walk. The tree is finally dumped to a new output file, now including the approximated density and an estimated interaction length at each point.

For some simulations, the estimated interaction length for particles was estimated to be several orders of magnitude apart. This was seen mostly on the far edges of the galaxy models where tidal tails are. This lead to some particles having a splat that consumed most of the visualization's extents. If there were a few such particles that overlapped one another, the resulting composition would undue any sense of realism. To combat that, the following equation was used to scale the alpha channel or transparency of the colored splat:

$$\alpha_i = \text{MAX} \left(l, \frac{1}{\log(h_i) - \log(h_{\min})} \right) \quad (\text{A.5})$$

The scale goes from l to 1, where l is the lower bound, and α is the scaling or correction factor. This made an adjustment that varied with the magnitude of the interaction length of each particle with the minimum value of the dataset. The intent of equation 5 is to scale the opacity between a user defined lower limit other than 0.0 (to ensure that there is some opacity), and an upper limit based on how the size of a particle's interaction length compares to the smallest interaction length across the entire dataset in an effort to further reduce splats of intensity that are many orders of magnitude larger than the smallest ones. Although useful, this did not do any better than when the user could specify a variable from their dataset to scale the opacity by, such as their own own value of an interaction length or neighborhood size. The final version of this implementation in VisIt leaves l at 1.0, mitigating its impact. In the future, l may become an input within VisIt's volume renderer's plotting options, or the user may recompile the software with their own value for l .

Finding the appropriate settings for controlling the opacity of the image is in itself an art for any analyst using volume rendering. As seen in A.8, VisIt allows the user to choose what fields in their dataset to scale to, how to map opacity across the range of values in the dataset, and how to map colors to values. After significant trial and error, our simulations from MASS99 worked best by scaling opacity with the variable being colored, and to apply a Gaussian fit to opacity profile, with the maximum of the curve centered on the maximum value of the dataset, with the tail going towards zero for the minimum value. The surface brightness of stars if computed may be a better candidate to define the opacity profile if that variable is computed and available. With careful choice of a transparency profile, sharp features such as tidal tails and spiral arms, can be seen in the visualizations.

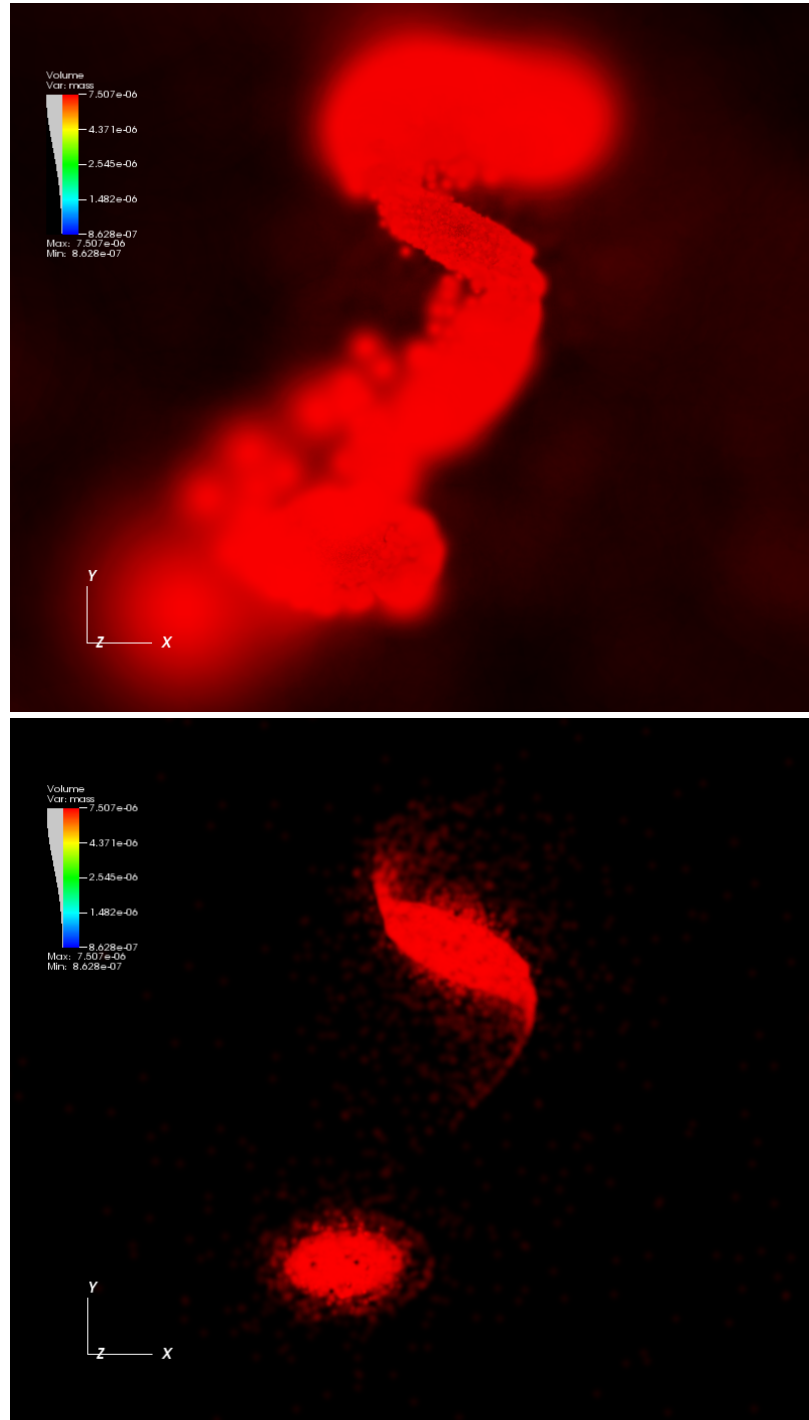


Figure A.7: The upper image shows a visualization of mass from two galaxies before using a more realistic estimate of the interaction length between particles, while the lower image shows mass with the length computed in MASS99. The image on the left does show both galactic discs, but the arms are poorly resolved. The refined interaction length shows much more refined features.

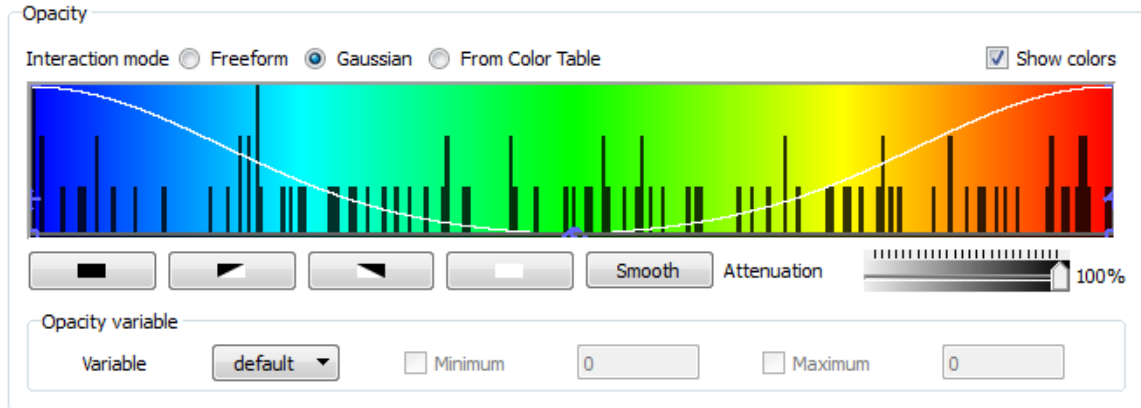


Figure A.8: VisIt offers many ways to define the alpha channel, i.e opacity or transparency, of the visualization.

In galaxy modeling, the areas of most interest are those with high densities (higher temperatures, higher star formation rates, greatest activity) while those with low density cover the largest areas and are the least interesting. In this way, the areas of greatest interest, such as galactic centers and spiral arms, will be more visible than areas of low activity. In future work, the color scale used can be tied to other properties of the simulation, such as element type or luminosity to better mimic faux colored galaxies commonly made available to the general public. Alternatively, the appropriate greyscale and property can be used to better represent the black and white images made available from many telescopes.

A.6 Summary

Volume rendering can be used to gain a better understanding of meshless datasets with the proper choice of algorithms and opacity definition. There now exists a general purpose splatting technique in Lawrence Livermore National Laboratory's open source visualization framework, VisIt, as of version 2.5.2. Although developed for the astrophysics community in mind to offer more ways of visualizing galaxy simulations, it was developed to support all meshless and other unstructured meshes, provided there's a way data can be assigned on a nodal basis. This is achieved principally through the combination

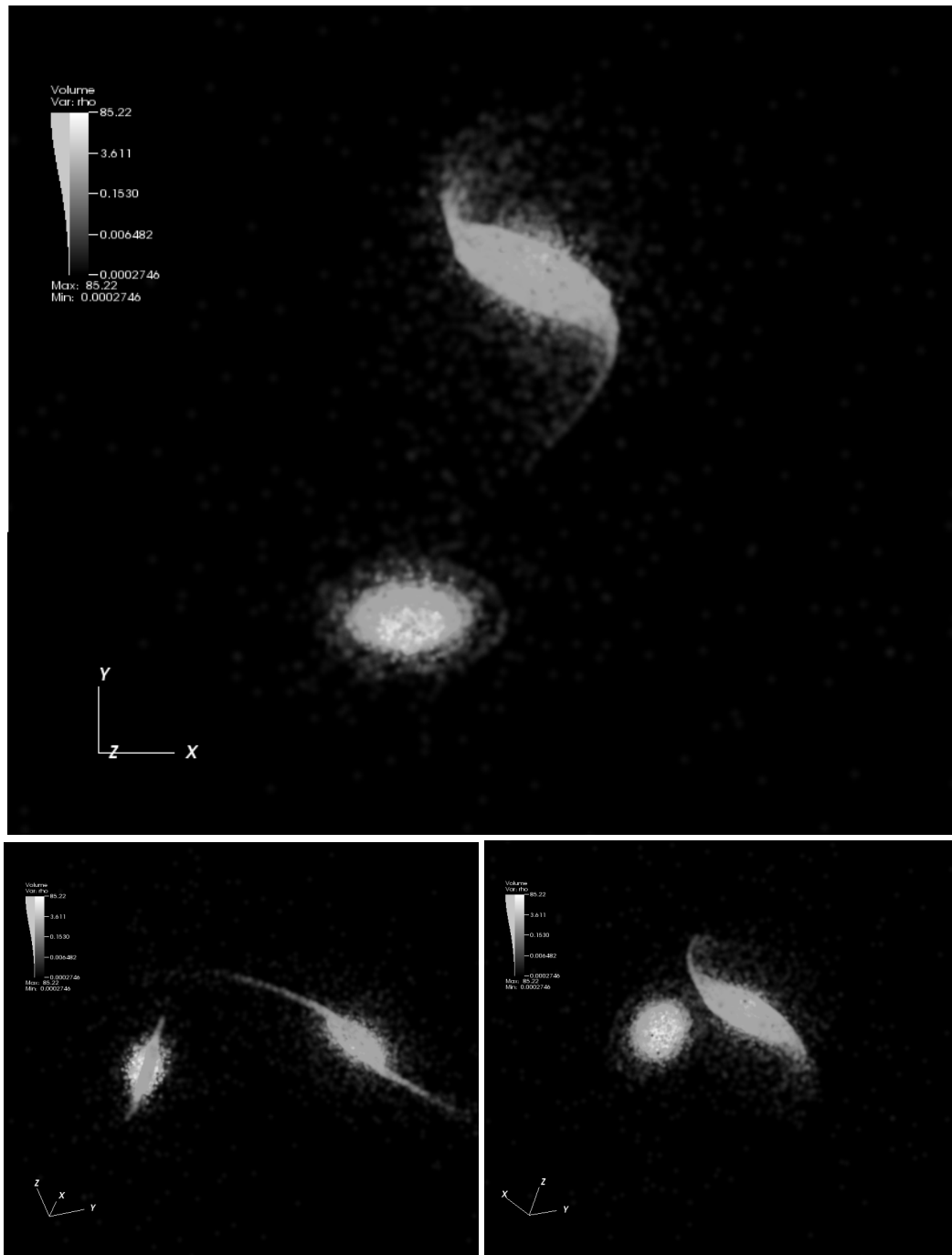


Figure A.9: Use of gradients to define the opacity, along with greyscales can better allow simulations to match photographs taken from telescopes.

of Delaunay Triangulation and SPH kernels. This capability allows the analyst to explore new visualization and analysis possibilities without the need of creating very specific visualization tools with limited use outside their intended application. Although this software has been designed to visualize interacting galaxy simulations, it can be used for almost any set of complex meshless data.

This software is available at <https://wci.llnl.gov/codes/visit>.

Bibliography

- Aarseth, S. J. and Fall, S. M. (1980). Cosmological N-body Simulations of Galaxy Merging. *The Astrophysical Journal*, 236:43–57.
- Antunes, A. and Wallin, J. (2001). Convergence on n-body plus SPH. In *Bulletin of the American Astronomical Society*, volume 199, page 1433.
- Antunes, A. and Wallin, J. (2007). Dynamical parameters for AM 0644741. *The Astrophysical Journal*, 670(1):261–268.
- Appel, A. W. (1985). An efficient program for many-body simulation. *SIAM Journal Sci. Stat. Computing*, 6:85–103.
- Arp, H. (1966). Atlas of peculiar galaxies. *The Astrophysical Journal Supplement Series*, 14:1.
- Balcells, M., Borne, K. D., and Hoessel, J. G. (1989). Interacting Binary Galaxies. VI - The Fast Encounter of NGC 2672 and NGC 2673 (Karachentsev 175, ARP 167). *The Astrophysical Journal*, 336:655–668.
- Barnes, J. and Hut, P. (1986). An hierarchical $O(n \log n)$ force calculation algorithm. *Nature*, 324:446–449.
- Barnes, J., Hut, P., and Teuben, P. (2010). Nemo: A stellar dynamics toolbox. Astrophysics Source Code Library.
- Barnes, J. E. (2011). Identikit 2: An algorithm for reconstructing galactic collisions. *Monthly Notices of the Royal Astronomical Society*, 413:2860–2872.

- Barnes, J. E. and Hernquist, L. (1992). Dynamics of interacting galaxies. *Annual Review of Astronomy and Astrophysics*, 30:705–742.
- Barnes, J. E. and Hibbard, J. E. (2009). Identikit 1: A modeling tool for interacting disk galaxies. *The Astronomical Journal*, 137:3071–3090.
- Billings, J. J. (2008). *Starscream User's Manual*. Oak Ridge National Laboratory.
- Binney, James & Tremaine, S. (1994). *Galactic Dynamics*. The Princeton University Press, Princeton, NJ, third edition.
- Blumenthal, G. R., Faber, S. M., Primack, J. R., and Rees, M. J. (1984). Formation of galaxies and large-scale structure with cold dark matter. *Nature*, 311:517–525.
- Boily, C. M., Kroupa, P., and Peñarrubia-Garrido, J. (2001). Efficient n-body realisations of axisymmetric galaxies and halos. *New Astronomy*, 6:27–42.
- Borne, K. D. (1984). Interacting binary galaxies. I - a numerical model and preliminary results. *The Astrophysical Journal*, 287:503–522.
- Borne, K. D. (1988a). Interacting Binary Galaxies. II - Matching Models to Observations. *The Astrophysical Journal*, 330:38–50.
- Borne, K. D. (1988b). Interacting Binary Galaxies. IV - Simulations, Masses, and Spatial Orientations for NGC 1587/1588 and NGC 7236/7237. *The Astrophysical Journal*, 330:61–77.
- Borne, K. D., Balcells, M., and Hoessel, J. G. (1988). Interacting Binary Galaxies. V - NGC 4782/4783 (3C 278): Unbound Colliders, Not a Supermassive Pair. *The Astrophysical Journal*, 333:567–585.
- Borne, K. D. and Hoessel, J. G. (1988). Interacting Binary Galaxies. III - Observations of NGC 1587/1588 and NGC 7236/7237. *The Astrophysical Journal*, 330:51–60.

- Borne, K. D. and Richstone, D. O. (1991). A Merger Scenario for NGC 7252 - A Tale of Two Tails. *The Astrophysical Journal*, 369:111–120.
- Bundy, Kevin, e. a. (2015). Overview of the sdss-iv manga survey: Mapping nearby galaxies at apache point observatory. *The Astrophysical Journal*, 798.
- Chandrasekhar, S. (1943). Dynamical friction. i. generation considerations: The coefficient of dynamical friction. *The Astrophysical Journal*, 97:255–262.
- Childs, H. (2011). *VisIt Python Interface Manual*. Lawrence Berkeley.
- Corrigan, A., Wallin, J., and Vesenjak, M. (2009). Visualization of meshless simulations using fourier volume rendering. *Computational Methods in Applied Sciences*, 11:291–305.
- Cunningham, A. J., Frank, A., Varnière, P., Mitran, S., and Jones, T. W. (2009). Simulating Magnetohydrodynamical Flow with Constrained Transport and Adaptive Mesh Refinement: Algorithms and Tests of the AstroBEAR Code. *The Astrophysical Journal Supplement*, 182:519–542.
- Darg, D. W. e. a. (2010). Galaxy zoo: The properties of merging galaxies in the nearby universe - local environments, colours, masses, star-formation rates and agn activity. *Monthly Notices of the Royal Astronomical Society*, 401(3):1552–1563.
- de Vaucouleurs, G. (1962). Classification of galaxies by form, luminosity and color. In McVittie, G. C., editor, *Problems of Extra-Galactic Research*, number 15, New York. International Astronomical Union Symposium, Macmillan Press.
- Evans, A. (2008). Galaxies gone wild!
- Ferrare, K. M. (2001). The interstellar environment of our galaxy. *Review of Modern Physics*, 73:1031–1066.
- Fryxell, B., Olson, K., Ricker, P., Timmes, F. X., Zingale, M., Lamb, D. Q., MacNeice, P.,

- Rosner, R., Truran, J. W., and Tufo, H. (2000). FLASH: An Adaptive Mesh Hydrodynamics Code for Modeling Astrophysical Thermonuclear Flashes. *The Astrophysical Journal Supplement*, 131:273–334.
- Gingold, R. A. and Monaghan, J. J. (1977). Smoothed particle hydrodynamics - Theory and application to non-spherical stars. *Monthly Notices of the Royal Astronomical Society*, 181:375–389.
- Hammer, F., Flores, H., Puech, M., Yang, Y. B., Athanassoula, E., Rodrigues, M., and Delgado, R. (2009). The hubble sequence: Just a vestige of merger events? *Astronomy and Astrophysics*, 507:1313–1326.
- Hernquist, L. (1993). N-body realizations of compound galaxies. *The Astrophysical Journal Supplement Series*, 86:389–400.
- Holincheck, A. (2013). *A Pipeline for Constructing a Catalog of Multi-method Models of Interacting Galaxies*. PhD thesis, George Mason University.
- Holincheck, A. and Wallin, J. F. (2015). Spam: A restricted three-body code for simulating interacting galaxies. *Astronomy and Computing*. submitted February 2015.
- Hubble, E. P. (1927). The classification of spiral nebulae. *The Observatory*, 50:276–281.
- Kang, H. e. a. (2004). A comparison of cosmological hydrodynamic codes. *The Astrophysical Journal*, 430:83–100.
- Kim, S. & Morris, M. (2003). Dynamical friction on star clusters near the galactic center. *The Astrophysical Journal*, 597:312–322.
- King, I. R. (1966). The structure of star clusters. iii. some simple dynamical models. *The Astronomical Journal*, 71(1):64–76.
- Lintott, C., Schawinski, K., Bamford, S., Slosar, A., Land, K., Thomas, D., Edmondson, E., Masters, K., Nichol, R. C., Raddick, M. J., Szalay, A., Andreescu, D., Murray, P., and

- Vandenberg, J. (2011). Galaxy Zoo 1: Data Release of Morphological Classifications for Nearly 900 000 Galaxies. *Monthly Notices of the Royal Astronomical Society*, 410:166–178.
- LSST Science Collaboration, Abell, P. A., Allison, J., Anderson, S. F., Andrew, J. R., Angel, J. R. P., Armus, L., Arnett, D., Asztalos, S. J., Axelrod, T. S., and et al. (2009). LSST Science Book, Version 2.0. *ArXiv e-prints*.
- Michie, R. W. and Bodenheimer, P. H. (1963). The Dynamics of Spherical Stellar Systems, II. *Monthly Notices of the Royal Astronomical Society*, 126:269.
- Monaghan, J. J. (1992). Smoothed particle hydrodynamics. *Astronomy and Astrophysics*, 30:543–574.
- Mortazavi, S. A. and Lotz, J. M. (2014). Dynamically modeling of major galaxy mergers - testing identikit using gadget sph simulations. In *American Astronomical Society*, volume 223 of *American Astronomical Society Meeting Abstracts*, page 246.45.
- Noguchi, M. (1998). Gas dynamics in interacting disc galaxies; fuelling of nuclei by induced bars. *Astronomy & Astrophysics*, 203:259–272.
- O’Shea, B. W., Bryan, G., Bordner, J., Norman, M. L., Abel, T., Harkness, R., and Kritsuk, A. (2004). Introducing Enzo, an AMR Cosmology Application. *ArXiv Astrophysics E-prints*.
- Pelupessy, F. I., van Elteren, A., de Vries, N., McMillan, S. L. W., Drost, N., and Portegies Zwart, S. F. (2013). The Astrophysical Multipurpose Software Environment. *Astronomy & Astrophysics*, 557:A84.
- Petsch, H. P. and Theis, C. (2008). Modeling merging galaxies using MINGA: improving restricted n-body by dynamical friction. *Astronomische Nachrichten*, 329:1046–1049.
- Privon, G. C., Barnes, J. E., Evans, A. S., Hibbard, J. E., Yun, M. S., Mazzarella, J. M., Armus, L., and Surace, J. (2013). Dynamical modeling of galaxy mergers using identikit. *The Astrophysical Journal*, 771:15.

- Scarpa, R. (2006). Modified newtonian dynamics, an introductory review. In *1st Crisis in Cosmology Conference*, volume 822 of *AIP Conference Proceedings*, pages 253–265.
- Schombert, J. M., Wallin, J. F., and Struck-Marcell, C. (1990). A Multicolor Photometric Study of the Tidal Features in Interacting Galaxies. *The Astronomical Journal*, 99:497–529.
- Springel, V. (2005). The cosmological simulation code gadget-2. *Monthly Notices of the Royal Astronomical Society*, 364(4):1105–1134.
- Springel, V., Di Matteo, T., and Hernquist, L. (2005). Modelling feedback from stars and black holes in galaxy mergers. *Monthly Notice of the Royal Astronomical Society*, 361:776–794.
- Springel, V. and White, S. D. M. (1999). Tidal Tails in Cold Dark Matter Cosmologies. 307:162–178.
- Struck, C. (2006). *Galaxy Collisions - Dawn of a New Era*. Astrophysics Update 2. Praxis Publishing Ltd, Chichester, UK.
- Sulehria, F. (2005). Astronomical illustrations and space art.
- Toomre, A., . T. J. (1972). Galactic bridges and tails. *The Astrophysical Journal*, 178:623–666.
- Toomre, A. (1977). Mergers and Some Consequences. In Tinsley, B. M. and Larson, D. Campbell, R. B. G., editors, *Evolution of Galaxies and Stellar Populations*, page 401.
- Trac, Hy & Pen, U.-L. (2003). A primer on eulerian computational fluid dynamics for astrophysics. *The Publications of the Astronomical Society of the Pacific*, 115(805):303–321.
- Vazza, F. e. a. (2001). A comparison of cosmological codes: Properties of thermal gas and shock waves in large-scale structures. *Monthly Notices of the Royal Astronomical Society*, 418:960–985.
- Villumsen, J. V. (1989). A new hierarchical particle-mesh code for very large scale cosmological n-body simulations. *The Astrophysical Journal Supplement Series*, 71(2):407–431.

- Wallin, J. F., Schombert, J. M., and Struck-Marcell, C. (1990). Observations and models of star formation in the tidal features of interacting galaxies. volume 3098, pages 727–730.
- Westover, L. A. (1990). Footprint evaluation for volume rendering. *Computer Graphics*, 24:367–376.
- Willett, K. W., Lintott, C. J., Bamford, S. P., Masters, K. L., Simmons, B. D., Casteels, K. R. V., Edmondson, E. M., Fortson, L. F., Kaviraj, S., Keel, W. C., Melvin, T., Nichol, R. C., Raddick, M. J., Schawinski, K., Simpson, R. J., Skibba, R. A., Smith, A. M., and Thomas, D. (2013). Galaxy Zoo 2: Detailed Morphological Classifications for 304,122 Galaxies from the Sloan Digital Sky Survey. *Monthly Notices of the Royal Astronomical Society*, 435:2835–2860.

Curriculum Vitae

Allen Harvey lives with his wife and children in Northern Virginia. He works as a computational scientist supporting and leading a wide variety of modeling and simulation efforts for the United States Department of Defense and Department of Homeland Security.